Fluid Mechanics of Environmental Interfaces

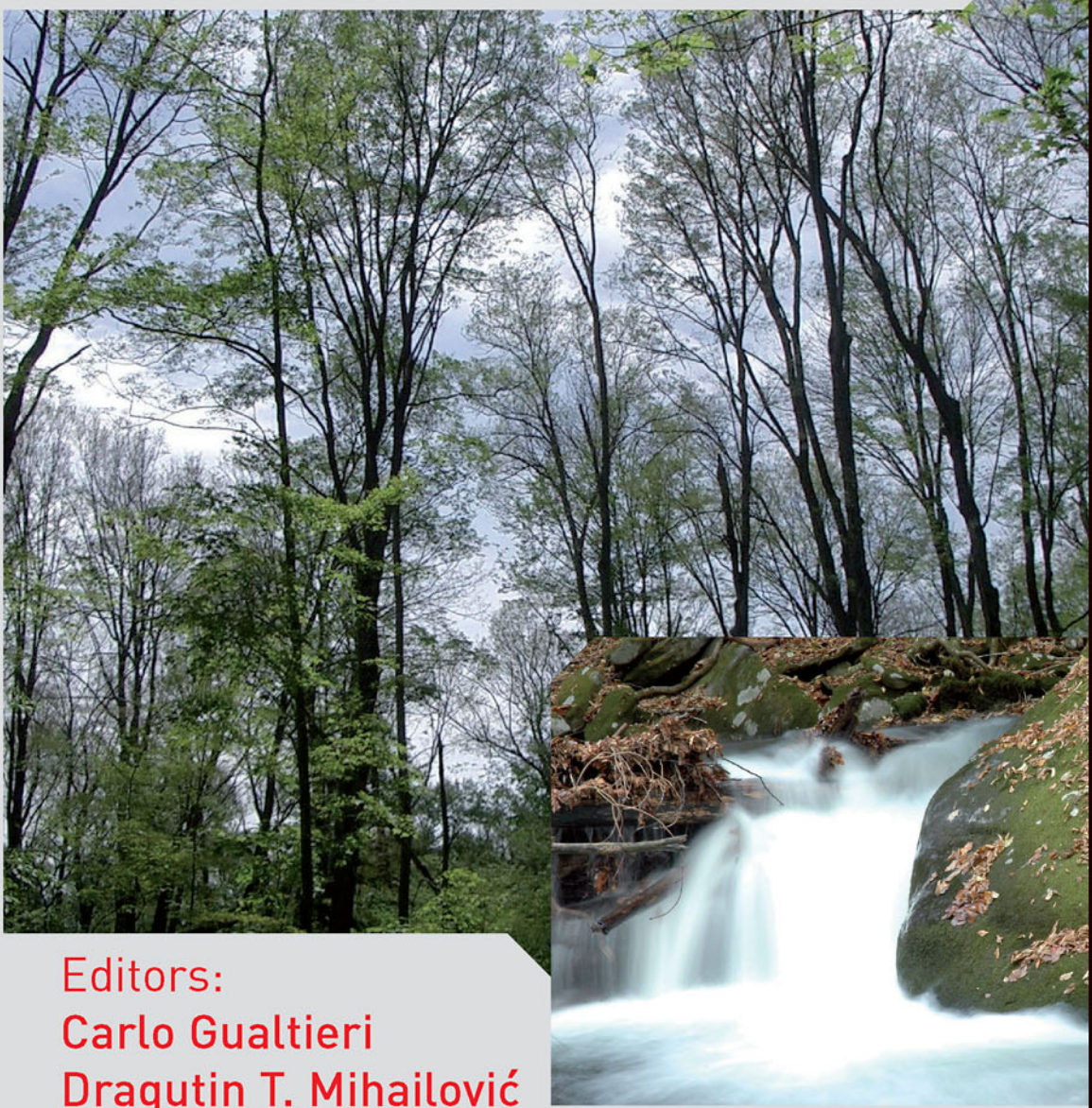

Editors:
Carlo Gualtieri
Dragutin T. Mihailović

Taylor & Francis
Taylor & Francis Group

FLUID MECHANICS OF ENVIRONMENTAL INTERFACES

BALKEMA – Proceedings and Monographs
in Engineering, Water and Earth Sciences

Dedicated to all teachers and students of the Gymnasium in Cacak (Serbia) established in 1837
Dragutin T. Mihailović

To my family
Carlo Gualtieri

Fluid Mechanics of Environmental Interfaces

Editors

Carlo Gualtieri
Hydraulic and Environmental Engineering Department
University of Napoli Federico II, Napoli, Italy

Dragutin T. Mihailović
Faculty of Agriculture, University of Novi Sad
Novi Sad, Serbia

Taylor & Francis
Taylor & Francis Group
LONDON / LEIDEN / NEW YORK / PHILADELPHIA / SINGAPORE

This edition published in the Taylor & Francis e-Library, 2008.

"To purchase your own copy of this or any of Taylor & Francis or Routledge's collection of thousands of eBooks please go to www.eBookstore.tandf.co.uk."

Taylor & Francis is an imprint of the Taylor & Francis Group, an informa business

Library of Congress Cataloging-in-Publication Data

Fluid mechanics of environmental interfaces / editors, Carlo Gualtieri, Dragutin T. Mihailović.
p. cm.
Includes index.
ISBN 978-0-415-44669-3 (hardcover : alk. paper)
1. Geophysics–Fluid models. 2. Fluid mechanics. 3. Atmospheric turbulence. 4. Hydrology.
5. Ocean-atmosphere interaction. I. Gualtieri, Carlo. II. Mihailović, Dragutin T.

QC809.F5F587 2008
551.5′2–dc22

2007040345

Published by: Taylor & Francis/Balkema
P.O. Box 447, 2300 AK Leiden, The Netherlands
e-mail: Pub.NL@tandf.co.uk
www.balkema.nl, www.taylorandfrancis.co.uk, www.crcpress.com

ISBN 0-203-89535-5 Master e-book ISBN

ISBN 13: 978-0-415-44669-3 (Print Edition)
ISBN 13: 978-0-203-89535-1 (e-book)

Table of contents

Preface VII

Biographies of the authors XI

1. Environmental fluid mechanics: Current issues and future outlook 1
B. Cushman-Roisin, C. Gualtieri & D.T. Mihailović

Part one—Processes at atmospheric interfaces

2. Point source atmospheric diffusion 17
B. Rajković, I. Arsenić & Z. Grsić

3. Air–sea interaction 49
V. Djurdjević & B. Rajković

4. Modelling of flux exchanges between heterogeneous surface and atmosphere 71
D.T. Mihailović & D. Kapor

5. Desert dust uptake-transport and deposition mechanisms—impacts of dust on radiation, clouds and precipitation 97
G. Kallos & P. Katsafados

Part two—Processes at water interfaces

6. Gas-transfer at unsheared free-surfaces 131
C. Gualtieri & G. Pulci Doria

7. Advective diffusion of air bubbles in turbulent water flows 163
H. Chanson

Part three—Processes at interfaces of biotic systems

8. Transport processes in the soil-vegetation-lower atmosphere system 199
D.T. Mihailović

9. Turbulence and wind above and within the forest canopy 221
B. Lalić & D.T. Mihailović

10. Boundary layer development over rigid submerged vegetation 241
P. Gualtieri & G. Pulci Doria

11. Mass transport in aquatic environments 299
G. Nishihara & J. Ackerman

Author Index 327
Subject Index 329

Preface

The field of Environmental Fluid Mechanics (EFM) abounds with various interfaces, and it is an ideal place for the application of new fundamental approaches leading towards a better understanding of interfacial phenomena. In our opinion, the foregoing definition of an environmental interface broadly covers the unavoidable multidisciplinary approach in environmental sciences and engineering also includes the traditional approaches in sciences that are dealing with an environmental space less complex than any one met in reality. An environmental interface can be also considered as a biophysical unit lying between the environment and the organization having the following major functions: (a) to prevent the harmful signals from being injected into the system directly and attacking the valuable structures and channels; (2) to unify the various directions from sub-systems and recursive operations towards the environment; and (3) to fully utilize the internal resources by resolving external variables. The wealth and complexity of processes at this interface determine that the scientists, as it often seems, are more interested in a possibility of non-linear dislocations and surprises in the behavior of the environment than in a smooth extrapolation of current trends and a use of the approaches close to the linear physics. In recent times, researches on fluid mechanics processes at the environmental interfaces have been increasingly undertaken but within different scientific fields and with various applicative objectives.

The aim of the book is to present a comprehensive overview of fluid mechanical processes at the several environmental interfaces. Hence, the matter collected in the book can be considered as a part of the broader context of Environmental Fluid Mechanics in which strong emphasis is placed on the processes involving the exchange of momentum, mass and heat across an environmental interface. The book is aimed at graduate students, doctoral students as well as researchers in civil and environmental engineering, environmental sciences, atmospheric sciences, meteorology, limnology, oceanography, physics, geophysics and applied mathematics. The book can be adopted as a textbook or supplementary reading for courses at the graduate level in environmental fluid mechanics, environmental hydraulics, physics of the atmosphere, water quality modeling, air quality modeling, atmospheric turbulence and bio-fluid mechanics.

Previous books within the EFM field covered only partially the topics presented here. In fact, books on atmosphere dynamics or on air pollution cover only the chapters in Part one of the book. Also, existing books on water quality issues deal only partially with the processes at the environmental interfaces of the hydrosphere. Furthermore, some topics treated in this book, such as momentum and mass-exchange in vegetated open channels, could be found only in papers published in scientific journals. It should be stressed that the book has the unique feature of covering a broad range of scientific knowledge where all the topics are considered from the point of view of the concept of environmental interface. Finally, the team of the contributing authors is mostly consisting of researchers with many years of experiences in the topics they are covering.

The book is organized in three parts with an introductive chapter by B. Cushman-Roisin, C. Gualtieri and D. Mihailović, where scope, scales, processes and systems of EFM are described and discussed together with an overview of EFM processes at environmental interfaces and of challenges to be expected in the future.

Part one deals with the processes at the atmospheric interfaces. First, the chapter by B. Rajković, I. Arsenić and Z. Grsić covers some theoretical aspects, including molecular

and turbulent diffusion, and several areas of modeling of atmospheric dispersion of a passive substance for a point source, such as *Gaussian* and *puff* models. Following this, the chapter by V. Djurdjević and B. Rajković introduces the basic concepts of the air–sea interactions, also discussing the influence of boundary layers on both sides of the air–water interface, and presents the most common approaches to air–sea exchange modeling together with results of sea surface temperature (SST) simulation for the Mediterranean sea obtained by a coupled model with specific modeling of fluxes. The next chapter, by D. Mihailović and D. Kapor is devoted to the modeling of flux exchanges between heterogeneous surfaces and the atmosphere. The three approaches commonly applied for calculating the transfer of momentum, heat and moisture from a grid cell comprised of heterogeneous surfaces are discussed. This begs for a combined method and highlights the uncertainties in the parameterization of boundary layer processes when heterogeneities exist over the grid cell. Part one ends with a chapter by G. Kallos that covers the matter related to transport and deposition of dust, the cycle of which is important in the atmosphere and ocean, since dust particles can have considerable impacts on radiation, clouds and precipitation. In this chapter, the state of the art for modeling dust production are reviewed and the impacts on atmospheric and marine processes are discussed.

Part two of the book covers some fluid mechanics processes at the interface between the atmosphere and inland free surface waters. The chapter by C. Gualtieri and G. Pulci Doria deals with gas-transfer at an unsheared free surface, which can have significant impacts on water quality in aquatic systems. First, the effects of the properties of the gas being transferred and of turbulence on gas-transfer rate are discussed. Then, conceptual models are proposed to calculate the gas-transfer rate, including recent developments resulting from both experimental and numerical methods. The next chapter by H. Chanson covers advection-diffusion of air bubbles in turbulent water flows. Herein, air bubble entrainment is defined as the entrainment or entrapment of undissolved air bubbles and air pockets by the flowing waters. After a review of the basic mechanisms of air bubble entrainment in turbulent water flows, it is shown that the void fraction distributions may be represented by analytical solutions of the advection-diffusion equation for air bubbles. Later the microstructure of the air–water flow is discussed, and it is argued that the interactions between entrained air bubbles and turbulence remain a key challenge.

Part three of the book deals with fluid mechanical processes at the interface between water or atmosphere and biotic systems. The chapter by D. Mihailović presents transport processes in the system comprised of the soil vegetation and lower atmosphere. The chapter shortly describes the interaction between land surface and atmosphere, such as interaction of vegetation with radiation, evaporation from bare soil, evapotranspiration, conduction of soil water through the vegetation layer, vertical movement in the soil, run-off, heat conduction in the soil, momentum transport, effects of snow presence, and freezing or melting of soil moisture. The chapter also includes a detailed description and explanation of governing equations, the representation of energy fluxes and radiation, the parameterization of aerodynamic characteristics, resistances and model hydrology. The next chapter by B. Lalić and D. Mihailović covers turbulence and wind above and within the forest canopy and is focused on forest architecture and on turbulence produced by the friction resulting from air flow encountering the forest canopy. An overview of different approaches oriented towards their parameterization (forest architecture) and modeling (turbulence) is presented. The chapter by P. Gualtieri and G. Pulci Doria deals with vegetated flows in open channels. Particularly, the equilibrium boundary layer developing on a submerged array of rigid sticks and semi-rigid grass on the vegetated bed is characterized based on experimental results carried out by the authors. The last chapter, by G. Nishihara and J. Ackerman discusses the interaction of fluid mechanics with biological and ecological systems. Transport processes in aquatic environments are considered for both pelagic and benthic organisms (those respectively

within the water column and at the bottom). The particular issues related to mass transfer to and from benthic plants and animals are considered in detail.

The editors wish to thank all the chapter authors for their continuous and dedicated effort that made possible the realization of this book. The editors also thank the anonymous reviewers of the project for their thoughtful and detailed suggestions that have improved both the contents and presentation of this book. The editors finally acknowledge with gratitude the assistance of the Editorial Office of Taylor & Francis and, especially, of Dr. Janjaap Blom and Richard Gundel.

Carlo Gualtieri
Dragutin T. Mihailović

Biographies of the authors

Josef Ackerman is the Associate Dean of the Faculty of Environmental Sciences at the University of Guelph, where he administers an interdisciplinary faculty that serves all academic units at the university. He is an Associate Professor in the Department of Integrative Biology where he conducts research on the physical ecology of aquatic plants and animals, as well as environmental issues. Most of this research is focused on small-scale fluid dynamic and ecological processes. He holds adjunct faculty positions in the School of Engineering at Guelph and the Environmental Science & Engineering Programs at the University of Northern British Columbia. Before coming to Guelph, he was a faculty member at the UNBC, where he played a leading role in founding the university's environmental science and environmental engineering programs and held the *Canada Research Chair in Physical Ecology and Aquatic Science*. He is currently an Associate Editor of the journals *Limnology & Oceanography* and *Aquatic Sciences.* Ackerman is the editor of one book and two special issues of international journals, and the author of over 45 peer-reviewed publications.

Ilija Arsenić is the Assistant of the Meteorology, Physics and Biophysics at the Department for Field and Vegetable Crops, Faculty of Agriculture, University of Novi Sad, Serbia. He conducts laboratory classes in Meteorology to the students of various courses and exercises in Biophysics to the students of Veterinary medicine at Faculty of Agriculture. Additionally, at the Faculty of Sciences he conducts laboratory classes in Atmospheric turbulence, Micrometeorology, Instrumental techniques and Air Pollution Modelling courses, and he teaches a course on Air Pollution Modelling to the students of Physics, Meteorology and Environmental Modelling. He received a B.S. in Physics and M.Sc. in Agrometeorology at the University of Novi Sad. His main research interest is the numerical modeling of air pollution transport, turbulent processes and processes connected to the dynamic meteorology. Great part of his activities is connected to the constructing and programming cluster computers at the OS level and parallelizing numerical models. Also, he has experience in constructing meteorological measurement sensors and devices and programming appropriate computer programs for them.

Hubert Chanson is a Professor in Civil Engineering, Hydraulic Engineering and Applied Fluid Mechanics, at the University of Queensland, Brisbane, Australia. His research interests encompass the design of hydraulic structures, experimental investigations of two-phase flows, coastal hydrodynamics, environmental hydraulics and natural resources. His publication record includes 12 books and over 350 international refereed papers. He authored the student textbook *The Hydraulics of Open Channel Flows: An Introduction* (1st edition 1999, 2nd edition 2004) currently used in 50 universities worldwide. In 2003, the IAHR presented Hubert Chanson with the 13*rd Arthur Ippen Award* for outstanding achievements in hydraulic engineering. The American Society of Civil Engineers, Environmental and Water Resources Institute (ASCE-EWRI) presented him with the 2004 award for the Best Practice paper in the *Journal of Irrigation and Drainage Engineering*. Prof. Chanson was invited to deliver keynote lectures in several international conferences and he lectured several short courses in Australia and overseas. He was member of the organizing committee of several scientific conferences. He also contributed as reviewer for over 50 among scientific journals and international conferences and as expert reviewers for research funding agencies.

He is also member of the *International Association of Hydraulic Engineering and Research* (IAHR) and of the *Institution of Engineers, Australia* (MIEng.Aust.). His Internet home page is http://www.uq.edu.au/∼e2hchans/.

Benoit Cushman-Roisin is Professor of Engineering Sciences at Dartmouth College, where he teaches a series of courses in environmental engineering and fluid mechanics in the Thayer School of Engineering. He received his B.Sc. in engineering physics at the University of Liège, Belgium, and his doctorate in geophysical fluid dynamics at the Florida State University, where he also taught physical oceanography. He later moved to Dartmouth College to teach fluid mechanics and environmental engineering, the intersection of which is environmental fluid mechanics. He is the author of the first introductory textbook on geophysical fluid dynamics (Prentice Hall, 1994) and the lead author of a monograph on the physical oceanography of the Adriatic Sea (Kluwer, 2001). He has authored a number of research articles on various aspects of numerical analysis, physical oceanography and fluid dynamics. He is also the founding and chief editor of *Environmental Fluid Mechanics*, a peer-reviewed journal published by Springer since 2001. His current research is devoted to the variability of coastal waters (with particular focus on the mesoscale variability in the Adriatic Sea), fluid instabilities, turbulent dispersion, and particle entrainment by jets. Aside from his academic position, Cushman-Roisin also advices various groups and companies on topics related to environmental quality, fluid mechanics and alternative energies.

Vladimir Djurdjević is teaching assistant at the department for Physics, Institute for Meteorology, Belgrade University. He graduated from Faculty of Physics, Department of Meteorology, in 1998 with the average grade of 9.80, the highest average in the history of the department. In 2002 he defended his master thesis *The air-sea interaction in the Mediterranean area*. His main area of interest is atmosphere and ocean modeling. Currently he is involved in the project SINTA, simulation of Mediterranean climate as regional climate problem. Starting from the climate integrations done by the Bologna climate model, which is a version of ECHAM-4 model he performs long term integrations (30 years) in the same mode as a limited area model does weather forecast. The model that is used is a coupled atmosphere-ocean model whose atmospheric component is NCEP's meso-scale (ETA) model and the ocean POM (Princeton Ocean Model). Using the same coupled model he does investigations of the air-sea interaction in the Mediterranean basin and in particular in the Adriatic sea. As a expert in ocean and atmospheric modeling he was invited to the University of Lisbon, Department of Oceanography, where he spent two months. Currently he is involved in three international projects related to the various aspects of the air-sea interaction and its influence in a localized area.

Zoran Grsić is currently head of the Micrometeorology and air pollution division in the Institute for nuclear sciences in Vinca, Belgrade. He received bachelors degree at Belgrade University, department for Physics, Institute for Meteorology. At the same department he received his M.Sc. degree. Most of his work concerns modeling of the pollution from industrial sources, but his main occupation was and is design and improvement of the acquisition network of the possible nuclear pollution near the nuclear reactor in Vinca and its modeling as a part of the comprehensible warning and accident management. He was and is involved in several international projects concerning the safety of a nuclear and chemical installations. Currently he is leading meteorologist in three national projects. The first one is in the project of the decommissioning of the nuclear reactor in Vinca, near Belgrade, the second one is: *Automated air quality system in industrial zone of Pancevo* and the third one: *Design of continual observing system for the assessment the influence of thermo power plant Nikola Tesla*, which is located in the vicinity of Belgrade. He is member of *Air Protection*

Society of Serbia, *Meteorological Society of Serbia* and *Balkan Environmental Association* (B.EN.A).

Carlo Gualtieri is currently Assistant Professor in Environmental Hydraulics at the Hydraulic and Environmental Engineering Department *G.Ippolito* of the University of Napoli *Federico II*. He received a B.Sc. in Hydraulic Engineering at the University of Napoli *Federico II*, where he received also a M.Sc. in Environmental Engineering. He finally received a Ph.D. in Environmental Engineering at the University of Napoli *Federico II*. Prof. Gualtieri has 85 peer-reviewed scientific papers, including 15 publications in scientific journals, 40 publications in conference proceedings, and 26 other refereed publications in subjects related to environmental hydraulics and computational environmental fluid mechanics, with over 60 papers, experimental investigations of two-phase flows, water supply networks management and environmental risk. He is also co-author of 2 textbooks on Hydraulics and author of a textbook on Environmental Hydraulics. He is member of the Editorial Board of *Environmental Modelling and Software (Elsevier)* and of *Environmental Fluid Mechanics (Springer)*. He contributed as reviewer in several scientific journals (e.g. Environmental Fluid Mechanics, Environmental Modeling and Software, Journal of Environmental Engineering ASCE, Journal of Hydraulic Engineering ASCE, Advances in Water Resources, Experiments in Fluids, Ecological Modelling, Journal of Coastal Research) and as external examiner for Ph.D thesis in foreign countries. He co-organized sessions dealing with environmental fluid mechanics in international conferences, such as *iEMSs 2004*, *iEMSs 2006*, *EMS 2007* and *iEMSs 2008*. He is also active as expert reviewer for research funding agencies in several countries. He is member of the International Scientific Advisory Board of the EU project *RRP-CMEP*, of the *American Society of Civil Engineers* (ASCE), of the *International Association of Hydraulic Engineering & Research* (*IAHR*) and of the *International Environmental Modelling & Software Society (iEMSs)*.

Paola Gualtieri is currently Associate Professor in Hydraulics and Hydraulic Measurements at the Hydraulic and Environmental Engineering Department *G.Ippolito* of the University of Napoli *Federico II*. She received a B.Sc. in Hydraulic Engineering at the University of Napoli *Federico II*, where she received also a M.Sc. in Environmental Engineering. She finally received a Ph.D. in Hydraulic Engineering at the University of Napoli *Federico II*. She is member of Ph.D. Program Board at the University of Napoli *Federico II*. Prof. Gualtieri produced about 50 scientific papers, including 2 textbooks, 2 chapters in international scientific books, 6 papers in international journals, 16 papers in international conferences, 13 papers in national conferences in subjects related to hydraulic measurements, turbulence in uniform and boundary layer flows, air entrainment at hydraulics structures, and, finally, environmental hydraulics with 14 papers. She contributed as reviewer for international conferences and as expert reviewer for research funding agencies in several countries. She is member of the *International Association of Hydraulic Engineering and Research* (IAHR) and of the *American Society of Civil Engineers* (ASCE).

Petros Katsafados is Lecturer at the Harokopio University of Athens, Department of Geography. He is also a senior research associate at the Atmospheric Modeling and Weather Forecasting Group – AM&WFG (http://forecast.uoa.gr). He is originally studied Mathematics and acquired a Bachelor degree in this subject at the National and Kapodistrian University of Athens (NKUA) on 1993. He then switched scientific field to Environmental Physics and he finally completed his Master degree from the School of Physics on 1996. As a postgraduate student he joined Atmospheric Modelling and Weather Forecasting Group (AM&WFG) of NKUA mainly participating in EU funded SKIRON project. Getting the achievements of this research he became a Ph.D. candidate on 1998 supervised by Prof.

Kallos head of AM&WFG. In his Ph.D. thesis factors that influence the forecast skill in numerical weather prediction were examined in conjunction with the development of a methodology for expanding the forecast period. The regional climatic patterns and variability for temporal periods, which may vary from medium-range to seasonal weather forecasts, were also analyzed throughout his thesis. On 2001 he took position as a senior research associate in the School of Physics at NKUA but he also continued the cooperation with AM&WFG. From that period up today he participated in a number of EU and national funded projects mainly related with regional climate dynamics and impacts (CIRCE), air-sea interactions (MFSTEP), natural and anthropogenic air pollution modelling (MEDUSE, ADIOS), wind energy applications (ANEMOS). Since 2002 he has 9 articles in international peer-reviewed journals and more than 21 announcements and publications in conference proceedings in subjects related to atmospheric physics and regional climate impacts. An additional 4 manuscripts are presently either under review with minor revisions or in preparation. He has also participated in more than 20 EU and national funded projects in 1 of them as coordinator.

George Kallos is Associate Professor at the University of Athens, School of Physics/Division of Applied Physics. He has also the position of Senior Research Associate at the SUNY/ASRC, Albany, NY. He leads the Atmospheric Modeling and Weather Forecasting Group – AM&WFG (http://forecast.uoa.gr). He has B.Sc. from University of Athens/School of Mathematics (1975), M.Sc. and Ph.D. in Geophysical Sciences/Atmospheric Sciences Division, Georgia Institute of Technology, School of Geophysical Sciences, U.S.A, (1985). He has 30 years of experience in atmospheric modeling working at the University of Athens, Georgia Institute of Technology, Colorado State University, SUNY/ASRC and National Center for Atmospheric Research (NCAR). His activities are related to atmospheric and climate modelling, air pollution wind and wave energy prediction. Dr. Kallos has 75 publications in scientific journals, 120 publications in conference proceedings, and 90 other publications in subjects related to atmospheric physics and chemistry. Most of them are related to atmospheric modeling. His published work has more than 1000 citations from others. He has participated in 65 projects; in 50 of them was coordinator. He serves as Associate Editor for the scientific journal *Environmental Fluid Mechanics* and he is member of the Editorial Board of the *Journal of Atmosphere-Ocean Systems – JAOS* **(**former *Global Atmosphere-Ocean Systems – GAOS*)**.** He contributed as reviewer in several scientific journals (e.g. JGR, GRL, JAS, MWR, JAM, J Climate, BLM, Atm. Env., QJRMS, ACP). He received the *International Union of Air Pollution Prevention Association – IUAPPA award* for his work on Atmospheric Modeling of the Long Range Transport and air quality work in the Mediterranean Region (2004).

Darko Kapor is Professor of Theoretical Physics at the Department of Physics, Faculty of Sciences, University of Novi Sad, Serbia. He teaches various theoretical and mathematical Physics courses to all Physics students, a course on Atmospheric Radiation to the students of physics and meteorology and history of physics for Physics teachers. He received a B.Sc. in Physics at the University of Novi Sad, his M.Sc. in Theoretical Physics at the University of Belgrade, Serbia and defended his Ph.D. Thesis in Theoretical Physics at the University of Novi Sad. Along with his teaching activities in Physics, he also teaches at the multidisciplinary studies of the Center for Meteorology and Environmental Modelling (CMEM) which is the part of the Association of Centers for Multidisciplinary and Interdisciplinary Studies (ACIMSI) of the University of Novi Sad. His main research interest is the theoretical condensed matter physics, where he is the head of the project financed by the Ministry for Science of the Republic of Serbia. During the last 15 years, he has developed an interest in the problems of theoretical meteorology and worked with the Meteorology group at the

Faculty of Agriculture and Faculty of Sciences. He is engaged in transferring the concepts and techniques of the theoretical physics to meteorology, for example to the problem of aggregated albedo for heterogeneous surfaces and more recently the problem of chaos.

Branislava Lalić is Assistant Professor of Meteorology, Physics and Biophysics at the Department for Field and Vegetable Crops, Faculty of Agriculture, University of Novi Sad, Serbia. She conducts laboratory classes in Meteorology to the students of various courses and in Biophysics to the students of Veterinary medicine at Faculty of Agriculture. Additionally, at the Faculty of Sciences she conducts laboratory classes in Atmospheric modeling course and she teaches a courses on Instrumental techniques and Applied meteorology to the students of Physics, Meteorology and Environmental Modelling. She received a B.Sc. in Physics at the University of Novi Sad, her M.Sc. in Meteorology at the University of Belgrade, Serbia and defended her Ph.D. Thesis in Meteorology and Environmental Modelling at the University of Novi Sad. Along with her teaching activities at Faculty of Agriculture and Faculty of Sciences she is involved in establishment and organization of the multidisciplinary studies at the Center for Meteorology and Environmental Modelling (CMEM) which is the part of the Association of Centers for Multidisciplinary and Interdisciplinary Studies (ACIMSI) of the University of Novi Sad. Her main research interest is the modeling of physical processes describing biosphere – atmosphere interaction and turbulent transfer between ground and the atmosphere.

Dragutin T. Mihailović is Professor of Meteorology and Biophysics at the Department of the Vegetable and Crops, Faculty of Agriculture, University of Novi Sad, Serbia. He is also the Professor of the Modelling Physical Processes at the Department of Physics, Faculty of Sciences at the same university and the Visiting Professor at the State University of New York at Albany. He teaches various theoretical and numerical meteorology courses to Physics and Agriculture students. He received a B.Sc. in Physics at the University of Belgrade, Serbia, his M.Sc. in Dynamics Meteorology at the University of Belgrade and defended his Ph.D. Thesis in Dynamics Meteorology at the University of Belgrade. He is head of the Center for Meteorology and Environmental Modelling (CMEM) which is the part of the Association of Centers for Multidisciplinary and Interdisciplinary Studies (ACIMSI) of the University of Novi Sad where he has teaching activities. His main research interest are the surface processes and boundary layer meteorology with application to air pollution modeling and agriculture. Recently, he has developed an interest for (i) analysis of occurrence of the deterministic chaos at environmental interfaces and (ii) modeling the complex biophysical systems using the category theory.

Gregory Nishihara is currently a JSPS (Japan Society for the Promotion of Science – U.S. National Institute of Health) post-doctoral fellow at the Faculty of Fisheries at Kagoshima University, Japan. He received a B.Sc. in Civil Engineering at the University of Hawaii at Manoa and was awarded a Ph.D. in the Science of Marine Resources from the United Graduate School of Agricultural Sciences at Kagoshima University. He received advanced training in the Physical Ecology Laboratory at the University of Guelph where he was a postdoctoral scientist. He is interested in examining the relationship between mass transport and fluid dynamic processes on the physiological and ecological processes of aquatic plants and macrophytes and is also interested in how the physical and biological processes interact in aquatic animals. Additionally, he is interested in developing and applying novel technologies to promote the responsible and efficient use of aquatic environments.

Guelfo Pulci Doria is currently Full Professor in Fluid Mechanics and Hydraulics at the Hydraulic and Environmental Engineering Department *G.Ippolito* of the University

of Napoli *Federico II*. He received a B.Sc. in Electronic Engineering at the University of Napoli *Federico II* in year 1966. From 1993 to 1999 he was head of the Hydraulic and Environmental Engineering Department *G.Ippolito* and in 1994–95 he was president of Napoli Water Supply Authority. He also was 5 times head and 15 times member of the Board of the Ph.D. Program at the University of Napoli *Federico II* and 3 times external reviewer of Ph.D. Program at the University of Roma 3. Since 1988 he was national coordinator in 10 National Research Groups funded by the Scientific Research National Department and in 1997 he was co-coordinator of EU funded research program *Waternet*. Prof. Pulci Doria produced about 160 scientific papers, including 4 textbooks, 3 chapters in international scientific books, 6 papers in international journals, 3 invited lectures in conferences, over 30 papers in international conferences and over 40 papers in national conferences. He contributed as reviewer for scientific journals and international conferences. His research interests encompass turbulence, hydraulic models and measurements, cavitation, air entrainment at hydraulic structures and, finally, environmental hydraulics with over 30 papers. He is member of the *International Association of Hydraulic Engineering and Research* (IAHR).

Borivoj Rajković is Associate Professor at the Faculty of Physics, University of Belgrade, where he teaches several courses for undergraduate and graduate students. He received his bachelors degree at Belgrade University, department for Mathematics, Mechanics and Astrophysics and Ph.D. from Princeton University, program in Geophysical Fluid Dynamics. His professional interests are in Numerical modeling of the atmosphere and ocean, Micrometeorology and Parameterization of physical processes in the Atmosphere. For several years he was joint professor at the University of Novi Sad where he is currently at the Center for Environmental Modeling and Ecological Studies (CIMSI). During 1993–95 he was visiting scientist at the World Laboratory in *LAND-3 project: Protection of the Coastal Marine Environment in the Southern Mediterranean Sea*. Currently he participates in the regional climate project, *Simulation of the Balkan climate in the 21st century* (SINTA) together with scientists from Italy. He is author of textbook on Micrometeorology and the author of over 18 peer-reviewed articles and book chapters.

CHAPTER ONE

Environmental fluid mechanics: Current issues and future outlook

Benoit Cushman-Roisin
Thayer School of Engineering, Dartmouth College
Hanover, New Hampshire, USA

Carlo Gualtieri
Hydraulic and Environmental Engineering Department
University of Napoli Federico II, Napoli, Italy

Dragutin T. Mihailović
Faculty of Agriculture, University of Novi Sad, Novi Sad, Serbia

1.1 FLUIDS IN THE ENVIRONMENT

All forms of life on earth are immersed in a fluid or another, either the air of the atmosphere or the water of a river, lake or ocean; even, soils are permeated with moisture. So, it is no exaggeration to say that life, including our own, is bathed in fluids. A slightly closer look at the situation further reveals that it is the mobility of fluids that actually makes them so useful to the maintenance of life, both internally and externally to living organisms. For example, it is the flow of air that our lungs that supplies oxygen to our blood stream. The forced air flow created by our respiration, however, is not sufficient; without atmospheric motion around us, we would choke sooner or later in our own exhaust of carbon dioxide. Likewise, most aquatic forms of life rely on the natural transport of water for their nutrients and oxygen. Our industrial systems, which release pollution on a continuing basis, would not be permissible in the absence of transport and dilution of nearly all emissions by ambient motions of air and water.

In sum, natural fluid motions in the environment are vital, and we have a strong incentive to study the naturally occurring fluid flows, particularly those of air in the atmosphere and of water in all its streams, from underground aquifers to surface flows in rivers, lakes, estuaries and oceans.

The study of these flows has received considerable attention over the years and has spawned several distinct disciplines: meteorology, climatology, hydrology, hydraulics, limnology and oceanography. Whereas the particular objectives of each of these disciplines, such as weather forecasting in meteorology and design of water-resource projects in hydraulics, encourage disciplinary segregation, environmental concerns compel experts in those disciplines to consider problems that are essentially similar: the effect of turbulence on the dispersion of a dilute substance, the transfer of matter or momentum across an interface, flow in complex geometries, the rise of a buoyant plume, and the impact of flow over a biotic system.

The study of environmental flows is also fully integrated in the contemporary emphasis on environmental impacts and sustainable life on planet Earth. According to physicists, the world scientific community will be occupied during the 21st century in large part by problems related to the environment, particularly those stemming from the concern over climate change (Rodhe *et al*., 2000) as well as many other problems spanning a wide range of spatial and temporal scales. This marks the first time in the history of science that environmental problems lie at the forefront of scientific research.

The following chapters of this book are illustrative of a number of these problems. The common points encourage interdisciplinarity to a degree that is increasing in proportion to the acuity of our environmental problems. This overlap between the various disciplines concerned with the environmental aspects of natural fluid flows has given rise to a body of knowledge that has become known as Environmental Fluid Mechanics. The interdisciplinary aspects become especially manifest in the study of processes at the interfaces between environmental systems.

1.2 SCOPE OF ENVIRONMENTAL FLUID MECHANICS

In the light of the preceding remarks, we can propose a definition: *Environmental Fluid Mechanics* (EFM) is the scientific study of naturally occurring fluid flows of air and water on our planet Earth, especially of those flows that affect the environmental quality of air and water. Scales of relevance range from millimeters to kilometers, and from seconds to years.

According to the preceding definition, EFM does not extend to fluid flows inside organisms, such as air flow in lungs and blood flow in the vascular system, although these can be classified as natural. Rather, these topics more properly belong to specialized biological and medical sciences, which have little in common with studies of outdoor fluid flows.

The preceding definition also distinguishes EFM from classical fluid mechanics, the latter being chiefly concerned with artificial (engineered) fluid motions: flows in pipes and around airfoils, in pumps, turbines, heat exchangers and other machinery that utilizes fluids. In so doing, it treats many different types of fluids and under vastly different pressures and temperatures (Munson *et al*., 1994). By contrast, EFM is exclusively concerned with only two fluids, air and water, and moreover under a relatively narrow range of ambient temperatures and pressures. Ironically, while classical fluid mechanics tends to view turbulence as a negative element, because it creates unwanted drag and energy loss, EFM accepts turbulence as beneficial, because it favors rapid dispersion and dilution.

The objective of EFM also differs from that of hydraulics, which deals exclusively with free-surface water flow (Chow, 1959; Sturm, 2001). Traditionally, problems in hydraulics have addressed the prediction and control of water levels and flow rates, but the realm of hydraulics has recently been shifting considerably toward environmental concerns (Singh and Hager, 1996; Chanson, 2004). This situation has arisen because it has now become equally important to estimate the effect of turbulent mixing, erosion and sedimentation, and their effects on water quality as it has been to calculate pressures against structures and predict floods. Because of its similarities with other natural fluid flows, the environmental component of hydraulics is incorporated in EFM.

Geophysical fluid dynamics, which studies the physics of atmospheric and oceanic motions on the planetary scale (Cushman-Roisin, 1994), is another branch of fluid mechanics that overlaps with EFM. In geophysical fluid dynamics, however, the strong effect of planetary rotation relegates turbulence to secondary status. Put another way, the two main ingredients of geophysical fluid dynamics are stratification and rotation, whereas those of EFM are stratification and turbulence.

Other cousin disciplines are limnology (study of lakes; ex. Imberger, 1998) and hydrology (study of surface and subsurface water; ex. Brutsaert, 2005). Table 1.1 recapitulates the commonalities and differences between EFM and its cousin disciplines highlighting their purpose, possibility of human control and the role of turbulence within them.

Table 1.1. Topical comparison between Environmental Fluid Mechanics and related disciplines.

	Environmental Fluid Mechanics	Fluid Mechanics	Geophysical Fluid Dynamics	Hydraulics	Hydrology
Air example	Sea breeze	Airfoil	Storm	–	–
Water example	Danube River	Pump	Gulf Stream	Dam	Watershed
Turbulence	Beneficial (Dilution)	Detrimental (Drag)	Secondary importance	Secondary importance	Unimportant
Human control	Limited	Dominant	Nil	Dominant	Limited
Purpose	Prediction & Decision	Design & Operation	Prediction & Warnings	Design & Operation	Prediction & Decision

Finally, it is worth situating the purpose of EFM among that of the other disciplines. Because no one can affect in any direct way the flow of air and water on planetary scales, geophysical fluid dynamics, meteorology and oceanography aim solely at the understanding and prediction of those flows. In contrast, the primary objectives of traditional fluid mechanics and hydraulics are design and operation. Environmental fluid mechanics finds its purpose between those extremes; like hydrology and limnology, it is aimed at prediction and decision. Indeed, typical problems in EFM concern the prediction of environmental-quality parameters that depend on natural fluid flows, such as bedload transports and pollution levels. EFM also extends into decision making. Decisions in the realm of EFM, however, do not address how natural fluid flows can be controlled or modified, but rather how inputs from human activities can be managed as to minimize their impact downstream. A typical example is the design of a smokestack (with decisions regarding its location, height, diameter and rate of output) in order to avoid certain levels of ground pollution within a certain radius around its base. Another pertinent example is the management of a lake that is used as a drinking water reservoir but is unfortunately contaminated by methyl tertiary-butyl ether (MTBE). This contaminant. which is an oxygenated compound that has been added to gasoline in the USA, is released in the lake by recreational vehicles. Since gas-transfer, that is volatilization, is believed to be the main removal process of MTBE from the lake, the assessment of MTBE volatilization rate is a critical point for the use of the lake for water supply (Gualtieri, 2006). This example points out another feature of EFM, namely that EFM processes often involve exchange processes between the boundaries of different systems, such as the interface between a water body and the atmosphere or between the atmosphere and the land surface. An overview of these processes will be proposed later in Section 1.5.

EFM thus considers only two fluids, air and water, and each within a relatively narrow range of values, never far from ambient temperatures and pressures, one may then be tempted to ask: Shouldn't such study be relatively straightforward? Why should an entire discipline be devoted to such a narrow object of inquiry? The answers to these questions lie in the several complexities which EFM needs to confront. First, the domain size is typically very large, large enough to enable a number of distinct processes to play simultaneous roles, and it is not uncommon to encounter a hierarchy of processes embedded into one another. For example, sea breeze near the seashore is a larger-scale manifestation of convection and at

the same time a smaller-scale component of the local meteorology. Second, the geometry is typically complex, with irregular topography and free surfaces. Third, processes at interfaces, the particular subject of this book, often play a controlling role in the entire system, and details matter for the whole. Fourth, fluid turbulence, although an incompletely known subject of physics, is central to friction, dispersion and dilution in environmental fluids.

1.3 STRATIFICATION AND TURBULENCE

Stratification and turbulence are two essential ingredients of EFM. Stratification occurs when the density of the fluid varies spatially, as in a sea breeze where masses of warm and cold air lie next to each other or in an estuary where fresh river water flows over saline seawater. Such situations with adjacent masses of lighter and denser fluid create buoyancy forces that strongly control the flow by either generating or restricting vertical motion.

1.3.1 Stratification

Stratification is to be distinguished from compressibility. Compressibility, or the variation of density under changing pressure, is responsible for the propagation of sound waves. Intuitively, it is evident that the propagation of sound waves (acoustics) is not relevant to environmental fluid motions. This is because the typical speeds associated with movements of air and water in nature are much less than the sound speed; *i.e.* the Mach number (ratio of fluid velocity to sound speed) is much less than one. In contrast to compressibility, stratification arises because density varies with temperature through what is commonly called thermal expansion: heat dilates the fluid[1], so that warm fluid expands and cold fluid contracts. This effect is often important in natural fluid systems because thermal contrasts across the system create buoyancy forces that may not be negligible, imparting to the fluid a tendency to arrange itself vertically with the denser fluid sinking to the lowest places and the lighter fluid floating on top. Such layering of the fluid according to density, from the heaviest at the bottom to the lightest at the top, is what is properly called stratification. But, the word stratification has been enlarged to encompass any situation in which density differences are important, regardless of whether they occur in the vertical or the horizontal or both, and whether they are caused by heat or another agent such as salinity (in seawater), moisture (in atmosphere), or suspended matter (in turbid water).

Although a certain degree of stratification is always present in environmental systems, its dynamical effects are not necessarily important in every single instance. There are indeed cases, such as shallow-river flows, where buoyancy forces exert a negligible effect among the other forces at play. To ascertain the importance of density stratification in a particular situation, we can use the following rule. Under the action of gravity, fluid masses of different densities tend to flow so that the heavier ones occupy the lower portion of the domain and the lighter ones the upper portion. In the absence of mixing along the way and of other forces besides gravity, the ultimate result would be a vertical arrangement of horizontal layers with density increasing monotonically downward, which corresponds to a state of least potential energy. The action of other forces, however, create motions that disturb such equilibrium, tending to raise heavier fluid and lower lighter fluid against their respective buoyancy forces. The result is an increase of potential energy at the expense of a portion of the kinetic energy contained in the motion. Therefore, the dynamical importance of stratification can be estimated by comparing the levels of potential and kinetic energies present in the system under consideration.

[1] With the exception of fresh water below 4°C.

In most environmental applications, fluid parcels (air or water) undergo only very moderate density variations. For example, a water parcel on the surface of a lake when subjected to solar heating that increases its temperature by 10°C (which almost never occurs) has its density reduced by less than 0.3%! By contrast, we think of the air in the atmosphere as being very compressible, and it is so, but nonetheless the compressibility of air is unimportant in most environmental situations, because air parcels traveling with winds remain within a narrow range of pressures and temperatures and experience density variations that are usually less than 5%. With this in mind, we can write the density ρ of the fluid (mass per volume, in kg/m^3), as the sum of two terms:

$$\rho = \rho_0 + \rho' \tag{1.1}$$

where ρ_0 is a constant and ρ' a variable but small perturbation. For ρ_0, we can adopt the following values:

- for air at standard temperature (15°C) and pressure (101.33 kPa): $\rho_0 = 1.225\ \text{kg/m}^3$;
- for freshwater at standard temperature (15°C) and atmospheric pressure $\rho_0 = 999\ \text{kg/m}^3$;
- for seawater at standard temperature (10°C) and salinity (35 ppt) $\rho_0 = 1027\ \text{kg/m}^3$.

If the density perturbation ρ' changes by a value $\Delta\rho$ over a height H of the fluid (height over which vertical excursions take place), so that a fluid parcel at some level z has a density equal to $\rho_0 + \Delta\rho/2$ and one at level $z + H$ a density equal to $\rho_0 - \Delta\rho/2$ (Figure 1.1), an exchange of volume V between those two parcels causes a rise in potential energy of the heavier one by $mgH = (\rho_0 + \Delta\rho/2)VgH$ and a simultaneous drop in potential energy of the lighter parcel by $(\rho_0 - \Delta\rho/2)VgH$. The net change in potential energy is $\Delta\rho VgH$. On the other hand, the kinetic energy is on the order of $mU^2/2$ per parcel, where U is a measure of the fluid velocity in the system (such as a velocity at some inlet). For the pair of parcels, this adds to $(\rho_0 + \Delta\rho/2)VU^2/2 + (\rho_0 - \Delta\rho/2)VU^2/2 = \rho_0 VU^2$. A comparison of potential energy to kinetic energy leads to forming the ratio:

$$Ri = \frac{gH\Delta\rho}{\rho_0 U^2} \tag{1.2}$$

after division by V. This ratio is called the *Richardson number*.

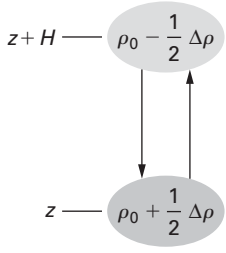

Figure 1.1. Exchange between fluid parcels of different densities and at different heights. Because each displacement is performed either against or with the force of gravity, the exchange causes a modification in potential energy.

The value of the dimensionless ratio Ri permits to determine the importance of stratification in a given system. If Ri is on the order of unity (say $0.1 < Ri < 10$, customarily

written as $Ri \sim 1$), a significant perturbation to the stratification can consume a major part of the available kinetic energy, thereby modifying the flow field significantly. Stratification is then important. If Ri is much greater than unity ($Ri >> 1$, or in practice $Ri > 10$), then there is insufficient kinetic energy to perturb the stratification in any significant way, and the latter greatly constrains the flow. But, on the other hand, when Ri is much less than unity ($Ri << 1$, or in practice $Ri < 0.1$), potential-energy variations created by vertical excursions of the fluid against their buoyancy forces cause a negligible drop in kinetic energy, and the stratification is easily erased by vertical mixing. In sum, stratification effects are negligible whenever $Ri << 1$ and important otherwise.

1.3.2 Turbulence

Turbulence is the term used to characterize the complex, seemingly random motions that continually result from instabilities in fluid flows. Turbulence is ubiquitous in natural fluid flows because of the large scales that these flows typically occupy. (The only significant exception is the subsurface flow in porous soils where motion is very slow.) By vigorously stirring the fluid, turbulence is an extremely efficient agent of dilution. This is a major advantage in environmental systems. On the other hand, turbulence comes with a substantial handicap: The complex motions that it generates are beyond any easy description, even by a statistical approach. Some specific types of turbulent flow, such as homogeneous turbulence and shear turbulence, can be described by limited theories and modeled with a good dose of empiricism, but a complete theory of turbulence has not yet been formulated.

The level of turbulence in a fluid system is estimated by comparing the amount of kinetic energy and the work of viscous forces. If ρ_0 is again the average density value in the system, U a typical velocity value, L a characteristic length of the domain (such as its width or height), and μ the viscosity of the fluid, then a measure of the kinetic energy per unit volume is $\rho_0 U^2/2$, while the dissipative work done by viscous forces per unit volume is $\mu U/L$. The ratio of these two quantities is (after removal of the factor 2 which is inconsequential in a definition):

$$Re = \frac{\rho_0 U L}{\mu} \tag{1.3}$$

This is the *Reynolds number*, ubiquitous in fluid mechanics. When Re is large, there is ample kinetic energy and comparatively weak viscous dissipation; the fluid flows relatively freely and is thus apt to exhibit complex spatial patterns and much temporal variability. This is the case of turbulence. Hence, turbulence occurs whenever the Reynolds number is large. There is rarely a precise value of the Reynolds number below which the flow is simply structured (laminar flow) and above which turbulence occurs, but the transition typically occurs at a Reynolds number of a few thousands. In environmental systems, with large values of L and small values of μ [$\mu = 1.8 \times 10^{-5}$ kg/m · s for air and 1.0×10^{-3} kg/m · s for water], the value of Re almost invariably exceeds 10^6, and the flow is turbulent. The questions that arise are how strong is the turbulence and what is its nature. Environmental fluid turbulence can be broadly divided into two types: *shear turbulence* and *convective turbulence*. Each type is characterized by a turbulent velocity scale, which can then be compared to the mean flow velocity.

In shear turbulence (also called wall turbulence), the turbulent velocity scale is the friction velocity u^*, defined as:

$$u^* = \sqrt{\frac{\tau}{\rho}}, \tag{1.4}$$

where ρ is the fluid density and τ is the stress occurring at the boundary (Pope, 2000, page 269). The greater the stress against the boundary, the greater the shear in the mean flow, and the greater its capacity to create turbulent eddies.

In convective turbulence, the turbulent velocity scale, usually denoted w^* because it measures the vertical velocity of rising or sinking thermals, is given by:

$$w^* = (\kappa \alpha g h Q)^{1/3} \tag{1.5}$$

where $\kappa = 0.41$ is the von Karman constant, α is the thermal expansion coefficient, g the earth's gravitational acceleration, h the height of the system, and Q the *kinematic* heat flux (actual heat flux divided by the fluid's density and heat capacity) (Cushman-Roisin, 1994, page 165). Which among u^* and w^* is largest and how the latter compares to the mean flow directly affect the importance of turbulence in an environmental flow.

The two ingredients of EFM, stratification and turbulence, act generally in competition with each other. Oftentimes, the buoyancy forces of stratification tend to quench turbulence, because vertical movements against buoyancy forces consume kinetic energy to increase potential energy. On the other hand, turbulent motions are capable of mixing the fluid and therefore of reducing the density differences that create stratification. An exception to the rule is convection, which occurs when an unstable, top-heavy stratification releases potential energy that feeds turbulent kinetic energy.

1.4 SCALES, PROCESSES AND SYSTEMS

Environmental problems appear different at different scales, requiring various approaches for their investigation and solution. Likewise, Environmental Fluid Mechanics takes different forms depending on the scale of investigation.

The shortest relevant length scale is that of the smallest turbulent eddy, called the Kolmogorov scale, where viscosity quenches turbulence. It is typically less than a millimeter in environmental fluid flows. Computer models cannot resolve this scale, but it is nonetheless important because it is near this scale that molecular diffusion occurs inside the flow and skin effects take place on the interfaces.

The next scale characterizing EFM motions is usually the local level, where the smaller geometrical dimensions of the system come into play, such as the overall roughness of a vegetated surface, the shape of buildings in an airshed, or the structure of a river channel. At this level, the focus is usually on resolvable details of the flow or the concentration field in the vicinity of a single source, such as the jet caused by the discharge of an industrial waste in a body of water or the plume originating from a release of hot gases from a smokestack (Figure 1.2). The understanding of such phenomena proceeds from studies of specific processes. The same process is likely to be present in different environmental systems under almost identical forms. For example, shear-flow instability occurs in the lower atmosphere, in estuaries and also in the near-surface circulation of a lake. Likewise, convective motions driven by top-heavy stratification follow similar dynamics regardless whether they occur in air or water. The same mathematical formulation will therefore be useful in more than one application.

At the next larger level, one considers entire systems, such as a stretch of river, an entire lake, an aquifer, or an urban airshed. In those systems, fluid motions result from several processes acting simultaneously. For example, lake dynamics are characterized by a mix of wind-driven currents, gravity waves, thermal stratification, and winter convection. As one proceeds toward longer scales, one begins to encounter systems of systems, for example, a hydrologic network consisting of multiple river branches and lakes, or the meteorology over a heterogeneous land area.

Figure 1.2. A smokestack plume. Note the turbulent billowing inside the plume, which is the cause of its gradual dispersion in the ambient atmosphere. (Photo by the first author).

Table 1.2 lists the typical length, velocity, and time scales of the most common environmental fluid processes and systems. Not surprisingly, larger systems evolve on longer time scales, with the exception of ocean tides. Depending on the size of the system under consideration, the spatial scale can be regional, continental or even global. As the scale increases, some processes may yield precedence to others. For example, as one approaches continental and global scales, turbulence becomes increasingly less important, and planetary rotation becomes dominant. At the limit of the entire globe, mass budgets (ex. of greenhouse gases) also become important because there is (almost) no escape from the earth.

1.5 EFM PROCESSES AT ENVIRONMENTAL INTERFACES

In Section 1.2, EFM was defined as the scientific study of naturally occurring fluid flows of air and water on our planet Earth, especially of those flows that affect the environmental quality of air and water. In fact, these flows carry various substances that can modify environmental quality or be considered as indicators of environmental quality. These substances of concern may be gases, solutes or solids, and they can be naturally present or be produced by human activities. Anthropogenic contaminants can often create severe hazards for both human and environmental health.

There are two primary modes of transport that fall under the scope of EFM are:

- *advection*, which is the transport by the flow of the fluid itself;
- *diffusion*, which is the transport associated with random motions within the fluid. These random motions occur at the molecular scale producing *molecular diffusion* or are caused by turbulence, causing *turbulent diffusion*. Molecular diffusion tends to be important in the close vicinity of interfaces, regulating for example the passage of a soluble gas between air and water, while turbulent diffusion tends to act mostly within the body of the system.

Table 1.2. Length, velocity and time scales of environmental fluid processes and systems.

	Horizontal length scale L	Vertical length scale H	Velocity scale U	Time scale T
Processes:				
Microturbulence	1–10 cm	1–10 cm	1–10 cm/s	few seconds
Shear turbulence	0.1–10 m	0.1–10 m	0.1–1 m/s	few minutes
Water waves	0.1–10 m	1–100 cm	1–10 m/s	seconds to minutes
Convection	10–1000 m	1–1000 m	0.1–1 m/s	hours, days or seasons
Atmospheric systems:				
Urban airshed	1–10 km	100–1000 m	1–10 m/s	hours
Sea breeze	1–10 km	100–1000 m	1–10 m/s	hours
Thunderstorms	1–10 km	100–5000 m	1–10 m/s	hours
Mountain waves	1–10 km	10–1000 m	1–10 m/s	days
Tornado	1–10 km	100–1000 m	100 m/s	minutes to hours
Hurricane	1–10 km	10 km	100 m/s	days to weeks
Weather patterns	1–10 km	10 km	1–10 m/s	days to weeks
Climatic variations	Global	50 km	1–10 m/s	decades and beyond
Water systems:				
Aquifers	1–1000 km	10–1000 m	1–10 m/s	seasons to decades
Wetlands	10–1000 m	1–10 m	1–10 m/s	days to seasons
Small stream	1–10 m	0.1–1 m	1–10 m/s	seconds to minutes
Major river	10–1000 m	1–10 m	1–100 cm/s	minutes to hours
Lakes	1–100 km	10–1000 m	1–10 m/s	days to seasons
Estuaries	1–10 km	1–10 m	0.1–1 m/s	hours to days
Oceanic tides	basin size	basin depth	0.1–10 m/s	hours
Coastal ocean	1–100 km	1–100 m	0.1–1 m/s	few days
Upper ocean	10–1000 km	100–1000 m	1–100 cm/s	weeks to decades
Abyssal ocean	global	basin depth	0.1–1 cm/s	decades and beyond

Moreover, a large number of substances of environmental concern are simultaneously subjected to various transformation phenomena:

- *physical transformation*, caused by physical laws, such as radioactive decay;
- *chemical transformation*, produced by chemical reactions, such as hydrolysis and photolysis;
- *biochemical transformation*, due to biological processes, such as the uptake of nutrients by organisms and oxidation of organic matter.

When they reduce the level of contamination or the pollution hazard, transformation phenomena are beneficial to the environment. There are occasions, however, when the transformation creates a new substance that has adverse effects, called a secondary pollutant. A most important example of this is the formation of tropospheric ozone from nitrogen oxides by photochemical reactions.

Both transport and transformation processes investigated by EFM can occur either within one of the environmental fluid systems (atmosphere, hydrosphere) or at the interface with

the lithosphere or biosphere. An *environmental interface* can be defined as a surface between two either abiotic or biotic systems that are in relative motion and exchange mass, heat and momentum through biophysical and/or chemical processes. These processes are fluctuating temporally and spatially. The study of interfaces is a crucial prerequisite toward a better understanding of the environment, but it is enormously complex and it is expected to occupy scientists for some significant time in the future (Mihailović and Balaz, 2007).

In EFM, four main environmental interfaces need be considered, which are: air–water, air–land, water–sediment, and water–vegetation interfaces. They are affected by the following processes:

- The *air–water interface* is subjected to momentum, heat and mass transfer. the main actor in *momentum transfer* is the shear stress exerted as the result of a difference between wind speed and direction in the air and the surface velocity in the water. The shear stress generates a wave field, part of which goes to creating surface drift currents. the accompanying *surface heat transfer* represents a relevant source or sink of heat in producing the thermal structure of a water body. Finally, several chemicals are transferred upward to the air or downward to the water depending on the substances involved and departure from equilibrium (Henry's Law). This process is termed *gas-transfer*. Hence, gas transfer of a volatile or semi-volatile chemical is a two-way process involving both dissolution by the water and volatilization into the air across an air–water interface. Finally, *air-entrainment* is the entrapment of undissolved air bubbles and air pockets by the flowing water (chanson, 2004);
- The *air–land interface* is a complex one that connects non-liquid terrestrial surfaces with the atmosphere. Examples are bare soil, desert, rocky land, ice, vegetative cover, buildings, and their non-homogeneous combinations. The physical state of the atmosphere is defined by its *temperature*, *humidity*, *wind speed*, and *pressure*. The question is: How does the atmosphere evolve its physical state? To answer this question we must determine the fluxes of *heat*, *energy* and *momentum* into and out of the air–land interface. A particular type of interface is the *biosphere*, which introduces characteristics of living organisms. The rates at which trace gasses and energy are transferred through the air–biosphere interface depend upon a *complex* and *non-linear* interplay among physiological, ecological, biochemical, chemical and edaphic (soil) factors as well as meteorological conditions;
- The *water–sediment interface*, which is very difficult to define precisely, is subjected to several complicated physical and chemical processes responsible for exchange of solids and solutes between the water column and the sediment bed. The physical processes involving the solids are *settling*, *sedimentation* and *resuspension*. settling is the downward movement of sediment particles due to their negative buoyancy. Sedimentation occurs once the settled particles reach the bottom and join the sediment bed, while resuspension is the process by which particles of the bed are entrained upward into the water column, usually by shear flow. Furthermore, *diffusive exchanges*, either molecular or turbulent and including *adsorption/desorption*, can occur between the water column and the sediment bed. Also, the bed solutes can be subjected to advection and diffusion. *Bioturbation* is the mixing of sediment by small organisms, usually worms, living in the upper layers of the sediment;
- The *water-vegetation interface* is a relatively new subject of study, which considers the interaction between the flowing waters and submerged and/or emerged vegetation. Besides the transfer of substances between vegetation and water, the problem is complicated by the fact that the vegetation can deform under the passage of the water flow.

The previous overview points to the number and complexity of EFM processes occurring at the interfaces among environmental systems and explain why theoretical, laboratory,

field and numerical studies have only begun recently to investigate EFM processes at environmental interfaces and to elucidate their role and effects on environmental quality.

1.6 CHALLENGES OF ENVIRONMENTAL INTERFACES MODELING

As previously outlined, the field of EFM abounds with various interfaces and can serve as an ideal platform for the application of new and fundamental approaches leading towards a better understanding of interfacial phenomena. The preceding definition of an environmental interface broadly covers the requisite multidisciplinary approach so necessary in environmental sciences and yet permits approach by well established scientific methods that have been developed to study the environment within approximations and assumptions designed to alleviate the complexity of the problems. Nonetheless, we anticipate that the next generation or two of EFM scientists will be confronted by the following challenges.

First is the seemingly perpetual problem of fluid turbulence. Without hoping for a miraculous new theory for all forms of fluid turbulence, EFM scientists are asked to continue forging new methods to deal effectively with its effects on environmental processes, particularly shear flow, convection, instabilities, and contaminant dispersion.

On the field side of the discipline, there is a strong need for observational techniques, including new instrumentation, to measure concentrations and fluxes in the very proximity of interfaces. This is particularly challenging not only because interfaces tend to be ill-defined at close range but also because instrumental probes run the risk of interfering with the situation that one is trying to observe in its natural manifestation. In that respect, remote sensing offers a unique advantage.

This leads us to another and relatively profound question: In which circumstances should we view the environmental interface as a fractal surface? And, if such is the case, how can this be accomplished most clearly and effectively in our models?

It goes without saying that computer models are ever more powerful. However, the time when a computer exists that will permit the simulation of an environmental system down to its micro-level (ex. urban-scale airshed model down to the size of an individual sediment particle or river model down to the size of an air bubble) is still in the distant future. Parameterization techniques will continue to be necessary for the undetermined future. Yet, these techniques are not stagnant; they need to evolve as the shortest resolved scale diminishes in the numerical models and as our discoveries and understanding of the factors at play demand the inclusion of evermore more processes in the models.

One particular need for in-depth inquiry, which arises in the context of environmental remediation, is the study of particle-particle interaction inside of a flowing fluid. The current state of the art remains largely empirical, and serious efforts need to be made to move gradually toward a science-based approach to the related processes.

At the opposite end of the spectrum, on the very largest spatial and temporal scales, EFM scientists are called to be ever more conscious of planetary limits and climatic implications. Acute questions concern the sustainability of water resources and the capacity of environmental systems (atmosphere, hydrosphere, lithosphere and biosphere) to assimilate our waste.

EFM modellers base their calculations on mathematical models for the simulation and prediction of different processes, which are most often non-linear, describing relevant quantities in the field of consideration (Monteith and Unsworth, 1990). Many investigators have proved that complex dynamical evolutions lead to chaotic regime. A small *tuning* of initial conditions may lead the numerical model to instability if the system is a chaotic one. The aforementioned instabilities can be generated in temporal fluctuations on all space-time scales ranging from turbulence to climate. These kinds of uncertainties tend to take place at

the interface between two environmental media. The land–air interface of the lower atmosphere and many other environmental interfaces are illustrative examples of the occurrence of irregularities in the temporal variation of some geophysical quantities (Figure 1.3).

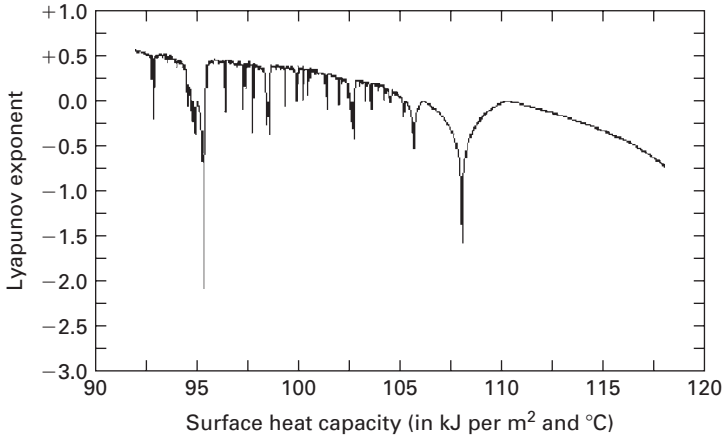

Figure 1.3. Dependence of Lyapunov exponent on soil surface heat capacity. The spectrum is obtained from dimensionless temperature as solution of the energy balance equation for the interface between land and lower atmosphere when the energy is exchanged by all three known mechanisms. Positive values correspond to temporal growth and hence chaotic behaviour.

APPENDIX—LIST OF SYMBOLS

List of Symbols

Symbol	Definition	Dimensions or Units
H	vertical length scale	[L]
L	characteristic length scale	[L]
Q	kinematic heat flux	$[\mathrm{K\,L\,T^{-1}}]$
Re	Reynolds number	
Ri	Richardson number	
T	time scale	[T]
U	fluid velocity	$[\mathrm{L\cdot T^{-1}}]$
V	volume exchanged	$[\mathrm{L^3}]$
g	gravitational acceleration constant	$[\mathrm{L\,T^{-2}}]$
h	system height	[L]
m	mass	[M]
u^*	shear or friction velocity	$[\mathrm{L\cdot T^{-1}}]$
z	vertical coordinate	[L]
$\Delta\rho$	change in density value	$[\mathrm{M\,L^{-3}}]$
α	thermal expansion coefficient	$[\mathrm{K^{-1}}]$
κ	Von Karman constant	
μ	fluid dynamic viscosity	$[\mathrm{M\,L^{-1}\,T^{-1}}]$
ρ	fluid density	$[\mathrm{M\,L^{-3}}]$
τ	shear stress	$[\mathrm{M\,L^{-1}\,T^{-2}}]$

REFERENCES

Brutsaert, W., 2005, *Hydrology: An Introduction*, Cambridge University Press, 618 pp.

Chanson, H., 2004, *Environmental Hydraulics of Open Channel Flows*, Elsevier Butterworth-Heinemann, 430 pp.

Chow, V. T., 1959, *Open-Channel Hydraulics*, McGraw-Hill, 680 pp.

Cushman-Roisin, B., 1994, *Introduction to Geophysical Fluid Dynamics*, Prentice Hall, 320 pp.

Gualtieri C., 2006, Verification of wind-driven volatilization models. *Environmental Fluid Mechanics*, **6**, pp. 1–24

Imberger, J., ed., 1998, *Physical Processes in Lakes and Oceans*, American Geophysical Union, 668 pp.

Mihailović, D., and Balaz, I., 2007, An essay about modelling problems of complex systems in environmental fluid mechanics. *Idojaras* (In press).

Monteith, J. L., and Unsworth, M., 1990, *Principles of Environmental Physics, Second Edition*. Elsevier, 304 pp.

Munson, B. R., Young, D. F., and Okiishi, T. H., 1994, *Fundamentals of Fluid Mechanics*, 2nd ed., John Wiley & Sons, 893 pp.

Pope, S. B., 2000. *Turbulent Flows*, Cambrige University Press, 771 pp.

Rodhe, H., Charlson, R. J., and Anderson, T., 2000, Avoiding circular logic in climate modeling. An editorial essay, *Clim. Change*, **44**, 409–411.

Singh, V. P., and Hager, W. H., eds., 1996, *Environmental Hydraulics*, Kluwer Academic Pub., 415 pp.

Sturm, T. W., 2001, *Open Channel Hydraulics*, McGraw-Hill, 493 pp.

Part one
Processes at atmospheric interfaces

CHAPTER TWO

Point source atmospheric diffusion

Borivoj Rajković
Institute for Meteorology, University of Belgrade, Belgrade, Serbia

Ilija Arsenić
Faculty of Agriculture, University of Novi Sad, Novi Sad, Serbia

Zoran Grsić
Institute of Sciences Vinča, Belgrade, Serbia

ABSTRACT

This chapter covers some theoretical aspects and several areas of modelling of atmospheric dispersion of a passive substance. After the introduction there is a section with fundamentals about molecular diffusion. It has a derivation of Fick's law including sinks and sources of a passive substance. Some simple cases of source and sinks are presented and their physical meaning discussed. In the end, we examine the point source substance diffusion in the case of a constant wind.

After molecular mechanism of diffusion, we look at its generalization, the turbulent diffusion, how it arises and its problems from the modelling point of view. Finally, we present some results like Taylor's theorem and Richardson's approach.

The second part of the chapter covers the economical models for the point source diffusion. The starting point is Gaussian model. First, we give a derivation of the concept and its several variants that are most common. Next, we discuss some of the limitations that are inherent to this approach, and present an example where one gets quite nice results in spite of all possible criticism of the Gaussian approach. The standard Gaussian model has serious problems in two situations, when the wind is changing either in time or in space or if the size of the domain is large. In order to address these problems modellers have taken the next step creating the concept of Puff models. Instead of a single puff and its advection downwind, together with the appropriate lateral spreading, now there is a series of such puffs, which are consequently released. Spreading and advection of each puff is done according to its position and the moment of release; thus, such model is able to take into account possible changes/variations both in time and space. We present the concept and its basic characteristics and then we offer some ideas of its potential. Finally, we show several examples where this approach had been used.

Whether we have Gaussian or Puff type model, in any case, we still have to be able to calculate the amount of the deposited substance on the ground at a given location. So, this chapter ends with subsection about the parameterizations of wet and dry deposition.

2.1 FOREWORD

It is clear that in the era of massive pollution of air, water and land, there is a great need for a reliable method of calculating spreading of various substances that are constantly injected in the atmosphere. The nature of the flow in the lowest part of the atmosphere makes this task quite a complicated one. So, we set an additional condition that method of calculation should have some degree of efficiency even if we have to sacrifice some of the features of the problem. Fortunately, a combination of empirical experience and theory that has been advanced in the last 100 years and the rapid progress in the computer power make it possible to approach the problem and have a decent level of success.

The usual starting point in the problem of diffusion of a passive substance is the so called "point" source which may be either instantaneous where we have a single "puff" emitted or continuous with a release that lasts for some time. From the methodological point of view, starting point can be molecular diffusion. After we have introduced basic concepts and given some results we can start with so called turbulent diffusion. This concept is trying to take into account the turbulent nature of the atmospheric flow. That turned out to be and still is a very complex problem yet unsolved. Some of the basic parameters, such as the variance of the substance concentration both in direction of the wind and in the lateral directions, are still not expressed in terms of the velocity fields. This is well known problem of the "closure" of the equations of motions. There are several approaches in solving this problem but none are complete solution of the problem. Fortunately, from the large accumulation of measurement data, values of these basic parameters are known with sufficient accuracy. In combination with some theory, they constitute an acceptable tool in solving the problem.

The class of models thus formed are Gaussian and later Puff type models. They are a combination of empirical experience and a classical Fick's approach to the problem of diffusion. From the pure theoretical point of view we have two important results/concepts in treatment of the turbulent diffusion, Taylor's theorem and Richardson's formulation of the problem. Taylor's theorem explains why turbulent diffusion is scale dependent problem and even makes a prediction of the spreading of a "cloud" of a passive substance at the very beginning stage and at the final stage. Beginning and final stage relative to the integral time scale. Interestingly, at about the same time Richardson developed a theory that offered a radical new approach to the solution of the problem. He substitutes a new variable the so-called *distance–neighbour function* that depends only on the scale of the spreading cloud for density distribution in x, y and z. From the mathematical point of view we are solving a partial differential equation by introducing an integral transformation which leads to a new equation of the same form as Fick's equation but with a *variable* coefficient of "viscosity". He managed to get the form of the new mixing coefficient using all available empirical data. Unfortunately, the theory does not contain the "inverse" transformation from the distance–neighbour function to the normal distribution of passive substance in 3-D (x, y, z) space. There is an alternative, at least in theory. We might seek the solution in the framework of full three dimensional prognostic model, very much like the ordinary problem of weather forecasting. The problem is that usually we do not have sufficient knowledge about the starting wind field structure and, even less, about the changes that occur at the boundaries of the domain in which we are trying to make the prediction.

So, for the time being if efficiency of the method is of paramount importance one would still work with a Gaussian type model with all its enlargements that will account for some of its deficiencies. If computer power is not an issue and the problem's setup allows, we can use Puff type model. In the end, we should mention the inverse modelling techniques, such as those based on the Bensian statistics or Kalman filtering.

2.2 DIFFUSION IN THE ABSENCE OF THE WIND

Diffusion is a term generally used for *molecular* dispersion of a passive substance consisting of gasses or very small particles. The basic quantity is concentration of the substance, χ, which can be either the number of particles in a unit volume and has dimension of $[L^{-3}]$, or the amount of mass in one kilogram of air expressed in non-dimensional units or the volume of gas in a unit volume of air. The assumption that particles are very small means that we can neglect the influence of gravity and effectively treat the substance as a gas.

In a relatively calm weather, the diffusion goes down the gradient of its concentration, i.e. from the region of higher concentration to the regions of smaller concentrations. The relation between flux, which is a mass of substance that is transported through the unit area in one second, and the gradient of concentration, can be expressed by Fick's law of diffusion. The basic assumption is that this transport is *proportional* to the gradient of the concentration. Let the sides of the elementary volume be along the coordinate axes then the flux through the unit area orthogonal to x-direction is

$$F(x) = -D\frac{\partial \chi}{\partial x}. \tag{2.1}$$

Constant of proportionality D can be derived from the molecular considerations within the framework of ideal gas. Its value is about $10^{-7}-10^{-5}$ $[LT^{-1}]$ depending on the kind of gas. For the air we have the number $Dair \approx 10^{-5}$. The minus sign in Equation (2.1) denotes that the transport is *down* the gradient of concentration. Convergence of that flux gives the rate of change for χ,

$$\frac{d\chi}{dt} = \frac{dF}{dx} \tag{2.2}$$

which, under Fick's assumption, becomes:

$$\frac{d\chi}{dt} = \frac{d}{dx}\left(D\frac{d\chi}{dx}\right). \tag{2.3}$$

In three dimensions we have

$$\frac{d\chi}{dt} = \nabla(D\nabla\chi). \tag{2.4}$$

Constant D is kept "behind" differential operator for the more general case of variable D. That is the case in turbulent diffusion when the flow is turbulent. Finally, if we have sources or sinks, with known rates *Src* and *Snk* the diffusion equation becomes:

$$\frac{\partial \chi}{\partial t} = \nabla(D\nabla\chi) + Src + Snk. \tag{2.5}$$

The *Src* measures the amount of gas being formed in a chemical transformation or the amount of pollutant that is emitted from a chimney or some other point or dispersed source, etc. The same goes for the *Snk* term. In order to avoid terminological confusion, we should note that in the equations of motion the whole diffusion term is viewed as the *Snk* term. So, solving Equation (2.5) means calculation of time evolution of spatial distribution for χ given source(s) and sink(s) with appropriate initial and boundary conditions.

Both, source and sink terms, may represent quite complicated processes so we have to make smaller or larger simplifications which is usually referred to as parameterization. For instance, in the case of a sink term, it is common that the rate of change is *proportional to the amount of the present passive substance*. This is often the case in chemical transformations. Its mathematical form is:

$$Snk = -\sigma\chi, \tag{2.6}$$

where σ is a constant whose meaning will be soon apparent.

In order to get better understanding of the physical meaning of this assumption, we will examine time evolution of χ in the windless case and no diffusion. In that case, one-dimensional version of the Equation (2.5) reduces to:

$$\frac{d\chi}{dt} + \sigma\chi = 0 \tag{2.7}$$

which has the solution

$$\chi_h(t) = \chi_0 \exp(-\sigma \cdot t) \tag{2.8}$$

presented in Figure 2.1, the upper panel. So, this form of the sink term gives the exponential decay of concentration with e^{-1} folding time of $\tau = 1/\sigma$, i.e. after τ seconds the concentration of substance roughly halves.

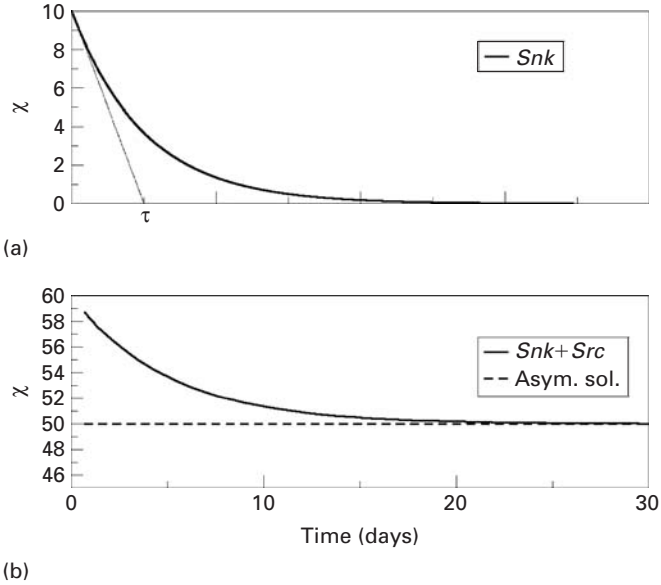

Figure 2.1. The upper panel shows the solution of Equation (2.7) while the lower one of Equation (2.9).

Coming back to the Equation (2.5), in its dimensional version for the *Src* term, we start with the simplest case of the constant source whose strength is equal to f, while the *Snk* term is still of the form in the Equation (2.6). These assumptions give

$$\frac{d\chi}{dt} + \sigma\chi = f. \tag{2.9}$$

Having in mind the solution from the previous case we seek the solution in the form:

$$\chi(t) = \chi_h(t)g(t) \tag{2.10}$$

with $\chi_h(t)$ as

$$\chi_h(t) = \chi_0 \exp(-\sigma \cdot t). \tag{2.11}$$

After inserting this in the equation we get:

$$\chi_h(t) = \chi_0 \exp(-\sigma \cdot t) + \frac{f}{\sigma} \tag{2.12}$$

presented in Figure 2.1, the lower panel.

The solution has two terms. The first term is transitional part of the solution and decays with time. For large time or more precisely for time, $t \approx \tau = 1/\sigma$ emerges a balance between source and sink terms:

$$\sigma\chi \approx Src. \tag{2.13}$$

That will always happen no matter how weak or strong is the source since the sink term is parameterized as proportional to the existing amount of passive material and is always able to "catch up" with the increase of material given by *Src*. But, the most problematic aspect of Equation (2.13) is that all "material" released stays very close to the point of release. So, a mechanism that will spread χ is still missing. The spreading is done by the second derivative, the "diffusion" term. To show that we add the diffusion term while for the source term we choose the point source whose strength is Q. One of the ways to represent point source is through Dirac's delta function. With respect to time we will still restrict ourselves to the steady case, i.e.

$$\sigma\chi = \nu\frac{d^2\chi}{dx^2} + Q\delta(x - x_0). \tag{2.14}$$

Sink term Diffusion Point Source

This is non homogeneous equation that can be solved using the Green's function approach. Away from the source we have

$$\sigma\chi_{\pm} = \nu\frac{\partial^2\chi_{\pm}}{\partial x^2}. \tag{2.15}$$

This is *homogeneous* differential equation with boundary conditions $\chi_{\pm} \to 0$ for $x \to \pm\infty$. Since the coefficients are constant we can immediately write solutions in the form:

$$\chi_{\pm} = C_{\pm} \exp\left[\pm\sqrt{\frac{\sigma}{\nu}}(x - x_0)\right]. \tag{2.16}$$

The non homogeneous solution is a superposition of the solutions with the continuity condition for $\chi(x)$ at $x = x_0$. The condition for the first derivative at the point $x = x_0$ we can get if we integrate Equation (2.14) around that point,

$$\sigma \int_{x_0+\frac{\varepsilon}{2}}^{x_0+\frac{\varepsilon}{2}} \chi dx = v \frac{d\chi}{dx}\bigg|_{x_0+\frac{\varepsilon}{2}} - v \frac{d\chi}{dx}\bigg|_{x_0-\frac{\varepsilon}{2}} + Q. \tag{2.17}$$

If ε is very small there is a balance:

$$v \frac{d\chi}{dx}\bigg|_{x_0+} - v \frac{d\chi}{dx}\bigg|_{x_0-} + Q = 0. \tag{2.18}$$

Together with the continuity of χ we get

$$\chi(x) = \frac{Q}{\sqrt{\sigma \cdot v}} \begin{cases} \exp\left[-\sqrt{\sigma/v}(x - x_0)\right], & x > x_0 \\ \exp\left[-\sqrt{\sigma/v}(x_0 - x)\right], & x < x_0 \end{cases}. \tag{2.19}$$

This solution, shown in the Figure 2.2, is symmetric on both sides of x_0 since we have the constant coefficients problem. So, in the case of molecular diffusion and sink term whose "activity" is proportional to the amount of the passive substance we get again exponential decay, but now in space, away from the point source. The width of the distribution is expressed through the ratio of σ/v. As before $\sigma \cdot \chi$ term keeps the passive substance close to the source while diffusion term spreads it away from the source.

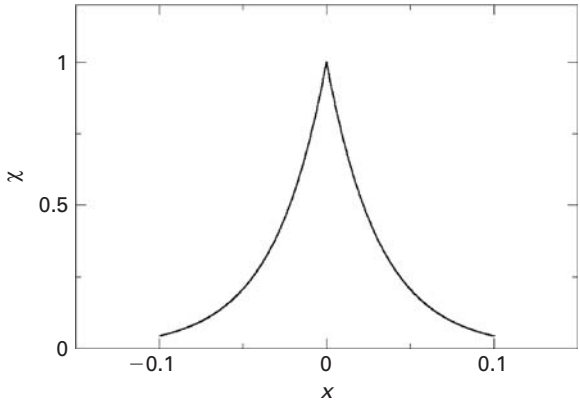

Figure 2.2. Graphical representation of the solution of the Equation (2.14). Note the *symmetry* in the x direction.

Relative strength of those two terms will decide how wide/narrow is the cloud of released material.

2.3 DIFFUSION IN THE PRESENCE OF WIND

Now we introduce motion in the problem i.e. of *advection* of a passive and conservative substance. A passive substance is a substance whose presence does not influence motion but is only carried around by the wind. For instance, water vapour can be viewed as such until condensation occurs. Smoke is another example. In small concentrations it can also be regarded as passive substance. But in the situation of a large volcano eruption, it can block the sun and therefore influence not only the motion but in the extreme event even the whole climate. In the conservative case we have

$$\frac{d\chi}{dt} = 0, \tag{2.20}$$

or explicitly

$$\frac{\partial \chi}{\partial t} + v \cdot \nabla \chi = 0. \tag{2.21}$$

If the velocities in the problem are much smaller then the speed of sound, we can assume that we have incompressible fluid for which continuity equation assumes quite simple form:

$$\nabla \cdot (v\chi) = 0. \tag{2.22}$$

This allows us to write conservation equation in the flux form as:

$$\frac{\partial \chi}{\partial t} + \nabla \cdot (v\chi) = 0. \tag{2.23}$$

Next we show (prove) that with the appropriate initial and boundary conditions the conservation equation with *Snk* as in Equation (2.6) and general *Src* term:

$$\frac{\partial \chi}{\partial t} + \nabla \cdot (v\chi) + \sigma\chi = f \tag{2.24}$$

has a unique solution.

Let us consider a cylindrical region G bounded by side with area S and at the top and bottom by surfaces *St* and *Sb*, respectively. We will denote the initial conditions with χ_0 and the boundary conditions with χ_s, valid at the sides of the cylinder S. For the velocity field we will assume the *no inflow condition*, i.e. normal velocity component is zero at S and that vertical velocity is also zero at the bottom and the top of the cylinder

$$\begin{aligned} u_n &= 0 \quad \text{at} \quad S \\ w &= 0 \quad \text{at} \quad z = 0;\ z = H. \end{aligned} \tag{2.25}$$

First we multiply Equation (2.24) with χ and get

$$\frac{\partial \chi^2}{\partial t} + \nabla \cdot (v\chi^2) + \sigma\chi^2 = f\chi. \tag{2.26}$$

If we integrate it over the domain V, over time $0 < t < T$ we get

$$\int_V \frac{\chi^2}{2} dV \Big|_{t=T} - \int_V \frac{\chi^2}{2} dV \Big|_{t=0} + \int_{t=0}^{T} dt \int_V \nabla \left(\frac{v\chi^2}{2} \right) + \sigma \int_{t=0}^{T} dt \int_V \chi^2 dV = \int_{t=0}^{T} dt \int_V f \chi \, dV. \tag{2.27}$$

We then apply Gauss–Ostrogradsky's theorem, the transformation of the volume integral into surface integral:

$$\int_V \nabla \cdot \left(\frac{v\chi^2}{2} \right) dV = \int_S \frac{u_n \chi^2}{2} \, ds \tag{2.28}$$

and get

$$\int_V \frac{\chi^2}{2} dV \Big|_{t=T} - \int_V \frac{\chi^2}{2} dV \Big|_{t=0} + \int_{t=0}^{T} dt \int_S \frac{u_n \chi^2}{2} \, ds + \sigma \int_{t=0}^{T} dt \int_V \chi^2 \, dV = \int_{t=0}^{T} dt \int_V f \chi \, dV. \tag{2.29}$$

Now let us introduce new variables u^+ and u^- defined as

$$u^+ = \begin{cases} u_n, u_n > 0 \\ 0, u_n < 0 \end{cases} \tag{2.30}$$

and

$$u^- = u_n - u^+. \tag{2.31}$$

With these definitions Equation (2.27) can be rewritten in the form

$$\int_V \frac{\chi^2}{2} dV \Big|_{t=T} + \int_{t=0}^{T} dt \int_S \frac{u_n^- \chi^2}{2} ds + \sigma \int_{t=0}^{T} dt \int_V \chi^2 dV = \int_V \frac{\chi^2}{2} dV \Big|_{t=0} - \int_{t=0}^{T} dt \int_S \frac{u_n^- \chi^2}{2} ds + \int_{t=0}^{T} dt \int_V f \chi \, dV. \tag{2.32}$$

Now suppose that there are two, *different*, solutions, χ_1, χ_2. In that case, due to the linearity of the governing equation their difference is also a solution, i.e.

$$\frac{\partial(\chi_2 - \chi_1)}{\partial t} + \nabla v(\chi_2 - \chi_1) + \sigma(\chi_2 - \chi_1) = 0. \tag{2.33}$$

If we introduce a new variable ξ, defined as,

$$\chi_2 - \chi_1 = \xi, \tag{2.34}$$

we have

$$\frac{\partial \xi}{\partial t} + \nabla \cdot v\xi + \sigma\xi = 0 \tag{2.35}$$

while the boundary conditions

$$u_n = 0 \quad \text{at} \quad S; \quad \text{with} \quad u_n < 0 \tag{2.36}$$

now become

$$\xi = 0 \quad \text{at} \quad S; \quad \text{with} \quad u_n < 0 \tag{2.37}$$

and the integral Equation (2.33) becomes

$$\int_V \frac{\xi^2}{2} dV \Bigg|_{t=T} + \int_{t=0}^{T} dt \int_S \frac{u_n^+ \xi^2}{2} ds + \sigma \int_{t=0}^{T} dt \int_V \xi^2 \, dV = 0 \tag{2.38}$$

Since all integrands are positive definite, the above relation is true only if $\xi = 0$, which means that

$$\chi_2 - \chi_1 = \xi. \tag{2.39}$$

With that we have proved the uniqueness of the solution of the diffusion equation.

Next we analyze the wind case, with the point source, in the same way that we analyzed the windless case. If we denote wind speed with u the governing equation is

$$u\frac{d\chi}{dx} + \sigma\chi = v\frac{d^2\chi}{dx^2} + Q\delta(x - x_0). \tag{2.40}$$

Away from the source we have homogeneous equation(s)

$$u\frac{d\chi_\pm}{dx} + \sigma\chi_\pm = v\frac{d^2\chi_\pm}{dx^2} \tag{2.41}$$

with the same boundary conditions as in the windless case $\chi_\pm \to 0$ for $x \to \pm\infty$. We seek particular solutions of Equation (2.41) in the form

$$\chi_\pm(x) = C_\pm \exp[\pm\lambda(x - x_0)] \tag{2.42}$$

which, upon the substitution, leads to the quadratic equation for λ

$$\lambda^2 + \frac{u}{v}\lambda - \frac{\sigma}{v} = 0 \tag{2.43}$$

with roots

$$\lambda_{\pm} = -\frac{u}{2v} \pm \sqrt{\frac{\sigma}{v} + \frac{u^2}{4v^2}}. \tag{2.44}$$

Due to the condition $\chi_+ \to 0$ as $x \to +\infty$ and because

$$\frac{u}{2v} < \sqrt{\frac{\sigma}{v} + \frac{u^2}{4v^2}} \tag{2.45}$$

we discard the λ solution.

From the continuity of $\chi\,(x)$ and its first derivative we finally get

$$\chi(x) = \frac{Q}{\sqrt{\sigma \cdot v}} \begin{cases} \exp\left[-\left(\sqrt{\dfrac{\sigma}{v} + \dfrac{u^2}{4v^2}} - \dfrac{u}{2v} \right)(x - x_0) \right], & x > x_0 \\ \exp\left[-\left(\sqrt{\dfrac{\sigma}{v} + \dfrac{u^2}{4v^2}} + \dfrac{u}{2v} \right)(x_0 - x) \right], & x \le x_0 \end{cases} \tag{2.46}$$

Depending on the sign of u (here we take $u > 0$) typical forms of these solutions are presented in the Figure 2.3.

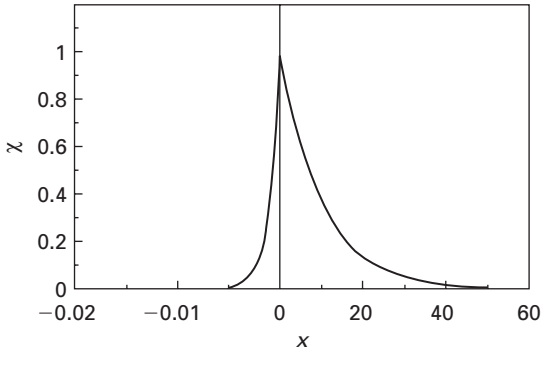

Figure 2.3. Graphical representation of the solution of the Equation (2.27). Note the *asymmetry* in the x direction.

Unlike the case of solution of Equation (2.14) this solution exhibits space *asymmetry* which is a consequence of the presence of wind. Upwind we have "narrowing" of the distribution while downwind "broadening" occurs.

2.4 TURBULENT DIFFUSION

So far we have had diffusion (spreading) of a passive substance by the molecular processes only. Due to the fact that diffusion coefficient is in that case a constant, mathematical treatment of that problem is relatively easy. But, if a passive substance is released into the atmosphere, most likely close to the ground, measurements show that spreading is much stronger, by several orders of magnitude, than the calculations for the molecular diffusion suggest. The reason for that is that flow near the ground is always turbulent. The main characteristic of such flows is that they consist of large number of eddies with very different sizes which constantly develop and decay. In the case of steady state turbulence, the distribution of number of eddies is approximately constant. Its shape depends on several parameters. The basic one is the amount of turbulent kinetic energy (TKE) and the next most important is viscosity. The size of TKE depends on the wind shear and local stability near the ground. The existence of eddies means that instead of molecular movement we have large number of bigger and smaller vortices that carry around passive substance, i.e. we have extremely complicated pattern of advection field resulting in very efficient diffusion. The biggest eddies are of the order of several hundreds of meters while the smallest one are small enough so that viscous dissipation is sufficient to transform all TKE into heat. This prevents the formation of even smaller vortices and we are referring to the size of these, smallest elements as Kolmogorof's scale. Because of such large difference from the ordinary diffusion a new name has been introduced turbulent diffusion.

Even such short description of the turbulent diffusion is sufficient to indicate that its mathematical treatment must be extremely difficult. The spread of a cloud of a passive substance results from the nonlinear interaction of the turbulent elements of the surrounding air and eddies of a passive substance. The nature of the nonlinear interaction is that it is local. To show that, let us assume that at a particular moment our cloud is very small relative to the turbulent element so it is embedded in it. In that case cloud will be carried around but without changes in its dimensions. This is depicted in the left sketch in Figure 2.4. Grey is the cloud while in white we have an air eddy. The opposite would be that we have very small eddies of air impinging on a relatively large cloud (the right part of the same figure, where in white are turbulent element of the air while in grey is the cloud). Air will just mix better the material inside the cloud but again without significant change in cloud's overall size. But, if we have interaction of the turbulent elements of roughly the same size as the cloud's (the central part of the same figure), then the "left"/ "right" edge of the cloud will be extended by the eddy there and thus roughly doubling the size of the cloud.

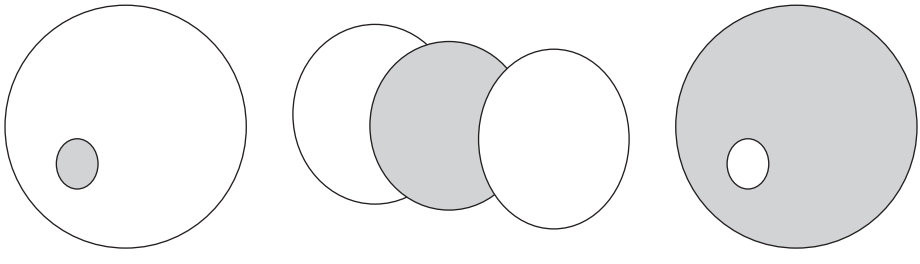

Figure 2.4. Sketch of the three possible situations in relative scales between turbulent elements (white) and cloud (grey).

The same conclusion comes from a simple analysis of the nonlinear ($u\partial_x u$) term[1] which will give somewhat more precise result as the above intuitive/graphical reasoning. The second fact that we must take into account is that larger elements have larger velocities. The locality of the interaction together with the velocity dependence on the size of the elements then explains the increase in diffusion rate.

2.5 TAYLOR'S THEOREM

In the introduction to the problem of calculating turbulent diffusion we have highlighted the fact that basic difficulty is in the fact that the rate of expansion of a cloud of a passive substance depends on the "size" of that cloud at that moment. That fact almost prevents us from the Fickian approach in the diffusion calculations. There is a beautiful explanation/picture of that situation which is encompassed in the so called Taylor's theorem. Let us first clarify several concepts that have been so far loosely defined or being surmised intuitively.

The first is the "size" of a cloud of a passive substance. Let us, for the sake of clarity, reduce the geometry to one dimension and let at $x = 0$ be a source of passive substance that continuously releases particles. Further let us assume that their size is very small like smoke, fine dust, pollen etc., so light that we will assume that these particles float in the surrounding air. Now as time passes the released particles will spread away from each other. A possible definition of the cloud size would be the distance from the furthest particle on the left to the furthest particle on the right. But, that is not very clever choice since we know that in every gas like air we have Maxwell's distribution of velocities and these furthest particles could be very far away but in negligible concentration. The more practical choice is through the following mathematical definition:

$$S = \overline{x_i^2}. \tag{2.47}$$

The advantage of this definition is that it takes into account the concentration as well as the distance of particles in the cloud. The mean wind (in the sense of Reynolds's decomposition, has only large scale variations larger then the size of the expanding cloud) will not influence the size of the cloud but rather carry it downstream without the changes in its geometry. That can be taken into account by introducing the movement of the centre of the cloud as the position of it median, i.e.

$$S = \overline{(x_m - x_i)^2} \tag{2.48}$$

with

$$x_m = \frac{1}{N}\sum_{n=1}^{N} x_i. \tag{2.49}$$

[1] Let us have two components with respective wave numbers k_1 and k_2. Then ($u\partial_x u$) will create $sink_1 x \cdot cosk_2 x \cdot sin(k_1 + k_2)x + sin(k_1 - k_2)x$ which means that we have two *new* components with wave numbers $(k_1 + k_2)$ and $(k_2 - k_1)$. If $k_1 >> k_2$ then $k_1 + k_2 \sim k_1$ and nothing new happens. The same goes for $k_1 - k_2 \sim k_1$. Only if $k_2 \sim k_1$ then we get $k_1 + k_2 \sim 2k_1$, i.e. creation of the new wave number (smaller eddy).

Since this is trivial extension of the windless case we will return to the zero wind case and analyze case given by the Equation (2.47). The question is how *fast* does a cloud spread. We will define the "speed" of the increase in size as

$$\frac{dS}{dt} = \frac{d}{dt}\overline{x_i^2}. \tag{2.50}$$

Since differentiating and averaging are commutative operations we have

$$\frac{dS}{dt} = \overline{\frac{d}{dt}x_i^2} \tag{2.51}$$

or

$$\frac{dS}{dt} = \overline{x_i \frac{dx_i}{dt}} = \frac{1}{2}\overline{x_i v_i}. \tag{2.52}$$

If we express the distance of the i-th particle through integral of its velocity, from the beginning of the release till the time t, we can write

$$\frac{dS}{dt} = \frac{1}{2}\overline{v_i \int_0^t v_i(\tau)\, d\tau}. \tag{2.53}$$

Since velocity at the time t is independent of the sequence of the integration and again integration and averaging are interchangeable operations we have

$$\frac{dS}{dt} = \frac{1}{2}\int_0^t \overline{v_i(t) v_i(\tau)\, d\tau}. \tag{2.54}$$

This is the increase of S at the moment t relative to the *beginning* of the release. But, of the greater interest is what is happening relative to this moment, i.e. we would like to change frame of reference, from the moment $t = 0$ to the moment t (see Figure 2.5). The time ξ in this new frame is related to τ as

$$t = \tau + \xi. \tag{2.55}$$

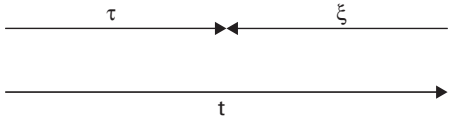

Figure 2.5. Sketch explaining the relation between time relative to the beginning of the release (τ) and time relative to this moment (ξ).

The Equation (2.54) then becomes

$$\frac{dS}{dt} = \frac{1}{2}\int_0^t \overline{v_i(t)v_i(t+\xi)}\, d\xi. \tag{2.56}$$

Using the definition of auto-correlation function:

$$R(t,\xi) = \frac{\overline{v_i(t)v_i(t+\xi)}}{\overline{v_i(t)^2}} \tag{2.57}$$

and concentrating to the case of the homogenous turbulence for which

$$R(t,\xi) = R(\xi), \tag{2.58}$$

we finally get

$$S(t) = \frac{1}{2}\overline{v_i^2}\int_0^t dt' \int_0^{t'} R(\xi)\, d\xi. \tag{2.59}$$

This relation constitutes the Taylor's theorem (Taylor, 1921). Provided that we know the shape of the auto-correlation function, we can calculate the size of the cloud at any moment. Unfortunately, it is even more difficult to get the form of $R(\xi)$, as it is obvious from its definition. So, it seems that we have not gained much. We have expressed the unknown S with another, perhaps even more complicated variable R. Well, if we wanted operational relation, we didn't get one but there are several, very important, points that are hidden in this result. Let us first concentrate to the very beginning of the cloud growth. If the time is really short, i.e. ξ is very small, we can assume that $R(\xi \approx 0) \approx 1$ which immediately gives the result:

$$S(t) = \frac{\overline{v_i^2}}{2}t^2 = const \cdot t^2. \tag{2.60}$$

Actually if we want something that has dimensions of length, we should introduce[2]

$$D = \sqrt{x_i^2} = const \cdot t. \tag{2.61}$$

These two relations are exact derivation and/or confirmation of experimental fact that cloud's expansion rate, in the early stages of expansion, increases with time. Now let us look at the other extreme, i.e. very "long" time after the start of the diffusion. What is very long is

[2] Variable D can serve as the definition of the cloud size.

not yet clear but it will soon become. One of the global parameters that characterizes every auto-correlation function is its integral time scale defined as

$$\int_0^\infty R(\xi)d\xi = T. \tag{2.62}$$

So, if t (or more precisely t') in Equation (2.61) is much larger then T the inner integral's value is close to T. That gives us as the result for D:

$$D = \sqrt{x_i^2} = const' \cdot \sqrt{t} \tag{2.63}$$

Equations (2.61) and (2.63) are telling us that at the beginning of diffusion cloud's size grows linear in time and as the process goes on its growth *slows* down and for the $t >> T$ reduces to the square root of time. The explanation of this result comes from the structure of turbulent flows which is the cause of the spreading. As we have explained earlier, turbulent character of the flow means that flow consists of many eddies of different sizes. Beside the distribution in size of even more importance is the distribution in speed. The fact that we must take into account is that *larger* elements have *larger velocities*. The locality of the interaction together with the velocity dependence on the size of the elements explains the *increase* in diffusion rate. At the beginning small elements are responsible for the turbulent diffusion. As the cloud grows larger, larger and faster elements are widening the cloud. This is seen as the increase of the diffusion rate. Once the cloud is comparable and bigger then the size of the elements with the largest kinetic energy the diffusion rate slows down since there are no more *new* elements faster than the previous one to take over further spreading.

2.6 THE RICHARDSON'S THEORY

Starting point of Richardson's (Richardson, 1926) theory was also the fact that diffusion depends on the scale of the cloud. Therefore he introduces a new variable, so called *distance–neighbour function* $q(l)$, defined as:

$$q(l) \equiv \frac{1}{N}\int_{-\infty}^{\infty} \chi(x)\chi(x+l)\,dx, \tag{2.64}$$

with

$$N = \int_{-\infty}^{\infty} \chi(x)\,dx \tag{2.65}$$

being number of the particles in the cloud which we assume that is *constant* in time. The name for $q(l)$ comes its definition:

- $\chi(x)$: is the number of particles on dx
- $(\chi(x)\,dx)/N$: is that number relative to the total number of particles

- $\chi(x+l)$: is number of particles, on *unit* length at the distance l meters away
- $(\chi(x)\,dx/N)\cdot\chi(x+l)$: is *relative* number of *neighbours* of all particles from section whose length is dx and is l meters away.

When we *add* them all we get a number of neighbours of each particle in a cloud at the relative distance of l meters. For better understanding let us consider a simple distribution $\chi\,(x)$ with constant concentration χ_0 over interval d starting at $x=a$ and 0 elsewhere:

$$\chi(x)=\begin{cases}0, & x<a\\ \chi_0, & a\le x\le a+d\\ 0, & x>a+d\end{cases}. \tag{2.66}$$

From the definition of $q(l)$ and using translation $x\to x+l$ we can show that $q(l)$ is an *even* function and therefore it is sufficient to calculate it only for $l>0$. From Equation (2.66) we get

$$\chi(x)\chi(x+l)=\begin{cases}0, & x<a\\ \chi_0^2, & a\le x\le a+d-l\\ 0, & x>a+d-l\end{cases}. \tag{2.67}$$

If we insert this into Equation (2.64) we get

$$q(l)=\begin{cases}0, & -d<l\\ \chi_0(1+l/d), & -d>l>0\\ \chi_0(1-l/d), & 0<l<d\\ 0, & d<l\end{cases}. \tag{2.68}$$

Both, $\chi(x)$ and its $q(l)$, are shown in Figure 2.6.

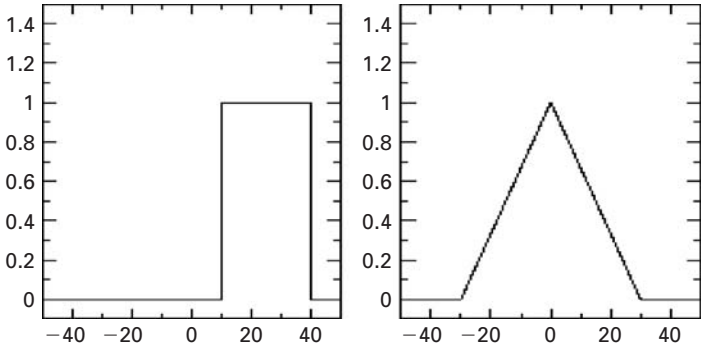

Figure 2.6. On the left, concentration distribution in arbitrary units. On the right, is the distance–neighbour function for that distribution.

The main advantage of $q(l,t)$ over $\chi(x,t)$ is that it depends on l and not on x, i.e. scale of the cloud is the only spatial variable in the problem.

If we want to switch to the new framework of $q(l)$ instead of $\chi(x,t)$ two questions arise. The first is if we can develop the equation for time *evolution* of $q(l,t)$? Given that we are successful in that, we face the second problem, can we create the *methodology* with which we can get the *inverse* $\chi(x,t)$ from $q(l,t)$?

To get the prognostic equation for $q(l,t)$ we start with Equation (2.64) by differentiating it

$$\frac{\partial q(l)}{\partial t} = \frac{1}{N}\int_{-\infty}^{\infty} \frac{\partial}{\partial t}(\chi\chi_l)\,dx = \frac{1}{N}\int_{-\infty}^{\infty} \chi_l \frac{\partial}{\partial t}\chi + \chi\frac{\partial}{\partial t}\chi_l\,dx. \tag{2.69}$$

Now, if the process is of the Fickian type then

$$\frac{\partial \chi}{\partial t} = K\frac{\partial^2 \chi}{\partial x^2} \tag{2.70}$$

and analogously

$$\frac{\partial \chi_l}{\partial t} = K\frac{\partial^2 \chi_l}{\partial x^2}. \tag{2.71}$$

Noticing that differentiation over x and over l are the same, Equation (2.71) can be rewritten as

$$\frac{\partial \chi_l}{\partial t} = K\frac{\partial^2 \chi_l}{\partial l^2}. \tag{2.72}$$

So, Equation (2.69) becomes:

$$\frac{\partial q(l)}{\partial t} = \frac{1}{N}\int_{-\infty}^{\infty} \left(\chi_l \frac{\partial^2 \chi_l}{\partial x^2} + \chi\frac{\partial^2 \chi_l}{\partial l^2}\right) dx. \tag{2.73}$$

If we transform integrand using several identities:

$$\chi_l\frac{\partial^2 \chi}{\partial x^2} + \chi\frac{\partial^2 \chi_l}{\partial l^2} = \frac{\partial^2}{\partial x^2}(\chi_l\chi) - 2\frac{\partial \chi}{\partial x}\frac{\partial \chi_l}{\partial l} - 2\chi\frac{\partial^2 \chi_l}{\partial l^2} + 2\chi\frac{\partial^2 \chi_l}{\partial l^2}, \tag{2.74}$$

$$2\frac{\partial \chi}{\partial x}\frac{\partial \chi_l}{\partial l} - 2\chi\frac{\partial^2 \chi_l}{\partial l^2} = \frac{\partial^2}{\partial x\,\partial l}(\chi\chi_l) \tag{2.75}$$

and

$$2\chi\frac{\partial^2 \chi_l}{\partial l^2} = \frac{\partial^2}{\partial l^2}(\chi\chi_l), \tag{2.76}$$

we finally get

$$\frac{\partial q(l)}{\partial t} = 2K\frac{\partial^2}{\partial l^2}\,q(l). \tag{2.77}$$

The meaning of this is that for the molecular mechanism of diffusion both descriptions, the one using $\chi(x)$ and the other using $q(l,t)$ are equally good. Next we generalize, Equation (2.77) in the form:

$$\frac{\partial q(l)}{\partial t} = \frac{\partial}{\partial l}\left[K(l)\frac{\partial}{\partial l}q(l)\right]. \tag{2.78}$$

Can we find (form) $K(l)$? To do that Richardson analyzed all the data, available to him at that time covering very wide range of scales from the synoptic ones to the smallest one, molecular scales (Figure 2.7). From these data he proposed that $K(l)$ should be

$$K(l) = 0.2l^{3/4}. \tag{2.79}$$

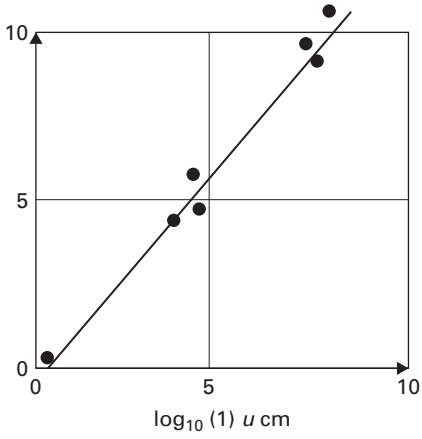

Figure 2.7. Deduced diffusion coefficient from measurements, observations of the processes from the synoptic scale to molecular one (black dots) and suggested linear interpolation of that data. Linear form for the logarithmic scales indicates power function for $K(l)$.

With this relation, Equation (2.78) is complete and ready to serve as the equation for the evolution in space and time for the variable q. The procedure would be as follows, for given concentration distribution we make integral transformation, defined in Equation (2.64), to form $q(l,0)$ and than integrate Equation (2.78) to get $q(l,t)$. What about the second step, the inversion procedure. Unfortunately, he was not successful in that as he was in the first part of the theory. Maybe that was the reason why he left this problem for over 25 years (Richardson, 1952) when he showed that for a limited class of concentration distributions he was able to perform the inversion part. Due to the fact that inversion for any $q(l,t)$ has not be found, general solution of turbulent diffusion problem using Richardson's approach remains still an open problem.

2.7 THE GAUSSIAN MODEL FOR A POINT SOURCE

From both, Taylor's theorem and Richardson's theory, we know that turbulent diffusion of a passive substance has difficulties in dealing with Fick's equation. But, none of them offers

an operational framework that can give an estimate of, for instance, how big is concentration of a passive pollutant around say a factory chimney or some other quasi-point source. There are two different situations regarding the manner in which the material is released. If we have emission with relatively short duration we talk about a puff. If, on the other hand, we have continuous source than we will call it a plume.

In our, highly industrial era number of sources is very large and we are forced to come with some approach that is relatively easy to handle and yet sufficiently accurate to answer the question of spatial distribution of concentration from a source that emits a pollutant into windy and unstable/stable atmosphere. The only possible approach is a combination of theory and experiment. The hope is that elements of the dispersion theory can be parameterized using the field measurements and the rest of it supplied from the Fick's equation. To fulfil that, in England in 1925 near city of Porton series of field experiments (Pasquill and Smith, 1983) were conducted in which a coloured gas was released and its concentration was measured. The purpose of the experiment was to find the spatial distribution of the released substance. The atmosphere was close to neutral with the wind of about 7 [LT^{-1}]. Concentration was measured downwind and in the direction perpendicular to that direction, roughly every 100 meters. From these data an approximate concentration distribution was deduced in the form of the exponential function

$$\chi(x_0, y) = \chi_0 \exp(-ay^r) \tag{2.80}$$

where x_0 is a point in the downwind direction, while y is horizontal distance perpendicular to the x axes. Following these preliminary results from various other experiments, Brahman *et al.* (1952) have analyzed the New Mexico experiments, Crozier and Seely (1955) have analyzed Australian experiments from 1953, Pasquill (1955, 1956) used data from another experiment at Porton, etc. From most of the experimental results general shape of the plume could be expressed as:

$$\chi(x, y, z) = Q \exp[-(by)^r - (cz)^s] \tag{2.81}$$

where x, y, z are distances relative to the source. Parameters b and c depend on the size of the plume in the respective direction. Constant Q is a measure of the rate of emission. If we assume that wind is constant throughout the considered period, the concentration takes the form of a plume whose main axis is downwind, with lateral spared in both directions. The effect of the wind is that it dilutes the concentration. The stronger the wind the smaller the concentration. The amount of the material that is diffused is determined by the strength of the source. Concentration is inversely proportional to the wind's strength,

$$\chi \approx \frac{1}{U}. \tag{2.82}$$

Like in the Taylor's theorem for the measure of lateral spread we take:

$$\sigma_i^2 = \frac{\int_0^\infty x_i^2 \chi dx_i}{\int_0^\infty \chi dx_i}, \quad i = 2, 3. \tag{2.83}$$

Let us note that from the conservation of mass we have:

$$\iint_{y,z} U\chi\, dy\, dz = Q. \tag{2.84}$$

Now, the expression using the above relations can be rewritten in the following way

$$\chi(x,y,z) = \frac{Q}{B_1\sigma_y\sigma_z}\left\{-\left[\left(\frac{\Gamma(3/r)}{\Gamma(1/r)}\right)^{r/2}\left(\frac{y}{\sigma_y}\right)^{r} + \left(\frac{\Gamma(3/s)}{\Gamma(1/s)}\right)^{s/2}\left(\frac{y}{\sigma_z}\right)^{s}\right]\right\}, \tag{2.85}$$

where

$$\frac{1}{B_1} = \frac{rs}{4U}\frac{[\Gamma(3/r)\Gamma(3/s)]^{1/2}}{[\Gamma(1/r)\Gamma(1/s)]^{3/2}}. \tag{2.86}$$

With $r = s = 2$ and using the relations:

$$\Gamma(n+1) = n\Gamma(n) \tag{2.87}$$

and

$$\Gamma(1/2) = \sqrt{\pi} \tag{2.88}$$

we get the so called standard Gaussian form of the plume

$$\chi(x_0,y,z) = \frac{Q}{\sqrt{2\pi}\sigma_y\sigma_z}\exp\left[-\frac{1}{2}\left(\frac{y^2}{\sigma_y^2} + \frac{z^2}{\sigma_z^2}\right)\right]. \tag{2.89}$$

In the end we want to have concentration relative to a fixed point, the beginning of the x axis, the usual position of the source. Then, taking into account the wind we have

$$\chi(x,y,z) = \frac{Q}{\sqrt{2\pi}U\sigma_y\sigma_z}\exp\left[-\frac{1}{2}\left(\frac{y^2}{\sigma_y^2} + \frac{z^2}{\sigma_z^2}\right)\right]. \tag{2.90}$$

All this is valid for the ground sources. If the height of the source is at H we have:

$$\chi(x,y,z) = \frac{Q}{\sqrt{2\pi}U\sigma_y\sigma_z}\exp\left[-\frac{1}{2}\left(\frac{y^2}{\sigma_y^2} + \frac{(z-H)^2}{\sigma_z^2} + \frac{(z+H)^2}{\sigma_z^2}\right)\right]. \tag{2.91}$$

The second term in z direction comes from the fact that with time cloud will spread so much that it will reach the ground. In that case, we can imagine a second source that is mirror image of the original positioned at $-H$ below the ground so that its contribution to the points above the ground starts exactly at the point where the original cloud touched the ground.

In the case of the short release time (puff) we have

$$\chi(x,y,z,t) = \frac{q}{\sqrt{(2\pi)^3}\sigma_x\sigma_y\sigma_z}\exp\left\{-\left[\frac{(x-Ut)^2}{2\sigma_x^2}+\frac{y^2}{2\sigma_y^2}\right]\right\} \times\left\{\exp\left[-\frac{(z-H)^2}{2\sigma_z^2}\right]+\exp\left[\frac{(z+H)^2}{2\sigma_z^2}\right]\right\}. \tag{2.92}$$

Even though we formally differentiate σ_x and σ_y the usual assumption is that there is isotropy in x and y. Obviously, parameters σ_i, $i=1,2,3$ are the centre of the Gaussian approach and most of the "meteorology" is hidden in them. They should reflect the local stability and the parameters that characterize turbulent flow. To express all that with a single number (two numbers) seems a difficult problem. Here again we insert as much of the empirical experience as we can. Actually our starting point, Equation (2.92) has the fact that flow is turbulent and therefore is characterized by lateral spread of passive substance (σ_y and σ_z). Taking into account stability of the atmosphere requires an additional effort. The first attempt is made by Pasquill (1961), later modified by Gifford (1961), and referred to as the Pasquill–Gifford (P–G) stability class. This collective work of several researchers in the interpretation of the available measurements resulted in formation of nomograms (Turner, 1969), shown in Figure 2.8, that have dependence of the σ's in y and z direction for quite wide range of distances. The dashed parts of the curves are actually *extrapolations* of the measured data. The whole range of possible stability states i.e. possible values of $\partial\Theta/\partial z$, where $\Theta(z)$ is potential temperature, were divided into seven categories, labeled as A-F. The next step is to determinate the category (class) using only the standard meteorological data, 2 meters temperature, 10 meters wind and cloud cover. Pasquill and Smith (1983) devised such a scheme presented in Table 2.1. Question of stability was covered only with the position of the Sun. The idea is that high Sun means warmer part of the day and warmer season in which we should expect unstable regime within the PBL. In the next table we show how these categories are determined.

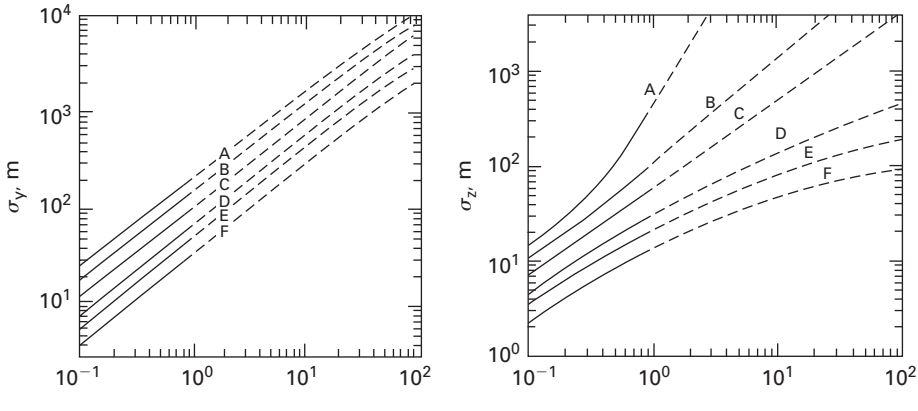

Figure 2.8. On the *left* panel we have downwind variation of the lateral diffusion coefficient σ_y while on the right we have the same for vertical coefficient σ_z.

Later, Briggs (1973) turned these graphs into analytical relations thus making them operational for computers. At this moment we must once again state the assumptions and the

Table 2.1. Determination of categories from wind speed, solar radiation and cloud cover data that is available from the routine measurements.

Surface(10 m) wind speed	Daytime			Nighttime	
	Incoming solar radiation			Cloudiness	
Ms^{-1}				>=4/8	<=3/8
<2	A	A–B	B	–	–
2–3	A–B	B	C	E	F
3–5	B	B–C	C	D	E
5–6	C	C–D	D	D	D
>6	C	D	D	D	D

validity of the results given so far. First from the measurements done over relatively small domains and therefore for the short periods, the concentration distribution in the directions normal to the wind directions was approximated by the exponential curves. These measurements and consequent fits have by their nature some spread. So in order to get formal similarity with the Fickian picture we set values of r and s to 2 because in that case we have *Gaussian* distributions. Beside the spatial variation we have also the question of the time averages. The shorter time average the closer we are to the actual situation. So we have 3 minutes, 10 minutes or hourly σ's. A parameterization has been proposed (Gifford and Hanna, 1973) that takes into account that for the longer times σ should increase:

$$\sigma(t > 10) = \sigma_{10} \left(\frac{t}{t_{10}} \right)^q \tag{2.93}$$

With σ_{10} are denoted values of σ for 10 minutes. Factor q has two values depending on the length of the time interval. Up to an hour $q = 0.2$ while for the longer time, 1 hour $< t <$ 100 hours $q = 0.25$.

In spite of the obvious crudeness of the calculation this approach has the advantage of being very straight forward and needs practically one number, wind at the point of release. Sun's height can be estimated from the astronomy. If there is an additional data, in particular temperature gradient near the ground ,we can refine the expressions for two basic parameters σ_y and σ_z. The concept of Pasquil–Gifford–Turner that σ is the only parameter describing the diffusion process was later parallel by the similarity approach. The group of models based on that concept of similarity has been proposed by several authors Golder (1972), Horst (1979), Nieuwstad (1980) and Briggs (1982) among others. The starting point of the theory is the well known Monin–Obukhov's theory with its length scale

$$L = \frac{\Theta_0 u_*^3}{\kappa \overline{w\theta_0}}. \tag{2.94}$$

The next step then is to relate σ_z to various parameters connected to the Monin–Obukhov's theory:

$$\sigma_y = \sigma_\theta U F_y(u_*, w_*, z/L, z_i) \tag{2.95}$$

and

$$\sigma_y = \sigma_\varphi U F_z(u_*, w_*, z/L, z_i). \tag{2.96}$$

In order to accomplish that, an extensive re-examination of almost all data from the field experiments was done. The basic problem comes from the formulation of Pasquil–Gifford–Turner concept that does not take into account neither sensible and latent heat flux nor z_0. Instead they have insolation alone. Golder in his 1972 paper was able to produce nomograms though made subjectively that relate on the one side pair z_0, L^{-1} to Pasquil–Gifford–Turner categories (A–F).

As an example of calculations that are based on the Gauss model we present estimates of possible pollution coming from a point source for the period of one year, Figure 2.9. The wind is measured at the height of 40 meters which is close to the height of the chimney, which is the possible source of pollution. Wind was averaged on hourly basis, what was taken into account when choosing appropriate σ.

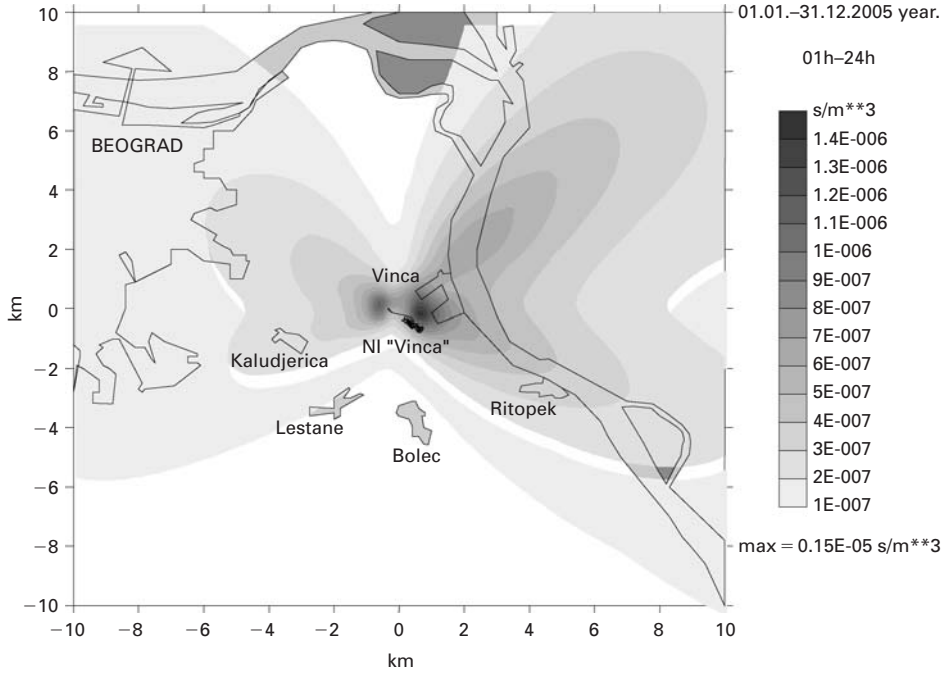

Figure 2.9. The annual concentrations for the year 2005 of a continuous point source for the nuclear facility Vinca near Belgrade, Serbia and Montenegro. Winds data are the standard hourly averaged wind with the direction of the prevailing wind. Wind was measured at the level of 40 meters, approximately the height of the possible source of pollution.

Due to the fast development of the 3-D models that calculate turbulent mixing coefficients from the prognostic equation for turbulent kinetic energy and are therefore considered as being capable to calculate (forecast) changing of concentration in time and space, we made a comparison between such a model (actually a 2-d version x–z plane) and Gaussian model whose results we have already shown in the previous example (Grsić, 1991) In a nut shell he

shows that the largest difference between the two models was not greater than 50%, being most of the time between 25% and 35%.

2.8 THE PUFF MODEL FOR A CONTINUOUS POINT SOURCE

As it was pointed in the introduction, Puff model is an attempt to generalize the Gaussian concept for non-stationary releases or spatially non-homogenous wind or for both. The continuous releases are treated as time–series consecutive instantaneous releases, puffs. The amount of substance q allocated to each puff is the release rate Q multiplied by the time interval Δt between two consecutive releases. So, as the time passes, *number* of puffs that have been released is growing. Each puff is carried around by the wind valid for that particular time interval. Beside changes of the position of the centre, the size of each puff also *increases* due to the turbulent diffusion. Figure 2.10 has the sketch of the actual meandering of the plume, upper panel and its approximation by the series of puffs consecutively released from the point source located at S, the lower panel. Beside puffs, we have grid of cells spanning the space in which we want to calculate concentration distribution. These cells are usually constant volume. Concentration in a cell is the *sum* of the contribution of all puffs, released up to that moment. If the index of receiving cell is denoted by *ic* and index of puffs as *ipf*, than the contribution of that puff is

$$\chi_{ic}(x_{ic}, y_{ic}, z_{ic}, n \cdot \Delta t) = \frac{Q \cdot \Delta t}{\sigma_{ipf}} \exp\left\{ -\left[\frac{(x_{ic} - x_{ipf})^2}{2\sigma_x^2} + \frac{(y_{ic} - y_{ipf})^2}{2\sigma_y^2} \right] \right\} \times \left\{ \exp\left[-\frac{(z_{ic} - z_{ipf})^2}{2\sigma_z^2} \right] + \exp\left[\frac{(2z_{inv} - z_{ipf})^2}{2\sigma_z^2} \right] \right\}, \quad (2.97)$$

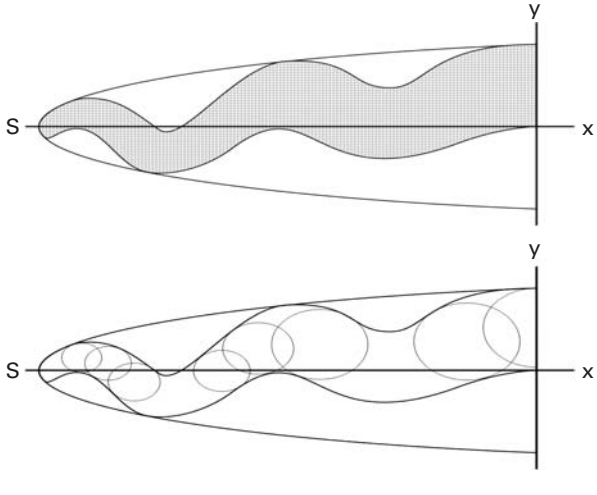

Figure 2.10. Top panel has the actual shape of the cloud and the lower panel represents it using several puffs. Actual number of puffs is usually larger than on the picture where we have reduced their number for better visibility. Also the edge of the real cloud on the top panel is smoothed near its borders.

where σ_{ipf} is defined as:

$$\sigma_{ipf} \equiv (2\pi)^{2/3}\sigma_{x,ipf}\,\sigma_{y,ipf}\,\sigma_{z,ipf}\,. \tag{2.98}$$

It is clear that computational effort in this approach could be several orders of magnitude bigger than the one in the case of the Gaussian plume approach. Two parameters are involved, telling us how often we release each puff and how high is the spatial resolution of the grid in which we calculate the concentration of a passive substance. Logistically (coding) it is also much more difficult. Model has to keep track of the position of each puff and those as the time passes can be large in number. Even when a puff leaves the domain it can come back due to changes of the wind direction. On the other hand, the linear nature of the cell concentration calculation makes this problem easy to parallelise and so run on a cluster rather than on a single processor machine.

Next we show an example of the puff approach to the calculation (Grsić and Milutinovic, 2000) of possible contamination by a continuous point source near the city of Novi Sad. Wind data has been reanalyzed from the anemograph tapes and 10 minutes averages were made. The stability of the atmosphere was characterized with the temperature gradient between temperature at 5 centimetres and 2 meters. Wind was measured at the standard height of 10 meters. The heights of the possible source, the petrochemical plant chimney, was at much greater height so we had to perform the vertical extrapolation of the wind data. Following Holstag and Ulden (1983) and Holstag (1984), Beljars (1982), Beljars and Holstag (1991) and using the Monin–Obukhov approach with the necessary modification for the strongly stable situations we extrapolated winds to 50 meters height.

We have also looked into the differences in the extrapolation results if other methods are used, namely if one has only standard 2 meters temperature. The main goal of the Holstag and Ulden and Holstag papers was exactly that. How, from standard measurements which have only 2 meters temperature, one can *estimate* heat fluxes and therefore use again the Monin–Obukhov approach. Figure 2.11 shows annually averaged diurnal cycle for the measured 10

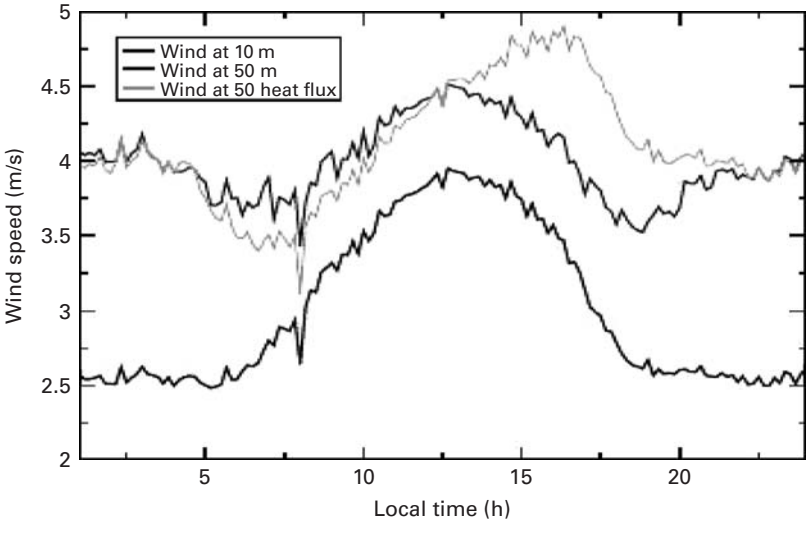

Figure 2.11. The annually averaged diurnal cycle for the measured 10 meters wind, black curve, wind extrapolated at 50 meters using temperature gradient, (grey curve) and wind extrapolated using heat flux estimate, (light grey curve).

meters wind, black curve, wind extrapolated at 50 meters using temperature gradient, (grey curve) and wind extrapolated using heat flux estimate, (light grey curve). Based on these winds we have made an *estimate* of the possible zones of influence. Our runs were 3 hours long and we made calculations twice a day. To estimate the influence of averaging period for the wind, 10 minutes versus 1 hour, we made a comparison of those two averages. This was repeated for all four seasons, 15th of January, 15th of March (Figure 2.12) and 15th of July and 15th of September (Figure 2.13). The year was 1998, for which we have the data of both, the wind and the temperature. The source strength was the same for all runs so the differences come from variations in wind and variations in the local stability between day and night and from their seasonal variations. As we can expect the spatial spread is larger in the case of 10 minute average. The seasonal variations of concentrations are presumably strongly influenced by the local stability rather than by the wind intensity variations.

2.9 DRY AND WET DEPOSITIONS

So far, we have assumed that the amount of passive substance was not changing except for the emission. However, there are many other mechanisms that might change the quantity of the pollutant. We can have a chemical transformation deposition on the ground by both dry and wet deposition, etc. We will concentrate only on the dry and wet depositions and their parameterizations.

The dry deposition occurs when turbulent eddies hit the ground so that material they carry sticks to it. The amount of the material that is deposited can be parameterized as

$$\chi_d = V_d \cdot \chi(x, y, z \approx 0) \tag{2.99}$$

where V_d is the so called deposition velocity, [LT^{-1}]. Its typical magnitude is about $\sim$1 mm/s. In the simplest case, it depends only upon the friction velocity u_* and the mean wind (Thykier–Nielsn and Larsen, 1982)

$$V_d = \frac{u_*}{U}. \tag{2.100}$$

In a more general case, there could be included the so called aerodynamic resistance (r_a), the resistance representing viscous sub-layer (r_v) and the resistance representing characteristics of the ground, bulk resistance (r_b). Then Equation (2.100) has three terms:

$$V_d = \frac{1}{r_a + r_v + r_b}. \tag{2.101}$$

There are two possibilities in treating the removed material. The first is the so called *source–depletion*, where we add all depositions downwind and subtract them from the source. The other, called *surface–depletion*, calculates the flux of material downwind and is represented as a negative source. The second one is more realistic but is computationally more complex. We should also take into account whether we have vapours (gases) or particles. In any case different materials have different deposition rates on different surfaces. We can find deposition parameters by direct measurements at the site and then use those numbers through some interpolation procedure. This is of course the best approach but is expensive in both, time and money.

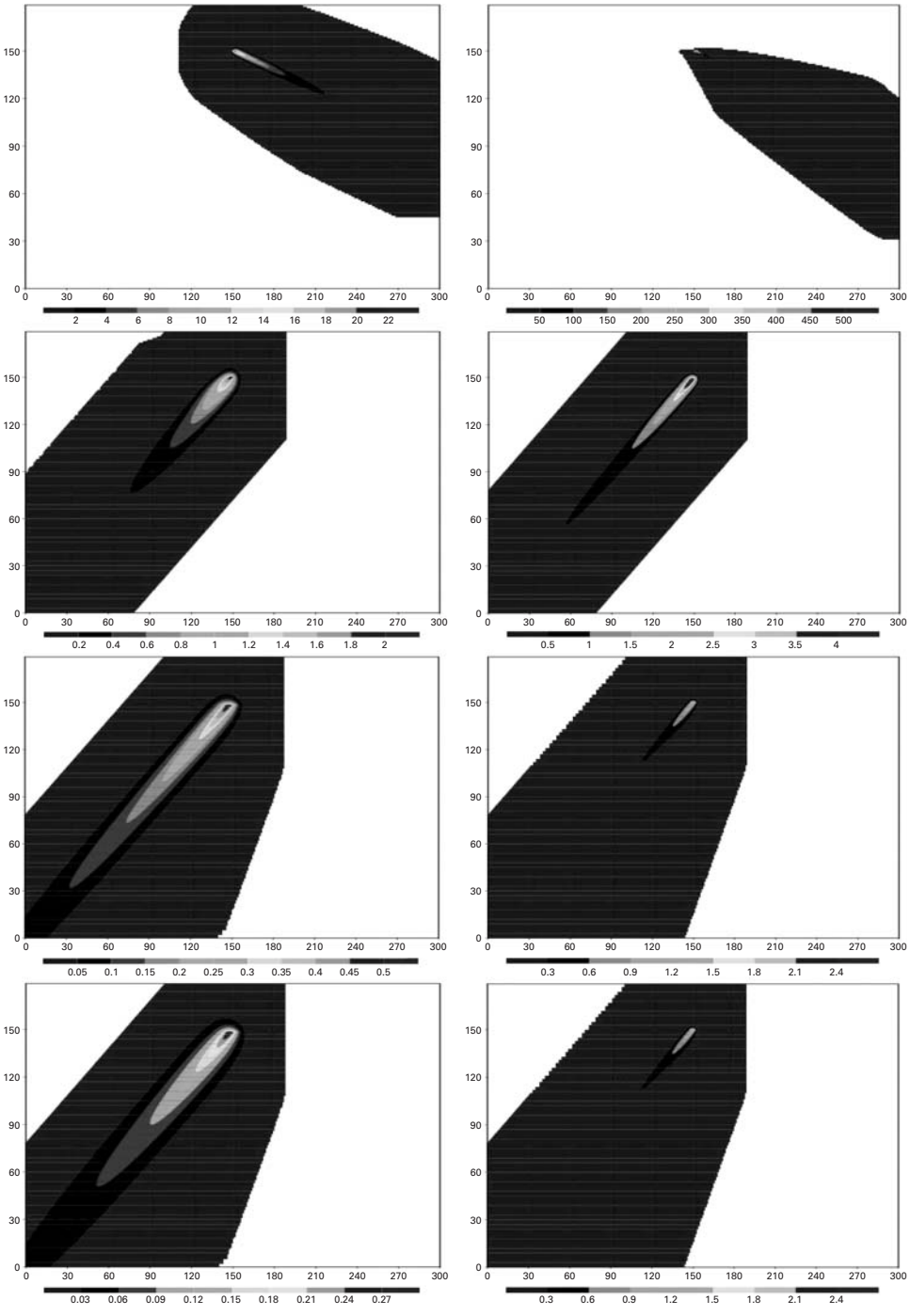

Figure 2.12. On the left concentration after 3 hours of continuous release. The upper two panels are for the 15th of January. The top panel is for the midnight and the one bellow is for the noon of the same day. The lower two panels are for the 15th of March again the upper for the midnight and the lower one for the noon. The winds are *hourly* averages. On the left, the same except for the winds which are 10 *minutes* averages.

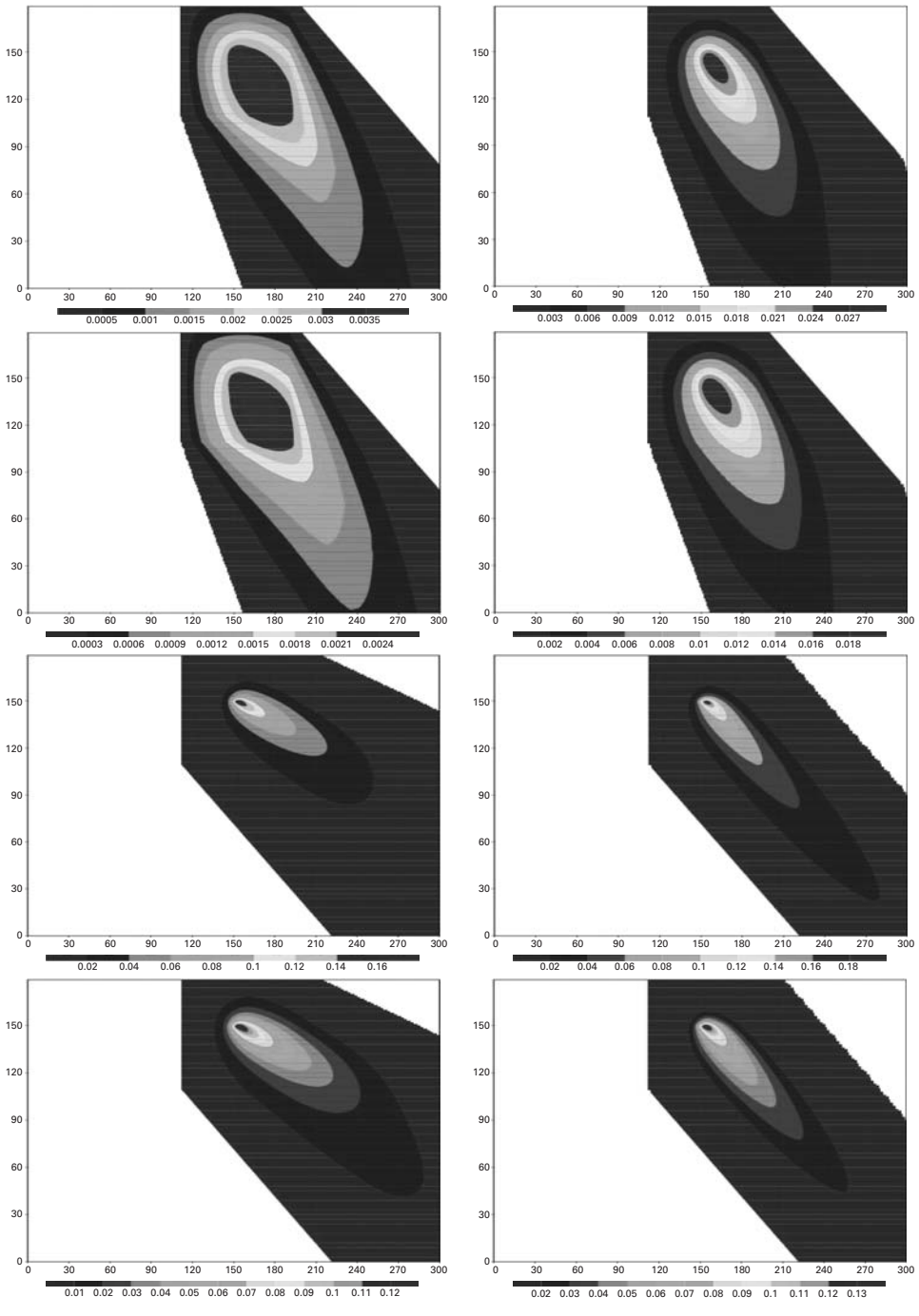

Figure 2.13. On the left concentration after 3 hours of continuous release. The upper two panels are for the 15th of June. The top panel is for the midnight and the one bellow is for the noon of the same day. The lower two panels are for the 15th of September again the upper for the midnight and the lower one for the noon. The winds are *hourly* averages. On the left, the same except for the winds which are 10 *minutes* averages.

Rain (snow) is a very successful removal mechanism for both gases and particles. A simple parameterization is with the introduction of the washout rate, W_r. It relates the removed concentration of the rain droplets C_o to the concentration in the rain χ_o, at some reference height

$$W_r = \frac{C_o}{\chi_o} \tag{2.102}$$

(Misra *et al.*, 1985). With the knowledge of W_r and χ_o, the flux of effluent to the surface due to the precipitation is

$$F_{prec} = \chi_o W_r P, \tag{2.103}$$

where P is the equivalent rainfall in, for instance, mm/hr. From Equation (2.103) we can define, in analogous way to the dry deposition velocity, the wet deposition velocity as

$$w_r = \frac{F_{prec}}{\chi_o} = W_r P. \tag{2.104}$$

APPENDIX—LIST OF SYMBOLS

List of Symbols

Symbol	Definition	Dimensions or Units
B_1	an arbitrary constant	
C_o	concentration in rain droplets	$[m^{-3}]$
D	an arbitrary constant or a measure of a cloud size	[m]
Dair	molecular diffusion of air	$[m^2\ s^{-1}]$
F	flux of substance through unit area orthogonal to x-direction	$[s^{-1}]$
F_{prec}	flux of effluent to surface due to precipitation	$[(ms)^{-1}]$
G	cylindrical region	
H	top of cylinder G, height of source	
K	diffusion coefficient	$[m^2\ s^{-1}]$
L	Monin-Obukhov's length scale	[m]
N	number of particles in a cloud	
P	equivalent rainfall	$[m\ s^{-1}]$
Q	release rate or strength of point source	$[kg\ kg^{-1}\ s]$
R	auto-correlation function	
S	area that by side bounds cylindrical region G, measure of a cloud size	$[m^2]$
Snk	sink of a substance	$[kg\ kg^{-1}\ s]$
Src	source of a substance	$[kg\ kg^{-1}\ s]$
St, Sb	top and bottom surfaces that bounds cylindrical region G	$[m^2]$
T	integral time scale	[s]
U	wind's strength, mean wind	$[m\ s^{-1}]$

(*Continued*)

List of Symbols

Symbol	Definition	Dimensions or Units
V	domain of integration	$[m^3]$
V_d	deposition velocity	$[m\,s^{-1}]$
W_r	washout rate	
a, b, c	arbitrary constants	
const	an arbitrary constant	
f	source strength	$[kg\,kg^{-1}\,s]$
i	index of a particle	
ic	index of receiving cell	
ipf	index of a puff	
k_1, k_2	wave numbers	$[m^{-1}]$
l	distance between any two particles in a cloud	[m]
q	distance-neighbour function, amount of substance	$[m^{-1}]$
r, s	constants in the distribution function	
r_a	aerodynamic resistance	$[s\,m^{-1}]$
r_b	bulk resistance	$[s\,m^{-1}]$
r_v	resistance representing viscous sub layer	$[s\,m^{-1}]$
t	time	[s]
Δt	time interval	[s]
u	x-component of velocity	$[m\,s^{-1}]$
u_n	component of velocity normal on the surface	$[m\,s^{-1}]$
u_*	friction velocity	$[m\,s^{-1}]$
u^+	arbitrary variable	
u^-	arbitrary variable	
v	y-component of velocity	$[m\,s^{-1}]$
$\boldsymbol{v}$	wind vector	$[m\,s^{-1}]$
v_i	i-th particle velocity	$[m\,s^{-1}]$
ν	diffusion coefficient	$[m\,s^{-1}]$
w	z-component of velocity	$[m\,s^{-1}]$
w_r	wet deposition velocity	
$w\theta_0$	mean vertical flux of heat	$[m\,K\,s^{-1}]$
x, y, z	distances, coordinates	[m]
x_0	position of the source of a passive substance	[m]
x_i	position of the i-th particle relative to the sources position	[m]
x_{ic}, y_{ic}, z_{ic}	coordinates of the ic-th cell	[m]
x_m	median of a cloud of particles	[m]
z_0	aerodynamic length	[m]
Γ	Gamma function	
Θ	mean potential temperature	[K]
Θ_0	mean potential temperature of the basic state	[K]
δ	Dirac's delta function	
ε	small interval	
κ	Von Karaman constant	
λ	an arbitrary constant	
ξ	difference between χ_2 and χ_1	$[kg\,kg^{-1}]$

(*Continued*)

List of Symbols

Symbol	Definition	Dimensions or Units
ξ	relative time	[s]
π	number pi	
σ	arbitrary constant	$[1\,m^{-2}]$
σ_i	measure of lateral spread	$[1\,m^{-2}]$
$\sigma_x, \sigma_y, \sigma_z$	diffusion coefficients in x, y and z direction	$[1\,m^{-2}]$
σ_{10}	values of σ for 10 averaged over minutes	$[1\,m^{-2}]$
σ_{ipf}	measure of the lateral spread of a cloud	$[1\,m^{-2}]$
τ	time constant	[s]
χ	concentration of a substance	$[kg\,kg^{-1}]$
χ_s	boundary conditions for χ	$[kg\,kg^{-1}]$
χ_0	initial conditions	$[kg\,kg^{-1}]$
χ_1, χ_2	two different solutions for χ	$[kg\,kg^{-1}]$
χ_{ic}	concentration of a passive substance for the *ic*-th cell	$[kg\,kg^{-1}]$
χ_d	deposited material	$[kg\,kg^{-1}]$
χ_h	homogenous part of solution	$[kg\,kg^{-1}]$
χ_o	initial concentration of a substance	$[kg\,kg^{-1}]$

REFERENCES

Beljars, A. C., 1982, The derivation of fluxes from profiles in perturbed areas. *Boundary–Layer Meteorology*, **24**, pp. 35–55.

Beljars, A. C., and Holstag, A. A. M., 1991, Flux parameterization over land surfaces for atmospheric models. *Journal of Applied Meteorology*, **30**, pp. 327–341.

Braham, R. R., Seely, B. K., and Crozier, W. D., 1952, A technique for tagging and tracing air parcels. *Transactions, American Geophysical Union*, **33**, pp. 825–833.

Briggs, G. A., 1982, Similarity forms for ground source surface layer diffusion. *Boundary–Layer Meteorology*, **23**, pp. 489–502.

Briggs, G. A., 1973, *Diffusion estimates for small emissions*, (Washington: U.S. Environmental Protection Agency).

Crozier, W. D. and Seely, B. K., 1955, Concentration distributions in aerosol plumes three to twenty two miles from a point source. *Transactions, American Geophysical Union*, **36**, pp. 42–50.

Gifford, F. A., 1961, Use of routine meteorological observations for estimating atmospheric dispersion. *Nuclear Safety*, **2**, pp. 47–51.

Gifford, F. A. and Hanna, S. R., 1973, Modelling urban air pollution. *Atmospheric Environment*, **7**, pp. 131–136.

Golder, D., 1972, Relations among stability parameters in the surface layer. *Boundary–Layer Meteorology*, **3**, pp. 47–58.

Grsić, Z., 1991, *Critical analysis of Gaussian diffusion models (master thesis, in Serbian*), (Belgrade: Institute for Meteorology, Belgarde University).

Grsić, Z. and Milutinovic, P., 2000, Automated meteorological station and the appropriate software for air pollution distribution assessment. In *Air Pollution Modelling and Its Application,* XIII, edited by Gryning, S. E. and Batchvarova, E.

Holstag, A. A. M., 1984, Estimates of diabatic wind speed profiles from near-surface weather observations. *Boundary–Layer Meteorology*, **29**, pp. 225–250.

Holstag, A. A. M. and Van Ulden, P., 1983, A simple scheme for daytime estimates of the surface fluxes from routine weather data. *Journal of Applied Meteorology*, **22**, pp. 517–529.

Horst, T., 1979, Lagrangian similarity modeling of vertical diffusion from ground-level sources. *Journal of Applied Meteorology*, **18**, pp. 733–740.

Misra, P. K., Chan, W. H., Chung, D. and Tang, A. J. S., 1985, Scavenging ratios of acidic pollutants and their use in long-range transport models. *Atmospheric Environment*, **19**, pp. 1471–1475.

Nieuwstad, F. T. M., 1980, Application of mixed-layer similarity to the observed dispersion from a ground-level source. *Journal of Applied Meteorology*, **19**, pp. 733–740.

Pasquill, F., 1961, The estimation of the dispersion of windborne material. *Meteorological Magazine*, **90**, pp. 33–49.

Pasquill, F., 1956, Meteorological research at Porton. *Nature*, **177**, pp. 1148–1150.

Pasquill, F., 1955, Preliminary studies of the distribution of particles at medium range from a ground-level point source. *Quarterly Journal of Royal Meteorological Society*, **81**, pp. 636–638.

Pasquill, F. and Smith, F. B., 1983, *Atmospheric Diffusion*, (New York: John Wiley and Sons).

Richardson, R. L., 1952, Transforms for the eddy–diffusion of clusters. *Proceedings of the Royal Society*, **A 214**, pp. 1–20.

Richardson, R. L., 1926, Atmospheric diffusion shown on a distance–neighbour graph. *Proceedings of the Royal Society*, **A 110**, pp. 709–737.

Taylor, G. I., 1921, Diffusion by Continuous Movements, *Proceedings of the London Mathematical Society*, **20**, pp. 196–212.

Thykier–Nielsen, S. and Larsen, S. E., 1982, *The Importance of Deposition for Individual and Collective Doses in Connection with Routine Releases from Nuclear Power Plants*, (Roskilde: RISO National Laboratory).

Turner, D. B., 1969, Workbook of atmospheric dispersion estimates. In *Office of Air Programs Publications*, **AP 26**, (Washington D.C.: Public Health Service Publ.), pp. 26–84.

CHAPTER THREE

Air–sea interaction

Vladimir Djurdjević & Borivoj Rajković
Institute for Meteorology, University of Belgrade, Belgrade, Serbia

ABSTRACT

This chapter will cover basic concepts of the air–sea interaction. It has three sections. After the introduction about the importance of the phenomenon, its two-way nature and scale (time and space) on which it is important, there is a section on exchange of momentum, energy and mass between the atmosphere and the ocean. Part of this section addresses some of the aspects of modelling approaches used in variety of problems which are connected to or influenced by the air–sea interaction. Air–sea exchanges are strongly influenced by the structures of both media near the atmosphere–ocean interface, notably boundary layers that are present in both media. Therefore, we give brief discussion of boundary layer structures and we examine in particular the role of the viscous sub-layer in the atmosphere. Then we present the most common approaches to the modelling of these exchanges. We start with some relatively simple concepts such as "Bulk" formulae and then present some more complex approaches. It is difficult to evaluate the quality of a particular model. We usually look into the effects of flux calculation and then, indirectly, we judge about the quality of a particular scheme or approach. Therefore, we present calculations of the sea surface temperature (SST) for the Mediterranean sea obtained by a coupled model with particular modelling of fluxes. Comparing observed and calculated SST's we offer some ideas about the quality of modelling in that case.

3.1 FOREWORD

The atmosphere and the ocean are interacting mutually over the area that covers five sevenths of the planet's surface. Just from this basic fact alone, we can expect that knowledge of this interaction is important if we wish to understand dynamical characteristics of both entities. This is really the case and the dynamical state of both atmosphere and ocean are in large determined by the interaction. This interaction works both ways and is determined by their dynamical and physical properties. First we point out the difference in densities of the atmosphere and the ocean. Typical density of the ocean is about 1025 [ML^{-3}], while density of the air is roughly 800 times smaller, from 1.2 to 1.3 [ML^{-3}]. Direct consequence of this large difference in densities is that the interaction occurs mostly over the surface where they are in contact. The second physical characteristic that strongly influences the nature of the interaction is the heat capacity. The heat capacity of the ocean is about four times larger than the heat capacity of the air, so the total heat capacity of the unit area column of air through the entire atmosphere is equal to the heat capacity of the unit area layer of the ocean whose depth is only about 2.5 meters. Or putting it differently, the heat that is needed to warm a column of air by one degree can be obtained just by cooling 2.5 meters of water by one degree. Another difference between the atmosphere and the ocean is the absorption of the incoming, short-wave radiation, which is the fundamental, external source

of energy that drives the whole atmosphere–ocean system. The basic difference comes from the fact that the atmosphere is quite weak absorber in that part of the solar spectrum (about 16%) while the ocean typically absorbs about 80% of the short wave radiation within its first 10 meters (Jerlov, 1976). That is why the ocean surface appears very dark on the satellite pictures. On the other side, the main source of energy for the atmosphere is the long-wave radiation that comes from both the ocean and the earth surface which radiate as almost black bodies at the respective surface temperatures. These differences in heat and absorption characteristics play dominant role in the way the ocean influences the state of the atmosphere. Large differences in the heat capacities of the land and the ocean are the main reason why temperature variations over oceans are much smaller compared to those over land. Vast heat capacity of the ocean makes it efficient storage of the heat in the summer part of the year. In that part of the year the net energy balance at the ocean surface is such that more energy is gained than lost to the atmosphere. During the rest of the year the accumulated energy is then available for the additional heating of the atmosphere while the ocean cools down because the energy balance at the its surface is negative. The evaporation from the ocean's surface is also an important part of the energy balance of the ocean–atmosphere system. It takes part of the ocean's energy which then becomes available for the atmosphere first through convection and then finally through the condensation in clouds. As a by-product we have moistening of the atmosphere which greatly influences its radiation properties and therefore its temperature. Atmosphere's influence on ocean works through two mechanisms. The first is already mentioned energy exchange involving exchange of radiation and heat through sensible and latent heat fluxes. The second influence is through mechanical forcing due to friction between the surface wind and the ocean.

Thus distribution of the surface winds decisively influences the structure of the ocean surface circulation. But again, due to the large differences in densities, velocities in the ocean are only about 10% of the velocities in the air, measured at reference height of 10 meters. Due to such large density of the water, ocean "carries" more easily the amount of momentum handed over by the atmosphere, and so, effectively atmosphere sees the ocean as a motionless surface. So close to the ocean surface, large wind shear develops which in turn leads to the fully developed turbulent regime. Ocean surface layer has its source of the momentum confined to its very top and that leads to the same consequence, as in the case of the atmosphere, that there is a fully developed turbulent regime. There is yet another way for the atmosphere to influence the ocean, through the precipitation created in the clouds. This influence is twofold, through the local increase of mass and thus creating barotropic component of pressure gradient force. In the past this was viewed as an important contributor to the ocean currents but now we know that this effect is about 30 times weaker then the effect of the surface winds. The second effect is effect of dilute/salt depending on the difference precipitation–evaporation. If this difference is positive, local salinity decreases thus reducing buoyancy in the top layer of the ocean, otherwise we have increase of buoyancy there. Both of these effects locally influence pressure field and therefore change existing pressure gradient force thus influencing the ocean circulation.

The air–sea interaction, in some degree, influences the whole spectrum of time and space scales in the atmosphere and in the ocean. Some more and some less. Generally, the longer time or space scales, the larger the influence of the interaction. But there are some phenomena, relatively small in space, that own their existence totally to the air–sea interaction. The land–sea breeze, which is an example of the forced circulation due to temperature contrast across land sea interface. Also there is a weak feedback coming from the shape of the wind stress in the vicinity of the land–sea boundary (Mellor, 1986, Rajković and Mellor, 1988). The next example is the case of formation and evolution of tropical cyclones. At the other end of the time and space spectrum are ENSO–El-Nino phenomena, seasonal variability of Somali jet, monsoons, etc. For these time scales and beyond year or decade, merging of the two components, atmosphere and ocean, into one inseparable system is inevitable.

In both media, in the vicinity of the mutual interface, there are well-developed boundary layers, so the interaction must "go through" them and is therefore strongly influenced first by molecular and then by turbulent nature of the motion there. Turbulent regime in the atmosphere is formed due to the existence of the strong velocity gradient as mentioned before. Buoyancy flux is the second contributor to the turbulent kinetic energy (TKE in the further text). In the case of the ocean, vertical gradient of the surface currents, caused by the "import" of the momentum flux from the atmosphere, is one of the sources of TKE. Buoyancy flux works in the same way as in the case of the atmosphere except that here precipitation or evaporation can also decrease/increase it. There is another source of buoyancy. That is solar short-wave radiation, its absorption with depth. Due to the seasonal difference in the solar radiation absorption, there is a seasonal shift in the sign of the buoyancy flux. It is often said that winter for ocean is like summer for the atmosphere. Atmospheric boundary layer (ABL), or as often referred to as planetary boundary layer (PBL) extends from several hundreds of meters for winter high latitude regions to several kilometres for the summer season and tropics. As we pointed earlier, temperature's vertical gradient and diurnal amplitude are much smaller over the ocean so the height of the ocean's BL can be several times smaller then the corresponding ABL over land. Atmospheric boundary layers are well defined in space, having relatively sharp upper boundary. This is clearly visible from the vertical soundings in the potential temperature but also in other fields (wind and humidity). In all these fields we see large vertical gradients which mark the end of ABL and the beginning of the so-called "free atmosphere". Both, atmospheric and oceanic boundary layers have double structure with the so-called surface layers in the vicinity of the interface and well-mixed layers further away. These surface layers are usually referred to as constant flux layers. Surface layers occupy about 10% of the whole boundary layer and are characterised by large vertical gradients of almost all variables. In the immediate vicinity of the interface, on both sides, there exist viscous sub layers with molecular transports as dominant mechanisms of momentum, heat and even mass (water vapour) transfer. Mixed layers, on the other, hand are characterised by small vertical gradients. Exchange between boundary layers and the rest of the atmosphere/ocean is greatly reduced by the existence of the strong gradients in density at their tops, especially in the case of the oceans with much colder water bellow the picnocline (region of steepest density gradient region). The ocean counterpart for the ABL is the thermocline layer. There are several ways of defining its depth. The simplest and often used way is to specify the depth where temperature gradient exceeds some predefined value. This is usually between 0.5 and 1 degree. Thermocline depth varies 1000 meters to 50 meters. Note that in the oceanographic practice term "surface layer" can have another meaning as the layer of water that in the past had been influenced by the atmosphere. That layer is usually somewhat deeper than the boundary layer itself.

In modelling air–sea interaction, the processes inside the viscous sub-layer have proved to be an important factor for the evolution of the whole ABL by influencing fluxes near the ocean surface (Janjic, 1994, Liu *et al.*, 1979). Regimes that develop in the viscous sub-layer are determined by a single parameter, the friction velocity. With weak winds and therefore small friction velocity, viscous mechanisms are important and should be taken into account. With the increase in wind and consequently development of waves, the influence of the viscous sub-layer reduces. Other mechanisms developed, such as direct exchange of momentum from the local pressure gradient forces exerted on the waves. In a very strong winds regime we can have direct transfer of water into atmosphere from the wave spray which leads to the complete collapse of the viscous sub-layer.

3.2 EXCHANGE OF THE MOMENTUM FLUXES

Consideration about the momentum exchange starts with the condition of continuity of fluxes across any surface, including the boundary surface between the atmosphere and the

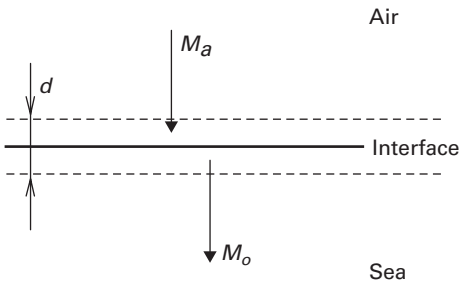

Figure 3.1. Schematic presentation of the air–sea boundary region. M_a is the momentum flux in the atmosphere while M_o is the momentum flux in the ocean.

ocean. If we assume that the boundary surface that separates two fluids is smooth and well defined as in Figure 3.1, then in the immediate vicinity of the interface we have

$$M_a = M_o, \tag{3.1}$$

where M_a is the momentum flux in the atmosphere while M_o is the momentum flux in the ocean. As it was mentioned several times, because water density is several times larger then air density, velocity of the sea currents needed to "carry" all the momentum that comes from the atmosphere is much smaller than the velocity of the air that "carries" the same amount of momentum. This fact is well known from the measurements. Typical air velocity is of the order of *meter*/second while typical surface currents velocity is of the order of *centimetres*/second. So from the atmosphere's perspective, the ocean is a motionless surface very much like the land, while from the ocean's perspective momentum flux that comes from the atmosphere is a considerably source of kinetic energy and is key factor in formation of the surface currents. Based on these considerations, for the atmosphere we impose the lower-boundary condition of zero velocity while for the ocean the upper-boundary condition is in terms of the momentum flux and is set equal to the atmospheres momentum flux as in Equation (3.1). Based on the measurements in neutral flows, oceanographers developed formulae that relate momentum flux to the wind strength, usually to its value at 10 meters. The coefficient that appears in those formulae is the so called *drag coefficient* and whole concept is known by that name. Large and Pond (1981) developed a simple algorithm consisting of a bulk formula for calculating the drag coefficient using only the wind velocity:

$$C_D = \begin{cases} 1.2 \cdot 10^{-3}, 4 \le U \le 11[LT^{-1}] \\ (0.49 + 0.065U) \cdot 10^{-3}, 11 \le U \le 25[LT^{-1}] \end{cases}. \tag{3.2}$$

The other well known formula that takes into account the SST in addition to the wind velocity is the Hellerman and Rosenstein (1983) formula

$$\begin{aligned} C_D = {} & \alpha_1 + \alpha_2 U + \alpha_3 (T_a - T_s) + \alpha_4 U^2 \\ & + \alpha_5 (T_a - T_s)^2 + \alpha_6 U (T_a - T_s)^2 \end{aligned}. \tag{3.3}$$

Vertical profile of the wind due to friction must increase upward from the land or sea and is characterized with strong vertical gradients, shear. They decrease with height and eventually the wind acquires velocity close to the geostrophic. The existence of the strong shear, near the sea/land surface, is the main reason why the flow is *turbulent* there. That

is the fundamental characteristic of that region which strongly influences all its transports, momentum, energy and any passive substance present there. Further away from this surface region, we still observe a turbulent regime but the generation of turbulence is of different nature there. The main source of turbulent kinetic energy is the local convective instability or buoyancy production. The whole layer of the atmosphere with turbulent regime is called Planetary Boundary Layer, PBL in the further text. Its vertical scale is of the order of 1 km with strong diurnal, seasonal and north south variations. The north–south variability comes from two factors. The first one is the position of the Sun resulting in the larger surface heating while the second one is the value of the Coriolis parameter. Both of them contribute to the generation of higher PBL at the low latitudes. The PBL turbulent fluxes are several orders of magnitude larger than the corresponding molecular and so there they are dominant mechanism in transporting of the momentum, energy, passive substances, etc.

Due to the difference in densities of water and air, there is no direct mixing between them, i.e. air cannot go "through" water and vice versa. This has a very strong impact on the scale and the mechanism of the exchange, which has to be completely *molecular* in the immediate vicinity of the surface. What are the scales of the relevant variables, length, velocity and momentum? How far up are these viscous fluxes important and where turbulent fluxes eventually take over and become dominant for the rest of the PBL?

Let us examine the simplest possible case of the flow over homogeneous flat surface with very large horizontal extension in comparison with the vertical extension. Further we assume constant pressure gradient force (PGF) and no rotation. In that case there exists a steady state solution in which PGF is balanced by the surface friction. Domain of interest is very close to the ground (that is why we can neglect the influence of the Coriolis term) so we neglect vertical advection by the mean wind. Due to the assumed homogeneity in x and y horizontal advection and divergence of Reynolds stresses are negligible in comparison with their vertical divergence. With all these assumptions made the x component of the equation of motion reduces from

$$\begin{aligned}&\frac{\partial U}{\partial t}+U\frac{\partial U}{\partial x}+V\frac{\partial U}{\partial y}+W\frac{\partial U}{\partial z}-fV\\&\quad=PGF+\frac{\partial}{\partial x}\left(\nu\frac{\partial U}{\partial x}-\overline{uu}\right)+\frac{\partial}{\partial y}\left(\nu\frac{\partial U}{\partial y}-\overline{uv}\right)+\frac{\partial}{\partial z}\left(\nu\frac{\partial U}{\partial z}-\overline{uw}\right)\end{aligned}\tag{3.4}$$

to

$$\frac{\partial}{\partial z}\left(\nu\frac{\partial U}{\partial z}-\overline{uw}\right)=-PGF\equiv A.\tag{3.5}$$

As it is traditional in the case of the turbulent flows, capital letters denote mean values while lower case letters denote deviations from these mean variables. Equation (3.3) expresses the balance between the acceleration due to the PGF and deceleration due to the convergence of the sum of turbulent x-momentum flux and viscous momentum flux, $\nu\,\partial U/\partial z$. If we integrate Equation (3.5) from the surface up to a level z we get

$$-\overline{uw}+\nu\frac{\partial U}{\partial z}=Az+B,\tag{3.6}$$

where B is the constant of integration. The boundary condition

$$\overline{uw}=0\tag{3.7}$$

at $z = 0$ leads to

$$B = \nu \left[\frac{\partial U}{\partial z} \right]_{z=0}. \tag{3.8}$$

Dimensions of B are $[L^2T^{-2}]$, that of squared velocity and since it is a consequence of the friction, its square root, is called "friction velocity" and is denoted either by u_* or by u_τ. Using this notation and having in mind that we are very close to the surface, balance relation (3.6) reduces to

$$-\overline{uw} + \nu \frac{\partial U}{\partial z} = u_*^2. \tag{3.9}$$

Due to the fact that the sum of two momentum fluxes has approximately a constant value, region where this approximation is valid is called the *constant flux layer*. The most important consequence of Equation (3.9) is that we have only two parameters in the problem. One is absolute constant, viscosity ν, while the other one is a *dynamical* variable, the friction velocity u_*, velocity scale in the problem. From these two and dimensional arguments we can form the length scale of the problem

$$z_0 = \frac{\nu}{u_*}. \tag{3.10}$$

With u_* and z_0 we can rewrite Equation (3.9) in the *non-dimensional* form

$$\frac{-\overline{uw}}{u_*^2} + \nu \frac{\partial (U/u_*)}{\partial (z/z_0)} = 1. \tag{3.11}$$

The above relation is illustrated in Figure 3.2 showing relative magnitudes of non-dimensional viscous flux versus non-dimensional turbulent flux in the vicinity of the wall. For $z \leq 0.3z_0$ the viscous mechanism is dominant, while for $z \geq 0.3z_0$ the turbulent mechanism prevails.

All this is valid for a very smooth and hard surface like a large area covered with ice. For the boundary layers over the water, the most commonly used relation for the value of z_0 is the one proposed by Charnock (1955)

$$z_0 = 0.0156 \frac{u_*^2}{g}, \tag{3.12}$$

where g is gravitational constant.

Calculation of the fluxes above the surface sub-layer has to take into account an additional factor, that of the local stability and, related to it, the existence of heat and humidity fluxes. There are several approaches to this problem but we will concentrate on the so-called Monin–Obukhov theory (M–O in the further text) following the presentation of Janjic (1995). Let us denote the vertical turbulent flux of momentum with M and assume that it depends on the vertical gradient of the mean wind, i.e. assume the eddy viscosity concept

$$\overline{uw} = M = -K_M \frac{dU}{dz}, \tag{3.13}$$

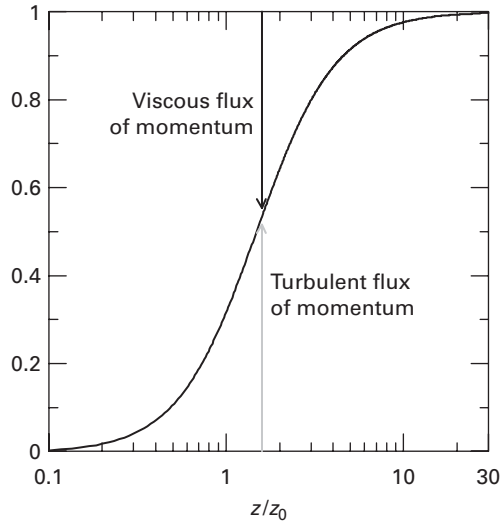

Figure 3.2. The relative magnitudes of non-dimensional viscous flux versus non-dimensional turbulent flux, in the vicinity of the wall.

where K_M is turbulent diffusivity coefficient for momentum. If we integrate Equation (3.13) from level z_1 to level z_2 with the assumption that M is *constant* within $[z_1, z_2]$ we get

$$U_2 - U_1 = M \int_{z_1}^{z_2} \frac{dz}{K_M} \frac{dU}{dz}. \tag{3.14}$$

Further if we define *bulk* mixing coefficient of momentum as:

$$\frac{z_2 - z_1}{K_{MB}} \equiv \int_{z_1}^{z_2} \frac{dz}{K_M}. \tag{3.15}$$

Equation (3.14) can be written as

$$M = K_{MB} \frac{U_2 - U_1}{z_2 - z_1}. \tag{3.16}$$

The starting point of the M–O theory is the theory valid for the *neutral* fluid. Namely, the law of the wall, which says that very close to the wall, in the region where turbulent momentum flux is constant (Equation (3.9)), mean velocity gradient is inversely proportional to the distance from the wall

$$\frac{\partial U}{\partial z} = \frac{u_*}{kz}. \tag{3.17}$$

This is a similarity law that says: if we *scale* properly velocity, then all the possible profiles of the velocity, close enough to the wall, will collapse to a single profile, and shear of all

these profiles are given by the above relation. The quantity u_* insures that the slope of the first derivative of $U(z)$ profile at $z=0$ is such that $U(z=0)=0$. So the complete dynamics of the neutral flow, in the law of the wall region, is determined by that single quantity. For instance, the appropriate length scale $z_0 = u_*/v$ is also derivative of the friction velocity. As we said, both the concept and form of the profiles (gradients) for the neutral flow were the starting point for the M–O theory whose generalization

$$\frac{\partial U}{\partial z} = \frac{u_*}{kz}\varphi_m\left(\frac{z}{L}\right) \equiv \frac{u_*}{kz}\varphi_m(\zeta) \tag{3.18}$$

was proposed by Obukhov (1946) and Monin and Obukhov (1953). The first part comes from the neutral case, while with the introduction of the new, universal function φ_m we take into account all the new moments of stratified flows. There are *two* new moments, heat flux between the surface and the air above it $w\theta_0$, and stability parameter $\beta = 1/\Theta_0$ with $\Theta_0 \approx 273°\text{K}$. From these three u_*, $w\theta_0$ and β the M–O theory suggests the new vertical length scale L

$$L = \frac{u_*^3}{\kappa\beta g w\theta_0}, \tag{3.19}$$

where κ is von Karman's constant while g is the gravitational constant. The reason why we have *one* unknown function φ_m of *one* variable $\zeta = z/L$ is that out of four variables, parameters z, u_*, $w\theta_0$ and β, only three are dimensionally independent. In that case, from the Buckingham's Pi theorem, the form of relation must be that of an unknown function, with *one* dimensionless variable. Once we have relation, we must show that it is, indeed, the universal function covering all possible ranges of winds (u_*) and all possible stable and unstable regimes ($w\theta_0$). Following the formulation of the M–O theory, a great deal of effort went into its verification. The best known is the so-called Kansas experiment (Businger *et al.,* 1971).

From the way that M–O theory was initiated, it is clear that we must have, as a boundary condition:

$$\lim_{\zeta\to 0}\varphi_m(\zeta) = 1, \tag{3.20}$$

From the definition of ζ, we see that such condition can be achieved either for $z \approx 0$ or for the close to neutral case with $w\theta_0 \approx 0$. With the boundary condition met, we get for the wind profile the logarithmic profile, which is always observed when the atmosphere is close to the neutral one. Now having the value for the gradient of the mean wind, we can rewrite Equation (3.14) as

$$U_2 - U_1 = \frac{u_*}{\kappa}\int_{z_1}^{z_2}\varphi_m(\zeta)\frac{d\zeta}{\zeta}. \tag{3.21}$$

Integrand of Equation (3.21) is singular for $\zeta = 0$ so we will add "suitable chosen zero" $\varphi_m(0) - \varphi_m(0)$ and group it as:

$$U_2 - U_1 = \frac{u_*}{\kappa}\left(\int_{z_1}^{z_2}(\varphi_m(\zeta) - \varphi_m(0))\frac{d\zeta}{\zeta} + \varphi_m(0)\int_{z_1}^{z_2}\frac{dz}{z}\right) \tag{3.22}$$

or with condition (3.20) we have

$$U_2 - U_1 = \frac{u_*}{\kappa}\left(\int_{z_1}^{z_2}(\varphi_m(\zeta)-1)\frac{d\zeta}{\zeta} + \ln\left(\frac{z_2}{z_1}\right)\right). \tag{3.23}$$

If we denote

$$\Psi_m(\zeta) \equiv \int_{z_1}^{z_2}(\varphi_m(\zeta)-1)\,\frac{dz}{z} \tag{3.24}$$

then we finally have

$$U_2 - U_1 = -\frac{u_*}{\kappa}\left[\Psi_m(\zeta) + \ln\left(\frac{z_2}{z_1}\right)\right]. \tag{3.25}$$

Functions $\varphi_m(\zeta)$ or $\Psi_m(\zeta)$ are the core of the M–O theory. The only way that these functions can be determined is through measurements and then looking for their best fit. Correspondence between measurements and their mathematical expression is not one to one and so there are several formulations for ϕ_m or Ψ_m. They are divided into two groups. The one is for the unstable stratification and the other one is for the stable stratification. From the already mentioned analysis of the Kansas experiment Businger et al. have proposed one set of Ψ_m. Here we present the form suggested by Mellor (2004)

$$\varphi_m(\zeta) \cong \begin{cases} (1+a_m\zeta)^{-1/3}; & \text{for the unstable case} \\ 1+5\zeta; & \text{for the stable case} \end{cases} \tag{3.26}$$

where a_m has value of 11.5. After definition

$$x \equiv (1-a_m\zeta)^{1/3} \tag{3.27}$$

Equations (3.26) become

$$\Psi_m(\zeta) \cong \begin{cases} -\dfrac{3}{2}\ln(x^2+x+1) + \sqrt{3}\arctan\dfrac{2x+1}{\sqrt{3}} + c; & \text{for the unstable case} \\ 5\zeta; & \text{for the stable case} \end{cases} \tag{3.28}$$

With the explicit form for Ψ, we can calculate K_{MB} and related fluxes provided that we know the values of U_1 and U_2 at levels z_1 and z_2, u_* and L. But L depends, beside u_*, on the surface heat flux $w\theta_0$, which makes the problem both implicit and transcendental. Since we have two unknowns (u_*, and $w\theta_0$) we must create another similar relation, but for the potential temperature Θ. That will be done later in this section.

Beside the problem of solving for K_{MB} and its counterpart for heat $K_{\Theta B}$, we must analyse the possible positions of levels z_1 and z_2. The upper one must be within the surface layer where the M–O theory applies. This may sometimes be a problem, when that is the height of the lowest level of a numerical model, which can have a relatively low vertical resolution and has in its domain points deep in the North (South), where the whole PBL is much shallower, hence its surface layer. If we are working with the standard measurements i.e. two-metres

temperatures and ten-metres winds, then we are well within the region of applicability of M–O theory. With the lower level, z_1, the situation is more complicated. From the geometry the lower boundary condition should be at $z = 0$ but due to singularity at $z = 0$, we usually set the lower boundary condition at some height z_0 above the surface. The idea is that below z_0 fluxes will remain constant. We had a similar quantity when we looked in the case of the neutral stratification. Over land z_0 is dominated by the form of the surface, local irregularities that most of the time are much higher than the one that z_0 has for the smooth surface. Beside the mathematical problems with lower boundary condition we must remember that in the foundations of M–O theory lies the assumption that fluxes are due to completely chaotic turbulent movement. In the case of the boundary layers over water, z_0, is very small which means that turbulent fluxes become comparable to the viscous one. Further, in the case of the weak winds, z_0, is so small that viscous fluxes completely take over. We will come back to this later, when we develop the theory that takes into account the existence of the viscous sub-layer. That this really should be taken into account comes from the experience with numerical weather prediction models (Janjic, 1994, 1996; Chan *et al.*, 1996).

We start the viscous sub-layer theory with the Liu *et al.*, 1979 paper. According to it, very close to the surface, we have the following relation:

$$U_1 - U_S = D_1\left[1 - \exp\left(-\frac{z_1 u_*}{D_1 \nu}\right)\right]\left(\frac{M}{u_*}\right), \tag{3.29}$$

where the subscript S stands for the surface while index 1 stands for the top of the viscous sub-layer. We will come back to the parameter $D_{1,\nu}$, the viscosity related coefficient and M is the momentum flux *above* the viscous sub-layer. In deriving Equation (3.29) Liu *et al.* have explicitly set the condition of continuity of fluxes across the boundary between the viscous sub-layer and the turbulent layer above. If we introduce definition

$$\xi = -\frac{z_1 u_*}{D_1 \nu} \tag{3.30}$$

and since its value is very small in the sub-layer, we have

$$1 - \exp(-\xi) \approx \xi \tag{3.31}$$

so the relation (3.29) becomes

$$U_1 - U_S = \frac{z_1 M}{\nu}, \tag{3.32}$$

where

$$z_1 = \frac{\xi \nu D_1}{u_*}. \tag{3.33}$$

The last relation effectively defines the viscous sub-layer height. From the combination of Equations (3.16) and (3.32) we get

$$\nu \frac{U_1 - U_S}{z_1} = K_{MB} \frac{U_2 - U_1}{\Delta z} \tag{3.34}$$

or

$$U_1 = \frac{1}{1 - \dfrac{z_1 K_{MB}}{\nu \Delta z}} U_S - \frac{\dfrac{z_1 K_{MB}}{\nu \Delta z}}{1 - \dfrac{z_1 K_{MB}}{\nu \Delta z}} U_2. \tag{3.35}$$

This relation states that velocity at the interface can be viewed as a weighted mean of the surface velocity and the velocity at the height z_2. So if we know parameters D_1 and ξ parameterization of the surface layer is complete. In most cases the value of U_1 is set to zero or is negligible relative to the value U_2, but not always. For instance, in the Gulf Stream there are regions with surface currents up to 2 [LT^{-1}], so that U_1 and U_2 are of the same order. According to Janjic (1995) there are three possible regimes (which need to be taken into account while calculating fluxes) regarding the existence of the viscous sub-layer. Furthermore, he proposes that the number which separates these regimes is the Reynolds number for z_0

$$R_e = \frac{z_0 u_*}{\nu} \tag{3.36}$$

with limits

$$z_0 = \max\left(0.018\frac{u_*}{g}, 1.59 \cdot 10^{-15}\right). \tag{3.37}$$

Regarding the momentum flux, if R_e is smaller then R_{e1} corresponding to the value for $u_{*1} = 0.225$ [LT^{-1}] we do include the viscous layer in the calculations. We will call this the *smooth* regime. If the friction velocity is greater than u_{*1} we neglect viscous sub layers influence. That regime is referred to as the *rough* regime. The idea is that having larger u_* the sea surface becomes wavy and there is pressure force upon the surface of the water enhancing the momentum exchange and thus surpassing the limits that viscosity imposes.

Regarding the value for the constant D_1 , Liu suggests parameterization in the form

$$D_1 = GR_e^{1/4}, \tag{3.38}$$

where G is a constant that depends on the flow regime. For the smooth regime Liu gives the value around 30 while for the other two regimes the value of $G \approx 10$ is the best fit to Mangarella *et al.* (1973) data. This approach has been successfully implemented in NCEP's limited area model and in the version of that model which is fully coupled with the POM (Princeton Ocean Model).

3.3 EXCHANGE OF THE HEAT FLUX

The problem of the heat flux exchange between the ocean and the atmosphere has some similarity with the problem of the momentum flux exchange, but there are also some differences. Geometry of the problem is depicted in Figure 3.3 showing various components of the energy exchange between the ocean and the atmosphere.

Assuming that we have balance of all energy components in the layer, whose depth is d, we can write the heat balance as:

$$H_o = (LW_a - LW_o) + H_a + LE + (SW_a - SW_o). \tag{3.39}$$

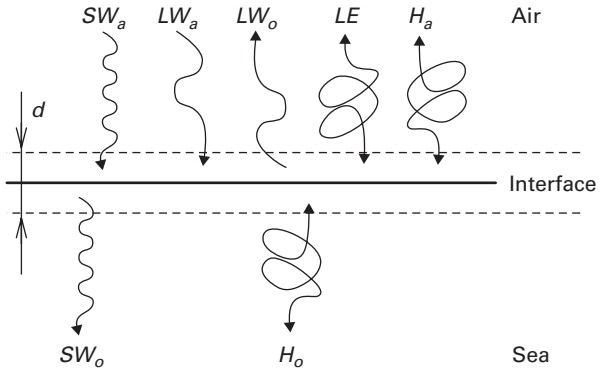

Figure 3.3. Various components of the energy exchange between the ocean and the atmosphere. SW_a is the solar short wave radiation, LW_a is the atmosphere's long wave radiation, LW_o is the ocean's long-wave radiation, LE and H_a are latent and sensible heat fluxes, SW_o is the solar short wave radiation that is absorbed by the ocean and H_o is ocean's sensible heat flux.

The terms in the brackets are the net long wave and short wave components of the radiation fluxes respectively. Analogous to the case of the momentum flux, we assume that sensible and latent heat fluxes can be expressed as:

$$H = \overline{w\theta} = -K_H \frac{d\Theta}{dz} \tag{3.40}$$

and

$$LE = \overline{wq} = -K_H \frac{dq}{dz}. \tag{3.41}$$

We also assume that the mixing coefficient is the same in both fluxes. Variable q is the specific humidity. Again as in the case of momentum integrating we get

$$H = -K_{HB} \frac{\Theta_2 - \Theta_1}{z_2 - z_1} \tag{3.42}$$

and

$$LE = -K_{HB} \frac{q_2 - q_1}{z_2 - z_1}. \tag{3.43}$$

The M–O theory for the heat fluxes has

$$\frac{\partial \Theta}{\partial z} = -\frac{\Theta_*}{\kappa z} \varphi_h(\zeta) \tag{3.44}$$

and

$$\frac{\partial q}{\partial z} = -\frac{q_*}{\kappa z} \varphi_h(\zeta) \tag{3.45}$$

with the scales for heat and humidity defined as $\Theta_* \equiv H/u_*$ and $q_* \equiv LE/u_*$. Again by integrating Equation (3.45) from z_1 to z_2 we obtain for Θ and q

$$\Theta_2 - \Theta_1 = -\frac{\Theta_*}{\kappa}\left[\Psi_h(\zeta) + \ln\left(\frac{z_2}{z_1}\right)\right] \tag{3.46}$$

and

$$q_2 - q_1 = -\frac{q_*}{\kappa}\left[\Psi_h(\zeta) + \ln\left(\frac{z_2}{z_1}\right)\right]. \tag{3.47}$$

As in the case of momentum, viscous sub-layer fluxes are introduced, for heat as

$$\Theta_1 - \Theta_S = D_2\left[1 - \exp\left(-\frac{z_{1T}u_*}{D_2\chi}\right)\right]\left(\frac{H}{u_*}\right) \tag{3.48}$$

and for the specific humidity as

$$q_1 - q_S = D_3\left[1 - \exp\left(-\frac{z_{1T}u_*}{D_3\lambda}\right)\right]\left(\frac{LE}{u_*}\right), \tag{3.49}$$

where χ and λ are molecular, heat and humidity viscous coefficients, Θ_S is sea surface temperature (henceforth SST) and q_S is specific humidity just above the water surface, which is assumed to have its saturation value. Using the assumption $z_{1q}u_*/D_1\lambda \approx 1$, Equations (3.46) and (3.48), and definitions of bulk coefficients we evaluate Θ_1 and q_1 as

$$\Theta_1 = \Theta_S\frac{1}{1 - \dfrac{z_{1T}K_{HB}}{\chi\Delta z}} - \Theta_2\frac{\dfrac{z_{1T}K_{HB}}{\chi\Delta z}}{1 - \dfrac{z_{1T}K_{HB}}{\chi\Delta z}} \tag{3.50}$$

and

$$q_1 = q_S\frac{1}{1 - \dfrac{z_{1q}K_{HB}}{\lambda\Delta z}} - q_2\frac{\dfrac{z_{1q}K_{HB}}{\lambda\Delta z}}{1 - \dfrac{z_{1q}K_{HB}}{\lambda\Delta z}}, \tag{3.51}$$

with definitions

$$z_{1T} = \frac{\xi\chi D_2}{u_*} \tag{3.52}$$

and

$$z_{1q} = \frac{\xi\lambda D_3}{u_*}. \tag{3.53}$$

The saturation value can be calculated either from the Clausius–Clapeyron relation or from some of the empirical relations that will cover wider range of validity in terms of temperature, like Teten's formula

$$e_{sat}(T) = 0.618 \exp\left(\frac{17.2T}{T + 237.3}\right), \tag{3.54}$$

where T is temperature of the air (water) in deg C and pressure is the standard pressure 1000 *mb's*. D_2 and D_3 can be expressed, like in the momentum case, as

$$D_2 = GR_e^{1/4} P_r^{1/2} \tag{3.55}$$

and

$$D_3 = GR_e^{1/4} S_c^{1/2}, \tag{3.56}$$

where G is constant whose value depends on the regime. Again we have three regimes with limiting R_e or corresponding u_* values. The first regime is the same one that we had for momentum, i.e. $u_* < u_*$ with $u_{*1} = 0.225$ [LT^{-1}]. The second regime is for $u_{*1} < u_* < u_{*2}$ where $u_{*2} = 0.7$ [LT^{-1}] while the third regime with $u_* > u_{*2}$. In the first two regimes we have viscous sub layer with temperature and humidity at the top of it as in Equations (3.50) and (3.51). In the third regime, r*ough with spray* we neglect the viscous calculations with the idea that with such strong winds waves are with spray causing direct injection of water into air.

Mellor (2004) has slightly different formulae for differences in potential temperature and humidity, analogous to

$$\begin{aligned} \Theta_2 - \Theta_1 &= -\frac{\Theta_*}{\kappa}\left[\Psi_h(\zeta) + \ln\left(\frac{z_2}{z_1}\right)\right] + F_{YK}\left(\frac{z_0 u_*}{\nu}, P_r\right) \\ q_2 - q_1 &= -\frac{q_*}{\kappa}\left[\Psi_h(\zeta) + \ln\left(\frac{z_2}{z_1}\right)\right] + F_{YK}\left(\frac{z_0 u_*}{\nu}, S_c\right). \end{aligned} \tag{3.57}$$

The two extra terms are corrections for the viscosity whose parameterization, according to the laboratory results (Yaglom and Kader, 1974), is

$$F_{YK} = 3.14\left(\frac{u_* z_0}{\nu}\right)^{1/2} (P_r^{2/3} - 0.2) + 2.11. \tag{3.58}$$

Numbers P_r and S_c are Prandtl's turbulent number and Shcmidt's number respectively.

The energy flux exchanges between the atmosphere and the ocean illustrate nicely two-way (or circular) nature of the energy flux as depicted in the sketch given in Figure 3.4. Part of the energy coming from the atmosphere represents the forcing factor for the ocean while on the other side ocean is also one of the sources of energy for the atmosphere.

Beside these energy exchanges, momentum input from the atmosphere is very important contributor to the formation of the surface currents while the energy fluxes are dominant contributors to the SST. Apart from the energy fluxes which operate *in situ* the other mechanism that influences the value of SST is advection done by the ocean currents through the advection process. For models of the atmosphere, the SST is either the lower boundary condition itself or determines (together with the air temperature) surface heat fluxes which again

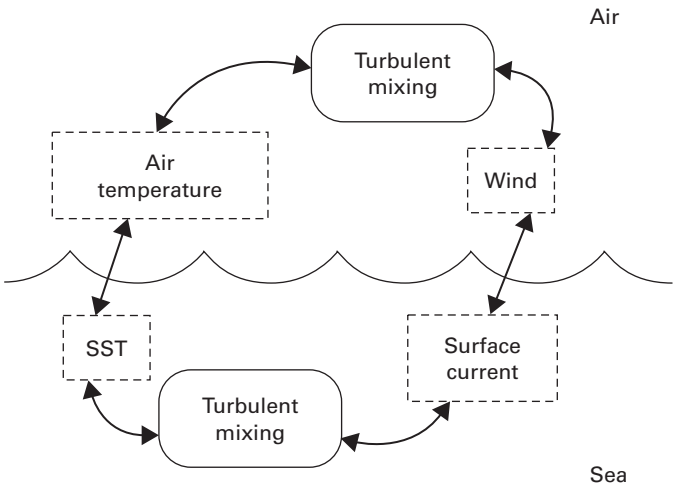

Figure 3.4. Sketch depicting the two-way nature of the atmosphere and the ocean interaction.

are the lower boundary conditions for other models. So for the SST forecast we need atmospheric fluxes while these atmospheric fluxes are in turn dependent on the SST. Very similar situation is with the mass where evaporation and precipitation and increase/decrease in the salinity of sea are two connected processes. We will come back to this in the next section.

We turn now to the radiation fluxes. In the situations without the knowledge of the surface long wave radiation fluxes oceanographers use empirical formulae with the net radiation $LW_a - LW_o$ being the most frequently calculated quantity. That can be done as suggested by May (1986)

$$LW = \lfloor \sigma \cdot T_a^4 (0.4 - 0.05 e_a^{1/2}) + 4\sigma \cdot T_a^3 (T_S - T_a) \rfloor (1 - 0.75 C^{3.4}), \tag{3.59}$$

where $\sigma = 5.6 \cdot 10^{-8}$ is the Boltzman's constant, T_a is two-metres temperature [in deg C], e_a is water vapour's partial pressure [in mb's], T_S is water temperature [in deg C] and C *is* cloud cover in ten's. For the flux of the short wave radiation we can use (Reed, 1977)

$$SW_a = Q_{TOT}(1 - 0.62C + 0.0019\beta)(1 - \alpha), \tag{3.60}$$

where C is again cloud cover, β is solar noon altitude in degrees and α albedo of the ocean. Q_{TOT} is defined as the sum of solar direct Q_{DIR} and diffuse Q_{DIFF} radiation, i.e.

$$Q_{TOT} = Q_{DIR} + Q_{DIFF}, \tag{3.61}$$

where

$$Q_{DIR} = Q_0 \tau \exp[-\sec(z)] \tag{3.62}$$

and

$$Q_{DIFF} = \frac{(1 - A_a)Q_0 - Q_{DIR}}{2}. \tag{3.63}$$

with $Q_0 = 1370$ [ML^2T^{-3}] being short wave flux at the top of the atmosphere, with τ as transmission coefficient of the atmosphere with the value of 0.7 while $A_a = 0.09$ is the absorption coefficient of the combined effect of the water vapour and the ozone (Rosati and Miyakoda, 1988 and Castellari *et al.*, 1997). Part of the incoming short wave radiation will partly penetrate the water and will be absorbed there. According to Paulson and Simson (1977), depth variation of that flux, due to the attenuation, can be calculated as

$$SW_o(z) = SW_a(re^{-z/a_1} + (1 - r)e^{-z/a_2}), \tag{3.64}$$

With SW_a as short wave flux at the ocean's surface while r, a_1 and a_2 are constants related to the optical properties of the water that, according to Jerlov (1976), can be classified into five groups. Values of these parameters depending on the group are given in Table 3.1.

Table 3.1. Values for the coefficients r, a_1 and a_2 for different types of sea water.

Jerlov type	I	Ia	Ib	II	III
r	0.58	0.62	0.67	0.70	0.78
a_1	0.35	0.60	1.0	1.5	1.4
a_2	23.0	20.0	17.0	14.0	7.9

Typical depth that sunlight can penetrate varies from 25 to 50 meters.

If we have values for SW_a and LW_a from measurements or from an atmospheric model as in the case of a numerical weather prediction model, LW_a can be treated as an independent term rather than part of the net radiation term. The ocean is also a source of the long wave radiation that can be calculated according to the Stephan–Boltzman's law for a grey body

$$LW_o = \varepsilon\sigma \cdot T_S^4, \tag{3.65}$$

with constant ε close to 1, $\varepsilon = 0.985$ (Gill, 1982). Temperature T_s is the SST in [deg K].

3.4 THE MASS AND SALINITY FLUXES

The question of mass and salinity fluxes, as part of the air–sea interaction, can be regarded as a single question because changes of the salinity of the sea can be viewed as the flux of the fresh water to/from the ocean. The diagram of that is shown in Figure 3.5.

The balance of these fluxes means

$$\rho_w w = E - P \tag{3.66}$$

where ρ_w is the density of the water, w is the vertical velocity in the ocean while E and P are fluxes of water vapour and liquid water (in precipitation) from the atmosphere. On the other hand, the salt balance can be depicted as in Figure 3.6 leading to

$$FS + \rho_w w S_w = 0, \tag{3.67}$$

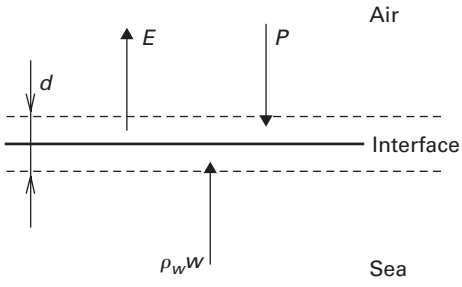

Figure 3.5. Diagram of mass flux. Flux of mass into the ocean, represented by the precipitation rate P, flux of mass out of the ocean, represented by the evaporation rate E, and flux of mass in the ocean $\rho_w w$ that balances the difference of the first two.

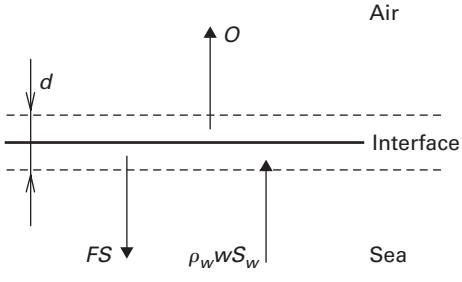

Figure 3.6. Fluxes contributing to the salt balance. Letter O denotes that atmospheric salt flux is zero. In the ocean we have diffusion of salt, FS and vertical flux of salt, $\rho_w w S_w$ due to the vertical advection.

where FS is diffusion of salt, $\rho_w w S_w$ is the vertical flux of salt due to the vertical advection, and S_w is salinity at the sea surface. Combining equations for the fluxes of mass and salinity we get

$$FS = -(E - P)S_w. \tag{3.68}$$

3.5 SIMULATIONS OF AIR–SEA INTERACTION OVER MEDITERRANEAN AREA

Starting with the climate modelling, the air–sea interaction was introduced as the basic factor in the large scale and longer term simulations. With the introduction of regional climate modelling, the spatial scale reduces but the time scale remains the same. That means that there is still a need for the air–sea interaction. Finally, with the extension of weather forecast periods beyond 5–7 days, the air–sea interaction found its place in the models for weather prediction (Miyakoda, 2002).

To approach such a problem, we have created coupled air–sea interaction model for a limited area (Djurdjević and Rajković, 2002) by coupling NCEP's Eta meso-scale atmospheric model (Janjic, 1984, 1994, Mesinger *et al*., 1988), as the atmospheric component, with POM (Princeton Ocean Model) (Mellor and Yamada, 1982, Mellor and Blumberg, 1985), as the ocean component. Exchanges of fluxes and SST were done interactively, after every physical time-step in the atmospheric model (∼360 s). For this exchange we made special coupler. Surface fluxes from Eta E-grid were interpolated on POM C-grid using bilinear

interpolation. The SST from C-grid was set on E-grid using simple averaging of all points that are inside the area of corresponding E-grid point (the resolution of the ocean model was about two times larger than the atmospheric model resolution). How good is such a model depends on the success of the coupling, which means how good are fluxes of energy and momentum that are exchanged between the two components of the model. That is not so easy to verify against direct observations so one can look at the SST as a variable most directly dependent on these exchanges.

Air–sea interaction in the Mediterranean area was analysed. The length of simulation was one year (2002). It is important to emphasize that the run was uninterrupted for the whole year, which means: start with a single initial field for both the atmosphere and the ocean, and then only updating at the boundaries. The ocean part was initialized from the MODB data set, which is monthly climatology of the Mediterranean sea. For the atmosphere part the German meteorological service, (Deutshen Wetterdienst or short DWD) data were used both for the initial and for the boundary conditions. The atmospheric boundary conditions were updated every six hours. The boundaries for the ocean were kept constant, i.e. no exchange through the boundaries.

The main topic is to verify the quality of computed fluxes. This will be done indirectly through verification of the SST. In Figure 3.7 we show time evolution of the mean SST for the whole Mediterranean sea. We can see that the annual variation was reproduced with remarkable accuracy. Even on shorter time scales, model was able to follow short scale variations of SST.

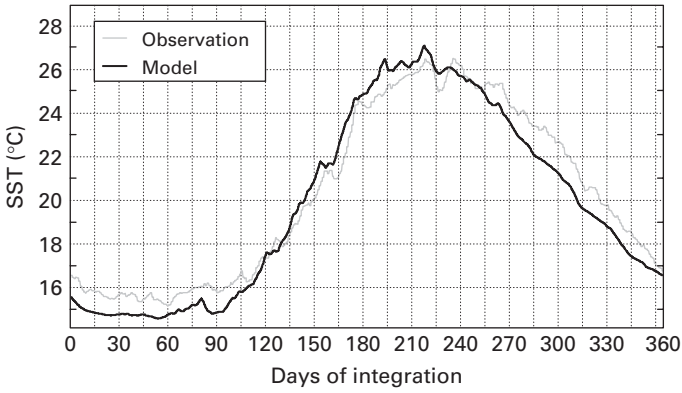

Figure 3.7. Mean SST for the Mediterranean sea.

To infer the influence of coupling on various results we have compared coupled and uncoupled runs, (Figure 3.8). For the uncoupled run we had specified the climatological SST, Reynolds climatology.

First we look into the coupled versus the uncoupled SST, which is presented in bottom panel of the figure. It is clear that differences are season dependent. They are stronger during the summer season. Since the atmosphere gets part of its moisture from the sea we looked into the area averaged diurnal accumulations of precipitation as well, middle panel in the same figure. The precipitation data cover almost whole of Serbia (south-east of Balkan peninsula), the area for which we had the data for that particular year. In general, both runs had surprisingly good precipitation forecasts. The annual accumulation for the observations was 721 mm, for the coupled model it was 750 mm and for the uncoupled it was 746 mm.

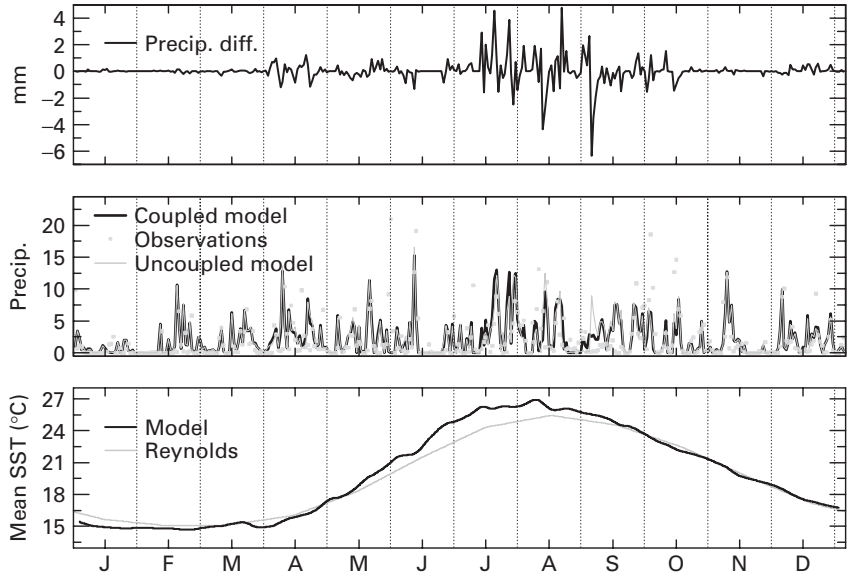

Figure 3.8. The bottom panel shows mean SST from the coupled run (black line) and, prescribed, climatological SST (grey line). The middle panel shows precipitation (cumulative diurnal) from the coupled run, black line, the same for the run with the climatological SST, grey line, and purple dots show observations of cumulative precipitation. The top panel shows differences in cumulative precipitation between coupled and uncoupled run.

Differences, top panel, were concentrated over the June, July and August period, what was also true for the diurnal averages. In comparison with the observations there is some scatter but, overall, coupled model does slightly better than the run with the climatological SST. This, of course, depends crucially on how far or on how close is the actual SST to the climatological one. Presumably, the reason that differences in the SST calculations lead to differences in the precipitation forecasts indicates that these differences come from the differences in the latent heat fluxes, so we have another indication of quality of flux calculations.

Using coupled air–sea model, the annual variation in average SST for the whole Mediterranean sea was reproduced with remarkable accuracy. That skill was maintained even on shorter time scales. Runs with prescribed climatological SST had also surprisingly good precipitation forecasts. Errors in the annual accumulation were less then 25 mm and 20 mm for coupled and uncoupled model respectively. Differences were concentrated over the June, July and August period. The same was valid in the case of diurnal accumulations.

APPENDIX—LIST OF SYMBOLS

List of Symbols

Symbol	Definition	Dimensions or Units
A	arbitrary constant	[m s^{-2}]
A_a	absorption combined coefficient of water vapour and ozone	

(*Continued*)

List of Symbols

Symbol	Definition	Dimensions or Units
B	constant of integration	$[m^2 s^{-2}]$
C	cloud cover in ten's	
D_1	constant	
D_2	constant	
D_3	constant	
E	flux of water vapour	$[kg\ m^{-2}\ s^{-1}]$
F_{YK}	surface layer correction term for viscosity part of fluxes	
FS	salt flux at sea surface	$[kg\ m^{-2} s^{-1}]$
G	constant	
H	heat flux in the vertical	$[K\ m\ s^{-1}]$
H_a	heat flux in the vertical in atmosphere	$[K\ m\ s^{-1}, W\ m^{-2}]$
H_o	heat flux in the vertical in ocean	$[K\ m\ s^{-1}, W\ m^{-2}]$
K_M	turbulent diffusivity coefficient for momentum	$[m^2 s^{-1}]$
K_{MB}	bulk turbulent diffusivity coefficient for momentum	$[m^2 s^{-1}]$
K_H	turbulent diffusivity coefficient for heat	$[m^2 s^{-1}]$
K_{HB}	bulk turbulent diffusivity coefficient for heat	$[m^2 s^{-1}]$
[L]	the dimension of length	
L	Monin–Obukhov length	[m]
LE	latent flux in the vertical	$[kg\ kg^{-1}\ ms^{-1}]$
LW	net long wave radiation flux	$[K\ m\ s^{-1}, W\ m^{-2}]$
LW_a	atmospheres long wave radiation flux	$[K\ m\ s^{-1}, W\ m^{-2}]$
LW_o	oceans long wave radiation flux	$[K\ m\ s^{-1}, W\ m^{-2}]$
M	momentum flux in the vertical	$[m^2 s^{-2}]$
M_a	momentum flux in the atmosphere	$[m^2 s^{-2}]$
M_o	momentum flux in the ocean	$[m^2 s^{-2}]$
P	flux of liquid water (precipitation)	$[kg\ m^{-2} s^{-1}]$
PGF	pressure gradient force	$[m\ s^{-2}]$
P_r	Prandtl's turbulent number	
Q_0	solar short wave flux at the top of the atmosphere	$[W\ m^{-2}]$
Q_{TOT}	total solar short wave radiation at surface	$[W\ m^{-2}]$
Q_{DIFF}	diffuse part of solar short wave radiation	$[W\ m^{-2}]$
Q_{DIR}	direct part of solar short wave radiation	$[W\ m^{-2}]$
R_e	Reynolds number	
S_c	Schmidt number	
S_W	salinity at the sea surface	[psu]
SW_a	short wave radiation flux at surface	$[K\ m\ s^{-1}, W\ m^{-2}]$
SW_o	part of short wave radiation flux in ocean	$[K\ m\ s^{-1}, W\ m^{-2}]$
[T]	the dimension of time	
T	temperature	[K]
T_a	air 2m temperature	[°C]
T_s	sea surface temperature	[°C]
U	mean wind velocity in x direction	$[m\ s^{-1}]$
V	mean wind velocity in y direction	$[m\ s^{-1}]$
W	mean wind velocity in z direction	$[m\ s^{-1}]$

(*Continued*)

List of Symbols

Symbol	Definition	Dimensions or Units
a_1	constant related to the optical properties of the water	[m]
a_2	constant related to the optical properties of the water	[m]
e_a	saturation water vapour partial pressure	[h Pa]
e_{sat}	saturation water vapour pressure	[h Pa]
f	Coriolis parameter	[s^{-1}]
g	gravitational acceleration constant	[m s^{-2}]
q	specific humidity (of water vapour)	[kg kg^{-1}]
q_s	surface specific humidity (of water vapour)	[kg kg^{-1}]
r	constant related to the optical properties of the water	
t	time	[s]
u_*	friction velocity	[m s^{-1}]
uu	kinematic flux of U-momentum in x direction	[m^2s^{-2}]
uv	kinematic flux of U-momentum in y direction	[m^2s^{-2}]
uw	kinematic flux of U-momentum in z direction	[m^2s^{-2}]
w	vertical velocity	[m s^{-1}]
$w\theta$	kinematic flux of heat in the vertical	[K m s^{-1}]
wq	kinematic flux of latent heat in the vertical	[kg kg^{-1} ms^{-1}]
z_o	aerodynamic length based on friction velocity	[m]
z_{1T}	viscous sub layer height for temperature	[m]
z_{1q}	viscous sub layer height for humidity	[m]
Θ	potential temperature	[K]
Θ_0	constant, characteristic potential temperature in the surface layer	[K]
Θ_S	surface potential temperature	[K]
Ψ	integral of surface layer stability correction terms	
α	albedo of the ocean surface	
β	stability parameter, solar noon altitude	[k^{-2}], [rad]
ε	emissivity of sea surface	
ζ	dimensionless height in the surface layer	
κ	von Karaman constant	
λ	heat molecular viscosity coefficient	[m^2s^{-1}]
ρ_w	density of the water	[kg m^{-3}]
σ	Boltzmann's constant	[W $m^{-2}K^{-4}$]
τ	atmospheric transmission coefficient	
υ	kinematic molecular viscosity	[m^2s^{-1}]
ϕ_h	surface layer stability correction term for heat	
ϕ_m	surface layer stability correction term for momentum	
χ	humidity molecular viscosity coefficient	[m^2s^{-1}]

REFERENCES

Businger, J. A., Wyngaard, J. C., Izumi, Y. and Bradley, E. F., 1971, Flux-profile relationship in the atmospheric boundary layer. *Journal of Atmospheric Science*, **28**, pp. 181–189.

Castellari, S., Pinardi, N. and Leaman, K., 1998, A model study of air–sea interactions in the Mediterranean Sea. *Journal of Marine Systems*, **18**, pp. 89–114.

Charnock, H., 1955, Wind stress on a water surface. *Quarterly Journal Royal Meteorological Society*, **81**, pp. 639–640.

Chen, F., Mitchell, K., Janjic, Z. I. and Baldwin, M., 1996, Land–surface parameterization in the NCEP Mesoscale Eta Model. In *Activities in Atmospheric and Oceanic Modelling*, No. 23, 4.4, (Geneva: CAS/JSC WGNE).

Djurdjević, V. and Rajković, B., 2002, Air–sea interaction in Mediterranean area. In *Spring Colloquium on the Physics of Weather and Climate "Regional weather prediction modelling and predictability"*, (Trieste: ICTP).

Gill, A. E., 1982, *Atmosphere–Ocean Dynamics*. (New York: Academic Press).

Janjic, Z. I., 1996, The surface layer parameterization in the NCEP Eta Model. In *Research Activities in Atmospheric and Oceanic Modelling*, 4.16–4.17, (Geneva: CAS/JSC WGNE).

Janjic, Z. I., 1995, The surface layer parameterization in Eta model. In Summer *School in Meteorology: Hydrological Cycle in Atmospheric Models*, Doc. 8, (Belgrade: Federal Hydro-meteorological Institute).

Janjic, Z. I., 1994, The step-mountain Eta coordinate model: Further developments of the convection, viscous sub-layer and turbulence closure schemes. *Monthly Weather Review*, **122**, pp. 927–945.

Janjic, Z. I., 1984, Non-linear advection schemes and energy cascade on semi-staggered grids. *Monthly Weather Review*, **112**, pp. 1234–1245.

Jerlov, N. G., 1976, *Marine Optics*, (Amsterdam: Elsevier Scientific Publishing Company).

Liu, W. T., Katsaros, K. B. and Businger, J. A., 1979, Bulk parameterization of air–sea exchanges of heat and water vapour including the molecular constraints at the interface. *Journal of Atmospheric Science*, **36**, pp. 1722–1735.

Mangarella, P. A., Chambers, A. J., Street, R. L. and Hsu, E. Y., 1973, Laboratory studies of evaporation and energy transfer through a wavy air–water interface. *Journal of Physical Oceanography*, **3**, pp. 93–101.

May, P.W., 1986, A brief explanation of Mediterranean heat and momentum flux conditions. NORDA Code 322, NSTL, MS 39529.

Mellor, G. L., 2004, *Users guide for a three-dimensional, primitive equation, numerical ocean model*, (Princeton: Princeton University).

Mellor, G. L., 1986, Numerical simulation and analysis of the mean coastal circulation of California. *Continental Shelf Research,* **6**, pp. 689–713.

Mesinger, F., Janjic, Z. I., Nickovic, S., Gavrilov, D., and Deaven, D. G., 1988, The step-mountain coordinate: model description and performance of alpine lee cyclogenesis and for a case of an alpine redevelopment. *Monthly Weather Review*, **116**, pp. 1493–1518.

Miyakoda, K., 2002, Strategy for regional Seasonal Forecast. In *Ocean Forecasting: Conceptual Basis and Applications*, edited by Pinardi, N. and Woods, J. D., (Berlin: Springer), pp. 179–199.

Monin, A. S. and Obukhov, A. M., 1954, Basic laws of turbulent mixing in the atmosphere near the ground. *Trudy Geophizicheskogo Instituta*, **24**, pp. 1963–1987.

Obukhov, A.M., 1946, Turbulence in thermally inhomogeneous atmosphere. *Trudy Geophizicheskogo Instituta*, **1**, pp. 95–115.

Paulson, C. A. and Simpson, J., 1977, Irradiance measurements in the upper ocean. *Journal of Physical Oceanography*, **7**, pp. 952–956.

Rajković, B. and Mellor, G. L., 1988, Coastal ocean response to atmospheric forcing. In *International Colloquium on Ocean Hydrodynamics, 19th—Small–Scale Turbulence and Mixing on the Ocean*, (Amsterdam: Elsevier Science Publishers), pp. 141–149.

Reed, R. K., 1977, On estimating insolation over the ocean. *Journal of Physical Oceanography*, **17**, pp. 854–871.

Rosati, A. and Miyakoda, K., 1988, A general circulation model for upper ocean simulation. *Journal of Physical Oceanography*, **18**, pp. 1601–1626.

Yaglom, A. M. and Kader, B. A., 1974, Heat and Mass Transfer between a rough wall and turbulent fluid flow at high Reynolds and Peclet numbers. *Journal of Fluid Mechanics*, **62**, pp. 601–623.

CHAPTER FOUR

Modelling of flux exchanges between heterogeneous surface and atmosphere

Dragutin T. Mihailović
Faculty of Agriculture, University of Novi Sad, Novi Sad, Serbia

Darko Kapor
Department of Physics, University of Novi Sad
Novi Sad, Serbia

ABSTRACT

In numerical models of atmospheric flow it is necessary to consider the properties of boundary-layer flow as averaged over the grid cell of the model. "Flux aggregation" is the process by which an effective horizontal average or aggregate of turbulent fluxes is formed over heterogeneous surfaces. The aggregated flux differs from spatial average of equilibrium fluxes in an area, due to nonlinear advective enhancement associated with local advection across surface transitions. Aggregated fluxes can be related to vertical profiles only above the blending height. The concept of so-called blending height has become frequently used approach to the Parameterization of areally averaged fluxes over heterogeneous surfaces. There are three approaches commonly taken for calculating the transfer of momentum, heat and moisture from a grid cell comprised of heterogeneous surfaces. They are: (a) "parameter aggregation", where grid cell mean parameters such as roughness length, albedo, leaf area index, stomatal resistance, soil conductivity, etc., are derived in a manner which attempts to incorporate in the best way the combined non-linear effects of each of different relatively homogeneous subregions ("tiles") over the grid cell; (b) "flux aggregation", where the fluxes are averaged over the grid cell, using a weighted average with the weights determined by the area covered by each tile; and (c) a combination of the "flux aggregation" and "parameter aggregation" methods. However, if large differences exist in the heterogeneity of the surfaces over the grid cell, then a combined method has to be applied. In "parameter aggregation" and "flux aggregation", numerical modellers usually either use the dominant type for the grid cell or make a simple linear average to determine grid cell averages of certain parameters. Both these methods lead to uncertainties in the Parameterization of boundary layer processes when heterogeneities exist over the grid cell. In this chapter we describe: (1) the concept of the blending height, (2) an approach for aggregation of aerodynamic surface parameters, (3) an approach for aggregation of albedo and (4) a combined method for calculating the surface temperature and water vapour pressure over heterogeneous surface.

4.1 FOREWORD

The effect of land surface heterogeneity on the atmosphere and on the surface energy balance has attracted widespread interest because understanding of this effect is fundamental to

a comprehensive knowledge of regional and global hydrometeorological processes. Moreover, many investigators are concerned that inadequate treatment of heterogeneity may weaken confidence in large-scale models, which do not resolve heterogeneity at scales smaller than the model grid. Several technical advances have spurred interest in heterogeneity further; not the least of which is the availability of satellite data. Remote sensing technology offers high-resolution data to quantify regional and global heterogeneity and make areal-average measurements representing the effective areal-average value of surface parameters. Computational advances and increased interest in climate, and therefore in the modelling of land–atmosphere interactions, have also promoted interest in surface heterogeneity (Michaud and Shuttleworth, 1997).

"Aggregation" generally refers to spatial averaging of some heterogeneous surface variable such as albedo, soil hydraulic properties, soil moisture, fraction of vegetation cover, surface temperature, surface reflectance, sensible heat flux, latent heat flux, surface resistance, aerodynamic resistance, or aspects of topography; or it refers to spatial averaging of some near-surface meteorological field such as temperature, humidity or precipitation. There is the question of how to "average" (arithmetically or logarithmically being two of the ways), and how to determine the size of the region over which averaging should be performed. This size depends on the degree of heterogeneity and whether there is a causal relationship between the variable being averaged and the quantity to be calculated in the model. There is a possibility that aggregation will fail when a heterogeneous variable has a nonlinear relationship with some other variable of interest. Moreover, aggregation strategies may be dependent on model formulation. Aggregation is a more limited enterprise than "scaling", because scaling seeks to find a basis for relating a phenomenon at one scale to an analogous phenomenon at other scales. Michaud and Shuttleworth (1997) emphasized that interest in the "aggregation problem" is motivated largely either by the desire to make efficient use of highly resolved spatial data, or by the desire to proceed confidently without utilisation of detailed data. In other words, it seeks to address the question, "How can we model variable processes spatially using a grid cell which is coarse enough to be economical, yet fine enough that results are not affected by sub-grid-scale variability?" However, the topic of aggregation is equally pertinent to the question of adequate spatial resolution of measurements; hence there is a need to investigate the effect of spatial resolution on the accuracy of remotely sensed measurements.

In numerical models of atmospheric flow it is necessary to consider the properties of boundary-layer flow as averaged over the grid cell of the model. "Flux aggregation" is process by which an effective horizontal average or aggregate of turbulent fluxes is formed over heterogeneous surfaces. The aggregated flux differs from spatial average of equilibrium fluxes in an area, due to nonlinear advective enhancement associated with local advection across surface transitions. Aggregated fluxes can be related to vertical profiles only above the blending height. The concept of so-called blending height has become frequently used approach to the Parameterization of areally averaged fluxes over heterogeneous surfaces (e.g. Wieringa, 1986; Mason, 1988; Claussen, 1990, 1991, 1995). For above the blending height modifications of air flow owing to changes in surface conditions will not be recognisable individually, but an overall stress or heat flux profile will exist, representing the surface conditions of a large area. This concept should be applicable to variation in surface conditions at scales considerably smaller than 10 km, i.e., for so-called disorganised or Type A landscapes (Shuttleworth, 1988). At these scales the concept of blending height has been tested by microscale models (e.g. Mason, 1988; Claussen, 1991). In flow over terrain inhomogeneities at scale larger than 10 km, i.e. over so-called organised or Type B landscapes, blending takes place essentially above the surface layer where Coriolis effect must not be ignored. Moreover, in Type B landscapes, secondary circulations may develop which mix momentum and energy throughout the planetary boundary layer efficiently and presumably affect surface fluxes (Claussen, 1995).

Until the middle of the last decade, the hydrologists and meteorologists have invested a large effort in making the theoretical and modelling background related to the aggregation of fluxes and parameters. Those efforts and results reached are comprehensively elaborated by Michaud and Shuttleworth (1997) through the Tucson Aggregation Workshop summary findings that will be given in this chapter in exactly the same form as it was done in the paper by aforementioned authors. They can be summarised as follows:

- Aggregation of land surface properties appears to be successful to within an accuracy of about 10% in many, but not all, circumstances. Stated more precisely, effective parameter values representing the areal averages of land surface properties in models of surface–atmosphere interactions have been calculated successfully from simple averaging rules, with the form of the latter being related to the nature of the variable being averaged (e.g. Shuttleworth, 1991). Patch-scale and meso-scale simulations show that energy fluxes calculated from these effective (aggregated) parameters can be within 10% of energy fluxes obtained from higher-resolution simulations (Dolman and Blyth, 1997; Noilhan *et al*., 1997; Sellers *et al*., 1997).

  Using a combination of wind tunnel experiments, theoretical analysis, and simulation, Raupach and Finnigan (1997) showed that the regional energy balance is insensitive to the presence of hills of moderate size, providing that the nature of the vegetation and soil at the surface and the soil water available to the vegetation are uniform. Aggregation of near-surface meteorology considered in isolation is likely to be successful for slopes up to 20%.

  The above successes are encouraging, but additional work is needed in (1) the aggregation of soil hydraulic properties, (2) lateral near-surface water and groundwater flow, and (3) examination of the effect of distinct lateral changes in vegetation height. In addition, some, but not all, researchers point to the need for additional work in the aggregation of soil moisture. Although there has been substantial progress in understanding scaling of ecohydrologically relevant soil parameters at plot and field scales (1–10 000 m^2) (Kabat *et al*., 1997), this progress has been little recognised by the large-scale meteorological modelling community; the applicability of these scaling procedures at large scales remains under-explored. In terms of soil moisture, several researchers (Wood, 1997; Sellers *et al*., 1997) have shown that neglecting small-scale moisture variability may compromise coarse-grid simulations of areal-average evaporation, though Sellers *et al*. (1997) view this as of secondary significance.
- Meso-scale heterogeneity in land surface properties is now known to be capable of generating meso-scale circulations, which can have a significant effect on vertical energy transfers within the atmosphere. Parameterization of this phenomenon, which would allow general circulation models to accommodate these additional sub-grid-scale atmospheric transport processes, is a topic of active research (Pielke *et al*., 1997). However, some researchers (Noilhan *et al*., 1997) view the need to provide such Parameterization with less urgency, drawing attention to the moderating effect of winds.
- The purpose of many aggregation studies is to provide information to refine or stimulate regional and global models of the interactions between soil, vegetation, energy, and water. The basic tools for regional ecohydrological modelling have already been developed and applied in mountainous terrain (Thornton *et al*., 1997). Adequate specification of finely resolved near-surface meteorology, particularly precipitation, is one of the difficulties that needs to be addressed, but there is currently no universally accepted procedure for doing this.
- Remotely sensed vegetation indices contain useful information on the bulk stomatal resistance and photosynthetic uptake of vegetation (Sellers *et al*., 1992), but the roles of vegetation type and nutrition on the interpretation of these indices require further investigation.

- Aggregation of remotely sensed measurements in sparse canopies can be accomplished with little error in some circumstances (such as aggregation of surface temperature from $1\,m^2$ to $1\,km^2$) but not others (such as aggregation of sensible heat to $1\,km^2$ (Moran *et al.*, 1997).

4.2 THE CONCEPT OF BLENDING HEIGHT

In the studies of the heterogeneous terrain, Wieringa (1986) suggested averaging momentum fluxes at a blending height. He interpreted the blending height as a height above which modifications of air flow owing to changes in surface conditions will not be recognised individually, but overall stress or heat flux exist, representing the surface conditions of a large area. Mason (1988) more explicitly defined the blending height l_b [L] as a scale height at which the flow is approximately in equilibrium with local surface and also independent of horizontal position. Using the latter definition, the momentum flux $-(\overline{uw'})[L^2T^{-2}]$ on average over a heterogeneous surface is

$$\left[-(\overline{uw'}) = \sum_i [-(\overline{uw'})_i]\right] = \kappa^2 U^2(l_b) \sum_i \frac{\sigma_c^i}{\ln\left(\frac{l_b}{z_0^i}\right)^2} \tag{4.1}$$

where square brackets denote a horizontal average, σ_c^i is fractional area covered by a patch i with the roughness length z_0^i[L]. $U[LT^{-1}]$ is mean wind speed and κ the von Karman constant (here $\kappa = 0.4$). An aggregated roughness length z_{0a}[L] can also be defined from Eq. (4.1), as

$$\frac{1}{\ln\left(\frac{l_b}{z_{0a}}\right)^2} = \sum_i \frac{\sigma_c^i}{\ln\left(\frac{l_b}{z_0^i}\right)^2}. \tag{4.2}$$

Mason (1988) provided a heuristic model, which indicates that

$$\frac{l_b}{L_c}\left(\ln\frac{l_d}{z_0}\right)^2 \approx 2k^2 \tag{4.3}$$

where L_c[L] is horizontal scale of roughens variations, and from Eq. (4.3) one can conclude that $l_b/L_c \approx O(10^{-2})$. Claussen (1991) deduced the blending height from numerical simulations of air flow over a surface with randomly varying roughness. He found that the sum of errors owing to the assumptions of horizontal homogeneity and equilibrium with the local surface attains a minimum at a height, which is roughly as large as the diffusion height scale l_d

$$\frac{l_b}{L_c}\left(\ln\frac{l_d}{z_0}\right) \approx c_i k \tag{4.4}$$

where the constant c_i should be $O(1)$. Claussen (1990) found $c_i = 1.75$. Using either estimate of blending height, Eq. (4.3) or (4.4), one obtains reasonably accurate estimates of an aggregated roughness length. Differences between estimates are small particularly when considering the inaccuracy in determining L_c. From simulations of air flow over randomly

varying surface conditions, Claussen (1991) inferred that L_c is the length scale at which on average the surface conditions change over a larger fetch.

4.2.1 Parameter aggregation

Provided L_c and σ_c^i are known, then the blending height and the aggregated roughness length can be obtained from Eqs. (4.2) and (4.3) or (4.4). The average momentum flux is finally computed from the aggregated roughness length. The computation of areally averaged fluxes from aggregated parameters will be called "parameter aggregation" in the following. Formally, an areally averaged flux $\langle \Phi \rangle$ is

$$\langle \Phi \rangle = f(\psi_a, \dots) \tag{4.5a}$$

where the vector of aggregated surface parameters is a function of surface parameters of each land type,

$$\psi_a = f(\psi_i). \tag{4.5b}$$

For example, z_{0a} is given by Eqs. (4.2), (4.3) or (4.4), but for an aggregated albedo α_a,

$$\alpha_a = \sum\nolimits_i \sigma_c^i \alpha_i.$$

4.2.2 Flux aggregation

In stratified flow, it has been proposed (e.g. Wood and Mason, 1991; Noilhan and Lacarrère, 1992) to apply the method of "parameter aggregation" also to estimation of areally averaged heat fluxes, i.e. by defining proper values of aggregated albedo, aggregated leaf area index, or aggregated stomatal resistances. However, "parameter aggregation" will fail if surface conditions vary strongly. For example, definition of an aggregated soil heat conductivity is cumbersome in the presence of water and soil. The heat flux into soil is predominantly conductive, whereas water advection or thermoclinic circulation could influence the heat flux into water. Likewise, it has been shown (e.g. Claussen, 1990; Blyth *et al*., 1993) that an aggregated stomatal resistance is impossible to find if the local resistances vary strongly.

A second complication arises as a result of the nonlinear relationship between turbulent fluxes and vertical mean profiles. For example, the vertical gradient of potential temperature can be positive on average over larger area, whereas the averaged heat flux is upward, because strong turbulence in small regions of unstable stratification can dominate the averaged heat flux, resulting in an averaged flux opposite to the averaged vertical gradient of potential temperature. This process is important in the winter polar zones (e.g. Stössel and Claussen, 1993; Claussen, 1995). To circumvent these problems, Claussen (1991) suggested computing momentum and heat fluxes at the blending height for each land-use type, which can be identified in the area under consideration. Consequently, the averaged surface fluxes are obtained by the average of surface fluxes on each land-use surface weighted by its fractional cover σ_c^i. This method is called "flux aggregation" in the following. Formally,

$$\langle \Phi \rangle = \sum_i \sigma_c^i \Phi_i \tag{4.6a}$$

where

$$\Phi_i = f(\psi_i, \dots). \tag{4.6b}$$

Fluxes Φ_i also depend on turbulent transfer coefficients, which in turn are functions some of the components ψ_i. The requirement of computing the surface fluxes for each land type at the blending height leads to a revised formulation of turbulent transfer coefficients which differs from the conventional formulation (Claussen, 1991).

4.3 AN APPROACH FOR AGGREGATION OF AERODYNAMIC SURFACE PARAMETERS OVER HETEROGENEOUS SURFACE

Numerical modellers usually either use the dominant surface type over the grid cell or a simple linear average to determine grid cell averages of surface parameters. Both methods have problems in parameterising the surface layer processes when large heterogeneities exist over the grid cell (Mason, 1988; Claussen, 1995; Hess and McAvaney, 1998). However, it is possible to make aggregation of some surface parameters over the grid cell in a more physical way as it is done by Mihailović *et al*. (2002). They suggested approaches for: (1) calculating the exchange of momentum between the atmosphere and heterogeneous surface, (2) deriving the equation for the wind speed profile in a roughness sublayer under neutral conditions, and (3) derivation of the aggregated roughness length and displacement height over the grid cell.

4.3.1 Mixing length and momentum transfer coefficient

We derive first an expression for the momentum transfer coefficient K_m [L^2T^{-2}] and the wind profile, under neutral conditions above a heterogeneous grid cell consisting of patches of vegetation, solid part (e.g. bare soil, rock, urban tile), and water. The non-uniformity of the vegetative part is expressed by the surface vegetation fractional cover σ_i representing the i type of vegetation cover filling the grid cell. Their sum takes values from 0 (when only solid surface or water are present) to 1 (when the ground surface is totally covered by plants). The non-uniformity of solid (solid parts of urban area, rock solid and bare soil) and liquid portions (sea, river, lake, water catchments) of the grid cell will be denoted by symbols δ_i and ν_i, representing the surface solid and water fractional cover respectively. The total sum of all these fractional covers must be equal to unity. A realistic surface of a grid cell is rather porous with patches of solid material, vegetative portions and free air spaces inside and around it, which can produce quite different modes of turbulence in comparison with a uniform underlying surface. Also, the designed underlying surface in the grid cell is a mosaic of patches of various sizes and different aerodynamic characteristics. Presumably, this mosaic will produce microcirculations with possible flow separations at leading and trailing edges, setting up a highly complex dynamic flow. In this section, we will not address the consequences of such non-uniformity of the vegetation part of the underlying surface. Instead, following calculations are based on the assumption that the underlying surface is a combination of the only three portions consisting of a vegetative portion, characterised with total fractional cover σ, a solid portion, characterised with total δ, and a liquid portion having total fractional cover $\nu = 1 - \sigma - \delta$.

As suggested by Mihailović *et al*. (1999), who introduced an expression for the mixing length over a grid cell consisting of vegetated and non-vegetated surface, the aggregated mixing length l_m^a [L] at level z[L] above a grid cell consisting of a heterogeneous surface as defined above, might be represented by some combination of their single mixing lengths.

If, as a working hypothesis, we assume a linear combination weighted by fractional cover, according to mixing length theory we can define l_m^a as

$$l_m^a = \kappa \left[\sum_{i=1}^{K} \sigma_i \varsigma_i (z - d_i) + \sum_{i=1}^{L} \delta_i z + \sum_{i=1}^{M} \nu_i z \right], \tag{4.7}$$

where σ_i, δ_i and ν_i are partial fractional covers for vegetation, solid part, and water surface, with K, L, and M as the maximum number of patches in the grid cell respectively, while d_i is zero displacement height for the ith vegetative part in the grid cell. Parameter ς_i is the dimensionless constant introduced by Mihailović *et al*. (1999) that depends on morphological and aerodynamic characteristics of the vegetative cover whose values vary according to the type of vegetative cover. The functional form of the parameter ς, considered as a function of leaf drag coefficient C_d and leaf area index LAI, was derived empirically by Lalić (1997) and Lalić and Mihailović (1998). They analysed the wind profiles in the sublayer above a broad range of vegetation [i.e. short grass (Morgan *et al*., 1971), tall grass (Jacobs and van Boxel, 1988) and forest (De Bruin and Moore, 1985)], using the maximum and minimum values of LAI for 20 types of vegetation listed in Delage and Verseghy (1995). Comparison of model simulations with observations showed a good agreement with the expression $\varsigma^2 = \sqrt{2}(C_d LAI)^{1/10}$ for short grass, $\varsigma^2 = 2(C_d LAI)^{1/5}$ for tall grass, and $\varsigma^2 = 4(C_d LAI)^{1/2}$ for forest.

The momentum transfer coefficient K_m for the non-homogeneous vegetative cover is

$$K_m = l_m^a u_m^a \tag{4.8}$$

here u_*^a [LT^{-1}] is a friction velocity above non-homogeneously covered grid cell. Replacing l_m^a, in Eq. (4.8), by the expression (4.7), we get

$$K_m = \kappa \left[\sum_{i=1}^{K} \sigma_i \varsigma_i (z - d_i) + \sum_{i=1}^{L} \delta_i z + \sum_{i=1}^{M} \nu_i z \right] u_*^a. \tag{4.9}$$

4.3.2 Wind profile

Using the assumption that the friction velocity u_*^a is equal to $l_m^a \, du/dz$ yields

$$u_*^a = \kappa \left[\left(\sum_{i=1}^{K} \sigma_i \varsigma_i + \sum_{i=1}^{L} \delta_i + \sum_{i=1}^{M} \nu_i \right) z - \sum_{i=1}^{K} \sigma_i \alpha_i d_i \right] \frac{du}{dz}. \tag{4.10}$$

This equation can be integrated to

$$u(z) = \frac{u_*^a}{\kappa} \frac{1}{\sum_{i=1}^{K} \sigma_i \varsigma_i + \sum_{i=1}^{L} \delta_i + \sum_{i=1}^{M} \nu_i}$$

$$\ln \left[\left(\sum_{i=1}^{K} \sigma_i \xi_i + \sum_{i=1}^{L} \delta_i + \sum_{i=1}^{M} \nu_i \right) z - \sum_{i=1}^{K} \sigma_i \varsigma_i d_i \right] + C_i \tag{4.11}$$

where C_i is an integration constant. If we introduce the following notations

$$\Lambda = \sum_{i=1}^{K} \sigma_i \varsigma_i + \sum_{i=1}^{L} \delta_i + \sum_{i=1}^{M} \nu_i \tag{4.12}$$

and

$$\Gamma = \sum_{i=1}^{K} \sigma_i \varsigma_i d_i, \tag{4.13}$$

then Eq. (4.11) can be written in a concise form

$$u(z) = \frac{u_*^a}{k} \frac{1}{\Lambda} \ln(\Lambda z - \Gamma) + C_i. \tag{4.14}$$

The constant C_i can be found if we introduce the assumption that the extrapolation of the wind profile given by Eq. (4.14) produces zero wind velocity at some height z_k[L] defined as

$$z_k = Z_0 + D \tag{4.15}$$

where

$$Z_0 = \frac{z_0}{\Lambda} \tag{4.16}$$

and

$$D = \frac{\Gamma}{\Lambda}. \tag{4.17}$$

The last two expressions can be considered as aggregated roughness length and displacement height over a non-homogeneous surface in the grid cell as in Mihailović *et al*. (1999) for the case of a surface consisting only of bare soil and vegetation patches.

The above condition can then be written as

$$0 = \frac{u_*^a}{\kappa} \frac{1}{\Lambda} \ln(\Lambda z_k - \Gamma) + C_i. \tag{4.18}$$

After substituting the expressions (4.15), (4.16) and (4.17) into Eq. (4.18), we find that the constant C_i is given by

$$C_i = \frac{u_*^a}{\kappa} \frac{1}{\Lambda} \ln z_0. \tag{4.19}$$

Finally, combining the expressions (4.14) and (4.18), we derive a wind profile in the roughness sublayer above the non-uniform surface in the grid cell under neutral conditions, which

can be written in the form

$$u(z) = \frac{u_*^a}{\kappa\Lambda} \ln \frac{z - D}{Z_0}. \tag{4.20}$$

In this wind profile, Z_0 and D, defined by Eqs. (4.16) and (4.17), represent the aggregated roughness length and displacement height above the grid cell, respectively. Note that the aerodynamic properties of different types of vegetation, expressed through the vegetation-type dependent parameter ς, are incorporated into the expressions for Λ and Γ and, thus, Z_0, D and $u(z)$.

4.3.3 Parameterization of roughness length and displacement height

Equation (4.14) can be used in numerical modelling of atmospheric processes above built-in urban areas and forest canopies since their dynamics exhibits many similarities as well as dissimilarities (Fernando *et al*., 2001). This wind profile can be also successfully applied to modelling processes above an urban grid cell (Mihailović *et al*., 2005; Lazic *et al*., 2002). In the Parameterization of the aggregated roughness length given by Eq. (4.16), it seems that a suitable choice would be to separate the vegetative, z_{0v} [L], and non-vegetative, z_{0n} [L], parts of the grid cell. Bearing in mind that the non-vegetative part includes solid and liquid fraction with roughness lengths z_{0s} [L] and z_{0l} [L] respectively, the aggregated roughness length may be written in the form

$$Z_0 = \frac{1}{\Lambda} \frac{\sigma z_{0v} + \delta z_{0s} + \nu z_{0l}}{\sigma + \delta + \nu}. \tag{4.21}$$

Since the sum of total fractional covers is equal to 1, the last expression can be simplified

$$Z_0 = \frac{\sigma z_{0v} + \delta z_{0s} + \nu z_{0l}}{\Lambda}. \tag{4.22}$$

For roughness length of solid and water fraction, we use a simple average having the form

$$z_{0s} = \frac{\sum_{i=1}^{L} \delta_i z_{0s}^i}{\sum_{i=1}^{L} \delta_i} \tag{4.23}$$

and

$$z_{0l} = \frac{\sum_{i=1}^{M} \nu_i z_{0l}^i}{\sum_{i=1}^{M} \nu_i}. \tag{4.24}$$

However, for the roughness length of the vegetative part, we will use a simple average in combination with the expression for the generalised roughness length (Mihailović *et al*.,

1999). In that case, we obtain

$$z_{0v} = \frac{\sum_{i=1}^{K} \frac{\sigma_i \varsigma_i^m}{\sigma_i(\varsigma_i - 1) + 1} z_{0v}^i}{\sum_{i=1}^{K} \sigma_i}, \tag{4.25}$$

where ς_i^m is a parameter for ith part of a vegetative cover in the grid cell, while m is a parameter that has a value of 2 according to Mihailović *et al*. (1999). The use of this parameter in the expression for the wind profile in the roughness layer gives systematically better results above the broad range of plant communities than the classical logarithmic wind profile (Mihailović *et al*., 1999).

Substituting (4.23), (4.24) and (4.25) into Eq. (4.16), we obtain the expression for the roughness length Z_0 as

$$Z_0 = \frac{1}{\Lambda}\left[\sum_{i=1}^{K} \frac{\sigma_i \varsigma_i^m}{\sigma_i(\varsigma_i - 1) + 1} z_{ov,i} + \frac{\sum_{i=1}^{L} \delta_i z_{0s}^i}{\sum_{i=1}^{L} \delta_i} + \frac{\sum_{i=1}^{M} \nu_i z_{ol,i}}{\sum_{i=1}^{M} \nu_i}\right]. \tag{4.26}$$

According to Eqs. (4.12), (4.13) and (4.17), the aggregated displacement height D has the form

$$D = \frac{\sum_{i=1}^{L} \varsigma_i \alpha_i d_i}{\sum_{i=1}^{K} \sigma_i \varsigma_i + \sum_{i=1}^{L} \delta_i + \sum_{i=1}^{M} \nu_i}. \tag{4.27}$$

Mihailović *et al*. (2002) have performed numerical tests comparing the aforementioned expressions for aggregated aerodynamic characteristics with some earlier approaches (Kondo and Yamazawa, 1986; Claussen, 1995). It was done by comparison of the wind profiles using the observations obtained in an urban area. They found that (1) there exists a better physical justification of the derivation of aggregate aerodynamic characteristics than in the case when aggregation is made by a simple averaging method, (2) in numerical experiments with different fractions of grid cell components the aggregated aerodynamic parameters show more realistic reproduction of the behaviour of observed features, and (3) the wind profile above the urban area obtained by Eq. (4.20) simulates more correctly the wind speed than the two other methods.

4.4 AN APPROACH FOR AGGREGATION OF ALBEDO OVER HETEROGENEOUS SURFACE

In the grid-based environmental models, numerical modellers usually make a simple averaging to determine the albedo as the grid cell-average albedo, a key variable in the

Parameterization of the land surface radiation and energy budgets (Wetzel and Boone, 1995; Jacobson, 1999; Hu *et al*., 1999). Recently, attempts go towards the calculation of the net shortwave radiation by combining the net albedo from different patches (Walko *et al*., 2000). However, a physics-based analysis indicates that there is a significant deviation of the albedo above such a heterogeneous surface from that calculated by simple averaging, seriously affecting the calculated values of quantities describing surface biophysical processes like land surface energy budgets, canopy photosynthesis and transpiration, urban area physics and snow melt, among others (Mihailović and Kallos, 1997; Delage *et al*., 1999). It is, therefore, important to understand the general behaviour and limitations of the approaches used for aggregating the albedo over a heterogeneous grid cell in current land surface models. With these issues in mind, this section considers a new approach for aggregating the albedo over a very heterogeneous surface in land surface schemes for use in grid-based environmental models following Kapor *et al*. (2002) and Mihailović *et al*. (2003). More precisely, they introduced a method for accounting for the effect of different height levels and nature of the surfaces present in a given grid cell. This procedure, although transparent, is rather cumbersome, so that we shall demonstrate it using a situation with rather simple geometry, i.e. a two-patch grid-cell with a simple geometrical distribution and different heights of its components. We start with a discussion of the basic assumptions of the approach, and then derive a general expression for the aggregated albedo. The derived expression for the albedo of this particular grid-cell is compared with the conventional approach, using a common Parameterization of albedo over the same grid cell (Oke, 1987).

First of all let us state the basic assumptions. We suppose that the basic constituent of the albedo, coming from the grid-cell, describes the diffuse, homogeneous single scattering of incoming radiation from a given surface. This simplifying assumption neglects the multiple scattering effect and the dependence of the albedo on the zenith angle of the incident radiation. Apparently, within this approach, the geometry plays an essential role. In our approach, a part of the radiation reflected from the lower surface is completely absorbed by the lateral sides of the surface lying on a higher level. Consequently, the idea is to calculate the ratio of the reflected energy lost in this manner by calculating the solid angle within which these lateral sides are seen from each point of the lower surface. It is important to stress here another assumption that differs this work from one of Schwerdtfeger (2002). We assume here that the observer (measuring instrument) is sufficiently high so that the whole grid-cell is seen under a small angle and the influence of height could be neglected.

To calculate the radiant energy flux dE/dt, we introduce the total intensity of radiation I obtained from the monochromatic intensity by integrating it over the entire range of the spectrum. Taking into account that within our approach I is a constant, we can write down our basic expression following Liou (2002)

$$\left(\frac{dE}{dt}\right) = I\, dS\ \cos\theta\, d\Omega, \tag{4.28}$$

where dS is the infinitesimal element of surface on which radiation comes or reflects from, $\cos\theta$ describes the direction of the radiation stream, while $d\Omega = \sin\theta\, d\theta\, d\varphi$ is the element of solid angle within which our differential amount of energy is confined to.

After stating our basic assumptions, we shall explain our analytic treatment for the most general case. Let us concentrate on the average albedo of the properly chosen grid-cell of the area S as presented in Fig. 4.1.

For simplicity we assume that this region consists of two surface types, with different albedos and heights. Accordingly, we assume that this grid-cell is divided into two subregions having the areas S_1 and S_2 with corresponding albedos α_1 and α_2 respectively, while the relative height of the higher surface is h. In order to define the position of a particular

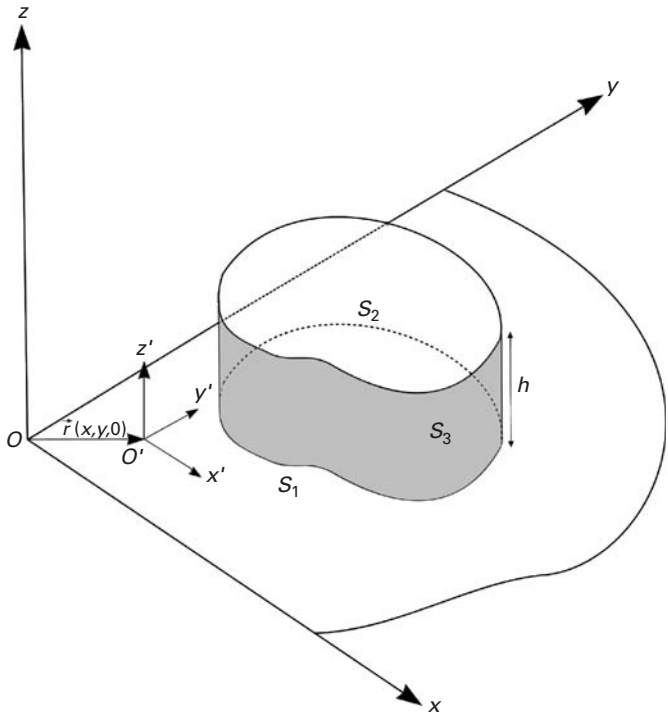

Figure 4.1. Schematic representation of the grid-cell of an arbitrary geometry consisting of two surfaces of the relative height *h*. Notation follows the text.

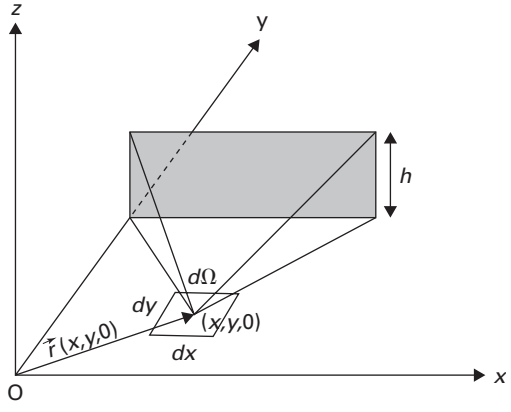

Figure 4.2. Schematic representation of the differential solid angle used in definition of $(dE/dt)_1$.

point we have to use the global (x, y, z) reference frame as well as the local reference frame (x', y', z') assigned to each point, which is used for the calculation of the solid angle under which the vertical boundary between two surfaces is seen from the given point (Fig. 4.2). Let us note that the local axes are parallel to the corresponding global ones. According to

the conventional approach, the average albedo $\overline{\alpha}_c$ over the grid-cell of an arbitrary geometry is given as

$$\overline{\alpha}_c = \alpha_1\sigma_1 + \alpha_2\sigma_2 \tag{4.29}$$

in terms of the fractional covers $\sigma_i = S_i/S$ $(i = 1, 2)$, where $S = S_1 + S_2$ is the total grid cell area.

Our idea is to introduce the "loss coefficient" k_l $(0 < k_l \leq 1)$, which measures the relative radiant flux lost from the reflected beam from the lower surface due to their non-zero relative height. We must emphasise that our basic assumption is that the flux of radiation that reaches the vertical boundary surface of the area S_3 (which lies in the plane orthogonal to the surfaces S_1 and S_2) is completely lost. This means that we are not taking into account the contribution of the radiation reflected from the surface S_3 to the total reflected flux of radiation. In that way we calculate the average albedo $\overline{\alpha}_n$ of this grid-cell as

$$\overline{\alpha}_n = (1 - k_l)\ \alpha_1\sigma_1 + \alpha_2\,\sigma_2. \tag{4.30}$$

One way of accounting the possible reflection from the vertical boundary would be to add the term including the albedo of the vertical boundary which, however, need not be equal to α_2 at all, which poses an additional problem. Finally, our definition of the loss coefficient brings us to the following relation

$$k_l = \frac{\left(\dfrac{dE}{dt}\right)_l}{\left(\dfrac{dE}{dt}\right)_h} \tag{4.31}$$

where $(dE/dt)_h = IS_1\pi$ is the amount of flux which the land surface of area S_1 emits into the upper half-space (Liou, 2002), while $(dE/dt)_1$ is the part of the total energy coming from surface S_1 towards surface S_3. Our definition of the loss coefficient is conceptually analogous to the idea of the sky-view factor introduced by Oke (1987). More precisely, his sky-view factor would be represented as $1 - k_l$ for the infinite obstacle case. This concept is currently used in some urban models for estimation of the trapping of solar radiation and outgoing longwave radiation flux by the urban street canyon system (Masson, 2000). Let us note that in our approach we are interested in aggregating the albedo so we do not consider the particular fluxes that are in the focus of the foregoing studies.

The amount of emitted flux reaching the vertical boundary is calculated as the sum of all infinitesimal amounts of radiant flux emitted from the infinitesimal surface element $dxdy$ (centred around the point with position vector $\vec{r}$), confined in the solid angle $d\Omega$ under which the element $dxdy$ "sees" the surface S_3 (Fig. 4.2). Let us note that we have chosen the lower surface to have $z = 0$ so it is omitted in the calculations.

Figures 4.3a and 4.3b show boundaries for the integration over the azimuth (φ_1, φ_u) and zenith (θ_1, θ_u) angles in terms of the global coordinates (x, y) of the given point, where the subscripts l and u denote the lower and upper boundary respectively. Accordingly, we can write down the following relation

$$\left(\frac{dE}{dt}\right)_l = I \iint\limits_S dxdy \int_{\varphi_l(\vec{r})}^{\varphi_u(\vec{r})} d\varphi \int_{\theta_l(\vec{r},\varphi)}^{\theta_u(\vec{r},\varphi)} \cos\theta \sin\theta\, d\theta. \tag{4.32}$$

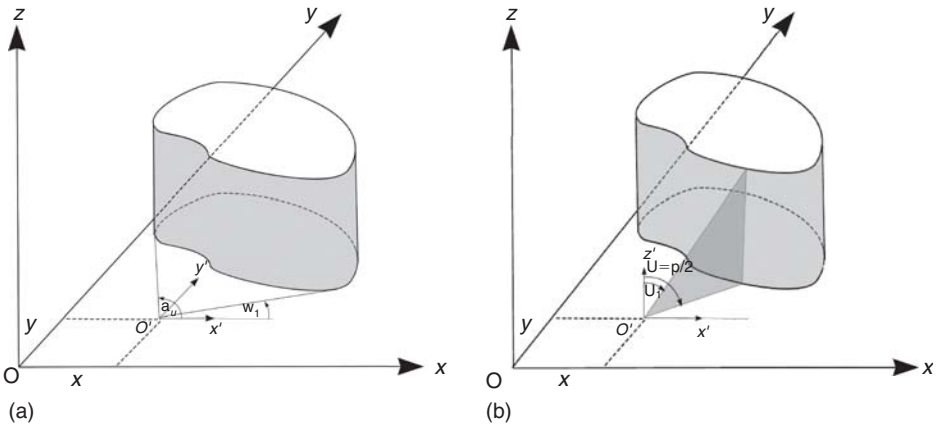

Figure 4.3. Definition of the boundaries for the integration over the local (a) azimuthal and (b) zenithal angle for the grid-cell of an arbitrary geometry.

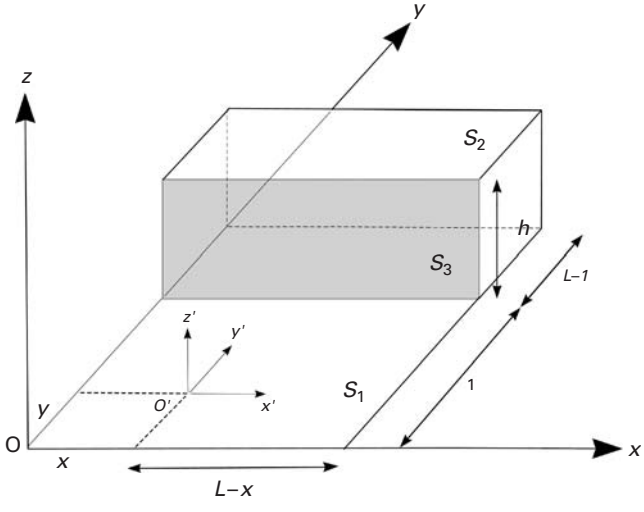

Figure 4.4. Schematic representation of the square grid-cell consisting of two surfaces of the relative height h. Notation follows the text.

Combining Eqs. (4.31) and (4.32), we can evaluate the loss coefficient k needed for calculating the average albedo given by Eq. (4.30).

In order to demonstrate this procedure, we shall apply this analytic treatment to a particular situation consisting of the square grid-cell with the edge size L presented in Fig. 4.4. For the sake of simplicity, we assume that this grid-cell is divided into two subregions having rectangular form. These two subregions have areas $S_1 = L \times l$ and $S_2 = L \times (L - l)$, with corresponding albedos α_1 and α_2 respectively, while the relative

height of the higher surface is h. Now $(dE/dt)_h = ILl\pi$ (while $(dE/dt)_1$ given by Eq. (4.32) becomes

$$\left(\frac{dE}{dt}\right)_l = I\int_0^l dy\int_0^L dx\int_{\varphi_l}^{\varphi_u}\int_{\theta_l}^{\theta_u}\cos\theta\sin\theta\ d\theta\, d\varphi \tag{4.33}$$

with

$$\varphi_l = arctg\frac{l-y}{L-x} \quad \varphi_u = \frac{\pi}{2} + arctg\frac{x}{l-y} \tag{4.34}$$

and

$$\theta_l = arctg\frac{l-y}{h\sin\varphi} \quad \theta_u = \frac{\pi}{2} \tag{4.35}$$

as defined in Kapor *et al*. (2002). Let us note that the expression for θ_l is valid for any $0 \le \varphi \le \pi$. Introducing the reduced dimensionless quantities

$$\widehat{x} = \frac{x}{L}, \quad \widehat{y} = \frac{y}{L}, \quad \widehat{l} = \frac{l}{L}, \quad \widehat{h} = \frac{h}{L},$$

our final result for the loss coefficient (4.31), as the function of the reduced relative height $\widehat{h}$ and reduced length $\widehat{l}$, after some substitutions can be presented as

$$\begin{aligned} k_l(\widehat{l},\widehat{h}) = \frac{1}{\widehat{l}\pi}\Bigg\{ & \widehat{l}\ arctg\frac{1}{\widehat{l}} - \sqrt{\widehat{h}^2+\widehat{l}^2}\ arctg\frac{1}{\sqrt{\widehat{h}^2+\widehat{l}^2}} + \widehat{h}\ arctg\frac{1}{\widehat{h}} \\ & + \frac{1}{4}(1-\widehat{l}^2)\Big[\ln(1+\widehat{l}^2) - \ln(1+\widehat{h}^2+\widehat{l}^2)\Big] \\ & + \frac{1}{4}\widehat{h}^2\ln(1+\widehat{h}^2+\widehat{l}^2) \\ & + \frac{1}{4}(1-\widehat{h}^2)\ln(1+\widehat{h}^2) + \frac{1}{4}\widehat{l}^2\Big[\ln\widehat{l}^2 - \ln(\widehat{h}^2+\widehat{l}^2)\Big] \\ & + \frac{1}{4}\widehat{h}^2\Big[\ln\widehat{h}^2 - \ln(\widehat{h}^2+\widehat{l}^2)\Big]\Bigg\} \end{aligned} \tag{4.36}$$

Let us now compare the effect of the two approaches given by expressions (4.29) and (4.30) (i.e. the conventional and proposed approaches) by analyzing some limiting cases. Expression (4.36) behaves as $h/(2l)$ for small h/l so it vanishes identically for $h = 0$. For $l \to 0$, and consequently $\widehat{l} \to 0$, it has a finite value equal to 1/2, and since σ_1 vanishes, average albedo tends to α_2, as it should. For further analysis, we have calculated the ratio of the average albedos obtained by the proposed and conventional approaches as

$$\Gamma = \frac{\overline{\alpha}_n}{\overline{\alpha}_c}. \tag{4.37}$$

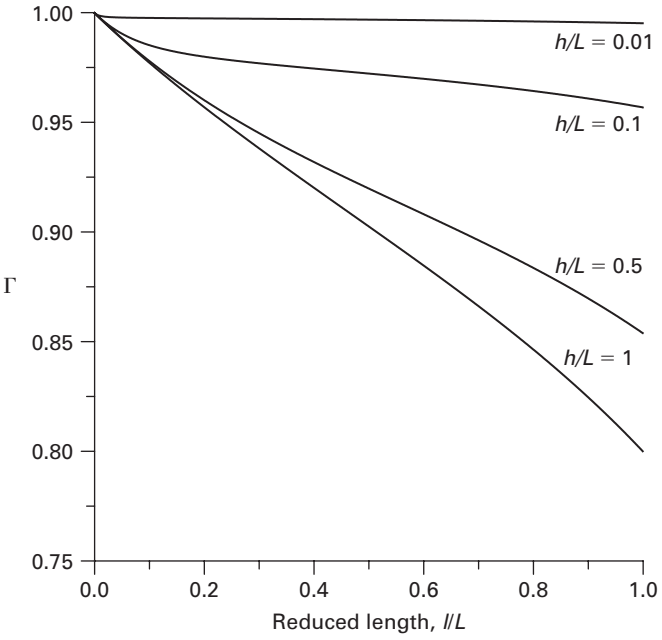

Figure 4.5. Dependence of Γ ratio on the reduced length l/L.

In the particular case $\alpha_1 = \alpha_2/2$ this ratio becomes

$$\Gamma = \frac{1 - [1 + k_l(\widehat{l}, \widehat{h})]\dfrac{\widehat{l}}{2}}{1 - \dfrac{\widehat{l}}{2}} \tag{4.38}$$

where $k_l(\widehat{l}, \widehat{h})$ is given by expression (4.36). Figure 4.5 depicts Γ as a function of the reduced length $\widehat{l} = l/L$ and considered the reduced relative height $\widehat{h} = h/L$ as the parameter. The inspection of this plot indicates that the albedo calculated by the proposed approach is always lower than the conventional one, decreasing non-linearly when $\widehat{l}$ increases. So the decrease in albedo is up to 20 percent for $\rho = 1$ and a reduced relative height of 1. These differences in albedo may have a significant impact on the calculation of the energy budget over the grid-cell. This study depicts another important property: for $\widehat{l} = L$, the loss coefficient does not vanish, but in fact remains finite with a value coming from

$$\lim_{\widehat{l}\to 1} k_l(\widehat{l}, \widehat{h}) = \frac{1}{4} + \frac{1}{\pi}\left(\sqrt{1+\widehat{h}^2}\, arctg\sqrt{1+\widehat{h}^2} - \widehat{h}\, arctg\widehat{h}\right) - \frac{1}{2}\left(\sqrt{1+\widehat{h}^2} - \widehat{h}\right) - \frac{1}{4\pi}\widehat{h}^2 \ln\frac{(1+\widehat{h}^2)^2}{(2+\widehat{h}^2)\widehat{h}^2}. \tag{4.39}$$

This is the consequence of the fact that a vertical surface at the edge of the grid-cell must have an impact to its albedo. This can be explained in a more extreme case by considering the albedo of a square grid-cell surrounded by vertical boundaries of height h. If we neglect the boundaries, its albedo would be equal to some value α. However, it can be seen very easily that due to the additivity of solid angles, the effective albedo is equal to α multiplied by the factor

$$\Lambda(\widehat{h}) = 1 - 4\kappa(1, \widehat{h}) \tag{4.40}$$

i.e. a factor whose magnitude is between 0 and 1. In fact, for $h = 0$, it is equal to 1, while for a large $\widehat{h}$ it vanishes. One should notice the importance of this effect for the calculations particularly in urban areas, where the height might be close or even larger than the cell size, so $\widehat{h}$ need not be small at all. For the small values of the reduced relative height $\widehat{h}$, the loss coefficient is proportional to $\widehat{h}$ what allows us in practical calculations in environmental modelling to use a rather simplified form of loss coefficient instead of its complete form given by the expression (4.36). In fact dimensional considerations indicate that this must be true in the most general case. More precisely, if there are more than two patches, the loss coefficient for any surface due to the presence of another (higher) surface should be always proportional to its relative height, so in the future work we shall use this approximation to study some practical situations.

To calculate the albedo of urban grid cells using the proposed method by aggregating their albedos over several patches included in the grid cell, we have to suppose that all patches have a rectangular form located to each other. This case can be treated analytically in principle, yet the expression is much more complex. So we decided to treat it by an empirical approach based on the knowledge of the behaviour studied above. Let us study any two patches having contact at some line (denoted by i and j; i, j enumerating patches). Expanding the expression (4.29) we obtained effective albedo of the lower surface (let us say i) as

$$\overline{\alpha}_n = \overline{\alpha}_{c(i,j)} - k_{l(i,j)}\alpha_i\sigma_i. \tag{4.41}$$

We know that the limiting expression for only two patches and small relative height is $k_{l(i,j)} = (h_j - h_i)/(2L)$. However, in practice the coefficient $k_{i,j}$ between two adjacent surfaces can be estimated by some empirical expressions based on dimensional consideration.

4.5 A COMBINED METHOD FOR CALCULATING THE SURFACE TEMPERATURE AND WATER VAPOUR PRESSURE OVER HETEROGENEOUS GRID CELL

In numerical modelling of surface layer processes, as mentioned above, two approaches are commonly taken for calculating the transfer of momentum, heat and moisture from a grid cell comprised of heterogeneous surfaces. They are: (1) "parameter aggregation", where grid cell mean parameters are derived in a manner which attempts to best incorporate the combined non-linear effects of each of different relatively homogeneous subregions ("tiles") over the grid cell and (2) "flux aggregation", where the fluxes are averaged over the grid cell, using a weighted average with the weights determined by the area covered by each tile; according to Hess and McAvaney (1997) and Hess and McAvaney (1998); there is also the third approach as a combination of the "flux aggregation" and "parameter aggregation" methods, the so-called combined method. When the underlying surface over

the grid cell is homogeneous, the turbulent transfer physics can be treated as (1) or (2) (Claussen, 1991, 1995). If large differences exist in the heterogeneity of the surfaces over the grid cell then a combined method has to be applied. The application of the aggregation method requires a control regarding its sensitivity to chaotic time fluctuations, realisability and proper aggregation of biophysical parameters relevant for calculating turbulent fluxes over the grid cell (Mihailović, 2002). However, when either the "flux aggregation" method or its combination with the "parameter aggregation" is used, then certain anomalies can arise through the "Schmidt paradox", leading to a situation of the occurrence of the countergradient transport between the surface and the lowest model level. In this section we will suggest a method that combines the "parameter aggregation" and the "flux aggregation" approaches in calculating the surface temperature of the heterogeneous grid cell.

In the following text we use angular brackets to indicate an average of certain physical quantity A over the grid cell, i.e.

$$\langle A \rangle = \sum_{i=1}^{NP} \xi_i A_i \tag{4.42}$$

where NP is the number of patches within a grid cell and ξ_i is fractional cover for the ith surface type. In "parameter aggregation" approach, the mean sensible heat flux $\langle H_0 \rangle$ and latent heat flux $\lambda \langle E_0 \rangle$, calculated over the grid cell, where λ is latent heat of vaporisation, are found by assuming, for example, the aerodynamic resistance representation, i.e.

$$\langle H_0 \rangle = \rho_p c_p \frac{\langle T_0 \rangle - T_a}{\langle r_a \rangle} \tag{4.43}$$

and

$$\lambda \langle E_0 \rangle = \frac{\rho_p c_p}{\gamma} \frac{\langle e_0 \rangle - e_a}{\langle r_a \rangle}, \tag{4.44}$$

where ρ_p is the air density, c_p is specific heat of air at constant pressure, γ is psychrometric constant, r_a is resistance between canopy air or ground surface and the atmospheric lowest model level, T is temperature and e is water vapour pressure. The subscript a indicates the atmospheric lowest model level and the subscript 0 indicates the surface or environment within the canopy. The $\langle r_a \rangle$ is defined as

$$\langle r_a \rangle = \langle r_s \rangle \delta \mu + \frac{1}{\kappa \langle u_* \rangle} \ln \frac{\langle z_a \rangle - \langle d \rangle (1 - \delta)}{\langle z_b \rangle - \langle d \rangle (1 - \delta)}, \tag{4.45}$$

where r_s is the bare soil surface resistance, δ ($\delta = 1$ for the bare soil, water and solid fraction; $\delta = 0$ for vegetative surface) and μ ($\mu = 1$ for the bare soil fraction; $\mu = 0$ for vegetative surface, water and solid fraction) are parameters, u_* is friction velocity, z_a is height of the lowest atmospheric model level, z_b is a height taking values z_0 and h_c (canopy height) for the barren/solid/water and vegetative part respectively. For r_s is used the empirical expression given by Shu Fen Sun (1982), i.e.

$$\langle r_s \rangle = d_1 + d_2 \langle w_1 \rangle^{-d_3} \tag{4.46}$$

where d_1, d_2 and d_3 are empirical constants (Mihailović and Kallos, 1997), while w_1 is the top soil layer volumetric soil moisture content. If the surface "flux aggregation" approach

is applied then the mean surface fluxes are given by

$$\langle H_0 \rangle = \rho_p c_p \sum_{i=1}^{NP} \xi_i \frac{T_{m,i} - T_a}{r_{a,i}} \tag{4.47}$$

$$\lambda \langle E_0 \rangle = \frac{\rho_p c_p}{\gamma} \sum_{i=1}^{NP} \xi_i \frac{e_{m,i} - e_a}{r_{a,i}}. \tag{4.48}$$

where the subscript m refers to the single patch in the grid cell (vegetation, bare soil, water urbanised area) whose temperature is calculated under the land surface scheme. However, according to Hess and McAvaney (1998), it seems that averaging temperatures over different patches in the grid cell, rather than the sensible heat flux, can be the source of problems. We will suggest an alternative method for their calculation diagnostically from Eqs. (4.43) and (4.44), when the grid-averaged fluxes are known from Eqs. (4.47) and (4.48). It is done by following the works of Hess and McAvaney (1998) and Mihailović *et al*. (2002). Since we have three unknowns, it is necessary to introduce the associated "parameter" and "flux aggregation" equations for momentum

$$\langle u_*^2 \rangle = \left[\frac{\kappa \Lambda}{\ln \dfrac{z_a - \langle D \rangle}{\langle Z_0 \rangle}} \right]^2 \langle F(\langle Ri_b \rangle, u_a, \langle T_0 \rangle, T_a) \rangle u_a^2, \tag{4.49}$$

and

$$\langle u_*^2 \rangle = \sum_{i=1}^{NP} \xi_i \left[\frac{\kappa \Lambda_i}{\ln \dfrac{z_a - D_i}{Z_{0,i}}} \right]^2 F_i[Ri_{b,i}, u_a, T_{m,i}, T_a] u_a^2 \tag{4.50}$$

where $\langle Z_0 \rangle$, $\langle D \rangle$ and Λ are given by Eqs. (4.26), (4.27) and (4.12), F represents the nonneutral modification, Ri_b is bulk Richardson number and u_a is wind speed at the lowest model level. Now, the mean averaged momentum flux is calculated from Eq. (4.50). If this value is substituted into Eq. (4.49) the resulting equation can be solved for $\langle F \rangle$. The "parameter aggregation" version of the aerodynamic resistance $\langle r_a \rangle$ can be now determined (since $\langle F \rangle$, $\langle Z_0 \rangle$, $\langle D \rangle$ and $\langle h_c \rangle$ are all known). Thus,

$$\langle r_a \rangle = \langle r_s \rangle \delta\mu + \frac{\left[\dfrac{\kappa \Lambda}{\ln \dfrac{z_a - \langle D \rangle}{\langle Z_0 \rangle}} \right]}{\kappa \left\{ \sum_{i=1}^{NP} \xi_i \left[\dfrac{\kappa \Lambda_i}{\ln \dfrac{z_a - D_i}{Z_{0,i}}} \right]^2 F_i[Ri_{b,i}, u_a, T_{g,i}, T_a] \right\}^{1/2}}$$

$$\ln \frac{z_a - \langle D\rangle(1-\delta)}{\langle z_b\rangle - \langle D\rangle(1-\delta)}. \tag{4.51}$$

Hence, the grid-averaged surface values of temperature and water vapour pressure can be found from Eqs. (4.43) and (4.44), i.e.

$$\langle T_0\rangle = \frac{\langle r_a\rangle\langle H_0\rangle}{\rho_p c_p} + T_a \tag{4.52}$$

and

$$\langle e_0\rangle = \frac{\langle r_a\rangle\gamma\lambda\langle E_0\rangle}{\rho_p c_p} + e_a \tag{4.53}$$

4.6 CONCLUSION

The aim of this chapter was to review various procedures for treating heterogenous grid cells, characteristic for realistic situations. It is shown that this variety of options demands that the choice of the approach should be made by the modeller, depending on the particular situation.

APPENDIX—LIST OF SYMBOLS

List of Symbols

Symbol	Definition	Dimensions or Units
C_d	a leaf drag coefficient	
C_i	an integration constant	
D	displacement height above the grid cell	
F	the nonneutral modification	
$\langle H_0\rangle$	the mean sensible heat flux calculated over the grid cell	[W m^{-2}]
I	the total intensity of radiation	[W m^{-2} sr^{-1}]
K, L, M	the maximum number of patches in the grid cell, respectively	
K_m	the momentum transfer coefficient	[m^2 s^{-2}]
L	the edge size of the square grid-cell [m]	
LAI	a leaf area index	
L_c	the horizontal scale of roughness variations	[m]
NP	the number of patches within a grid cell	
Ri_b	the bulk Richardson number	
S	the total grid cell area	[m^2]
dS	the infinitesimal element of surface on which radiation comes or reflects from	[m^2]
S_1, S_2	the areas of the subregions of the grid-cell with corresponding albedos α_1 and α_2 respectively	[m^2]

(*Continued*)

List of Symbols

Symbol	Definition	Dimensions or Units
S_3	the area which lies in the plane normal to the surfaces S_1 and S_2	[m^2]
T	the temperature	[K]
U	the mean wind speed	[$m\,s^{-1}$]
Z_0	the aggregated roughness length above the grid cell	[m]
a	the subscript which indicates the atmospheric lowest model level	
c_i	the constant	
c_p	specific heat of air at constant pressure	[$J\,kg^{-1}\,K^{-1}$]
d_1, d_2	empirical constants	
d_3	empirical constant	
d_i	the zero displacement height for the ith vegetative part in the grid cell	[m]
dE/dt	the radiant energy flux	[W]
e	the water vapour pressure	[Pa]
h	the relative height of the higher surface	
h_c	canopy height	[m]
$\widehat{h}$	the reduced relative height	
k_l	the "loss coefficient",which measures the relative radiant flux lost from the reflected beam from the lower surface due to their nonzero relative height	
$\widehat{l}$	the reduced length	
l_b	the blending height as a scale height at which the flow is approximately in equilibrium with local surface and also independent of horizontal position	[m]
l_d	the diffusion height scale	[m]
l_m^a	the aggregated mixing length at level z	[m]
m	a parameter; the subscript refers to the single patch in the grid cell (vegetation, bare soil, water urbanised area)	
r_a	the resistance between canopy air or ground surface and the atmospheric lowest model level	
r_s	the bare soil surface resistance	
u_a	wind speed at the lowest model level	[$m\,s^{-1}$]
u_*	friction velocity	[$m\,s^{-1}$]
u_*^a	a friction velocity above non-homogeneously covered grid cell	[$m\,s^{-1}$]
$-(\overline{uw'})$	the momentum flux on average over a heterogeneous surface	[$m^2\,s^{-2}$]
w_1	the top soil layer volumetric soil moisture content	
z	level above a grid cell	[m]

(*Continued*)

List of Symbols

Symbol	Definition	Dimensions or Units
z_{0a}	an aggregated roughness length	[m]
z_{0l}	an aggregated roughness length over the liquid fraction of the grid cell	[m]
z_{0n}	an aggregated roughness length over the non-vegetative part of the grid cell	[m]
z_{0s}	an aggregated roughness length over the solid fraction of the grid cell	[m]
z_{0v}	an aggregated roughness length over the vegetative part of the grid cell	[m]
z_a	the height of the lowest atmospheric model level	[m]
z_b	a height taking values z_0 and H (canopy height) for the barren/solid/water and vegetative part, respectively	[m]
$\langle\Phi\rangle$	an areally averaged flux	
Φ_i	the fluxes which in turn are functions some of the components ψ_i	
α_a	an aggregated albedo	
$\overline{\alpha}_c$	the average albedo over the grid-cell of an arbitrary geometry	
$\overline{\alpha}_n$	the average albedo of the grid-cell	
γ	psychrometric constant	
δ	the total fractional cover for a solid portion; parameter	
δ_i	a partial fractional cover for a solid part	
ς	the vegetation-type dependent parameter	
ς_i	the dimensionless constant, parameter	
ς_i^m	a parameter for ith part of a vegetative cover in the grid cell	
ξ_i	the fractional cover for the ith surface type	
θ_1, θ_u	the zenithal angles where the subscripts $l$and u denote the lower and upper boundary, respectively	
κ	Von Karman constant	
λ	latent heat of vaporisation	$[\mathrm{J\,kg^{-1}}]$
$\lambda\langle E_0\rangle$	latent heat flux calculated over the grid cell	$[\mathrm{W\,m^2}]$
μ	parameter	
ν	the total fractional cover for a liquid portion	
ν_i	a partial fractional cover for a water surface	
ρ_p	the air density	$[\mathrm{kg\,m^{-3}}]$
φ_1, φ_u	the azimuthal angles, where the subscripts $l$and u denote the lower and upper boundary, respectively	
σ	the total fractional cover for a vegetative portion	
σ_c^i	a fractional area covered by a patch i with the roughness length z_0^i	
σ_i	a partial fractional cover for vegetation	

(*Continued*)

List of Symbols

Symbol	Definition	Dimensions or Units
ψ_a	the vector of aggregated surface parameters	
ψ_i	the surface parameters of each land type	
$d\Omega$	the element of solid angle within which our differential amount of energy is confined to	
0	the subscript which indicates the surface or environment within the canopy	

REFERENCES

Claussen, M., 1990, Area-averaging of surface fluxes in a neutrally stratified, horizontally inhomogeneous atmospheric boundary layer. *Atmospheric Environment*, **24a**, pp. 1349–1360.

Claussen, M. 1991, Estimation of areally-averaged surface fluxes. *Boundary-Layer Meteorology*, **30**, pp. 327–341.

Claussen, M., 1995, Flux aggregation at large scales: on the limits of validity of blending height. *Journal of Hydrology*, **166**, pp. 371–382.

Delage, Y. and Verseghy, D., 1995, Testing the effects of a new land surface scheme and of initial soil moisture conditions in the Canadian global forecast model. *Monthly Weather Review*, **123**, pp. 3305–3317.

Delage, Y., Wen, L. and Belanger, J.M., 1999, Aggregation of parameters of the land surface model CLASS. *Atmosphere-Ocean*, **37**, pp. 157–178.

De Bruin, H.A.R. and Moore, C.J., 1985, Zero-plane displacement and roughness length for tall vegetation, derived from a simple mass conservation hypothesis. *Boundary-Layer Meteorology* **42**, pp. 53–62.

Dolman, A.J. and Blyth, E.M., 1997, Patch scale aggregation of heterogeneous land surface cover for mesoscale meteorological models. *Journal of Hydrology*, **190**, pp. 252–268.

Fernando, H.J.S., Lee, S.M., Anderson, J., Princevac, M., Paradyjak, E. and Grossman-Clarke, S., 2001, Urban fluid mechanic: Air circulation and contaminant dispersion in cities. *Environmental Fluid Mechanics*, **1**, pp. 107–164.

Hess, G.D. and McAvaney, B.J., 1997, Note on computing screen temperatures humilities and anemometer-height winds in large-scale models. *Australian Meteorological Magazine*, **46**, pp. 109–115.

Hess, G.D. and McAvaney, B.J., 1998, Realisability constraints for land-surface schemes. *Global and Planetary Change*, **19**, pp. 241–245.

Hu, Z., Islam, S. and Jiang, L., 1999, Approaches for aggregating heterogeneous surface parameters and fluxes for mesoscale and climate models. *Boundary-Layer Meteorology*, **93**, pp. 313–336.

Jacobs, A.F.G. and van Boxel, J.H., 1988, Changes of the displacement height and roughness length of maize during a growing season. *Agricultural and Forest Meteorology*, **42**, pp. 53–62.

Jacobson, M.Z., 1999, *Fundamentals of atmospheric modeling*, (Cambridge University Press, The Edinburgh Building, Cambridge).

Kabat, P., Hutjes, R.W.A. and Feddes, R.A., 1997, The scaling characteristics of soil pammews: From plot scale heterogeneity to subgrid parametexization. *Journal of Hydrology*, **190**, pp. 364–397.

Kapor, D., Mihailović, D.T., Tosic, T., Rao, S.T. and Hogrefe, C., 2002, An approach for the aggregation of albedo in calculating the radiative fluxes over heterogeneous surfaces in atmospheric models. In *Integrated Assessment and Decision Support Proceedings of the First Biennial Meeting of the International Environmental Modelling and Software Society, 24–27 June, Lugano (Switzerland)*, Vol. 2, edited by Rizzoli, A.E. and Jakeman, A.J., pp. 448–453.

Kondo, J. and Yamazawa, H., 1986, Aerodynamic roughness over an inhomogeneous ground surface. *Boundary-Layer Meteorology*, **35**, pp. 331–348.

Lalić, B., 1997, *Profile of wind speed in transition layer above the vegetation*, University of Belgrade, Masters Thesis, (in Serbian).

Lalić, B. and Mihailović, D.T., 1998, Derivation of aerodynamic characteristics using a new wind profile in the transition layer above the vegetation. *Research Activities in Atmospheric and Oceanic Modelling*, **27**, pp. 4.25–4.26.

Lazic, J., Mihailović, D.T., Lalić, B., Arsenić, I. and Hogrefe, C., 2002, Land air surface scheme (LAPS) for use in urban modelling. In *Integrated Assessment and Decision Support Proceedings of the First Biennial Meeting of the International Environmental Modelling and Software Society, 24–27 June, Lugano (Switzerland),* Vol. 2, edited by Rizzoli, A.E. and Jakeman, A.J., pp. 448–453.

Liou, K.-N., 2002, *An introduction to atmospheric radiation, Second Edition,* (Academic Press, Inc., NY).

Mason, P.J., 1988, The formation of areally averaged roughness lengths. *Quarterly Journal of Royal Meteorological Society*, **114**, pp. 399–420.

Masson, V., 2000, A physically-based scheme for the urban energy budget in atmospheric models. *Boundary-Layer Meteorology*, **94**, pp. 357–397.

Michaud, J.D. and Shuttleworth, W.J., 1997, Executive summary of the Tucson Aggregation Workshop. *Journal of Hydrology*, **190**, pp. 176–181.

Mihailović, D.T., 2002, Environmental Modeling of physical, biophysical and chemical processes in the atmosphere plant-soil-interaction: How Nonlinearity Affects the Solutions?, In *Integrated Assessment and Decision Support Proceedings of the First Biennial Meeting of the International Environmental Modelling and Software Society, 24–27 June, Lugano (Switzerland)*, Vol. 2, edited by Rizzoli, A.E. and Jakeman, A.J., pp. 383–388.

Mihailović, D.T., Lalić, B., Rajković, B. and Arsenić, I., 1999, A roughness sublayer wind profile above non-uniform surface. *Boundary-Layer Meteorology*, **93**, pp. 425–451.

Mihailović, D.T. and Kallos, G., 1997, A sensitivity study of a coupled-vegetation boundary-layer scheme for use in atmospheric modelling. *Boundary-Layer Meteorology*, **82**, pp. 283–315.

Mihailović, D.T., Kapor, D., Hogefre, C., Lazic, J. and Tosic, T., 2003, Parameterization of albedo over heterogeneous surfaces in coupled land-atmosphere schemes for environmental modelling, Part I: Theoretical background. *Environmental Fluid Mechanics*, **4**, pp. 57–77.

Mihailović, D.T., Rao, S.T., Hogefre, C. and Clark, R., 2002, An approach for the aggregation of aerodynamic parameters in calculating the turbulent fluxes over heterogeneous surfaces in atmospheric models. *Environmental Fluid Mechanics*, **2**, pp. 315–337.

Mihailović, D.T., Rao, S.T., Alapaty, K., Ku, J.Y., Arsenić, I. and Lalić, B., 2005, A study on the effects of subgrid-scale representation of land use on the boundary layer evolution using a 1-D model. *Environmental Modelling and Software*, **20**, pp. 705–714.

Moran, M.S., Humes, K.S. and Pinter, Jr. P.J., 1997, The scaling characteristics of remotely sensed variables for sparsely-vegetated heterogeneous landscapes. *Journal of Hydrology*, **190**, pp. 338–363.

Morgan, D.L., Pruitt, W.O. and Lourence, F.J., 1971, Analysis of energy, momentum, and mass transfers above vegetative surfaces. *Research and Development Technical*

Report ECOM 68-G10-F, (Department of Water Science and Engineering, University of California, Davis, U.S.A.).

Noilhan, J. and Lacarrère, P., 1992, GCM gridscale evaporation from mesoscale modelling, In: *Proceedings of a workshop held at ECMWF on fine-scale modelling and the development of parameterization schemes, 16–18 September 1991, European Centre for Medium-Range Weather Forecasts*, (Reading, UK), pp. 245–274.

Noilhan, J., Lacarrère, P., Dohuan, A.J. and Blyth, E., 1997, Defining area-average parameters in meteorological models for land surfaces with mesoscale heterogeneity. *Journal of Hydrology*, **190**, pp. 302–316.

Oke, T.R., 1987, *Boundary layer climates, 2nd Edition*, (Methuen, London, New York).

Pielke, R.A., Zeng, X., Lee, T.J. and Dahr, GA., 1997, Mesoscale fluxes over flat landscapes for use in larger scale models. *Journal of Hydrology*, **190**, pp. 317–337.

Raupach, M.R. and Finnigan, J.J., 1997, The influence of topography on meteorological variables and surface-atmosphere interactions. *Journal of Hydrology*, **190**, pp. 182–213.

Schwerdtfeger, P., 2002, Interpretation of airborn observation of the albedo. *Environmental Modelling and Software*, **17**, pp. 51–60.

Sellers, P.J., Heiser, M.D. and Hall, F.G., 1992, Relations between surface conductance and spectral vegetation indices at intermediate (100 m^2 to 15 km^2) length scales. *Journal of Geophysical Research*, **97(D17)**, pp. 19 033–19 059.

Sellers, P.J., Heiser, M.D., Hall, F.G., Verma, S.B., Desjardins, R.L., Schuepp, P.M. and MacPherson, J.I., 1997, The impact of using area-averaged land surface properties- topography, vegetation condition, soil wetness in calculations of intermediate scale (approximately 10 km^2) surface-atmosphere heat and moisture fluxes. *Journal of Hydrology*, **190**, pp. 269–301.

Shuttleworth, J.W., 1988, Macrohydrology-the new challenge for process hydrology. *Journal of Hydrology*, **100**, pp. 31–56.

Shuttleworth, J.W., 1991, The Modellion Concept. *Reviews of Geophysics*, **29**, pp. 585–606.

Stössel, A. and Claussen, M. 1993, A new atmospheric surface-layer scheme for a large-scale sea–ice model. *Climate Dynamics*, **9**, pp. 71–80.

Sun, S.F., 1982, *Moisture and heat transport in a soil layer forced by atmospheric conditions*. M.S. Thesis, Department of Civil Engineering, University of Connecticut.

Thornton, P.E., Running, S.W. and White, M.A., 1997, Generating surfaces of daily meteorological variables over large regions of complex terrain. *Journal of Hydrology*, **190**, pp. 214–251.

Wetzel, P.J. and Boone, A. 1995, A Parameterization for Atmosphere-Cloud-Exchange (PLACE): Documentation and testing of a detailed process model of the partly cloudy boundary layer over heterogeneous land. *Journal of Climate,* **8**, pp. 1810–1837.

Wieringa, J., 1986, Roughness-dependent geographical interpolation of surface wind speed averages. *Quarterly Journal of Royal Meteorological Society*, **112**, pp. 867–889.

Walko, R.L., Band, L.E., Baron, J., Kittel, T.G.F., Lammers, R., Lee, T.J., Ojima, D., Pielke, R.A., Taylor, C., Tague, C., Tremback, C. J. and Vidale, P.L., 2000, Coupled atmosphere-biophysics-hydrology models for environmental modeling. *Journal of Applied Meteorology*, **39**, pp. 931–944.

Wood, E.F., 1997, Effects of soil moisture aggregation on surface evaporative fluxes. *Journal of Hydrology*, **190**, pp. 398–413.

Wood, N. and Mason, P.J., 1991, The influence of stability on effective roughness lengths for momentum and heat transfer. *Quarterly Journal of Royal Meteorological Society*, **117**, pp. 1025–1056.

CHAPTER FIVE

Desert dust uptake-transport and deposition mechanisms—impacts of dust on radiation, clouds and precipitation

G. Kallos & P. Katsafados
School of Physics, University of Athens, Athens, Greece

ABSTRACT

Desert dust cycle is considered as important in the atmosphere and the ocean. Dust particles can have considerable impacts on radiation, clouds and precipitation. Perturbations on dust cycle are considerable on climate for various reasons. Deserts dust can reduce the incoming radiation near surface, can warm middle tropospheric layers and therefore affect precipitation or can assist in the formation of small water droplets and therefore suppress precipitation, or finally, in combination with sea salt and anthropogenic pollutants (like sulfates) can form gigantic CCNs that behave like Ice Nucleus (IN) and enhance precipitation and creation of storms. Dust deposition can affect significantly the marine biological and radiative processes.

The mechanism for dust production is very complicated and depends on several parameters like friction velocity, soil composition and granulation, soil moisture etc. The transport a deposition processes depend not only on atmospheric conditions but also on dust particle size and geometry. Small dust particles can be transported in long distances. For example Saharan dust can cross Mediterranean in less than a day while the cross-Atlantic path can last one or two weeks. Almost 10^8 tons of Saharan dust is deposited over the Mediterranean waters every year. The same amount is deposited over Europe.

In this chapter the state of the art dust production mechanisms will be reviewed and the impacts on the atmospheric and marine processes will be discussed.

5.1 INTRODUCTION

One of the most important sources of Particulate Matter (PM) in the atmosphere is the soil dust produced by the aeolian activity. Soil dust is extracted from desert, arid and semi-arid regions and transported to short and long distances (from a few centimetres to thousands of kilometres). Agricultural and other human activities are also considerable sources of mineral dust. It is considered as an important climate modifier because: (1) it affects the backscattering and absorption of solar and terrestrial radiation (Miller and Tegen, 1998), (2) it reduces the incoming solar radiation at the earth's surface by a considerable amount (up to 10% under extreme events) and therefore produces a cooling that masks the global warming (Ramanathan *et al.*, 2001; Alpert *et al*., 1998), (3) it is causing mid tropospheric warming by absorbing of radiation and on that way it stabilizes the lower troposphere and affects the water budget (Levin *et al.*, 2005). Because the dust source areas are near regions with fragile water budget, perturbations in production can

affect precipitation and water budget. Since dust production is affected by soil moisture, perturbations in the water cycle in arid and semi-arid regions can affect the dust cycle. The feedback between dust, cloud formation and precipitation is not straightforward but is very complicated (Levin *et al.*, 1996). The entire system becomes more complicated when other factors like sea-salt spraying and/or anthropogenic pollutants (aerosols) coexist (Levin *et al*., 2005). Under such circumstances, the effects on cloud and precipitation are not fully understood yet.

Almost one third of the earth's land surface is desert, arid land with sparse vegetation and very small amounts of rainfall. The deserts may be areas covered by sand, rocks gravels and rarely some plants can be found. Mineral deposits like salt can be found in the surface as a result of transport and erosion. Erosion is due to various reasons like temperature differentiation, friction between various sizes of stones, water and mainly aeolian activity.

Soil dust consists of particle with diameter ranging from submicron to tens of microns. The particle size is function of various parameters related to the way they have been created as well as the composition and the origin (Tegen and Fung, 1994). The transport and deposition is subject of the particle size and composition as well as turbulence and wind strength.

The estimated annual global mineral dust production is at the range of 1000–5000 $Mtyr^{-1}$ (Andreae, 1996). Comparing this amount with the annual production of sulphate aerosols at global scale that is at the range of several hundreds of $Mtyr^{-1}$ someone can see immediately a difference of at least one to two orders of magnitude.

One of the most known source areas of mineral dust is the Saharan desert that extends also to the Middle East and Arabian Peninsula. Dust mobilized from this region can be transported hundreds and thousands of kilometres away towards Mediterranean and Europe as well as towards the Atlantic and Indian Oceans. As Guerzoni and Chester (1996), Kallos *et al.* (2005) and Kallos *et al.* (2007), found it the amount of Saharan dust deposited over the Mediterranean waters is of the order to 10^8 $Mtyr^{-1}$. Similar amount is crossing the Mediterranean and transported towards Europe. The amounts deposited over the Atlantic Ocean are even higher (Kallos *et al.*, 2006, 2007). The other deserts known for their high productivity of dust particles are the Gobi desert, the desert of Namibia, Australia, Peru, SW USA and other smaller. Smaller amounts of desert dust are produced from the areas around lakes with specific characteristics, mainly with high amounts of salt and other minerals (e.g. Salt Lake in Utah, southern Aral, the area around the Caspian Sea, Deal Sea).

The impacts of dust in the atmosphere and climate have been briefly mentioned previously (Miller and Tegen, 1998; Andreae, 1996). The impacts of the deposited desert dust on the ocean surface and therefore the marine environments are also considerable (Martin and Fitzwater, 1988). Desert dust can cause radiative and heat perturbations at the ocean top, it can affect phytoplankton and other kind of marine productivity and of course, it can affect fluxes of important chemical species in the atmosphere like di-methyl-sulfate (DMS). Desert dust in the ocean can trigger various biochemical reactions between dust ingredients and the marine environment. Key elements like iron, phosphorus and other micronutrients (Guerzoni *et al*., 1999).

Desert dust can affect also fauna and flora. Deposition of dust over plants can affect photosynthesis, evapotranspiration and heat exchange. It can act also as fertilizer.

The urban air quality in many regions around the world is affected from desert dust transport on many ways as described in Rodriguez *et al.* (2001) and Papadopoulos *et al.* (2003) among others (e.g. by increasing the PM concentration at levels above the imposed regulations, by reducing visibility, by reducing the incoming solar radiation, by deposited over surfaces in buildings etc and then by re-suspension can be in the atmosphere). For example, most of the South European cities cannot meet the imposed European Union air quality standards on PM concentrations. Health effects are also associated with desert dust outbreaks (Rodriguez *et al.*, 2001; Kallos *et al.*, 2007).

Because of the importance of the dust cycle in the atmosphere, biosphere and hydrosphere, the dust cycle in the atmosphere (production, transport deposition) and its main properties will be further analyzed in the next sections.

5.2 PHYSICAL PROCESSES

The desert dust cycle is considered as a complex geophysical process. It involves soil erosion and atmospheric processes. The impacts of the desert dust on environment and climate are several. They are ranging from modifications on radiative transfer mechanisms (short and long wave), air quality degradation in urban environments, modification of water budget especially in arid and semi-arid regions and is associated with desertification and aridity. The transported and deposited dust material significantly affects the marine environment because it may significantly modify the marine biochemistry after deposition to ocean waters (Martin and Fitzwater, 1988). As it was found by Li *et al.* (1996) desert dust plumes are responsible for a negative radiative forcing of approximately 1 Wm^{-2} that is leading in about -0.2 K cooling of the lower troposphere (Alpert *et al.* 1998). Effects on construction materials, rain acidification, and visibility degradation have also been reported. They also pointed out that dust aerosols are an important source of inaccuracies in numerical weather prediction and especially in General Circulation Models (GCMs) used for climate research. It is also worth mentioning that some intense dust storms catastrophically affect the regions in the neighbourhood of dust sources, causing loss of human life and economic damage. Dust plumes can affect remote locations significantly, because they increase the PM concentrations and especially the fine ones (PM2.5) and therefore they can have significant health effects. According to Barkan *et al.* (2004) the highest aerosol index values in North Africa and Arabian Peninsula were estimated during June and July while the area around Lake Chad, has demonstrated local maximum values and, contrary to the other sources, is active throughout the year. These estimations were made by analyzing the TOMS instrument data for a period of fourteen years (1979–1992).

Dust mobilization exhibits a seasonal variability of the dust mobilization that depends on the source characteristics as well as the global atmospheric circulation (Ozsoy *et al*., 2001). The dust production in the highest productive area of North Africa and Arabian Peninsula is subject of seasonal variability and the characteristics of general circulation of planetary scale. During winter and spring, the Mediterranean region is affected by two upper air jet streams: the polar front jet stream, normally located over Europe, and the subtropical jet stream, which is typically located over northern Africa. The combined effects of these westerly jets in late winter and spring support the propagation of extratropical cyclones towards the East and Southeast, resulting in dust plume intrusion in the Mediterranean (Figure 5.1).

During the transient and cold seasons, most of the dust events that transport significant amounts of dust from Saharan towards the Mediterranean Sea and Europe occur. These seasons are characterized by the low index circulation of the year as described by Papadopoulos *et al*. (2003) and Rodriguez *et al*. (2001). During summer, the amount of produced and transported dust is almost twice as large as in winter (Husar *et al*., 1997). The highest amounts of mobilized dust in Sahara are transported towards the tropical Atlantic, Caribbean Sea and even North America with the aid of the easterlies (Perry *et al*., 1997).

The dust storm is created by the injection of dust particles in the atmosphere. This injection is function of various parameters like wind shear, the size and the composition of the particles, and the soil moisture. Soil particles can move in three different ways namely creeping, saltation, and suspension:

- Creeping is the rolling and/or sliding of particles along the ground. Creeping is supported by light winds and low particle granulation.

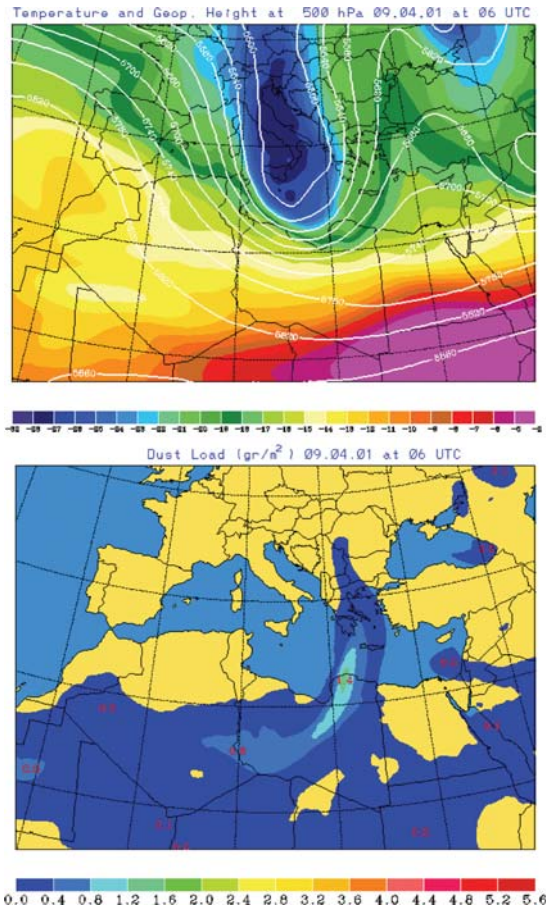

Figure 5.1. Synoptic conditions favour the dust transfer from the North Africa towards Eastern Mediterranean. The plots depict the geopotential height (gpm) with the temperature (C) at 500 hPa and the dust load (in gr m^{-2}). The figure obtained from the Skiron/Eta operational cycle and it is valid for 9th April 2001 at 06UTC.

- Saltation is the kind of soil particle movement through a series of jumps or skips. When the particles are lifted into the atmosphere, they start drifting for approximately farther downwind before they fall down again. The horizontal drifting is for approximately four times the vertical lifting. When the particles return to ground, they hit other particles or the ground and then they jump up again and progress forward. Smaller particles can be produced during the impact.

Suspension is the process that occurs when soil particles (usually sediment materials) lifted into the air and remain aloft by winds. If the particles are sufficiently small and the upward air motion is able to support the weight of the individual grains, they will hold aloft. The larger particles settle due to gravitational force while the smaller ones remain suspended and transported by turbulence. The amount of the suspended particles is function of wind speed: strong winds can assist in suspension of larger particles. The suspended particles are moving initially by turbulence and later by the organized flow patterns. The organized strong flow pattern (mesoscale and/or synoptic scale) can lift up the dust particles by thousands of

meters and transported horizontally downwind hundreds or thousand of kilometres. Large-scale turbulence or updrafts assist in suspending the soil particles until they settle down by gravitational forcing and/or wet scavenging and deposition processes. Regularly, the smaller particles (usually of the size of PM2.5 and less) are transported the larger distances while particles of size higher than PM10 are deposited faster over smaller distances (a few kilometres to a few hundreds of kilometres).

5.3 PARTICLE SIZE AND SETTLING VELOCITY

Soil dust particles belong to one of the three major types of aerosols namely (a) continental or desert aerosols, (b) industrial aerosols and (c) volcanic aerosols. Soil dust particles (called also continental aerosols) are of a wide range in diameter. Usually they are of diameter of submicron to a few tens of μm. The particulate portion of an aerosol is referred to as Particulate Matter (PM). PM is a collective term used for very small solid and/or liquid particles found in the atmosphere. The geometry, size, composition and in general, physical and chemical properties is varying significantly. Particle size can range from 0.001 to 500 μm (Seinfeld and Pandis, 1998). Particles larger than 2.5 μm are called as "coarse" particles; while the others with diameter from 0.1 to 2.5 μm are called as "fine". The smaller particles (less than 0.1 μm) are called as "ultra fine". There are two categories that well known the so-called PM2.5 and PM10 and define particles with diameters less than 2.5 μm and 10 μm respectively. The range of horizontal transport of the particles is function of the size and composition. In general, particles of the category PM2.5 behave as perfect gases because the gravitational settling is negligible. Particles of size PM10 are heavier and therefore the gravitational settling is larger and deposit in relatively small to moderate distances. The particles that are larger than PM10 deposit quickly near the sources.

Since the gravitational settling for soil particles of the category PM2.5 is very small, they are subject for long-range transport. Transport scales of 1000 km are characteristic in such cases. A common phenomenon associated with such kind of transport of dust particles is the "red snow" or "mad rain" encountered in Northern Europe, Asia or even North America. Soil particles larger than PM10 usually are transported in distances ranging from a few meters to a few kilometres. While the transport of such particles is not a subject of long range transport, their effects are significant near the sources and for the production of smaller particles as they collide with others while falling down (saltation). According to Alfaro *et al.* (1997), the size distributions of the aerosols released by silt and clay soil textures have medium respective diameters of 1.6, 6.7 and 14.2 μm. The total mass of released dust depends on particle size distribution. Tegen and Fung (1994) suggested four size particle categories resulting from the structure of desert soils based on content of clay, small silt, large silt and sand. For each size category k, typical radius (R_k), density (ρ_k), and the ratio between the mass available for uplift and the total mass (γ_k)[$\mathrm{kg \cdot kg^{-1}}$] are summarized in Table 5.1. Typically, the mass of clay particles is approximately 1–2 orders of magnitude smaller than the particles in the range 1–10 μm. The size of the silt particles are ranging from 1 to 25 μm.

The wet and turbulent dry deposition processes are the main mechanisms for removal of particles less than 10 μm. Particles larger than 10 μm are basically removed by gravitational settling. The sand particles are large and cannot participate in the longer-term atmospheric transport. Although, their role in dust storms is considerable near the source areas since high amounts of sand mass are lifted and drifted with the turbulence eddies, especially in the area of density current. Such phenomena are responsible for mobilization of large amounts of sand towards areas adjacent to dust sources and hence the expansion of desertification.

The dust particles that are moving within the atmosphere will continue doing it as long as the upward motion is greater than the speed at which the particles fall through air. The

Table 5.1. Main characteristics of typical dust particles (Source: Nickovic *et al.*, 2001).

k	Type	Typical particle radius R_k (μm)	Particle density ρ_{pk} (g cm^{-3})	γ_k
1	Clay	0.73	2.50	0.08
2	Silt, small	6.1	2.65	1.00
3	Silt, large	18	2.65	1.00
4	Sand	38	2.65	0.12

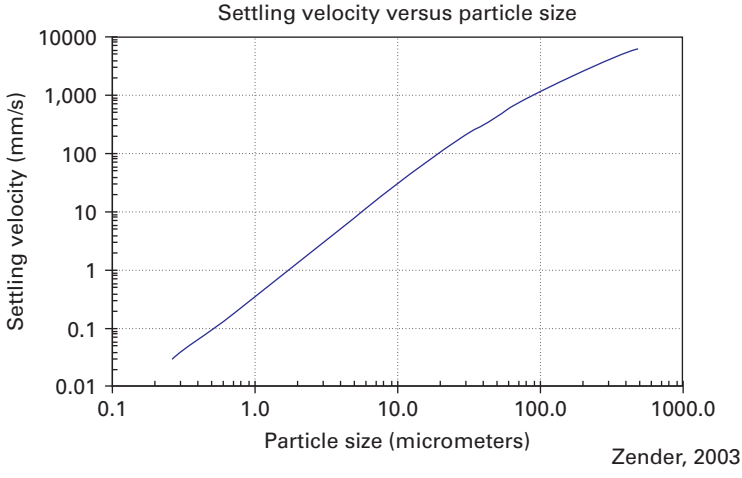

Figure 5.2. The settling velocity, as a function of particle size (source:http://www.meted.ucar.edu).

relationship between the falling speed (or settling velocity) and the particle size is shown in Figure 5.2. As we can see, particles capable of travelling great distances are these with diameters less than 20 μm since the falling speed is about 0.1 m $\cdot$ s^{-1}. Particles larger than 20 micrometers in diameter fall disproportionately faster. The PM10 particles fall at about 0.03 m $\cdot$ s^{-1}. Fine particles fall with very low speeds ($\sim$0.001 m $\cdot$ s^{-1}). Finest clay particles settle very slowly and therefore can be transported very large distances under favourable synoptic weather conditions. This is especially true over oceans under anticyclonic conditions where wet removal processes do not exist.

5.4 SOURCE REGIONS

The dust particles encountered in most of the deserts are clay particles with diameters less than 2 μm, silt particles with size ranging from 2 to 50 μm, and sand-size particles that are greater than 75 μm. Therefore, areas that contain soil particles with such characteristics can act as dust sources under the appropriate weather conditions. The source areas favouring the production of fine particles appropriate for long-range transport are these with fine-grained soils, rich in clay and silt. Areas with large soil particles (sand) can act as sources for dust storms of local scale.

A considerable amount of soil dust is taken up by the wind from arid or semi-arid areas around the globe and then transported to smaller or larger distances. Smaller amounts can be produced from other areas and human activities, mainly agricultural areas and/or roads, under certain circumstances. From all dust sources, the Saharan desert is the major production area. The estimates of soil dust emissions exhibit significant variations. The large variations can be attributed to the frequent spatial inhomogeneities in soil properties and the incapability of the existing methodologies to cover such issues on an accurate way. Therefore, the figures provided for the dust production on annual base are subject to assumptions made in the methodology of the calculations such as the surface properties, particle granulation, soil moisture characteristics and of course rate of scavenging. Older estimated emissions are of the range of 500 to 5000 million tons per year. Recent ones suggest the range of 1000 to 3000 million tons per year as more realistic. The dust emissions from Saharan desert are of the range of 130 and 760 million tons per year. The range of emitted dust between 260 and 710 million tonnes per year has been also provided in the literature (Callot *et al.*, 2000; Prospero, 1996; Swap *et al.*, 1992). The dust emission by itself is not an accurate estimate of the phenomenon because someone has to take in the account suspension time scales and range of transport. Most of the emitted dust settles down quickly producing usually producing smaller particles that are emitted later and transported over longer distances.

There is strong relationship between dust production areas and aridity or with low annual rainfall amounts (usually with rainfall $<$200–250 mm/year). The so called "dust belt" extends from Western Africa to Middle East, the Arabian Peninsula and East almost up to Himalaya. This is the most "productive" area for dust. The main reason is the small amount of rain, the composition of soil, the daily temperature range and in general the geomorphological characteristics of the area (e.g. ephemeral playa-lakes, rivers, lakes and steams, and in general drainage basins in the proximity of mountains without vegetation). Usually, these ephemeral formations during the wet season collect eroded soils that are exposed to re-suspension processes during the dry season (Querol *et al.*, 2002).

Mapping the dust production areas and characterization of their productivity is an important issue due to various implications of dust in the environment, water management and climate. A major effort devoted towards this direction by Prospero *et al.* (2002). In this work, they used satellite data (Total Ozone Mapping Spectrometer TOMS data) to identify the dust regions and their characteristics on global scale. According to Prospero *et al.* (2002), the largest and most persistent sources are located at the latitudes of the subtropical high of the Northern Hemisphere, mainly in a broad "dust belt" that extends from the west coast of North Africa, over the Middle East, Central and South Asia, to China. There are some mountainous regions (e.g., Afghanistan, Iran, Pakistan, and China) that are significant dust sources, especially the valleys between mountain peaks. Considerable amounts of produced dust are also outside of this belt. In particular, there are areas in the Southern Hemisphere with remarkable dust activity as in Namibia, Australia, Peru etc. Other dust production areas associated with human impacts are well documented, e.g., the Caspian and Aral Seas, Tigris-Euphrates River Basin, SW North America, and the loess lands in China. Of course, the largest and most active sources are located in areas where there is little or no human presence.

The most active dust sources are associated with topographic lows or they are in areas with frequent exchange between mountains and valleys of highlands as shown in Figure 5.3. In this figure, a typical desert area in SW Algeria is shown where hills and valleys are in a stripe formation (NASA photo).

The Mediterranean Region is affected by dust storms very often. Every day, there is a region of the Mediterranean Sea where North African dust is deposited. In addition, Europe and especially Southern Europe, receives similar amounts of dust as the Mediterranean Sea. This is especially true during late spring and summer (Guerzoni and Chester, 1996; Prospero, 1996; Moulin *et al*., 1998). The most important sources of the dust are eastern Algeria, Tunisia, Libya, and Egypt.

Figure 5.3. Dust uptake areas in NE Algeria. Stripe formation of the uptake areas with sand dunes and dust-salt mixture. Source NASA. Photo taken from the International Space Program, Photo ISS013-E-75141, 2 September 2006. Available from http://earthobservatory.nasa.gov/Newsroom/NewImages.

The most important dusts sources of the planet have been identified, described, and grouped by Prospero *et al.* (2002). Following the work of Prospero *et al.* (2002), the most important dust sources with their major characteristics are briefly described below:

Mauritania and Western Sahara: This is an area with important sources that contribute to the production of dust plumes directed towards the Atlantic Ocean. They become active early in the year and remain productive until late Fall with peak production during summer months. High productivity is partially due to drainage activities during winter and partially due to trade wind systems.

Mali, Mauritania, Niger and the Ahaggar Mountains: This area contains some of the most productive sources all over the world. This is due to existence of several sand dunes evident in many locations, the composition of the soil (high granulation), and the absence of precipitation (very seldom) and the presence of trade wind systems in the area, mainly the easterlies. The area is habituated by a very small amount of people with negligible agricultural activities. The most productive period is late spring to late Fall and the suspended dust is primarily directed towards the Atlantic Ocean and secondarily to other directions according to the prevailing weather systems. A certain amount of dust, especially the large particles contribute to the expansion of desertification in the surrounding areas.

Lake Chad Basin and the Bodele Depression: This is the most productive dust area of the world. It contributes to the dust plumes directed towards West, East and North. The dust areas remain productive during all seasons with minima during late autumn. There is always dust in the air for most of the regions of this large area. The soil consists of sediments that are rich in clay amounts and therefore dust clouds can form easily even with light winds due to high granulation. Production is enhanced also from the activity of drainage formations in

many places. Sand dunes that are continuously productive all over the year cover large areas (hundreds of kilometres towards each direction). Most of the sub-regions and especially the Bodele are the main contributors of dust plumes directed towards Atlantic, Gulf of Guinea and also towards Mediterranean.

Tunisia and Northeast Algeria: This area has some very productive areas at various elevations. The most productive dust areas are in locations where temporal salt lakes are temporarily formed. The dust particles suspended from this area have different hygroscopicity and therefore they affect the cloud formation and precipitation. In addition to high hygroscopicity the dust particles from these areas are of mixed alluvial, silt and clay type. The drainage activity and the formation of the seasonal lakes enhance the dust productivity during the dry period of the year. The most productive period of the year is spring and autumn. The salty-water lakes (called chotts) and the associated dust source regions lie in the lee of the Atlas mountains and therefore receive small amounts of precipitation (approximately 100 mm on annual base) not adequate to keep water during the dry season.

Libyan and Egyptian Desert: A large area that extends from Eastern Libya to Egypt is dust productive during most of the year, with the most intensive period during spring and autumn. The northern part of this area is a low-lying region where water is drained from the surrounding areas forming the "wadis". These areas are highly productive after the rainy season or temporal rains. The dust productive areas are often broken by the oases. These dust sources are of alluvial type and contribute significantly in the dust storm formation towards the Mediterranean Sea and Europe.

Sudan, Ethiopian highlands and Horn of Africa: This is a large area with large variability in dust sources. The maximum productivity is from May to July. The productivity is moving towards North at the beginning of summer and then again southward during fall. There are areas with sand dunes while other productive areas at the Sudan highlands with rich in clay soils. Wadi-type formations can be encountered too. Runoff formations in the Ethiopian, Somali and Eritrean high lands turn in high productive regions after drying out. The dust production from these regions is transported towards the Red Sea, the Gulf of Aden and the Indian Ocean. Very often, the dust plumes are mixed with biomass burning that is a seasonal procedure in agricultural or semi-arid areas.

5.5 WIND AND TURBULENCE

Having defined the dust sources, one must turn to the characteristics of the wind field which play a key role in moving and lofting the dust particles. The initial dust and sand particles that will move (at wind speeds of 5–13 $m \cdot s^{-1}$) are those whose diameter ranges from 0.08 to 1 mm (80–1000 micrometers). For both larger and smaller particles to move, stronger winds are required. Apparently, the impact created by saltation of the initial particles when lifted can cause the smaller particles to be hurled aloft.

Generally speaking, in order to mobilize dust, winds at the surface need to be 15 knots or greater. The Table 5.2 shows an overview of wind speeds required to lift particles in different source environments.

Once a dust storm starts, even when wind speeds slow to below initiation levels, it can maintain the same intensity. The reason lays in the fact that the bond between the dust particles and the surface is broken and saltation mechanism allows dust to lift. For a perfectly laminar flow, the mobilized particles would move in a thin layer across the desert floor. In order that a dust storm be created, it is necessary to get that dust up in the air. Substantial turbulence in the atmospheric boundary layer is typically required for the lofting of dust.

Table 5.2. Threshold dust-lofting wind speed for different desert environments (source:http://www.meted.ucar.edu).

Environment	Threshold wind speed ($m \cdot s^{-1}$)
Fine to medium sand in dune-covered areas	4.50–6.70
Sandy areas with poorly developed desert pavement	8.95
Fine material, desert flats	8.95–11.16
Alluvial fans and crusted salt flats (dry lake beds)	13.40–15.60
Well-developed desert pavement	18.90

Typically, the turbulence and horizontal roll vortices that loft the dust up and away from the surface are created by the wind shear. It stands to reason that dust storms will be favoured by an unstable boundary layer, since vertical motions are required to loft the particles. So, a stable boundary layer suppresses updrafts and inhibits dust raise. In similar way, the vertical extent of dust lofting is limited by a low-level inversion. Due to the lack of vegetation, dust-prone regions can experience extreme daytime heating of the ground causing the establishment of an unstable boundary layer, which deepens as the amount of heating increases. Thus, it is the mid-latitude deserts, with their extreme daytime temperatures, which are particularly prone to an unstable boundary layer. On the other hand, dry desert air leads to a wide diurnal temperature cycle. Strong radiative cooling leads to rapid heat loss after sunset, the lowest atmosphere is cooled, resulting in a surface-based inversion with potentially strong effects on blowing dust.

Such inversion suppresses vertical motions in the boundary layer so it becomes hard to lift dust. A 10-knot wind may raise dust during the day, but at night it may not. However, formation of a surface-based inversion will have little effect to the dust already in suspension higher in the atmosphere. Furthermore, sufficiently strong winds will inhibit formation of an inversion or even remove one that has already formed. In this case, one can blowing dust.

5.6 FRICTION VELOCITY

It has been previously discussed, that even for a strong wind, the wind must be sufficiently turbulent to loft dust, under the conditions of a reasonably unstable atmospheric environment. A single parameter that expresses wind speed, turbulence, and stability is the friction velocity. More technically, dust mobilization is proportional to the flux of momentum, or stress, into the ground. It turns out that a friction velocity of 60 centimetres per second is typically required to raise dust. Friction velocity u^* ($cm \cdot s^{-1}$) is defined as:

$$u^* = \frac{V_s \cdot \kappa}{\ln(z_s/z_0) - \psi_m \cdot (z_s/L)} \tag{5.1}$$

where:
V_S is the wind speed [L T^{-1}] at the midpoint z_s [L] of the surface layer,
κ is the von Karman constant,
z_0 is the surface roughness ($z_0 = 0.01$ for the desert) [L],
ψ_m is the stability parameter for momentum, and
L is the Monin-Obukhov length [L]. For neutral conditions, $z_s/L = 0$ and $\psi_m = 0$.

In daytime, the atmosphere over the desert is usually unstable so that $z_s/L < 0$ and $\psi_m > 0$, and more momentum is transferred to the ground. Table 5.3 presents some typical values of

Table 5.3. Typical values of friction velocity (u^*) for different values of threshold wind velocity (Vt) under neutral and unstable conditions (source:http://www.meted.ucar.edu).

$Vt(\mathrm{m}\cdot\mathrm{s}^{-1})$	u^*	
	Neutral ($z_s/L=0$)	Unstable ($z_s/L=2$)
5	29	35
8	46	55
11	64	77

u^* for different values of threshold wind velocity (Vt) under neutral and unstable conditions (Westphal *et al.*, 1988).

5.7 DIFFUSION EQUATION

The dust cycle in the atmospheric environment is in general, described by a set of K independent Euler-type prognostic continuity equations for dust concentration of the form:

$$\frac{\partial C_k}{\partial t} = -u\frac{\partial C_k}{\partial x} - v\frac{\partial C_k}{\partial y} - (w - v_{gk})\frac{\partial C_k}{\partial z} - \nabla(K_H \nabla C_k) - \frac{\partial}{\partial z}\left(K_Z \frac{\partial C_k}{\partial z}\right) + \left(\frac{\partial C_k}{\partial t}\right)_{SOURCE} - \left(\frac{\partial C_k}{\partial t}\right)_{SINK} \tag{5.2}$$

where:
K indicates the number of the particle size bins ($k = 1,\ldots,K$),
C_k is the dust concentration of a k-th particle size bin [$\mathrm{kg}\cdot\mathrm{m}^{-3}$],
u and v are the horizontal velocity components [L T],
w is the vertical velocity [L T],
v_{gk} is the gravitational settling velocity [L T],
∇ is the horizontal nabla operator,
K_H is the lateral diffusion coefficient [$\mathrm{L}^2\ \mathrm{T}^{-1}$],
K_Z is the turbulence exchange coefficient [$\mathrm{L}^2\ \mathrm{T}^{-1}$],
$(\partial C_k/\partial t)_{SOURCE}$ is the dust production rate normally over the dust source areas [$\mathrm{kg\,m}^{-3}\cdot\mathrm{s}^{-1}$], and
$(\partial C_k/\partial t)_{SINK}$ is the sink term which includes both wet and dry deposition fractions [$\mathrm{kg\,m}^{-3}\cdot\mathrm{s}^{-1}$].

The total concentration C [$\mathrm{kg}\cdot\mathrm{m}^{-3}$] is a weighted sum of concentrations of K particle size classes:

$$C = \sum_{k=1}^{K} \delta_k C_k; \quad \sum_{k=1}^{K} \delta_k = 1 \tag{5.3}$$

Here, δ_k denotes a mass fraction of the k-th particle category [$\mathrm{kg}\cdot\mathrm{kg}^{-1}$], to be specified in 5.10.1 paragraph.

Once the dust particles are released into the atmosphere they are lofted high into the boundary layer but eventually they will return to surface. Sooner or later, the dust particles will settle, although, some of them may travel half way around the globe before that happens. There are three main processes that mobilize dust particles into the atmospheric environment. These are:

- dispersion of dust,
- gravity-driven settling of dust, and
- entrainment of dust in precipitation.

5.8 DISPERSION OF DUST

The dispersion causes the fanning of a dust plume as it moves downstream from its source region. It is assumed as a dilution process and the more air is mixed with a plume, the more dilution there will be and the more the plume spreads out and disperses. You would see a similar effect if you poured dye into a river and watched how the colour faded as the water moved downstream. It is important to note that dispersion processes always act to dilute; laws of physics take care that plume never re-concentrates.

Figure 5.4 shows a (highly idealized) view of dispersion of a plume from a point source as it moves downstream. The concentration has not a uniform pattern throughout the plume. It remains highest in the centre of the plume while it reduces away from the centre.

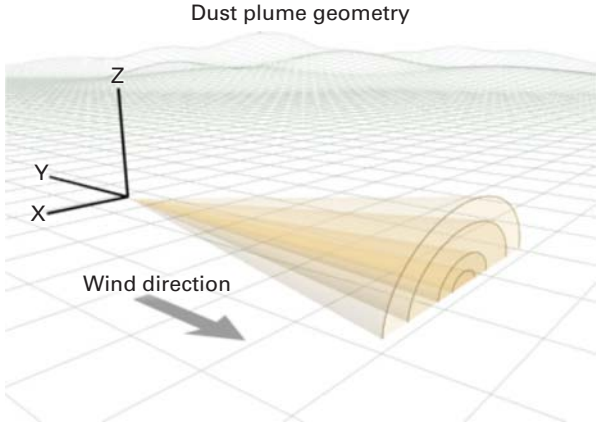

Figure 5.4. Schematic representation of the dust dispersion (source:http://www.meted.ucar.edu).

Turbulence primarily governes the dispersion since it mixes ambient air with the plume. The increase of the rate at which the plume disperses is directly related to the increase in turbulence. Three types of turbulence participate in the dispersion procedure: the mechanical turbulence, the turbulence caused by shear, and the turbulence caused by buoyancy.

- Mechanical turbulence is caused by air flowing over rough features, such as hills, trees and buildings.
- Turbulence from shear can result from the vertical variation of wind speed and/or direction.

- Buoyancy turbulence can be caused by bubbles of air rising due to the diurnal heating of the ground and it is governed by the stability of the atmosphere (Figure 5.5).

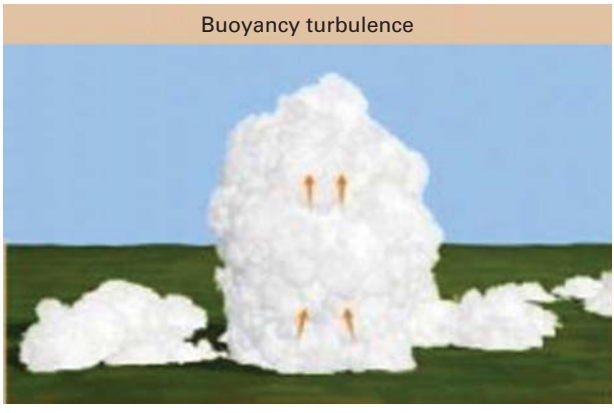

Figure 5.5. The buoyancy turbulence (source:http://www.meted.ucar.edu).

It is important to note in the case of dust plumes that turbulence not only acts to disperse the plume, it also acts to keep the dust particles in suspension. With no turbulence present, dust particles are generally settled at a rate of 300 metres per hour. However, this is strongly dependent on synoptic and mesoscale conditions so the rate at which the dust settles will be slowed down by the establishment of an unstable atmospheric environment.

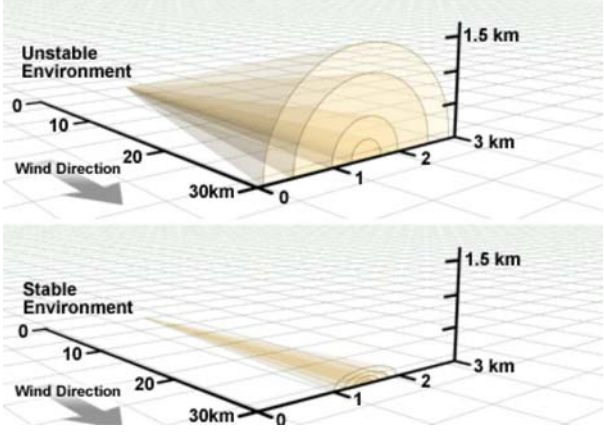

Figure 5.6. Dispersion and atmospheric stability (source: http://www.meted.ucar.edu).

We have mentioned already that unstable conditions favour the lofting of dust and the formation of dust storms. Atmospheric stability also has a strong influence on how dust disperses. Figure 5.6 depicts the difference of the dispersion of dust plumes generated under stable and unstable conditions. The plume dispersion is intensified in both horizontal and vertical directions in case of an unstable environment. This effect is significantly more

pronounced for vertical dispersion. With stable atmosphere, the dust remains relatively concentrated vertically, compared to dispersion under unstable conditions, while under neutral conditions, the plume will spread roughly equally in horizontal and vertical directions.

5.9 SETTLING OF DUST

Dry and wet deposition consist the main mechanisms of PM removal from the atmospheric environment. The term "wet deposition" is used if the aerosols are scavenged by precipitation, whereas if they are removed by gravitational settling it is referred as dry deposition. Different particle sizes are removed by different mechanisms.

Ultrafine particles, with diameter less than 0.1 μm, are mainly removed by coagulation whose rate is determined by the mobility of ultrafine particles and by the mass concentration of the entire aerosol population. Wet deposition is the main removal process for aerosols in the 0.1–10 μm size range. Particles in this size range are most efficient in acting as Cloud Condensation Nuclei (CCN). This range covers also coarser particles. For particles coarser than 10μm, dry deposition or sedimentation becomes significant.

However, particle size plays an important role in both lifting and settling thresholds. For example, long periods of dust haze in arid areas result from longer suspension times for finer particles result. Particles between 10 and 50 micrometers fall at about 1,000 feet per hour. This correlation has been used successfully to determine the lifespan of extended dust devils in the desert southwest of the United States. Another application was to estimate the settling of suspended dust in New Mexico after large-scale dust storms. Settling is actually grouping by particle size, with the largest falling out first and the smallest falling out last. Consequently, near the source area there will settle larger and heavier particles, with the smaller ones settling farther away.

We already defined dry deposition or sedimentation as the downward movement of PM due to gravitational settling. In general, the sedimentation velocity (v_s) [L T] can be obtained by equating the drag force and the weight of particles:

$$v_s = \frac{d_p^2 \rho_p g}{18\eta} \tag{5.4}$$

where η is the dynamic viscosity [Pa s], d_p is the diameter of the particles [μm], g is the gravitational acceleration (9.80 ms^{-2}) and ρ_p is the particle density. The sedimentation velocity becomes significant for particles coarser than 10 μm. The dry deposition velocity (v_d) is obtained if the sedimentation velocity is divided by the concentration near the surface $C_p[\mathrm{kg} \cdot \mathrm{kg}^{-1}]$. The dry deposition rate $D_d[\mathrm{kg\,m}^{-2} \cdot \mathrm{s}^{-1}]$ is then defined as the mass of the PM deposited per surface area unit during the time unit:

$$D_d = v_d M \tag{5.5}$$

where M corresponds to the mass concentration immediately adjacent to the surface $[\mathrm{kg} \cdot \mathrm{m}^{-3}]$ (Meszaros, 1999).

Most dust particles "love water" i.e. they are hygroscopic. Any precipitation will effectively remove dust from the troposphere due to this affinity to moisture. The removal mechanism of particles known as in-cloud scavenging occurs when aerosol particles are removed from the atmosphere by condensation. In fact, atmospheric particles usually form the nucleus of precipitation and may act as CCN. When condensation exists in the atmosphere, deposition of the CCN particles occurs. Additional particles present in the atmosphere are washed out by precipitation. This process is called below-cloud scavenging

(or wash-out). In the below-cloud mechanism, depending on the particle size, there occur two processes: Fine and ultrafine particles with diameters below 0.5–1 μm are removed by diffusion due to their Brownian motion. Coarser particles are removed by their inertial deposition onto cloud droplets or ice crystals.

Due to both scavenging processes, precipitation water contains chemical species which affect the precipitation acidity. Precipitation is considered acidic when pH is lower than 5.6, which is the equilibrium pH of pure water and CO_2 atmospheric concentrations (Granat, 1972). This acid rain damages vegetation, building materials and affects the biogeochemical functioning of ecosystems. The main contributor to acidity in rain is the sulphuric acid is but also nitric acid can contribute to acidification. Figure 5.7 represents the stages of the wet deposition. More detailed formulation on dry and wet deposition processes is provided later.

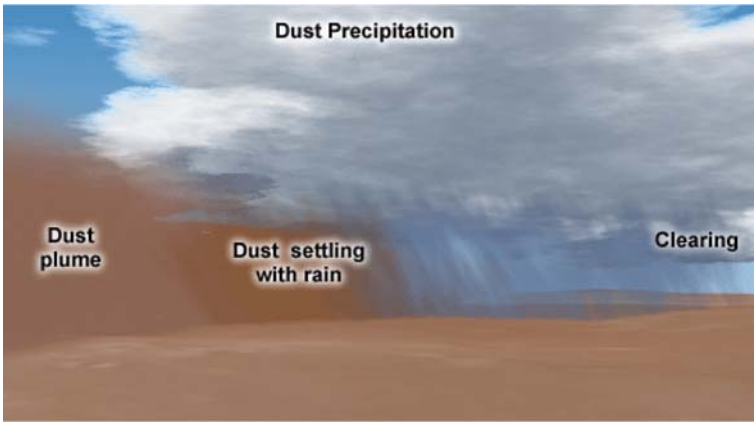

Figure 5.7. The wet deposition stages (source http://www.meted.ucar.edu).

5.10 THE FORMULATION OF THE DUST CYCLE

This paragraph introduces a formulation for the description of the dust cycle in the atmosphere. It consists of a sophisticated scheme for the dust production and concentration which are estimated by a set of K independent Euler-type equations. Equation (5.2) offers the general form of these equations. An advanced parameterization scheme for the dry and wet deposition is also included.

In order to provide atmospheric driving conditions for dust parameters this formulation is combined with the Skiron/Eta atmospheric model on a fully coupled way. The dynamics of the model is based on: large-scale numerical solutions controlled by conservation of integral properties (Arakawa, 1966; Janjic, 1977; Janjic, 1984), energetically consistent time-difference splitting (Janjic, 1979; Janjic, 1997), and the step-like mountain representation (Mesinger, 1984; Mesinger *et al.*, 1988). A conservative positive definite scheme (Janjic, 1997) has been applied for horizontal advection of passive substances (including dust concentration). The physics incorporated consists of: the viscous sublayer models over water (Janjic, 1994) and over land (Zilitinkevitch, 1995), the surface layer scheme based on the similarity theory (Janjic, 1996b), a turbulence closure scheme based on Kolmogorov-Heisenberg theory (Janjic, 1996a), the Betts-Miller-Janjic deep and shallow moist convection scheme (Betts, 1986; Janjic, 1994), the land surface scheme (Chen *et al.*,

1996), the grid-scale precipitation scheme (Zhao and Carr, 1997), and the radiation scheme (Lacis and Hansen, 1974; Fels and Schwartzkopf, 1975).

5.10.1 Surface concentration

The movement of dust particles is mainly caused by the larger particles with diameters greater then 10 μm which break soil cohesion forces and release finer particles into the atmosphere, this is saltation (bombardment) process (Alfaro *et al.*, 1997). The key role in the wind erosion processes is played by the surface features of the atmosphere and soil which regulate the amount of the released dust. The momentum flux from the atmosphere determines the quantity of mobilized dust, while on the other hand, soil conditions (soil structure, wetness, and coverage) dictate if and how much dust will finally be injected into the atmosphere.

The lower boundary condition in modelling simulations can be chosen either as surface flux or surface concentration. The "flux" approach is applied in most of the dust models (Westphal *et al.*, 1987; Marticorena and Bergametti, 1995; Tegen and Fung, 1994).

Two groups of parameters govern the released surface concentration of mobilised particles and the corresponding surface vertical flux. The first group relates to the structure and state of soil, while the second one describes the turbulent state of the surface atmosphere. The flux dependence on friction velocity is a subject where there is no full agreement among different authors. For example Gillette and Passi (1988) proposed that the vertical dust flux F_S [μgr $\cdot$ m^{-2} $\cdot$ s^{-1}] should be represented by a function of friction velocity, which asymptotically approaches the forth power of friction velocity:

$$F_S = const \times u_*^4 \left(1 - \frac{u_{*t}}{u_*}\right) \quad for\, u_* \geq u_{*t} \tag{5.6}$$

Here, u_* is the friction velocity [L T], and u_{*t} is its threshold value below which dust production ceases [L T]. Another functional form for vertical flux was used by Tegen and Fung (1994):

$$F_S = const \times u_*^2 (u_* - u_{*t}) \quad for\, u_* \geq u_{*t} \tag{5.7}$$

However, the work of Shao *et al.* (1993), based on wind tunnel experiments does not support relationships (5.6) and (5.7). Their study instead proposes the following parametric formula for dust surface fluxes:

$$F_S = const \times u_*^3 \left[1 - \left(\frac{u_{*t}}{u_*}\right)^2\right] \quad for\, u_* \geq u_{*t} \tag{5.8}$$

which reasonably well agrees with the wind tunnel measurements. Nickovic *et al.* (2001) developed their dust production scheme using this relation as a starting point. They also introduced parameters α, β, and γ to describe the effects of the soil structure and particle size distribution (Table 5.1). Thus the definition of the dust productivity factor is given:

$$\delta_k = \alpha \gamma_k \beta_k \tag{5.9}$$

Here, the subscript k denotes particle size categories. β includes the influence of soil textures [kg $\cdot$ kg^{-1}] and typical values are presented in Table 5.4 while parameter γ corresponds to the ratio between the mass available for uplift and the total mass of a specific

Table 5.4. Correspondence between texture classes and soil types, and relative contributions of clay/sand/silt.

l	ZOBLER texture classes	Cosby soil types	β_{kl}			
			Clay	Small silt	Large silt	Sand
1	coarse	loamy sand	0.12	0.08	0.08	0.80
2	medium	silty clay loam	0.34	0.56	0.56	0.10
3	fine	Clay	0.45	0.30	0.30	0.25
4	coarse-medium	sandy loam	0.12	0.18	0.18	0.70
5	coarse-fine	sandy clay	0.40	0.10	0.10	0.50
6	medium-fine	clay loam	0.34	0.36	0.36	0.30
7	coarse-medium-fine	sandy clay loam	0.22	0.18	0.18	0.60

particle size category [$\mathrm{kg} \cdot \mathrm{kg}^{-1}$] (Table 5.1). Grid points which act as desert dust sources in the model are specified using arid and semi-arid categories of the global vegetation data set. This can be done by mapping global vegetation data into the horizontal model grid and then counting numbers of desert points falling into Skiron/Eta model grid boxes. Parameter α which is the fraction of a grid point area covered by desert surface is calculated by:

$$\alpha = \frac{\text{number of dust points in model grid box}}{\text{total number of vegetation points in model grid box}} \tag{5.10}$$

The effective surface vertical flux can be defined by:

$$F_{Sk}^{EFF} = \delta_k F_S \tag{5.11}$$

Nickling and Gillies (1989), expressed the surface concentration under neutral stability conditions, in terms of vertical surface flux as:

$$C_{Sk} = const \times \frac{F_{Sk}^{EFF}}{\kappa u_*} \tag{5.12}$$

Combining (5.8)–(5.12) the surface concentration is calculated as:

$$C_{Sk} = const \times \delta_k u_*^2 \left[1 - \left(\frac{u_{*tk}}{u_*} \right)^2 \right] \quad for\, u_* \geq u_{*tk} \tag{5.13}$$

The value of the dimensional empirical constant is $2.4 \times 10^{-4}\,\mathrm{m}^{-5} \cdot \mathrm{kg} \cdot \mathrm{s}^2$.

5.10.2 Threshold friction velocity

The soil wetness and particle size strongly determine the threshold friction velocity at which the soil erosion starts. Soil water which water resists in the soil due to capillary forces on surfaces of the soil grains, and due to molecular adsorption, increases the threshold friction velocity, therefore reducing the amount of dust injected into the atmosphere.

The soil moisture effects are included in the formulation of u_{*t} following the method of Fecan *et al.* (1999). The maximal amount of the adsorbed water w' [$\mathrm{cm}^3 \cdot \mathrm{cm}^{-3}$] is an

increasing function of the clay fraction in the soil. Based on empirical data, Fecan *et al.* (1999) estimate w' to be a second order polynomial function of clay fraction in soil:

$$w' = 0.0014(\%\text{clay})^2 + 0.17(\%\text{clay}) \tag{5.14}$$

Combining (5.14) and β_k from Table 5.4, one can establish a correspondence between w' and the seven considered texture classes, as given in Table 5.5.

Table 5.5. Correspondence between soil texture classes and w'.

l	Cosby soil types	w'_l (%)
1	loamy sand	2.5
2	silty clay loam	6.8
3	Clay	11.5
4	sandy loam	2.5
5	sandy clay	10.0
6	clay loam	6.8
7	sandy clay loam	3.5

Following available experimental data, the threshold velocity is defined in (5.15) as:

$$\begin{aligned} u_{*tk} &= U_{*tk} && \text{for } w \le w' \quad \text{(dry soil)} \\ u_{*tk} &= U_{*tk}\sqrt{1 + 1.21(w - w')^{0.68}} && \text{for } w > w' \quad \text{(wet soil)} \end{aligned} \tag{5.15}$$

Here, w corresponds to the ground wetness [$\text{cm}^3 \cdot \text{cm}^{-3}$]. Following Bagnold (1941), one defines the threshold friction velocity for dry soil as:

$$U_{*tk} = A_k\sqrt{2gR_k\frac{\rho_{pk} - \rho_a}{\rho_a}} \tag{5.16}$$

where g is gravity, and ρ_{pk} and ρ_a are particle and air densities, respectively. The parameter A_k is the function of the particle Reynolds number $(Rr)_{pk} = (2R_k U_{*tk})/\nu$ only and $\nu = 0.000015\,\text{m}^2\text{s}^{-1}$ is the molecular diffusivity for momentum [$\text{m}^2 \cdot \text{s}^{-1}$]. For the considered four particle sizes distribution, $A_k = \{1, 0.7, 0.4, 0.25\}$ is specified using available empirical data (White, 1979).

The Bagnold-type relation for the threshold friction velocity assumes that there is no flux bellow U_{*tk}, yet observations indicate that when u_* decreases, the soil erosion does not stop immediately as soon as sub-threshold conditions are reached (Jackson, 1996). It is suggested that the particles are carried forward due to inertia for a period, effectively maintaining the transport longer then predicted. In order to avoid underestimation of dust production by parameterizing the inertial effect, the cases shown schematically in Figure 5.8 are treated in the following way:

a) Fluxes start to operate when $u_* < u_{*ts} = 0.9 \times U_{*tk}$ (at time step t_1) increases to the value $u_* > U_{*tk}$ (at time step t_2).
b) Fluxes are still operating when $u_* > U_{*tk}$ (at time step t_2) falls to the value $u_{*ts} < u_* < U_{*tk}$ (at time step t_3).

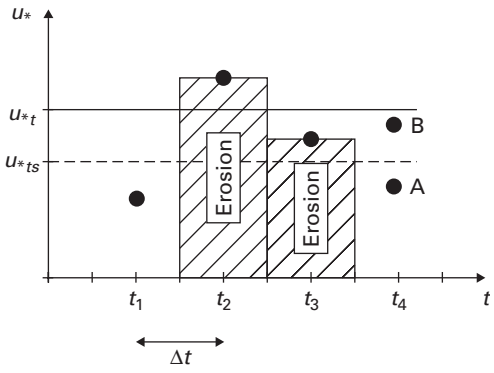

Figure 5.8. Conceptual model describing dust production under sub-threshold friction velocity conditions. At model time step t_1, u_* is bellow u_{*t} and there is no dust production. At t_2, u_* exceeds u_{*t} and dust production starts. At t_3, u_* is bellow the threshold (u_{*t}) but above the sub-threshold value ($u_{*ts} = 0.9\ u_{*t}$) and there is still dust production driven by inertial forces. At t_4, dust production is ceased if either u_* is bellow u_{*ts} (point A) or even it increases but stays bellow the threshold (point B) (Source: Nicković *et al.*, 2001).

c) Fluxes are ceased when $u_{*ts} < u_* < U_{*tk}$ (at time step t_3) stays in the interval $[u_{*ts}, U_{*tk}]$ or decreases to $u_* < u_{*ts}$ (at time step t_4).

5.10.3 Viscous sublayer effects

There are two atmospheric layers operating over the oceans in the Skiron/Eta model: a thin viscous sublayer located just above the surface where vertical transport is realised through molecular diffusion, and a layer above with fluxes defined by turbulent mixing (Janjic, 1994). Features of the viscous sublayer are described by different regimes depending on surface turbulent conditions.

There exists a physical similarity of mass/heat/momentum exchange over surfaces with mobilized particles such as sea and deserts surfaces (Chamberlain, 1983 and Segal, 1990). The viscous sublayer formulation is applied to the dust concentration and the dust source term in the concentration equation (5.2), following Janjic (1994), is represented by:

$$\left(\frac{\partial C_k}{\partial t}\right)_{SOURCE} = -\frac{F_{Sk}}{\Delta z} \tag{5.17}$$

Here, Δz represents the depth of the lowest atmospheric layer [L], k is the subscript denoting the particle size class, and F_{Sk} is the turbulent flux of dust concentration above the viscous sublayer [$\mathrm{kg \cdot m^{-2} \cdot s^{-1}}$]. The turbulent flux can be approximated in terms of the viscous sublayer parameters as:

$$F_{Sk} = \nu \frac{C_{0k} - C_{Sk}}{z_C} \tag{5.18}$$

The subscript 0 denotes values at the interface of the viscous and turbulent layers; the subscript S denotes the surface values. The depth of the viscous sublayer is approximated by:

$$z_C = \frac{0.35 MRr^{0.25} Sc^{0.5} \nu}{u_*} \tag{5.19}$$

Here, M is a parameter varying for different turbulent regimes, and u_* is the friction velocity. The roughness Reynolds number Rr and the Schmidt number Sc are defined by:

$$Rr = \frac{z_0 u_*}{\nu}, \quad Sc = \frac{\nu}{\lambda} \tag{5.20}$$

where λ is the particle diffusivity $[\mathrm{m}^2 \cdot \mathrm{s}^{-1}]$, and $z_0 = \max(0.018(u_*^2/g), 1.59 \times 10^{-5})$ (Zoumakis and Kelessis, 1991).

Following Janjic (1994), the viscous sublayer for dust transport is assumed to operate in the following regimes: smooth and transitional, rough, and very rough, depending on Rr (or, equivalently, on u_*). Transitions between regimes are assumed to occur at $u_{*r} = 0.225\,\mathrm{m\,s}^{-1}$ and $u_{*s} = 0.7\mathrm{m\,s}^{-1}$. Following observational data, it is defined $M = 30$ for the smooth regime, and $M = 10$ otherwise.

The particle diffusivity λ is much smaller than ν (Businger, 1986). In the wind-tunnel experiments of Chamberlain *et al.* (1984), synthetic particles with diameter $0.65\,\mu\mathrm{m}$ are used, having diffusivity coefficients $\lambda = 4.8 \times 10^{-9}\,\mathrm{m^2 s^{-1}}$ for smooth and transitional flow, and $\lambda = 3.0 \times 10^{-8}\,m^2 s^{-1}$ for rough conditions. For very rough turbulent regime it is applied $\lambda = 7.0 \times 10^{-8}\,\mathrm{m^2 s^{-1}}$.

The smooth regime stops to operate when the friction velocity exceeds u_{*r} and the flow enters into the rough regime. In this case, the viscous sublayer for momentum is "turned off", while the viscous sublayer for the other parameters (including dust) continues to function until the next critical value u_{*s} is achieved. The rough regime transits at this point, to the very rough regime characterized by fully developed turbulence. At this stage, the viscous sublayer for dust is completely ceased and extensive mobilization of dust particles starts.

The expression (5.18) can alternatively be defined in terms of turbulent conditions above the viscous sublayer:

$$F_{Sk} = K_S \frac{C_{LMk} - C_{0k}}{\Delta z} \tag{5.21}$$

Here, K_S is the surface-mixing coefficient for concentration $[\mathrm{L^2 T^{-1}}]$, and LM denotes the first level of the free atmosphere above the viscous syblayer. K_S is assumed equivalent to the mixing coefficient for heat and moisture. The surface-mixing coefficient is calculated according to the Monin–Obukhov method (Janjic, 1996b).

The lower boundary condition for concentration is obtained from the requirement that the fluxes (5.7) and (5.21) are matched at the interface of the viscous and turbulent layers:

$$C_{0k} = \frac{C_{Sk} + \omega C_{LMk}}{1 + \omega} \tag{5.22}$$

Here,

$$\omega = \frac{\left(\dfrac{K_S}{\Delta z}\right)}{\left(\dfrac{\lambda}{z_C}\right)} \tag{5.23}$$

which has a role of weighting factor in (5.22). From (5.21) and (5.22) the surface flux is finally calculated as:

$$F_{Sk} = K_S^* \frac{C_{LMk} - C_{Sk}}{\Delta z} \tag{5.24}$$

Here, C_{Sk} is defined by (5.13), and

$$K_S^* = \frac{1}{1+\omega} K_S \tag{5.25}$$

is a conventional similarity-theory mixing coefficient but corrected by viscous effects.

5.10.4 Shear-free convection effects

Overheated desert surfaces may generate strong uprising thermal plums. Even in the absence of surface wind shear they are associated with significant upward vertical transport. In such cases the calculation of the surface fluxes should not be based on (5.24), but following the method of Zilitinkevich *et al.* (1998).

The reason is that under the shear-free convection conditions, the friction velocity vanishes, which causes a singularity in calculation of surface fluxes if a traditional approach (e.g. the Monin–Obukhov theory) is applied. In Skiron/Eta model, the method of Beljaars (1994) is applied which avoids this difficulty by adding to the turbulent kinetic energy a term with the kinetic energy of the near-surface wind induced by the large-scale eddies (Janjic, 1996b), thus preventing the friction velocity and the Obukhov length to get nonzero values. Beljaars' correction converts the surface buoyancy flux $(\overline{w'T'})_S$ [L T] into the turbulent kinetic energy of the near-surface wind. The fraction of the surface buoyancy flux converted into the turbulent kinetic energy is assumed to be

$$U_B^2 = (1.2 \times W^*)^2 \tag{5.26}$$

where the convective scale velocity [L T^{-1}] is defined by

$$W^* = \left[\frac{1}{273} \times gh(\overline{w'T'}) \right]^{1/3} \tag{5.27}$$

Here, h is the depth of the convective boundary layer [L]. The Beljaars correction is performed in practice by adding U_B to the wind speed at the upper boundary of the surface layer.

Shear-free flow is characterized by strong convection with narrow uprising motion created by buoyancy driven structures. Such structures generate a surface convergence, which is superimposed on the mean wind. In the shear-free regime, the flow yields its own velocity shear characterized by the 'minimum friction velocity' U_* and the "minimum Monin-Obukhov length", L_* [L]. Under these conditions, a well-developed planetary boundary layer combined with a relatively smooth roughness height characterize the flow. Here, the shear-free convective dust flux is estimated using the 'aerodynamic' mixing coefficient

$$K_{AC} \equiv \frac{F_S}{U_* \Delta C_A} \tag{5.28}$$

rather then using the bulk coefficient (5.25). The expression (5.28) is valid in a broad range of turbulent conditions, for $10^{-10} \le z_{0u}/h \le 10^{-5}$. Here, z_{0u} is the roughness length for momentum. The concentration "aerodynamic increment" is formulated by

$$\Delta C_A \equiv C_{AS} - C_{LM} = \left(C_S - \frac{F_C}{\kappa U_*} \ln \frac{z_{0u}}{z_{0C}} \right) - C_{LM} \tag{5.29}$$

where, $\kappa = 0.4$ is the von Karman constant, C_{LM} is the lowest atmospheric level concentration [kg · m^{-3}], C_S is the surface concentration defined by (5.13), and C_{AS} is the concentration extrapolated logarithmically downwards to the level $z = z_{0u}$ [kg · m^{-3}]. Following Zilitinkevich *et al.* (1998), the following approximations are used:

$$\frac{U_*}{W_*} = 0.36 \left(\frac{z_{0h}}{h}\right)^{0.1} \tag{5.30a}$$

and

$$K_{AC} = \frac{1}{4.4 \left(\dfrac{h}{z_{0u}}\right)^{0.1} - 1.5} \tag{5.30b}$$

Using (5.28), (5.29) and (30), the surface flux at shear-free atmospheric layers is finally calculated as:

$$F_S = \frac{0.36 \left(\dfrac{z_{0u}}{h}\right) W_*(C_S - C_{LM})}{\dfrac{1}{\kappa} \ln \dfrac{z_{0u}}{z_{0C}} + 4.4 \left(\dfrac{z_{0u}}{h}\right)^{-1} - 1.7} \tag{5.31}$$

5.11 DUST SINKS

5.11.1 Dry deposition

The scheme of Georgi (1986) is used for the parametrization of the dry part of particle deposition on the Earth surface. This scheme includes processes of deposition by surface turbulent diffusion and Brownian diffusion, gravitational settlement, and interception and impaction on the surface roughness elements. Thus the dry deposition velocity v_{dep} [L T] is parameterised by:

$$v_{dep} = \frac{1}{\dfrac{1}{v_{SL}} + \dfrac{1}{f_{B0} v_{IL}}} \tag{5.32}$$

Here, v_{SL} is the turbulent deposition velocity in the layer between z_S and 10 m [L T]; v_{IL} is the turbulent deposition velocity at the top of the viscous sublayer z_S, and f_{B0} [L T] is the empirical constant, which takes into account effect of the blow-off over the vegetation surfaces. The velocity v_{SL} is expressed as

$$v_{SL} = C_{D10} U_{10} \frac{\sqrt{C_{D10}}}{\sqrt{C_{D0}} - \sqrt{C_{D10}}} \tag{5.33}$$

where, drag coefficients $C_{D10} = u_*^2 / U_{10}^2$ and $C_{D0} = u_*^2 / U_{Z_S}^2$ and the velocities U_{10} and U_{Z_S} are specified with respect to the to the heights $z = 10$ m and z_S.

The parameterization of the velocity v_{IL}

$$v_{IL} = G \sqrt{C_{D10}} u_* \tag{5.34}$$

includes the function G introduced by Georgi (1986) which reflects the properties of particles (size, composition) and depositing surfaces (roughness, texture, vegetation coverage). It is given by

$$G = \frac{B_{St}}{\sqrt{C_{D0}}} \tag{5.35}$$

where B_{St} is the particle surface Stanton number. Moreover, G can be divided into a sum of contributions from the Brownian diffusion, interception and impaction (Slinn, 1982):

$$G = G_{BD} + G_{\text{int}} + G_{imp} \tag{5.36}$$

G is separately considered for two kinds of surfaces: surfaces with turbulent regimes ranging from smooth to rough conditions, and surfaces covered by vegetation.

The first kind of surfaces includes sea, bare soil and ice surfaces. There. Basic assumption is $f_{B0} = 1$. Over such surfaces, parameters $1/\sqrt{C_{D0}}$ and G are represented by expressions as shown in Table 5.6 (Georgi, 1986). Here, $St = (v_g u_*^2)/(\nu g)$ is the Stokes number, where the gravitational settling velocity at the lowest model level is defined as

$$(v_{gk})^{LM} = \frac{2g\rho_{pk}R_k^2}{9\nu} \tag{5.37}$$

Here, $g = 9.8\,\text{m}\,\text{s}^{-1}$ is the gravitation acceleration; R_k and ρ_{pk} are the radius [L] and density [g cm^{-3}] of a k-th particle size class, respectively, as given in Table 5.1.

Equations (5.32)–(5.37) and Tables (5.1) and (5.6) completely determine the deposition velocity v_{dep}.

Table 5.6. Values of $1/\sqrt{C_{D0}}$ and G for different turbulent regimes.

Turbulent regime defined according to Rr (equation 5.18)	$\frac{1}{\sqrt{C_{D0}}}$	G
$Rr < 0.13$	13.5	$S_c^{-2/3} + 4.27\frac{St^2}{St^2+400}$
$0.13 < Rr < 2.00$	$6.432Rr^{-0.3634}$	$0.6667Rr^{-0.2}Sc^{-0.538Rr^{-0.105}} + 2.225Rr^{-0.3634}\frac{St^2}{St^2+400}$
$Rr > 2.00$	5	$0.6849Rr^{-0.25}Sc^{-0.5} + 1.75\frac{St^2}{St^2+400}$

The parameterization proposed by Georgi (1986) is applied for surfaces covered by vegetation. The parameters and constants dependent on vegetation types are defined as shown in Table 5.7. Over vegetation surfaces, Georgi (1986) defines:

$$G = \sqrt{\frac{\eta_e}{c_{dm}}} \tag{5.38}$$

Table 5.7. Parameters related to deposition over surfaces covered by vegetation which depend on vegetation types.

M	Vegetation types according to Dorman/Sellers	c_d	c_v	A_s	$(1/\sqrt{C_{D0}})_m$
1	Broadleaf-evergreen trees	0.5	0.16	0	2.0
2	Broadleaf-decidious trees	0.5	0.16	0	2.0
3	Broadleaf and neadleleaf trees	0.5	0.16	0	2.0
4	Neadleleaf-evergreen trees	0.4	0.12	0	2.5
5	Neadleleaf-decidious trees	0.4	0.12	0	2.5
6	Breoadfeaf trees with groundcover	0.4	0.12	0	2.5
7	Groundcover only or cultivations	0.3	0.08	1.4×10^{-5}	3.5
8	Broadleaf shrubs with perennial groundcover	0.35	0.09	3.2×10^{-5}	3.0
9	Broadleaf shrubs with groundcover	0.35	0.09	3.2×10^{-5}	3.0
10	Dwarf trees and shrubs with groundcover	0.35	0.09	3.2×10^{-5}	3.0

where c_{dm} is the local drag coefficient for vegetation depending upon m different vegetation types (see Table 5.7); η_e is the efficiency of vegetation to collect the aerosol. The collection efficiency is approximated by:

$$\eta_e = \eta_{BD} + \eta_{int} + \eta_{imp} + \eta_s \tag{5.39}$$

Here, the subscripts denote Brownian diffusion, interception, impaction and collection by small elements, respectively.

The collection efficiency for Brownian diffusion is given by

$$\eta_{BD} = c_{vm} Sc^{-1.3} \tag{5.40}$$

where the local viscous drag coefficient c_{vm} depends upon m different vegetation types (see Table 5.7).

The collection efficiency for interception depends on particle size k and it is specified as

$$\eta_{int} = \frac{F_k^2}{a} \tag{5.41}$$

where $F_k = R_k/a$, R_k is the radius of the k-th particle class, and $a = 0.5$ mm is the average obstacle radius.

The collection efficiency for interception by smaller vegetation elements is defined by

$$\eta_s = A_{sm} F_{sk} \ln(1 + F_{sk}) \tag{5.42}$$

where $F_{sk} = R_k/a_s$, $a_s = 10\,\mu$m. The factor A_{sm} is the ratio between areas of small collectors and area of the roughness elements, which depends upon different vegetation types m (see Table 5.7).

Finally, the collection efficiency for impaction is approximated by

$$\eta_{imp} = \frac{St_a^{3.2}}{(St_a + 0.6)^{3.2}} \tag{5.43}$$

where, $St_a = v_g u_*/ga$ is the Stanton number over vegetation surfaces.

For particle deposition over surfaces covered by vegetation, different function is applied $f_{BO} = 1/(e^{\sqrt{St_a}})$. The parameter $(1/\sqrt{C_{D0}})_m$ used in calculations over vegetation surfaces ranges from 2–3.5 for different vegetation types m, as given in Table 5.7.

Finally, (5.39) can be rewritten using (5.40)–(5.43), as:

$$\eta_e = c_v Sc^{-1.3} + \frac{F^2}{2} + \frac{St_a^{3.2}}{(St_a + 0.6)^{3.2}} + A_s R_s \ln(1 + R_s) \tag{5.44}$$

The dry deposition velocity v_{dep} (5.32) is fully determined with equations (5.33)–(5.44). Its contribution to the source term in Equation (5.2) is then defined as:

$$\left(\frac{\partial C}{\partial t}\right)_{SINKddep} = -\left(\frac{C v_{dep}}{\Delta z}\right)^{LM} \tag{5.45}$$

5.11.2 Wet deposition

The wet removal of dust concentration can be estimated by using the precipitation water. The rate of dust scavenged by precipitation is calculated as

$$\left(\frac{\partial C}{\partial t}\right) = -\phi \frac{\partial}{\partial z}\left(C \frac{\partial P}{\partial t}\right) \tag{5.46}$$

where $\partial P/\partial t$ is the precipitation rate [L T], and the washout parameter is given the constant value $\phi = 5 \times 10^5$. The deposition on the surface is then calculated by

$$\left(\frac{\partial C}{\partial t}\right)_{SINKwdep} = -\phi \left(\frac{C}{\Delta z}\frac{\partial P}{\partial t}\right)^{LM} \tag{5.47}$$

where LM is the lowest atmospheric layer.

APPENDIX—LIST OF SYMBOLS

List of Symbols

Symbol	Definition	Dimensions or Units
A_k	function of the particle Reynolds number	
A_{sm}	ratio between areas of small collectors and area of the roughness elements, which depends upon different vegetation types m	
B_{St}	particle surface Stanton number	
C	total concentration	[kg m^{-3}]
C_{AS}	concentration extrapolated logarithmically downwards to the level $z = z_{0u}$	[kg m^{-3}]
C_k	dust concentration of a k-th particle size bin	[kg m^{-3}]

(*Continued*)

List of Symbols

Symbol	Definition	Dimensions or Units
C_{LM}	lowest atmospheric level concentration	[kg m^{-3}]
C_p	concentration near the surface	[kg kg^{-1}]
C_{Sk}	surface concentration	[kg m^{-3}]
D_d	dry deposition rate	[kg m^{-2} s^{-1}]
F_S	vertical dust flux	[μgr m^{-2} s^{-1}]
F_{Sk}^{EFF}	effective surface vertical flux	[μgr m^{-2} s^{-1}]
F_{Sk}	turbulent flux of dust concentration above the viscous sublayer	[kg m^{-2} s^{-1}]
G	function which reflects the properties of particles and depositing surfaces	
K	number of the particle size bins (k = 1, . . ., K)	
K_{AC}	aerodynamic mixing coefficient	
K_H	lateral diffusion coefficient	[m^2 s^{-1}]
K_S	surface-mixing coefficient for concentration	[m^2 s^{-1}]
K_Z	turbulence exchange coefficient	[m^2 s^{-1}]
L	Monin–Obukhov length	[m]
L_*	minimum Monin–Obukhov length	[m]
LM	lowest atmospheric layer	
M	mass concentration immediately adjacent to the surface	[kg m^{-3}]
M_t	parameter varying for different turbulent regimes	
Re	Reynolds number	
R_k	radius of a k-th particle size class	[m]
Rr	roughness Reynolds number	
Sc	Schmidt number	
St	Stokes number	
St_a	Stanton number over vegetation surfaces	
U_{*tk}	threshold friction velocity for dry soil	[m s^{-1}]
U_B^2	fraction of the surface buoyancy flux converted into the turbulent kinetic energy	[m^2 s^{-2}]
V_s	wind speed at the midpoint z_s of the surface layer	[m s^{-1}]
W^*	convective scale velocity	[m s^{-1}]
c_{dm}	local drag coefficient for vegetation	
c_{vm}	local viscous drag coefficient	
d_p	diameter of the particles	[μm]
f_{B0}	empirical constant, which takes into account effect of the blow-off over the vegetation surfaces	
g	gravitational acceleration constant	[m s^{-2}]
h	depth of the convective boundary layer	[m]
k	size category	
m	number of different vegetation types	
u, v	horizontal velocity components	[m s^{-1}]
u_*	friction velocity	[m s^{-1}]
u_{*t}	threshold value of the friction velocity bellow which dust production ceases	[m s^{-1}]

(*Continued*)

List of Symbols

Symbol	Definition	Dimensions or Units
u_{*ts}	sub-threshold friction velocity	$[\mathrm{m\,s^{-1}}]$
v_s	sedimentation velocity	$[\mathrm{m\,s^{-1}}]$
w	vertical velocity	$[\mathrm{m\,s^{-1}}]$
w_g	ground wetness	$[\mathrm{cm^3\,cm^{-3}}]$
w'	volumetric soil moisture	$[\mathrm{cm^3\,cm^{-3}}]$
$(\overline{w'T'})_S$	surface buoyancy flux	[m s]
z_C	depth of the viscous sublayer	[m]
z_s	midpoint of the surface layer	[m]
z_{0u}	roughness length for momentum	[m]
z_0	surface roughness	[m]
Δz	depth of the lowest atmospheric layer	[m]
α	fraction of a grid point area covered by desert surface	
β	influence of soil textures	$[\mathrm{kg\,kg^{-1}}]$
γ	ratio between the mass available for uplift and the total mass of a specific particle size category	$[\mathrm{kg\,kg^{-1}}]$
γ_k	ratio between the mass available for uplift and the total mass	$[\mathrm{kg\,kg^{-1}}]$
δ_k	mass fraction of the k-th particle category	$[\mathrm{kg\,kg^{-1}}]$
η	dynamic viscosity	[Pa s]
η_{BD}	collection efficiency for Brownian diffusion	
η_e	efficiency of vegetation to collect the aerosol	
η_{imp}	collection efficiency for impaction	
η_{int}	collection efficiency for interception	
s η_s	collection efficiency for interception by smaller vegetation elements	
κ	von Karman constant	
λ	particle diffusivity	$[\mathrm{m^2\,s^{-1}}]$
ν	molecular diffusivity for momentum	$[\mathrm{m^2\,s^{-1}}]$
v_{dep}	dry deposition velocity	$[\mathrm{m\,s^{-1}}]$
v_{gk}	gravitational settling velocity	$[\mathrm{m\,s^{-1}}]$
$(v_{gk})^{LM}$	gravitational settling velocity at the lowest model level	$[\mathrm{m\,s^{-1}}]$
v_{IL}	turbulent deposition velocity at the top of the viscous sublayer z_S	$[\mathrm{m\,s^{-1}}]$
v_{SL}	turbulent deposition velocity in the layer between z_S and 10 m	$[\mathrm{m\,s^{-1}}]$
ρ_a	air density	$[\mathrm{kg\,m^{-3}}]$
ρ_p	particle density	$[\mathrm{g\,cm^{-3}}]$
ρ_{pk}	density of a k-th particle size class	$[\mathrm{g\,cm^{-3}}]$
$(\partial C_k/\partial t)_{SOURCE}$	dust production rate normally over the dust source areas	$[\mathrm{kg\,m^{-3}\cdot s^{-1}}]$
$(\partial C_k/\partial t)_{SINK}$	sink term which includes both wet and dry deposition fractions	$[\mathrm{kg\,m^{-3}\cdot s^{-1}}]$
$\partial P/\partial t$	precipitation rate	$[\mathrm{m\,s^{-1}}]$
ϕ	washout parameter	
ψ_m	stability parameter for momentum	
∇	horizontal nabla operator	

REFERENCES

Alfaro, S. C., Gaudichet, A., Gomes, L. and Maille, M., 1997, Modeling the size distribution of a soil aerosol produced by sandblasting. *Journal of Geophysical Research,* **102**, pp. 11239–11249.

Alpert, P., Kaufman, Y.J., Shay-El, Y., Tanre, D., Da Silva, A., Schubert, S. and Joseph, J.H., 1998, Quantification of dust-forced heating of the lower troposphere, *Nature*, **395**, pp. 367–370.

Andreae, M. O., 1996. Raising dust in the greenhouse, *Nature*, **380**, pp. 389–340.

Arakawa, A., 1966, Computational design for long-term numerical integration of the equations of fluid motion: Two dimensional incompressible flow. Part I, *J. Comp. Phys*. **1**, pp. 119–143.

Bagnold, R. A., 1941, *The Physics of Blown Sand and Desert Dunes,* pp. 265, Morrow, New York.

Barkan, J., Kutiel, H. and Alpert, P., 2004, Climatology of Dust Sources in North Africa and the Arabian Peninsula, Based on TOMS Data, *Indoor Built Environ 2004*, pp. 13: 407–419.

Beljaars, A.C.M., 1994, The parameterization of surface fluxes in large-scale models under free convection, *Quarterly Journal of the Royal Meteorological Society,* **121**, pp. 255–270.

Betts, A., 1986, A new convective adjustment scheme. Part I: Observational and theoretical basis, *Quarterly Journal of the Royal Meteorological Society,* **112**, pp. 677–693.

Businger, J.A., 1986, Evaluation of the accuracy with which dry deposition can be measured with current micrometeorological techniques, *Journal of Climatology and Applied Meteorology*, **25**, pp. 1100–1124.

Callot, Y., Marticorena, B. and Bergametti, G., 2000, Geomorphologic approach for modelling the surface features of arid environments in a model of dust emissions: Application to the Sahara desert, *Geodin. Acta*, **13(5)**, pp. 245–270.

Chamberlain, A.C., Garland, J.A. and Wells, A. C., 1984, Transport of gasses and particles to surfaces with widely spaced roughness elements, *Boundary-Layer Meteorology*, **24**, pp. 343–360.

Chamberlain, A.C., 1983, Roughness length of sea, sand and snow, *Boundary-Layer Meteorology*, **25**, pp. 405–409.

Chen F., Mitchell, K., Janjic, Z. and Baldwin, M., 1996, Land-surface parameterization in the NCEP Mesoscale Eta Model, *Research Activities in Atmospheric and Oceanic Modelling, WMO, Geneva*, CAS/JSC WGNE, **23**, 4.4.

Fecan, F., Marticorena, B. and Bergametti, G., 1999, Parameterization of the increase of the Aeolian erosion threshold wind friction velocity due to soil moisture for arid and semi-arid areas. *Annales Geophysicae*, **17**, pp. 194–157.

Fels, S.B. and Schwartzkopf, M.D., 1975, The simplified exchange approximation: A new method for radiative transfer calculations, *Journal of Atmospheric Science*, **32**, pp. 1475–1488.

Georgi, F., 1986, A particle dry-deposition parameterization scheme for use in tracer transport models, *Journal of Geophysical Research*, **91**, pp. 9794–9806.

Gillette, D.A. and Passi, R., 1988, Modeling dust emission caused by wind erosion, *Journal of Geophysical Research*, **93**, pp. 14233–14242.

Granat, G., 1972, On the relation between pH and the chemical composition in atmospheric precipitation, *Tellus*, **24**, pp. 550–560.

Guerzoni, S. and Chester, R. (Eds), 1996, *The Impact of Desert Dust Across the Mediterranean*, Kluwer Academic, Norwell, Mass.

Guerzoni, S., Chester, R., Dulac, F., Herut, B., Loye-Pilot, M.-D., Measures, C., Migon, C., Molinaroli, E., Moulin, C., Rossini, P., Saydam, C., Soudine, A. and Ziveri, P. 1999, The

role of atmosphere deposition in the biogeochemistry of the Mediterranean Sea, *Prog. Oceanogr.* **44**, pp. 147–190.

Husar, R.B., Prospero, L.M. and Stowe, L.L., 1997, Characterization of tropospheric aerosols over the oceans with the NOAA advanced very high resolution radiometer optical thickness operational product, *Journal of Geophysical Research*, **102**, pp. 16889–16909.

Jackson, D.W.T., 1996, Potential inertial effects in Aeolian sand transport: preliminary results, *Sedimentary Geology,* **106**, pp. 193–201.

Janjic, Z.I., 1997, Advection scheme for passive substance in the NCEP Eta Model, in: *Research Activities in Atmospheric and Oceanic Modeling*, edited by Ritchie, H., (WMO, Geneva, CAS/WGNE).

Janjic, Z.I., 1996a, The Mellor-Yamada Level 2.5 turbulence closure scheme in the NCEP Eta Model, in: *Research Activities in Atmospheric and Oceanic Modeling*, edited by Ritchie, H., (WMO, Geneva, CAS/WGNE), **4**, pp. 4.15.

Janjic, Z.I., 1996b, The Surface Layer Parameterization in the NCEP Eta Model, in: *Research Activities in Atmospheric and Oceanic Modeling*, edited by Ritchie, H. (WMO, Geneva, CAS/WGNE), **4**, pp. 4.16–4.17.

Janjic, Z.I., 1977, Pressure gradient force and advection scheme used for forecasting with steep and small scale topography, *Contrib. Atm. Phys*., **50**, pp. 186–199.

Janjic, Z.I., 1979, Forward–backward scheme modified to prevent two-grid-interval noise and its application in sigma coordinate models, *Contrib. Atm. Phys*., **52**, pp. 69–84.

Janjic, Z.I., 1984, Non-linear advection schemes and energy cascade on semi-staggered grids, *Monthly Weather Review*, **112**, pp. 1234–1245.

Janjic, Z.I., 1994, The Step-mountain Eta Coordinate Model: Further Developments of the Convection, Viscous Sublayer and Turbulence Closure Schemes, *Monthly Weather Review*, **122**, pp. 927–945.

Kallos, G., Papadopoulos, A., Katsafados, P. and Nickovic, S., 2006: Trans-Atlantic Saharan dust transport: Model simulation and results. *Journal of Geophysical Research-Atmosphere*, **111**, doi: 10.1029/2005JD006207.

Kallos, G., Astitha, M., Katsafados, P. and Spyrou, C., 2007, Long-Range Transport of Anthropogenically and Naturally Produced PM in the Mediterranean and North Atlantic: Present Status of Knowledge, *Journal of Applied Meteorology and Climatology*, (in press).

Kallos, G., Katsafados, P., Spyrou, C. and Papadopoulos, A., 2005, Desert dust deposition over the Mediterranean Sea estimated with the SKIRON/Eta, *4th EuroGOOS Conference,* 6–9 June 2005, Brest, France.

Lacis, A.A. and Hansen, J.E., 1974, A parameterization of the absorption of air-solar radiation in the earth's atmosphere, *Journal of Atmospheric Sciences*, **31**, pp. 118–133.

Levin, Z., Teller, A., Ganor, E. and Yin, Y., 2005, On the interactions of mineral dust, sea-salt particles and clouds: A measurement and modeling study from the Mediterranean Israeli Dust Experiment campaign, *Journal of Geophysical Research*, **110**, D20202, doi:10.1029/2005JD005810.

Levin, Z., Ganor, E. and Gladstein, V., 1996, The Effects of Desert Particles Coated with Sulfate on Rain Formation in the Eastern Mediterranean, *Journal of Applied Meteorology*, **35**, pp. 1511–1523.

Li, X., Maring, H., Savoie, D., Voss, K. and Prospero, M., 1996, Dominance of mineral dust in aerosol light-scattering in the North Atlantic trade winds, *Nature*, **380**, pp. 416–419.

Marticorena, B., and Bergametti, G., 1995, Modeling the atmospheric dust cycle: 1. Design of a soil-derived dust emission scheme, *Journal of Geophysical Research,* **100**, pp. 16415–16430.

Martin, J.M. and Fitzwater, S.E., 1988, Iron deficiency limits phytoplancton growth in the north–east Pacific subarctic *Nature*, **331**, pp. 341–343.

Mesinger, F., 1984, A blocking technique for representation of mountains in atmospheric models, *Rivista di Meteorologia Aeronautica*, **44**, pp. 195–202.

Mesinger, F., Janjic, Z.I., Nickovic, S., Gavrilov, D. and Deaven, D.G., 1988, The step-mountain coordinate: model description and performance for cases of Alpine lee cyclogenesis and for a case of an Appalachian redevelopment, *Monthly Weather Review*, **116**, pp. 1493–1518.

Meszaros, E., 1999, Fundamentals of atmospheric aerosol chemistry, Akdemiai Kiado.

Miller, R.L. and Tegen, I., 1998, Climate Response to soil dust aerosols, *Journal of Climate*, **11**, pp. 3247–3267.

Moulin, C., Lambert, C.E., Dayan, U., Masson, V., Ramonet, M., Bousquet, P., Legrand, M., Balkanski, Y.J., Guelle, W., Marticorena, B., Bergametti, G. and Dulac, F., 1998, Satellite climatology of African dust transport in the Mediterranean atmosphere, *Journal of Geophysical Research*, **103**, pp. 13137–13144, 10.1029/98JD00171.

Nickling, W.G. and Gillies, J.A., 1989, Emission of fine-grained particulates from desert soils, *Paleoclimatology and Paleometeorology: Modern and Past Patterns of Global Atmospheric Transport,* edited by Leinen, M. and Sarnthein, M., (Kluwer Academic Publishers), pp. 133–165.

Nickovic, S., Kallos, G., Papadopoulos, A. and Kakaliagou, O., 2001, A model for prediction of desert dust cycle in the atmosphere, *Journal of Geophysical Research*, **106**, pp. 18113–18129.

Ozsoy, E., Kubilay, N., Nickovic, S. and Moulin, C., 2001, A hemisphere dust storm affecting the Atlantic and Mediterranean in April 1994: Analyses, modeling, ground-based measurements and satellite observations, *Journal of Geophysical Research*, **106**, pp. 18439–18460.

Papadopoulos A., Katsafados, P., Kallos, G., Nickovic, S., Rodriguez, S. and Querol, X., 2003, Contribution of Desert Dust Transport to Air Quality Degradation of Urban Environments, Recent Model Developments. *26th NATO/CCMS ITM on Air Pollution Modeling and its Application*, ISBN 0-306-48464-1, pp. 279–286.

Perry, K.D., Cahill, T.A., Eldred, R.A. and Dutcher, D.D., 1997, Long-range transport of North African dust to the eastern Union States, *Journal of Geophysical Research*, **102**, pp. 11225–11238.

Prospero, J.M., Ginoux, P., Torres, O., Nicholson, S.E. and Gill, T.E., 2002, Environmental characterization of global sources of atmospheric soil dust identified with the nimbus 7 total ozone mapping spectrometer (TOMS) absorbing aerosol product, *Rev. of Geophys.*, **40**, doi:10.1029/2000RG000095.

Prospero, J.M., 1996, Saharan dust transport over the North Atlantic Ocean and Mediterranean: An overview, in *The Impact of Desert Dust Across the Mediterranean*, edited by Guerzoni, S. and Chester, R., (Kluwer Acad., Norwell Mass.), pp. 133–151.

Querol, X., Alastuey, A., Rodriguez, S., Viana, M.M., Artinano, B., Salvador, P., Mantilla, E., Santos, S.G.D., Patier, R.F., Rosa, J.D.L., Campa, A.S.D.L. and Menedez M., 2002, Interpretation de series temporales (1996–2000) de niveles de particulas en suspension en Espana, Ministerio de Medio Ambiente, Madrid.

Ramanathan, V., Crutzen, P.J., Lelieveld, J., Mitra, A.P., Althausen, D., Anderson, J., Andreae, M.O., Cantrell, W., Cass, G.R., Chung, C.E., Clarke, A.D., Coakley, J.A., Collins, W.D., Conant, W.C., Dulac, F., Heintzenberg, J., Heymsfield, A.J., Holben, B., Howell, S., Hudson, J., Jayaraman, A., Kiehl, J.T., Krishnamurti, T.N., Lubin, D., McFarquhar, G., Novakov, T., Ogren, J.A., Podgorny, I.A., Prather, K., Priestley, K., Prospero, J.M., Quinn, P.K., Rajeev, K., Rasch, P., Rupert, S., Sadourny, R., Satheesh, S.K., Shaw, G.E., Sheridan, P. and Valero, F.P.J., 2001, Indian Ocean Experiment: An integrated analysis of the climate forcing and effects of the great Indo-Asian haze. *Journal of Geophysical Research*, **106**, pp. 28371–28398.

Rodriguez, S., Querol, X., Alastuey, A., Kallos, G. and Kakaliagou, O., 2001. Saharan dust inputs to suspended particles time series (PM10 and TSP) in Southern and Eastern Spain, *Atmospheric Environment*, **35/14**, pp. 2433–2447.

Segal, M., 1990, On the impact of thermal stability on some rough flow effects over mobile surfaces, *Boundary-Layer Meteorology*, **52**, pp. 193–198.

Seinfeld, J.H. and Pandis, S.N., 1997, *Atmospheric Chemistry and Physics: From Air Pollution to Climate Change*, (New York: Wiley-Interscience), ISBN 0471178160.

Shao, Y., Raupach, M.R. and Findlater, P.A., 1993, Effect of saltation bombardment on the entrainment of dust by wind, *Journal of Geophysical Research,* **98**, pp. 12719–12726.

Slinn, W.G.N., 1982, Prediction for particle deposition to vegetative canopies, *Atmospheric Environment*, **16**, pp. 1785–1794.

Swap, R., Garstang, M., Greco, S., Talbot, R. and Kallberg, P., 1992, Sahara dust in the Amazon basin, *Tellus*, **44**, pp. 133–149.

Tegen, I. and Fung, I., 1994, Modeling of mineral dust in the atmosphere: Sources, transport and optical thickness, *Journal of Geophysical Research*, **99**, pp. 22897–22914.

Westphal, D.L., Toon, O.B. and Carlson, T.N., 1988, A case study of Mobilization and transport of Saharan dust, *Journal of Atmospheric Sciences*, **45**, pp. 2145–2175.

Westphal, D.L., Toon, O.B. and Carlson, T.N., 1987, A two-dimensional numerical investigation of the dynamics and microphysics of Saharan dust storms*, Journal of Geophysical Research*, **92**, pp. 3027–3049.

White, B.R., 1979, Soil transport by winds in Mars, *Journal of Geophysical Research*, **84**, pp. 4643–4651.

Zhao, Q. and Carr, F.H., 1997, A Prognostic Cloud Scheme for Operational NWP Models, *Monthly Weather Review*, **125**, pp. 1931–1953.

Zilitinkevich, S.S., 1995, Non-local turbulent transport: pollution dispersion aspects of coherent structure of convective flows, in *Air Pollution III—Volume I. Air Pollution Theory and Simulation,* edited by. Power, H., Moussiopoulos, N. and Brebbia, C.A., (Computational Mechanics Publications, Southampton Boston), pp. 53–60.

Zilitinkevich, S.S., Grachev, A.A. and Hunt, J.C.R., 1998, Surface frictional processes and non-local heat/mass transfer in the shear-free convective boundary layer, in *Buoyant Convection in Geophysical Flows*, edited by Plate, E.J. *et al.* (Kluwer Acad Norwell, Mass), pp. 83–113.

Zoumakis, N.M. and Kelessis, A.G., 1991, The dependence of the bulk Richardson number on stability in the surface layer, *Boundary Layer Meteorology*, **57**, 407–414.

Part two
Processes at water interfaces

CHAPTER SIX

Gas-transfer at unsheared free-surfaces

Carlo Gualtieri & Guelfo Pulci Doria
Hydraulic and Environmental Engineering Dept.
University of Napoli Federico II, Napoli, Italy

6.1 FOREWORD

Transport processes through the gas–liquid interfaces are of paramount importance in a number of areas of industrial engineering, such as chemical and mechanical engineering, and for geophysical and environmental systems. In such systems, gaseous pollutants may be directly exchanged between air and water in either direction across the air–water interface. Gas fluxes being transferred can be upward to the air or downward to the water depending on the substances involved. Thus, *gas transfer* is a two-way process involving both gas absorption, i.e. air to water, and volatilization, i.e. water to air, across an air–water interface, for a volatile or semi-volatile chemical. In the environmental fluid mechanics field, for processes at the free surfaces of terrestrial water bodies, early interest related the absorption of atmospheric oxygen in natural waters. This process is also termed as atmospheric reaeration. Since dissolved oxygen (DO) is commonly considered as the main indicator of aquatic ecosystem health, reaeration is one of the most relevant source of DO in the water bodies, whose DO level are depleted by natural causes or the discharge of organic matter (USEPA, 1985; Chapra, 1997). The volatilization of many chemicals, such as mercury, PCBs, PAHs and pesticides, has been widely recognized as an important process determining the transport, fate, and chemical loadings of these contaminants in the atmosphere and in large water bodies, such as lakes, estuaries and oceans (USEPA, 1997). Also, the assessment of volatilization rate of environmentally important compounds of low molecular weight such as benzene, chloroform, methylene chloride, and toluene from rivers and streams contaminated by spills or industrial discharges has been subject of continuing interest. Therefore the estimation of both reaeration and volatilization rate is a key issue in the application of a modeling framework of dissolved oxygen balance or of contaminant transport and fate (Chapra, 1997).

More recently, the exchange of moisture, carbon dioxide (CO_2) and other greenhouse gases between the atmosphere and the oceans or the lakes have become important because of their impact on global warming. It is estimated that approximately 30–40 per cent of man-made CO_2 is taken up by the oceans, but these estimates are significantly affected by the uncertainties in the prediction of gas-transfer rate at the air–water interface (Banerjee and MacIntyre, 2004).

Despite the significant theoretical, laboratory, field and numerical studies, research efforts have not yet achieved a complete understanding of gas-transfer process. Also, predictive models currently available are not yet able to predict its rate in all the environmental and hydrodynamic conditions. In the hydraulic and environmental engineering field several

empirical equations have been long proposed to estimate both reaeration and volatilization rates, but recent studies have demonstrated that these equations cannot have a general application (Melching and Flores, 1999; Gualtieri *et al.*, 2002; Gualtieri, 2006). Therefore, intensive researches are currently carried on to gain insight into the complex mechanisms of gas-transfer and to develop a physically sound and reliable predictive equation of gas-transfer rate.

First of all, we can define *gas-transfer* as an *interphase mass-transfer process* that occurs at the air–water interface if a non-equilibrium condition between the air phase and the water phase exists for a chemical. The equilibrium or non-equilibrium condition generally depends on chemical potential of the considered species within the phase involved, which is related to concentration, which is simpler to be measured. Thus, the transport of material between phases is controlled by the gradient in concentration across the interface, which represents the *driving force* of the gas-transport process. As a result of this gradient, a flux of the chemical moves through the air–water interface. Also, this flux should be related to the characteristics of transport processes near the air–water interface. These processes can occur at the molecular scale and are also affected by turbulence because the flow in the atmosphere and in the water body is turbulent. Thus, a first qualitative assessment of gas-transfer process would lead to state that a gas-transfer flux $J_{g\text{-}t}$ driven by concentration gradient could be generally expressed using Fick's law (Thibodeaux, 1997) as:

$$J_{g\text{-}t} = -(D_m + D_t) \cdot \frac{dC}{dz} \tag{6.1}$$

where D_m and D_t are, respectively, the molecular and *turbulent* or *eddy* diffusion coefficient and dC/dz is the concentration gradient of the species being transferred, where z is the vertical coordinate. Notably, the gas being transferred is assumed to be distributed uniformly in the bulk fluid. Also, the magnitude of the eddy diffusion coefficient D_t in the natural environment is usually many times larger than molecular diffusivity D_m.

Equation (6.1) points out that gas-transfer process depends on the physicochemical characteristics of the substance being transferred and on the interaction between turbulence in the atmosphere and/or in the water body, on one hand, and the air–water interface, on the other. The latter feature introduces a second critical point that is related to the relative importance of the gas-phase, i.e. the atmosphere, and of the water-phase, i.e. the water body, on gas-transfer process. It is likely that sometimes one phase can prevail and transport processes occurring within this phase should be better investigated to gain insight into gas-transfer process. Third, another critical point is expected to be related to where the turbulence is produced, i.e. whether close to the air–water interface or far from it, since the interplay between turbulent motions and the interface should be different.

The previous short discussion suggests to divide the subject and to organize the chapter as follows. Section 2 explains how the physicochemical characteristics of the substance being transferred affect gas-transfer process and they can control which phase governs the process. Section 3 provides a discussion on how turbulence generally interacts with the air–water interface a for a substance being controlled by the water phase. This discussion highlights that a more detailed approach requires to consider separately conditions where turbulence is produced far from the air–water interface, that is an unsheared interface, and where turbulence is produced close to the interface, that is a sheared interface. Thus, Section 4 deals with the gas-transfer at an unsheared air–water interface. First of all, dimensional analysis of gas-transfer process is presented to achieve a robust theoretical framework where suitable modelling efforts can be developed. After then, classical and more recent modeling approaches starting from Lewis-Whitman two films theory are discussed. Both approaches based on *global* and *local* properties of turbulence are presented. Moreover, results from

both laboratory and field studies together with those coming from numerical simulations are also considered to elucidate physical features of the gas-transfer process and to assess models performances. Finally, conclusive remarks are drawn also highlighting the areas where future research would be useful.

6.2 GAS-TRANSFER—INFLUENCE OF GAS CHARACTERISTICS

The previous short discussion pointed out that gas-transfer process is governed by the interplay of turbulent and molecular transport processes. Hence Equation (6.1) includes molecular diffusivity, which depends on the characteristics of both the gas being transferred and the fluid, air or water, where the transfer occurs. However, there is another important characteristics of the gas involved in the transfer that should be considered. In fact, it is well known that if a vessel of gas-free distilled water is exposed to the atmosphere, gaseous compounds, such as oxygen or carbon dioxide, cross the air–water interface and enter into solution. The process will continue until a fixed level of the gas for a given temperature will be reached. In other words, an equilibrium is established between the partial pressure of the gas in the atmosphere and the concentration in the water phase. This equilibrium can be expressed by Henry's law as:

$$p = H_e\, C_{sat} \tag{6.2}$$

where p is the partial pressure, H_e is Henry's constant and C_{sat} is the saturation concentration of the gas into the water. From equation (6.2) Henry's constant is the ratio of the partial pressure of the gaseous phase to the solubility of the gas in the water phase. Equation (6.2) points out that at a fixed partial pressure of the gas, saturation concentration of the gas and hence its solubility decreases with the increasing value of H_e.

Equation (6.2) could be also presented in dimensionless form using the ideal gas law:

$$pVol = n_m\, R\, T_a \tag{6.3}$$

where Vol is the volume of the gas, n_m is the number of moles, and T_a is absolute temperature in K. Finally, R is the universal gas constant, which is equal to 8.314. From Equation (6.3), the molar concentration of the gas could be expressed in terms of its partial pressure as:

$$C = \frac{n}{Vol} = \frac{p}{R\, T_a} \tag{6.4}$$

which can be introduced into Equation (6.2) to yield:

$$H = \frac{H_e}{R\, T_a} = \frac{C}{C_{sat}} \tag{6.5}$$

where H is the dimensionless Henry's constant.

Table 6.1 lists the values of Henry's constants He and H at 25°C for some substances in the field of environmental fluid mechanics.

The influence of temperature on He or H and, hence, on C_{sat} was already introduced but the saturation concentration of a gas is affected also by two other parameters, water salinity and partial pressure variations due to elevation. Some empirical equations were developed to predict how these factors influence saturation of dissolved oxygen (Chapra,

Table 6.1. Values of Henry's constants H and H_e at 25°C.

Chemical	Source	M – g/mole	H_e – $Pa \cdot m^3 \cdot mole^{-1}$	H
Aroclor 1016	Chapra, 1997	257.9	3.35E+01	1.35E−02
Aroclor 1242	Chapra, 1997	266.5	3.85E+02	1.55E−01
Aroclor 1248	Chapra, 1997	299.5	3.59E+02	1.45E−01
Aroclor 1254	Chapra, 1997	328.4	1.46E+02	5.91E−02
Aroclor 1260	Chapra, 1997	375.7	7.17E+02	2.89E−01
Mean PCBs	Chapra, 1997	305.6	2.18E+02	8.78E−02
Al drin	Various	364.91	1.67E+00	6.72E−04
Dieldrin	Various	380.91	1.09E+00	4.38E−04
Lindane	Various	290.83	3.33E−01	1.34E−04
Toxaphene	Chapra, 1997	430	5.72E+03	2.31E+00
Benzene	Rathbun, 1998	78.11	5.57E+02	2.24E−01
Naphthalene	Rathbun, 1998	128.2	5.60E+01	2.26E−02
Methylbenzene	Rathbun, 1998	92.14	6.38E+02	2.57E−01
Ethylbenzene	Rathbun, 1998	106.17	7.56E+02	3.05E−01
Chlorobenzene	Rathbun, 1998	112.6	3.58E+02	1.44E−01
Trichloromethane	Rathbun, 1998	257.9	3.91E+02	1.58E−01
Trichloroethylene	NIST, 2000	266.5	1.07E+03	4.34E−01
1,2-Dichloroethane	Rathbun, 1998	299.5	1.14E+02	4.60E−02
MTBE	Various	328.4	6.43E+01	2.59E−02
Mercury	Various	375.7	1.25E+03	5.03E−01

1997). These equations point out that saturation concentration of dissolved oxygen decreases as temperature and water salinity increase. On the other hand, saturation concentration increases with the increasing pressure.

The influence of Henry's constant on gas-transfer process can be pointed out considering a volume of fluid across the air–water interface. A qualitative approach shows that the interface due to the surface tension of the fluid could be considered as a semi-solid *wall*. Thus, approaching to the interface, turbulent motions become increasingly damped and molecular transport takes control over turbulent transport. Considering for now only mass transport, it can be expected that a *diffusive* or *concentration* boundary sublayer (CBL) develops on both sides of the interface, while outside these sublayers turbulence governs transport processes (Fig. 6.1). At this point, we limit the discussion to this but important details on the interplay of turbulence and these sublayers will be further provided.

Figure 6.1 relates to a flux from the atmosphere to a waterbody, such as in the reaeration process. To enter the bulk water, the gas must cross both the CBLs. Recall that the gas-transfer process is related to a non-equilibrium condition holding between the air phase and the water phase. Thus, we can assume according to Equation (6.1) that the gas flux is proportional to the concentration gradient existing between the interface and the bulk fluid through a coefficient. First, the gas must move through the CBL on the air-side and the gas flux $J_{g\text{-}t\text{-}gas}$ is:

$$J_{g\text{-}t\text{-}gas} = k_g(C_g - C_i) \tag{6.6a}$$

where $C_g - C_i$ are gas concentration in the bulk gas and at the air–water interface, respectively, and k_g is the gas-transfer velocity in the CBL on the air-side. Concentrations are

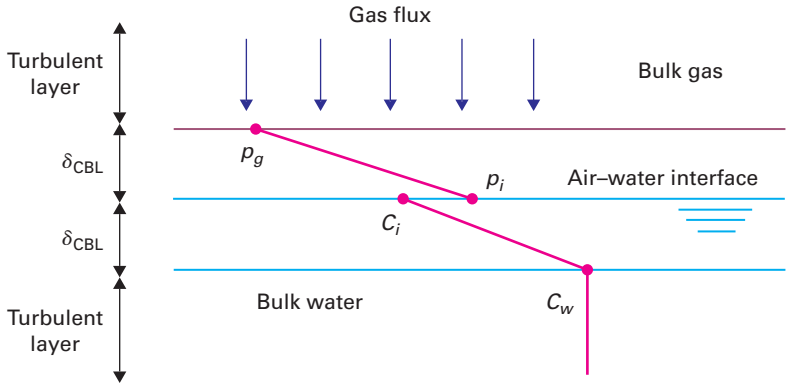

Figure 6.1. Sketch of gas-transfer across the air–water interface.

related to pressures by Equation (6.4), so Equation (6.6a) yields:

$$J_{g\text{-}t\text{-}gas} = \frac{k_g}{R\,T_a}(p_g - p_i) \tag{6.6b}$$

where $p_g - p_i$ are gas pressure in the bulk gas and at the interface, respectively.

Similarly, the gas must cross the CBL on the water-side and the gas flux moving across this CBL is:

$$J_{g\text{-}t\text{-}water} = k_w\,(C_i - C_w) \tag{6.7a}$$

where C_w is gas concentration in the bulk water and k_w is the gas-transfer velocity in the CBL on the water-side. Since at the interface equilibrium holds, Equation (6.2) allows to express the concentration at the interface C_i in Equation (6.7a) as a function of the pressure at the interface p_i to yield:

$$p_i = H_e\left(\frac{J_{g\text{-}t\text{-}water}}{k_w} + C_w\right) \tag{6.7b}$$

while Equation (6.6b) yields:

$$p_i = p_g - \frac{RT_a\,J_{g\text{-}t\text{-}gas}}{k_g} \tag{6.6c}$$

Equations (6.6c) and (6.7b) can be equated and solved for the gas flux J_{g-t} as:

$$J_{g-t} = \frac{1}{\dfrac{1}{k_w} + \dfrac{R\,T_a}{H_e\,k_g}}\left(\frac{p_g}{H_e} - C_w\right) \tag{6.8a}$$

which points out as the gas-transfer process depends on the equivalent concentration gradient existing between the gas phase and the water phase. Equation (6.8a) can be also expressed as:

$$J_{g\text{-}t} = K_L\left(\frac{p_g}{H_e} - C_w\right) \tag{6.8b}$$

where K_L, which is equal to:

$$K_L = \frac{1}{\dfrac{1}{k_w} + \dfrac{R\,T_a}{H_e\,k_g}} = k_w \frac{H_e}{H_e + R\,T_a(k_w/k_g)} \tag{6.9}$$

is called *gas-transfer coefficient*. Equation (6.9) confirms that the gas-transfer process depends also on gas characteristics, that is the value of Henry's constant H_e. Inspection of (6.9) highlights that chemicals with high H_e are rapidly purged from the water, whereas chemicals with low H_e tend to stay in solution. Also, we can note that Equation (6.9) shows that the process encounters a resistance moving across the CBLs which is analogous to that of two resistors in series in an electrical circuit. In other words, the total resistance to gas transfer R_{tot} depends on each resistance in the water and gaseous CBL as:

$$R_{tot} = R_g + R_w \tag{6.10}$$

where R_g and R_w are the resistance in the CBLs on the air-side and water-side, respectively:

$$R_g = \frac{R\,T_a}{H_e\,k_g} \quad R_w = \frac{1}{k_w} \tag{6.11}$$

Therefore, depending on the relative magnitudes of H_e, k_g, and k_w, the process may be controlled by the water, the gas, or both CBLs. Particularly, the influence of the water CBL can be quantified as:

$$\frac{R_w}{R_{tot}} = \frac{R_w}{R_g + R_w} = \frac{\dfrac{1}{k_w}}{\dfrac{R\,T_a}{H_e\,k_g} + \dfrac{1}{k_w}} = \frac{H_e}{H_e + R\,T_a(k_w/k_g)} \tag{6.12}$$

Few data are available for gas transfer coefficients k_w and k_g. In the open ocean a value of 8.3×10^{-3} m/s is commonly used for k_g (Rathbun and Tai, 1982). Field and laboratory data show that the gas-film coefficient k_g is typically in the range from 3.00×10^{-3} to 3.00×10^{-2} m/s, whereas k_w lies between is 5.00×10^{-6} to 5.00×10^{-5} m/s (Schwarzenbach *et al*., 1993). In lakes, k_w varies from 1.16×10^{-6} to 1.16×10^{-4} m/s and k_g from 1.39×10^{-3} to 1.39×10^{-1} m/s (Chapra, 1997). These values correspond to a range from 0.1 to 10 m/day for k_w and from 120 to 12 000 m/day for k_g. Thus, the ratio k_w/k_g generally is in the range from 0.001 to 0.01, with the higher values in small lakes due to lower k_g because of wind sheltering (Chapra, 1997).

Table 6.1 showed that H_e can significantly change among different substances and Equation (6.12) demonstrates that the ratio R_w/R_{tot} increases with the increasing value of the Henry's constant. Thus, the higher the Henry's constant, the more the control of gas-transfer process shifts to the CBL on the water-side.

Recently, the values of ratio R_w/R_{tot} for 20 environmental contaminants was evaluated (Gualtieri, 2006). The considered contaminants were 6 different *PCBs*; 4 *pesticides*, aldrin, dieldrin, lindane and toxaphene; 2 *aromatic hydrocarbons*, benzene and naphtalene; 2 *alkyl-benzenes*, methylbenzene and ethylbenzene; 2 *halogenated alkanes*, chloroform and 1,2-dichloroethane; and, finally, chlorobenzene, trichloroethylene (TCE), methyl

Table 6.2. Values of gas-transfer coefficients k_w, k_g and their ratio k_w/k_g.

	High	Mean	Low
$k_w - m/s$	1.157E−04	1.157E−05	1.157E−06
$k_g - m/s$	1.389E−01	1.389E−02	1.389E−03
Ratio k_w/k_g	8.33E−02	8.33E−04	8.33E−06

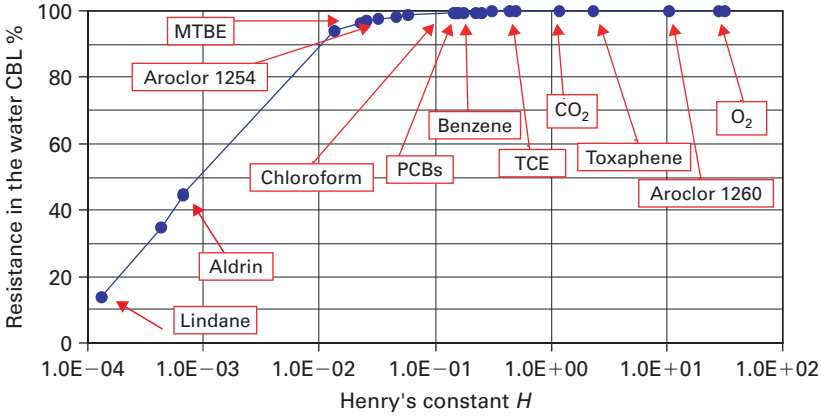

Figure 6.2. Resistance to gas-transfer in the water CBL.

tertiary-butyl ether (MTBE), and mercury. Mean values of H_e for a temperature of 25°C were applied. Also, three values were considered for the ratio k_w/k_g here. They were obtained coupling maximum, minimum, and mean value for k_w with the minimum, maximum, and mean value for k_g and they are listed in Table 6.2. The percentage resistance to the mass-transfer in the liquid CBL finally was estimated. Results for the *mean* conditions are shown in Figure 6.2, where the data for some environmentally important gases, such as ammonia, sulfur dioxide, carbon dioxide, nitrogen and oxygen, are also presented. Results showed that lindane, dieldrin, and aldrin are controlled by the gaseous CBL, whereas the remaining chemicals are controlled by the CBL on the water-side. This is the case of sparingly soluble gases such as O_2 and CO_2.

Noticeably, if a lower value of the ratio k_w/k_g is applied, the control shifts to the liquid CBL. Hence, results in Figure 6.2, where the ratio k_w/k_g is equal to $k_w/k_g = 8.33 \times 10^{-4}$, are representative of *mean* conditions. If the ratio R_w/R_{tot} is nearly equal to unity, then Equation (6.9) yields that gas-transfer velocity in the CBL on the water-side is equal to gas-transfer velocity, that is:

$$K_L \approx k_w \tag{6.13}$$

which means that the gas-transfer process is affected only by fluid mechanics processes in the water body.

The forthcoming discussion will be addressed to gas-transfer process for a substance being controlled by the CBL on the water-side, which is a very common condition for the gas-transfer in the environmental fluid mechanics field.

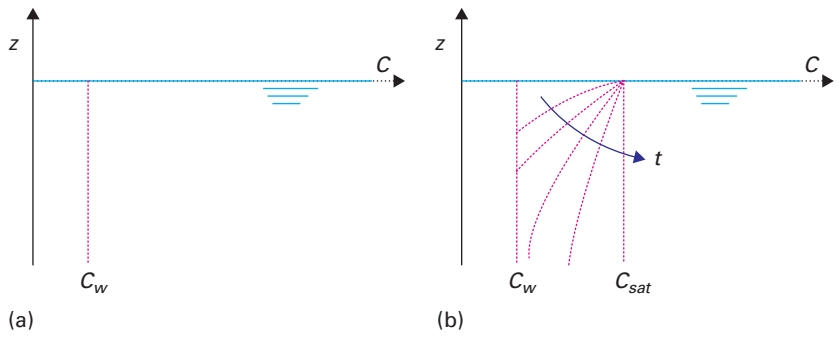

Figure 6.3. Gas-transfer in a stagnant water body.

6.3 GAS-TRANSFER—INFLUENCE OF TURBULENCE

Characterizing turbulence influence on gas-transfer across air–water interface has been proved to be difficult since this influence depends on relative phase velocities, roughness of surfaces at the interface, frictional and adhesive forces, surface tensions and several other parameters (Weber and DiGiano, 1996), and complex, anisotropic effects of the free surface on turbulence further complicate the modeling effort as well (Moog and Jirka, 1999). However, to introduce how turbulence generally interacts with the air–water interface for a substance being controlled by the water phase, we can start to consider a stagnant water body, where hydrodynamics processes have negligible effects on gas-transfer, as illustrated in Figure 6.3 (Socolofsky and Jirka, 2002).

If the water body has along its depth a uniform initial concentration C_w, which is lower than saturation concentration C_{sat} (Fig. 6.3a), we can define the following initial condition:

$$C(z,0) = C_w \tag{6.14}$$

The air–water interface is then instantaneously exposed to an infinite source of the gas. Since $C_w < C_{sat}$, the gas tends to cross the interface and to dissolve into the water. The process will continue until the water body will reach over all the depth saturation concentration. Dissolution reaction is a fast reaction but the movement of the gas inside the water is controlled by diffusion (Fig. 6.3b). One-dimensional advection-diffusion equation in the vertical direction could be applied to study this case, neglecting advection term since the fluid is stagnant:

$$\frac{\partial C}{\partial t} = D_m \frac{\partial^2 C}{\partial z^2} \tag{6.15}$$

where Equation (6.14) defines initial condition and the boundary conditions are:

$$\begin{aligned} C(-\infty,t) &= C_w \\ C(0,t) &= C_{sat} \\ C(0,0) &= C_{sat} \\ C(z,0) &= C_w \end{aligned} \tag{6.16}$$

Note that the presented case corresponds to that of diffusion in a semi-infinite medium from a constant concentration source. Thus, the solution is:

$$\frac{C\,(z,t) - C_w}{C_{sat} - C_w} = 1 - erf\left(\frac{-z}{\sqrt{4\,D_m\,t}}\right) \tag{6.17}$$

where the minus sign inside the error function is needed since z is negative downward. Equation (6.17) can be used to derive the flux across the air–water interface. According to Fick's law, the one-dimensional diffusive flux is:

$$J_{g\text{-}t\text{-}z} = -D_m \left.\frac{\partial C}{\partial z}\right|_{z=0} \tag{6.18a}$$

Substituting the solution above, the flux becomes:

$$J_{g\text{-}t\text{-}z}(t) = -(C_{sat} - C_w)\sqrt{\frac{D_m}{\pi\,t}} \tag{6.18b}$$

which demonstrates that the flux increases with the molecular diffusivity of the gas into the water and with the gradient existing to saturation. The gas-transfer flux can be also expressed as:

$$J_{g\text{-}t\text{-}z}(t) = -K_L(C_{sat} - C_w) \tag{6.19}$$

where the gas-transfer coefficient is given by:

$$K_L = \sqrt{\frac{D_m}{\pi\,t}} \tag{6.20}$$

The thickness of the CBL on the water-side can be evaluated, after some algebra, as:

$$\delta_{\mathrm{CBL}} = \sqrt{2\,D_m\,t} \tag{6.21}$$

which shows that the CBL in a stagnant water body grows deeper indefinitely in time and with the molecular diffusivity of the exchanged gas. This result holds when turbulence is absent and it should seen as an idealized, very unlikely case. However, it could be considered as a starting point of a discussion about the effects of turbulence on gas-transfer process.

As previously outlined, the interface due to the surface tension of the fluid could be considered as a semi-solid *wall*. Therefore, momentum and mass transport processes are expected to be governed by the interplay between turbulent and molecular transport within an hierarchal structure of layers: the *turbulent layer* (TL), the *velocity boundary sublayer* (VBL) and the aforementioned *diffusive* or *concentration boundary sublayer* (CBL).

Far from the interface, in the turbulent boundary layer, both momentum and mass transport is dominated by turbulent motions, that provide full vertical mixing. Thus, the main body of gaseous and liquid phases are assumed to be well-mixed with the gas profile practically uniform at the bulk concentration. In the turbulent layer, momentum and mass transport processes can be related to the turbulent eddy viscosity ν_t and to the turbulent eddy diffusivity D_t, respectively. Reynolds analogy allows to consider these parameters having the same order of magnitude, that is:

$$\nu_t \approx D_t \tag{6.22}$$

They are related by the turbulent Schmidt number Sc_t:

$$Sc_t = \frac{\nu_t}{D_t} \tag{6.23}$$

which is approximately equal to the unity, that is turbulent momentum and mass transport have the same strength, which is higher than that of transport processes occurring at the molecular scale. In other words, in the natural environment, within the turbulent layer, $\nu_t >> \nu$ and $D_t >> D_m$, where ν is the kinematic viscosity of the fluid and D_m is the molecular diffusivity of the gas into the fluid. Strictly reasoning, the vertical mass-transport is a combination of molecular and turbulent diffusion and the vertical diffusivity K_v is the sum of molecular D_m and turbulent eddy diffusivity D_t, but we can assume that turbulent diffusion is predominant. Turbulent eddy diffusivity D_t can be also related to the dissipation rate of turbulent kinetic energy ε. In fact, in steady turbulence, the rate of energy transfer from one scale to the next is the same for all scales and it is per unit mass of fluid equal to ε. On the other hand, under certain conditions, assuming a balance between total kinetic energy related to Reynolds stresses and the viscous dissipation, a logarithmic profile structure holds and the dissipation ε could be expressed as (Wüest and Lorke, 2003:

$$\varepsilon = \frac{u^{*3}}{\kappa z} \tag{6.24}$$

where u^* is the friction velocity and κ is Von Kármán constant $\kappa = 0.41$. Typical turbulent layers heights range from several meters to several tens or hundreds of meters in lakes and oceans, respectively, and several hundreds of meters to kilometres in the atmosphere (Lorke and Peeters, 2006).

Approaching to the air–water interface, at scales where viscous forces play a relevant role, turbulent eddies are increasingly damped as they approach closer than their length scale. Thus, turbulent momentum and mass transport mechanisms become weaker and someway increasingly comparable with those occurring at the molecular scale. Both ν_t and D_t decrease steeply assuming values which may be comparable with those of ν and D_m respectively. We could expect that approaching to the interface, molecular transport takes control over turbulent transport and momentum and mass boundary sublayers develop on both sides of the air–water interface (Fig. 6.4). The first sublayer is termed *velocity boundary sublayer* (VBL) and the second is called *diffusive* or *concentration boundary*

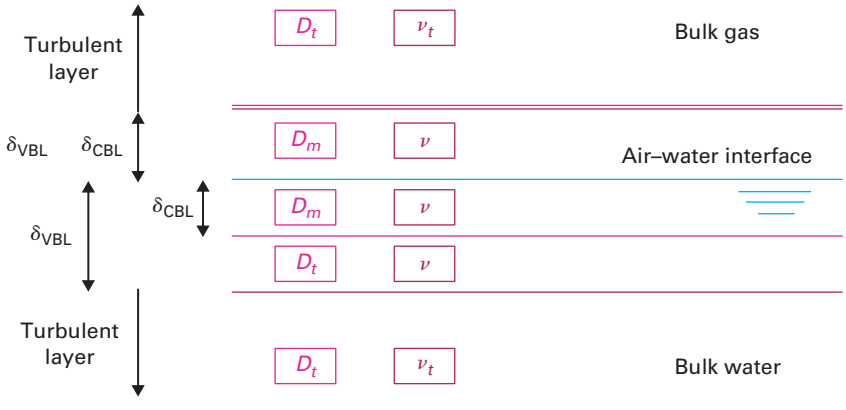

Figure 6.4. Hierarchal structure of layers at the air–water interface.

sublayer (CBL). Their thicknesses are δ_{VBL} and δ_{CBL}, respectively. Note that sometimes a difference is underlined between diffusive and concentration sublayers. The latter is related to a concentration gradient and it is also called *outer concentration sublayer*, the former is the region where that gradient is linear and it is also termed *inner concentration sublayer* (Magnaudet and Calmet, 2006). Hence, the diffusive sublayer would be a component of the CBL. However, in the following discussion we will not distinguish the diffusive sublayer from the CBL. Inside the VBL momentum transport is governed by fluid viscosity. Inside the CBL mass transport is controlled by the molecular diffusivity of the gas in the fluid. The relative thickness of these sublayers is related to the importance of diffusion of momentum and diffusion of mass by molecular transport. This can be expressed through the ratio of the kinematic viscosity to the molecular diffusivity of the gas into the fluid:

$$Sc = \frac{\nu}{D_m} \tag{6.25}$$

which is the Schmidt number. In other words, the Schmidt number describes the relative intensity of momentum and mass transport processes occurring at the molecular scale. In the air, Sc is close to 1 and the sublayers have about the same thickness. For example, Sc is for CO_2, NH_3 and H_2O equal to 0.83, 0.53 and 0.56, respectively (Jähne and Haußecker, 1998).

The situation is completely different in the liquid phase since within the range of temperature typical of environmental processes, water kinematic viscosity is in the order of $1 \times 10^{-6}\,m^2/s$, whereas molecular diffusivity of a gas into water is in the order of $1 \times 10^{-9}\,m^2/s$ resulting in a Sc in the order of 10^3. Therefore in the water phase the diffusion of mass is much more slower than the diffusion of momentum and the mass boundary sublayer is significantly thinner than the viscous boundary sublayer. Also, in contrast to the air phase, Sc depends significantly on temperature, in turn making the gas transport inside the water phase temperature-dependent. Notably, ν decreases with temperature, while D_m increases with temperature. Hence Sc decreases with the increasing temperature. For example, the Schmidt number for dissolved oxygen and cyclohexane is in the range from 950 to 440 and from 2223 to 985, respectively if temperature is ranging from 10 to 25°C (Gualtieri, 2005b).

Since we are dealing with the gas-transfer process for a substance being controlled by the CBL on the water-side, further details must be provided about the structure of velocity and concentration boundary sublayers in the water phase. As previously outlined, approaching to the air–water interface from the water side, the velocity boundary layer is first encountered. Inside the VBL the velocity gradient is constant and its thickness δ_{VBL} could be defined as the distance below the interface where D_t equates water kinematic viscosity ν. The height δ_{VBL} could be scaled with the friction velocity u^* in the turbulent layer below as (Lorke and Peeters, 2006):

$$\delta_{VBL} = \frac{11\,\nu}{u^*} \tag{6.26}$$

and δ_{VBL} is typically $\delta_{VBL} \approx 10^{-3} \div 10^{-4}$ m.

Inside the VBL, although turbulent diffusion is damped, the rate of strain of scalar tracer concentration fields creates enhanced concentration gradients, which increase transport due solely to molecular diffusion (Lorke and Peeters, 2006). Thus, mixing rates of tracers in the velocity boundary layer are still higher than those occurring at the molecular scale and measured concentration profiles are usually well mixed up to a certain distance from the interface. Approaching further to the air–water interface, turbulent eddy diffusivity D_t decreases down to the molecular diffusivity D_m. This defines the thickness δ_{CBL} of the CBL,

where the transport due to the eddies becomes negligible compared to molecular diffusion and a linear concentration gradient holds up to the interface since viscous straining is no more capable to increase mixing above that occurring at the molecular scale. Therefore, it should be expected that the thickness of the concentration boundary sublayer would be related to the level of turbulence in the TL and to the *strength* of both momentum and mass transport mechanisms occurring at the molecular scale. The former using u^* was related to δ_{VBL}. The latter is represented from Equation (6.22) by the Schmidt number Sc. Also, D_t was assumed to be dependent from the vertical distance from the interface z. Therefore, δ_{CBL} could be expressed as:

$$\delta_{\mathrm{CBL}} = \frac{\delta_{\mathrm{VBL}}}{Sc^{\alpha}} \tag{6.27}$$

where α is a coefficient which is usually assumed to be between 1/3 and 1/4 (Wüest and Lorke, 2003).

Equation (6.27) demonstrates that δ_{CBL} is solute-specific and is slightly temperature-dependent, as Sc changes with temperature. If $\alpha = 1/3$, Eq. (6.27) shows that δ_c is for the substances of environmental concern range from 1/13 to 1/6 the thickness of the velocity boundary layer δ_{VBL} (Gualtieri, 2005a). Sometimes, since $Sc \approx 10^3$ and $Sc^{1/3} \approx 10$, δ_{CBL} is approximated as $\delta_{\mathrm{CBL}} = 0.1 \cdot \delta_{\mathrm{VBL}}$ and it is typically $\delta_{\mathrm{CBL}} \approx 10^{-4} \div 10^{-5}$ m, that is tens or hundreds of microns. Interestingly, the previous discussion holds also at the sediment-water interface, where the same hierarchal structure of turbulent and viscous layers exists and the same key parameters control momentum and mass transport processes (Lorke and Peeters, 2006).

At this point a fundamental question arises: how turbulence interacts with the outlined structure of layers? It may be expected that turbulent eddies moving randomly over the water depth delivering periodically water parcels from the bulk liquid close to the air–water interface. After their arrival at the interface, the effect of the eddies is twofold (Socolofsky and Jirka, 2002);

- first, they erode the boundary sublayers structure, thereby limiting the growth of the concentration boundary sublayer thickness, δ_{CBL}. Also, since the concentrations in bulk fluid and at the interface are independent of δ_{CBL}, this effect increases the concentration gradient; hence, according to equation (6.1), the gas-transfer flux is larger than in the stagnant case;
- second, turbulent eddies moved up to the air–water interface cause motion within the concentration boundary sublayer, thereby increasing the effective diffusivity. Thus, the gas-transfer flux is again larger than in the stagnant case.

Furthermore, if, for example, reaeration is the considered gas-transfer process, water parcels carried by the turbulent eddies from the bulk liquid to the air–water interface are characterized by low concentration of dissolved oxygen. Upon their arrival to the interface, they are exposed to dissolved oxygen source and enriched by molecular diffusion until turbulent eddies bring again them down in the bulk water increasing dissolved oxygen levels there.

This brief discussion points out that the general effect of turbulence is to increase gas-transfer flux but also that molecular diffusion is still expected to be a rate-limiting process. However, this general outcome should be considered only as a starting point for a more detailed analysis which requires to consider where turbulence is produced. Three cases can occur:

- *unsheared interface*, also sometimes termed as *bottom-shear generated turbulence*. In fact, if the winds are lights, fluid motions and turbulence that can be observed near

the air–water interface are generated elsewhere. This is typical of open channel flows, such as streams and rivers, where turbulence is generated at the bottom wall and is then self-transported towards the free surface. Another case is if turbulence is produced in the shear layer between subsurface currents flowing at different velocities. In both cases, these turbulence structures then impinge at the free surface producing effects as boils that can be easily seen at the surface of rivers. Turbulence can finally produced by heat losses that give rise to natural convective motions on the liquid side (Banerjee and Macintyre, 2004). Furthermore, the turbulence structure near the free surface can have a close relationship with surface-wave fluctuations and the froude number of the flow;

- *sheared interface*, also termed as *wind-shear generated turbulence*, which refers to lakes or the sea when the wind blows above an almost still air–water interface. When a significant winds blowing over the free surface, drift currents and wind-waves due to the wind shear across the air–water interface are produced. In this case the turbulence generation occurs at the interface itself giving rise to phenomena that are qualitatively different with regard to the gas-transfer. Also, at moderate wind speed, microbreaking starts changing the structure of turbulence at the air–water interface and affecting gas-transfer rate. Moreover, in lakes, oceans and wetlands, when cooling occurs, turbulence at the air–water interface is induced by heat loss but usually largest heat loss are related to evaporation due to high winds. So at a wind sheared interface, turbulence is also due to convection motions in the water volume (Banerjee and MacIntyre, 2004). Finally, at high winds, wave breaking with air entrainment significantly affects gas-transfer;
- *combined wind-stream turbulence*. When both air flow and water flow together exist and bed shear and interfacial shear are simultaneously present in the water layer. This conditions typically hold in large rivers and estuaries.

Section 6.4 will discuss in detail *bottom-shear generated turbulence*, proposing a dimensional analysis of the gas-transfer process and presenting a review of experimental results, conceptual models and numerical simulations available in the literature to gain insight into this process and to estimate its rate.

6.4 GAS-TRANSFER AT AN UNSHEARED INTERFACE

In open channel flows, such as streams and rivers, the surface turbulence is mainly generated at the bottom boundary of the streams or in the shear layer between subsurface currents flowing at different velocities. In both cases turbulence structures could then impinge on the air–water interface producing effects as boils that can be easily seen at the surface of rivers and that can affect the gas-transfer process. Thus, since surface turbulence is generated elsewhere, this case can be termed as *bottom-shear generated turbulence* (Nakayama, 2000) and the air–water interface is accordingly called *unsheared interface* or *shear-free interface* (Banerjee and MacIntyre, 2004; Magnaudet and Calmet, 2006).

The structure of fluid motions in the bottom-shear generated turbulence and their effect on the region near the air–water interface have been experimentally investigated in a number of studies, which used different techniques such as laser-Doppler velocimetry and optical probe, digital particle image velocimetry (DPIV) and video cameras, laser-induced fluorescence (LIF) (Rashidi and Banerjee, 1988; Komori *et al.*, 1989; Kumar *et al.*, 1998; Herlina and Jirka, 2004). First, Rashidi and Banerjee (1988) using high speed videos observed periodic ejection of intensely turbulent fluid with low streamwise momentum from the wall into the relatively quiescent bulk fluid. Between the bursts and the interface, a high speed region with steep velocity gradient developed. Hence, the motion of bursts toward the interface was forced to slow down and then to turn back to the wall, giving rise to characteristics rolling

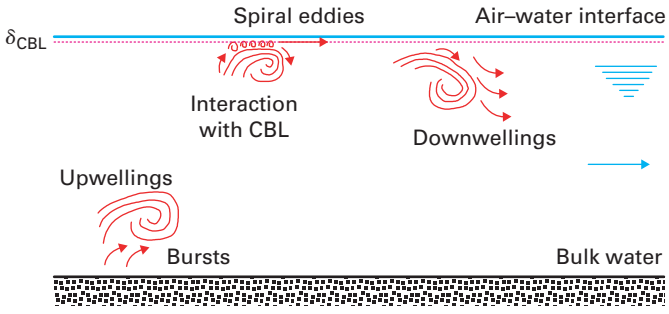

Figure 6.5. Coherent structures involved in the gas-transfer process.

structures, which rotate clockwise if the flow was viewed as going from left to right (Rashidi and Banerjee, 1988). Komori *et al*. (1989) observed that large-scale turbulent eddies ejected by bursting from the buffer region of the bottom moved upward to the interfacial region and arrived at the free-surface. Also, they successfully related these bursting motions to the gas-transfer process. In a more detailed study, three types of persistent coherent structures were observed near the air–water interface (Fig. 6.5), that is upwellings, downwellings or downdrafts, and spiral eddies (Kumar *et al.*, 1998). Upwellings, also called splats, were produced by large active structures (bursts) originated in the sheared region at the channel bottom and impinged on the free surface. They moved with it for some time, but the vanishing of the vertical velocity at the surface then forced upwellings to stretch in the horizontal and roll up resulting in the creation of downwelling structures, also termed antisplats, when two neighbouring upwellings collided, which moved back to the flow. At the edges of the upwellings were seen to be generated spiral eddies, typically attached to the free surface. These eddies often merged if rotating in the same direction, and form pairs if rotating in the opposite directions. Spiral eddies persisted for long period and they were finally destructed by merging, by new upwellings impinging on them upward, and by viscous dissipation (Kumar *et al.*, 1998).

The first step of the proposed study of gas-transfer process at an unsheared interface is to develop a proper dimensional analysis which would consider all the parameters that are likely to be involved in that process. These parameters should reflect both the fluid and gas properties, and the hydrodynamics of the flow. As presented in Subsection 6.4.1, dimensional analysis can provide a general relation for the gas-transfer rate, where this rate is related with parameters describing the hydrodynamics and environmental conditions of the mean flow.

However, Section 6.3 already pointed out that turbulence close to the air-interface where the concentration boundary layer is embedded is a key factor affecting the transport rate across the interface. Also, the aforementioned experimental studies revealed almost at a basic level of understanding the mechanism of interaction between turbulent coherent structures and air–water interface. Hence, several conceptual models were proposed in the literature to relate gas-transfer rate with hydrodynamics parameters representing the turbulence conditions at the interface. These parameters can represent both *global* and *local* properties of turbulence. These models are reviewed and discussed in Subsection 6.4.2 starting from the classical two-film model to the latest models proposed in the literature to account near-surface turbulence characteristics. More recently, numerical methods have been applied to investigate gas-transfer process to overcome difficulties still existing in the experimental techniques. Particularly, both Direct Numerical Simulation (DNS) and Large Eddy Simulation (LES) were applied allowing detailed determination of velocity and concentration fields very near the air–water interface, as described and discussed in Subsection 6.4.3. Finally,

Subsection 6.4.4 compares results from both conceptual models and numerical simulations with available experimental data.

6.4.1 Dimensional analysis

Dimensional analysis usually starts with the selection of the parameters affecting the process being modelled. Considering now a channel with wide rectangular section so that the hydraulic radius $R_h \approx 4h$ and the shape factor $\psi = h/W$ is always very low. Gas-transfer process should be affected by the following parameters (Gualtieri *et al.*, 2002; Gualtieri *et al.*, 2006):

- natural constants and fluid properties, such as the gravitational acceleration constant g, the water density ρ, the water dynamic viscosity μ, and the water surface tension T_s;
- gas exchanged properties, such as the molecular diffusion coefficient D_m;
- flow properties, such as the mean depth h, the mean streamflow velocity u, the energy line slope J_e, the channel bed slope J_b and the roughness coefficient of colebrook-white equation ε_{cw}.

Note that some literature empirical equation contain other parameters, such as Froude number Fr, friction velocity u^*, water discharge Q and kinetic turbulent energy dissipation rate per unit mass ε, which can be all expressed through the listed parameters. Water density ρ and the water dynamic viscosity μ can be combined to form water kinematic viscosity ν, that is $\nu = \mu/\rho$. Also, the water surface tension, T_s, was transformed into a kinematic parameter as $\tau_s = T_s/\rho$. Hence, the process can be considered as kinematic. Thus, it holds:

$$K_L = f_1[D_m, \tau_s, \nu, g, h, u, J_e, J_b, \varepsilon_{cw}] \tag{6.28}$$

Assuming as fundamental quantities the water mean depth h and the molecular diffusivity D_m, a proper dimensional analysis leads to:

$$Sh = f_2[Sc, We, Re, Fr, J_e, J_b, S] \tag{6.29a}$$

where Sh, Sc, We, Re, and Fr are the classical Sherwood number, Schmidt number, Weber number, Reynolds number, and Froude number, respectively. Sh, Re and We are defined as:

$$Sh = \frac{K_L \cdot h}{D_m} \tag{6.30}$$

$$Re = \frac{u \cdot 4h}{\nu} \tag{6.31}$$

$$We = \frac{u^2 \cdot h}{\tau_s} \tag{6.32}$$

Finally, the relative roughness S is:

$$S = \frac{\varepsilon_{cw}}{4h} \tag{6.33}$$

Equation (6.29a) provides the dimensionless gas-transfer rate in an open channel for liquid-controlled chemicals. This equation holds whatever is the gas involved in the gas-transfer. Also, in Equation (6.29a) the temperature influence is directly accounted for through the temperature dependent parameters, such as *Sc*, *We* and *Re*. This represents an advantage respect to the common application of a temperature corrective coefficient, such as the classical θ of Van't Hoff-Arrhenius equation (Chapra, 1997).

Equation (6.29a) can be modified. First of all, assuming that uniform flow conditions hold, the energy line slope J_e and the channel bed slope J_b are equal, that is $J_e = J_b$. Second, the Froude number in Equation (6.29a) could be discarded since it can be expressed using S, Re and J_e (Gualtieri *et al.*, 2002). In fact, classical Darcy-Weisbach equation states:

$$J_e = \frac{f}{4}\frac{u^2}{h\,2\,g} = \frac{f}{8}Fr^2 \tag{6.34}$$

where f is the friction factor, that in a turbulent flow is $f = f(Re, S)$. Hence, Equation (6.34) yields:

$$J_e = \frac{f(Re, S)}{8}Fr^2 \tag{6.35}$$

where Fr, S, Re and $J_e = J_b$ are correlated. Therefore, the Froude number can be expressed as:

$$Fr = \sqrt{\frac{8\,J_b}{f(Re, S)}} = Fr(J_b, Re, S) \tag{6.36}$$

and Equation (6.29a) yields:

$$Sh = f_3[Sc, We, Re, J_b, S] \tag{6.29b}$$

Third, as a first approximation, the influence of *We* could be discarded. Thus, Equation (6.29b) yields:

$$Sh = f_4[Sc, Re, J_b, S] \tag{6.29c}$$

where Sherwood number is affected by only *Sc*, *Re*, J_b and S. Note that f_4 function in Equation (6.29c) must be defined using experimental data.

6.4.2 Conceptual models of gas-transfer process at an unsheared interface

In Section 6.3 it was already pointed out that the concentration boundary sublayer interacts with turbulent motions close to the air–water interface. Hence, CBL characteristics are expected to usually change with the space and the time depending on turbulence parameters. However, key point is to relate gas-transfer rate with hydrodynamics parameters representing the turbulence conditions at the interface.

The earliest and simplest model for K_L is the Lewis-Whitman model. It states that a stagnant film exists very near the interface. The gas moves across the film only by molecular diffusion. From the discussion in Section 6.3 it may be derived that the concept of the stagnant film implies that the concentration boundary sublayer exhibits a kind of time and space-averaged thickness δ_{CBL}, that may be considered as having a constant value. Due to the

steady uniform laminar flow in the film region, there is a linear concentration profile within the CBL and the gas flux $J_{g\text{-}t}$ is:

$$J_{g\text{-}t} = -D_m \cdot \left.\frac{dC}{dz}\right|_{z=0} = -D_m \cdot \frac{C_{sat} - C_w}{\delta_{\mathrm{CBL}}} \tag{6.37}$$

where C_w is gas concentration at $z = \delta_{\mathrm{CBL}}$. Equations (6.19) and (6.37) yield:

$$K_L = \frac{D_m}{\delta_{\mathrm{CBL}}} \tag{6.38}$$

Therefore, in this model, K_L is linearly proportional to D_m, as compared to the square-root dependence obtained in the stagnant case. This is due to the different concentration distribution holding in the two cases. However, Lewis-Whitman model does not provide any physical insight about δ_{CBL} prediction. Furthermore, since CBL characteristics are changing reflecting system hydrodynamics, the basic assumption of this model cannot mostly properly capture the physical mechanism that controls the concentration boundary layer thickness. Nevertheless, some models were recently proposed to provide an estimation of the thickness δ_{CBL} of the CBL to introduce in Equation (6.38). First, Atkinson *et al.* (1995) has considered two approaches; the first one compares molecular and turbulent diffusivities, while the second one relates δ_{CBL} to the smallest eddies in the flow according to the Kolmogorov microlength scale η (Atkinson *et al.*, 1995). This is the smallest scale of turbulent flow, at which turbulent kinetic energy is converted to heat. From dimensional analysis Kolmogorov microlength η can be defined as:

$$\eta \propto \frac{\nu^{3/4}}{\varepsilon^{1/4}} \tag{6.39}$$

The first approach considers that the vertical profile of turbulent diffusivity can be estimated using Elder's analysis (Elder, 1959). As the shear stress τ is a linear function of depth in open channel flow $\tau = \tau_b \cdot (z/h)$, a velocity profile must be assumed to estimate the gradient velocity. Using a logarithmic profile and assuming that the thickness of diffusive layer δ_{CBL} is the depth below the air–water interface where molecular viscosity ν is comparable with eddy viscosity ν_t, after some simplifications, it can be shown that:

$$\delta_{\mathrm{CBL}} \approx c_1 \cdot \frac{\nu}{u^*} \cdot Sc^{-1/3} \tag{6.40}$$

where c_1 is a constant that can be set equal to $c_1 = 10$. From Equations (6.38) and (6.40), it yields:

$$K_L = \frac{D_m}{10 \cdot \nu} \cdot u^* \cdot Sc^{1/3} \tag{6.41}$$

The second approach proposed by Atkinson relates δ_{CBL} with the smallest eddies in the flow. Starting from Kolmogorov microlength scale η, as defined by Equation (6.39), after some algebra, δ_{CBL} can be estimated as (Atkinson *et al.*, 1995):

$$\delta_{\mathrm{CBL}} \cong c_2 \left(\frac{\nu^3 \cdot h}{u^3}\right)^{1/4} \tag{6.42}$$

where c_3 is a numerical constant, that is $c_2 = 2$. From Equations (6.38) and (6.42), K_L can be obtained as:

$$K_L = \frac{D_m}{2}\left(\frac{u^3}{\nu^3 \cdot h}\right)^{1/4} \tag{6.43}$$

Gualtieri and Gualtieri, comparing the laminar boundary sublayer at the air–water interface with the bottom classic laminar sublayer, have proposed another model to estimate the thickness δ_{CBL} of the concentration boundary layer (Gualtieri and Gualtieri, 2004). The bottom sublayer lies on a solid boundary, which has an infinite surface tension. On the other hand, the VBL is below the air–water interface which can be considered, due to its surface tension, as a semi-solid boundary. To follow this analogy a first velocity distribution in the VBL can be defined starting from the velocity distribution in the laminar sublayer near the bottom, which is known. Furthermore, in the laminar sublayer near the bottom, introducing the expression of bottom shear stress $\tau_b = \rho \cdot u^{*2}$ into the Newtonian expression for τ_b, a linear velocity distribution can be derived for the bottom sublayer. Applying the analogy between the air–water interface and the bottom, a second velocity distribution can be derived for the VBL below the water surface. Comparing these velocity distributions in the VBL at the air–water interface, its thickness δ_{VBL} can be derived. Finally, from Equations (6.27) and (6.38), gas-transfer coefficient K_L can be obtained as:

$$K_L = (D_m)^{2/3}\left(\frac{g \cdot J_b}{2 \cdot \nu \cdot Re_{g\text{-}t}}\right)^{1/3} \tag{6.44}$$

where $Re_{g\text{-}t}$ is a specific gas-transfer Reynolds number, which from the proposed approach should be $<< 25$ and should be calibrated from experimental data. Analysis of a large amount experimental field data collected in stream and rivers allowed to calibrate $Re_{g\text{-}t}$ as $Re_{g\text{-}t} = 0.750$ (Gualtieri and Gualtieri, 2004). Equation (6.44) can be modified to derive an equation comparable with *LE* and *SE* model, which is:

$$K_L^* = c_3 Sc^{-2/3}\, Re^{*-1/3} \tag{6.45}$$

where the exponent of *Re** is intermediate between those from *LE* and *SE* models. Also, it should be noted that the exponent of *Sc* in Equation (6.45), that is $-2/3$, is that expected for a solid boundary or for a film-covered water surface (Jähne and Haußecker, 1998; Banerjee and MacIntyre, 2004).

The models based upon the concept of *surface-renewal* assume that the fluid elements inside the CBL are periodically *refreshed* by turbulent eddies acknowledging the central role played by turbulence. The mechanism of *surface-renewal* is related to turbulent eddies that periodically bring liquid parcels from the bulk liquid to the air–water interface. During the short period of time spent at the interface, the liquid elements are exposed to the atmosphere and subjected to the gas-transfer process by molecular diffusion. After that, turbulent motions move again the water parcels down to the bulk liquid. The described cycle is a *surface-renewal event* and its frequency is a function of the turbulent characteristics of the flow. In this case, the concentration boundary sublayer is allowed to grow from zero depth until at some point the turbulence suddenly replaces the water parcel in the CBL, that is a renewal event occurs, and the sublayer growth starts over from the beginning. The CBL thickness is assumed larger than the depth that can be penetrated by molecular diffusion during the time of exposure to the atmosphere.

Key-point of *surface-renewal* models is the definition of the time between two renewal events. The first model based upon the outlined concepts is the *penetration model* by Higbie. The Higbie model assumes that all the liquid elements have the same time t_r of exposure at the air–water interface. The time t_r is often called *contact time* or *renewal time*. The governing transport equation and the initial condition and boundary conditions are the same as in the stagnant case, that is Equations (6.14), (6.15) and (6.16). Hence, the solution for the gas-transfer flux is Equation (6.18b), but it is valid during the time between two renewal events. The average flux of gas during one cycle is (Thibodeaux, 1997):

$$J_{g\text{-}t} = -(C_{sat} - C_w)\sqrt{\frac{4\,D_m}{\pi t_r}} \tag{6.46}$$

and the gas-transfer coefficient is:

$$K_L = \sqrt{\frac{4\,D_m}{\pi t_r}} \tag{6.47}$$

The basic assumption proposed by Higbie about the same exposure time of the water parcels was improved by Danckwerts, who introduced a random replacement time function, termed *surface-age distribution function*, which was more typical of what might be expected from a turbulent fluid. This function represents the probability that a parcel is exposed for a time t before being replaced by a new water element from the bulk fluid (Thibodeaux, 1997); this function if $t_{\text{-}avg}$ is the average renewal time is:

$$\varphi = r\,exp(-r\,t) \tag{6.48}$$

where $r = 1/t_{r\text{-}avg}$ is the fractional *renewal rate*; thus, water parcels can remain at the surface for variable times that may be any value from zero to infinity. Averaging $\pi/4$ term disappears and the average gas flux is:

$$J_{g\text{-}t} = -(C_{sat} - C_w)\sqrt{D_m\,r} \tag{6.49}$$

and the gas-transfer coefficient is:

$$K_L = \sqrt{D_m\,r} \tag{6.50}$$

which indicates that the gas-transfer rate is proportional to the frequency at which a renewal event occurs. Both Higbie and Danckwerts models have the weakness that their key parameter, that is t_r and r, respectively, is neither known nor immediately related to the turbulence near the air–water interface. As previously outlined, Komori *et al.* (1989) suggested that surface renewal eddies were originated in bursting phenomena occurring in the buffer region of the wall. Low speed fluid was ejected toward the interface from a wall burst, the fluid moved up to the surface to form a *surface-renewal patch*, and a downdraft developed after the interaction. They successfully correlated the frequency of both surface renewal and bursting and obtained that gas-transfer rate was proportional to the square-root of the surface renewal frequency confirming Equation (6.50) (Komori *et al.*, 1989). However, further studies pointed out a more complex interaction between the free surface and the ejections from sheared region near the channel bed. Hence, the measurements of *surface-renewal*

eddies are difficult to correlate with K_L, because the investigators themselves have to define what constitutes a *surface-renewal eddy* (Tamburrino and Gulliver, 2002).

Despite these difficulties, the *renewal rate r* may expected to be a characteristics of turbulent eddies and further research efforts were addressed to relate it with turbulence. We have already recalled that a characteristic feature of turbulent flow is the presence of a wide range of eddy sizes, ranging from the flow domain, i.e. integral scale eddies, to smaller sizes, i.e. Kolmogorov scale eddies (Pope, 2000). It is a common statement that the large eddies transfer their energy to the smaller ones. First, this transfer is efficient and very little kinetic energy is lost (Pope, 2000). When the eddies become small enough, in the order of Kolmogorov scale in size, viscosity takes over and the energy is damped out and converted into heat. This process is usually described as a turbulence cascade. Turbulent energy production and dissipation are almost in equilibrium in the intermediate region of a stream, whereas near the free surface dissipation is predominant (Nezu and Nakagawa, 1993; Nakayama, 2000). The dissipation rate of turbulent kinetic energy ε can be measured directly or calculated. Experimental data demonstrated that ε can be scaled as (Moog and Jirka, 1999):

$$\varepsilon \propto \frac{u^{*3}}{h} \tag{6.51}$$

As previously outlined, the scale at which turbulent kinetic energy is converted to heat is the Kolmogorov microlength scale η, which estimates the smallest turbulent eddies. This stage is characterized by an eddy Reynolds number approximately equal to 1, if the eddy Reynolds number is defined using the characteristic length and the velocity of smallest eddies. This reflects the idea that at these smallest scales of motion, the inertial strength of the eddy is approximately equal to its viscous transport strength, i.e. eddy viscosity $\nu_t = \nu$ (Pope, 2000).

At this point, two extreme estimates for r can be applied: one for the case that the concentration boundary layer is renewed by integral-scale eddies, that is called the *large-eddy* estimate, and another one for the case that the concentration boundary layer is renewed by Kolmogorov-scale eddies, that is called the *small-eddy* estimate (Moog and Jirka, 1999). In both cases, turbulence is assumed to be homogeneous and isotropic and this hypothesis is of course critical in the interfacial region.

In the first estimate, it could be assumed that the surface layer could be divided into a series of rotational cells having diameter and velocity proportional to h and u_{rms}, which is the root-mean-square value of turbulent velocity fluctuations, respectively. Also, the velocity of cells could be scaled by u^*. Thus, r parameter can be considered as $r \propto u*/h$. Inserting this into Equation (6.50) and non-dimensionalizing, the *large-eddy model (LE)* by Fortescue and Pearson (1967) states that (Moog and Jirka, 1999):

$$K_L^* = \frac{K_L}{u_{rms}} \approx \frac{K_L}{u^*} \propto Sc^{-1/2} Re^{*-1/2} \tag{6.52}$$

where K_L^* is the dimensionless gas-transfer rate and $Re*$ is the shear Reynolds number, which is defined as $Re* = u^* \cdot h/\nu$.

In the second estimate, considering the attenuation of vertical fluctuations due to the free surface, it could be assumed that smaller eddies may contribute to surface renewal (Moog & Jirka, 1999). They are dissipated by viscosity. Integrating a roll cell model over a wave number spectrum containing an inertial sub-range, it follows:

$$K_L \propto Sc^{-1/2} \cdot (\varepsilon \cdot \nu)^{1/4} \tag{6.53}$$

This is the *small-eddy model (SE)* by Banerjee *et al.* (1968), where energy dissipation may be also enhanced by many factors, such as wind shear, wave breaking, natural convection, rain (Banerjee and McIntyre, 2004). This model, considering Equation (6.43), gives (Moog & Jirka, 1999):

$$K_L^* \approx \frac{K_L}{u^*} \propto Sc^{-1/2} Re^{*-1/4} \tag{6.54}$$

Comparison between Equations (6.52) and (6.54) shows that the large-eddy and small-eddy models differ only by the Reynolds number exponent, so that these models have the general form:

$$K_L^* \approx \frac{K_L}{u^*} \propto Sc^{-1/2} Re^{*n} \tag{6.55}$$

where $n = -1/2$ holds for the *large-eddy* model and $n = -1/4$ holds for the *small-eddy* model.

A different expression for both *large-eddy* and *small-eddy* models can be derived considering that:

$$u^* = u\left(\frac{f}{8}\right)^{1/2} \tag{6.56}$$

where f is the Darcy-Weisbach friction coefficient. If gas-transfer rate K_L is non-dimensionalized using the mean streamflow velocity u, those models become:

$$\frac{K_L}{u} \propto Sc^{-1/2} Re^{-1/2} \left(\frac{f}{8}\right)^{1/4} \tag{6.57}$$

$$\frac{K_L}{u} \propto Sc^{-1/2} Re^{-1/4} \left(\frac{f}{8}\right)^{3/8} \tag{6.58}$$

for *large-eddy* and *small-eddy* models, respectively. Notably, in Equations (6.57) and (6.58) the boundary type of the flow are directly taken into account by the friction coefficient. Interestingly, Theofanous *et al.* (1976) suggested that there is a smooth transition between low *Re* values, where large-scale eddies control gas transfer, and high *Re* values, where small-scale eddies dominate. The transition occurs at $Re^* = 500$. In order to compare *large-eddy* and *small-eddy* models, Moog and Jirka (1999) carried out experimental works in open channel flow with shear Reynolds number Re^* from 350 to 4200. First, they observed that measurements in stirred tanks supported *small-eddy* model. Second, from their experimental data, they obtained $n = -0.29$, which supported *small-eddy* model and yielded (Moog and Jirka, 1999):

$$K_L^* = 0.161 Sc^{-1/2} Re^{*-1/4} \tag{6.59}$$

However, observations at low Reynolds number suggest that large coherent structures such as bursts and upwellings are responsible for interfacial transport. Hence, to solve this conflict they argued that both scales would be involved in gas-transfer process in a framework termed *chain saw* model (Moog and Jirka, 1999). Large scale motions transport turbulent

energy to the interface, creating active zones or *patches* for the gas-transfer. Within these zones, the transfer is controlled by small eddies at a rate which is related to near-surface turbulent dissipation rate. Moreover, the variation in active area decreases with the increasing Re^*, leading to the successful scaling of *small-eddy* model at higher Re^* and confirming Theofanous suggestion (Moog and Jirka, 1999).

Since both *large-eddy* and *small-eddy* models are based on a *global* property of turbulence, the next theoretical step in the literature was to relate gas-transfer process directly to a *local* property of turbulence, that is the turbulence characteristics near the air–water interface. Hanratty (1991) argued that, since the CBL is very thin, the derivative in z-direction is much larger that in the other directions. Hence, using a coordinate system embedded on the interface, the advection-diffusion equation for the gas in a turbulent flow near a free surface may be simplified as:

$$\frac{\partial C}{\partial t} + w' \frac{\partial \overline{C}}{\partial z} = D_m \frac{\partial^2 C}{\partial z^2} \tag{6.60}$$

where C and $\overline{C}$ are instantaneous concentration and its temporal mean, respectively, and w' is the fluctuating velocity normal to the interface. A series-expansion and order-of-magnitude analysis near the interface yielded the following relation for w' (McCready *et al*., 1986):

$$w' \approx \frac{\partial w'}{\partial z} z \tag{6.61}$$

where the vertical velocity gradient very near to the air–water interface is also called β parameter. This gradient is changing with the time and the distance parallel to the interface and is function of flow turbulence. Equation (6.60) highlights the importance of β parameter for the gas-transfer process. Note that the vertical velocity gradient $\partial w'/\partial z$ is unequal to zero when at the water surface 2D continuity equation in a control volume that moves vertically is not satisfied, that is:

$$\frac{\partial u'}{\partial x} + \frac{\partial v'}{\partial y} \neq 0 \tag{6.62}$$

where u' and v' are the fluctuating velocity in the streamwise direction x and in the spanwise direction y, respectively, which are both tangential to the interface. Indeed, on a free water surface tangential velocity fluctuations are possible. Hence, from 3D continuity equation, the vertical velocity gradient may be derived as:

$$\beta = \frac{\partial w'}{\partial z} = -\left(\frac{\partial u'}{\partial x} + \frac{\partial v'}{\partial y} \right) \tag{6.63}$$

where the term in brackets is termed *surface divergence.* The physical meaning of Equation (6.62) or (6.63) is that there are convergence or divergence zone at the water surface, that is surface fluid elements are dilated or contracted due to turbulent motions that bring bulk fluids to the interface (Jähne and Haußecker, 1998; Banerjee and McIntyre, 2004). Thus, if free-surface turbulence can be measured or estimated, Equation (6.63) provides the value of β parameter which is related to gas-transfer rate.

The surface divergence cannot be predicted without a theory. Hence the *blocking theory* by Hunt and Graham (1978) was used by Banerjee (1990) to relate surface divergence to the far-field turbulence characteristics when they are homogeneous and isotropic. Using

this approach, gas-transfer coefficient for an unsheared interface and high *Sc* was derived as (Banerjee, 1990):

$$K_L = c_4\, u\, Sc^{-1/2} Re^{-1/2} [0.3(2.83\, Re^{3/4} - 2.14\, Re^{2/3})]^{1/4} \tag{6.64}$$

which is also termed as *surface divergence (SD)* model. The quantity within the brackets is the square of the nondimensional surface divergence. This model applies also to a rigid slip surface because Hunt and Graham theory holds for this case. However, since the air–water interface is mobile and can deform following the motions on the liquid side, the surface divergence for a deformable interface may be expected to be less and the constant c_4 using experimental data was equated to 0.20 (Banerjee and MacIntyre, 2004). Equation (6.64) is asymptotic to $Re^{-1/2}$ at small *Re* and almost to $Re^{-1/4}$ at large *Re*, which is in line with *LE* and *SE* models and confirms Theofanous suggestion. Also, in Equation (6.64) the friction factor is not present.

Following surface divergence approach, other researchers proposed predictive equations different from Equation (6.64). Tamburrino and Gulliver (2002) measured free surface turbulence in a fully developed, open channel flow and estimated β parameter. They argued that high values of β were not a primary result of large upwellings moving to the air–water interface. The spatial scales of β were more closely related to the high velocity gradients of surface vorticity, which can originated by large upwelling, but were not previously identified as source of surface renewal (Tamburrino and Gulliver, 2002). Using previous experimental data, they finally proposed that (Tamburrino and Gulliver, 2002):

$$K_L* \approx \frac{K_L}{u*} \propto 0.24\, Sc^{-1/2} S_{\beta\max}{*}^{-1/2} \tag{6.65}$$

where $S_{\beta\max}*$ is dimensionless maximum value of the β spectrum.

Later, Sugihara and Tsumori (2005) carried out experiments in oscillating-grid turbulent flows to investigate the relation between gas-transfer rate and turbulence characteristics at the air–water interface. They obtained the following relation (Suhihara and Tsumori, 2005):

$$K_L = 0.30(D_m \beta_{rms})^{1/2} \tag{6.66}$$

where β_{rms} is the root mean square of the vertical velocity gradient at the interface. Equation (6.66) may be rewritten as (Sugihara and Tsumori, 2005):

$$\frac{K_L}{k^{1/2}} = 0.18\, Sc^{-1/2}\, Re_{k\varepsilon}^{-1/4} \tag{6.67}$$

where is k is turbulent kinetic energy and $Re_{k\varepsilon}$ is a turbulent Reynolds number defined with k and ε parameters, that is $Re_{k\varepsilon} = k^2/\varepsilon\,\nu$. Note that the exponent $-1/4$ of Reynolds number would support the *small-eddy* model, Equation (6.55).

Recently, Xu *et al*. used an innovative particle image velocimetry-based measurement method to investigate interfacial turbulence and to assess β parameter (Xu *et al*., 2006). Several distinctly different flow conditions, including turbulence induced by wind shear from above, turbulence generated from the bottom and a combination of simultaneously contributing conditions from above and beneath the interface, were investigated. They suggested a general predictive equation to correlate the gas-transfer rate with the surface divergence (Xu *et al.*, 2006):

$$K_L = 0.20\, Sc^{-1/2}\, (\beta_{rms}\nu)^{1/2} \tag{6.68}$$

6.4.3 Numerical simulation of gas-transfer process at an unsheared interface

Despite the rapid evolution of investigation techniques, especially in the last two decades, experimental methods cannot yet provide all the data required to a complete knowledge of gas-transfer process. In fact, to understand gas-transfer process, it is needed to perform simultaneous analyses of concentration and velocity fluctuations in the interfacial region in terms of both statistics and turbulent structures. If laser-induced fluorescence (LIF) technique allows to reveal the concentration distribution within the CBL (Münsterer and Jähne, 1998; Herlina and Jirka, 2004) and microprobes are capable to follow concentration fluctuations (Chu and Jirka, 1992), these techniques still have difficulties in resolving the uppermost layer of the flow. On the other hand, particle image velocimetry provides an adequate picture of turbulence characteristics near the air–water interface (Kumar *et al*., 1998; Xu *et al*., 2006). Thus, the application of high-resolution numerical simulations has been increasingly proposed to provide a detailed and precise determination of velocity and concentration fields very near to the air–water interface.

The first numerical method applied was the Direct Numerical Simulation (DNS) of time-dependent three-dimensional Navier-Stokes equations, which have often been used in the field of physics and engineering. Several studies on gas-transfer process based on DNS are available in literature (Komori *et al.*, 1993; Nagaosa, 1999; Handler *et al.*, 1999; Shen *et al.*, 2001). These studies sometimes confirmed findings of previous experimental or theoretical works but often provided detailed, novel insights on three-dimensional structures responsible for surface renewal and its net contribution to the dynamics of free-surface turbulence. Numerical results pointed out that vertical motions were restrained in the interfacial region by the damping effect, and the turbulent kinetic energy associated with them was redistributed mainly to the spanwise motions through the pressure fluctuation (Komori *et al.*, 1993). Also, they confirmed that large-eddies generated by bursts in the wall region were advected up to the free-surface producing *surface-renewal events* (Komori *et al.*, 1993; Nagaosa, 1999). To be more in details, two types of vortex tubes were observed below the free surface (Nagaosa, 1999). The first type were elongated, near-horizontal, quasi-streamwise vortices, parallel to the main stream and the free surface. The interactions between these vortices and the air–water interfaces produced splats and antisplats at the free surface. The balance of intercomponent energy transfer between the spanwise and surface–normal direction via the pressure-strain effect was determined by the splats and antisplats, which furthermore are responsible for *surface renewal events* at the free surface. The second type were the surface-attached vortices, which were perpendicular to the interface and were established by connections of quasi-streamwise vortices to the free surface. The surface-attached vortices did not produce splats and antisplats at the interface. Hence, the direct contribution of the surface-attached vortices to the dynamics of the free surface turbulence, for example, the intercomponent energy transfer or turbulent gas-transfer across the free surface, is believed to be very small (Nagaosa, 1999). Overall, DNS results confirmed the close link between bursting phenomena from the bottom region, on one hand, and interfacial turbulence and gas-transfer process, on the other. Also, studies based on DNS provided detailed statistics of the dynamics and concentration fields and of the structure interfacial turbulence which are still beyond the capabilities of laboratory experiments.

However, the main limitation of these DNS studies arises from their low Reynolds number. In fact, the aforementioned studies were carried out for a shear Reynolds number Re^* and Schmidt or Prandtl number Sc or Pr ranging from 150 to 180 and 1 to 5, respectively (Komori *et al.*, 1993; Nagaosa, 1999; Handler *et al.*, 1999; Shen *et al.*, 2001). Hence, Schmidt number were very far from the typical values of substances being involved in the gas-transfer process at the free-surface of streams and rivers. Also, in that range of Re^* the free surface lies within the logarithmic layer of the mean velocity profile. Therefore, the turbulence *seen* by the free surface is strongly anisotropic and interacts directly with the dynamics of the bed region

(Magnaudet and Calmet, 2006). This makes the near-surface velocity and concentration fields observed in these DNS studies quite specific for low Reynolds number wall-bounded shear flows and do not allows to extend some of their conclusions to the environmental flows. Therefore, it should be very useful to perform numerical simulation with higher Reynolds number to investigate instantaneous and statistical structure of velocity and concentration fields in free-surface flows where turbulence is closer to isotropy and almost independent from the way it is generated in the bed region (Magnaudet and Calmet, 2006). However, it is well known that in the DNS the number of grid points required to capture the smallest scales grows with the Reynolds number and the Schmidt number like $Sc^3Re^{9/4}$ (Pope, 2000). To overcome this limitation, Large Eddy Simulation (LES) has been recently applied to study the structure of interfacial velocity and concentration fields and the mechanism of gas-transfer process assuming that the small-scales do not prevail in this process (Calmet and Magnaudet, 1998; Magnaudet and Calmet, 2006).

Calmet and Magnaudet (1998) first applied LES to investigate gas-transfer across a flat, shear-free interface for a shear Reynolds number Re^* of 1280 and two values of Schmidt number, that is $Sc = 1$ and $Sc = 200$. They demonstrated that the concentration boundary sublayer is the related to the viscous boundary sublayer as:

$$\delta_{\mathrm{CBL}} = \frac{\delta_{\mathrm{VBL}}^{1/2}}{Sc^{1/2}} \tag{6.69}$$

which confirms results later obtained by Lorke *et al.* for the sediment-water interface (Lorke *et al.*, 2003). Moreover, the analysis of vertical velocity and concentration fluctuation w' and C' revealed that the dynamics of the concentration field was closely correlated with large-scale structures present near the air–water interface confirming that the driving mechanism of gas-transfer is the *surface-renewal* by the structures coming from the bottom wall (Calmet and Magnaudet, 1998). In fact, large-structures that reach the interface ($w' > 0$), that is upwellings, or move downward from it ($w' < 0$), that is downwellings, carried low ($C' < 0$) and high ($C' > 0$) concentration, respectively. Also, the analysis of horizontal motions confirmed the role of surface divergence β, that is $\beta > 0$ corresponded to upwellings motions and compression of the interface and $\beta < 0$ corresponded to downwellings motions and dilatation of the interface (Calmet and Magnaudet, 1998). Finally, LES results were used to estimate gas-transfer rate. Comparison with both *large-eddy* and *small-eddy* models, which assume homogeneous and isotropic turbulence, could not allow to prefer one model on the other one (Calmet and Magnaudet, 1998).

More recently, Large Eddy Simulation was again applied by Magnaudet and Calmet (2006) investigate gas-transfer across a flat unsheared interface of a turbulent channel flow for a shear Reynolds number Re^* of 1280 over a wide range of Schmidt number, that is from 1 to 200. LES results provided a detailed picture of the structure of the uppermost layers below the air–water interface. In fact, they identified an inner concentration sublayer, where mean concentration profile was linear, and an outer concentration sublayer, where root-mean-square concentration fluctuation grew up from zero at the surface to a maximum at the outer edge (Magnaudet and Calmet, 2006). This difference is analogous to that previously underlined between diffusive and concentration sublayers. Also, the thickness of the inner and the outer CBL was proportional to $Sc^{-1/2}\,Re^{-3/4}$ and $Sc^{-1/2}\,Re^{-1/4}$, respectively. Hence, the former corresponds to the Batchelor microscale. Notably, Lorke *et al.*, (2003) demonstrated that the scaling of the diffusive sublayer height with the Batchelor microscale provided an adequate description of the sediment-water exchange of oxygen observed in the field (Lorke *et al.*, 2003). When plotted against the dimensionless distance to $Sc^{1/2}zu/\nu$, the near-surface profiles of the normalized concentration variance and of all terms contributing to its budget were shown to be independent of the Schmidt number (Magnaudet and Calmet, 2006). Moreover, LES results pointed out that the region where w' grows linearly

with the distance from the interface, that is the Kolmogorov sublayer, evolved with $Re^{-3/4}$, whereas the viscous boundary sublayer thickness scaled with $Re^{-1/2}$. The simultaneous analysis of near-surface velocity and concentration fluctuations confirmed the central role of upwellings and downwellings and the typical horizontal size of these structures is found to be about $2L_I$, corresponding to the turbulence macroscale. Also, the thickness of the diffusive boundary sublayer was seen to undulate slightly, owing to the alternate compression and dilation induced by the upwellings and downwellings (Magnaudet and Calmet, 2006). The high-concentration structures driven by the downwellings mostly took the form of *needles* penetrating the bulk flow and represented the main way by which a gas could be transferred from the interface down to the bulk fluid. Obviously, due to LES characteristics, this picture could describe only horizontal large-size structures, whereas other methods could capture concentration smaller size structures. Finally, by a frequency analysis of the concentration equation, Magnaudet and Calmet demonstrated that the $Re^{-3/4}$ scaling of the inner CBL resulted directly in the scaling of K_L with the variance of the surface divergence β elevated to $1/4$:

$$K_L \approx D_m^{1/2} \left(\bar{\beta}^2\right)^{1/4} \tag{6.70}$$

which in turns, since $\bar{\beta}^2 \approx \varepsilon/\nu$, implies that (Magnaudet and Calmet, 2006):

$$\frac{K_L}{u} \approx Sc^{-1/2}\, Re^{-1/4} \tag{6.71}$$

which is identical to the *small-eddy* model. However, Equation (6.71) derived only by the $Re^{-3/4}$ scaling of the inner CBL and did not mean that gas-transfer process is controlled by the small scale eddies, but, on the contrary, the role of large-scale structures such as upwellings and downwellings, remained, according to Magnaudet and Calmet (2006), dominant, as also highlighted by experimental observations (Rashidi and Banerjee, 1988; Komori *et al.*, 1989; Kumar *et al.*, 1998). Interestingly, Equation (6.71) supports the recent experimental results by Sugihara and Tsumoto (2005), that is Equation (6.67).

6.5 CONCLUSIVE REMARKS

Gas-transfer across the turbulent air–water interface of a surface water body is a relevant process in the environmental fluid mechanics area. The movement through this interface of oxygen, carbon dioxide, nitrogen and toxic chemicals can greatly affect water quality levels.

In this chapter the gas-transfer of sparingly soluble gas, such as oxygen, carbon dioxide and many environmental contaminants, across the free surface of rivers and streams was discussed in details in terms of experimental measurements and observations, predictive models and numerical simulations. The transfer of these substances across the air–water interface is controlled by the processes occurring in a thin region below the interface. Also, in open channel flows turbulence is mostly generated at the channel bottom wall and is then self-transported towards the free surface. Hence, this condition leads to define the air–water interface as *unsheared* or *shear-free*. Both experimental and numerical studies as well as theoretical analysis have pointed out the role played by turbulence characteristics into the gas-transfer process. Turbulent structures produced in the bed region move upward to the free surface and interact with it producing a renewal of the near-surface layers of flow, which controls the gas-transfer process. Although the classic analysis leading to the *surface renewal* theory by Higbie and Danckwerts can be considered as an adequate general *picture* of the process, considerable efforts are currently produced to understand how turbulent coherent structures affect *surface-renewal*. Hence, conceptual models proposed to describe this process and to predict its rate K_L have tried to relate it to both global and local properties

of turbulence. The models based on *global* properties, such as *large-eddy* and *small-eddy* models, relate K_L to the Schmidt number and the turbulent Reynolds number of the flow, which is defined with the aid of the integral length scale and some velocity scale. They basically differ on the range of scales which is assumed to control the gas-transfer process, that is large scale or small scale. However, to solve this conflict, it was proposed that both scales would be involved in the process and their relative importance would depend on the value of turbulent Reynolds number. More recently, models based on *local* properties of turbulence, that is interfacial turbulence characteristics, were proposed. Basic concept of these models is the *surface divergence*, that is β parameter, which is the vertical velocity gradient. This parameter is related to the horizontal velocity fluctuations. Recent numerical simulations were able to resolve both velocity and concentration fields near the air–water interface. Numerical results have pointed out that positive and negative values of β correspond to large-structures reaching the interface or moving downward from it, carrying low and high concentration.

Despite these important advances in gas-transfer understanding and modelling, many efforts are still needed to achieve a complete knowledge of this process. First, even if recent developments in experimental techniques are encouraging, they still require improvements to made measurements very close to the air–water interface, in the uppermost layers of the flow, which control the transfer of the gas across the free surface. Also, it is very important that detailed measurements of concentration field would be linked with simultaneous measurements of near-surface velocity field. Second, even if numerical methods have provided detailed and precise determination of velocity and concentration fields very near to the air–water interface pointing out relevant features of the interaction between turbulence and gas-transfer process, these methods should be extended to higher both Schmidt and Reynolds numbers to encompass typical conditions existing in streams and rivers. Also, the influence of the turbulent anisotropy on the relationship between gas-transfer rate and Reynolds number should be further investigated. Finally, future modelling efforts should be addressed to take into account the role of all the turbulent scales in the gas-transfer process.

APPENDIX—LIST OF SYMBOLS

List of Symbols

Symbol	Definition	Dimensions or Units
C	concentration	$[M \cdot L^{-3}]$
$\overline{C}$	temporal mean concentration	$[M \cdot L^{-3}]$
C_g	gas concentration in the bulk gas	$[M \cdot L^{-3}]$
C_i	gas concentration at the air–water interface	$[M \cdot L^{-3}]$
C_{sat}	gas concentration at saturation	$[M \cdot L^{-3}]$
C_w	gas concentration in the bulk water	$[M \cdot L^{-3}]$
D_m	molecular diffusion coefficient	$[L^2\ T^{-1}]$
D_t	turbulent diffusion coefficient	$[L^2\ T^{-1}]$
Fr	Froude number	
H_e	dimensional Henry constant	$[M \cdot L^2 \cdot T^{-2} \cdot mole^{-1}]$
H	dimensionless Henry constant	
J_b	channel bed slope	
J_e	energy line slope	
$J_{g\text{-}t}$	gas-transfer flux	$[M\ L^{-2}\ T^{-1}]$

(*Continued*)

List of Symbols

Symbol	Definition	Dimensions or Units
$J_{g\text{-}t\text{-}gas}$	gas-transfer flux across the CBL on the air-side	$[M\,L^{-2}\,T^{-1}]$
$J_{g\text{-}t\text{-}z}$	gas-transfer flux in the vertical direction	$[M\,L^{-2}\,T^{-1}]$
$J_{g\text{-}t\text{-}water}$	gas-transfer flux across the CBL on the water-side	$[M\,L^{-2}\,T^{-1}]$
K_L	gas-transfer coefficient	$[L \cdot T^{-1}]$
K_L^*	dimensionless gas-transfer coefficient	
L_I	turbulent integral scale	[L]
Q	water discharge	$[L^3 \cdot T^{-1}]$
R	universal gas constant	$[M \cdot L^2 \cdot T^{-2} \cdot K^{-1} \cdot mole^{-1}]$
R_g	gas-transfer resistance in the CBL on the air-side	$[T \cdot L^{-1}]$
R_{tot}	total resistance to the gas-transfer	$[T \cdot L^{-1}]$
R_w	gas-transfer resistance in the CBL on the water-side	$[T \cdot L^{-1}]$
R_h	channel hydraulic radius	[L]
Re	Reynolds number	
Re^*	shear Reynolds number	
$Re_{g\text{-}t}$	gas-transfer Reynolds number	
$Re_{k\varepsilon}$	turbulent k-ε Reynolds number	
S	relative roughness	
Sc	Schmidt number	
Sc_t	turbulent Schmidt number	
Sh	Sherwood number	
$S^*_{\beta\max}$	dimensionless maximum value of the β spectrum	
T_a	absolute temperature	[K]
T_s	water surface tension	$[M\,T^{-2}]$
Vol	gas volume	$[L^3]$
We	Weber number	
c_1, c_2, c_3, c_4	numerical constants	
f	Darcy-Weisbach friction factor	
g	gravitational acceleration constant	$[L\,T^{-2}]$
h	channel water mean depth	[L]
k	turbulent kinetic energy per unit mass	$[L^2\,T^{-2}]$
k_g	gas-transfer velocity in the CBL on the air-side	$[L \cdot T^{-1}]$
k_w	gas-transfer velocity in the CBL on the water-side	$[L \cdot T^{-1}]$
n_m	number of moles	
p	gas partial pressure	$[M \cdot L^{-1} \cdot T^{-2}]$
p_g	gas pressure in the bulk gas	$[M \cdot L^{-1} \cdot T^{-2}]$
p_i	gas pressure at the air–water interface	$[M \cdot L^{-1} \cdot T^{-2}]$
r	renewal rate	$[T^{-1}]$
t	time	[T]
t_r	renewal time	[T]

(*Continued*)

List of Symbols

Symbol	Definition	Dimensions or Units
$t_{r\text{-}avg}$	average renewal time	[T]
u	mean streamflow velocity	$[L \cdot T^{-1}]$
u_{rms}	root-mean-square of turbulent streamflow velocity	$[L \cdot T^{-1}]$
u*	shear velocity	$[L \cdot T^{-1}]$
u'	fluctuating velocity in the streamwise direction x	$[L \cdot T^{-1}]$
v'	fluctuating velocity in the spanwise direction y	$[L \cdot T^{-1}]$
w'	fluctuating velocity normal to the interface	$[L \cdot T^{-1}]$
z	vertical coordinate	[L]
β_{rms}	root mean square of β	$[T^{-1}]$
$\bar{\beta}^2$	variance of surface divergence	$[T^{-2}]$
δ_{CBL}	thickness of the concentration boundary layer	[L]
δ_{VBL}	thickness of the velocity boundary layer	[L]
ε	dissipation rate of turbulent kinetic energy per unit mass	$[L^2\ T^{-3}]$
ε_{cw}	Colebrook-White roughness coefficient	[L]
η	Kolmogorov microlength scale	[L]
θ	temperature correction factor for K_L	
κ	Von Karman constant	
μ	water dynamic viscosity	$[M\ L^{-1}\ T^{-1}]$
ν	water kinematic viscosity	$[L^2\ T^{-1}]$
ν_t	water turbulent kinematic viscosity	$[L^2\ T^{-1}]$
ρ	Water density	$[M\ L^{-3}]$
τ	Shear stress	$[M\ L^{-1}\ T^{-2}]$
τ_b	bed shear stress	$[M\ L^{-1}\ T^{-2}]$
$\tau_s = T_s/\rho$	ratio between water surface tension and water density	$[L^3\ T^{-2}]$
φ	surface-age distribution function	
ψ	Shape factor of stream transverse section	

REFERENCES

Atkinson, J. F., Blair, S., Taylor, S., and Ghosh, U., 1995, Surface aeration, *J. Environmental Engineering Division*, *ASCE*, **121**, 1, January–February 1995, pp. 113–118

Banerjee, S., 1990, Turbulence structure and transport mechanisms at interface, *Proceedings of IX Heat Transfer Conference*, Keynote Lectures, **1**, pp. 395–418

Banerjee, S., Rhodes, E., and Scott, D. S., 1968, Mass transfer through falling wavy liquid films in turbulent flow, *Ind. Eng. ChE. Fundamentals*, **7**, pp. 22–28

Banerjee, S., and MacIntyre, S., 2004, The air–water interface: turbulence and scalar exchange, in *Advances in Coastal and Ocean Engineering* (P.L.F. Liu ed.), 9, World Scientific, Hackensack, N. J., USA, pp. 181–237

Calmet, I., and Magnaudet, J., 1998, High-Schmidt number mass transfer through turbulent gas–liquid interfaces, *Int. J. Heat and Fluid Flow*. **19**, pp. 522–532

Chapra, S. C., 1997, *Surface water quality modeling*, McGraw-Hill, New-York, USA

Chu, C. R. and Jirka, G. H., 1992, Turbulent gas flux measurements below the air–water interface of a grid-stirred tank, *Int. J. Heat and Mass Transfer*. **35**, pp. 1957–1968

Elder, J. W., 1959, The dispersion of marked fluid in turbulent shear flow, J. Fluid Mech., **5**, pp. 544–560

Fortescue, G. E. and Pearson, J. R. A., 1967, On gas absorption into a turbulent liquid, *Chem. Engr. Science*, **22**, pp. 1163–1176

Gualtieri, C., Gualtieri P., and Pulci Doria, G., 2002, Dimensional analysis of reaeration rate in streams. *Journal of Environmental Engineering*, *ASCE*, **128**, n. 1, January 2002, pp. 12–18

Gualtieri, C., and Gualtieri P., 2004, Turbulence-based models for gas transfer analysis with channel shape factor. *Environmental Fluid Mechanics*, **4**, n.3, September 2004, pp. 249–271

Gualtieri C., Pulci Doria G., and D'Avino, A., 2006, Gas-transfer coefficient in a smooth channel. An equation based on dimensional analysis. *Proceedings of XXX Hydraulics and Waterworks Conference*, Rome, Italy, September 10/15, 2006

Gualtieri C., 2005a, Discussion on Higashino, M., Stefan, H.G., and Gantzer, C.J.: Periodic diffusional mass transfer near sediment/water interface: Theory. J. Env. Eng., ASCE, vol. 129, n. 5, May 2003, pp. 447–455. *Journal of Environmental Engineering, ASCE*, **131**, n. 1, January 2005, pp. 171–172

Gualtieri C., 2005b, Discussion on Chu, C.R., and Jirka, G.H.: Wind and stream induced reaeration. J. Env. Eng., ASCE, vol. 129, n. 12, December 2003, *Journal of Environmental Engineering, ASCE*, **131**, 8, August 2005, pp. 1236–1238

Gualtieri C., 2006, Verification of wind-driven volatilization models. *Environmental Fluid Mechanics*, **6**, n. 1, February 2006, pp. 1–24

Handler, R. A., Saylor, J. R., Leighton, R. I., and Rovelstad, A. L., 1999, Transport of a passive scalar at a shear-free boundary in fully developed turbulent open channel flow, *Physics of Fluids*, **11**, 9, September 1999, pp. 2607–2625

Hanratty, T. J., 1991, Effect of gas flow on physical absorption, In *Gas-transfer at Water Surfaces*, edited by Wilhelm, S.C., and Gulliver, J.S., New York, ASCE, pp. 10–33

Herlina, and Jirka, G. H., 2004, Application of LIF to investigate gas transfer near the air–water interface in a grid-stirred tank, *Experiments in Fluids*, **37**, pp. 341–349

Hunt, J. C. R., and Graham, J. M. R., 1978, Free stream turbulence near plane boundaries, *J.Fluid Mechanics*. **84**, Part 2, pp. 209–235

Jähne, B., and Haußecker, H., 1998, Air–water gas exchange, *Annual Review of Fluid Mechanics*, **30**, pp. 443–468

Komori, S., Murakami, Y., and Ueda, H., 1989, The relationship between surface-renewal and bursting motions in an open channel flow, *J. Fluid Mechanics*. **203**, pp. 103–123

Komori, S., Nagaosa, R., Murakami, Y., Chiba, S., Ishii, K., and Kuwahara. K., 1993, Direct numerical simulation of three-dimensional open-channel flow with zero-shear gas-liquid interface, *Physics of Fluids*, **5**, 1, January 1993, pp. 115–125

Kumar, S., Gupta, R., and Banerjee, S., 1998, An experimental investigation of the characteristic of free-surface turbulence in channel flow, *Physics of Fluids*, **10**, 2, February 1998, pp. 437–456

Lorke, A., Müller, B., Maerki, M., and Wüest, A., 2003, Breathing sediments: The control of diffusive transport across the sediment-water interface by periodic boundary-layer turbulence. *Limnology and Oceanography*, **48**, n. 6, pp. 2077–2085

Lorke, A., and Peeters, F., (2006), Toward a unified scaling relation for interfacial fluxes, *Journal of Physical Oceanography*, **36**, May 2006, pp. 955–961

Magnaudet, J., and Calmet, I., 2006, Turbulent mass transfer through a flat shear-free surface, *J. Fluid Mechanics* **553**, pp. 155–185

McCready, M. A., Vassiliadou, E., and Hanratty, T. J., 1986, Computer simulation of turbulent mass transfer at a mobile interface, *AIChE Journal*, **32**, 7, July 1986, pp. 1108–1115

Melching, C. S., and Flores, H. E., 1999, Reaeration equations derived from U.S. Geological Survey database. *J. Environmental Engineering*, *ASCE*, **125**, 5, May 1999, pp. 407–414

Moog, D. B., and Jirka, G. H., 1999, Air–water gas transfer in uniform channel flow. *J. Hydraulic Engineering*, *ASCE*, **125**, 1, January 1999, pp. 3–10

Münsterer, T., and Jähne, B., 1998, LIF measurements of concentration profiles in the aqueous mass boundary layer, *Experiments in Fluids*, **25**, pp. 190–196

Nagaosa, R., 1999, Direct numerical simulation of vortex structures and turbulent scalar transfer across a free surface in a fully developed turbulence, *Physics of Fluids*, **11**, 6, June 1999, pp. 1581–1595

Nakayama, T., 2000, *Turbulence and coherent structures across air–water interface and relationship with gas-transfer*, PhD Thesis, Kyoto University, Japan

Nezu, I., and Nakagawa, H., 1993, *Turbulence in open-channel flows*, IAHR Monograph Series, Balkema, Rotterdam, The Netherlands

NIST, 2000, Standard Reference Database Number 69. February 2000

Pope, S. B., 2000, *Turbulent flows*, Cambridge University Press, Cambridge, U.K.

Rashidi, M., and Banerjee, S., 1988, Turbulence structure in free-surface channel flows, *Physics of Fluids*, **31**, 9, September 1998, pp. 2491–2503

Rathbun, R. E., and Tai, D. Y., 1982, Volatilization of organic compounds from streams, *Journal of Environmental Engineering Division*, *ASCE*, **108**, 5, October 1982, pp. 973–989

Rathbun, R. E., 1998, Transport, behavior and fate of volatile organic compounds in streams. *U.S. Geological Survey Professional Paper 1589*, Washington, DC

Schwarzenbach, R. P., Gschwend, P. M., and Imboden, D. M., 1993. *Environmental organic chemistry*. Wiley-Interscience, New York, USA

Shen, L., Triantafyllou, G. S., and Yue, D. K. P., 2001, Mixing of a passive scalar near a free surface, *Physics of Fluids*, **13**, 4, April 2001, pp.913–926

Socolofsky, S. A., and Jirka G. H., (2002), *Environmental Fluid Mechanics. Part I: Mixing, Transport and Transformation*, Engineering Lectures, Institut für Hydromechanik, University of Kalsruhe, Germany

Sugihara, Y., and Tsumori, H., 2005, Surface-renewal eddies at the air–water interface in oscillating-grid turbulence, in *Proceedings of Environmental Hydraulics and Sustainable Management* (Lee and Lam eds.), Taylor & Francis Group, London, U.K., pp. 199–205

Tamburrino, A., and Gulliver, J. S., 2002, Free-surface turbulence and mass transfer in a channel flow, *AIChE Journal*, **48**, 12, December 2002, pp. 2732–2743

Theofanous, T. G., Houze, R. N., and Brumfield, L. K., 1976, Turbulent mass transfer at free, gas–liquid interfaces, with applications to open-channel, bubble and jet flows, *Int. J. Heat Mass Transfer*. **19**, pp. 613–624

Thibodeaux, L. J., 1996, *Environmental chemodynamics*. John Wiley&Sons, Chichester, U.K.

USEPA, 1985, *Rates, constants and kinetics formulation in surface water quality modeling*. U.S. EPA, Office of Research and Development, Environmental Research Laboratory, Athens, GA, USA, 1985

USEPA, 1997, *Deposition of air pollutants to the Great Waters*, U.S. EPA, Office of Air Quality Planning and Standards, Research Triangle Park, NC, USA

Weber, W. J., and DiGiano, F. A., 1996, *Process dynamics in environmental systems*. John Wiley&Sons, Chichester, U.K.

Wüest, A., and Lorke, A., 2003, Small-scale hydrodynamics in lakes. *Annual Review in Fluid Mechanics*, **35**, pp. 373–412

Xu, Z. F., Khoo, B. C., and Carpenter K., 2006, Mass transfer across the turbulent gas–water interface, *AIChE Journal*, **52**, 10, October 2006, pp. 3363–3374

CHAPTER SEVEN

Advective diffusion of air bubbles in turbulent water flows

Hubert Chanson
University of Queensland, Brisbane, Australia

7.1 INTRODUCTION

The exchange of air between the atmosphere and flowing water is usually called air entrainment, air bubble entrainment or self-aeration. The continuous exchange between air and water is most important for the biological and chemical equilibrium on our planet. For example, the air–water mass transfer at the surface of the oceans regulates the composition of the atmosphere. The aeration process drives the exchange of nitrogen, oxygen and carbon dioxide between the atmosphere and the sea, in particular the dissolution of carbon dioxide into the oceans and the release of supersaturated oxygen to the atmosphere. Another form of flow aeration is the entrainment of un-dissolved air bubbles at the air–water free-surface. Air bubble entrainment is observed in chemical, coastal, hydraulic, mechanical and nuclear engineering applications. In Nature, air bubble entrainment is observed at waterfalls, in mountain streams and river rapids, and in breaking waves on the ocean surface. The resulting "white waters" provide some spectacular effects (Figs. 7.1 to 7.4). Figure 7.1 illustrates the air bubble entrainment at a 83 m high waterfall with a lot of splashing and spray generated at nappe impact. Figure 7.2 shows some air entrainment in a hydraulic jump downstream of a spillway, and Figure 7.3 presents some air bubble entrainment at a plunging breaking wave. Figure 7.4 highlights the free-surface aeration downstream of the Three Gorges dam that may be seen from space (Fig. 7.4B).

Herein we define air bubble entrainment as the entrainment or entrapment of un-dissolved air bubbles and air pockets that are advected within the flowing waters. The term air bubble is used broadly to describe a volume of air surrounded continuously or not by some liquid and encompassed within some air–water interface(s). The resulting air–water mixture consists of both air packets within water and water droplets surrounded by air, and the flow structure may be quite complicated.

Further the entrainment of air bubbles may be localised at a flow discontinuity or continuous along an air–water free-surface: i.e., singular or interfacial aeration respectively. Examples of singular aeration include the air bubble entrainment by a vertical plunging jet. Air bubbles are entrained locally at the intersection of the impinging water jet with the receiving body of water. The impingement perimeter is a source of both vorticity and air bubbles. Interfacial aeration is defined as the air bubble entrainment process along an air–water interface, usually parallel to the flow direction. It is observed in spillway chute flows and in high-velocity water jets discharging into air.

After a review of the basic mechanisms of air bubble entrainment in turbulent water flows, it will be shown that the void fraction distributions may be modelled by some analytical solutions of the advective diffusion equation for air bubbles. Later the micro-structure of the air–water flow will be discussed and it will be argued that the interactions between entrained air bubbles and turbulence remain a key challenge.

Figure 7.1. Air bubble entrainment at a water fall—Chute Montmorency, Québec, Canada on 6 June 2004 (Fall height : 83 m)—Top: general view from downstream. Bottom: details of the free-surface (shutter speed: 1/1,000 s).

Figure 7.2. Air bubble entrainment in a hydraulic jump at the downstream end of a spillway chute—Chain Lakes dam spillway, Southern Alberta, Canada, June 2005 (Courtesy of John Rémi)—Looking downstream, with a discharge of about 300 m^3/s—Note the "brownish" dark colour of the flow caused by the suspended load and the "white" waters downstream of the hydraulic jump highlighting the air bubble detrainment.

Figure 7.3. Air entrainment at wave breaking—Anse des Blancs, Le Conquet, France on 19 April 2004 during early ebb tide (Shutter speed 1/200 s).

(A) Bottom outlet operation on 20 October 2004-Q = 1700m^3/s per jet, V = 35 m/s (Shutter speed 1/1,000 s).

(B) "While water" created by the outlets viewed from space on 14 May 2006—NASA image created by Jesse Allen, Earth Observatory, using ASTER data made available by NASA/GSFC/MITI/ERSDAC/JAROS, and U.S./Japan ASTER Science Team

Figure 7.4. Free-surface aeration by interfacial aeration and plunging jet motion at the Three Gorges dam, central Yangtze river (China).

7.2 FUNDAMENTAL PROCESSES

7.2.1 Inception of air bubble entrainment

The inception of air bubble entrainment characterises the flow conditions at which some bubble entrainment starts. Historically the inception conditions were expressed in terms of a time-averaged velocity. It was often assumed that air entrainment occurs when the flow

velocity exceeds an onset velocity V_e of about 1 m/s. The approach is approximate and it does not account for the complexity of the flow nor the turbulence properties. More detailed studies linked the onset of air entrainment with a characteristic level of normal Reynolds stress(es) next to the free-surface. For example, Ervine and Falvey (1987) and Chanson (1993) for interfacial aeration, Cummings and Chanson (1999) for plunging jet aeration, Brocchini and Peregrine (2001). Although present knowledge remains empirical and often superficial, it is thought that the inception of air entrainment may be better described in terms of tangential Reynolds stresses.

In turbulent shear flows, the air bubble entrainment is caused by the turbulence acting next to the air–water interface. Through this interface, air is continuously being trapped and released, and the resulting air–water mixture may extend to the entire flow. Air bubble entrainment occurs when the turbulent shear stress is large enough to overcome both surface tension and buoyancy effects (if any). Experimental evidences showed that the free-surface of turbulent flows exhibits some surface "undulations" with a fine-grained turbulent structure and larger underlying eddies. Since the turbulent energy is high in small eddy lengths close to the free surface, air bubble entrainment may result from the action of high intensity turbulent shear close to the air–water interface.

Free-surface breakup and bubble entrainment will take place when the turbulent shear stress is greater than the surface tension force per unit area resisting the surface breakup. That is:

$$|\rho_w * v_i * v_j| > \sigma * \frac{\pi * (r_1 + r_2)}{A} \quad \text{inception of air entrainment} \tag{7.1}$$

where ρ_w is the water density, v is the turbulent velocity fluctuation, (i, j) is the directional tensor (i, j = x, y, z), σ is the surface tension between air and water, $\pi*(r_1 + r_2)$ is the perimeter along which surface tension acts, r_1 and r_2 are the two principal radii of curvature of the free surface deformation, and A is surface deformation area. Equation (7.1) gives a criterion for the onset of free-surface aeration in terms of the magnitude of the instantaneous tangential Reynolds stress, the air/water physical properties and the free-surface deformation properties. Simply air bubbles cannot be entrained across the free-surface until there is sufficient tangential shear relative to the surface tension force per unit area.

Considering a two-dimensional flow for which the vertical structures next to the free-surface have axes predominantly perpendicular to the flow direction, the entrained bubbles may be schematised by cylinders of radius r (Fig. 7.5). Equation (7.1) may be simplified into:

$$|\rho_w * v_i * v_j| > \frac{\sigma}{\pi * r} \quad \text{cylindrical bubbles} \tag{7.2a}$$

where x and y are the streamwise and normal directions respectively. For a three-dimensional flow with quasi-isotropic turbulence, the smallest interfacial area per unit volume of air is the sphere (radius r), and Equation (7.1) gives:

$$|\rho_w * v_i * v_j| > \frac{\sigma}{2 * \pi * r} \quad \text{spherical bubbles} \tag{7.2b}$$

Equation (7.2) shows that the inception of air bubble entrainment takes place in the form of relatively large bubbles. But the largest bubbles will be detrained by buoyancy and this yields some preferential sizes of entrained bubbles, observed to be about 1 to 100 mm in prototype turbulent flows (e.g. Cain 1978 and Chanson 1993,1997).

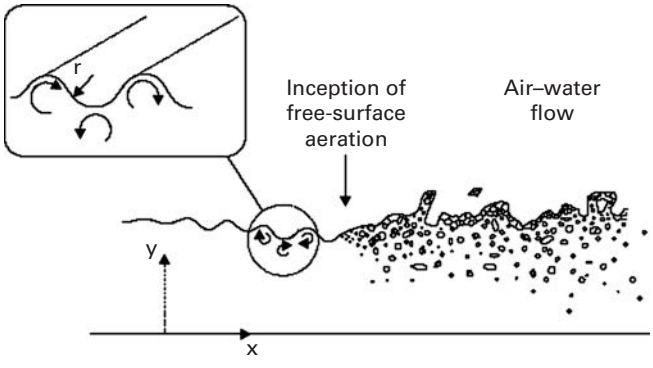

Figure 7.5. Inception of free-surface aeration in a two-dimensional flow.

7.2.2 Bubble breakup

The size of entrained air bubbles in turbulent shear flows is an important parameter affecting the interactions between turbulence and air bubbles. Next to the entrainment point, a region of strong mixing and momentum losses exists in which the entrained air is broken into small bubbles while being diffused within the air–water flow.

At equilibrium, the maximum bubble size in shear flows may be estimated by the balance between the surface tension force and the inertial force caused by the velocity changes over distances of the order of the bubble size. Some simple dimensional analysis yielded a criterion for bubble breakup (Hinze 1955). The result is however limited to some equilibrium situations and it is often not applicable (Chanson 1997, pp. 224–229).

In air–water flows, experimental observations of air bubbles showed that the bubble sizes are larger than the Kolmogorov microscale and smaller than the turbulent macroscale. These observations suggested that the length scale of the eddies responsible for breaking up the bubbles is close to the bubble size. Larger eddies advect the bubbles while eddies with length-scales substantially smaller than the bubble size do not have the necessary energy to break up air bubbles.

In turbulent flows, the bubble break-up occurs when the tangential shear stress is greater than the capillary force per unit area. For a spherical bubble, it yields a condition for bubble breakup:

$$|\rho_w * v_i * v_j| > \frac{\sigma}{d_{ab}} \quad \text{spherical bubble} \tag{7.3a}$$

where d_{ab} is the bubble diameter. Equation (7.3a) holds for a spherical bubble and the left handside term is the magnitude of the instantaneous tangential Reynolds stress. More generally, for an elongated spheroid, bubble breakup takes place for:

$$|\rho_w * v_i * v_j| > \sigma * \frac{\pi * (r_1 + r_2)}{2 * \pi * r_1 * \left(r_1 + r_2 * \dfrac{\text{Arc sin}\left(\sqrt{1 - \dfrac{r_1^2}{r_2^2}}\right)}{\sqrt{1 - \dfrac{r_1^2}{r_2^2}}} \right)} \quad \text{elongated spheroid} \tag{7.3b}$$

where r_1 and r_2 are the equatorial and polar radii of the ellipsoid respectively with $r_2 > r_1$. Equation (7.3b) implies that some turbulence anisotropy (e.g. v_x, $v_y >> v_z$) must induce some preferential bubble shapes.

7.3 ADVECTIVE DIFFUSION OF AIR BUBBLES. BASIC EQUATIONS

7.3.1 Presentation

Turbulent flows are characterised by a substantial amount of air-water mixing at the interfaces. Once entrained, the air bubbles are diffused through the flow while they are advected downstream. Herein their transport by advection and diffusion are assumed two separate additive processes; and the theory of superposition is applicable.

In the bubbly flow region, the air bubble diffusion transfer rate in the direction normal to the advective direction varies directly as the negative gradient of concentration. The scalar is the entrained air and its concentration is called the void fraction C defined as the volume of air per unit volume of air and water. Assuming a steady, quasi-one-dimensional flow, and for a small control volume, the continuity equation for air in the air–water flow is:

$$\text{div}(C * \vec{V}) = \text{div}(D_t * \overrightarrow{\text{grad}}\ C - C * \vec{u}_r) \tag{7.4}$$

where C is the void fraction, $\vec{V}$ is the advective velocity vector, D_t is the air bubble turbulent diffusivity and $\vec{u}_r$ is the bubble rise velocity vector that takes into account the effects of buoyancy. Equation (7.4) implies a constant air density, neglects compressibility effects, and is valid for a steady flow situation.

Equation (7.4) is called the advective diffusion equation. It characterises the air volume flux from a region of high void fraction to one of smaller air concentration. The first term (C∗V) is the advective flux while the right handside term is the diffusive flux. The latter includes the combined effects of transverse diffusion and buoyancy. Equation (7.4) may be solved analytically for a number of basic boundary conditions. Mathematical solutions of the diffusion equation were addressed in two classical references (Carslaw and Jaeger 1959, Crank 1956). Since Equation (7.4) is linear, the theory of superposition may be used to build up solutions with more complex problems and boundary conditions. Its application to air-water flows was discussed by Wood (1984, 1991) and Chanson (1988, 1997).

7.3.2 Buoyancy effects on submerged air bubbles

When air bubbles are submerged in a liquid, a net upward force is exerted on each bubble. That is, the buoyancy force which is the vertical resultant of the pressure forces acting on the bubble. The buoyant force equals the weight of displaced liquid.

The effects of buoyancy on a submerged air bubble may be expressed in terms of the bubble rise velocity u_r. For a single bubble rising in a fluid at rest and in a steady state, the motion equation of the rising bubble yields an exact balance between the buoyant force (upwards), the drag force (downwards) and the weight force (downwards). The expression of the buoyant force may be derived from the integration of the pressure field around the bubble and it is directly proportional to minus the pressure gradient $\partial P/\partial z$ where P is the pressure and z is the vertical axis positive upwards. In a non-hydrostatic pressure gradient, the rise velocity may be estimated to a first approximation as:

$$u_r = \pm(u_r)_{Hyd} * \sqrt{\frac{\left|\frac{\partial P}{\partial z}\right|}{\rho_w * g}} \tag{7.5}$$

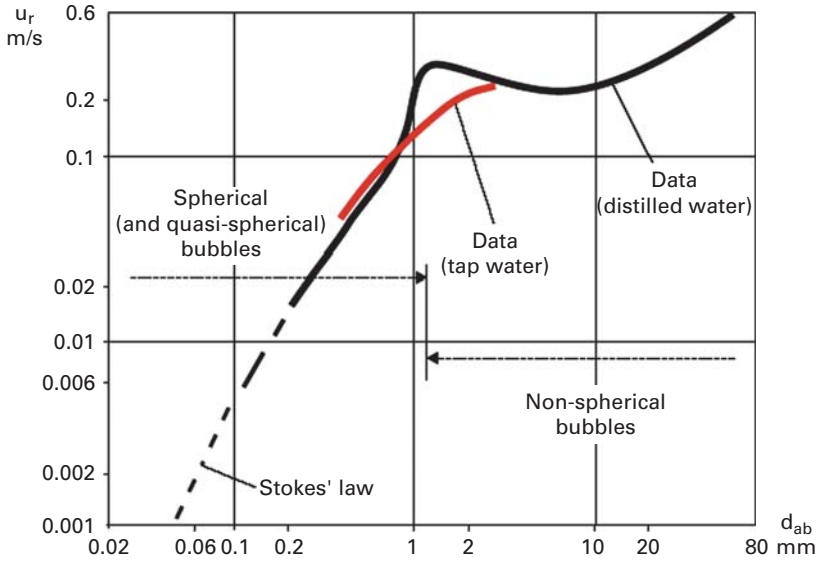

Figure 7.6. Bubble rise velocity in still water.

where $(u_r)_{Hyd}$ is the bubble rise velocity in a hydrostatic pressure gradient (Fig. 7.6), ρ_w is the liquid density, herein water, and z is the vertical direction positive upwards. The sign of the rise velocity u_r depends on the sign of $\partial P/\partial z$. For $\partial P/\partial z < 0$, u_r is positive. Experimental results of bubble rise velocity in still water are reported in Figure 7.6. Relevant references include Haberman and Morton (1954) and Comolet (1979a,b).

7.3.3 A simple application

Let us consider a two-dimensional steady open channel flow down a steep chute (Fig. 7.7). The advective diffusion equation becomes:

$$\frac{\partial}{\partial x}(V_x * C) + \frac{\partial}{\partial y}(V_y * C) = \frac{\partial}{\partial x}\left(D_t * \frac{\partial C}{\partial x}\right) + \frac{\partial}{\partial y}\left(D_t * \frac{\partial C}{\partial y}\right) - \frac{\partial}{\partial x}(-u_r * \sin\theta * C) - \frac{\partial}{\partial y}(u_r * \cos\theta * C) \qquad (7.6)$$

where θ is the angle between the horizontal and the channel invert, x is the streamwise direction and y is the transverse direction (Fig. 7.7). In the uniform equilibrium flow region, the gravity force component in the flow direction is counterbalanced exactly by the friction and drag force resultant. Hence $\partial/\partial x = 0$ and $V_y = 0$. Equation (7.6) yields:

$$0 = \frac{\partial}{\partial y}\left(D_t * \frac{\partial C}{\partial y}\right) - \cos\theta * \frac{\partial}{\partial y}(u_r * C) \qquad (7.7a)$$

where D_t is basically the diffusivity in the direction normal to the flow direction.

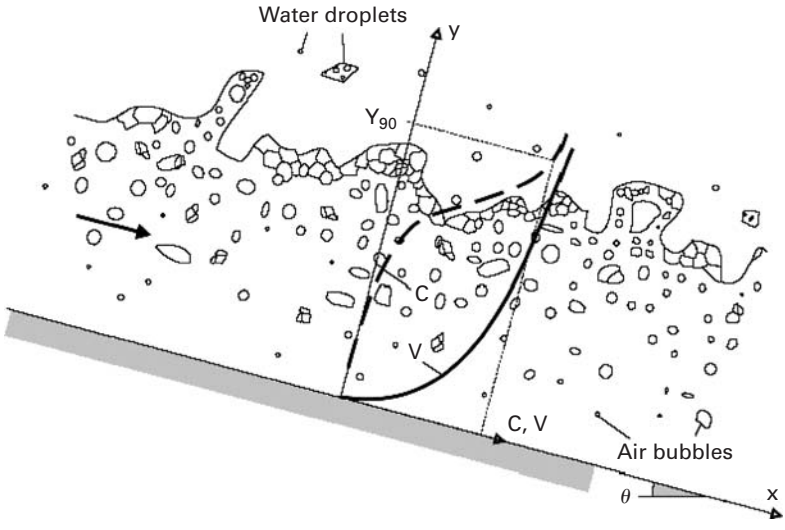

Figure 7.7. Self-aeration in a high-velocity open channel flow.

At a distance y from the invert, the fluid density is $\rho = \rho_w * (1 - C)$ where C is the local void fraction. Hence the expression of the bubble rise velocity (Eq. (5)) becomes:

$$u_r = (u_r)_{Hyd} * \sqrt{1 - C} \tag{7.8}$$

Equation (7.8) gives the rise velocity in a two-phase flow mixture of void fraction C as a function of the rise velocity in hydrostatic pressure gradient. The buoyant force is smaller in aerated waters than in clear-water. For example, a heavy object might sink faster in "white waters" because of the lesser buoyancy.

The advective diffusion equation for air bubbles may be rewritten in dimensionless terms:

$$\frac{\partial}{\partial y'}\left(D'^{*}\frac{\partial C}{\partial y'}\right) = \frac{\partial}{\partial y'}(C * \sqrt{1 - C}) \tag{7.7b}$$

where $y' = y/Y_{90}$, Y_{90} is the characteristic distance where $C = 0.90$, $D' = D_t/((u_r)_{Hyd} * \cos\theta * Y_{90})$ is a dimensionless turbulent diffusivity and the rise velocity in hydrostatic pressure gradient $(u_r)_{Hyd}$ is assumed a constant. D' is the ratio of the air bubble diffusion coefficient to the rise velocity component normal to the flow direction time the characteristic transverse dimension of the shear flow.

A first integration of Equation (7.7a) leads to:

$$\frac{\partial C}{\partial y'} = \frac{1}{D'} * C * \sqrt{1 - C} \tag{7.9}$$

Assuming a homogeneous turbulence across the flow (D' = constant), a further integration yields:

$$C = 1 - \tanh^2\left(K' - \frac{y'}{2 * D'}\right) \tag{7.10}$$

where K′ is an integration constant and tanh(x) is the hyperbolic tangent function. The void fraction distribution (Eq. (7.10)) is a function of two constant parameters: the dimensionless diffusivity D′ and the dimensionless constant K′. A relationship between D′ and K′ is deduced at the boundary condition $C = 0.90$ at $y' = 1$:

$$K' = K* + \frac{1}{2 * D'} \tag{7.11}$$

where $K* = \tanh^{-1}(\sqrt{0.1}) = 0.32745015\ldots$ If the diffusivity is unknown, it can deduced from the depth averaged void fraction C_{mean} defined as:

$$C_{mean} = \int_0^1 C * dy' \tag{7.12}$$

It yields:

$$C_{mean} = 2 * D'^{*} \left(\tanh\left(K* + \frac{1}{2 * D'} \right) - \tanh(K*) \right) \tag{7.13}$$

7.4 ADVECTIVE DIFFUSION OF AIR BUBBLES. ANALYTICAL SOLUTIONS

In turbulent shear flows, the air bubble entrainment processes differ substantially between singular aeration and interfacial aeration. Singular (local) air entrainment is localised at a flow discontinuity: e.g., the intersection of the impinging water jet with the receiving body of water. The air bubbles are entrained locally at the flow singularity: e.g., the toe of a hydraulic jump (Fig. 7.2). The impingement perimeter is a source of air bubbles as well as a source of vorticity. Interfacial (continuous) aeration takes place along an air–water free-surface, usually parallel to the flow direction: e.g., spillway chute flow (Fig. 7.7). Across the free-surface, air is continuously entrapped and detrained, and the entrained air bubbles are advected in regions of relatively low shear.

In the following paragraphs, some analytical solutions of Equation (7.4) are developed for both singular and interfacial air entrainment processes.

7.4.1 Singular aeration

7.4.1.1 Air bubble entrainment at vertical plunging jets

Considering a vertical plunging jet, air bubbles may be entrained at impingement and carried downwards below the pool free surface (Fig. 7.8). This process is called plunging jet entrainment. In chemical engineering, plunging jets are used to stir chemicals as well as to increase gas–liquid mass transfer. Plunging jet devices are used also in industrial processes (e.g. bubble flotation of minerals) while planar plunging jets are observed at dam spillways and overfall drop structures. A related flow situation is the plunging breaking wave in the ocean (Fig. 7.3).

The air bubble diffusion at a plunging liquid jet is a form of advective diffusion. For a small control volume and neglecting the buoyancy effects, the continuity equation for air bubbles becomes:

$$\text{div}(C\vec{V}) = \text{div}(D_t * \overrightarrow{\text{grad}}\, C) \tag{7.14}$$

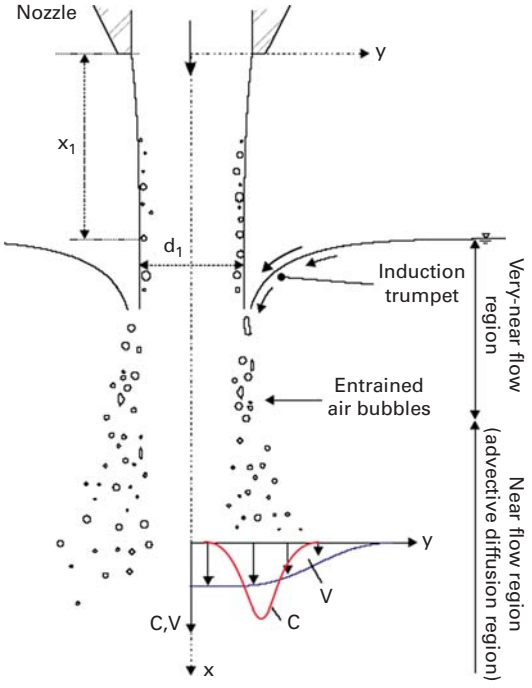

Figure 7.8. Advection of air bubbles downstream of the impingement of a vertical plunging jet.

In Equation (7.14), the bubble rise velocity term may be neglected because the jet velocity is much larger than the rise velocity.

For a circular plunging jet, assuming an uniform velocity distribution, for a constant diffusivity (in the radial direction) independent of the longitudinal location and for a small control volume delimited by streamlines (i.e. stream tube), Equation (7.14) becomes a simple advective diffusion equation:

$$\frac{V_1}{D_t} * \frac{\partial C}{\partial x} = \frac{1}{r} * \frac{\partial}{\partial y}\left(y * \frac{\partial C}{\partial y}\right) \tag{7.15}$$

where x is the longitudinal direction, y is the radial distance from the jet centreline, V_1 is the jet impact velocity and the diffusivity term D_t averages the effects of the turbulent diffusion and of the longitudinal velocity gradient.

The boundary conditions are: $C(x < x_1, y \leq d_1/2) = 0$ and a circular source of total strength Q_{air} at $(x - x_1 = 0, y = d_1/2)$ where d_1 is the jet diameter at impact (Fig. 7.8). Equation (7.15) can be solved analytically by applying a superposition method. The general solution of the advective diffusion equation is:

$$C = \frac{Q_{air}}{Q_w} * \frac{1}{4 * D^{\#} * \dfrac{x - x_1}{d_1/2}} * \exp\left(-\frac{1}{4 * D^{\#}} * \frac{\left(\dfrac{y}{d_1/2}\right)^2 + 1}{\dfrac{x - x_1}{d_1/2}}\right) * I_o\left(\frac{1}{2 * D^{\#}} * \frac{\dfrac{y}{d_1/2}}{\dfrac{x - x_1}{d_1/2}}\right)$$

Circular plunging jet (7.16)

where I_o is the modified Bessel function of the first kind of order zero and $D^{\#} = D_t/(V_1 * d_1/2)$.

For a two-dimensional free-falling jet, the air bubbles are entrapped at the point sources ($x = x_1$, $y = +d_1/2$) and ($x = x_1$, $y = -d_1/2$). Assuming an uniform velocity distribution, for a diffusion coefficient independent of the transverse location and for a small control volume (dx, dy) limited between two streamlines, the continuity equation (Eq. (7.14)) becomes a two-dimensional diffusion equation:

$$\frac{V_1}{D_t} * \frac{\partial C}{\partial x} = \frac{\partial^2 C}{\partial y^2} \tag{7.17}$$

where y is the distance normal to the jet centreline (Fig. 7.8). The problem can be solved by superposing the contribution of each point source. The solution of the diffusion equation is:

$$C = \frac{1}{2} * \frac{Q_{air}}{Q_w} * \frac{1}{\sqrt{4 * \pi * D^{\#} * \dfrac{x - x_1}{d_1}}} * \left(\exp\left(-\frac{1}{4 * D^{\#}} * \frac{\left(\dfrac{y}{d_1} - 1\right)^2}{\dfrac{x - x_1}{d_1}} \right) + \exp\left(-\frac{1}{4 * D^{\#}} * \frac{\left(\dfrac{y}{d_1} + 1\right)^2}{\dfrac{x - x_1}{d_1}} \right) \right)$$

Two-dimensional plunging jet (7.18)

where Q_{air} is the entrained air flow rate, Q_w is the water flow rate, d_1 is the jet thickness at impact, and $D^{\#}$ is a dimensionless diffusivity: $D^{\#} = D_t/(V_1 * d_1)$.

Discussion

Equations (7.16) and (7.18) are the exact analytical solutions of the advective diffusion of air bubbles (Eq. (7.4)). The two-dimensional and axi-symmetrical solutions differ because of the boundary conditions and of the integration method. Both solutions are three-dimensional solutions valid in the developing bubbly region and in the fully-aerated flow region. They were successfully compared with a range of experimental data.

7.4.1.2 Air bubble entrainment in a horizontal hydraulic jump

A hydraulic jump is the sudden transition from a supercritical flow into a slower, subcritical motion (Fig. 7.9). It is characterised by strong energy dissipation, spray and splashing and air bubble entrainment. The hydraulic jump is sometimes described as the limiting case of a horizontal supported plunging jet.

Assuming an uniform velocity distribution, for a constant diffusivity independent of the longitudinal and transverse location, Equation (7.14) becomes:

$$V_1 * \frac{\partial C}{\partial x} + u_r * \frac{\partial C}{\partial y} = D_t * \frac{\partial^2 C}{\partial y^2} \tag{7.19}$$

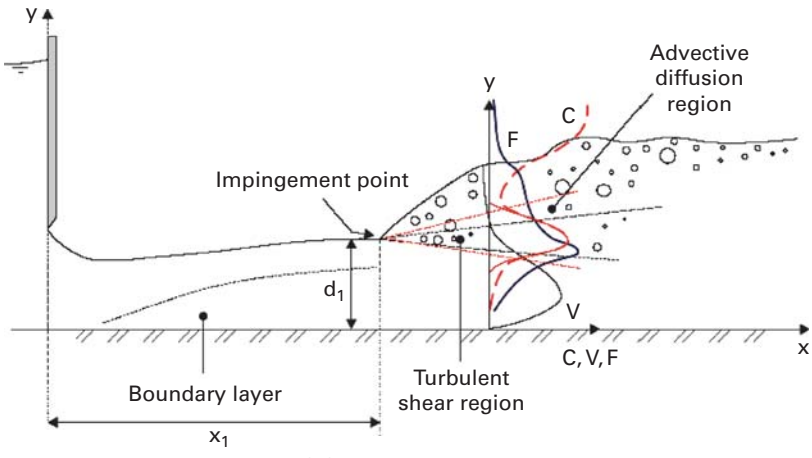

(A) Definition sketch

(B) Hydraulic jump in a rectangular channel ($V_1/\sqrt{g*d_1} = 7$, $\rho_w*V_1*d_1/\mu_w = 8.1\ E{+}4$) —Flow from left to right

Figure 7.9. Advection of air bubbles in a horizontal hydraulic jump.

where V_1 is the inflow velocity and the rise velocity is assumed constant. With a change of variable ($X = x - x_1 + u_r/V_1 * y$) and assuming $u_r/V_1 << 1$, Equation (7.19) becomes a two-dimensional diffusion equation:

$$\frac{V_1}{D_t} * \frac{\partial C}{\partial X} = \frac{\partial^2 C}{\partial y^2} \tag{7.20}$$

In a hydraulic jump, the air bubbles are supplied by a point source located at ($X = u_r/V_1 * d_1$, $y = +d_1$) and the strength of the source is Q_{air}/W where W is the channel width.

The diffusion equation can be solved by applying the method of images and assuming an infinitesimally long channel bed. It yields:

$$C = \frac{Q_{air}}{Q_w} * \frac{1}{\sqrt{4 * \pi * D^{\#} * X'}} * \left(\exp\left(-\frac{1}{4 * D^{\#}} * \frac{\left(\frac{y}{d_1} - 1\right)^2}{X'} \right) + \exp\left(-\frac{1}{4 * D^{\#}} * \frac{\left(\frac{y}{d_1} + 1\right)^2}{X'} \right) \right) \tag{7.21}$$

where d_1 is the inflow depth, $D^{\#}$ is a dimensionless diffusivity: $D^{\#} = D_t/(V_1 * d_1)$ and:

$$X' = \frac{X}{d_1} = \frac{x - x_1}{d_1} * \left(1 + \frac{u_r}{V_1} * \frac{y}{x - x_1}\right)$$

Equation (7.21) is close to Equation (7.18) but the distribution of void fraction is shifted upwards as a consequence of some buoyancy effect. Further the definition of d_1 differs (Fig. 7.9). In practice, Equation (7.21) provides a good agreement with experimental data in the advective diffusion region of hydraulic jumps with partially-developed inflow conditions.

7.4.2 Interfacial aeration

7.4.2.1 Interfacial aeration in a water jet discharging into the atmosphere

High velocity turbulent water jets discharging into the atmosphere are often used in hydraulic structures to dissipate energy. Typical examples include jet flows downstream of a ski jump at the toe of a spillway, water jets issued from bottom outlets (Fig. 7.10B) and flows above a bottom aeration device along a spillway. Other applications include mixing devices in chemical plants and spray devices. High-velocity water jets are used also for fire-fighting jet cutting (e.g. coal mining), with Pelton turbines and for irrigation (Fig. 7.10C).

Considering a water jet discharging into air, the pressure distribution is quasi-uniform across the jet and the buoyancy effect is zero in most cases. For a small control volume, the advective diffusion equation for air bubbles in a steady flow is :

$$\text{div}(C\,\vec{V}) = \text{div}(D_t * \overrightarrow{\text{grad}}\, C) \tag{7.14}$$

For a circular water jet, the continuity equation for air becomes:

$$\frac{\partial}{\partial x}(C * V_1) = \frac{1}{y} * \frac{\partial}{\partial y}\left(D_t * y * \frac{\partial C}{\partial y}\right) \tag{7.22}$$

where x is the longitudinal direction, y is the radial direction, V_1 is the jet velocity and D_t is the turbulent diffusivity in the radial direction.

Assuming a constant diffusivity D_t in the radial direction, and after separating the variables, the void fraction:

$$C = \mathbf{u} * \exp\left(-\frac{D_t}{V_1} * \alpha_n^2 * x\right)$$

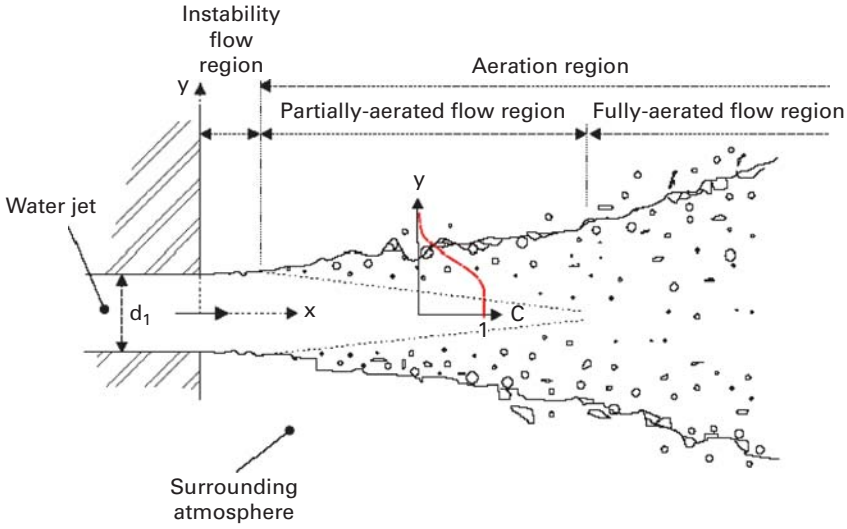

(A) Definition sketch

(B) High-velocity water jet at Three Gorgas dam—9 m by 7 m jet, V_1 = 35 m/s, high-shutter speed (1/1,000 s)

Figure 7.10. Advective dispersion of air bubbles in a turbulent water jet discharging into air.

(C) Circular water jet (irrigation water canon)—d_1 = 0.0275 m, V_1 = 22.5 m/s, high-shutter speed (1/1,000 s)

Figure 7.10. (*Continued*)

is a solution of the continuity equation provided that u is a function of y only satisfying the Bessel's equation of order zero:

$$\frac{\partial^2 \mathbf{u}}{\partial y^2} + \frac{1}{y} * \frac{\partial \mathbf{u}}{\partial y} + \alpha_n^2 * \mathbf{u} = 0 \tag{7.23}$$

At each position x, the diffusivity D_t is assumed a constant independent of the transverse location y. The boundary conditions are $C = 0.9$ at $y = Y_{90}$ for $x > 0$ and $C = 0$ for $x < 0$. An analytical solution is a series of Bessel functions:

$$C = 0.9 - \frac{1.8}{Y_{90}} * \sum_{n=1}^{+\infty} \frac{J_o(y * \alpha_n)}{\alpha_n * J_1(Y_{90} * \alpha_n)} * \exp\left(-\frac{D_t}{V_1} * \alpha_n^2 * x\right) \tag{7.24}$$

where J_o is the Bessel function of the first kind of order zero, α_n is the positive root of: $J_o(Y_{90} * \alpha_n) = 0$, and J_1 is the Bessel function of the first kind of order one. Equation (7.24) was numerically computed by Carslaw and Jaeger (1959) for several values of the dimensionless diffusivity $D'' = D_t * x/(V_1 * Y_{90}^2)$.

Equation (7.24) is valid close to and away from the jet nozzle. It is a three-dimensional solution of the diffusion equation that it is valid when the clear water core of the jet disappears and the jet becomes fully-aerated.

For a two-dimensional water jet, assuming an uniform velocity distribution, and for a constant diffusivity independent of the longitudinal and transverse location, Equation (7.14) becomes:

$$V_1 * \frac{\partial C}{\partial x} = D_t * \frac{\partial^2 C}{\partial y^2} \tag{7.25}$$

where V_1 is the inflow depth. Equation (7.25) is a basic diffusion equation (Crank 1956, Carslaw and Jaeger 1959).

The boundary conditions are: $\lim(C(x > 0, y \to +\infty)) = 1$ and $\lim(C(x > 0, y \to -\infty)) = 1$, where the positive direction for the x- and y-axes is shown on Figure 7.10A. Note that, at the edge of the free-shear layer, the rapid change of shear stress is dominant. The effect of the removal of the bottom shear stress is to allow the fluid to accelerate. Further downstream the acceleration decreases rapidly down to zero.

The analytical solution of Equation (7.25) is:

$$C = \frac{1}{2} * \left(2 + \text{erf}\left(\frac{\frac{y}{d_1} - \frac{1}{2}}{2 * \sqrt{\frac{D_t}{V_1 * d_1} * \frac{x}{d_1}}} \right) + \text{erf}\left(\frac{\frac{y}{d_1} + \frac{1}{2}}{2 * \sqrt{\frac{D_t}{V_1 * d_1} * \frac{x}{d_1}}} \right) \right) \quad (7.26)$$

where d_1 is the jet thickness at nozzle, erf is the Gaussian error function, and the diffusivity D_t averages the effect of the turbulence on the transverse dispersion and of the longitudinal velocity gradient. The boundary conditions imply the existence of a clear-water region between the air-bubble diffusion layers in the initial jet flow region as sketched in Figure 7.10A.

The two-dimensional case may be simplified for a two-dimensional free-shear layer: e.g. an open channel flow taking off a spillway aeration device or a ski jump. The analytical solution for a free shear layer is:

$$C = \frac{1}{2} * \left(1 + \text{erf}\left(\frac{\frac{y}{d_1}}{2 * \sqrt{\frac{D_t}{V_1 * d_1} * \frac{x}{d_1}}} \right) \right) \quad (7.27)$$

where $y = 0$ at the flow singularity (i.e. nozzle edge) and $y > 0$ towards the atmosphere.

7.4.3 Discussion

The above expressions (Sections 7.4.1 & 7.4.2) were developed assuming a constant, uniform air bubble diffusivity. While the analytical solutions are in close agreement with experimental data (e.g. Chanson 1997; Toombes 2002; Gonzalez 2005; Murzyn *et al.*, 2005), the distributions of turbulent diffusivity are unlikely to be uniform in complex flow situations. Two well-documented examples are the skimming flow on a stepped spillway and the flow downstream of a drop structure (Fig. 7.11).

For a two-dimensional open channel flow, the advective diffusion equation for air bubbles yields:

$$\frac{\partial}{\partial y'}\left(D' * \frac{\partial C}{\partial y'} \right) * \frac{\partial}{\partial y'}(C * \sqrt{1 - c}) \quad (7.7b)$$

where $y' = y/Y_{90}$, Y_{90} is the characteristic distance where $C = 0.90$, and $D' = D_t/((u_r)_{Hyd} * \cos\theta * Y_{90})$ is a dimensionless turbulent diffusivity that is the ratio of the air bubble diffusion coefficient to the rise velocity component normal to the flow direction time the characteristic transverse dimension of the shear flow. In a skimming flow on a stepped chute (Fig. 7.11A), the flow is extremely turbulent and the air bubble diffusivity distribution may be

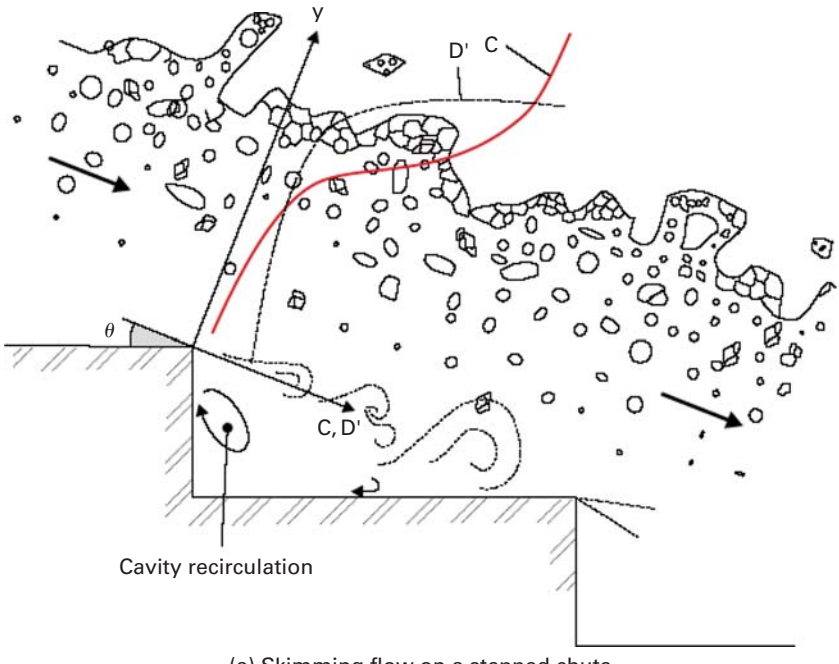

(a) Skimming flow on a stepped chute

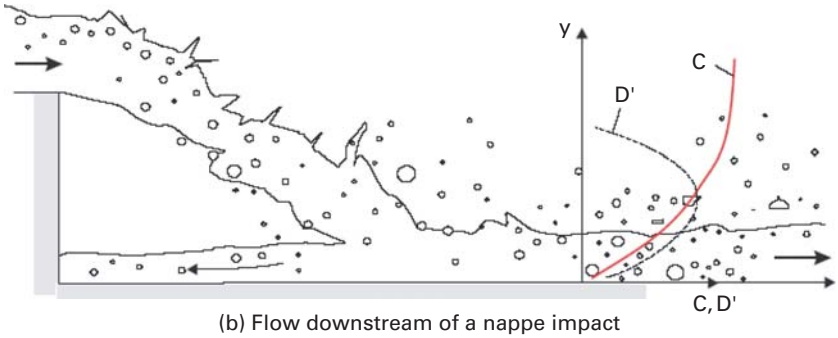

(b) Flow downstream of a nappe impact

Figure 7.11. Advective dispersion of air bubbles in highly-turbulent open channel flows.

approximated by:

$$D' = \frac{D_o}{1 - 2 * \left(y' - \frac{1}{3}\right)^2} \tag{7.28}$$

The integration of the air bubble diffusion equation yields a S-shape void fraction profile:

$$C = 1 - \tan h^2 \left(K' - \frac{y'}{2 * D_o} + \frac{\left(y' - \frac{1}{3}\right)^3}{3 * D_o} \right) \tag{7.29}$$

where K' is an integration constant and D_o is a function of the mean void fraction only :

$$K' = K^* + \frac{1}{2 * D_o} + \frac{8}{81 * D_o} \quad \text{with } K^* = 0.32745015\ldots \tag{7.30}$$

$$C_{mean} = 0.7622 * (1.0434 - \exp(-3.614 * D_o)) \tag{7.31}$$

Equations (7.28) and (7.29) are sketched in Figure 7.11A. They were found to agree well with experimental measurements at step edges.

Downstream of a drop structure (Fig. 7.11B), the flow is fragmented, highly aerated and extremely turbulent. A realistic void fraction distribution model may be developed assuming a quasi-parabolic bubble diffusivity distribution :

$$D' = \frac{C * \sqrt{1 - C}}{\lambda * (K' - C)} \tag{7.32}$$

The integration of Equation (7.7b) yields :

$$C = K' * (1 - \exp(-\lambda * y')) \tag{7.33}$$

where K' and λ are some dimensionless functions of the mean air content only :

$$K' = \frac{0.9}{1 - \exp(-\lambda)} \tag{7.34}$$

$$C_{mean} = K' - \frac{0.9}{\lambda} \tag{7.35}$$

Equations (7.32) and (7.33) are sketched in Figure 7.11B. In practice, Equation (7.33) applies to highly-aerated, fragmented flows like the steady flows downstream of drop structures and spillway bottom aeration devices, and the transition flows on stepped chutes, as well as the leading edge of unsteady surges. Note that the depth-averaged air content must satisfy $C_{mean} > 0.45$.

7.5 STRUCTURE OF THE BUBBLY FLOW

In Sections 7.3 and 7.4, the advective diffusion equation for air bubbles is developed and solved in terms of the void fraction. The void fraction is a gross parameter that does not describe the air–water structures, the bubbly flow turbulence nor the interactions between entrained bubbles and turbulent shear. Herein recent experimental developments are discussed in terms of the streamwise flow structure and the air-water time and length scales.

7.5.1 Streamwise particle grouping

With modern phase-detection intrusive probes, the probe output signals provide a complete characterisation of the streamwise air-water structure at one point. Figure 7.12 illustrates the operation of such a probe. Figure 7.12B shows two probes in a bubbly flow, while Figure 7.12A presents the piercing of air bubbles by the probe sensor. Some simple signal

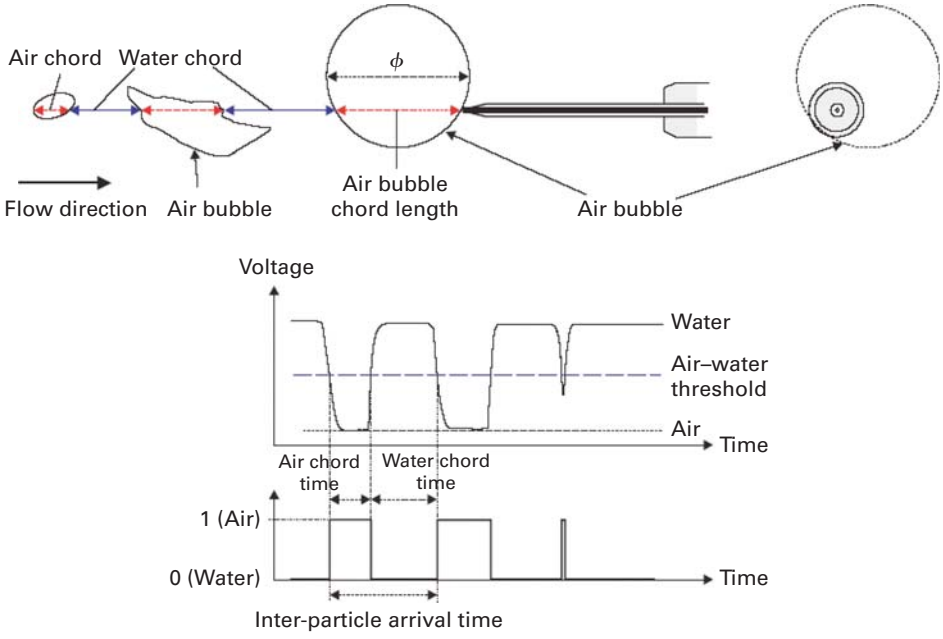

(a) Sketch of a phase-detection intrusive probe and its signal output

(b) Photograph of two single-tip conductivity probes side-by-side in a hydraulic jump ($Fr_1 = 7.9$, $\rho_w * V_1 * d_1 / \mu_w = 9.4\ E + 4$)—flow from right to left

Figure 7.12. Phase-detection intrusive probe in turbulent air–water flows.

processing yields the basic statistical moments of air and water chords as well as the probability distribution functions of the chord sizes.

In turbulent shear flows, the experimental results demonstrated a broad spectrum of bubble chords. The range of bubble chord lengths extended over several orders of magnitude

including at low void fractions. The distributions of bubble chords were skewed with a preponderance of small bubbles relative to the mean. The probability distribution functions of bubble chords tended to follow a log–normal and gamma distributions. Similar findings were observed in a variety of flows encompassing hydraulic jumps, plunging jets, dropshaft flows and high-velocity open channel flows.

In addition of void fraction and bubble chord distributions, some further signal processing may provide some information on the streamwise structure of the air–water flow including bubble clustering. A concentration of bubbles within some relatively short intervals of time may indicate some clustering while it may be instead the consequence of a random occurrence. The study of particle clustering events is relevant to infer whether the formation frequency responds to some particular frequencies of the flow. Figure 7.13 illustrates some occurrence of bubble pairing in the shear layer of a hydraulic jump. The binary pairing indicator is unity if the water chord time between adjacent bubbles is less than 10% of the median water chord time. The pattern of vertical lines seen in Figure 7.13 is an indication of patterns in which bubbles tend to form bubble groups.

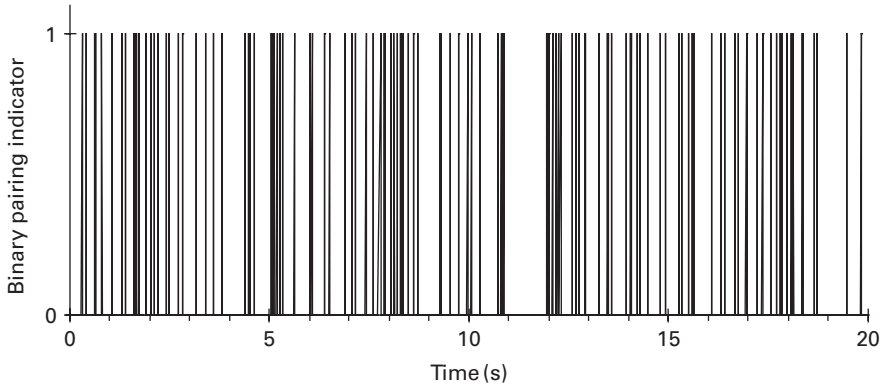

Figure 7.13. Closely spaced bubble pairs in the developing shear layer of a hydraulic jump—$Fr_1 = 8.5$, $\rho_w * V_1 * d_1/\mu_w = 9.8\ E + 4$, $x - x_1 = 0.4$ m, $d_1 = 0.024$ m, $y/d_1 = 1.33$, $C = 0.20$, $F = 158$ Hz.

One method is based upon the analysis of the water chord between two adjacent air bubbles (Fig. 7.12A). If two bubbles are closer than a particular length scale, they can be considered a group of bubbles. The characteristic water length scale may be related to the water chord statistics: e.g., a bubble cluster may be defined when the water chord was less than a given percentage of the mean water chord. Another criterion may be related to the leading bubble size itself, since bubbles within that distance are in the near-wake of and may be influenced by the leading particle.

Typical results may include the percentage of bubbles in clusters, the number of clusters per second, and the average number of bubbles per cluster. Extensive experiments in open channels, hydraulic jumps and plunging jets suggested that the outcomes were little affected by the cluster criterion selection. Most results indicated that the streamwise structure of turbulent flows was characterised by about 10 to 30% of bubbles travelling as parts of a group/cluster, with a very large majority of clusters comprising of 2 bubbles only. The experimental experience suggested further that a proper cluster analysis requires a high-frequency scan rate for a relatively long scan duration. However the analysis is restricted to the streamwise distribution of bubbles and does not take into account particles travelling side by side.

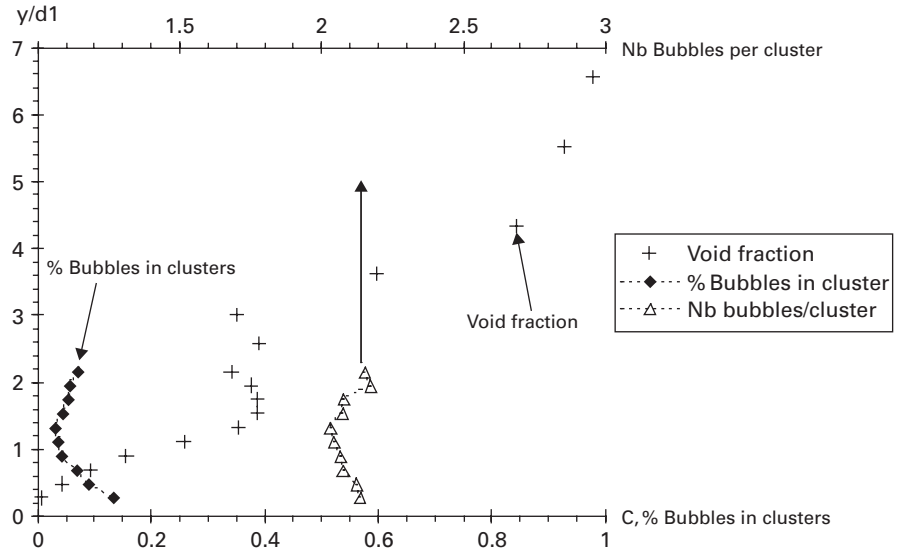

Figure 7.14. Bubble clustering in the bubbly flow region of a hydraulic jump: percentage of bubbles in clusters, average number of bubbles per cluster and void fraction—Cluster criterion: water chord time $<10\%$ median water chord time—$Fr_1 = 8.5$, $\rho_w * V_1 * d_1/\mu_w = 9.8\,E+4$, $x - x_1 = 0.3$ m, $d_1 = 0.024$ m.

Some typical result is presented in Figure 7.14. Figure 7.14 shows the vertical distribution of the percentage of bubbles in clusters (lower horizontal axis) and average number of bubbles per cluster (upper horizontal axis) in the advective diffusion region of a hydraulic jump. The void fraction distribution is also shown for completeness. The criterion for cluster existence is a water chord less than 10% of the median water chord. For this example, about 5 to 15% of all bubbles were part of a cluster structure and the average number of bubbles per cluster was about 2.1.

For a dispersed phase, a complementary approach is based upon an inter-particle arrival time analysis. The inter-particle arrival time is defined as the time between the arrival of two consecutive bubbles recorded by a probe sensor fixed in space (Fig. 7.12A). The distribution of inter-particle arrival times provides some information on the randomness of the structure. Random dispersed flows are those whose inter-particle arrival time distributions follow inhomogeneous Poisson statistics assuming non-interacting point particles (Edwards and Marx 1995a). In other words, an ideal dispersed flow is driven by a superposition of Poisson processes of bubble sizes, and any deviation from a Poisson process indicates some unsteadiness and particle clustering.

In practice, the analysis is conducted by breaking down the air–water flow data into narrow classes of particles of comparable sizes that are expected to have the same behaviour (Edwards and Marx 1995b). A simple means consists in dividing the bubble/droplet population in terms of the air/water chord time. The inter-particle arrival time analysis may provide some information on preferential clustering for particular classes of particle sizes.

Some results in terms of inter-particle arrival time distributions are shown in Figure 7.15 for the same flow conditions and at the same cross-section as the data presented in Figure 7.14. Chi-square values are given in the figure captions. Figure 7.15 presents some inter-particle arrival time results for two chord time classes of the same sample (0 to 0.5 msec and 3 to 5 msec). For each class of bubble sizes, a comparison between data and Poisson distribution gives some information on its randomness. For example, Figure 7.15A shows

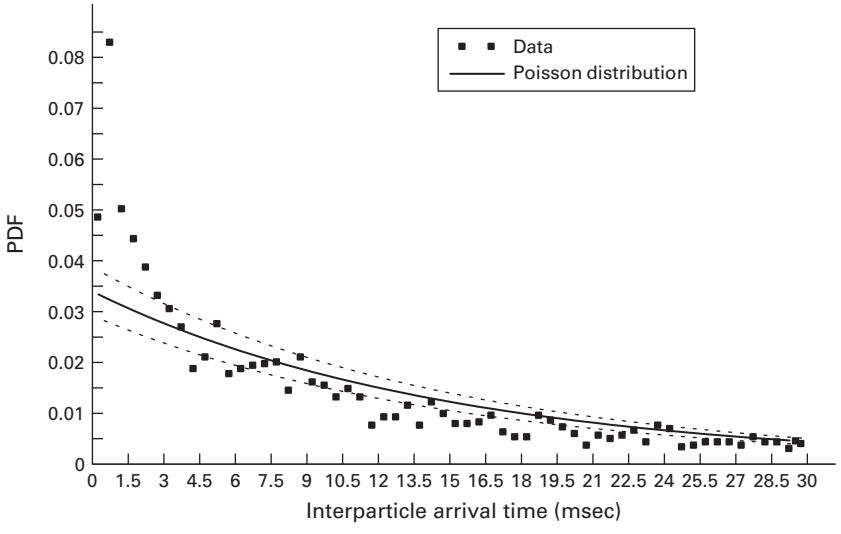

(a) Inter-particle arrival time distributions for bubble chord times between 0 and 0.5 msec, 3055 bubbles, $\chi^2 = 461$

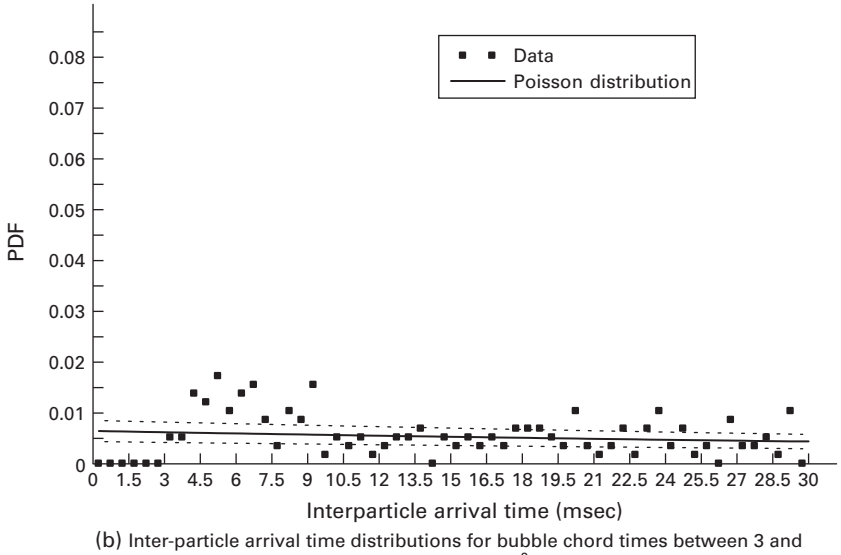

(b) Inter-particle arrival time distributions for bubble chord times between 3 and 5 msec, 581 bubbles, $\chi^2 = 110$

Figure 7.15. Inter-particle arrival time distributions in the bubbly flow region of a hydraulic jump for different classes of air chord times—Comparison between data and Poisson distribution—Expected deviations from the Poisson distribution for each sample are shown in dashed lines—$Fr_1 = 8.5$, $\rho_w * V_1 * d_1/\mu_w = 9.8\ E + 4$, $x - x_1 = 0.3$ m, $d_1 = 0.024$ m.

that the data for bubble chord times below 0.5 msec did not experience a random behaviour because the experimental and theoretical distributions differed substantially in shape. The second smallest inter-particle time class (0.5–1 msec) had a population that was 2.5 times the expected value or about 11 standard deviations too large. This indicates that there was a higher probability of having bubbles with shorter inter-particle arrival times, hence some

bubble clustering occurred. Simply the smallest class of bubble chord times did not exhibit the characteristics of a random process.

Altogether both approaches are complementary, although the inter-particle arrival time analysis may give some greater insight on the range of particle sizes affected by clustering.

7.5.2 Correlation analyses

When two or more phase detection probe sensors are simultaneously sampled, some correlation analyses may provide additional information on the bubbly flow structure. A well-known application is the use of dual tip probe to measure the interfacial velocity (Fig. 7.16). With large void fractions ($C > 0.10$), a cross-correlation analysis between the two probe sensors yields the time averaged velocity:

$$V = \frac{\Delta x}{T} \tag{7.36}$$

where T is the air–water interfacial travel time for which the cross-correlation function is maximum and Δx is the longitudinal distance between probe sensors (Fig. 7.16). Turbulence levels may be further derived from the relative width of the cross-correlation function:

$$Tu = 0.851 * \frac{\sqrt{\tau_{0.5}^2 - T_{0.5}^2}}{T} \tag{7.37}$$

where $\tau_{0.5}$ is the time scale for which the cross-correlation function is half of its maximum value such as: $R_{xy}(T + \tau_{0.5}) = 0.5 * R_{xy}(T)$, R_{xy} is the normalised cross-correlation function, and $T_{0.5}$ is the characteristic time for which the normalised auto-correlation function equals: $R_{xx}(T_{0.5}) = 0.5$ (Fig. 7.16). Physically, a thin narrow cross-correlation function ($(\tau_{0.5} - T_{0.5})/T << 1$) must correspond to little fluctuations in the interfacial velocity, hence a small turbulence level Tu. While Equation (7.37) is not the true turbulence intensity u'/V, it is an expression of some turbulence level and average velocity fluctuations.

More generally, when two probe sensors are separated by a transverse or streamwise distance, their signals may be analysed in terms of the auto-correlation and cross-correlation functions R_{xx} and R_{xy} respectively. Figure 7.12B shows two probe sensors separated by a transverse distance Δz, while Figure 7.16 presents two probe sensors separated by a streamwise distance Δx. Practically the original data set may be segmented because the periodogram resolution is inversely proportional to the number of samples and it could be biased with large data sets (Hayes 1996).

Basic correlation analysis results include the maximum cross-correlation coefficient $(R_{xy})_{max}$, and the integral time scales T_{xx} and T_{xy} where:

$$T_{xx} = \int_{\tau=0}^{\tau=\tau(R_{xx}=0)} R_{xx}(\tau) * d\tau \tag{7.38}$$

$$T_{xy} = \int_{\tau=\tau(R_{xy}=(R_{xy})_{max})}^{\tau=\tau(R_{xy}=0)} R_{xy}(\tau) * d\tau \tag{7.39}$$

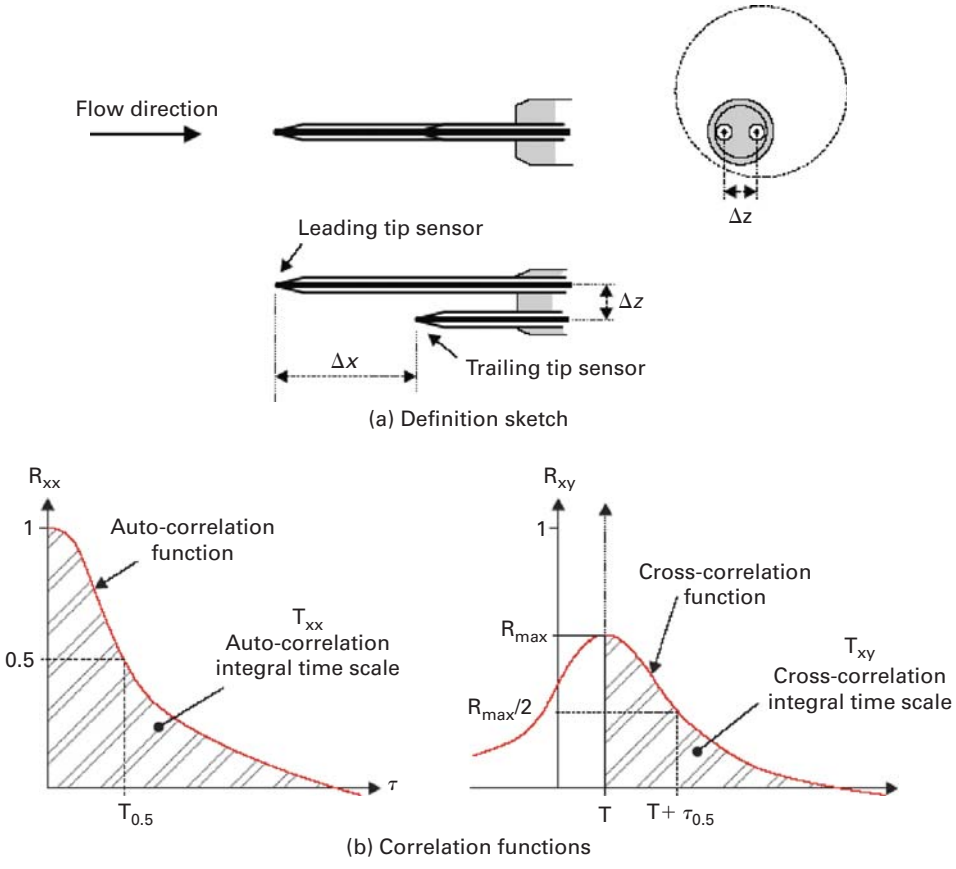

Figure 7.16. Dual sensor phase detection probe.

where R_{xx} is the normalised auto-correlation function, τ is the time lag, and R_{xy} is the normalised cross-correlation function between the two probe output signals (Fig. 7.16). The auto-correlation integral time scale T_{xx} represents the integral time scale of the longitudinal bubbly flow structure. It is a characteristic time of the eddies advecting the air–water interfaces in the streamwise direction. The cross-correlation time scale T_{xy} is a characteristic time scale of the vortices with a length scale y advecting the air–water flow structures. The length scale y may be a transverse separation distance Δz or a streamwise separation Δx.

When identical experiments are repeated with different separation distances y ($y = \Delta z$ or Δx), an integral turbulent length scale may be calculated as:

$$L_{xy} = \int_{y=0}^{y=y((R_{xy})_{max}=0)} (R_{xy})_{max} * dy \tag{7.40}$$

The length scale L_{xy} represents a measure of the transverse/streamwise length scale of the large vertical structures advecting air bubbles and air–water packets.

A turbulence integral time scale is:

$$\mathbf{T} = \frac{\int_{y=0}^{y=y((R_{xy})_{max}=0)} (R_{xy})_{max} * T_{xy} * dy}{L_{xy}} \tag{7.41}$$

T represents the transverse/streamwise integral time scale of the large eddies advecting air bubbles.

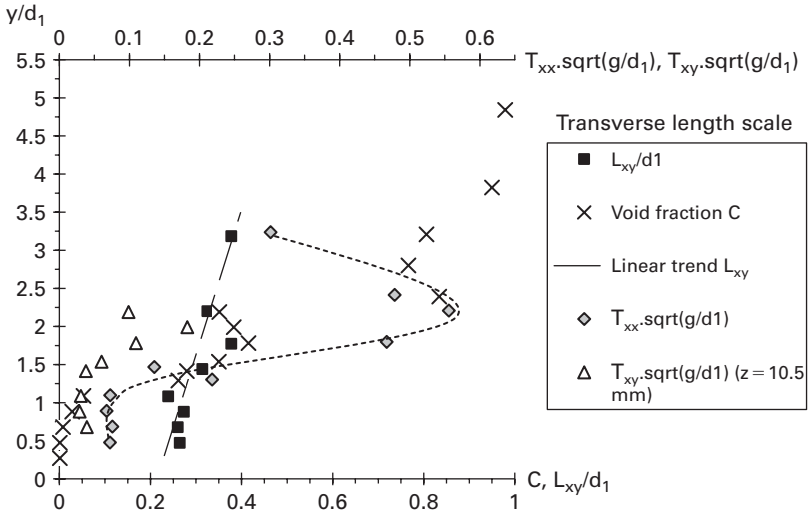

Figure 7.17. Dimensionless distributions of auto- and cross-correlation time scales $T_{xx} * \sqrt{g/d_1}$ and $T_{xy} * \sqrt{g/d_1}$ (transverse time scale, $y = \Delta z = 10.5$ mm), and transverse integral turbulent length scale L_{xy}/d_1 in a hydraulic jump—$Fr_1 = 7.9$, $\rho_w * V_1 * d_1/\mu_w = 9.4\ E + 4$, $x - x_1 = 0.1$ m, $d_1 = 0.0245$ m.

Figures 7.17 to 7.19 present some experimental results obtained in a hydraulic jump on a horizontal channel and in a skimming flow on a stepped channel. In both flow situations, the distributions of integral time scales showed a marked peak for $0.4 \leq C \leq 0.6$ (Figs. 7.17 and 7.18). Note that Figure 7.17 presents some transverse time scales T_{xy} while Figure 7.18 shows some longitudinal time scales T_{xy}. The distributions of transverse integral length scales exhibited some marked differences that may reflect the differences in turbulent mixing and air bubble advection processes between hydraulic jump and skimming flows. In Figure 7.19, the integral turbulent length scale L_{xy} represents a measure of the transverse size of large vertical structures advecting air bubbles in the skimming flow regime. The air–water turbulent length scale is closely related to the characteristic air–water depth Y_{90}: i.e., $0.05 \leq L_{xy}/Y_{90} \leq 0.2$ (Fig. 7.19). Note that both the integral turbulent length and time scales were maximum for about $C = 0.5$ to 0.7 (Figs. 7.18 & 7.19). The finding emphasises the existence of large-scale turbulent structures in the intermediate zone ($0.3 < C < 0.7$) of the flow, and it is hypothesised that these large vortices may play a preponderant role in terms of turbulent dissipation.

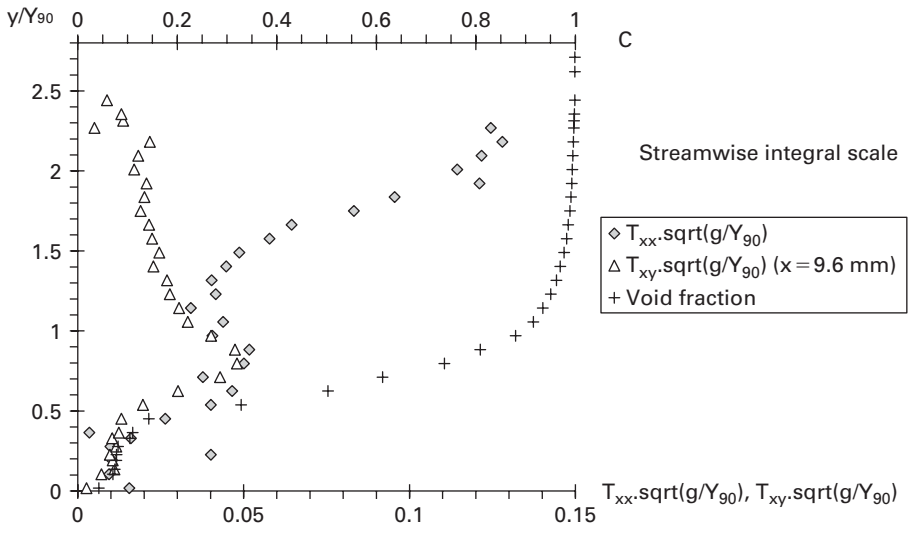

Figure 7.18. Dimensionless distributions of auto- and cross-correlation time scales $T_{xx} * \sqrt{g/Y_{90}}$ and $T_{xy} * \sqrt{g/Y_{90}}$ (longitudinal time scale, $y = \Delta x = 9.6$ mm) in a skimming flow on a stepped chute—$d_c/h = 1.15$, $\rho_w * V * d/\mu_w = 1.2\ E + 5$, Step 10, $Y_{90} = 0.0574$ m, $h = 0.1$ m, $\theta = 22°$.

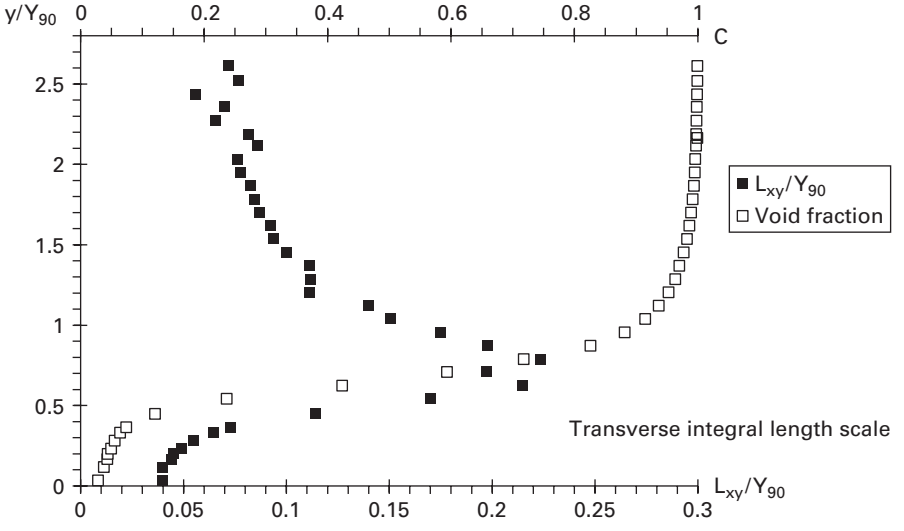

Figure 7.19. Dimensionless distributions of transverse integral turbulent length scale L_{xy}/Y_{90} in a skimming flow on a stepped chute—$d_c/h = 1.15$, $\rho_w * V * d/\mu_w = 1.2\ E + 5$, Step 10, $Y_{90} = 0.0598$ m, $h = 0.1$ m, $\theta = 22°$.

7.6 CONCLUDING REMARKS

In turbulent free-surface flows, the strong interactions between turbulent waters and the atmosphere may lead to some self-aeration. That is, the entrainment/entrapment of air bubbles that are advected within the bulk of the flow and give a 'white' appearance to the waters. In Nature, free-surface aerated flows are encountered at waterfalls, in mountain

Figure 7.20. Dettifoss waterfall, Iceland (Courtesy of Paul Guard)—Fall height: 44 m, chute width: 100 m.

rivers and river rapids, and when wave breaking occurs on the ocean surface. 'White waters' provide always spectacular effects (Fig. 7.20). While classical examples include the tidal bore of the Qiantang river in China, the Zambesi rapids in Africa, and the 980 m high Angel Falls in South America, 'white waters' are observed also in smaller streams and torrents. The rushing waters may become gravitationless in waterfalls, impacting downstream on rocks and water pools where their impact is often surrounded by splashing, spray and fog (e.g. Niagara Falls). Man-made self-aeration is also common, ranging from artistic fountains to engineering and industrial applications.

The entrainment of air bubbles may be localised at a flow discontinuity or continuous along an air–water free-surface. At a flow singularity, air bubbles are entrained locally at the impinging point and they are advected in a region of high shear. Interfacial aeration is the air bubble entrainment process along an air–water interface that is parallel to the flow direction. A condition for the onset of air bubble entrainment may be expressed in terms of the tangential Reynolds stress and the fluid properties. With both singular and interfacial aeration, the void fraction distributions may be modelled by some analytical solutions of the advective diffusion equation for air bubbles.

The microscopic structure of turbulent bubbly flows is discussed based upon some developments in metrology and signal processing. The results may provide new information on the air–water flow structure and the turbulent eddies advecting the bubbles. However the interactions between entrained air bubbles and turbulence remain a key challenge for the 21st century researchers.

7.7 MATHEMATICAL AIDS

Definition	Expression	Remarks
Surface area of a spheroid (radii r_1, r_2)	$A = 2 * p * r_1^2 + p * \frac{r_2^2}{\sqrt{1 - \frac{r_2^2}{r_1^2}}} * \mathrm{Ln}\left(\frac{1 + \sqrt{1 - \frac{r_2^2}{r_1^2}}}{1 - \sqrt{1 - \frac{r_2^2}{r_1^2}}}\right)$	r_1: equatorial radius, r_2: polar radius. Oblate spheroid ($r_1 > r_2$).
	$A = 2 * p * r_1 * \left(r_1 + r_2 * \frac{\mathrm{Arcsin}\left(\sqrt{1 - \frac{r_1^2}{r_2^2}}\right)}{\sqrt{1 - \frac{r_1^1}{r_2^2}}}\right)$	Prolate spheroid ($r_1 < r_2$).
Bessel function of the first kind of order zero	$J_o(u) = 1 - \frac{u^2}{2^2} + \frac{u^4}{2^2 * 4^2} - \frac{u^6}{2^2 * 4^2 * 6^2} + \cdots$	also called modified Bessel function of the first kind of order zero.
Bessel function of the first kind of order one	$J_1(u) = \frac{u}{2} - \frac{u^3}{2^2 * 4} + \frac{u^5}{2^2 * 4^2 * 6} - \frac{u^7}{2^2 * 4^2 * 6^2 * 8} + \cdots$	
Gaussian error function	$\mathrm{erf}(u) = \frac{2}{\sqrt{p}} * \int_0^u \exp(-t^2) * dt$	also called error function.

APPENDIX—LIST OF SYMBOLS

List of Symbols

Symbol	Definition	Dimensions or Units
A	bubble surface area	$[L^2]$
C	void fraction defined as the volume of air per unit volume of air and water	
C_{mean}	depth-averaged void fraction	

(*Continued*)

List of Symbols

Symbol	Definition	Dimensions or Units
D'	ratio of air bubble diffusion coefficient to rise velocity component normal to the flow direction time the characteristic transverse dimension of the shear flow	
D_t	air bubble turbulent diffusion coefficient	$[L^2\ T^{-1}]$
D_0	dimensionless function of the void fraction	
$D^{\#}$	dimensionless air bubble turbulent diffusion coefficient	
F	air bubble count rate defined as the number of bubbles impacting the probe sensor per second	[Hz]
Fr_1	inflow Froude number of a hydraulic jump	
J_0	Bessel function of the first kind of order zero	
J_1	Bessel function of the first kind of order one	
K'	dimensionless integration constant	
L_{xy}	integral turbulent length scale	[L]
P	pressure	$[N\ L^{-2}]$
Q_{air}	entrained air flow rate	$[L^3 \cdot T^{-1}]$
Q_{water}	water discharge	$[L^3 \cdot T^{-1}]$
R_{xx}	normalized auto-correlation function	
R_{xy}	normalized cross-correlation function	
T	air–water interfacial travel time for which R_{xy} is maximum	[T]
T	transverse/streamwise turbulent integral time scale	[T]
$T_{0.5}$	characteristic time for which $R_{xx} = 0.5$	[T]
T_{xx}	auto-correlation integral time scale	[T]
T_{xy}	cross-correlation integral time scale	[T]
Tu	turbulence intensity	
V_e	onset velocity for air entrainment	$[m\ s^{-1}]$
V_x	streamwise velocity	$[m\ s^{-1}]$
V_y	transverse velocity	$[m\ s^{-1}]$
V_1	jet impact velocity or inflow velocity in the hydraulic jump	$[m\ s^{-1}]$
$\vec{V}$	advective velocity vector	$[m\ s^{-1}]$
Y_{90}	characteristic distance where $C = 0.90$	[L]
d_{ab}	air bubble diameter	[L]
d_1	jet thickness at impact or inflow depth in hydraulic jump	[L]
erf	Gaussian error function	
g	gravitational acceleration constant	$[L\ T^{-2}]$
r	radius of sphere	[L]
r_1	radius of curvature of the free surface deformation	[L]
r_2	radius of curvature of the free surface deformation	[L]
r_1	equatorial radius of the ellipsoid	[L]
r_2	polar radius of the ellipsoid	[L]
t	time	[T]
$\overrightarrow{u_r}$	bubble rise velocity vector	$[m \cdot s^{-1}]$
u_r	bubble rise velocity	$[m \cdot s^{-1}]$
u_r	bubble rise velocity in a hydrostatic pressure gradient	$[m \cdot s^{-1}]$
v_i	turbulent velocity fluctuation in the streamwise direction	$[m \cdot s^{-1}]$

(*Continued*)

List of Symbols

Symbol	Definition	Dimensions or Units
v_j	turbulent velocity fluctuation in the normal direction	$[m \cdot s^{-1}]$
x	longitudinal/streamwise direction	[L]
x_1	distance between the gate and the jump toe	[L]
y	transverse or radial direction	[L]
y′	dimensionless transverse or radial direction: $y' = y/Y_{90}$	
z	vertical direction positive upward	[L]
Δx	longitudinal distance between probe sensors	[L]
Δy	transverse distance between probe sensors	[L]
α_n	positive root for $J_0 = (Y_{90} * \alpha_n) = 0$	
θ	angle between the horizontal and the channel invert	
λ	dimensionless function of the mean air content	
μ_w	water dynamic viscosity	$[M\ L^{-1}\ T^{-1}]$
ρ_w	water density	$[kg\ m^{-3}]$
σ	surface tension between air and water	$[N\ m^{-1}]$
τ	time lag	[T]
$\tau_{0.5}$	time scale for which $R_{xy} = 0.5 * R_{xy}(T)$	[T]

REFERENCES

Brocchini, M. and Peregrine, D.H. (2001). "The Dynamics of Strong Turbulence at Free Surfaces. Part 1. Description." *Jl Fluid Mech.*, Vol. 449, pp. 225–254.

Cain, P. (1978). "Measurements within Self-Aerated Flow on a Large Spillway." *Ph.D. Thesis*, Ref. 78-18, Dept. of Civil Engrg., Univ. of Canterbury, Christchurch, New Zealand.

Carslaw, H.S. and Jaeger, J.C. (1959). "Conduction of Heat in Solids." *Oxford University Press*, London, UK, 2nd ed., 510 pages.

Chanson, H. (1988). "A Study of Air Entrainment and Aeration Devices on a Spillway Model." *Ph.D. thesis*, Ref. 88-8, Dept. of Civil Engrg., University of Canterbury, New Zealand.

Chanson, H. (1993). "Self-Aerated Flows on Chutes and Spillways." *Jl of Hyd. Engrg.*, ASCE, Vol. 119, No. 2, pp. 220–243. Discussion : Vol. 120, No. 6, pp. 778–782.

Chanson, H. (1997). "Air Bubble Entrainment in Free-Surface Turbulent Shear Flows." *Academic Press*, London, UK, 401 pages.

Comolet, R. (1979). "Vitesse d'Ascension d'une Bulle de Gaz Isolée dans un Liquide Peu Visqueux." ('The Terminal Velocity of a Gas Bubble in a Liquid of Very Low Viscosity.') *Jl de Mécanique Appliquée*, Vol. 3, No. 2, pp. 145–171 (in French).

Comolet, R. (1979). "Sur le Mouvement d'une bulle de gaz dans un liquide." ('Gas Bubble Motion in a Liquid Medium.') *Jl La Houille Blanche*, No. 1, pp. 31–42 (in French).

Crank, J. (1956). "The Mathematics of Diffusion." *Oxford University Press*, London, UK.

Cummings, P.D. and Chanson, H. (1999). "An Experimental Study of Individual Air Bubble Entrainment at a Planar Plunging Jet." *Chem. Eng. Research and Design*, Trans. IChemE, Part A, Vol. 77, No. A2, pp. 159–164.

Edwards, C.F. and Marx, K.D. (1995a). "Multipoint Statistical Structure of the Ideal Spray, Part I: Fundamental Concepts and the Realization Density." *Atomizati & Sprays*, Vol. 5, pp. 435–455.
Edwards, C.F. and Marx, K.D. (1995b). "Multipoint Statistical Structure of the Ideal Spray, Part II: Evaluating Steadiness using the Inter-particle Time Distribution." *Atomizati & Sprays*, Vol. 5, pp. 435–455.
Ervine, D.A. and Falvey, H.T. (1987). "Behaviour of Turbulent Water Jets in the Atmosphere and in Plunge Pools." *Proc. Instn Civ. Engrs., London*, Part 2, Mar. 1987, 83, pp. 295–314. Discussion: Part 2, Mar.–June 1988, 85, pp. 359–363.
Gonzalez, C.A. (2005). "An Experimental Study of Free-Surface Aeration on Embankment Stepped Chutes." *Ph.D. thesis*, Department of Civil Engineering, The University of Queensland, Brisbane, Australia, 240 pages.
Haberman, W.L. and Morton, R.K. (1954). "An Experimental Study of Bubbles Moving in Liquids." *Proceedings*, ASCE, 387, pp. 227–252.
Hayes, M.H. (1996). "Statistical, Digital Signal Processing and Modeling." *John Wiley*, New York, USA.
Hinze, J.O. (1955). "Fundamentals of the Hydrodynamic Mechanism of Splitting in Dispersion Processes." *Jl of AIChE*, Vol. 1, No. 3, pp. 289–295.
Murzyn, F., Mouaze, D. and Chaplin, J.R. (2005). "Optical Fibre Probe Measurements of Bubbly Flow in Hydraulic Jumps" *Intl Jl of Multiphase Flow*, Vol. 31, No. 1, pp. 141–154.
Toombes, L. (2002). "Experimental Study of Air–Water Flow Properties on Low-Gradient Stepped Cascades." *Ph.D. thesis*, Dept of Civil Engineering, The University of Queensland.
Wood, I.R. (1984). "Air Entrainment in High Speed Flows." *Proc. Intl. Symp. on Scale Effects in Modelling Hydraulic Structures*, IAHR, Esslingen, Germany, H. Kobus editor, paper 4.1.
Wood, I.R. (1991). "Air Entrainment in Free-Surface Flows." *IAHR Hydraulic Structures Design Manual No. 4*, Hydraulic Design Considerations, Balkema Publ., Rotterdam, The Netherlands, 149 pages.

Bibliography

Brattberg, T. and Chanson, H. (1998). "Air Entrapment and Air Bubble Dispersion at Two-Dimensional Plunging Water Jets." *Chemical Engineering Science*, Vol. 53, No. 24, Dec., pp. 4113–4127. Errata : 1999, Vol. 54, No. 12, p. 1925.
Brattberg, T., Chanson, H. and Toombes, L. (1998). "Experimental Investigations of Free-Surface Aeration in the Developing Flow of Two-Dimensional Water Jets." *Jl of Fluids Eng.*, Trans. ASME, Vol. 120, No. 4, pp. 738–744.
Brocchini, M. and Peregrine, D.H. (2001b). "The Dynamics of Strong Turbulence at Free Surfaces. Part 2. Free-surface Boundary Conditions." *Jl Fluid Mech.*, Vol. 449, pp. 255–290.
Carosi, G. and Chanson, H. (2006). "Air–Water Time and Length Scales in Skimming Flows on a Stepped Spillway. Application to the Spray Characterisation." *Report No. CH59/06*, Div. of Civil Engineering, The University of Queensland, Brisbane, Australia, July, 142 pages.
Cartellier, A. and Achard, J.L. (1991). "Local Phase Detection Probes in Fluid/Fluid Two-Phase Flows." *Rev. Sci. Instrum.*, Vol. 62, No. 2, pp. 279–303.
Chang, K.A., Lim, H.J. and Su, C.B. (2003). "Fiber Optic Reflectometer for Velocity and Fraction Ratio Measurements in Multiphase Flows." *Rev. Scientific Inst.*, Vol. 74, No. 7, pp. 3559–3565. Discussion & Closure: 2004, Vol. 75, No. 1, pp. 284–286.

Chanson, H. (1989). "Study of Air Entrainment and Aeration Devices." *Jl of Hyd. Res.*, IAHR, Vol. 27, No. 3, pp. 301–319.
Chanson, H. (2002a). "Air–Water Flow Measurements with Intrusive Phase-Detection Probes. Can we Improve their Interpretation?." *Jl of Hyd. Engrg.*, ASCE, Vol. 128, No. 3, pp. 252–255.
Chanson, H. (2002b). "An Experimental Study of Roman Dropshaft Operation: Hydraulics, Two-Phase Flow, Acoustics." *Report CH50/02*, Dept of Civil Eng., Univ. of Queensland, Brisbane, Australia, 99 pages.
Chanson, H. (2004a). "Environmental Hydraulics of Open Channel Flows." *Elsevier Butterworth-Heinemann*, Oxford, UK, 483 pages.
Chanson, H. (2004b). "Unsteady Air–Water Flow Measurements in Sudden Open Channel Flows." *Experiments in Fluids*, Vol. 37, No. 6, pp. 899–909.
Chanson, H. (2004). "Fiber Optic Reflectometer for Velocity and Fraction Ratio Measurements in Multiphase Flows. Letter to the Editor" *Rev. Scientific Inst.*, Vol. 75, No. 1, pp. 284–285.
Chanson, H. (2006). "Air Bubble Entrainment in Hydraulic Jumps. Similitude and Scale Effects." *Report No. CH57/05*, Dept. of Civil Engineering, The University of Queensland, Brisbane, Australia, Jan., 119 pages.
Chanson, H. (2007). "Bubbly Flow Structure in Hydraulic Jump." *European Journal of Mechanics B/Fluids*, Vol. 26, No. 3, pp. 367–384 (DOI:10.1016/j.euromechflu. 2006.08.001).
Chanson, H. (2007). "Air Entrainment Processes in Rectangular Dropshafts at Large Flows." *Journal of Hydraulic Research*, IAHR, Vol. 45, No. 1, pp. 42–53.
Chanson, H., Aoki, S. and Hoque, A. (2006). "Bubble Entrainment and Dispersion in Plunging Jet Flows: Freshwater versus Seawater." *Jl of Coastal Research*, Vol. 22, No. 3, May, pp. 664–677.
Chanson, H. and Carosi, G. (2007). "Turbulent Time and Length Scale Measurements in High-Velocity Open Channel Flows." *Experiments in Fluids*, Vol. 42, No. 3, pp. 385–401 (DOI 10.1007/s00348-006-0246-2).
Chanson, H. and Manasseh, R. (2003). "Air Entrainment Processes in a Circular Plunging Jet. Void Fraction and Acoustic Measurements." *Jl of Fluids Eng.*, Trans. ASME, Vol. 125, No. 5, Sept., pp. 910–921.
Chanson, H. and Toombes, L. (2002). "Air-Water Flows down Stepped chutes: Turbulence and Flow Structure Observations." *Intl Jl of Multiphase Flow*, Vol. 28, No. 11, pp. 1737–1761.
Crowe, C., Sommerfield, M. and Tsuji, Y. (1998). "Multiphase Flows with Droplets and Particles." *CRC Press*, Boca Raton, USA, 471 pages.
Cummings, P.D. (1996). "Aeration due to Breaking Waves." *Ph.D. Thesis*, Dept. of Civil Engrg., University of Queensland, Australia.
Cummings, P.D. and Chanson, H. (1997a). "Air Entrainment in the Developing Flow Region of Plunging Jets. Part 1 Theoretical Development." *Jl of Fluids Eng.*, Trans. ASME, Vol. 119, No. 3, pp. 597–602.
Cummings, P.D. and Chanson, H. (1997b). "Air Entrainment in the Developing Flow Region of Plunging Jets. Part 2: Experimental." *Jl of Fluids Eng.*, Trans. ASME, Vol. 119, No. 3, pp. 603–608.
Gonzalez, C.A. and Chanson, H. (2004). "Interactions between Cavity Flow and Main Stream Skimming Flows: an Experimental Study." *Can Jl of Civ. Eng.*, Vol. 31.
Gonzalez, C.A., Takahashi, M. and Chanson, H. (2005). "Effects of Step Roughness in Skimming Flows: an Experimental Study." *Research Report No. CE160*, Dept. of Civil Engineering, The University of Queensland, Brisbane, Australia, July, 149 pages.
Heinlein, J. and Frtisching, U. (2006). "Droplet Clustering in Sprays." *Experiments in Fluids*, Vol. 40, No. 3, pp. 464–472.

Jones, O.C. and Delhaye, J.M. (1976). "Transient and Statistical Measurement Techniques for two-Phase Flows: a Critical Review." *Intl Jl of Multiphase Flow*, Vol. 3, pp. 89–116.
Luong, J.T.K. and Sojka, P.E. (1999). "Unsteadiness in Effervescent Sprays." *Atomization & Sprays*, Vol. 9, pp. 87–109.
Noymer, P.D. (2000). "The Use of Single-Point Measurements to Characterise Dynamic Behaviours in Spray." *Experiments in Fluids*, Vol. 29, pp. 228–237.
Straub, L.G. and Anderson, A.G. (1958). "Experiments on Self-Aerated Flow in Open Channels." *Jl of Hyd. Div.*, Proc. ASCE, Vol. 84, No. HY7, paper 1890, pp. 1890-1 to 1890-35.
Toombes, L. and Chanson, H. (2007). "Surface Waves and Roughness in Self-Aerated Supercritical Flow." *Environmental Fluid Mechanics*, Vol. 5, No. 3, pp. 259–270 (DOI 10.1007/s10652-007-9022-y).
Wood, I.R. (1983). "Uniform Region of Self-Aerated Flow." *Jl Hyd. Eng.*, ASCE, Vol. 109, No. 3, pp. 447–461.

Internet resources

Chanson, H. (2000). "Self-aeration on chute and stepped spillways—Air entrainment and flow aeration in open channel flows." *Internet resource*.
(Internet address: http://www.uq.edu.au/~e2hchans/self_aer.html)
Chanson, H. and Manasseh, R. (2000). "Air Entrainment at a Circular Plunging Jet. Physical and Acoustic Characteristics—Internet Database." *Internet resource*.
(Internet address: http://www.uq.edu.au/~e2hchans/bubble/)
Cummings, P.D. and Chanson, H. (1997). "Air Entrainment in the Developing Flow Region of Plunging Jets. Extended Electronic Manuscript." *Jl of Fluids Engineering—Data Bank*, ASME (Electronic Files: 6,904 kBytes).
(Internet address: http://www.uq.edu.au/~e2hchans/data/jfe97.html)
Open access research reprints in air-water flows
(Internet address: http://espace.library.uq.edu.au/list.php?terms=chanson)
(Internet address: http://eprint.uq.edu.au/view/person/Chanson,_Hubert.html)

Part three
Processes at interfaces of biotic systems

CHAPTER EIGHT

Transport processes in the soil-vegetation-lower atmosphere system

Dragutin T. Mihailović
Faculty of Agriculture, University of Novi Sad, Novi Sad, Serbia

ABSTRACT

The interaction of the land surface and the atmosphere may be summarised as follows: interaction of vegetation with radiation, evaporation from bare soil, evapotranspiration which includes transpiration and evaporation of intercepted precipitation and dew, conduction of soil water through the vegetation layer, vertical movement in the soil, run-off, heat conduction in the soil, momentum transport, effects of snow presence and freezing or melting of soil moisture. Consequently, the processes parameterized in the land surface schemes can be divided into three parts: thermal and hydraulic processes, bare soil transfer processes and canopy transport processes. The chapter shortly describes these processes through a land surface scheme capturing the main processes in the soil-vegetation-lower atmosphere system. The biophysical processes in vegetation are elaborated using so-called "sandwich" representation where the vegetation is treated as a block of constant-density porous material "sandwiched" between two constant-stress layers with an upper boundary (the height of the canopy top) and a lower boundary (the height of the canopy bottom). For description of the transport processes in the soil, the three-soil layer approach is used. The chapter also includes a detailed description and explanation of governing equations, the representation of energy fluxes and radiation, the parameterization of aerodynamic characteristics, resistances and model hydrology. A special attention will be devoted to consideration of "K"-theory within and above canopy.

8.1 FOREWORD

The land surface is important in atmospheric modelling as it controls a number of key processes. The brightness of the surface (its albedo) determines how much of the incoming solar radiation is absorbed and how much is reflected. The total absorbed radiation is partitioned by the surface into land-atmosphere fluxes of heat and moisture, and a ground heat flux which may heat the soil or melt any lying snow. The nature of this partitioning affects the near surface conditions (for example, freely evaporating surfaces are cooler than dry surfaces) and also atmospheric processes such as cumulus convection. Surface flux partitioning is dependent on both the land cover and its hydrological state.

As experience with numerical modelling of atmospheric processes has progressed over the decades, the atmospheric modelling community has come to recognise that various aspects of the atmosphere–ecosystem–ocean system, which once were thought to play a relatively minor role, are actually very important in atmospheric circulations. Ecosystem, soil processes and their effect on the atmosphere are certainly in this category. Most mesoscale and global atmospheric models of 20 years ago either ignored or treated in an extremely simple manner interactions of the atmosphere with underlying soil and vegetated surfaces. Now,

field and modelling studies have demonstrated that these interactions are extremely important in both long-term climate simulations and short-term weather forecasting applications (Dickinson 1995; Pielke *et al.*, 1998). Moreover, recent numerical studies strongly suggest that land-use change may cause significant weather, climate, and ecosystem change (Chase *et al.*, 1998; Baron *et al.*, 1998; Stohlgren *et al.*, 1998; Pielke *et al.*, 1999). Because the role of these interactions has become recognised, parameterizations of vegetation and soil processes have progressively become more sophisticated over the years in order to treat the complexities of the physical system. Soil–vegetation–atmosphere transfer (SVAT) schemes employed in general circulation, mesoscale, and small-scale atmospheric numerical models have become increasingly sophisticated (Deardorff 1978; Avissar *et al.*, 1985; Dickinson *et al.*, 1986; Sellers *et al.*, 1986; Noilhan and Planton 1989; Mihailović *et al.*, 1993; Acs 1994; Bosilovich and Sun 1995; Viterbo and Beljaars 1995; Pleim and Xiu 1995; Cox *et al.*, 1999; Walko *et al.*, 2000; Mihailović *et al.*, 2004). Also, our ability to sense characteristics of the land surface remotely has improved dramatically, enabling much better data to be used as inputs to the more sophisticated parameterizations (Loveland *et al.*, 1991; Lee *et al.*, 1995).

The Land Air Parameterization Scheme (LAPS) is one such SVAT scheme that has been developed at University of Novi Sad to be a component of any environmental model for agricultural purposes. The current version of LAPS is a representation of surface features that include vegetation, soil, lakes and oceans, and their influence on each other and on the atmosphere. LAPS includes prognostic equations for soil temperature and moisture for multiple layers, vegetation temperature, and surface water including dew and intercepted rainfall, and temperature and water vapour mixing ratio of canopy air. Exchange terms in these prognostic equations include turbulent exchange, heat conduction, and water diffusion and percolation in the soil, long-wave and short-wave radiative transfer, transpiration, and precipitation. This chapter provides a description of the current version of LAPS.

8.2 SCHEME STRUCTURE AND BASIC EQUATIONS

The net radiation absorbed by the canopy and soil is assumed to be partitioned into sensible heat, latent heat, and storage terms, as

$$R_{ng} = \lambda E_g + H_g + C_g \frac{\partial T_g}{\partial t} \tag{8.1}$$

$$R_{nf} = \lambda E_f + H_f + C_f \frac{\partial T_f}{\partial t} \tag{8.2}$$

where R_n is absorbed net radiation [MT^{-3}], λ is latent heat of vaporisation [$\mathrm{L}^2\mathrm{T}^{-2}$], E is evapotranspiration rate [$\mathrm{ML}^{-2}\mathrm{T}^{-1}$], H is sensible heat flux [MT^{-3}], C is heat capacity [$\mathrm{M}\theta^{-1}\mathrm{T}^{-2}$], T is surface (canopy or soil) temperature [θ]. The subscripts f, g refer to the canopy and soil respectively. The deep soil temperature [θ], T_d, is calculated from the equation (Mihailović *et al.*, 1999)

$$R_{ng} = \lambda E_g + H_g + \sqrt{365\pi}\frac{C_g}{2}\frac{\partial T_d}{\partial t} \tag{8.3}$$

The prognostic equations for the water stored on the canopy [L], w_f, is

$$\frac{\partial w_f}{\partial t} = P_f - E_{wf}/\rho \tag{8.4}$$

where ρ is water density [ML^{-3}], P_f is water amount retained on the canopy [LT^{-1}], E_{wf} the evaporation rate of water from the wetted fraction of canopy [$ML^{-2}T^{-1}$]. When the conditions for dew formation are satisfied, the condensed moisture is added to the interception store, w_f. The parameterization of the soil content is based on the concept of the three-layer model (Mihailović, 1996). The governing equations take the form

$$\frac{\partial \vartheta_1}{\partial t} = \frac{1}{D_1}\left\{P_1 - F_{1,2} - \frac{E_g + E_{tf,1}}{\rho} - R_0 - R_1\right\} \tag{8.5}$$

$$\frac{\partial \vartheta_2}{\partial t} = \frac{1}{D_2}\left\{F_{1,2} - F_{2,3} - \frac{E_{tf,2}}{\rho} - R_2\right\} \tag{8.6}$$

$$\frac{\partial \vartheta_3}{\partial t} = \frac{1}{D_3}\{F_{2,3} - F_3 - R_3\} \tag{8.7}$$

where ϑ_i is volumetric soil water content [L^3L^{-3}] in the ith layer, P_1 is infiltration rate of precipitation into the upper soil moisture store [LT^{-1}]; D_i is thickness of the ith soil layer [L], $F_{i,i+1}$ is water flux between i and $i+1$ soil layer [LT^{-1}], F_3 is gravitational drainage flux from recharge soil water store [LT^{-1}], $E_{tf,1}$ and $E_{tf,2}$ are canopy extraction of soil moisture by transpiration from the rooted first and second soil layers [$ML^{-2}T^{-1}$] respectively; R_0 is surface run-off [LT^{-1}]; and R_i is subsurface run-off from the ith soil layer [LT^{-1}].

Eqs. (8.1)–(8.3) are solved using an implicit backward method, i.e.,

$$T_g^{n+1} = T_g^n + \frac{\Gamma_f^n\left(\frac{\partial \Gamma_g}{\partial T_f}\right)^n + \Gamma_g^n\left[\frac{C_f}{\Delta t} - \left(\frac{\partial \Gamma_f}{\partial T_f}\right)^n\right]}{\left(\frac{\partial \Gamma_f}{\partial T_g}\right)^n\left(\frac{\partial \Gamma_g}{\partial T_f}\right)^n - \left[\frac{C_f}{\Delta t} - \left(\frac{\partial \Gamma_f}{\partial T_f}\right)^n\right]\left[\frac{C_g}{\Delta t} - \left(\frac{\partial \Gamma_g}{\partial T_g}\right)^n\right]} \tag{8.8}$$

$$T_f^{n+1} = T_f^n + \frac{\Gamma_g^n\left(\frac{\partial \Gamma_g}{\partial T_f}\right)^n + \Gamma_f^n\left[\frac{C_g}{\Delta t} - \left(\frac{\partial \Gamma_g}{\partial T_g}\right)^n\right]}{\left(\frac{\partial \Gamma_f}{\partial T_g}\right)^n\left(\frac{\partial \Gamma_g}{\partial T_f}\right)^n - \left[\frac{C_f}{\Delta t} - \left(\frac{\partial \Gamma_f}{\partial T_f}\right)^n\right]\left[\frac{C_g}{\Delta t} - \left(\frac{\partial \Gamma_g}{\partial T_g}\right)^n\right]} \tag{8.9}$$

$$T_d^{n+1} = T_d^n + \frac{\Gamma_g}{\frac{\sqrt{365\pi}}{2\Delta t}C_g - \left(\frac{\partial \Gamma_g}{\partial T_d}\right)} \tag{8.10}$$

where: $\Gamma_f = R_{nf} - \lambda E_f - H_f$, $\Gamma_g = R_{ng} - \lambda E_g - H_g$, and Δt is time step. Eqs. (8.4)–(8.6) are solved using an explicit time scheme.

8.3 REPRESENTATION OF ENERGY FLUXES

Our treatment of the energy fluxes may be classified as the so-called "resistance" representation. Schematic diagram of the Land–Air Parameterization Scheme (LAPS) is shown in Fig. 8.1. The transfer pathways for latent sensible heat fluxes are shown on the left- and right-hand sides of the diagram respectively. The fluxes of sensible and latent heat from

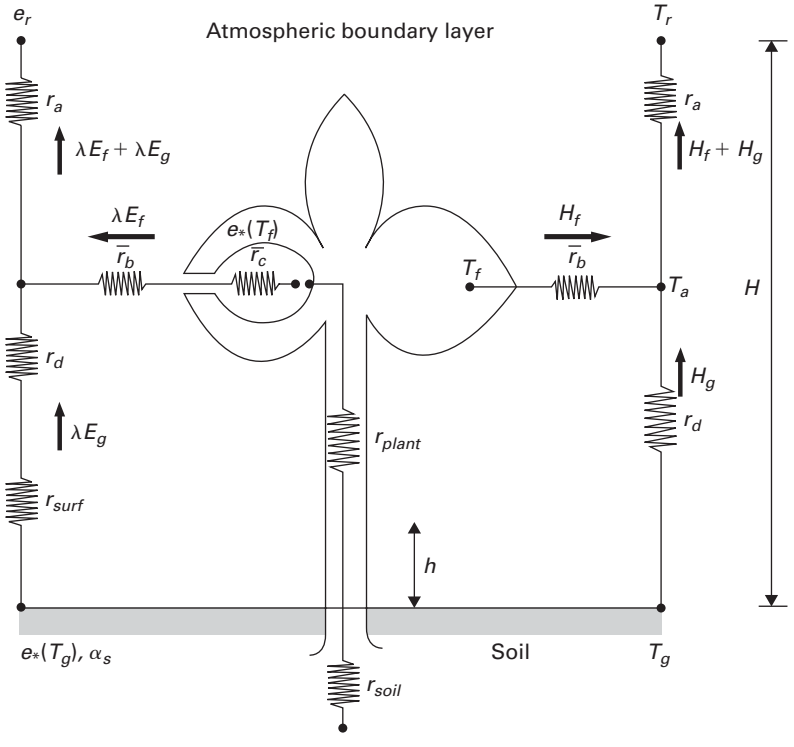

Figure 8.1. Schematic diagram of the Land–Air Parameterization Scheme (LAPS). The transfer pathways for latent sensible heat fluxes are shown on the left- and right-hand sides of the diagram respectively.

the soil and canopy are represented by electrical analogue models in which the fluxes are proportional to potential differences (in temperature or vapour pressure) and inversely proportional to resistances, which are equivalent to the inverse integrals of conductances over a specified length scale. The fluxes in Eqs. (8.1)–(8.3) are parameterized as follows.

The latent heat flux from canopy vegetation to canopy air space is given by

$$\lambda E_f = \frac{\rho_p c_p}{\gamma}[e_*(T_f) - e_a]\left(\frac{w_w}{\bar{r}_b} + \frac{1 - w_w}{\bar{r}_b + \bar{r}_c}\right), \tag{8.11}$$

where ρ_p, c_p are the density and specific heat of air $[\mathrm{ML}^{-3}, \mathrm{L}^2\mathrm{T}^{-2}\theta^{-1}]$, γ is the psychrometric constant $\times 10^2$ $[\mathrm{ML}^{-1}\mathrm{T}^{-2}\theta^{-1}]$, $e_*(T_f)$ is saturated vapour pressure at temperature $T_f \times 10^2 [\mathrm{ML}^{-1}\mathrm{T}^{-2}]$; e_a is canopy air space vapour pressure $[\mathrm{ML}^{-1}\mathrm{T}^{-2}]$, w_w is wetted fraction of canopy, $\bar{r}_b$ is bulk canopy boundary layer resistance $[\mathrm{TL}^{-1}]$ and $\bar{r}_c$ is bulk canopy stomatal resistance $[\mathrm{TL}^{-1}]$.

The evaporation rate E_{wf} from the wetted portion of canopy, with wetted fractions denoted by $w_w$according to Eq. (8.11) is

$$\lambda E_{wf} = \frac{\rho_p c_p}{\gamma}[e_*(T_f) - e_a]\frac{w_w}{\bar{r}_b}. \tag{8.12}$$

The fraction of the foliage that is wet, w_w, is parameterized according to Deardorff (1978). Transpiration occurs only from dry leaf and it is only outwards. This physiological process is parameterized with the equation

$$\lambda E_{tf} = \frac{\rho_p c_p}{\gamma}[e_*(T_f) - e_a]\frac{1 - w_w}{\overline{r}_b + \overline{r}_c} \tag{8.13}$$

where E_{tf} is the transpiration rate from foliage [$ML^{-2}T^{-1}$]. Dew formation occurs when $e_*(T_f) \leq e_a$. In that case the condensed moisture is added to the surface interception store, w_f. The transpiration rate is zero under this condition.

The latent heat flux from soil surface is parameterized as

$$\lambda E_g = \frac{\rho_p c_p}{\gamma}\frac{\alpha_s e_*(T_g) - e_a}{r_{surf} + r_d}(1 - \sigma_c) \tag{8.14}$$

where α_s is a factor to correct for soil dryness (Mihailović *et al.*, 1995), $e_*(T_g)$ is saturated vapour pressure at temperature T_g [$ML^{-1}T^{-2}$]; r_{surf} is soil surface resistance [TL^{-1}], r_d is aerodynamic resistance between soil surface and canopy air space [TL^{-1}], and σ_c is vegetation cover in fractional units.

The sensible heat fluxes from canopy, H_f, and soil surface H_g are parameterized as

$$H_f = \frac{2(T_f - T_a)}{\overline{r}_b}\rho_p c_p \tag{8.15}$$

$$H_g = \frac{(T_g - T_a)}{r_d}\rho_p c_p \tag{8.16}$$

where T_a is canopy air space temperature [θ].

Air within the canopy has negligible heat capacity, so the sensible heat flux from the canopy, H_f, and from the soil surface, H_g, must be balanced by the sensible heat flux to the atmosphere, H_t

$$H_t = H_g + H_f = \frac{(T_a - T_r)}{r_a}\rho_p c_p \tag{8.17}$$

where r_a is aerodynamic resistance [TL^{-1}], and T_r is air temperature at the reference height z_r[θ]. Similarly the canopy air is assumed to have zero capacity for water storage so that the latent heat flux from canopy air space to reference height in the atmospheric boundary layer, λE_t, balances the latent heat flux from canopy vegetation to canopy air space, λE_f, and the latent heat flux from soil surface to the canopy air space, λE_g

$$\lambda E_t = \lambda E_g + \lambda E_f = \frac{\rho_p c_p}{\gamma}\frac{(e_a - e_r)}{r_a} \tag{8.18}$$

where e_r is vapour pressure of the air at reference height [$ML^{-1}T^{-2}$] within the atmospheric boundary layer. The canopy air space temperature, T_a, and canopy air space vapour pressure,

e_a, are determined diagnostically from Eqs. (8.17) and (8.18), i.e.,

$$T_a = \frac{\dfrac{2T_f}{\bar{r}_b} + \dfrac{T_g}{r_d} + \dfrac{T_r}{r_a}}{\dfrac{2}{\bar{r}_b} + \dfrac{1}{r_d} + \dfrac{1}{r_a}} \tag{8.19}$$

and

$$e_a = \frac{\dfrac{1}{r_a} + \dfrac{\alpha_s e_*(T_g)(1-\sigma_c)}{r_{surf} + r_d} + e_*(T_f)\left[\dfrac{w_w}{\bar{r}_b} + \dfrac{1-w_w}{\bar{r}_b + \bar{r}_c}\right]}{\dfrac{1}{r_a} + \dfrac{1-\sigma_c}{r_{surf} + r_d} + \left[\dfrac{w_w}{\bar{r}_b} + \dfrac{1-w_w}{\bar{r}_b + \bar{r}_c}\right]} \tag{8.20}$$

8.4 PARAMETERIZATION OF RADIATION

The net radiation absorbed by the canopy, R_{nf}, and the soil surface, R_{ng}, [MT^{-3}] is calculated as a sum of short- and long wave radiative flux,

$$R_{nf} = R_f^s + R_f^l \tag{8.21}$$

and

$$R_{ng} = R_g^s + R_g^l \tag{8.22}$$

The short-wave radiation absorbed by the canopy, R_f^s, and the soil surface, R_g^s, [MT^{-3}] is

$$R_f^s = R_o^s(\sigma_f - \alpha_f)[1 + (1-\sigma_f)\alpha_g] \tag{8.23}$$

and

$$R_g^s = R_o^s(1-\sigma_f)(1 + \alpha_g + \alpha_f\alpha_g) \tag{8.24}$$

where R_o^s is incident downward-directed short-wave flux [MT^{-3}], assumed to be known as the forcing variable, σ_f is the fractional cover of vegetation and α_g and α_f are soil-surface albedo and canopy albedo respectively. The variability of ground albedo with soil wetness is parameterized in accordance with Idso *et al.* (1975). There is no distinction between direct and diffuse radiation and it is assumed that albedo does not vary with zenith angle. Both short-wave and long-wave radiation are reflected once between the soil surface and canopy.

The long-wave radiative fluxes absorbed by the canopy, R_f^l, and the soil surface, R_g^l, [MT^{-3}] are

$$R_f^l = R_o^l\sigma_f\varepsilon_f - 2\sigma_f\varepsilon_f\sigma_B + \sigma_f\varepsilon_f[R_o^l\sigma_B(1-\varepsilon_f)T_f^4 + \varepsilon_g\sigma_B T_g^4] \tag{8.25}$$

and

$$R_g^l = \varepsilon_g[R_o^l(1-\sigma_f) + \varepsilon_f\sigma_f\sigma_B T_f^4 + \sigma_f\varepsilon_g(1-\varepsilon_f)\sigma_B T_g^4 - \sigma_B T_g^4] \tag{8.26}$$

where σ_B is the Stefan-Boltzman constant [$MT^{-3}\theta^{-4}$], ε_f and ε_g are emissivities of the canopy and the soil surface respectively, and R_o^l the incident downward long-wave radiation prescribed as the forcing variable.

8.5 PARAMETERIZATION OF RESISTANCES

8.5.1 Aerodynamic resistances

The aerodynamic resistances r_a, r_b and r_d are described as

$$r_a = \int_{h_a}^{H} \frac{1}{K_s} dz + \int_{H}^{z_r} \frac{1}{K_s} dz, \tag{8.27}$$

$$r_d = \int_{z_g}^{h} \frac{1}{K_s} dz + \int_{h}^{h_a} \frac{1}{K_s} dz, \tag{8.28}$$

$$\frac{1}{\overline{r}_b} = \int_{h_a}^{H} \frac{\overline{L}_d\sqrt{u(z)}}{C_s P_s} dz, \tag{8.29}$$

where H is the canopy height [L]; K_s is turbulent transfer coefficient within and above the canopy [L^2T^{-1}] in the intervals (h_a, H) and (H, z_r) respectively; z_g is effective ground roughness length [L]; h[L] is the canopy bottom height (the height of the base of the canopy, see Fig. 8.2); $\overline{L}_d$ is the area-averaged stem and leaf area density (also called canopy density), which is related to leaf area index (LAI) as $LAI = \overline{L}_d(H-h)$; $u(h)$ is the wind speed; C_s the transfer coefficient [$L^{-1/2}T^{1/2}$] and P_s the leaf shelter factor. According to Sellers *et al.* (1986), the position of the canopy source height, h_a, can be estimated by obtaining the centre of gravity of the $1/\overline{r}_b$ integral. Thus,

$$\int_{h}^{h_a} \frac{\overline{L}_d}{r_b} dz = \int_{h_a}^{H} \frac{\overline{L}_d}{r_b} dz = \frac{1}{2}\int_{h}^{H} \frac{\overline{L}_d}{r_b} dz = \frac{1}{2\overline{r}_b}. \tag{8.30}$$

We may obtain h_a by successive estimations until the foregoing equality is reached.

The wind speed above the canopy $u(z)$ is considered as

$$u(z) = \frac{u_*}{\kappa}\left[\ln\frac{z-d}{z_0} - \psi_m(z/L)\right], \tag{8.31}$$

where u_* is friction velocity [LT^{-1}]; κ is the von Karman constant, z_0 roughness length over the non-vegetated surface, $\psi_m(z/L)$ the stability function for momentum and L

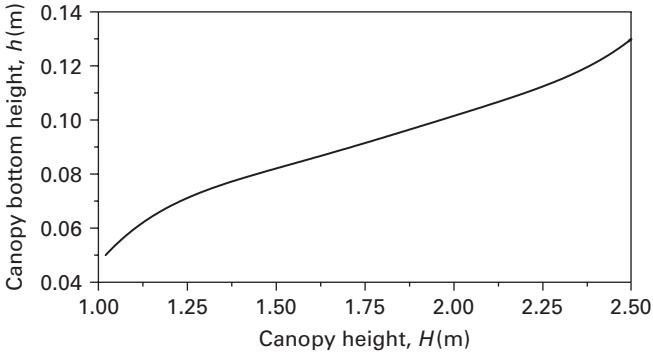

Figure 8.2. Calculated values of the canopy bottom height (h) as a function of the canopy height (H) for tall grass vegetation. The fitting curve is drawn using data from Dubov *et al.* (1978), Sellers and Dorman (1987), Mihailović and Kallos (1997), and Mihailović *et al.* (2000).

Monin-Obuhkov length. The function $\psi_m(z/L)$ is given for stable conditions ($z/L > 0$) by $4.7z/L$ and for unstable ($z/L < 0$) by

$$\psi_m(z/L) = -2\ln\left[\frac{(1+x)}{2}\right] - \ln\left[\frac{(1+x^2)}{2}\right] + 2\tan^{-1}(x) - \frac{\pi}{2} \tag{8.32}$$

where $x = [1 - 15z/L]^{1/4}$ (Paulson, 1970). For wind profile within short- and tall-grass canopies we used a form that approximates the wind profile within the tall-grass canopy fairly well (Brunet *et al.*, 1994; Mihailović *et al.*, 2004), i.e.,

$$u(z) = u(H)\exp\left[-\frac{1}{2}\beta\left(1 - \frac{z}{H}\right)\right], \tag{8.33}$$

where $u(H)$ is the wind speed at the canopy height [LT^{-1}]; and β is extinction parameter defined as

$$\beta^2 = \frac{2C_d\overline{L}_d(H-h)H}{\sigma}. \tag{8.34}$$

According to Mihailović *et al.* (2004), the value of the scaling length, σ, is defined as

$$\sigma = \frac{2C_{dg}^2 H}{C_d\overline{L}_d(H-h)}, \tag{8.35}$$

where C_{dg} is the leaf drag coefficient estimated from the size of the roughness elements of the ground (Sellers *et al.*, 1986), i.e.,

$$C_{dg} = \frac{\kappa^2}{\left[\ln\dfrac{h}{z_g}\right]^2}. \tag{8.36}$$

In Eq. (8.23) z_g is the effective roughness length. Beneath the canopy bottom height the wind speed follows a classical logarithmic profile in the form

$$u(z) = \frac{u(H)\exp\left[-\frac{1}{2}\beta\left(1-\frac{h}{H}\right)\right]}{\ln\frac{h}{z_g}}\ln\frac{z}{z_g}. \tag{8.37}$$

Bearing in mind the aforementioned parameterization, the three aerodynamic resistances, r_a, r_b, and r_d, and the canopy bottom height h_a are calculated following Mihailović *et al.* (2004)

$$r_a = \frac{1}{u_*}\left\{\frac{2\kappa H}{\sigma\beta\ln\frac{H-d}{z_0}}\left[\exp\left[\frac{1}{2}\beta\left(1-\frac{h_a}{H}\right)\right]-1\right]+\frac{1}{k}\ln\frac{z_r-d}{H-d}\right\}, \tag{8.38}$$

$$r_b = \frac{1}{\sqrt{u_*}}\frac{\beta C_s P_s\sqrt{k}}{4H\overline{L}_d\sqrt{\ln\frac{H-d}{z_0}}\left[1-\exp\left[-\frac{1}{4}\beta\left(1-\frac{h_a}{H}\right)\right]\right]}, \tag{8.39}$$

$$r_d = \frac{1}{u_*}\left\{\frac{2\kappa H}{\sigma\beta\ln\frac{H-d}{z_0}}\left[\exp\left[\frac{1}{2}\beta\left(1-\frac{h}{H}\right)\right]-\exp\left[\frac{1}{2}\beta\left(1-\frac{h_a}{H}\right)\right]-1\right]+\frac{\exp\left[\frac{1}{2}\beta\left(1-\frac{h}{H}\right)\right]}{\kappa\ln\frac{H-d}{z_0}}\ln^2\frac{h}{z_g}\right\}, \tag{8.40}$$

$$h_a = H\left\{1+\frac{4}{\beta}\ln\frac{1+2\exp\left[-\frac{1}{4}\beta\left(1-\frac{h}{H}\right)\right]}{3}\right\}. \tag{8.41}$$

For the forest canopy the wind profile is calculated from the differential equation (Mihailović *et al.*, 2004)

$$\frac{d}{dz}\left(K_s\frac{du}{dz}\right) = \sigma_c\frac{C_d\overline{L}_d(H-h)}{H}u^2 \tag{8.42}$$

describing the wind profile within a canopy architecture that is considered as a block of constant-density porous material placed between two heights, H and h (Sellers *et al.*, 1986; Mihailović and Kallos 1997). In this equation z is the vertical coordinate. In the case of dense vegetation ($\sigma_c = 1$), Eq. (8.42) reduces to the well-known equation for the dense vegetation. Otherwise, when $\sigma_c = 0$, Eq. (8.42) leads, by a proper choice of integration constant, to the wind profile over a bare soil. We can use Eq. (8.42) for calculating the wind speed within a vegetation canopy after we assume a functional form of K_s as it usually done. However, inadequacy of this approach lies in the fact that the behaviour of K_s must be given *a priori*, i.e. presupposed by experience (Mihailović *et al.*, 2006). After taking the derivative of Eq. (8.42) over z, we obtain a differential equation of the first order and first degree, where K_s is an unknown function, i.e.,

$$\frac{du}{dz}\frac{dK_s}{dz} + \frac{d^2u}{dz^2}K_s = \sigma_c \frac{C_d \overline{L}_d (H-h)}{H} u^2. \tag{8.43}$$

Solution to this equation can be found if the wind speed is treated as a linear combination of two terms, expressing behaviour of the wind speed over dense and sparse vegetation. Thus,

$$u(z) = \sigma_c u(H) \exp\left[-\frac{1}{2}\alpha\left(1 - \frac{z}{H}\right)\right] + (1-\sigma_c)\frac{u_*}{\kappa}\left[\ln\frac{z}{z_b} - \psi_m(z/L)\right], \tag{8.44}$$

where α is an unknown constant to be determined, $u(H)$ the wind speed at the canopy height, u_* the friction velocity, k the von Karman constant, z_b the roughness length over the non-vegetated surface, $\psi_m(z/L)$ the stability function and L Monin-Obuhkov length (Paulson, 1970). The function $\psi_m(z/L)$ is given for stable conditions ($z/L > 0$) by $\psi_m(z/L) = 4.7z/L$ and for unstable ($z/L < 0$) by

$$\psi_m(z/L) = -2\ln\left[\frac{(1+x)}{2}\right] - \ln\left[\frac{\left(1+x^2\right)}{2}\right] + 2\tan^{-1}(x) - \frac{\pi}{2} \tag{8.45}$$

where $x = [1 - 15z/L]^{1/4}$. The first term in the expression (8.44) is used to approximate the wind profile within the vegetation canopy (Brunet *et al.*, 1994; Mihailović *et al.*, 2004), while the second term simulates the shape of wind profile above bare soil. After we introduce (8.44) into Eq. (8.43), and rearrange, we reach

$$\frac{dK_m}{dz} + a(z)K_m = b(z), \tag{8.46}$$

where

$$a(z) = \frac{\frac{1}{4H^2}\alpha^2\sigma_c u(H) e^{-\frac{1}{2}\alpha\left(1-\frac{z}{h_c}\right)} + (1-\sigma_c)\frac{u_*}{\kappa}\left[-\frac{1}{z^2} + \psi_m''(z/L)\right]}{\frac{1}{2H}\alpha\sigma_c u(H) e^{-\frac{1}{2}\alpha\left(1-\frac{z}{h_c}\right)} + (1-\sigma_c)\frac{u_*}{\kappa}\left[\frac{1}{z} + \psi_m'(z/L)\right]} \tag{8.47}$$

and

$$b(z) = \left[\sigma_c u(H) e^{-\frac{1}{2}\alpha\left(1-\frac{z}{h_c}\right)} + (1-\sigma_c)\frac{u_*}{\kappa}\left[\ln\frac{z}{z_b} + \psi_m(z/L)\right]\right]^2 \times \frac{\sigma_c \dfrac{C_d \overline{L}_d (H-h)}{H}}{\dfrac{1}{2H}\alpha\sigma_c u(H) e^{-\frac{1}{2}\alpha\left(1-\frac{z}{h_c}\right)} + (1-\sigma_c)\dfrac{u_*}{\kappa}\left[\dfrac{1}{z} + \psi_m'(z/L)\right]}, \tag{8.48}$$

with $\psi_m'(z/L) = d\psi_m(z/L)/dz$ and $\psi_m''(z/L) = d^2\psi_m(z/L)/dz^2$.

It is interesting to analyse the nature of the solution, K_s, of the Eq. (8.46) with the initial condition defined as $K_s(z_1) = K_s^0 > 0$, where z_1 is some certain height within the canopy: (i) the solution is unique and defined over the interval $[z_1, \infty)$, that follows from the fact that the functions $a(z)$ and $b(z)$ are defined and continuous over the interval indicated; (ii) the solution is positive, that comes from the analysis of the field of directions of the given equation or more precisely due to $b(z) > 0$ and (iii) the solution is stable that can be seen from the following analysis. When $z \to \infty$ we have $a(z) \approx \alpha/(2H)$ and $b(z) \approx B\exp[\alpha z/(2H)]$. Now, Eq. (8.46) takes the form

$$\frac{dK_c}{dz} + \frac{\alpha}{2H}K_c = Be^{\frac{\alpha z}{2h_c}}, \tag{8.49}$$

where

$$B = \frac{2\sigma_c^2 u^2(H) C_d \overline{L}_d (H-h)}{\alpha H}. \tag{8.50}$$

The particular solution of this equation has the form $A\exp[\alpha z/(2H)]$, where A is a constant, which can be obtained after substituting the particular solution in Eq. (8.49). If we follow this procedure we get $A = BH/\alpha$. So, in this case, i.e., $z \to \infty$, the solution of Eq. (8.49) is asymptotically stable, it behaves as $A\exp[\alpha z/(2H)]$ for any given A. For the fixed α, Eq. (8.49) can be solved using the finite-difference scheme

$$K_m^{n-1} = K_m^n - \Delta z\left\{b^n(z) - a^n(z)K_m^n\right\}, \tag{8.51}$$

where n is the number of the spatial step in the numerical calculating on the interval $[H, h]$, while Δz is the grid size defined as $\Delta z = (H-h)/N$, where N is a number indicating an upper limit in number of grid size used. The calculation of the turbulent transfer coefficient for momentum starts from the canopy top with a boundary condition defined as

$$K_s^N(h_c) = \kappa^2 u(h_c)\left[\frac{\sigma_c(h_c-d)}{\ln\dfrac{h_c-d}{z_0}} + \frac{(1-\sigma_c)h_c}{\ln\dfrac{h_c}{z_b}}\right] \tag{8.52}$$

where d is the displacement height while z_0 is the canopy roughness length calculated according to Mihailović *et al.* (1999). The procedure then goes backwards down to the

canopy bottom height, h, which is defined according to Mihailović *et al.* (2004). To obtain parameter α we use an iterative procedure that does not end until the condition

$$\left| \sum_{i=1}^{N} u_i^{m+1} - \sum_{i=1}^{N} u_i^{m} \right| < \mu \tag{8.53}$$

is reached, where m is a number of iteration while μ is less then 0.001. Having this parameter we can calculate the wind profile on the interval $[H, h]$ according to Eq. (8.43). Beneath the canopy bottom height, the wind profile has the logarithmic shape (Sellers *et al.*, 1986; Mihailović *et al.*, 2004), i.e.,

$$u(z) = u(H) \left[\frac{\sigma_c e^{-\frac{1}{2}\alpha\left(1-\frac{h}{H}\right)}}{\ln \dfrac{h}{z_b}} + \frac{1-\sigma_c}{\ln \dfrac{H}{z_b}} \right] \ln \frac{z}{z_b}. \tag{8.54}$$

8.5.2 Surface, root and plant resistances

The resistances to the transport of water vapour from within the canopy and upper soil layer to the adjacent exterior air are defined as the bulk canopy stomatal resistance, $\bar{r}_c$, and soil surface resistance, r_{surf}, respectively. Combining dependence of $\bar{r}_c$ on solar radiation, air temperature, atmospheric water vapour pressure deficit and water stress (Jarvis, 1976; Dickinson *et al.*, 1986) is parameterized as

$$\bar{r}_c = \frac{r_{s\,min}}{LAI} \frac{1 + \dfrac{1.1\langle F_f \rangle}{R_0 LAI}}{\dfrac{1.1\langle F_f \rangle}{R_0 LAI} + \dfrac{r_{s\,min}}{r_{s\,max}}} [1.0 - 0.0016(298 - T_r)^2]^{-1}$$

$$\{1 - \eta[e_*(T_f) - e_r]\}^{-1} \Phi_2^{-1} \tag{8.55}$$

where $r_{s\,min}$, $r_{s\,max}$ are the minimum and maximum of stomatal resistance [TL^{-1}]; R_0 is limit value of 100 [MT^{-3}] for canopies; and η the canopy-dependent empirical parameter that is equal to 0.025×10^2[$\mathrm{M}^{-1}\mathrm{LT}^2$]. In this model the value of 5000 [TL^{-1}] for r_{smax} is used. The factor Φ_2 takes into account the effect of water stress on the stomatal resistance and is parameterized following Mihailović and Kallos (1997), i.e.

$$\Phi_2 = \begin{cases} 1 & \vartheta_a > \vartheta_{fc} \\ 1 - \left(\dfrac{\vartheta_{wil}}{\vartheta_a} \right)^{1.5} & \vartheta_{wil} \le \vartheta_a \le \vartheta_{fc} \\ 0 & \vartheta_a < \vartheta_{wil} \end{cases} \tag{8.56}$$

where ϑ_a is the mean volumetric soil water content in the first and second soil layers [$\mathrm{L}^3\mathrm{L}^{-3}$]; ϑ_{wil} is volumetric soil water content at wilting point [$\mathrm{L}^3\mathrm{L}^{-3}$]; and ϑ_{fc} volumetric soil water content at field capacity [$\mathrm{L}^3\mathrm{L}^{-3}$].

The soil surface resistance, r_{surf}, is parameterized using the empirical expression given by Sun (1982), i.e.,

$$r_{surf} = d_1 + d_2\langle\vartheta_1\rangle^{-d_3} \tag{8.57}$$

where d_1, d_2 [TL^{-1}] and d_3 are empirical constants (Mihailović, 2003) , while ϑ_1 is the top layer volumetric soil water content [L^3L^{-3}].

The leaf water potential ψ_l [L] describing the water transfer pathway from root zone to leaf is calculated following Van der Honert (1948),

$$\psi_l = \frac{\psi_r - z_t - E_{tf}(r_{plant} + r_{soil})}{\rho} \tag{8.58}$$

where ψ_r is soil moisture potential in the root zone [L], z_t is height of the transpiration source [L] that is equal to canopy source height, r_{plant} is plant resistance [T] imposed by the plant vascular system prescribed as a variable (Mihailović, 2003), r_{soil} is resistance of the soil and root system [T], and ρ is water density [ML^{-3}].

The soil water potential in the root zone, ψ_r, is parameterized as an average term obtained by summing the weighted soil water potentials of the soil layers from the surface to the rooting depth [L], z_d, i.e.

$$\psi_r = \frac{\sum_0^{z_d} \psi_i D_i}{z_d} \tag{8.59}$$

where ψ_i is soil water potential of the ith soil layer [L]. The soil water potential [L], ψ_i, is parameterised as it is usually done, after Clapp and Hornberger (1978),

$$\psi_i = \psi_s \left(\frac{\vartheta_i}{\vartheta_s}\right)^{-B} \tag{8.60}$$

where ψ_s is soil water potential at saturation [L], ϑ_i is volumetric soil moisture content of the ith soil layer [L^3L^{-3}], ϑ_s is its value at saturation while B is soil type constant. The depth-averaged resistance r_{soil} to water flow from soil to roots, is parameterized according to Federer (1979)

$$r_{soil} = z_d \left(\frac{R_r}{D_d} + \frac{\alpha_j}{K_r}\right) \tag{8.61}$$

where α_j is parameterized as

$$\alpha_j = \frac{\left\{V_r - 3 - 2\ln\left[\frac{V_r}{1 - V_r}\right]\right\}}{8\pi D_d} \tag{8.62}$$

where R_r is resistance per unit root length [TL^{-1}], D_d is root density [L^3L^{-3}], V_r is volume of root per unit volume of soil [L^3L^{-3}], and K_r is mean soil hydraulic conductivity in the

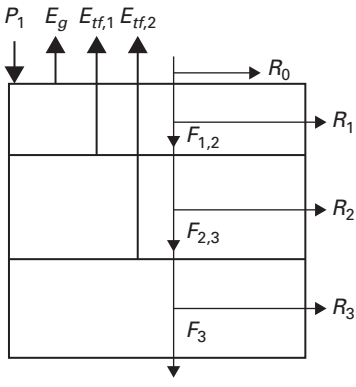

Figure 8.3. Schematic diagram of hydrology in the Land–Air Parameterization Scheme (LAPS).

root zone [LT^{-1}] expressed as function of ψ_r

$$K_r = K_c \left(\frac{\psi_s}{\psi_r} \right)^{\frac{2B+3}{B}} \tag{8.63}$$

where K_c is saturated hydraulic conductivity [LT^{-1}].

8.6 PARAMETERIZATION OF HYDROLOGY

Moving from top to bottom of the soil water column, the LAPS has the three layers (Fig. 8.3). The governing equations for the three volumetric soil moisture content are given by Eqs. (8.5)–(8.7). The precipitation P_1 that infiltrates into the top soil layer is given by

$$P_1 = \begin{cases} min(P_0, K_s) & \vartheta_1 < \vartheta_s \\ 0 & \vartheta_1 < \vartheta_s \end{cases} \tag{8.64}$$

where P_0 is effective precipitation rate [LT^{-1}] on the soil surface given by

$$P_0 = P - (P_f - D_f), \tag{8.65}$$

P is precipitation rate above the canopy [LT^{-1}], P_f is rate of interception (inflow) for the canopy [LT^{-1}], and D_f is rate of drainage of water stored on the vegetation (outflow) for the canopy [LT^{-1}]. P_f is given by

$$P_f = P(1 - e^{-\mu})\sigma_c \tag{8.66}$$

where μ is a constant depending on the leaf area index. It is assumed that the interception, if the rainfall can be considered via the expression describing the exponential attenuation

(Sellers *et al.*, 1986), D_f is given by

$$D_f = \begin{cases} 0 & w_f < w_{max} \\ P_f & w_f < w_{max} \end{cases} \tag{8.67}$$

The transfer of water between adjacent layers $F_{i,i+1}$ [LT^{-1}] is given by

$$F_{i,i+1} = K_{ef}\left[2\frac{\psi_i - \psi_{i+1}}{D_i - D_{i+1}}\right] + 1 \tag{8.68}$$

where ψ_i is soil moisture potential [L] of the ith layer, obtained by Eq. (8.60), and K_{ef} is effective hydraulic conductivity [LT^{-1}] between soil layers given by

$$K_{ef} = \frac{D_i K_i - D_{i+1}K_{i+1}}{D_i + D_{i+1}}. \tag{8.69}$$

In Eq. (8.69) K_i is hydraulic conductivity [LT^{-1}] of the ith soil layer determined by the empirical formula

$$K_i = K_{si}\left(\frac{\vartheta_i}{\vartheta_s}\right)^{2B+3} \tag{8.70}$$

where K_{si} is hydraulic conductivity at saturation [LT^{-1}] of the ith soil layer. The gravitational drainage from the bottom soil layer is defined by

$$F_3 = K_{si}\left(\frac{\vartheta_3}{\vartheta_s}\right)^{2B+3} \sin(x) \tag{8.71}$$

while x is mean slope angle (Sellers *et al.*, 1986; Abramopoulos *et al.*, 1988). The schematic diagram representing the drainage and run-off in the LAPS is shown in Fig. 8.3. The surface run-off R_0[LT^{-1}] is computed as

$$R_0 = P_1 - min(P_1, K_s). \tag{8.72}$$

The subsurface run-off R_i[LT^{-1}] is calculated for each soil layer using the expressions

$$R_1 = F_{1,2} - min(F_{1,2}, K_s) \tag{8.73}$$

$$R_2 = F_{2,3} - min(F_{2,3}, K_s) \tag{8.74}$$

$$R_3 = F_3 - min(F_3, K_s). \tag{8.75}$$

At the end of the time step, Δt, the value Γ_i is calculated as

$$\Gamma_i = \frac{D_i}{\Delta t}[\vartheta_i^k + A_i \Delta t - \vartheta_{fc}] \tag{8.76}$$

where ϑ_i^k is the volumetric soil moisture content at the beginning of k time step while A_i representing the terms on the right side of Eqs. (8.5)–(8.7). If the condition $\Gamma_i > 0$ is satisfied

Γ_i becomes run-off, which is added to corresponding subsurface run-off R_i. Consequently, at the end of the time step, the calculated value of the volumetric soil moisture content ϑ_i^{k+1} takes the value ϑ_{fc}.

8.7 CONCLUDING REMARKS

In this chapter is given a detailed description of parameterization of the transport processes in soil-vegetation-lower atmosphere system by LAPS scheme. In designing this scheme, an effort is invested for finding a compromise between an accurate description of the main physical processes and the resolution of the number of prescribed input parameters. Land surface schemes such as LAPS aim to simulate the surface flux partitioning using an Ohm's law analogue in which surface to atmosphere fluxes are proportional to a potential difference and inversely proportional to a resistance. For sensible heat, the potential difference is the surface temperature minus the atmospheric temperature. The resistance is purely aerodynamic, and depends on the roughness of the surface, the wind speed and the atmospheric stability. For the latent heat flux the potential difference is taken as the saturated water vapour pressure at the surface temperature minus the atmospheric vapour pressure at the reference level, and the resistance depends on which moisture store is being depleted.

The hydrological state of the land surface is defined in terms of the vertical profile of soil moisture and the water lying on plant leaves or puddled on the soil surface. Evaporation from the canopy is subject to the same aerodynamic resistance as the sensible heat flux. However, evaporation from the soil and transpiration through plants is subject to an additional surface resistance. For bare soil this is related to the requirement for moisture to diffuse to the soil surface before it can evaporate. For vegetated surfaces the additional resistance represents the control that "stomata" exert over transpiration. They are open and closed in response to changes in solar radiation, temperature or soil moisture. The soil moisture that the vegetation can access for transpiration depends on the root depth and the vertical profile of soil moisture. In its configuration, LAPS updates the soil moisture in three vertical layers. The other key changes in LAPS relate directly to the surface energy balance depending on soil surface, canopy temperatures and canopy air space temperatures. The surface temperatures are calculated from the energy balance equations for bare soil and canopy surfaces, while the canopy air space temperature is calculated diagnostically from the sensible heat flux to the atmosphere balancing the sensible heat flux from the canopy and from the soil surface.

APPENDIX—LIST OF SYMBOLS

List of Symbols

Symbol	Definition	Dimensions or Units
C	heat capacity	$[\mathrm{J\,kg^{-1}\,K^{-1}}]$
C_s	transfer coefficient	$[\mathrm{m^{-1/2}\,s^{1/2}}]$
D_d	root density	$[\mathrm{m^3\,m^{-3}}]$
D_f	rate of drainage of water stored on the vegetation (outflow) for the canopy	$[\mathrm{ms^{-1}}]$
D_i	thickness of the ith soil layer	[m]
E	evapotranspiration rate	$[\mathrm{kg\,m^{-2}\,s^{-1}}]$
$F_{i,i+1}$	water flux between i and $i+1$ soil layer	$[\mathrm{ms^{-1}}]$

(*Continued*)

List of Symbols

Symbol	Definition	Dimensions or Units
E_{tf}	transpiration rate from foliage	[kg m^{-2} s^{-1}]
$E_{tf,1}$	canopy extraction of soil moisture by transpiration from the rooted first soil layer	[kg m^{-2} s^{-1}]
$E_{tf,2}$	canopy extraction of soil moisture by transpiration from the rooted second soil layer	[kg m^{-2} s^{-1}]
E_{wf}	evaporation rate of water from the wetted fraction of canopy	[kg m^{-2} s^{-1}]
F_3	gravitational drainage flux from recharge soil water store	[ms^{-1}]
H	canopy height	[m]
H_f, H_g	canopy and soil sensible heat flux respectively	[W m^{-2}]
K_c	saturated hydraulic conductivity	[ms^{-1}]
K_{ef}	effective hydraulic conductivity	[ms^{-1}]
K_i	hydraulic conductivity	[ms^{-1}]
K_r	mean soil hydraulic conductivity in the root zone	[ms^{-1}]
K_s	turbulent transfer coefficient within and above the canopy	[m^2 s^{-1}]
K_{si}	hydraulic conductivity at saturation	[ms^{-1}]
P	precipitation rate above the canopy	[ms^{-1}]
P_0	effective precipitation rate	[ms^{-1}]
P_f	water amount retained on the canopy	[ms^{-1}]
P_1	infiltration rate of precipitation into the upper soil moisture store	[ms^{-1}]
R_0	surface run-off	[ms^{-1}]
R_i	subsurface run-off from the ith soil layer	[ms^{-1}]
R_f^l	long-wave radiative fluxes absorbed by the canopy	[W m^{-2}]
R_g^l	long-wave radiative fluxes absorbed by the soil surface	[W m^{-2}]
R_n	absorbed net radiation	[W m^{-2}]
R_{nf}	net radiation absorbed by the canopy	[W m^{-2}]
R_{ng}	net radiation absorbed by the soil surface	[W m^{-2}]
R_f^s	short-wave radiation absorbed by the canopy	[W m^{-2}]
R_g^s	short-wave radiation absorbed by the soil surface	[W m^{-2}]
R_o^s	incident downward-directed short-wave flux	[W m^{-2}]
R_r	resistance per unit root length	[s m^{-1}]
T	surface (canopy or soil) temperature	[K]
T_a	canopy air space temperature	[K]
T_d	the deep soil temperature	[K]
T_f	surface canopy temperature	[K]
T_g	surface soil temperature	[K]
T_r	air temperature at the reference height z_r	[K]
V_r	volume of root per unit volume of soil	[m^3 m^{-3}]
$a(z), b(z)$	functions of the vertical coordinate z	

(*Continued*)

List of Symbols

Symbol	Definition	Dimensions or Units
c_p	specific heat of air	[J kg^{-1} K^{-1}]
d	the displacement height	[m]
d_1, d_2, d_3	empirical constants	[s m^{-1}]
$e_*(T_f)$	saturated vapour pressure at temperature T_f	[Pa]
$e_*(T_g)$	saturated vapour pressure at temperature T_g	[Pa]
e_a	canopy air space vapour pressure	[Pa]
e_r	vapour pressure of the air at reference height within the atmospheric boundary layer	[Pa]
h	the canopy bottom height (the height of the base of the canopy)	[m]
h_a	the position of the canopy source height	[m]
m	number of iteration	
n	the number of the spatial step in the numerical calculating on the interval $[H, h]$	
$\overline{r}_b$	bulk canopy boundary layer resistance	[s m^{-1}]
$\overline{r}_c$	bulk canopy stomatal resistance	[s m^{-1}]
r_a	aerodynamic resistance	[s m^{-1}]
r_d	aerodynamic resistance between soil surface and canopy air space	[s m^{-1}]
r_{plant}	plant resistance imposed by the plant vascular system	[s]
$r_{s\ min}$	minimum of stomatal resistance	[s m^{-1}]
$r_{s\ max}$	maximum of stomatal resistance	[s m^{-1}]
r_{soil}	resistance of the soil and root system	[s]
r_{surf}	soil surface resistance	[s m^{-1}]
u_*	the friction velocity	[m s^{-1}]
$u\,(H)$	the wind speed at the canopy height	[m s^{-1}]
$u\,(h)$	the wind speed at the canopy bottom height	[m s^{-1}]
$u\,(z)$	the wind speed above a canopy	[m s^{-1}]
w_f	the water stored on the canopy	[m]
w_w	wetted fraction of canopy	
x	mean slope angle	[°]
z	the vertical coordinate	[m]
z_I	some certain height within the canopy	[m]
z_0, z_b	the roughness length over the non-vegetated surface	[m]
z_d	the rooting depth	[m]
z_g	effective ground roughness length	[m]
z_r	the reference height	[m]
z_t	height of the transpiration source that is equal to canopy source height	[m]
Δt	time step	[s]
Δz	the grid size	[m]

(*Continued*)

List of Symbols

Symbol	Definition	Dimensions or Units
α	an unknown constant	
α_f, α_g	canopy albedo and soil surface albedo, respectively	
α_s	a factor to correct for soil dryness	
β	extinction parameter	
γ	the psychrometric constant	$[\mathrm{Pa\,K^{-1}}]$
$\varepsilon_f, \varepsilon_g$	emissivities of the canopy and the soil surface, respectively	
η	the canopy-dependent empirical parameter	$[\mathrm{Pa^{-1}}]$
ϑ_1	the top layer volumetric soil water content	$[\mathrm{m^3\,m^{-3}}]$
ϑ_a	the mean volumetric soil water content in the first and second soil layers	$[\mathrm{m^3\,m^{-3}}]$
ϑ_{fc}	volumetric soil water content at field capacity	$[\mathrm{m^3\,m^{-3}}]$
ϑ_i^k	the volumetric soil moisture content at the beginning of k time step	$[\mathrm{m^3\,m^{-3}}]$
ϑ_i	volumetric soil water content in the ith layer	$[\mathrm{m^3\,m^{-3}}]$
ϑ_s	volumetric soil moisture content at saturation	$[\mathrm{m^3\,m^{-3}}]$
ϑ_{wil}	volumetric soil water content at wilting point	$[\mathrm{m^3\,m^{-3}}]$
κ	Von Karman constant	
λ	latent heat of vaporisation	$[\mathrm{J\,kg^{-1}}]$
λE_f	the latent heat flux from canopy vegetation to canopy air space	$[\mathrm{W\,m^{-2}}]$
λE_g	the latent heat flux from soil surface to the canopy air space	$[\mathrm{W\,m^{-2}}]$
λE_t	the latent heat flux from canopy air space to reference height in the atmospheric boundary layer	$[\mathrm{W\,m^{-2}}]$
μ	parameter; a constant depending on the leaf area index	
ρ	water density	$[\mathrm{kg\,m^{-3}}]$
ρ_p	air density	$[\mathrm{kg\,m^{-3}}]$
σ	the value of the scaling length	
σ_B	the Stefan-Boltzman constant	$[\mathrm{W\,m^{-2}\,K^{-4}}]$
σ_c	vegetation cover in fractional units	
σ_f	fractional cover of vegetation	
ψ_i	soil water potential of the ith soil layer; soil moisture potential of the ith layer	[m]
ψ_l	the leaf water potential describing the water transfer pathway from root zone to leaf	[m]
$\psi_m(z/L)$	the stability function for momentum	
ψ_r	soil moisture potential in the root zone	[m]
ψ_s	soil water potential at saturation	[m]

REFERENCES

Abramopoulos, F., Rosenzweig, C. and Choudhury, B., 1988, Improved ground hydrology calculations for global climate models (GCMs): Soil water movement and evapotranspiration. *Journal of Climate*, **l**, 921–941.

Acs, F., 1994, A coupled soil–vegetation scheme: Description, parameters, validation, and sensitivity studies. *Journal of Applied Meteorology*, **33**, 268–284.

Avissar, R., Avissar, P., Mahrer, Y. and Bravdo, B., 1985, A model to simulate response of plant stomata to environmental conditions. *Agricultural and Forest Meteorology*, **64**, 127–148.

Baron, J.S., Hartman, M.D., Kittel, T.G.F., Band, L.E., Ojima, D.S. and Lammers, R.B., 1998, Effects of land cover, water redistribution, and temperature on ecosystem processes in the South Platte Basin. *Ecological Applications*, **8**, 1037–1051.

Bosilovich, M. and Sun, W., 1995, Formulation and verification of a land surface parameterization for atmospheric models. *Boundary-Layer Meteorology*, **73**, 321–341.

Brunet, Y., Finnigan, J.J. and Raupach, M.R., 1994, A wind tunnel study of air flow in waving wheat: Single-point velocity statistics. *Boundary-Layer Meteorology*, **70**, 95–132.

Chase, T.N., Pielke, Sr.R.A., Kittel, T.G.F., Baron, J.S. and Stohlgren, T.J., 1998, Potential impacts on Colorado Rocky Mountain weather and climate due to land use changes on the adjacent Great Plains. *Journal of Geophysical Research*, **104**, 16673–16690.

Clapp, R.B. and Hornberger, G.M., 1978, Empirical equations for some soil hydraulic properties. *Water Resources Research*, **14**, 601–604.

Cox, P.M., Betts, R.A., Bunton, C.B., Essery, R.L.H., Rowntree, P.R. and Smith, J., 1999, The impact of new land surface physics on the GCM simulation of climate and climate sensitivity. *Climate Dynamics*, **15**, 183–203.

Deardorff, J.W., 1978, Efficient prediction of ground surface temperature and moisture, with inclusion of a layer of vegetation. *Journal of Geophysical Research*, **83**, 1889–1903.

Dickinson, R.E., 1995, Land–atmosphere interaction. *Reviews of Geophysics*, **33**, 917–922.

Dickinson, R.E., Henderson-Sellers, A., Kennedy, P.J. and Wilson, M.F., 1986, Biosphere–Atmosphere Transfer Scheme for the NCAR Community Climate Model, NCAR Tech. Rep. NCAR/TN-2751 STR, (Available from NCAR, P.O. Box 3000, Boulder, CO 80307-3000) p. 69.

Dubov, A.S., Bikova, L.P. and Marunich, S.V., 1978, *Turbulence inside a canopy.* (Gidrometeoizdat, Leniningrad) (In Russian).

Federer, C.A., 1979, A soil-plant-atmosphere for transpiration and availability of soil water. *Water Resources Research*, **15**, 555–562.

Idso, S., Jackson, R., Kimball, B. and Nakagama, F., 1975, The dependence of bare soil albedo on soil water content. *Journal of Applied Meteorology*, **14**, 109–113.

Jarvis, P.G., 1976, The interpretation on the variations in leaf water potential and stomatal conductance found in canopies in the field. *Philosophical Transactions of the Royal Society*, **B273**, 593–610.

Lee, T.J., Pielke, R.A. and Mielke, P.W.Jr., 1995, Modeling the clear-sky surface energy budget during FIFE87. *Journal of Geophysical Research*, **100**, 25585–25593.

Loveland, T.R., Merchant, J.W., Ohlen, D.O. and Brown, J.F., 1991, Development of a land-cover characteristics database for the conterminous U.S. *Photogrammetric Engineering and Remote Sensing*, **57**, 1453–1463.

Mihailović, D.T., 1996, Description of a land–air parameterization scheme (LAPS). *Global and Planetary Change*, **13**, 207–215.

Mihailović, D.T., 2003, Implementation of Land–Air Parameterization Scheme (LAPS) in a limited area model. *Final Report, The New York State Energy Conservation and Development Authority*, (Albany, NY).

Mihailović, D.T. and Kallos, G., 1997, A sensitivity study of a coupled soil-vegetation boundary layer scheme for use in atmospheric modeling. *Boundary-Layer Meteorology*, **82**, 283–315.

Mihailović, D.T., Rajković, B., Lalić, B. and Dekic, Lj., 1995, Schemes for parameterizing evaporation from a non-plant-covered surface and their impact on partitioning the surface energy in land–air exchange parameterization. *Journal of Applied Meteorology*, **34**, 2462–2475.

Mihailović, D.T., Pielke, R.A.Sr., Rajković, B., Lee, T.J. and Jeftic, M., 1993, A resistance representation of schemes for evaporation from bare and partly plant-covered surfaces for use in atmospheric models. *Journal of Applied Meteorology*, **32**, 1038–1054.

Mihailović, D.T., Kallos, G., Arsenić, I.D., Lalić, B., Rajković, B. and Papadopoulos, A., 1999, Sensitivity of soil surface temperature in a force-restore equation to heat fluxes and deep soil temperature. *International Journal of Climatology*, **19**, 1617–1632.

Mihailović, D.T., Alapaty, K., Lalić, B., Arsenić, I., Rajković, B. and Malinovic, S., 2004, Turbulent transfer coefficients and calculation of air temperature inside the tall grass canopies in land-atmosphere schemes for environmental modeling. *Journal of Applied Meteorology*, **43**, 1498–1512.

Mihailović, D.T., Lalić, B., Eitzinger, J., Malinovic, S. and Arsenić I., 2006, An approach for calculation of turbulent transfer coefficient for momentum inside vegetation canopies. *Journal of Applied Meteorology and Climatology*, **45**, 348–356.

Mihailović, D.T., Lee, T.J., Pielke, R.A., Lalić, B., Arsenić, I., Rajković, B. and Vidale, P.L., 2000, Comparison of different boundary layer schemes using single point micrometeorological field data. *Theorethical and Applied Climatology*, **67**, 135–151.

Noilhan, J. and Planton, S., 1989, A simple parameterization of land surface processes in meteorological models. *Monthly Weather Review*, **117**, 536–549.

Paulson, C.A., 1970, The mathematical representation of wind speed and temperature in the unstable atmospheric surface layer, *Journal of Applied Meteorology*, **9**, 857–861.

Pielke, R.A.Sr., Avissar, R., Raupach, M., Dolman, H., Zeng, X. and Denning, S., 1998, Interactions between the atmosphere and terrestrial ecosystems: Influence on weather and climate. *Global Change Biology*, **4**, 101–115.

Pielke, R.A.Sr., Walko, R.L., Steyaert, L., Vidale, P.L., Liston, G.E. and Lyons, W.A., 1999, The influence of anthropogenic landscape changes on weather in south Florida. *Monthly Weather Review*, **127**, 1663–1673.

Pleim, J. and Xiu, A., 1995, Development and testing of a surface flux and planetary boundary layer model for application in mesoscale models. *Journal of Applied Meteorology*, **34**, 16–32.

Sellers, P.J. and Dorman, J.L., 1987, Testing the simple biosphere model (SiB) using point micrometeorological and biophysical data. *Journal of Applied Meteorology*, **26**, 622–651.

Sellers, P.J., Mintz, Y., Sud, Y. and Dalcher, A., 1986, A simple biosphere model (SiB) for use within general circulation models. *Journal of Atmospheric Sciences*, **43**, 505–531.

Stohlgren, T.J., Chase, T.N., Pielke, R.A., Kittel, T.G.F. and Baron, J.S., 1998, Evidence that local land use practices influence regional climate, vegetation, and stream flow patterns in adjacent natural areas. *Global Change Biology*, **4**, 495–504.

Sun, S.F., 1982, *Moisture and heat transport in a soil layer forced by atmospheric conditions*. M.S. Thesis, Department of Civil Engineering, University of Connecticut.

Van der Honert, X., 1948, Water transport as a catenary process, *Discussions of the Faraday Society*, **3**, 146–153.

Viterbo, P. and Beljaars, A., 1995, An improved land-surface parameterization scheme in the ECMWF model and its validation. *Journal of Climate*, **8**, 2716–2748.

Walko, R.L., Band, L.E., Baron, J., Kittel, T.G.F., Lammers, R., Lee, T.J., Ojima, D., Pielke, R.A.Sr., Taylor, C., Tague, C., Tremback, C.J., Vidale, P.L., 2000, Coupled atmosphere-biophysics-hydrology models for environmental modeling. *Journal of Applied Meteorology*, **39**, 931–944.

CHAPTER NINE

Turbulence and wind above and within the forest canopy

Branislava Lalić & Dragutin T. Mihailović
Faculty of Agriculture, University of Novi Sad, Novi Sad, Serbia

ABSTRACT

The forest has a strong influence on vertical profiles of micrometeorological variables within and above the canopy. Especially pronounced variations of all variables between ground level and crown top are primarily generated by the forest architecture. When wind encounters forest canopy, the drag of the foliage removes mean momentum of wind producing turbulent eddies. Dissipation of mean flow kinetic energy within and below the forest crown usually has been described through vertical gradient of wind speed. The accuracy of within-canopy wind profile calculation is related to assumed forest architecture and to adopted approach for parameterization of momentum turbulent fluxes. This chapter is focused on forest architecture and on turbulence produced by friction exerted when air flow encounters forest canopy. An overview of different approaches oriented towards their parameterization (forest architecture) and modelling (turbulence) is presented.

9.1 INTRODUCTION

The definition of the lower boundary condition is of great importance in dynamic environmental models (atmospheric, hydrological and ecological), especially in the presence of vegetation. Forest is a vegetation system covering more than 20% of land-based globe. Also, the atmosphere 'feels' the presence of trees up to a few hundred meters from the ground, depending on tree height. Therefore, forest as an underlying surface is often met in atmospheric and environmental models of different scales. As a dynamical source and sink of momentum, heat, water (vapour) and pollution, forest plays a crucial role in land–atmosphere-interaction modelling. To describe that role it is important to understand mechanism of forest canopy—atmosphere interaction processes. Key element of these processes is the turbulent transfer above and within the forest canopy strongly affected by forest architecture, its thermal characteristics and significant drag of foliage. Consequently, many current vegetation–atmosphere as well as the environmental models require more specific information about the forest structure describing the leaf area density variation with height in order to provide a better estimate of energy, mass and momentum exchange (Mix *et al.*, 1994; Zeng and Takahashi, 2000). In the past decades, a fair amount of literature has been accumulated that deals with the closuring problem and values of the various coefficients that must be specified in order to solve equations of motion for turbulent flow above and within the canopy. This chapter describes different approaches in designing forest canopy architecture based on leaf area index, LAI or leaf area density, LAD, as key structural characteristics. Vertical transfer of momentum, considered in this chapter, is restricted to

horizontally homogeneous, extensive forest over which the mean wind is steady and unidirectional. We have selected here the parameterizations of turbulent transfer above and within the forest canopy based on first order closure model, i.e. modified K-theory.

9.2 MODELLING THE FOREST ARCHITECTURE

The forest architecture is most commonly quantified by the amount of leaves and stems, and their spatial distribution represented by leaf area index, LAI [L^2L^{-2}] and leaf area density, LAD [$L^2\ L^{-3}$], respectively. Following the definitions of these two characteristic quantities, the relation between them could be written in the form:

$$LAI = \int_0^{h_c} LAD(z)\, dz, \tag{9.1}$$

where h_c[L] is the forest height.

However, it is extremely difficult to measure in practice these quantities inside the forest canopy. Some authors try either to provide alternative methods for measuring (Meir *et al.*, 2000), or for estimating (Law *et al.*, 2001b) the leaf area index, LAI and leaf area density, LAD, inside the different forest communities. Levi and Jarvis (1999) suggested an empirical relation for the leaf area index, LAI based on an inclusion of the forest optical characteristics,

$$LAI = -\frac{\ln \tau_H(\theta_s)}{K(\theta_s)} \tag{9.2}$$

where τ_H is the transmittance of whole canopy ("bulk" transmittance) for radiation in photosynthetic waveband and K is an extinction coefficient which is a function of solar zenith angle, θ_s and leaf inclination angle distribution. Unfortunately, calculation of leaf area index, LAI using Eq. (9.2) is restricted to homogeneous forest and low values (less than $6\,m^2\,m^{-2}$) of LAI. In contrast to this and other similarly established approaches, Gower (Gower *et al.*, 1999) emphasized that the direct measurement is the only reliable method for dense forest canopies having high values of LAI ($LAI > 6\,m^2\,m^{-2}$).

Simplest parameterization of leaf area density, LAD, related to an ideal canopy with a homogeneous crown and negligible amount of vegetation below it, could be expressed in the form

$$LAD(z) = \begin{cases} LAD_0 & h_c/2 \le z \le h_c \\ 0 & 0 \le z \le h_c/2 \end{cases} \tag{9.3}$$

where LAD_0 [$L^2\ L^{-3}$] is the leaf area density of forest crown (Watanabe and Kondo, 1990). Recently, the scientific community dealing with the environmental problems tends to derive physically more realistic empirical expressions for leaf area density, LAD, based on available observational data archives. One of the expressions among their limited collection, based on photographic method, is suggested by Meir *et al.* (2000). The photographs are being taken horizontally from the tower at different heights, using as a target a white meteorological balloon raised into the canopy at the known distance, l[L]. From these hemispherical

photographs, one could determine the fraction of transmitted light through the canopy layer, τ_z as an estimate of probability, P_z, of a beam of light passing through a horizontal plane of leaves at height z within a forest canopy. Taking into account the relation between probability P_z and path length L_z through which the light comes to level z,

$$L_z = -\ln P_z, \tag{9.4}$$

leaf area density, *LAD* for each canopy layer could be calculated as

$$LAD(z) = \frac{L_z}{l}. \tag{9.5}$$

Unfortunately, this method for leaf area density, *LAD* calculation can be used only in a limited number of situations when hemispherical photographs for different canopy layers are made.

A more sophisticated approach to leaf area density *LAD*, parameterization was suggested by Lalić and Mihailović (2004). On the basis of measured spatial distribution of leaves and stems, they derived the relation for *LAD(z)* taking into account tree height h_c, maximum value of leaf area density L_m and corresponding height z_m as key parameters of the forest canopy structural characteristics (Kolic, 1978; Mix *et al.*, 1994; Law *et al.*, 2001a) in the form:

$$LAD(z) = L_m \left(\frac{\mathrm{h_c} - z_m}{\mathrm{h_c} - z}\right)^n \exp\left[n \cdot \left(1 - \frac{\mathrm{h_c} - z_m}{\mathrm{h_c} - z}\right)\right],$$
$$\text{where } n = \begin{cases} 6 & 0 \le z < z_m \\ 1/2 & z_m \le z \le \mathrm{h_c} \end{cases}. \tag{9.6}$$

Parameter n was found from analysis of minimum root-mean-square error (RMSE) for different measured leaf area density distribution data sets. Results of these analyses pointed out that the best choice is $n = 0.5$ for range $z \ge z_m$ and $n = 6$ for $z < z_m$. According to the classification based on z_m and h_c parameters (Kolic, 1978), all forest canopies can be divided into the three groups: 1) $z_m = 0.2\, h_c$ (oak and silver birch), 2) $0.2\, h_c < z_m < 0.4\, h_c$ (common maple) and 3) $z_m = 0.4\, h_c$ (pine), where in the bracket is a typical representative. Following this classification, empirical relation for leaf area density *LAD* described by Eq. (9.6) could be applied in the broad range of forest canopies.

9.3 TURBULENCE AND WIND ABOVE THE FOREST

In atmospheric models for different scales the underlying surface consists of patches of bare soil and plant communities with different morphological parameters. Experimental evidence indicates that there is a significant departure of the wind profile above a vegetative surface from that predicted by the logarithmic relationship, which gives the values which are greater than the observed. This situation can seriously disturb the real physical picture concerning the transfer of momentum, heat and water vapour from the surface into the atmosphere, particularly above the forest. In this section we generalise the calculation of exchange of momentum between the atmosphere and non-homogeneous vegetative surface and derive a general equation for the wind speed profile in a roughness sublayer under neutral conditions. Furthermore, these results are extended to non-neutral cases.

9.3.1 Definition of problem and motivations

Under thermally neutral conditions, steady-state flow over horizontally bare soil can be described by the well-known logarithmic law (e.g., Monin and Yaglom, 1971)

$$u(z) = \frac{u_{*g}}{\kappa} \ln \frac{z}{z_{0g}} \tag{9.7}$$

where $u(z)[\mathrm{L\,T^{-1}}]$ is the horizontal velocity at height z[L], $u_{*g}[\mathrm{LT^{-1}}]$ is the friction velocity for a bare soil, which, physically, represents the shear stress $\tau = \rho_a u_{*g}$ where $\rho_a[\mathrm{ML^{-3}}]$ is the air density, κ is the Von Karman constant taken to be 0.41 (Högström, 1985) and z_{0g} [L] the roughness length of a bare soil. For vegetative surfaces, where the obstacle size has the same order of magnitude as a measuring height, Eq. (9.7) is modified as

$$u(z) = \frac{u_*}{\kappa} \ln \frac{z - d}{z_0} \tag{9.8}$$

where u_* [L T^{-1}] is the friction velocity over the vegetation surface, d [L] the displacement height—the mean height in the vegetation on which the bulk aerodynamic drag acts (Thom, 1971) and z_0 [L] the roughness length. According to this expression, the wind speed is zero at height $d + z_0$, but the logarithmic profile cannot be extrapolated so far downwards. When the quantities d and z_0 are known the whole profile above a vegetative surface can be obtained if the wind at a single level as well as the ratio u_*/κ are known. For the non-neutral atmosphere, Eqs. (9.7) and (9.8) have to be modified due to stability effects (Businger *et al.*, 1971).

In order to illustrate differences between these two cases, in the treatment of the lower boundary conditions, for example in surface schemes in atmospheric models, we will form a ratio u_{*g}/u_*, which is equal to $ln[(z-d)/z_0]/ln[z/z_{0g}]$, at the height z where the velocities given by Eqs. (9.7) and (9.8) are the same. This ratio, for several plant communities is plotted in Fig. 9.1, where displacement heights and roughness lengths used have their standard

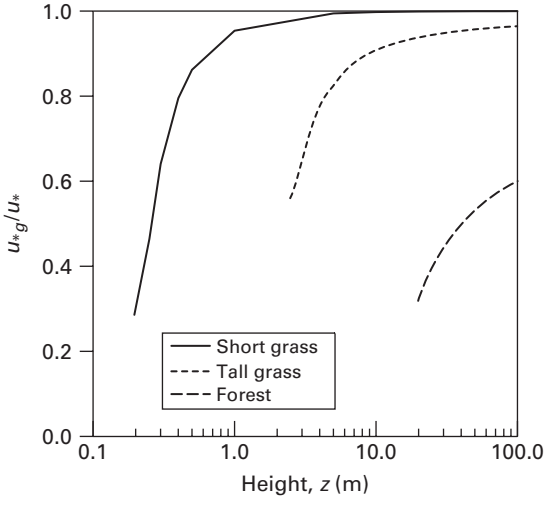

Figure 9.1. Ratio of the friction velocities over bare soil, u_{*g} and different vegetative surfaces, u_* plotted against the height z at which their wind velocities have the same value.

values for corresponding plant communities. Apparently, transfer of momentum between short grass and the atmosphere does not differ so much from the corresponding exchange when a bare soil is underlying surface. However, over tall grass the transfer of momentum into the atmosphere is more intensive since the u_*, which can be identified as the velocity scale of the eddies near the surface, becomes greater than u_{*g}. Difference in these velocity scales physically can be explained by the fact that the mixing length of the eddies above a vegetative surface is shorter than the mixing length above a bare soil.

However, Eq. (9.8) is not valid when height z is between the vegetation (of mean height h_c) and some height z^* representing the lower limit of the roughness sublayer. Its order of magnitude can vary between $z* \cong d + 10z_0$ (De Bruin and Moore, 1985) and $z* \cong d + 20z_0$ (Tennekes, 1982). In roughness sublayer Eq. (9.8) is not valid because we are then too close to roughness elements (tall grass, trees, etc.) when the turbulence is generated by the flow around them (Garratt, 1978; De Bruin and Moore, 1985). The depth of the roughness sublayer depends on the value of displacement height d which accounts for an upward shift in the whole profile above a vegetative cover. Since z_0 is around ten percent of the canopy height then the thickness of roughness sublayer can vary between one and two canopy heights. Consequently, an improper treatment of the wind profile in roughness sublayer, systematically gives the values of shear stress and latent heat flux which can significantly deviate from observed values. In models of biosphere–atmosphere exchange when underlying vegetative surface consists of patches of bare soil and plant communities with different morphological parameters, the level of inhomogeneity in the cover has to be taken into account in addition to a spatially varying displacement height. This is of importance in the design of a new generation of land surface parameterization schemes for use in atmospheric models on scales where the patchiness of the surface is resolved (Mihailović and Kallos, 1997).

Experimental evidence indicates that in the roughness sublayer above a vegetative surface, particularly forest canopy, there is a significant departure of the wind profile from that predicted by the logarithmic relationship, giving values which are greater than observed ones (Wilson *et al.*, 1982; Shaw and Pereira, 1982; Sellers *et al.*, 1986). This problem was comprehensively considered by Garratt (1978) and Raupach and Thom (1981). They have noted that estimates of turbulent transfer coefficient K_m [$\mathrm{ML^{-1}T^{-1}}$] above a vegetative surface h_c were 1.5–2.0 times larger than as the simple extrapolation of Eq. (9.8) would indicate. Using this estimation Eq. (9.8) can be modified, so that in roughness sublayer it takes the form

$$u(z) = \frac{u_*}{\alpha_G \kappa} \ln \frac{z - d}{z_0} \tag{9.9}$$

where α_G is a dimensionless constant estimated to be between 1.5 and 2.0 (Raupach and Thom, 1981; Massman, 1987) resulting in 1.5–2.0 times smaller values for the wind speed than it would be expected from Eq. (9.8). Let us note that logarithmic profile given by Eq. (9.9) can only be valid for the lower part of the roughness sublayer. Some other expressions with correct matching behaviour can be found in Raupach *et al.* (1980) and Raupach (1980).

9.3.2 Exchange of momentum above a non-uniform underlying surface under neutral conditions

We will derive an expression for the turbulent transfer coefficient K_m and the wind profile, under neutral conditions, above a non-uniform underlying surface whose non-uniformity is expressed by the surface vegetation fractional cover σ_f, which takes the values from 0 (bare

soil) to 1 when the ground surface is totally covered by plants. A realistic surface is rather porous, with patches of bare soil and free air spaces inside it, and vegetative portion which can produce quite different modes of turbulence in comparison with an uniform underlying surface which is either bare soil or surface covered with vegetation. Vegetative part of the underlying surface is a mosaic of patches of various size and different aerodynamic characteristics. Presumably, this mosaic will produce micro circulation with possible flow separations at leading and trailing edges setting up a highly complex dynamic flow. In this paper we will not address the consequences of such non-uniformity of the vegetation part of the underlying surface. Instead, the underlying surface will be considered as a combination of the only two homogeneous portions consisting of vegetative portion, characterized with fractional cover σ_f and the bare portion, characterized with fractional cover $1-\sigma_f$. Bearing in mind such assumption we will try to do the previously mentioned calculations.

We will start from the description of the logarithmic profile which is consistent with the following assumptions. Similarly as in the molecular gas theory, an exchange coefficient can be derived as the product of a velocity and mixing length. For molecules the mixing length can be identified with the mean free path, but for eddies above a canopy with displacement height d it is assumed that it is proportional to a corrected height $z-d$. The proportionality factor is given by von Karman's constant k, so the mixing height l_m^c[L] is given by

$$l_m^c = \kappa(z-d) \tag{9.10}$$

which is a broadly employed expression for the mixing length in the free air above a vegetative surface in the surface layer (in further text this approach will be denoted as the "old approach"). For $d=0$, Eq. (9.10) represents the mixing length over a bare soil, thus it becomes $l_m^b = \kappa z$ which is bigger than l_m^c. Undoubtedly, in the reality there is no situation when the underlying vegetative surface is as dense and smooth as it is assumed in deriving the mixing length given by Eq. (9.10). As we mentioned above, a natural surface is very porous and consists of vegetative surface with patches of bare soil, producing quite unpredictable mode of turbulence inside and above the vegetative surface. Experimental results by Garratt (1978) support this point. According to them, in the roughness sublayer above a vegetative surface, the mixing length l_m^α, which is bigger than l_m^c, can be written in the form $l_m^\alpha = \alpha\kappa(z-d)$ where α is a dimensionless constant representing corrected value of the mixing length in the roughness sublayer. For further consideration we will use the mixing length in the form

$$l_m^\alpha = \alpha_G\kappa(z-d) \tag{9.11}$$

where α is replaced by α_G which is defined above in Eq. (9.9). However, the eddies, with the mixing length given by Eq. (9.11), are still generated above a dense and smooth vegetative surface. In order to take into account its non-uniformity we have considered it as a block of porous material consisting of bare soil and vegetative patches which can be described by the vegetation fractional cover σ_f, with values between 0 and 1. The number of eddies generated above the underlying surface defined in such a way consists of: 1) eddies generated above the vegetative part whose number is proportional to σ_f and 2) eddies generated above the bare soil part with the factor of proportionality $(1-\sigma_f)$. Thus, their mixing length l_m could be used as a linear combination of mixing lengths l_m^α and l_m^b, i.e., $l_m = \sigma_f l_m^\alpha + (1-\sigma_f) l_m^b$. Let us note that a linear combination of the single lengths is not the only way of deriving a mixing length l_m accounting for the non-uniformity of the surface. Consequently, mixing lengths over a non-uniform surface would almost be different and it seems that the suggestion for a linear aggregation scheme for an effective mixing length is a simplified assumption. However, from a practical and a physical point of view this assumption might be acceptable

because it is more complex than the commonly used one. After setting $l_m^{\alpha} = \alpha\kappa(z-d)$, the mixing lengths l_m takes the form

$$l_m = \sigma\alpha\kappa(z-d) + (1-\sigma)\kappa z \tag{9.12}$$

where α is the dimensionless constant introduced above which depends on morphological and aerodynamic characteristics of the vegetative cover whose value varies depending on the type of vegetative cover. In this study α is considered as a function of leaf drag coefficient C_{dg}, and leaf area index LAI, i.e., $\alpha = \alpha\,(C_{dg} \cdot \mathrm{LAI})$. For $\sigma_f = 1$, Eq. (9.12) becomes Eq. (9.11) while for $\sigma_f = 0$ it reduces to the expression for the mixing length for a bare soil. The turbulent transfer coefficient K_m for the non-homogenous vegetative cover is

$$K_m = l_m U_* \tag{9.13}$$

where U_* [$\mathrm{L\,T^{-1}}$] is a friction velocity above non-homogeneously covered surface. Replacing l_m, in this equation, by the expression (9.12) we get

$$K_m = \kappa\{[\sigma(\alpha-1)+1]z - \sigma\alpha d\}U_*. \tag{9.14}$$

The functional form of the parameter α was derived empirically by Lalić (1997). More details about this parameter can be found in Mihailović *et al.* (1999) and Chapter 3 of this book. Mihailović *et al.* (1999) found that this parameter has a typical value for forest about 1.6 while other vegetation communities have the values closer to 1.

Another characteristic of the family of lines representing the mixing length l_m, is that they cross each other at a single point, at height z_l[L], where this height does not depend on the vegetation fractional cover σ_f. The height z_l can be calculated from the condition

$$[\sigma_1(\alpha-1)+1]z_l - \sigma_1\alpha d = [\sigma_2(\alpha-1)+1]z_l - \sigma_2\alpha d \tag{9.15}$$

where σ_1 and σ_2 indicate different vegetation fractional covers. Solving this equation for z_l we obtain

$$z_l = \frac{\alpha}{\alpha-1}d. \tag{9.16}$$

This expression explicitly shows that the point where the mixing length l_m and the turbulent transfer coefficient K_m do not depend on the vegetation fractional cover σ_f, is located at infinity where the condition that $\alpha = 1$ is satisfied. Mathematically, it means that all lines, obtained for different values of α, tend towards the line representing the "old approach". Physically, it seems that the influence of surface patchiness on the mixing length vanishes at some height z_l, however, re-emerging again above it. This situation can be explained by introducing two more degrees of freedom in the expression for the mixing length [Eq. (9.12)] in addition to the ones allowed by Eq. (9.10). Consequently, combining α and σ_f parameters we can find such a combination that makes l_m independent of surface patchiness. This dependence vanishes exactly at height z_l. Replacing this height, given by Eq. (9.16), in Eq. (9.14) we obtain $l_m = \kappa z_l$. It means that, at z_l, the mixing length is only a function of the displacement height and α. The tendency of the lines representing mixing length l_m to approach the line representing the "old approach" is more emphasized for the low height vegetation than for the taller one. Since the expression (9.14), for $\alpha = 1$, is not defined, the only physical conclusion that can be derived is that Eq. (9.10) can not be obtained as

a special case of Eq. (9.12). This is not surprising because Eq. (9.12) is derived by taking into account the presence of underlying surfaces with different vegetation fractional covers, while Eq. (9.10) is not based on such an assumption. For the taller vegetation the height, z_l, where the crossover point is located, becomes lower while the lines representing the different vegetation fractional covers are more apart. The lower location of z_l, in comparison with its location for the low height vegetation, can come from the fact that this height is closer to the canopy height [Eq. (9.14)] than it is in the case of the lower vegetation. Also, these lines show a tendency of shifting towards the right side of the domain bounded by the lines obtained by the "old approach" and approach suggested by Garratt (1978).

9.3.3 Wind profile above a non-uniform underlying surface under neutral conditions

Using the foregoing assumption that the friction velocity U_* is equal to $l_m\, du/dz$ yields

$$U_* = \kappa\{[\sigma(\alpha - 1) + 1]z - \sigma\alpha d\}\frac{du}{dz}. \tag{9.17}$$

This equation can be integrated to

$$u(z) = \frac{U_*}{\kappa}\frac{1}{\sigma(\alpha - 1) + 1}\ln\{[\sigma(\alpha - 1) + 1]z - \sigma\alpha d\} + C_i \tag{9.18}$$

where C_i is an integration constant. This constant can be found if we introduce the assumption that the extrapolation of wind profile (9.18) gives zero wind velocity at some height z_k defined as

$$z_k = Z_0 + D \tag{9.19}$$

where

$$Z_0 = \frac{f(\alpha, m)\, z_0}{\sigma(\alpha - 1) + 1} \tag{9.20}$$

and

$$D = \frac{\sigma\alpha d}{\sigma(\alpha - 1) + 1} \tag{9.21}$$

are generalized roughness length and displacement height, respectively and $f(\alpha, m)$ is an arbitrary function representing the dependence of Z_0 on introduced aerodynamic characteristic $\alpha = \alpha\,(LAI \cdot C_{od})$, and m denotes an arbitrary constant. Since the experimental evidence indicates that the vegetative underlying surface is rougher than it is described by the classical logarithmic profile it means that Z_0 has to be higher than z_0. Below we have assumed that the function $f(\alpha, m)$ has a power form, i.e. $f(\alpha, m) = \alpha^m$ which increases monotonically with respect to α.

Then the above condition can be written as

$$0 = \frac{U_*}{\kappa}\frac{1}{\sigma(\alpha - 1) + 1}\ln\{[\sigma(\alpha - 1) + 1]z_k - \sigma\alpha d\} + C_i. \tag{9.22}$$

After substituting the expressions (9.19), (9.20) and (9.21) in the condition (9.22), we find that the constant C_i is given by

$$C_i = -\frac{U_*}{\kappa}\frac{1}{\sigma(\alpha-1)+1}\ln \alpha^m z_0. \tag{9.23}$$

Finally, combining the expressions (9.19) and (9.23) we reach a wind profile in the roughness sublayer above the non-uniform vegetative surface under neutral conditions (hereafter referred to as the "new profile"), which can be written in the form

$$u(z) = \frac{U_*}{\kappa}\frac{1}{\sigma(\alpha-1)+1}\ln\frac{z-\dfrac{\sigma\alpha d}{[\sigma(\alpha-1)+1]}}{\dfrac{\alpha^m z_0}{[\sigma(\alpha-1)+1]}} \tag{9.24}$$

or shortly

$$u(z) = \frac{U_*}{\kappa}\frac{1}{\sigma(\alpha-1)+1}\ln\frac{z-D}{Z_0} \tag{9.25}$$

if we use the definitions (9.14) and (9.15) representing the generalized roughness length and displacement height respectively.

Comparing the expressions (9.8) and (9.25) we can see that the "new profile" explicitly includes the dependence of the wind on the non-uniformity of the underlying vegetative surface while the "old logarithmic profile" or [profile given by Eq. (9.8)] does not. Moreover, the "old logarithmic profile" interprets the underlying vegetative surface as a smooth one regardless of whether the surface is uniformly covered by the vegetation or not. The same conclusion can be emphasized for the wind profile given by Eq. (9.9) which will be referred to as the "Garratt's logarithmic profile". This profile, established on the basis of the experimental evidence, is a special case of the "new profile" for $\sigma_f = 1$, $\alpha = \alpha_G$ and $m = 1$ where α_G is taken to be 1.5. Note that the profile given by Eq. (9.8) can be formally obtained from Eq. (9.24) for $\sigma_f = 1$ and $\alpha = 1$.

In the "new logarithmic profile", given by Eq. (9.24), we still have not determined the value of the constant m. So, now we are going to focus on this constant. The "old logarithmic profile" gives systematically higher values of the wind speed in comparison with the observations. It could be an indicator that the underlying surface is much rougher than it is represented by this profile. This fact can be expressed as

$$D + Z_0 \geq d + z_0, \tag{9.26}$$

which, after substituting expressions (9.19) (with $f(\alpha, m) = \alpha^m$) and (9.20), after some rearrangement, takes the form

$$\alpha^m - \sigma\alpha - (1-\sigma)\left(1 + \frac{d}{z_0}\right) \geq 0. \tag{9.27}$$

This inequality can be used for the estimation of the value of the parameter m. First of all we may say that m should be significantly greater than 1 since for $m = 1$ the inequality (9.27)

is satisfied only for $\sigma_f = 1$ and $\alpha = 1$, i.e. when the Z_0 and D reduce to the roughness length and displacement height for the "old logarithmic profile". When $\alpha \neq 1$, the lower limit of the parameter m can be estimated from this inequality using empirical profile data. Analysing the wind profiles measured above a broad range of forest we have found that an optimum value for the parameter m is 2. With this value of m, the expression (9.24) for the wind profile which will be used in this study has the form

$$u(z) = \frac{U_*}{\kappa} \frac{1}{\sigma(\alpha - 1) + 1} \ln \frac{[\sigma(\alpha - 1) + 1]z - \sigma\alpha d}{\alpha^2 z_0}. \tag{9.28}$$

The expressions for aerodynamic parameters Z_0 and D and friction velocity U_* for forest, derived from continuity conditions, can be found in Mihailović *et al.* (1999)

9.3.4 Exchange of momentum and heat above a non-uniform vegetative surface under non-neutral conditions

As mentioned before, the exchange process can be considered as a result of movement of eddies, carrying heat and momentum. It was assumed that the velocity U_* of the eddies was of the order of $l_m\, du/dz$ where l_m is a characteristic length. Looking dimensionally we can conclude that the accelerations, caused by the friction forces, are of the order U_*^2/l_m or $l_m(du/dz)^2$. Under non-neutral conditions eddies may be also generated by buoyancy, the forces caused by density differences between the air in the eddy and the surrounding air. Buoyancy acceleration is of the order of $\Delta\Theta g/T_A$, where $\Delta\Theta[\theta]$ is the difference between the potential temperatures above and inside the canopy, g $[\mathrm{LT}^{-2}]$ the gravity acceleration and $T_A[\theta]$ is the mean ambient temperature. Since the difference $\Delta\Theta$ is of the order $l_m d\Theta/dz$ then the ratio of the buoyancy and friction acceleration is given by

$$Ri_g = \frac{g\dfrac{d\Theta}{dz}}{T_A\left(\dfrac{du}{dz}\right)^2} Pr_t \tag{9.29}$$

which is commonly used expression for the gradient Richardson's number, Ri_g and where Pr_t is the turbulent Prandtl number. This number and the Monin-Obukhov length L[L], whose precise derivation can be found in Monin and Obukhov (1954) and Priestly (1959), are the most widely used parameters characterizing the degree of non-neutrality. The Monin-Obukhov length L can be considered as the height above the displacement height, where buoyancy forces and friction forces are approximately equal. L may be given as

$$L = \frac{T_A U_*^2}{\kappa g l_m \dfrac{d\Theta}{dz}}. \tag{9.30}$$

Following the Monin-Obukhov theory we introduced the dimensionless height parameter denoted by ζ

$$\zeta = \frac{z - D}{L}. \tag{9.31}$$

According to Mihailović *et al.* (1999), this approach causes changes in the dimensionless height parameter ζ. Furthermore, these changes cause changes in the Φ_m and Φ_h functions in the case of non-neutrality when calculating the exchange coefficients for momentum K_m and heat transfer $K_h$are being calculated. These coefficients may be written as

$$K_m = \kappa U_* \{\Gamma_1 z - \sigma\alpha d\}/\Phi_m \tag{9.32}$$

and

$$K_h = \kappa U_* \{\Gamma_1 z - \sigma\alpha d\}/\Phi_h \tag{9.33}$$

where

$$\Gamma_1(\sigma, \alpha) = \sigma(\alpha - 1) + 1.$$

Functions Φ_m and Φ_h are, according to Businger *et al.* (1971),

$$\Phi_m = (1 - 15\zeta)^{-0.25} \quad \text{unstable} \quad \zeta < 0 \tag{9.34a}$$

$$\Phi_m = (1 + 4.7\zeta) \quad \text{stable} \quad \zeta > 0 \tag{9.34b}$$

$$\Phi_h = 0.74(1 - 9\zeta)^{-0.5} \quad \text{unstable} \quad \zeta < 0 \tag{9.35a}$$

$$\Phi_h = 0.74(1 + 4.7\zeta) \quad \text{stable} \quad \zeta > 0. \tag{9.35b}$$

Relations (9.34) and (9.35) are derived for air column over very homogeneous terrain. Certainly, it does not guarantee that their form will not be unaltered over a patchy surface. We assumed that the relations (9.34) and (9.35) can be maintained. The only differences between correction factors Φ_m and Φ_h, for homogeneous and non-homogeneous underlying surface, come from different values of the parameter ζ where its dependence on the vegetation fractional cover σ_f, is implicitly incorporated. Consequently, we have adapted correction factors Φ_m and Φ_h.

In the literature, alternative solutions can be found for the formulation of the effect of non-neutrality on the profiles of the exchange coefficients. A detailed elaboration of this subject concerning its theoretical and practical aspects is given by Goudriaan (1977). Following him we have derived the expression for the Monin-Obukhov length L in the form

$$L = \frac{T_A U_*^2 \int_{z_1}^{z_r} \frac{\Phi_h}{z' - D} dz'}{\Gamma_1 \kappa^2 g \Delta\Theta} \tag{9.36}$$

where the difference $\Delta\Theta$ for two heights $z_1 = D + Z_0$ and z_r an arbitrary reference level above it, is taken as $\Theta(z_r) - \Theta(z_1)$, which is negative under unstable conditions and positive under stable ones. However, the value of U_*, which is needed in Eq. (9.38) must be derived from a general profile defined by

$$\frac{du}{dz} = \frac{U_* \Phi_m}{\kappa\{\Gamma_1 z - \sigma\alpha d\}}. \tag{9.37}$$

Integration of this equation gives

$$u_r = \frac{U_*}{\kappa} \int_{D+Z_0}^{z_r} \frac{\Phi_m}{\Gamma_1 z' - \sigma\alpha d} dz' \tag{9.38}$$

where *ur* is the wind speed at the reference level. If we want to take into account the effect of non-neutrality then Eqs. (9.31), (9.34), (9.35), (9.36), and (9.38) must be solved simultaneously. In the stable case ($\zeta > 0$) the integration in Eqs. (9.36) and (9.38) can be done analytically. Otherwise, in the unstable conditions ($\zeta < 0$), the calculations must be done iteratively.

9.4 TURBULENCE AND WIND WITHIN THE FOREST

The main motive for studying turbulent flow within the forest is to understand processes governing momentum, mass and energy exchange between the atmosphere and forest canopy. Additionally, during the XX century the scientific community emphasised the importance of wind behaviour for the movement of spores, pollen and particles within and just above the vegetation canopy (Pingtong and Hidenori, 2000; Pinard and Wilson, 2001) as well as for the forest fires spread rate. Ecological and financial effects of forest fires have revealed a definite need for better understanding of wind profiles within and above forest (Curry and Fons, 1938).

In this section we present results of turbulent transfer parameterization within the homogeneous and non-homogeneous canopy. The first-order closure techniques based on K-theory for calculating the Reynolds' stresses within the canopy are described. Limitations of the traditionally parametrized canopy structure and the turbulent transfer coefficient for the forest canopy are considered. In addition, some approaches to turbulent transfer parameterization are presented using the forest morphological characteristics. We will focus on the momentum transfer parameterization since heat and mass transfer are treated in analogous manner.

9.4.1 Short overview of turbulent transfer parameterization within the canopy

The vertical distribution of momentum within different plant communities has usually been modelled by assuming steady and unidirectional wind and negligible pressure gradient force. Under these conditions, the time- and volume-averaged equation for the mean momentum within vegetation (Raupach *et al.*, 1986) turns into a relation describing balance between the vertical shear stress change and a drag force:

$$\frac{1}{\rho_a} \frac{\partial}{\partial z}(-\overline{uw}) = C_{dg} LAD(z) u^2, \tag{9.39}$$

where $\overline{uw}$[M $L^{-1}T^{-2}$] is vertical shear (Reynolds') stress describing turbulent transfer of x-component of momentum in z-direction.

Early modelling studies (Cowan, 1968; Thom, 1971) were based on K-theory supposing that the turbulent momentum flux is equal to the product of an eddy viscosity, represented by turbulent transfer coefficient K_m [$ML^{-1}T^{-1}$], and the local gradient of mean wind velocity. Hence Eq. (9.39) could be written in the form:

$$\frac{1}{\rho_a} \frac{\partial}{\partial z}\left(K_m \frac{du}{dz}\right) = C_{dg} LAD(z) u^2. \tag{9.40}$$

Various assumptions have been made regarding the behaviour of K_m within the canopy. They could be classified as follows:

a) K_m is proportional to wind speed, u ($K_m \propto u$) (Cowan, 1968; Denmead, 1976);
b) K_m depends on canopy height, h_c ($K_m \propto K_m(h_c)$) (Jarvis *et al.*, 1976);
c) K_m is a product of local gradient of mean wind velocity du/dz [T^{-1}] and mixing length within the canopy l_{mc} [L] (Inoue, 1963; Raupach and Thom, 1981; Baldocchi and Meyers, 1988)

$$K_m = l_{mc}^2 \frac{\partial u}{\partial z}. \tag{9.41}$$

During the decade of K-theory application, it become obvious that this model can not provide accurate predictions of wind velocity in lower part of plant canopy where near-zero vertical gradient wind velocity is frequently observed (Shaw, 1977). Corsin (1974) has pointed out that the application of this, also called small-eddy closure technique, (Stull, 1988) is limited to the places where the length scales of flux-carrying motions have to be much smaller than the scales associated with average gradients (Zeng and Takahashi, 2000). Unfortunately, many measurements have shown that the air flow within and just above the canopy is dominated by turbulence with vertical length scales at least as large as the vegetation height (Kaimal and Finigan, 1994). To provide a more reliable insight into the nature of momentum transfer processes within the canopy, some authors suggested higher-order closure models (Wilson and Shaw, 1977; Meyers and Paw, 1987).

As an alternative solution to not-using these closure techniques appears a non-local first-order closure model developed by Zeng and Takahashi (2000). In this model turbulent momentum flux is divided into two parts: one, diffused by the smaller-scale eddies and parameterized according to conventional K-theory; and the other, transported by large-scale eddies as a result of non-local transport caused by shear between air flows above and within canopies. However, vertical shear stress is parameterized in the form:

$$-\overline{uw} = K_m \frac{du}{dz} + C_g u_r (u_r - u) \frac{z}{h_c}, \tag{9.42}$$

where u_r [LT^{-1}] is a wind speed at reference height above vegetation and C_g [ML^{-3}] is an coefficient.

9.4.2 Single layer approach for parameterization of turbulent transfer within the canopy

In the case of homogeneous canopy ($LAD(z) = \text{const.}$), according to Eq. (9.1), leaf area density $LAD(z)$ can be calculated as:

$$LAD(z) = \frac{LAI}{h_c}. \tag{9.43}$$

Substituting $LAD(z)$ from Eq. (9.43) into Eq. (9.39), balance between the vertical shear stress change and drag force takes the form:

$$\frac{1}{\rho_a} \frac{\partial}{\partial z}(-\overline{uw}) = C_{dg} \frac{LAI}{h_c} u^2. \tag{9.44}$$

Assumption that K_m is proportional to wind speed u and that coefficient of proportionality σ is a constant ($K_m = \sigma u$), leads to well known Cowan's profile (Cowan, 1968):

$$u(z) = u(h_c)\left[\frac{\sinh\left(\beta_c \frac{z}{h_c}\right)}{\sinh \beta_c}\right]^{1/2}, \tag{9.45}$$

where $u(h_c)$ is the wind speed at the canopy top, h_c is the canopy height and β_c is the extinction factor defined for wind profile within the canopy:

$$\beta_c^2 = \frac{2h_c C_{dg} LAI}{\sigma}. \tag{9.46}$$

Using the third assumption for K_m, defined by Eq. (9.41), and supposing that mixing length l_{mc} is a constant within the whole canopy space, Inoue (1963) derived exponential wind profile in the form:

$$u(z) = u(h_c)\exp\left[-a_c\left(1 - \frac{z}{h_c}\right)\right], \tag{9.47}$$

where a_c is the canopy coefficient.

Using the wind profile within the canopy given by Eq. (9.48) and taking into account non-uniformity of underlying surface, Mihailović *et al.* (2006) assumed wind profile within the vegetation in the form:

$$u(z) = \sigma_f u(h_c) e^{-\frac{1}{2}\beta_1\left(1-\frac{z}{h_c}\right)} + (1-\sigma_f)\frac{u_*}{\kappa}\ln\frac{z}{z_0}. \tag{9.48}$$

They supposed that the first term on right-hand side of Eq. (9.48) describes well vertical transport of momentum within homogeneously vegetated part of canopy, while the second term is responsible for the turbulence above a bare soil situated within canopy space. β_1 appearing in Eq. (9.48) is the extinction factor obtained by an iterative procedure.

9.4.3 Two-layer approach for parameterization of turbulent transfer within the canopy

The assumption that canopy is a homogeneous medium could be appropriate in the case of grass and tall grass canopy space. However, forest canopy is extremely heterogeneous due to the complexity in tree structure and presence of two specific layers, crown and stands, affecting the transport of momentum into atmosphere on the following way. The absorption of momentum between the crown top and the bottom is 70–90%, depending on the crown depth and the density. The attenuation of momentum, below the bottom of the crown, is rather small up to the roughness layer, where the rest of the air momentum is transferred to the ground due to molecular transport.

According to the observations, wind profile within the forest canopy may significantly deviate from the profiles proposed by Cowan (1968) and Inoue (1963). One should not be

surprised since both relations are derived supposing that plant canopy is a homogeneous one, which is not acceptable in the case of forest canopy. In order to adequately describe within-canopy vertical momentum transfer, Lalić and Mihailović suggested (Lalić, 1997; Lalić and Mihailović, 1998; Lalić and Mihailović, 2002a; Lalić and Mihailović, 2002b; Lalić *et al.*, 2003) an empirical expression for the wind profile within the forest based on two-layer canopy model in the form:

$$u(z) = \begin{cases} u_h \left[\dfrac{\cosh \beta_c \left(\dfrac{z - z_d}{h_c} \right)}{\cosh \beta_c \left(1 - \dfrac{z_d}{h_c} \right)} \right]^{\frac{5}{2}} & z_d < z \leq h \\ C_h \, u(h_c) & z_0 < z \leq z_d \end{cases} \tag{9.49}$$

where: z_d is the crown bottom height and C_h is a constant. According to Massman (1987), factor β_c is equal to $4C_{dg}LAI/(\alpha^2\kappa^2)$. In the case of forest canopy, bearing in mind that smoothness or roughness of canopy from atmospheric point of view is an effect of the amount of leaves and their roughness, α can be parameterized as $\alpha^2 = 4(C_{dg}LAI)^{1/4}$ (Lalić, 1997; Lalić and Mihailović, 1998). In creating the foregoing profile, the evidence that comes from the observations of the wind profile within the forest was taken into account. After the comparisons of the wind profile observed and the wind profile defined by Eq. (9.49) it becomes obvious that two-layer approach in parameterization of forest canopy structure produces minimum deviation from the observation particularly in the layer occupied by the tree crown, where the absorption of momentum is mostly emphasized.

The wind profile defined by Eq. (9.49) requires an additional assumption in defining the momentum transfer coefficient, K_m i.e. turbulent diffusivity within the forest. Instead of commonly used assumption for K_m in the form $K_m(z) = \sigma u(z)$, describing the turbulence through the whole environment occupied by plants, we have introduced another one. For simplicity, σ is often assumed to be a constant regardless of the structure of the canopy vegetation. However, in the case of the forest this idea can be applied just in some part of its environment. Thereby, we have assumed that in the crown of the forest $(h_c > z \geq z_d)\sigma$ can be considered as a function of height z, i.e. $\sigma = \sigma(z)$, while below it $(z_d > z \geq z_0)\sigma$ remains constant. Thus, the momentum transfer coefficient can be written in the form:

$$K_m(z) = \begin{cases} \sigma(z) u(h_c) \left[\dfrac{\cosh \beta_c \left(\dfrac{z - z_d}{h_c} \right)}{\cosh \beta_c \left(1 - \dfrac{z_d}{h_c} \right)} \right]^{\frac{5}{2}} & z_d < z \leq h_c \\ \sigma_d C_h \, u(h_c) & z_0 < z \leq z_d \end{cases} \tag{9.50}$$

where σ_d is assumed to be a constant.

The functional form of $\sigma(z)$ may be found as the solution of the differential equation describing the shear stress within the canopy according to K-theory and supposing that each of two layers is a homogeneous one

$$\frac{d}{dz} \left(K_m \frac{du}{dz} \right) = \frac{C_{dg}LAI}{h_c} u^2. \tag{9.51}$$

Using expressions (9.49) and (9.50) for $u(z)$ and $K_m(z)$, the solution to Eq. (9.51) has the following form:

$$\sigma(z) = \frac{2\ C_{dg} LAI\ h_c}{7\ \beta_c^2 ch^6 \beta_c \left(\dfrac{z - z_d}{h_c}\right)} \left[1 + \sinh^2 \beta_c \left(\frac{z - z_d}{h_c}\right) + \frac{3}{5} \sinh^4 \beta_c \left(\frac{z - z_d}{h_c}\right) + \frac{1}{7} \sinh^6 \beta_c \left(\frac{z - z_d}{h_c}\right)\right]. \tag{9.52}$$

The quantities z_d, C_h and σ_d included in the foregoing expressions should be derived following continuity conditions (continuity of wind speed, turbulent momentum transfer coefficient and continuity of their first derivative) at forest height and crown bottom height.

APPENDIX—LIST OF SYMBOLS

List of Symbols

Symbol	Definition	Dimension or Units
C_h	constant	
C_i	integration constant	[m s^{-1}]
C_{dg}	the leaf drag coefficient estimated from the size of the roughness elements of the ground	
D	generalized displacement height	[m]
K	is an extinction coefficient	
K_m	turbulent transfer coefficient	[m^2 s^{-1}]
L	Monin-Obuhkov length	[m]
LAI	leaf area index	[m^2 m^{-2}]
LAD	leaf area density	[m^2 m^{-3}]
LAD_0	leaf area density of forest crown	[m^2 m^{-3}]
$\overline{L}_d$	the area-averaged stem and leaf area density (also called canopy density)	[m^2 m^{-2}]
L_m	maximum value of leaf area density	[m^2 m^{-3}]
L_z	path length through which the light comes to level z	
P_z	probability of a beam of light passing through a horizontal plane of leaves at height z	
Pr_t	turbulent Prandtl number	
Ri_g	gradient Richardson's number	
T	surface (canopy or soil) temperature	[K]
T_A	mean ambient temperature	[K]
U_*	friction velocity above non-homogeneously covered surface	[m s^{-1}]
Z_0	generalized roughness length	[m]
a_c	canopy coefficient	
c_g	coefficient	[kg m^{-3}]

(*Continued*)

List of Symbols

Symbol	Definition	Dimension or Units
d	displacement height	[m]
du/dz	local gradient of mean wind velocity	[s^{-1}]
g	gravitational acceleration constant	[m s^{-2}]
h_c	canopy height	[m]
l	mixing length above a non-homogeneously covered surface	[m]
l_m^b	mixing length above the bare soil	[m]
l_m^c	mixing length above the canopy	[m]
l_{mc}	mixing length within the canopy	[m]
l_m^α	the mixing length in the roughness sublayer above a vegetative surface	[m]
u_{*g}	friction velocity for a bare soil	[m s^{-1}]
u_*	the friction velocity	[m s^{-1}]
$u(h_c)$	the wind speed at the canopy height	[m s^{-1}]
$u(z)$	the wind speed	[m s^{-1}]
u_r	wind speed at reference height above vegetation	[m s^{-1}]
$\overline{uw}$	vertical shear stress	[kg $m^{-1}s^{-2}$]
z	the vertical coordinate	[m]
z_l	some certain height within the canopy	[m]
z_0	the roughness length	[m]
z_{0g}	roughness length of a bare soil	[m]
z_d	crown bottom height	[m]
z_g	effective ground roughness length	[m]
z_k	zero wind velocity height	[m]
z_m	corresponding height	[m]
z_r	the reference height above vegetation	[m]
$\Delta\Theta$	difference between the potential temperatures above and inside the canopy	[K]
Φ_h	correction factor for heat	
Φ_m	correction factor for momentum	
α	dimensionless constant representing corrected value of the mixing length in the roughness sublayer	
α_G	dimensionless constant estimated to be between 1.5 and 2.0	
β_1	extinction factor	
β_c	extinction parameter for within canopy wind profile	
ζ	dimensionless height parameter	
θ_s	solar zenith angle	[°]
κ	Von Karman constant	
ρ_a	the air density	[kg m^{-3}]
σ	coefficient of proportionality	
σ_d	constant	
σ_f	vegetation cover in fractional units	
τ_H	transmittance of whole canopy	
τ_z	transmittance of canopy layer at height z	

REFERENCES

Baldocchi, D.D. and Meyers T.P., 1988, Turbulence structure in a deciduous forest. *Boundary-Layer Meteorology*, **43**, pp. 345–364.

Businger, J.A., Wyngaard, J.C., Izumi, Y.I. and Bradley E.F., 1971, Flux-Profile Relationships in the Atmospheric Surface Layer. *Journal of Atmospheric Sciences*, **28**, pp. 181–189.

Corrsin, S., 1974, Limitations of gradient transport model in random walks and in turbulence. *Advances in Geophysics*, **18A**, pp. 25–60.

Cowan, I.R., 1968, Mass, heat and momentum exchange between stands of plants and their atmospheric environment. *Quarterly Journal of Royal Meteorological Society*, **94**, pp. 523–544.

Curry, J.R. and Fons, W.L., 1938, Transfer of heat and momentum in the lowest layers of the atmosphere. *Great Britain Meteorological Office Geophysics*. Memoir No. **65**, pp. 66.

De Bruin, H.A.R. and Moore, C.J., 1985, Zero-Plane Displacement and Roughness Length for Tall Vegetation, Derived From a Simple Mass Conservation Hypothesis. *Boundary-Layer Meteorology*, **42**, pp. 53–62.

Denmead, O.T., 1976, Temperate cereals. In *Vegetation and the Atmosphere,* Vol. 2, Edited by Monteith, J.L. (Academic Press, New York, U.S.A.), pp. 1–31.

Garratt, J.R., 1978, Flux Profile Relations above Tall Vegetation. *Quarterly Journal of Royal Meteorological Society,* **104**, pp. 199–211.

Goudriaan, J., 1977, *Crop Micrometeorology: A Simulation Study.* (Wageningen Center for Agricultural Publishing and Documentation).

Gower, S.T., Kucharik, C.J. and Norman J.M., 1999, Direct and indirect estimation of leaf area index, f_{APAR} and net primary production of terrestrial ecosystems. *Remote Sensing of Environment*, **70**, pp. 29–51.

Högström, U., 1985, Von Karman's Constant in Atmospheric Boundary Layer Flow: Reevaluated. *Journal of Atmospheric Sciences*, **42**, pp.263–270.

Inoue, E., 1963, On the turbulent structure of air flow within crop canopies. *Journal of Meteorological Society of Japan*, **41**, pp. 317–325.

Jarvis, P.G., James, B. and Landsberg J.J., 1976, Coniferous forest. In *Vegetation and the Atmosphere*, Vol. 2, Edited by Monteith, J.L. (Academic Press, New York, U.S.A.), pp. 171–240.

Kaimal, J.C. and Finnigan, J.J., 1994, *Atmospheric Boundary Layer Flows. Their Structure and Measurement*, (Oxford University Press, New York, U.S.A.).

Kolic, B., 1978, *Forest ecoclimatology*. University of Belgrade, Yugoslavia, (In Serbian).

Lalić B., 1997, *Profile of Wind Speed in Transition Layer above the Vegetation*, Master Thesis, University of Belgrade, Serbia, (in Serbian).

Lalić, B. and Mihailović, D.T., 1998, Derivation of aer?dynamic characteristics using a new wind profile in the transition layer above the vegetation. *Research Activities in Atmospheric and Oceanic Modelling*, **27**, pp. 4.17–4.19.

Lalić, B. and Mihailović, D.T., 2002a, A new approach in parameterisation of momentum transport inside and above forest canopy under neutral conditions. *Intergrated Assesment and Decision Support. Proceedings of the 1st biennial meeting of the International Environmental Modelling and Software Society*, Vol. **2**, University of Lugano, Switzerland 24/27 June, pp. 436–441.

Lalić, B. and Mihailović, D.T., 2002b, New approach to parameterisation of momentum transport within tall vegetation. *Extended Abstracts, 18th International Conference on Carpathian Meteorology*, 7/11 October 2002, Belgrade (Serbia), pp. 91–93.

Lalić, B. and Mihailović, D.T., 2004, An Empirical Relation Describing Leaf Area Density inside the Forest for Environmental Modelling. *Journal of Applied Meteorology*, **43**, pp. 641–645.

Lalić, B., Mihailović, D.T., Rajković, B., Arsenić, I.D. and Radlovic, D., 2003, Wind profile within the forest canopy and in the transition layer above it. *Environmental Modelling & Software*, **18**, pp. 943–950.

Law, B.E., Cescatti, A. and Baldocchi, D.D., 2001a, Leaf area distribution and radiative transfer in open-canopy forests: implications for mass and energy exchange. *Tree Physiology*, **21**, pp. 777–787.

Law, B.E., Kelliher, F.M., Baldocchi, D.D., Anthoni, P.M., Irvine, J., Moore, D. and Van Tuyl, S., 2001b, Spatial and temporal variation in respiration in a young ponderosa pine forest during a summer drought. *Agricultural and Forest Meteorology*, **110**, pp. 27–43.

Levi, P.E. and Jarvis, P.G., 1999, Direct and indirect measurements of LAI in millet and fallow vegetation in HAPEX-Sahel. *Agricultural and Forest Meteorology*, **97**, pp. 199–212.

Massman, W., 1987, A Comparative Study of some Mathematical Models of the Mean Wind Structure and Aerodynamic Drag of Plant Canopies. *Boundary-Layer Meteorology,* **40**, pp. 179–197.

Meir, P., Grace, J. and Miranda, A.C., 2000, Photographic method to measure the vertical distribution of leaf area density in forests. *Agricultural and Forest Meteorology*, **102**, pp. 105–111.

Meyers, T. and Paw, K.T., 1987, Modelling the Plant Canopy Micrometeorology with Higher-Order Closure Principles. *Agricultural and Forest Meteorology*, **41**, pp. 143–163.

Mihailović, D.T. and Kallos, G., 1997, A Sensitivity Study of a Coupled Soil- Vegetation Boundary-Layer Scheme for Use in Atmospheric Modelling. *Boundary-Layer Meteorology.* **82**, pp. 283–315.

Mihailović, D.T., Lalić, B., Rajković, B. and Arsenić, I., 1999, A roughness sublayer wind profile above non-uniform surface. *Boundary-Layer Meteorology*, **93**, pp. 425–451.

Mihailović, D.T., Lalić, B., Eitzinger, J., Malinovic, S. and Arsenić, I., 2006, An Approach for Calculation of Turbulent Transfer Coefficient for Momentum inside Vegetation Canopies. *Journal of Applied Meteorology and Climatology*, **45**, pp. 348–356.

Mix, W., Goldberg, V. and Bernhardt, K.H., 1994, Numerical experiments with different approaches for boundary layer modelling under large-area forest canopy conditions. *Meteorologische Zeitschrift*, **3**, pp. 187–192.

Monin, A.S. and Obukhov, A.M., 1954, Basic Regularity in Turbulent Mixing in the Surface Layer in the Atmosphere. *Trudi Geofizicheskovo Instituta Akademii Nauk USSR,* No. **24**.

Monin, A.S. and Yaglom, A.M. 1971, *Statistical Fluid Mechanics: Mechanics of turbulence*. Vol. 1, (The MIT Press, Cambridge, U.S.A.).

Pinard, J.D.J. and Wilson, J.D., 2001, First and second order closure models for wind in a plant canopy. *Journal of Applied Meteorology*, **40**, pp. 1762–1768.

Pingtong, Z. and Hidenori, T., 2000, A first order closure model for the wind flow within and above vegetation canopies. *Agricultural and Forest Meteorology,* **103**, pp. 301–313.

Priestly, C.H.B., 1959, *Turbulent transfer in the lower atmosphere*, (The University Chicago Press, Chicago, U.S.A.).

Raupach, M.R., 1980, Conditional Statistics of Reynolds Stress in Rough-Wall and Smooth-Wall Turbulent Boundary Layers. *Journal of Fluid Mechanics*, **108**, pp. 363–382.

Raupach, M.R. and Thom, A.S., 1981, Turbulence in and above Plant Canopies. *Annual Review of Fluid Mechanics*, **13**, pp. 97–129.

Raupach, M.R., Thom, A.S. and Edwards, I., 1980, A Wind Tunnel Study of Turbulent Flow Close to Regularly Arrayed Rough Surfaces. *Boundary-Layer Meteorology*, **18**, 373–397.

Raupach, M.R., Coppin, P.A. and Legg, B.J., 1986, Experiments on scalar dispersion within a model plant canopy. Part I: The turbulence structure. *Boundary-Layer Meteorology*, **35**, 21–52.

Sellers, P.J., Mintz, Y., Sud, Y.C. and Dachler, A., 1986, A Simple Biosphere Model (SiB) for Use within General Circulation Models. *Journal of Atmospheric Sciences*, **43**, pp. 505–531.

Shaw, R.H., 1977, Secondary wind speed maxima inside plant canopies. *Journal of Applied Meteorology*, **16**, pp. 514–521.

Shaw, R.H. and Pereira, A.R., 1982, Aerodynamic Roughness of a Plant Canopy: A Numerical Experiment. Agricultural Meteorology, **26**, pp. 51–65.

Stull, R.B., 1988, *An Introduction to Boundary Layer Meteorology*, (Kluwer Academic Publishers).

Tennekes, H., 1982, Similarity Relations, Scaling Laws and Spectral Dynamics. In *Atmospheric Turbulence and Air Pollution Modelling*, Edited by Nieuwstadt, F.T.M. and van Dop, H. (D. Reidel Publ. Co., Dordecht, Holland), pp. 37–64.

Thom, A.S., 1971, Momentum Absorption by Vegetation. *Quarterly Journal of the Royal Meteorological Society*, **97**, pp. 414–428.

Watanabe, T. and Kondo, J., 1990, The Influence of canopy structure and density upon the mixing length within and above vegetation. *Journal of the Meteorological Society of Japan*, **68**, pp. 227–235.

Wilson, N.R. and Shaw, R.H., 1977, A higher order closure model for canopy flow. *Journal of Applied Meteorology*, **16**, pp. 1197–1205.

Wilson, J.D., Ward, D.P., Thurtell, G.W. and Kidd, G.E., 1982, Statistics of Atmospheric Turbulence within and above a Corn Canopy. *Boundary-Layer Meteorology*, **24**, pp. 495–519.

Zeng, P. and Takahashi, H., 2000, A first order closure model for the wind flow within and above vegetation canopies. *Agricultural and Forest Meteorology*, **103**, pp. 301–313.

CHAPTER TEN

Boundary layer development over rigid submerged vegetation

Paola Gualtieri & Guelfo Pulci Doria
Hydraulic and Environmental Engineering Department
University of Napoli Federico II, Napoli, Italy

ABSTRACT

This chapter deals with a topic which is new in international literature, that is the boundary layer behaviour flowing in a channel over a vegetated surface. For sake of brevity and clearness, only the zero pressure gradient equilibrium boundary layer on one side, and the rigid submerged vegetation on the other, have been taken into consideration.

First of all, there is a long introductory paragraph, which reminds the main literature knowledge on two single topics (boundary layers and vegetated surfaces); this paragraph has been conceived also for teaching purposes.

Afterwards, the results of a long-term research, carried out by the authors, are reported. the topic is tackled mainly in experimental way, using an LDA facility. Basically, local mean velocity value distributions have been measured in different flow test sections, and, consequently, they have been suitably modelled too. Eight different vegetation typologies have been experimentally considered: six of them with sparse vegetation, and two with dense vegetation. Unlike what is customary in international literature, in case of sparse vegetation, velocity distributions have been thinly measured up to the bottom of the current. Modelling has been performed always referring to suitable non dimensional quantities, and it regards the whole height of the velocity distributions, including the current layers flowing through the same vegetation.

Data processing gave intriguing results on holding or not holding of boundary layers equilibrium characteristics, as a function of the different considered vegetation typologies. In the Conclusion paragraph, new hypotheses, to go further in this research type, are given too.

10.1 BASIC LITERATURE CONCEPTS AND AIM OF THE CHAPTER

10.1.1 The boundary layer

10.1.1.1 The standard boundary layer

The boundary layer concept was first introduced by L. Prandtl (Prandtl, 1904). When a fluid of little viscosity, such as air or water, flows past a streamlined solid body at high Reynolds number, the effect of viscosity should be small. Therefore, the flow may be regarded as frictionless and can be examined through the theory of irrotational motions.

However, this theory cannot be used to calculate what happens in the immediate proximity of the body, because the correlated phenomena are primarily due to viscous friction. Prandtl proposed the idea that the effect of viscosity in the flow should be confined to a very thin

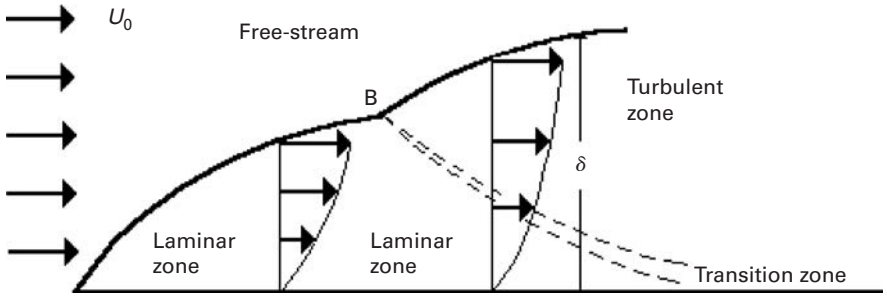

Figure 10.1. Sketch of a turbulent boundary layer.

layer of flow, in the immediate vicinity of the solid surface, where the condition of no slip results in a rather high velocity gradient which, in its turn, generates internal friction caused by fluid viscosity. Prandtl used the term "Boundary Layer" to describe this thin fluid layer. Figure 10.1 is a schematic diagram of the boundary layer flow simplest case.

In this figure, the submerged body is a very simple long flat plate of negligible thickness, immersed in a uniform flow of velocity u_0, with zero angle of attack. In this case, the boundary layer flow develops on both sides of the plate. The figure shows only the upper side.

Within the boundary layer, therefore, a velocity gradient appears in the direction normal to the plate, so that velocity values increase from zero at the plate, up to u_0 far from the plate. This behaviour describes the idea of velocity distribution in the normal direction.

The boundary layer thickness is another important concept. There are many definitions of such a concept. The simplest one is that the boundary layer thickness can be considered as the distance from the plate, where velocity attains 99% of the value of u_0 (δ_{99}). This is not the only definition of boundary layer thickness, as will be shown later. It is evident, in any case, that the boundary layer thickness grows with distance from the leading edge of the plate, due to the rising influence of this obstacle. This behaviour is schematised in Figure 10.1. It is possible to consider the flow over the plate as being composed of the rotational boundary layer near the plate, up to a distance equal to its thickness; and an external irrotational flow beyond this distance: this external flow will be hereafter called the free-stream. In the ideal configuration, the free-stream shows an infinite thickness, whereas in practical realizations its thickness will necessarily be a finite but very large value.

The boundary layer zone nearer to the leading edge presents laminar flow, but, not far from it, the internal friction generates turbulence into the same flow. As a consequence, there is a first laminar boundary layer zone and an ensuing turbulent boundary layer zone much more developed. In the turbulent zone, the boundary layer thickness grows quicker than in the laminar zone. In any case, also in the turbulent zone, a very very thin viscous sublayer is always present near the body surface. On the contrary, in the free-stream, the flow is considered to be laminar and irrotational everywhere.

The so described boundary layer will hereafter be called "Standard Boundary Layer".

The same characteristics are present also in the case of a lightly curved streamlined body surface, and, also in this case, the boundary layer will be referred to as a standard boundary layer. Consequently, the standard boundary layer can refer both to a flat plate and a streamlined body.

In the standard boundary layer over a flat plate already described, both the u_0 value and the pressure (or piezometric head, in case of water flow) value in the free-stream are constant. On the contrary, in case of a lightly curved streamlined body, the u_0 value and the pressure (or piezometric head) value in the free-stream are often variable, because of the streamlined

body's surface curvature. In this second case, the u_0 and the pressure (or piezometric head) gradients in the flow direction can be either constant or variable. In particular, if these gradients are constant, the standard boundary layer is called an equilibrium boundary layer. The case of constant u_0 value and constant pressure (or piezometric head) value can obviously be considered as the simplest case of equilibrium boundary layer, with zero value of u_0 and pressure (or piezometric head) gradients.

A noteworthy characteristic of equilibrium boundary layers is the possibility of defining a non-dimensional theoretical velocity distribution which fits experimental data in all the successive sections of the same boundary layer, save the points internal to the viscous sublayer. The simplest profiles of this velocity distribution are the so-called power and logarithmic distribution laws, both referring to the friction velocity $u^* = (\tau/\rho)^{1/2}$ with τ shear stress at the wall and ρ fluid density. Hereafter, we will concentrate on the second distribution law, in particular in the case of a smooth surface, which has a theoretical background, and is particularly valid for high Reynolds number flows, and can be presented as follows:

$$\frac{u}{u^*} = \frac{1}{0.39}\ln\left(\frac{yu^*}{\nu}\right) + 5.56 \tag{10.1}$$

with y being the distance from the plate and ν the kinematic viscosity. The 0.39 value is a historically very important parameter, generally defined through the symbol "κ", and whose name, in international literature, is "von Kármán Constant". This formulation was already present, for instance, in the very famous Schlichting test dated 1955. These days, a 0.4 value is generally attributed to the "von Kármán Constant".

During those years, Coles (1956), following some previous ideas of Clauser (1956), proposed a logarithmic corrected mean velocity distribution law which resulted in few changes to the constants, but added a new term, called the "wake term". Therefore, this law was called "Coles Wake Law". The new formulation was the following one:

$$\frac{u}{u^*} = \frac{1}{0.4}\ln\left(\frac{yu^*}{\nu}\right) + 5.1 + \frac{\Pi}{0.4}W\left(\frac{y}{\delta}\right) \tag{10.2}$$

This law was considered valid for high Reynolds numbers. The W function was a universal one, and was called the wake function. Coles gave its values as a table, but these values could be furnished also as $W(y/\delta) = 1 - \sin\{\pi[2(y/\delta) - 1]/2\}$, whereas the Π parameter value depends on the pressure (or piezometric head) gradient: for zero value of the gradient, the Π parameter has a value of 0.55. Finally, it is worth noting that the δ thickness was practically defined as the value through which the theoretical equation fitted the experimental points, and its value was a little more than the (δ_{99}) value.

A very common and useful way to present the Coles Wake Law is in the "velocity defect" shape. In this shape, the u_0 velocity of the free-stream appears in the following way:

$$\frac{u - u_0}{u^*} = \frac{1}{0.4}\ln\left(\frac{y}{\delta}\right) + \frac{\Pi}{0.4}\left[W\left(\frac{y}{\delta}\right) - W(1)\right] \tag{10.3}$$

As it is well known, the "Coles Wake Law" was affected by an important failure: its derivative, where $y = \delta$ is different from zero. Dean (1976), following Granville's ideas (1976), proposed a new mean velocity distribution law, where he could eliminate the Coles law failure. His law, however, (and this fact has not been underlined yet) is not continuous in its second derivative, always at $y = \delta$. The authors of this Chapter (Gualtieri and Pulci Doria,

1998) proposed a correction in the Coles law relative to the specific case of zero gradient, in order to overcome also this last failure.

10.1.1.2 The boundary layer with turbulent free-stream

As clarified in the previous paragraph, the hydrodynamic laws governing the standard boundary layer, and in particular the equilibrium boundary layer, are now reasonably well understood, though it is obvious that further research is required. In particular, in the aforementioned hydrodynamic condition, the value of the pressure (or piezometric head) gradient along the flat plate is the most important parameter which fixes the local mean velocity distribution along the direction orthogonal to the plate.

A more sophisticated type of boundary layer flow is the one rising when the free-stream is a turbulent one. This is obviously an important type of boundary layer, as, for instance, the presence of turbulence in streams of various types is a very frequent condition, and often the boundary layers eventually rising within them are of this type. This type of boundary layer will be hereafter defined as "Standard Boundary Layer with turbulent Free-Stream"; if the pressure (or piezometric head) gradient of the free-stream is constant, it will be possible to speak of an "Equilibrium Boundary Layer with turbulent Free-Stream".

Up to the present time, the impact of free-stream turbulence on fully turbulent boundary layers has been investigated in several experimental, analytical and computational studies.

Many of these studies deal with the effects of free-stream turbulence on the main statistical turbulence quantities and, in particular, with the local mean velocity distribution laws (Bandypadhyay 1992; Blair 1983a, b; Castro, 1984; Charnay *et al*., 1971, 1976; Evans 1985; Evans and Horlock 1974; Hancock and Bradshaw 1983; Hancock and Bradshaw 1989; Hoffmann and Mohammady 1991; Huffman *et al*., 1972; Kline 1960; Mc Donald and Kreskowsky 1974; Meier and Kreplin 1980; Robertson and Holt 1972).

Going back to the previous example, Coles believed that, in the case of an equilibrium boundary layer with turbulent free-stream, his own "wake law" could represent also this type of boundary layer, as he assumed that the presence of turbulence in the free-stream would have the same consequences on velocity distribution as an adverse pressure gradient.

In 1990, one of the authors (Pulci Doria and Taglialatela, 1990) developed a new velocity distribution law that can be applied to equilibrium boundary layers, with turbulent free-stream and zero pressure (or piezometric head) gradient, which took into account the presence of turbulence at $y = \delta$ and also the hydrodynamic requirement of having the derivative in that point equal to zero. The Pulci Doria Taglialatela (PDT) distribution was always presented in a "velocity-defect" shape, and was characterized by the presence, within it, of the u_0', which is the root-mean-square of velocity fluctuations at $y = \delta$. In fact, the PDT distribution is the following one:

$$\frac{u - u_0}{u^*} = \frac{1}{0.4}\ln\left(\frac{y}{\delta}\right) - \frac{0.0774}{0.4} - \frac{1.182}{0.4}\left(1 - \frac{u_0'}{u^+}\right) + \frac{1}{0.4}F\left(\frac{y}{\delta}\right) + \frac{1}{0.4}\left(1 - \frac{u_0'}{u^+}\right)F'\left(\frac{y}{\delta}\right) \tag{10.4}$$

As can be seen, the formula holds two experimentally based functions (F and F') of the non dimensional variable y/δ. The values of these functions are shown in Table 10.1. This distribution is valid up to a value of 1.0–1.2 for the ratio u_0'/u^*. Finally, it is worth stressing that the thickness δ of this distribution is once more defined as the value through which the theoretical equation fitted the experimental points, and its value is 1.25 times as large as

Table 10.1. Values of functions (F and F') of the non dimensional variable y/δ within PDT velocity distribution in an equilibrium turbulent free-stream zero pressure gradient smooth bottom boundary layer.

y/δ	F	F'	y/δ	F	F'	y/δ	F	F'
0.03	0.0084	0.000	0.10	0.0400	0.000	0.60	0.1272	1.008
0.05	0.0148	0.000	0.15	0.0728	0.009	0.70	0.1296	1.156
0.06	0.0180	0.000	0.20	0.0880	0.074	0.80	0.1340	1.182
0.07	0.0232	0.000	0.30	0.1080	0.277	0.90	0.1224	1.182
0.08	0.0272	0.000	0.40	0.1192	0.525	0.95	0.1056	1.182
0.09	0.0220	0.000	0.50	0.1252	1.008	1.00	0.0744	1.182

the δ of Coles. Experimental examples of boundary layers treated either through the Coles distribution or the PDT distribution are reported in the authors' paper (Gualtieri *et al.*, 2004).

Before going on with other questions, it is worth noting a few works that represent some fundamental milestones with regard to the study of boundary layers. First of all, we have to remember the very recent 8th English edition of Schlichting work (Schlichting and Gerstein, 2003). Two very important reviews, which appeared in the last few years, are those by Sreenivasan, in 1989, and Gad-el-Hak and Bandyopadhyay, in 1994. Finally, the review by George and Castillo, dated 1997, was not a traditional one, as it established a theory and experiment evaluation methodology based entirely on the averaged Navier-Stokes equations: a methodology which was applied to the fundamental zero pressure gradient equilibrium boundary layer.

10.1.1.3 Local boundary layer experimental surveys

The greatest part of international boundary layer research deals with air boundary layers obtained in air gallery devices. Nonetheless, there is some research on water boundary layers, one author who recently carried out research being Balachandar. His works deal either with standard boundary layers, created through a flat plate inserted within a water current {within which we can recall, for instance, the initial one (Balachandar *et al.*, 2001)}, and with boundary layers created through a new technique, directly within an open channel. Because of the proximity of this technique to the one used by the authors, in particular by one of the authors since 1983 (Greco and Pulci Doria, 1983), many of the former author papers, relative to this subject, are here cited (Balachandar and Ramachandran, 1999; Tachie *et al.*, 2000; Tachie *et al.*, 2001; Tachie *et al.*, 2003).

Also the authors of the present Chapter worked in previous years on boundary layers with free-stream turbulence (Gualtieri and Pulci Doria, 1997, 1998a, b, 1999, 2001, 2003; Pulci Doria 1991), performing their experimental tests in a water boundary layer instead of air.

The papers produced dealt with the influence of free-stream turbulence on boundary layer thickness and the main statistical turbulent quantities, and on the possibility of conceiving a particular boundary layer model. In particular, some of them (Gualtieri and Pulci Doria 1998b; Pulci Doria 1991) dealt with the mean velocity distribution problem. The boundary layers investigated were always equilibrium boundary layers with zero value of piezometric head gradient.

The important characteristic of the experimental equipment used by the authors was that the boundary layer was obtained on the bottom of a rectangular channel, coming out from

Figure 10.2. Overall view of the plant.

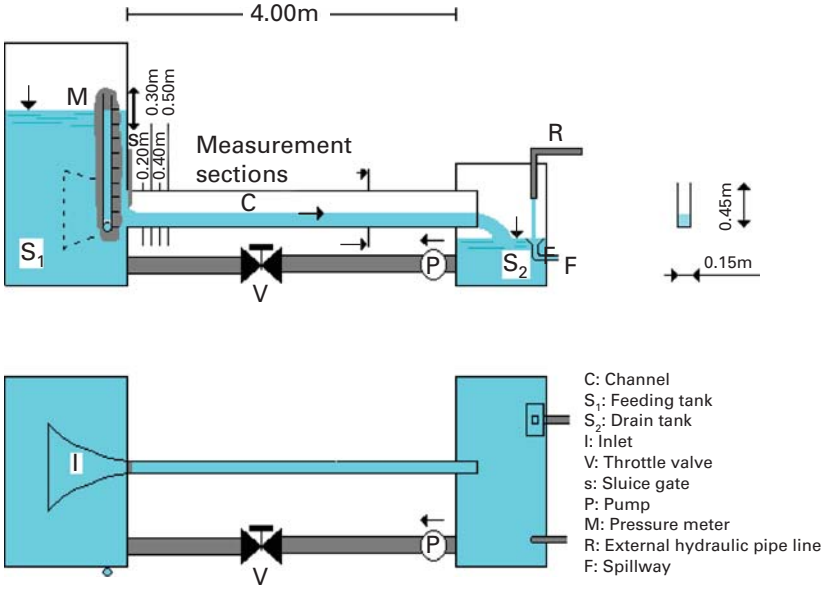

Figure 10.3. Scheme of the experimental plant.

a tank. This is an alternative way to obtain boundary layer streams. This type of flow was first used some decades ago by Russo Spena (Russo Spena, 1954, 1957).

In particular, in order to carry out the experiments, the plant shown in Figs. 10.2 and 10.3 was used.

The main device of the experimental plant was a channel 4 m long and 15 cm wide, with variable slope, with Plexiglas walls and bottom, coming out from a feeding tank supplied by a circulation pump, which took water from the drain tank downstream.

The tank fed the channel through a rectangular adjustable sluice gate. The inlet towards the sluice gate was modelled through a suitable Plexiglas device.

In this channel, it was possible to measure the height of the water in the tank, the height of the sluice gate, the slope of the channel, as well as the height of the water in every cross section of the channel itself.

In the first sections of the channel, a boundary layer was generated on the bottom.

The boundary layer thickness increased in the subsequent sections along the channel, till it reached the same value as the height of the circulating flow, at a distance, from the inlet of the channel, depending on the dynamic characteristics of the flow itself.

Attention was paid to way in which the boundary layer was generated, in order to ensure that what was being dealt with was an effective standard boundary layer stream.

As a matter of fact, in a standard boundary layer, as already stated in paragraph 10.1.1.1, the free-stream thickness should be very large (in theory, infinitely large) and the stream under investigation should be very wide (in theory, infinitely wide), in order to avoid the effects of lateral walls. Otherwise the flow in the channel investigated might not be considered to be a real standard boundary layer.

Nevertheless, even if these conditions are not met, that such a stream could be considered indeed a standard boundary layer had been confirmed in some past studies by one of the authors, since the years of his first major paper about this matter (Greco and Pulci Doria, 1983). The agreement among the distributions of the main statistical characteristics of the turbulence, obtained in these types of streams and those found in literature with reference to standard boundary layer air flows confirmed this. This agreement has been consistently confirmed in subsequent papers by this author.

Recently, the authors of this Chapter, in order to go deeper into the matter, performed a specific measurement survey (Gualtieri *et al*., 2004). The object of the survey was to experimentally and directly verify that the stream, in a channel coming out from the tank through a rectangular orifice, like the one in Figs. 10.2 and 10.3, is really an equilibrium boundary layer with turbulent free-stream.

In order to develop such direct verification, the authors set up the experimental equipment in the following way. Four different flow conditions were established in the channel characterized by different openings of the sluice gate and, therefore, by different values of the height in the vena contracta and the free-stream thickness. The head on the vena contracta was kept constant in the four conditions, so that the free-stream velocity was the same in every flow condition. Consequently, the flow-rate was different in the four flow conditions. The bottom of the channel had always a suitable slope to make the free channel surface horizontal *(in particular it was always the same)*. Therefore, the piezometric head of water flow on the bottom was constant along the channel, and consequently, the boundary layers were in equilibrium. In particular, in Table 10.2, the four values of the channel slope, the head in the tank on the vena contracta, the height in the vena contracta, the flow rate, the velocity in the free-stream are scheduled for each flow condition (run).

In each flow condition (run), the water stream was investigated in four streamwise locations (test sections) in the channel, 20 cm, 30 cm, 40 cm and 50 cm downstream of the flow inlet. In particular, measurements of local mean velocity distributions, in the vertical axis of each test section, were performed through velocity measurements at many experimental points (almost twenty) for each vertical axis, using an LDA system with a tracker and a frequency-shifter.

Afterwards, all the mean velocity data, in the four runs and relative to the four test sections, were collected in a single diagram (Fig. 10.4). In particular, following some experimental data, in each test section a δ_{COLES} and a δ_{PDT} value, not depending on the particular run,

Table 10.2. Flow characteristics.

Run	Slope	Head(cm)	Height in vena contracta(cm)	Q(dm^3/s)	u_0 (m/s)
Run 1	0.25%	10.34	4.62	9.87	1.424
Run 2	0.25%	10.34	5.56	11.88	1.424
Run 3	0.25%	10.34	3.68	7.86	1.424
Run 4	0,25%	10.34	3.02	6.45	1.424

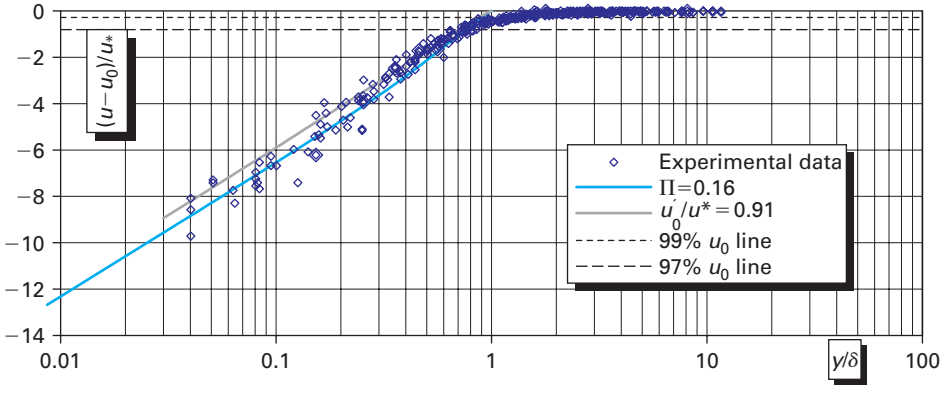

Figure 10.4. Experimental data, Coles and Pulci Doria—Taglialatela wake laws for any section and in all runs.

had been chosen. Finally, both the Coles and Pulci Doria-Taglialatela laws were drawn in the diagram: a 0.16 Π value was chosen for the first one, and a 0.91 value of the ratio u_0'/u^* for the second one.

It can be observed that both laws fit well the experimental data, especially in proximity of the frontier between the boundary layer and the free-stream; that is, where the influence of the turbulence in the second one is stronger.

On the basis of all the results of this research, it was possible to state that the four flows considered (relative to different sluice gate openings) were equilibrium boundary layer streams (with turbulent Recovery Layer). In particular:

1) The slopes of the four flows, needed to keep piezometric head constant, were always the same;
2) The experimental local mean velocities, in the four test sections and in the four flow conditions, superimposed perfectly.

Therefore, these two results showed that, even giving an infinitely thick free-stream, the channel slope and velocity distribution properties would always be the same. Moreover:

3) The four currents behaved as equilibrium boundary layers in their non dimensional velocity distributions relative to different test sections superimposed on one another;
4) For all the four currents, the experimental local mean velocities fitted well with classical velocity distribution laws in a boundary layer.

Without doubt, these currents presented all the characteristic behaviours of equilibrium boundary layers (with turbulent free-stream).

A last observation about these measurements is that, in some cases (lower streams and test sections far from the inlet), the stream height does not approach the height of the chosen δ values: nevertheless, the stream (up to the height to which it arrives) behaves as a boundary layer in any case, and this property will be widely used in what follows.

10.1.2 The vegetated surfaces

10.1.2.1 The problem of currents flowing over vegetated beds and the different possible vegetation models.

The study of the effects that the vegetation in the natural and artificial beds has on the characteristics of the stream flowing down in them (with particular reference to the flow resistance and to the flow rate) can be traced back to Chézy, who devoted himself to it at the end of the eighteenth century.

Typical examples of the effects of vegetation on water flow are the following ones: the decrease of the water velocity and the raising of the water levels i.e. the reduction of flow discharge capacity; the encouragement of the deposition of suspended sediment; the change of the magnitude and the direction of the currents within the channel, causing or reducing local erosion; the interference with the use of the water for conveyance, navigation, swimming and fishing.

Such effects depend mainly on height, density, distribution and stiffness and type of vegetation. These characteristics may change with the season, e.g. the flow resistance may increase in the growing season and diminish in the dormant season.

Much of the earlier studies on the hydraulic effects of vegetation were concentrated on determining roughness coefficient rather than obtaining a better understanding of the physical processes. Typically, a conventional method considered for head loss evaluation in vegetated channels was to select a suitable value of Manning's roughness coefficient n, which grouped all the sources of flow resistance, including vegetation (Chow, 1959).

Anyway, in the past, vegetation on river beds has been considered just as a source of flow resistance, and for this reason it has been usually eliminated.

Now, vegetation is no longer regarded merely as an obstruction to the movement of the water, but rather as a means for providing stabilization for banks and channels, habitat and food for animals, and pleasing landscapes for recreational use. Therefore the preservation of vegetation is of great relevance for the ecology of natural and artificial systems. For this reason, the study of the effects of vegetation on the hydrodynamic behaviour of the rivers represents one of the most basic knowledge required by engineers.

Recently mean flow and turbulence characteristics in presence of vegetation have been studied especially in presence of vegetation for the case of atmospheric flows over plants canopies. One of the main motivations was for understanding the transport processes in natural environments.

The developments of this research topic have given raise to interesting effects regarding the hydraulic research on vegetated open-channel flows. Consequently, numerous studies both experimental and numerical, have been carried out in order to examine closely not only the problems relative to the determination of the flow resistance of the streams on vegetated bottom, but also the main hydrodynamic characteristics of these streams, as the mean flow and the turbulent structures, and, therefore, the related transport processes of pollutants, heat, sediments.

With reference to the kind of vegetation, the investigations may be classified into two groups, the first one relative to rigid vegetation, the second one relative to flexible vegetation.

Rigid vegetation may be modelled through wooden or metallic cylinders, or through natural plants; flexible vegetation may be modelled through plastic strips or through grass or other vegetation types. Moreover these models of vegetation may have different densities, and the effects of wholly or partially submerged vegetation may be examined.

Usually, these studies are concerned with uniform or steady flows.

In (Lopez and Garcia, 1997), a brief review of the works concerning the interactions between vegetation and either atmospheric or free-surface flows is reported.

In the following paragraphs 10.2 and 10.3 of this Chapter the effects on a turbulent boundary layer flow of two different models of rigid fully submerged vegetation will be described. The first model is realized through brass cylinders of different heights and densities, arranged in rectangular or square shapes; the second one is realized through a synthetic grass carpet.

Therefore, it has been deemed suitable to report a brief review of the more recent papers concerning the effects of fully submerged rigid vegetation on uniform or steady flows.

10.1.2.2 Literature review about rigid fully submerged artificial vegetation

As stressed in previous paragraph 10.1.2.1, here a brief review of the recent papers concerning the effects of fully submerged rigid vegetation on uniform or steady flows will be exposed. Sometimes also cases of partially emerging vegetation, or flexible vegetation will be also considered, if suitable to better clarify either the more important (for our sakes) previously considered cases or the specific authors thoughts. The main part of the papers regards clearly artificial vegetation; only a few ones are devoted to natural like vegetation.

It is suitable to stress, once and for all, that in describing the different authors' papers, often their own words have been used, for the sake of signify their thought in the better way it would be possible.

Every paper that has been examined and deeply described is reported in the following through authors names and publication year. Sometimes the actual papers description is preceded by a brief record of its background The papers are referred in their temporal sequence, so that a kind of a vegetation researches history is generated.

(Tsujimoto *et al*., 1992)

The interactions between flow and vegetation differ for different species of water plant. When the vegetation layer over a bed is thin and the flow inside the vegetation is negligible, the bed may be treated as a rough bed. But, when the vegetation layer is thicker and the flow inside the vegetation cannot be neglected, the interaction between the faster flow over the vegetation and the slower flow inside the vegetation must play an important role in the turbulence.

In (Tsujimoto *et al*., 1992), this thicker vegetation case is investigated, as regards to rigid plants. The turbulence characteristics of a uniform flow developing in an open channel, with vertical rigid cylinders of the same diameter and height, set at equal spacing in a square pattern, as model of thicker rigid vegetation, are experimentally investigated in a laboratory flume. Based on the experimental data, the classical turbulence model (mixing-length model) is modified by focusing on the interaction between the flows over and through the cylinders to describe the velocity profile from the flume bed to the water surface.

In this study the "projected area of vegetation per unit volume of water in the flow direction" (dimensionally $[L^{-1}]$) is defined "so small" that the net and the apparent velocities of the flow in the vegetation layer can be considered equal.

The results obtained, neglecting the bottom shear stress in comparison with the additional resistance due to the vegetation, can be summarized as follows. When the flow depth is smaller than the vegetation height, there is a uniform velocity in the vegetation layer and the Reynolds stress is zero; the turbulence intensity is not zero but it is very small.

When the flow depth is larger than the vegetation height, the turbulence characteristics in the free-surface flow region are little affected by the vegetation layer, while, the flow in the vegetation layer is strongly affected by the faster surface flows.

In particular, at the interface between the vegetation layer and the surface-flow region, the profiles of the velocity distributions show an elbow, the profiles of the turbulence intensity and Reynolds stress show a peak, indicating that the flow is characterized by the shear at this level, and suggesting an active momentum exchange there.

The profiles of the induced velocity and Reynolds stress in the vegetation layer are roughly approximated by exponential functions, with exponents respectively β and α representing the turbulent structure in the vegetation layer, and with the presence of two parameters, u_k and τ_k, representing, respectively the velocity and the shear intensity at the interface between the vegetation layer and the surface-flow region.

The β and u_k values also determine the boundary conditions for the velocity and the velocity gradient at the interface between vegetation layer and surface flow region.

With the induced velocity profile in the vegetation layer approximated by an exponential function, a method to correct the energy slope, which is difficult to determine experimentally, is proposed. This correction results in a reduction in the scatter of the data, showing the relations among α, β u_k and τ_k.

An analytical model describing the turbulence structure in the vegetation layer, which leads to relations among α, β and u_k was derived by assuming the Reynolds stress distributes exponentially in the vegetation layer

(Shimizu and Tsujimoto, 1994)

In (Shimizu and Tsujimoto, 1994), the characteristics of a turbulent flow developing over a submerged vegetated layer are numerically analyzed with a k–ε turbulence model.

In order to describe the boundary accurately, the flow within a vegetation layer cannot be treated as a two dimensional flow. Thus the equation governing the flow was spatially averaged as in a porous medium and the effect of individual roughness elements was taken into account, neglecting the geometry of individual vegetation elements, by an averaged local drag force (averaged in a calculation mesh). Therefore, the presence of individual vegetation elements was accounted for the spatially averaged drag force acting upon individual elements. Such a technique was introduced in analyzing canopy flow in the field of meteorology by (Wilson and Shaw, 1977).

Then the modified equations were obtained by adding the drag terms due to vegetation not only to the momentum equation, but also to the k–ε turbulence model standard equations.

The calculations based on the present model were executed for uniform flow conditions in an open-channel vegetation, and the results were compared with turbulence measurements made in flume (Tsujimoto *et al*., 1992), in order to determine the numerical values of the parameters involved in the model, and to certificate the applicability of the model for flow over vegetation layers with different densities.

Not only the velocity profiles but also the statistical properties of turbulence can be described by the calculation based on the present model, where the specified model parameters can be rather universal, at least under the conditions of flow with idealized homogeneous vegetation. In fact, varying pattern of vegetation may bring about heterogeneous flow, often with secondary currents.

Moreover the calculated results were consistent with previous analysis, where an exponential distribution of the Reynolds stress in the vegetation layer was assumed, and the macroscopic force balance was considered in the vegetation layer, while a mixing length model was applied to the surface flow.

The present model was also applied to unestablished flow over a vegetation layer. In fact, when the flow is introduced to the vegetated bed, a transient process occurs where the turbulent characteristics change longitudinally until they reach an equilibrium state

sufficiently downstream. The longitudinal changes of the profiles of mean velocity and Reynolds stress in the transient process were calculated by assuming, for simplicity, that the water surface elevation is parallel to the bed.

The comparison between calculated longitudinal change of the mean velocity profile and the measured data demonstrates the applicability of the model to non uniform flow conditions. The comparison of the calculated Reynolds stress distribution with the measured one shows that the present model can also explain the transient change of Reynolds stress distribution.

Therefore, the numerical results showed a good agreement with the measurements in the flume where the depth in the vegetated reach was tried to be kept as constant as possible and, therefore, the comparisons demonstrate the applicability of the model also to non-uniform conditions.

The study suggests that the proposed numerical model can be considered a good representation of flow over a vegetated bed.

(Kutija and Hong, 1996)

In (Kutija and Hong, 1996), a numerical model is described, developed to help in deepening the understanding of flexible submerged vegetation-induced resistances in steady uniform flow, and, in particular, by following the effects of the various parameters involved. The basic model is a one-dimensional vertical mixing model which is coupled to the equation of conservation of momentum in the horizontal direction. It is used as a tool for investigating the influences of different parameters on the total resistance. The model addresses both rigid and flexible vegetation. In case of rigid vegetation, the most significant parameters are the properties of the height, the diameter and the density of the vegetation itself. In case of flexible vegetation, the role of the reed height is taken over by the effective reed height, which depends on the bending of the reed itself, due to the flow of the water.

The shear term is approximated within this model in two ways. In the surface flow layer, it is modelled as a turbulent shear stress approximated by a mixing length theory; in the vegetation layer, it is modelled according to the eddy-viscosity theory.

But comparing data from inflexible vegetation (Tsujimoto and Kitamura, 1990) with the results of the model, it became obvious that the eddy-viscosity approximation was not suitable for the whole height of the vegetation layer, especially near the tip of the reed, but only for a part (p) of the height of the vegetation layer, which is influenced by the density, the diameter and the stiffness of the reed. The rest of the height of the vegetation layer was modelled in the same manner as the surface flow.

In case of flexible vegetation, the effective height of any representative reed used in the evaluation of the drag force is influenced by the bending of the reed due to the flow of the water. The deflection of the reed can be calculated according to the standard cantilever beam theory (e.g. Timoshenko, 1955). As result of the bending, the effective height of vegetation is reduced, which means that the height over which the load is acting is also reduced and this reduced load causes less bending that would result with the full effective reed height: it is necessary to use an iterative procedure, which is stopped when a prescribed difference between the load height and the effective reed height is reached. It is obvious that in case of flexible vegetation the additional flow resistance is a result of more complex interactions than in case of rigid vegetation. Therefore, further study should be directed to establishing the interrelationship among the effective height of vegetation and the reed properties.

The additional force term due to vegetation, in the layer above the vegetation is equal to zero, while in the vegetation layer it is defined as a function of the density of reeds, the flow velocity, the drag coefficient, the diameter of one reed and the effective height of vegetation.

Some data from (Tsujimoto and Kitamura, 1990) were used for verification of the model with fixed, inflexible vegetation, due to the lack of experimental data relative to flexible vegetation.

In order to describe the influence of different parameters on the flow resistance, a simple example is used, relative to conditions present in floods planes of the river Rhine in the Netherlands. The Authors observe that they do not introduce dimensionless combinations of the variables involved in the model, in order to leave all such possibility open at this stage. The influence of each parameter involved in the model is investigated by changing one parameter at time from the initial set of data and comparing the results with the ones obtained by the initial set of data. However not all these parameters are independent of each other. That means that when only a parameter is changed and all the others are kept constant, a not fully realistic situation might be obtained, which might lead to premature and possibly incorrect conclusions.

It results that the computational parameters as the grid step and the time step do not much influence the flow resistance; the hydraulic parameters as the water depth influences the flow resistance; the Chézy coefficient does not much influence it; the parameters connected with the turbulence model as p and α (an empirical coefficient) influence the flow resistance; the reed geometries and characteristics as the density, the height, the diameter and the stiffness are important parameters for assessing the flow resistance.

Once calibrated, the model can be added, as a module, into an existing two-dimensional nearly-horizontal flow model.

However, the model still needs to be verified using field measurements taken in presence of flexible vegetation.

(Klopstra *et al*., 1997)

In (Klopstra *et al*., 1997), results from studies on hydraulic roughness of vegetation reported in literature are used for development and verification of a physically based model of vertical flow velocity profile and hydraulic roughness of submerged tall vegetation such as reeds. The velocity profile of submerged vegetation is treated separately for the vegetation layer and the surface flow region. The two profiles are smoothly matched through boundary conditions at the interface.

For the vegetation layer, the Authors start from the momentum equation, assuming uniform and steady flow. The turbulent shear stress can be described by the concept of Boussinesq. In conformity with the turbulence models described in (Rodi, 1980) the eddy viscosity is assumed to be characterised by the product of a velocity scale and a length scale of the large scale turbulence, which is responsible of the vertical transport of momentum. In conformity with (Tsujimoto and Kitamura, 1990), the characteristic velocity scale is assumed to be represented by the flow velocity distribution. The characteristic length scale α is assumed to be independent of z. Transforming and solving the momentum equation, the velocity profile for the vegetation layer is established. The only unknown parameter is the characteristic length scale α.

For the surface flow region the Prandtl's mixing length model is adopted, resulting in the well-known logarithmic velocity profile. The virtual bed level of such a profile does not coincide with the top of the vegetation but appears to lie under that level.

From the average flow velocity in the vertical, which follows from the integrals of the velocity distribution in the vegetation layer and in the surface flow region, the hydraulic roughness expressed as the value of Chézy coefficient, can be obtained, through a complex explicit expression, when vegetation characteristics, water depth and characteristic length scale α are known.

The model verification is assessed in two successive steps: (1) comparison with measured flow velocity profiles from flume experiments by varying the characteristic length scale α in such a way that the shape of the measured velocity is represented; (2) comparison with measured hydraulic roughness values from flume experiments.

The first verification step shows that the characteristic length scale α is not independent of z. To make the analytical model generally applicable, α has been correlated to hydraulic

and vegetation characteristics as the water depth and the height of the vegetation elements. With this relation for α, the model is tested again and the comparison among the hydraulic roughness values calculated with the model and the corresponding ones measured from flume experiments reported in literature, is good.

Models results for field situations show that , under certain conditions, e.g. α exceeds the values for which the relation for α was fitted, the calculated virtual bed level appears to lie up the top of the vegetation. This, in combination with the resulting low Chézy-values, shows the need for additional research either on the validity of the modelling concepts or on the relation for α. This study should be combined with a profound field measurement program (or on large scale flume experiments) so as to validate the study results.

(Meijer and van Velzen, 1998)

In (Meijer and Van Velzen, 1998), the physically based model developed by (Klopstra *et al*., 1997), that predicts the vertical flow velocity profile in the vegetation layer and in the surface flow region separately, and the hydraulic roughness of submerged vegetation, is considered. It is a physically based model, with one empirical parameter (the characteristic turbulence length scale α), to be determined by physical model tests. Different shear-stress descriptions are applied for the vegetation layer and the surface flow region. The analytical model had been validated by results from literature, based on scale model tests. It had not been validated for field condition yet, due to the lack of data.

In this paper an extensive set of flume experiments on prototype-scale, carried out in 1997 and 1998, is discussed, in order to verify the applicability of the analytical model for fields conditions. Vegetation is simulated, respectively, in 1997 with steel bars, in 1998 with natural reeds, as verification in a more realistic situation. The density is defined as bars or reeds per m^2; their values were, respectively, 256 and 64 bars per m^2, and 256 reeds per m^2.

The results of the flow measurements carried out using steel bars, show that the analytical model describe the measured flow profiles quite well and moreover, on the basis of the experiments, the prediction of the empirical parameter is improved. In particular, the dependence of α on the water depth and on the vegetation height, is confirmed, although through a different relation, while the α-value is proved to be independent of the vegetation density. The comparison among the Chézy hydraulic roughness values calculated with the model and the corresponding ones measured on prototype-scale flume experiments, is good, due to the fact that the Chézy coefficients are relatively insensitive to deviations in α value. Therefore the α parameter is the empirical element in the analytical model with the highest uncertainty.

According to the Authors, the tests with the steel bars can be considered as fundamental research, whereas the tests with the natural reed should be regarded as a verification of a more realistic situation. The results of the flow measurements carried out using natural reed show that near the surface the velocities seem to be somewhat underestimated. It should be noticed some unresolved questions as that the α-function validated for steel bars, is not necessary valid for the natural reed and that an average reed height might not represent the varying reed height well.

Anyway, although the model does not incorporate the effects of variable diameters and heights, tufts and the bending of the reed stalks, the results seem to confirm the applicability of the model for the prediction of the hydraulic roughness of natural reed vegetation.

Moreover the Authors point out that in these studies only the average flow velocity in one direction was involved. There are still a lot of unused data available in the other two dimensions which can be used, e.g., for improve the α-function, involving the turbulent characteristics.

(Lopez and Garcia, 2001)

In (Lopez and Garcia, 2001), the ability of numerical algorithms, based on two equation closures of turbulence (k–ε and k–ω formulations), to model the mean flow and the turbulence structure in open-channel flows with rigid, submerged vegetation is studied. From a mathematical point of view, the flow of water through and above vegetation presents new challenges due to the 3D nature of the turbulence, which represents a highly nonhomogeneous flow field. From an engineering perspective, a 1D description of the problem is commonly desirable.

A methodology to transform the 3D problem into an 1D framework, developed for atmospheric flows through plant canopies by (Raupach and Shaw, 1982), were applied to vegetated open channels. In particular, (Raupach and Shaw, 1982) proposed two schemes, by averaging the conservation equations over space and time.

In particular, in the first one (scheme I), the equations that describe the instantaneous flow field are locally time averaged over an horizontal plane large enough to obtain mean values independent of spatial variations due to the turbulence and the canopy structure. In the second one (scheme II), the three dimensional flow structures is first locally time averaged, to filter fluctuations due to the turbulence, and then spatially averaged to eliminate variations in space, due to the canopy structure.

With this methodology, drag related terms arise as a consequence of the averaging procedure, and it is clear that the simple addition of drag related to body forces in the momentum equation is incorrect, since the dispersive fluxes are not included. The budget of turbulent kinetic energy, irrespective of the averaging scheme, is composed of sources, sinks and transport terms. Two characteristic processes act as turbulent kinetics generators, i.e., transferring energy from larger scales (either mean flow or larger eddies) toward turbulent fluctuations in space or time at smaller scale: (1) the work of Reynolds and dispersive stresses against mean velocity gradients, which contribute to the generations of fluctuations in time and spatial perturbations of time-averaged velocities; (2) the work of mean flow or large eddies against pressure differences due to obstacles.

There are two limiting cases worth being analyzing. The first one is considered in the already remembered work of Raupach and Shaw (1982) and concerns the case when the length scale of canopy elements (and of their wakes, or in other words the scale of the wake-generated turbulence) is much larger than the Kolmogorov microscale, so that the viscous term becomes negligible. In this situation, the work of the mean flow against pressure differences becomes equal to the wake-production term for the turbulent fluctuations in time.

The second one concerns the case when the length scale of canopy elements (and of their wakes, or in other words the scale of the wake-generated turbulence) is much smaller (or even of the order of) than the Kolmogorov microscale. In this situation almost all the energy is spent in the generation of spatial fluctuations, and is therefore directly dissipated into heat. In this situation, there is a negligible contribution from the wakes to the spatial average of the turbulent fluctuations in time.

The first one of these situations seems to be common to atmospheric flow, whereas the second situation is more common to water flows with relatively low plant concentrations. This is reasonable, considering the Kolmogorov microscale is smaller in air than in water. In addition, the characteristic length scales of canopy elements in atmospheric flows can be expected to be in general much larger than those found in water flows.

The numerical closure schemes selected for the study are the k–ε and the k–ω models. Following the common practice in turbulence closure schemes, it is assumed (and experimentally validated) that the total averaged vertical turbulent transport of longitudinal momentum, in the presence of vegetation, can be modelled using an eddy viscosity approach. Boundaries conditions at the bed account for the presence of vegetation, and algebraic

expression to estimate the different components of the Reynolds stress tensor (proposed by (Rodi, 1976)), was slightly modified for the extra turbulence generation due to the plants.

Numerical results were compared to experimental observations on mean flow and turbulence structure of open channel with cylindrical wooden dowels (arranged in a staggered pattern with variable density, expressed as frontal area of obstructions per unit volume), to simulate rigid, submerged vegetation, made at the Ven Te Chow Hydrosystems Laboratory, University of Illinois.

Both models accurately predicted experimental observations on mean flow and turbulent quantities (up to the second-order statistics), and provided very good representation of the production, inertial diffusion, and dissipation terms in the turbulent kinetic energy budget. No significant difference was found between the numerical performance of either model. Flow resistance measured in terms of Manning's n, shows an almost constant value close to one corresponding to non-vegetated channels up to some threshold plant density. A linear increase is observed once this limit is exceeded. This work shows the need to average flow measurements taken in vegetated waterways in both space and time to obtain meaningful observations. The challenge for future work is to extend the predictive capabilities of the numerical models developed for "idealized" vegetation to the case of natural one.

(Stone and Tao Shen, 2002)

Well-established flow resistance formulas, have long been used to analyze river flows. However, the resistance characteristics of relatively smooth boundaries roughened with large roughness elements are not well understood.

Flow resistance due to cylindrical roughness can provide a better understanding of the resistance in vegetated channels. Many studies attempted to extend the conventional flow resistance formulas to account for the effect of vegetation with empirically determined resistance coefficients. However, those studies were not able to provide methods applicable to a wide range of vegetation conditions.

Moreover, the understanding of flow resistance in channels with rigid vegetation stems provides the basis for analyzing flow resistance with flexible stems. Kutija and Hong (1996), as already remembered, demonstrated that formulas developed for rigid vegetation could be extended to include the effects of stem flexure by an iterative method using a simple cantilever beam theory.

Recently, most studies focused on velocity profiles and turbulent characteristics of vegetated channel instead of developing resistance laws and conveyance formulas.

In this paper, the hydraulics of a flow in an open channel with circular cylindrical roughness is experimentally studied. The laboratory study consists of an extensive set of velocity profiles for flow with emergent and submerged cylindrical stems of the same height and of various diameters. The stems are distributed with staggered geometries, with different concentrations (defined as the number of stems per unit bed area).

Open channel flow with submerged cylindrical roughness can be envisioned as two interacting flow layers: the roughness layer or the stem layer, which is the lower layer containing the cylindrical stems, and the surface layer, above the stem layer, containing no part of the roughness.

An emergent condition can be considered as a limiting condition of a submerged one with no surface layer.

In general, the flow velocity in the stem layer is significantly smaller than in the surface layer, due to the drag imparted by the stems. The effect of the bed friction on the shape of the velocity profile is important only very near the bed where the profiles decrease to zero.

Due to the interaction of the surface and the stem layers, the submerged condition is much more complicated than the emergent condition.

Consider a steady, uniform, open channel flow with submerged cylindrical stems of equal length distributed uniformly over the channel bed. For a control volume of unit bed area

extending from the bed to the water surface, the momentum balance in the streamwise direction gives that the streamwise component of the weight of the water mass can be given by the resistance due to the drag around the cylinders within the stem layer and the bed shear stress. The area concentration is the fraction of the bed area occupied by stems, expressed through the number of stems per unit plan area of bed and the stem diameter.

The stem drag force per unit bed area is expressed through the drag force for a single cylinder in an array of identical cylinders, and the depth-averaged velocity of the constricted section in the stem layer. Therefore, the drag force is expressed in term of the velocity in the stem layer, instead of the often-used apparent vegetation layer velocity defined as the discharge in stem layer over the gross cross-sectional area. Moreover, in this study bed friction is included for completeness, although it is generally amounted to less than 3% of the total channel resistance.

Therefore, the friction slope of the channel flow may be considered as composed of contributions from bed resistance and stem resistance.

The expression of the apparent vegetation layer velocity can be rewritten in terms of the velocity in the stem layer. Moreover, it is hypothesized a relationship between the channel velocity (called apparent channel velocity) and the maximum velocity in the stem layer. Combining these expressions it is obtained a flow resistance formula based on the stem drag coefficient and a velocity coefficient.

Experimental data are used to determine these coefficients and to validate the preceding analysis.

In particular, the emergent flow data are used for drag coefficients calculations because there is no surface layer to complicate the analysis. An average value of the coefficient is determined. Moreover, it is used to calculate the apparent vegetation layer velocity and the results were compared with measured values for the emergent as well as submerged cases, obtained from this investigation and those from Fenzl (1962) and Tsujimoto and Kitamura (1990), including a wide range of roughness and hydraulic conditions. It is showed a generally close agreement between the calculated and the measured values of the apparent vegetation layer velocity values.

The velocity coefficient is calculated. An examination of the flume data suggested that it may be proportional to the wetted stem length/flow depth ratio. To verify this, all the data from the present study, as well those of Fenzl (1963) and Tsujimoto and Kitamura (1990) are plotted together, using dimensionless variables, including both emergent and submerged conditions and a wide range of roughness and hydraulic conditions.

Therefore, a flow resistance formula is obtained for channels with cylindrical roughness, valid for both emergent and submerged cases.

The effect of vegetation flexibility is not considered in this study. Therefore, additional research would be desirable to validate the applicability of the rigid vegetation model developed in this study to flexible vegetation conditions.

(Cui J. and Neary V.S., 2002)

Vegetation causes flow resistance and affects local flow and turbulence properties, including the local streamwise velocity and the shear stress distribution.

Field and laboratory investigations have related vegetative resistance parameters, such as drag coefficients and Manning's n values, plant properties, including height, density and flexibility (e.g. Kouwen and Unny, 1973; Shimizu and Tsujimoto, 1994). This information has aided the development of semi-empirical formulas for calculating bulk flow parameters and spatially averaged velocity profiles (Klopstra *et al*., 1997; Freeman *et al*., 1998).

Elucidations of more complex flow and transport processes requires more detailed investigations, namely measurements and modelling of vertical and transversal profiles of flow energy and turbulence properties. Such investigations require advanced experimental

instruments (e.g. LDA and PIV) and CFD modelling techniques (e.g. Reynolds averaged Navier-Stokes (RANS) and Large Eddy Simulation (LES)).

Computational fluid dynamics (CFD) models that describe open channel flows with vegetative resistance have only recently been developed (Shimizu and Tsujimoto, 1994; Lopez and Garcia, 1998; Tsujimoto and Kitamura, 1998; Neary 2000, Fischer-Antze *et al*., 2001).

These models close the RANS equations using two-equation isotropic turbulence models. With the exception of Neary (2000), who employed the near-wall k–ω model, the remaining investigators used the more popular k–ε with the near-wall functions. Such models provide detailed localized descriptions of the flow and the turbulence field, including profiles of the streamwise velocity and Reynolds shear stress, but provide only limited descriptions of the turbulence field.

The present work considers fully developed flow with simulated rigid vegetation as investigated by Shimizu and Tsujimoto (1994) in their laboratory study. The objectives are: (1) to validate a LES model with the experimental measurements of Shimizu and Tsujimoto (1994); (2) to investigate the effects of the vegetation layer on the turbulence field, including the turbulence intensities and the anisotropy of the Reynolds stresses.

The LES model developed by (Cui, 2000) is modified to include vegetative drag terms in the streamwise momentum equation. Near the bed and the edge of the vegetation layer, the mesh is densely distributed to resolve the step gradients of the mean flow and turbulence properties.

As with the RANS models, LES provides reasonably good predictions for the vertical velocity profiles and the Reynolds shear stress, when compared to the experimental measurements. LES also provides reasonably good results for the streamwise turbulence intensity. Neither model predicts the bulge in the measured streamwise velocity profile near the bed. The bulge in the measured streamwise velocity profile near the bed is most likely due to the streamwise vorticity produced by individual vegetation elements, and can not be resolved with the present model representation. A refined model that solves the flow around individual vegetation elements should therefore provide better agreement in this region.

(Neary V.S., 2003)

Numerical modeling studies by Shimizu and Tsujimoto (1994) and Lopez and Garcia (1997) are representative of recent attempts to simulate steady uniform flow through rigid submerged vegetation of uniform density.

These models close the RANS equations using the standard k–ε turbulence model with wall functions. They introduce a sink term representing vegetative drag to the RANS equations.

The k (turbulent kinetic energy) and ε (dissipation) transport equation were also modified by introducing the drag-related turbulence production terms.

Differences between these two numerical modelling studies relate to the treatment of the drag coefficient and the weighting coefficients. For the drag coefficient, Lopez and Garcia (1997) kept it constant; citing the experiments of Dunn *et al*. (1996) whereas Shimizu and Tsujimoto (1994) adjusted its value in a range, to achieve a good fit with measured velocity and Reynolds stress profiles. For the weighting coefficients, Lopez and Garcia (1997) selected values (based on a theoretical argument first presented by Burke and Stolzebach (1983)) different from the corresponding ones selected by Shimizu and Tsujimoto (1994) (based on calibration).

Comparing these two numerical model studies is somewhat arbitrary due to the different approaches used for selecting the model coefficients.

The objective of (Neary V.S., 2003) work is to develop and validate a CFD model that employs a near-wall k (turbulent kinetic energy) and ω (specific dissipation or dissipation per unit kinetic energy) turbulence closure that calculates the flow and turbulence properties all the way to the channel bottom. For vegetated waterways dominated by form drag, the

k–ω closure offers no obvious advantage over the k–ε models with wall functions. However, the near-wall k–ω closure has been demonstrated to be the model of choice for predicting bed-shear stress over a wide range of roughness types (Patel and Yoon, 1995; Neary, 1995). Therefore, the model should yield more accurate predictions than the k–ε model with wall functions when both bed shear and form drag affect flow resistance.

However, an important question is to validate the use of the near-wall k–ω closure model for the case of steady uniform flow through rigid submerged vegetation of uniform density. The detailed laboratory measurements of Shimizu and Tsujimoto (1994) are used to compare model calculations.

A fully developed one-dimensional open-channel flow with submerged rigid vegetation is modelled within the portion of flow occupied by vegetation by adding a vegetative drag term to the x-momentum equation and additional turbulence production terms to the k–ω transport equations.

This study discusses both treatments of the model coefficients adopted by Shimizu and Tsujimoto (1994) and by Lopez and Garcia (1997), discussed above.

An evaluation of these two modelling strategies indicates that, for similar treatment of the model coefficients, the use of the near-wall k–ω model produces results similar to previous models that employed the standard k–ε models with wall functions.

Moreover, reasonable predictions of streamwise velocity and Reynolds stress profiles can be achieved by adopting universal values for all model coefficients, but the calculated energy gradient can have significant error. The study also indicates that predictions of streamwise turbulence intensity are significantly improved by adopting for the weighting coefficients, the calibrated values rather than the theoretically based ones.

(Uittenbogaard R., 2003)

The paper (Uittenbogaard, 2003) is dedicated to modelling the turbulent flow over and through vegetation in water of limited depth. The perspective of the paper is innovative at all, as it is based on the use of concepts relative to turbulent flow along and through porous media, considering the vegetation as it was a porous medium. A rather long paragraph is therefore devoted to a survey on turbulent flow along and through porous media. Some important differences are stressed relative to different volume-averaging methods, depending on whether the sub-pore scale of turbulent kinetic energy is considered or just the larger-scales that survive the volume averaging. Another observation regards the question if it is better to use a multi-scale k–ε turbulence model or a single k–ε turbulence model extended to all length scales, and the choice falls upon the last one. The last observation regards questions about the permeability or flow resistance.

Having the aforementioned literature at his disposal, and having also a vast experience with testing and applying a 3D shallow-water solver and in parallel with a simpler so-called 1 DV model, the author could realize a new model for turbulent flow over and through a current flowing over bed covered by submerged, rigid or flexible, vegetation. The complete model is based on two momentum equations for the orthogonal horizontal velocity components, possibly subjected to rotation. But, for comparison with straight channel experiments, the model version which is presented is related to the Reynolds-averaged pore velocity in horizontal x-direction as a function of the vertical co-ordinate. The complete model includes a suite of eddy-viscosity based turbulence models, but in particular for the purpose of the paper only the k–ε model and a so-called low-Re version of the k–ε model are referred to. The essential limitation of the model is the assumption that the flow is uniform in horizontal direction.

After having developed the main characteristics of the model, the author presents some comparisons of its forecasts with the turbulence properties derived by the experiments referred in (Nepf and Vivoni, 2003) and also (López and Garcia, 2001) and (Meijer and Van Velzen, 1999). The first flume had a vegetation height of 160 mm with a water depth of

440 mm or of 280 mm; the second flume of 120 mm and 340 mm respectively, the third flume of 900 mm and 2090 mm respectively. In relation to the first flume figures are presented in which, referring to some statistic properties of the current (local mean values of velocity, Reynolds stresses, turbulent kinematic viscosity, non dimensional turbulent kinetic energy), comparisons are performed between experimental data and modelled data.

In relation to the second and the third flume, only local mean values of velocity are considered. In the two last comparisons experimental and modelled data agree very well, whereas in the first comparisons agreement is worse: author attributes this partial lack of agreement to the circumstance that the flume of Nepf and Vivoni is too high in respect of its width (280 mm).

In conclusion the author is rather satisfied with its model forecasts, even if he believes that some particular must be deepened.

(Choi S. and Kang H., 2004)

Stream flows over a vegetated bottom boundary are quite common in nature. Mean flow and turbulence characteristics of open-channel flows over rough boundary are studied either by laboratory measurements or numerical computations. In many engineering problems in fluid mechanics and hydraulics, the k–ε model has been widely employed perhaps due to the well-established empirical coefficients of the model. However, yet in 2004, none of the existing turbulence models were truly universal, and thus, each model needed to be tuned to specific flows. The k–ε model and similar models based upon the eddy viscosity concept made a basic assumption that the Reynolds stress is aligned with the velocity gradient. This assumption is valid only for simple shear flows. However, even for open-channel flows over a smooth bed, the bottom boundary and the free surface tend to reduce vertical turbulence intensity, and the decreased amount of turbulence intensity is redistributed to the ones in the streamwise and the transverse directions (Nezu and Nakagawa, 1993). Therefore, it can be easily deduced that the vegetation layer will increase the level of non-isotropy of turbulence, which motivated the application of non-isotropic turbulence model to vegetated open-channel flows in the present study.

Shimizu and Tsujimoto (1994) computed vertical distributions of mean and turbulent flow structures by using the k–ε model. Lopez and Garcia (1997) simulated flow structures of vegetated open-channel flows by using the k–ε model and compared the computed profiles with their experimental results. Neary (2003) simulated the open-channel flows with submerged vegetation using the k–ω model and suggested the weighting coefficients in the transport equations.

The considered study is an application of the Reynolds stress model (RSM) to vegetated open-channel flows, where cylinders of simulated vegetation are uniformly distributed. Averaged equations in both time and space dimensions are used. Assuming that the flow is at high Reynolds number in a wide open-channel, the momentum equation in the streamwise direction is expressed. The Reynolds stress due to the spatially fluctuating velocity is ignored because it is believed to be extremely small compared to the Reynolds stress due to the turbulent momentum transfer (Lopez and Garcia, 1997).

Now, beside the RMS model, three other turbulence models are considered in the paper for sake of comparison.

In the k–ε model, the values of the weighting coefficient for the drag due to vegetation suggested by Lopez and Garcia (1997) are used.

In the algebraic stress model (ASM), for the Reynolds stress, proposed firstly by Rodi (1979), the values of the empirical coefficients suggested by Shimizu and Tsujimoto (1994), are used.

In the Reynolds stress model, for the computation of pressure-strain term, the Speziale, Sarkar and Gatsky's model (1991) is employed. For diffusion and dissipation rate of Reynolds stress, Mellor and Herring's model (1973) is used.

The turbulence models, previously introduced, are applied to plain open-channel flows over smooth bed and open-channel flows with submerged and emergent vegetation. Moreover, the suspended load transported by vegetated open-channel flows is evaluated by using the Reynolds stress model.

Measurement data from Lopez and Garcia (1997) are used for comparison with numerical simulations. It is seen that the RMS predicts the mean velocity and turbulence intensity better than the algebraic stress model or k–ε model, especially above the height of vegetation.

With reference to the Reynolds stress profile, over the entire depth, the simulated profile by RMS and ASM are nearly the same and they match the measured data slightly better than the k–ε model.

With reference to the eddy viscosity profile, below the vegetation height, the eddy viscosity by the RMS is quite uniform except the region close to the bottom while the eddy viscosity by the k–ε model is the smallest, and the measured data lie between the profiles by the k–ε model and the RSM; above the vegetation height, the k–ε model and the ASM result in similar profiles, whereas the RMS yields larger values. Particularly, above the vegetation height, it can be said that the RSM simulates the eddy viscosity better.

However, more comparisons using another data set would consolidate the current finding.

For open channel flow with emergent vegetation, the RMS, the ASM and the k–ε model are employed in computation. Comparison are made with experimental data by Nepf and Vivoni (2000). They used flexible cylinders with artificial stems to model vegetation. However, near the bottom, the RMS predicts the mean velocity profile best. Towards the slowly surface, all computed profiles are indistinguishable and agree well with measured data. The RMS simulates the turbulence intensity profile better than the ASM and the k–ε model. The Reynolds stress profile agree well with measured data. The Reynolds stress profile is almost zero over the whole depth. All computed Reynolds stress profile agree well with measurements. The turbulent kinetic energy budget profile shows that the wake production balances dissipation rate over the entire depth except for the region close to the bottom where the shear production is dominant over the wake production.

However, more comparisons using another data set would consolidate the current finding. The challenges for the future of this model clearly include to extend it to natural vegetation.

(Poggi D., Porporato A., Ridolfi L., Albertson J. D., and Katul G. G., 2004)

In (Poggi *et al*., 2004) paper an innovative phenomenological model of the effect of vegetation density on canopy sub-layer (CSL) turbulence is established. The paper starts from the observation that the canonical form of atmospheric flow near the land surface, in the absence of a canopy, resembles a rough-wall boundary layer, whereas, in the presence of an extensive and dense canopy, the flow within and just above the foliage behaves as a perturbed mixing layer. Moreover the paper stresses the circumstance that up to 2004 no analogous formulation existed for intermediate canopy densities.

In order to create and validate the phenomenological model four steps were passed through.

The first step was an experimental one. Experiments were conducted in a re-circulating flume; the model canopy was composed of an array of vertical stainless steel cylinders with densities from 67 rods m^{-2} (a very poor density) till 1072 rods m^{-2} (a very high density). The velocity was measured by using a two-component LDA: 11 measurement locations were used, and at each location a profile of 15 vertical measurement locations was established through runs of 300s every one at the sampling frequency of 2500–3000 hz; finally a space and time mean was adopted in all the statistical analyses performed. Moreover, visualization experiments was conducted by injecting red rhodamine at several vertical layers which were lighted by a laser light split in a thin sheet to identify and photograph the dominant vortices at every level of canopies.

The second step was to perform statistics of the measured data. The performed statistics were first of all: mean velocity, variances, skewness and flatness factors, shear stresses. These statistics were presented for all the density cases, and the comparison clearly showed that, going from the less dense toward the most dense canopies, these statistics changed from rough-wall boundary layer type to perturbed mixing layer type, with all the intermediate possibilities. A second type of statistics was the quadrant analysis and the last type was the spectral analysis and visualization; these last analyses could show the vorticity characteristics of the flow: from both visualization and spectral analysis it was clear that the region inside the canopy, irrespective of density, is dominated by energetic motions controlled by length scales reflecting the local canopy geometry.

The third step was to create the phenomenological model. The created model decomposes the space within the CSL into three distinct zones: the deep zone in which the flow field is shown to be dominated by vortices connected with von Kármán vortex streets; the second zone, which is near the canopy top and presents a superposition of attached eddies and Kelvin-Helmoltz waves produced by inflection instability in the mean longitudinal velocity profile; the uppermost zone, where the flow follows the classical surface-layer similarity theory. In particular, in the second zone the flow is considered to be a superposition of a mixing layer and a rough-wall boundary layer with the superposition weights defined by canopy density. Finally the model equations were numerically integrated with suitable boundary conditions, and gave the possibility to obtain theoretic mean velocity and Reynolds stresses profiles.

The fourth final step was to compare the results obtainable from the model with the experimental data, and this comparison shows a good theoretic reproduction of mean velocity and Reynolds stresses profiles with the experimental data for a wide range of vegetation densities.

Authors conclude stating that with the advancement of remote sensing technology it is likely that broad space-time data mapping of canopy roughness densities should become readily available and that the proposed model will provide a mechanistic bridge from the roughness density maps to vertical transport predictions.

(Keijzer M. *et al.*, 2005)

This paper presents a necessarily brief treatise about derivation of several equations to model the water depth dependant resistance induced by submerged vegetation in wetlands and floodplains. Two of the expressions of the roughness coefficient studied here were created through an analysis and a process of derivation upon the extensive literature on this subject. A third expression was obtained using a variant of genetic programming.

In case of submerged vegetation, the first expression is based on the method of the effective water depth, that models only two of the four zones that in the velocity profile can be observed: in particular, the zone inside the vegetation sufficiently away from the bed and from the top of the vegetation, and the zone above the vegetation. By summing up the discharge per unit width of each zone a general expression for the Chézy resistance coefficient can be derived.

The second expression is based on an analytical method that attempts to model the velocity inside the vegetation by analytically solving the momentum equation for flow through and over the vegetation, represented as rigid cylinders.

Solving the partial differential equation for the velocity profile inside the vegetation layer using boundaries conditions, at the bed and at the top of the vegetation, furthermore assuming a logarithmic velocity profile above the vegetation, connecting with the profile underneath, such second expression for the Chézy resistance coefficient can be obtained.

The third expression of the roughness coefficient was obtained using a variant of genetic programming. The data used for training the genetic programming created expression were

generated by a 1DV turbulence model (Uittenbogaard, 2003). It can be argued that using such generated data defeats the purpose of finding an expression. But vegetation resistance is a typical 3-dimensional problem due to the water depth dependency. A full dynamical model thus operates on a 3D grid, which is computationally expensive. An analytical solution to the problem of resistance induced by vegetation, which includes water depth dependency, makes 2-dimensional, depth-averaged modelling possible, allowing for faster model computations and the possibility to apply the model to larger areas.

To ultimate test the created model, a dataset of laboratory flume experiments was collected from independent experimental studies. This data is not used for training, but kept aside to validate the created expression.

In particular, it can be seen that the expression based on the genetic programming results are in better agreement with the experimental dataset, than the manually induced formulations, both in their performance on synthetic training and laboratory testing data, and in the economy of detail that needs to be modelled.

This means that the genetic programming engine can be used as a hypothesis generator in scientific discovery. Not only is genetic programming capable of producing equations that are comparable or better than their human derived competitors, but also it can produce expressions that are amenable to further analysis and manual improvement. The equation developed with the aid of genetic programming and modified using theoretical considerations is currently the most accurate and elegant formulation of resistance induced by submerged vegetation.

The authors conclude that, due to simplicity and accuracy of this formulation, a hydraulic engineer can simply calculate the resistance induced by vegetation using a simple expression, instead of setting up a complicated and computationally expensive model.

(Defina and Bixio, 2005)

A review of recent studies dealing with a one-dimensional flow through rigid vegetation, shows that there are two different approaches to determine the velocity profile through and above submerged vegetation: a two-layer approach, which separately describes flow in the vegetation layer and in the upper layer, and a suitable modified k–ε model, in which the drag due to vegetation is taken into account not only in the momentum equation, but also in the equations for k and ε.

In the study described here, these two models were revised and extended to consider plant geometry and drag coefficient variable with depth. In order to give a complete description of turbulence structure within and above the canopy, a turbulent kinetic energy budget equation was added to the two-layer model. In fact, the mixing length approach used to compute the eddy viscosity in the two-layer model provides limited information on the turbulence structure.

Numerical simulations were then performed with both models to reproduce the flow field in the presence of real and artificial vegetation. The results of these simulations were then compared with available experimental data reported in literature. These data were from laboratory experiments where vegetation was simulated using simple rigid cylinders, plastic plants, and real vegetation.

With reference to the mean flow structure, good agreement between the results of the models and experimental measurements was found for velocity and shear stress distributions along the vertical. Interestingly, for the plant prototypes used by Nepf and Vivoni (2000) and the Spartina anglica used by Shi *et al*. (1995), the use of a variable with depth, vegetation density and drag coefficient, made it possible to improve the prediction of the velocity and the shear stress profiles inside the canopy. Furthermore, the *s*-shaped velocity profiles characterized by the local maximum and minimum velocities along the vertical, were accurately reproduced.

With reference to the turbulence structure, both models correctly predict the depth-averaged eddy viscosity. In fact, eddy viscosity profiles are fairly accurately predicted by the two-layer model. The k–ε model, on the other hand, does not accurately predict the behaviour of eddy viscosity within the vegetation layer. In this layer, the model predicts a parabolic profile and generally overestimates the experimental values. It is worth noting that the eddy viscosity is quite sensitive to average drag coefficient, while it seems unaffected by the assumption of constant or variable parameters.

The turbulent kinetic energy (TKE) budget illustrates the importance of the physical processes that govern turbulent fluid motions. The presence of vegetation adds a further dimension to the balance since new regions of turbulence production are created in the shear layer at the top of the canopy and in the wakes of the plant elements. The different length scales involved must be considered carefully. The wake-generated TKE has a length scale proportional to the dimensions of the elements in the canopy (i.e. the stem diameter), which is generally much smaller than the scale of the shear-generated turbulence, determined by the plant height. Therefore, when the scale of the wake-generated turbulence is smaller than the Kolmogorov microscale, which is commonly the case in aquatic flows with relatively low plant densities, most of the mean flow energy extracted by the plant drag is quickly dissipated into spatial fluctuations. So, in view of the above discussion, the TKE equation can be rewritten. Some terms of the TKE budget are represented together with the normalized TKE profile as calculated by the two models for an experiment developed by Nepf and Vivoni (2000). Two different sets of weighting coefficients suggested by Lopez and Garcia (2001) and Shimizu and Tsujimoto (1994), respectively, were used in the calculations. Both the models overpredict the normalized turbulent kinetic energy when the first set of weighting coefficient is used, particularly in the vegetation layer. Slightly better results are obtained when using the second set of weighting coefficients. Nonetheless, neither models is able to predict the concave-shaped profile seen in the experimental measurements when approaching the bottom.

After the turbulent kinetic energy k and the dissipation rate ε are computed, the streamwise turbulence intensity can be calculated using an algebraic stress model. Both the proposed sets of weighting coefficients lead to unsatisfactory results from the two models. In fact, most of the available experimental data clearly show concave-shaped profiles of streamwise turbulence intensity within the vegetation layer, while the models always show convex-shaped profiles. This discrepancy is probably due to the highly non isotropic character of the flow, which cannot be described by present models. However, there is also some uncertainty in the experimental data because measuring flow velocity in the presence of vegetation is quite difficult given that the spatial variation of the mean flow field makes it necessary to consider a large number of measurements location.

Nepf and Vivoni (2000) observed that the flow through a submerged canopy can be divided into two regions: the "vertical exchange zone" in the upper canopy, where the vertical turbulent exchange with the overlying water has a significant influence on the momentum balance, and the "longitudinal exchange zone", near the bottom, where the vertical turbulent transport of momentum is negligible and the pressure gradient is balanced by the vegetative drag. The distance from the bottom of the limit between the two zones is called penetration depth. The penetration depth of turbulent stress inside the canopy was estimated according to different criteria, based on the analysis of vertical profiles of Reynolds stress, velocity and total transport of turbulent kinetic energy. The results of the two models confirmed the experimentally observed trend of the penetration depth, although with some limits.

To sum up, both models proved to be effective in predicting velocity and shear stress, but not quantitative turbulence. Future research efforts should focus on modelling the turbulence generated by the interaction between flow and vegetation.

(Ben Meftah M. *et al.*, 2005)

Most efforts to study vegetal effects on a current have concentrated on analyzing rigid and flexible submerged vegetation. For a large part, research on vegetated open channels has focused on flow resistance due to vegetation, in particular on the determination of the friction factor and the drag coefficient in the flow resistance law, by means of analytical models and laboratory flumes.

Less is known about the local effect of the vegetation when it is characterized by a very low concentration. Indeed, in this conditions, it is not possible to consider the flow field homogeneous and so assign constant values to parameters such as the resistance index, the bed-friction velocity and/or the drag force, for the whole channel.

The rood topic of the present work is the investigation of the hydrodynamic effects of both rigid and flexible vegetation on a crossflow, in terms of velocity and turbulence distribution. The research is limited to the case of relatively low current velocities and flow depth higher than the height of vegetation, which is identical for both rigid and flexible type, in absence of current.

Different configurations as vegetation type, flow depth and velocity were investigated in the laboratory flume. In particular, metallic cylinders with rough lateral surface were used to simulate rigid plants, while commercial broom acted as surrogate of the flexible vegetation. For all the configurations the vegetation was taken submerged; different relative submergences have been considered.

Emphasis is put on assigning a minimal density to the artificial plants, as it is expected that in non-uniform, bed-friction conditions in the channel, a local analysis is needful for better understanding the phenomenon. Therefore, to capture spatial variability within the array, multiple measurements points were set between each two consecutive elements on the three principle directions.

Therefore, in order to study the variations of the velocity distribution around both rigid and flexible individual elements, several analysis of the velocity component data into the flume have been carried out, along longitudinal and horizontal sections. To better highlight the local effect of the artificial vegetation on the crossflow, velocity, data have been processed and plotted either at different longitudinal distances from the plants, or on horizontal planes at different levels.

In the vegetation layer, the current is subject to a strong slow motion due to the presence of the close elements. Near the top of the vegetation, both the local velocity and its gradient increase progressively, producing at the vertical profile an evident inflection point and the typical S shape, as reported in literature. Upon the vegetation, the velocity gradient decreases, with the concavity directed upward. These differences decrease as we move away upstream or downstream from the stem, and are particular evident for rigid elements.

It is noticeable that the isolevel contours around the rigid plants are not circular but elliptical with major axis parallel to the longitudinal direction, which reveals the anisotropy of vegetation stem effects over the hydrodynamic flow distribution. Moreover, the current is particularly delayed by the presence of flexible elements, while with rigid cylinders the normalized flow velocity at the middle longitudinal section of two arrays reach the unit value or slightly larger, which means the negligence of the vegetation stem effects as long as going away from it.

Nevertheless, the aim of the research at this stage has been the investigation of the particular hydraulic path of the flow inside the vegetated zone, and just on its top, and the detection of different behaviour due to the particular kind of plants. The normalized longitudinal velocity component profiles obtained around the flexible elements match those related to rigid ones, with minimum velocity values in proximity of each stem, while away from the stem, the velocity tends to rich the average value of the current in the flume in absence of vegetation. As a first remark, this result can be justified by the particularly

low vegetation density chosen for the experimental work. On the contrary, at the top of vegetations, the flow pattern is quite different, and the presence of rigid elements seems not to disturb the current, which means that velocity values keep constant along the whole transversal section, while the flexible vegetation branches make the horizontal velocity profiles more irregular.

With reference to the turbulent characteristics, turbulence intensity and Reynolds stresses distributions have been obtained, with the intention of highlighting the influence of different kind of vegetation on the turbulent behaviour of the current. However, a different behaviour is recognizable for the kinds of artificial vegetations. In particular, for rigid rods, non-dimensional values of turbulence intensity peak just below the rod top, maintaining same maximum independently of the hydraulic flume conditions. On the contrary, the maximum streamwise turbulence occurs above the element tops for the flexible canopy situation, particularly when the relative submergence is small. In fact, for small and intermediate relative submergence, coherent structures cannot develop their whole size.

Moreover, the vertical Reynolds stress distributions in the channel with flexible and rigid vegetation have been plotted. Again, the flexible vegetation shifts the Reynolds stress peak at higher level in the flow, above the canopy, than the single rigid element.

As final analysis, the transversal Reynolds stress distributions in the channel with flexible and rigid vegetation have been plotted. Alternate of positive and negative transversal Reynolds stress distribution, between stems, implies the formation of clocks and anti-clockwise vortices.

(Huthoff F. *et al.*, 2006)

For open channel flow over rough surfaces, several relations exist that relate the average flow velocity to a roughness height that reflects the resistance of the bed. However, when the bed is covered with large roughness elements such as vegetation, or cylindrical elements, these methods are theoretically no longer valid.

In the current work, flow over vegetation is described by an average-velocity model where distinct flow characteristics are attributed to two separate flow layers. These two regions will be referred to as the surface layer and the resistance layer.

In this paper, a two-layer scaling model is proposed that treats the flow field above and in between the roughness elements separately, and, when combined, gives a description of the depth-averaged velocity of the entire flow field.

When a flow field is penetrated by vegetation, turbulent vortices are created in the wake behind the protruding stems. Consequently, in addition to the resistance at the bed, drag effects around the individual plant stems cause the flow to slow down. This is the case of emergent vegetation.

Whenever cylindrical elements become submerged, the flow in the surface layer has a higher average velocity than in the resistance layer, because in this layer no drag due to the stems is experienced. The energy losses in the surface layer are entirely due to the shear stress near the top of the resistance layer, which balances the gravitational force that drives the flow. Subsequently, the shear stress between surface and resistance layer (i.e. the interface shear) also causes the flow in top of the resistance layer to speed up (i.e. the characteristics S shape velocity profile). The force balance, with an extra component due to the surface layer, yields for the scaling expression of the average velocity in the resistance layer, in case that the stems are submerged.

Based on physical principles and scaling assumptions, the well-known Manning/Strickler equation can be derived for the case of rough channel flow (Gioia and Bombardelli, 2002). The main principles behind the derivation are: a simple force balance, scaling of turbulent fluctuations to the average flow velocity, and the concept of a constant energy dissipation rate when large eddies break down into small ones (known as Kolmogorov scale). The Authors follow the same line of reasoning to describe the depth-averaged flow over submerged rigid

cylinders, i.e. for the surface layer, arriving to a scaling expression of the average velocity in the surface layer, including an unknown scaling length in terms of measurable geometric parameters, which can be specified from comparison with laboratory experiments.

When comparing the derived scaling expression of the average velocity in the resistance layer to results from flume experiments, very good agreement is found.

With reference to the scaling expression of the average velocity in the surface layer, several combination of available length scale were attempted. It is turn out that the spacing between the cylindrical stems gives the best agreement between calculated data and measured ones of the scaling expression of the average velocity in the surface layer. It is expected that this is no longer the case when the height of the cylinders is smaller than the distance between them. Future work of the authors will be focussed on the characteristics of such a scaling length when geometric variability among the resistance elements exist. Eventually, the aim will be to describe flow over natural vegetation, which involves further complications as stems flexibility, or leaves and side branches that individual plants may have.

(Ghisalberti M. and Nepf H., 2006)

In this paper flume experiments were conducted with rigid and flexible model vegetation to study the structure of coherent vortices (a manifestation of the Kelvin-Helmhotz instability) and vertical transport in shallow vegetated shear flows. This is a relatively innovative approach to the topic, as takes into account the non steady phenomena. In particular the vortex coherent structures are taken into consideration.

The rigid model canopies consisted of circular wooden cylinders arranged randomly in holes drilled plexiglass boards. Velocity measurements were taken simultaneously by three 3D acoustic Doppler velocimeters (ADV) and the vertical profiles consisted of 30 ten-minute velocity records collected at a sampling frequency of 25 Hz. The flexible model vegetation was designed to mimic eelgrass. Each model plant consisted of a stem region and six thin blades, based on the typical morphology of Massachusets Bay eelgrass: wooden dowels were used to mimic the eelgrass stem. In this case the experimental technique hold four 3D ADV and also a digital video camera used to determine the maximum plant height and the monami (phenomenon that will be described afterwards) amplitude. Finally, to characterize the impact of plant flexibility on the flow, the oscillatory nature of both the velocity field and the plant height had to be characterized, so that series of $u'v'$ and together oscillations of three particular blades, coloured red, green and blue, were considered.

As for qualitative experimental results, the vortex street generated in flows with submerged vegetation creates a pronounced oscillation in the velocity profile, with the velocity near the top of a model canopy varying by a factor of three during vortex passage. This oscillation, and the vortex structures themselves, did not encompass entire thickness of the shear layer (in particular do not arrive till the flume bottom, but only till a particular lower limit of the vegetation height), which is on the contrary unconfined by the free surface. However, the mixing length of momentum varies little in the entire flow overlying the canopy and, relative in particular to flows over rigid vegetation, within canopy geometry the oscillation has the effect of decreasing the amount of turbulent vertical momentum transport in the shear layer. In turn, this velocity oscillation drives the coherent waving of flexible canopies so that in case of flexible submerged aquatic vegetation, the response of the full system to the steady stronger currents is a progressive, synchronous, large-amplitude waving, termed monami by Ackerman and Okubo (1993).

This last phenomenon allows to use the flexible vegetation to study the vortex cycle: using a waving plant to determine the phase in the vortex cycle, each vortex is shown to consist of a strong sweep at its front (during which the canopy is most deflected), followed by a weak ejection at its rear (when the canopy height is at a maximum). Whereas in unobstructed mixing layers the vortices span the entire layer, they encompass only 70% of the flexibly obstructed shear layer studied here.

Generally speaking, measurements distinguished among four zones: above shear layer zone, upper shear layer zone, exchange zone, wake zone; moreover measurements distinguished also among the three cases of rigid canopy, still flexible canopy and waving canopy. Profiles of mean velocities, shear stresses, vertical mixing length, turbulence intensities, and also oscillations of bin-averaged values of plant height and of velocity profiles, are considered, and these quantities are studied also within a quadrant analysis.

Finally, remembering that, by using a waving plant to determine phase in the vortex cycle, each vortex is shown to consist of a strong sweep at its front followed by a weak ejection at its rear, the Reynolds stress generation by the vortex appears to respond to the oscillating instantaneous plant height: that is, the greatest penetration toward the bed of large-scale turbulence occurs when the canopy is at its most prone. Accordingly, it is imperative that the motions of the fluid and canopy are coupled in models of flow over flexible vegetation. The last remark is that the highly structured vertical transport within both rigid and flexible canopies is dominated by sweeps (to a degree dependent upon the drag density), while that in the unobstructed flow is dominated by ejections.

(Nezu I., *et al.*, 2006)

There are a lot of knowledge and valuable data in air flows over and within the vegetation canopies. In contrast, the vegetated rivers and the open-channel flows have only recently been investigated.

In particular, while the friction law and resistance of vegetation have in past decades studied intensively, a lot of uncertainties remain concerning the coherent structures, dispersive effects and turbulent energy transport properties.

These topics have been highlighted in this experimental work, where turbulence measurements in the whole depth region from the bottom-bed to the free surface, in a vegetated canopy open-channel flows have been conducted, in order to investigate dispersive properties and turbulence structure, by varying the vegetation density.

To reveal the effects of vegetation on turbulent structure, it is of essential importance to consider the horizontal space averaging in the time averaging Navier-Stokes equations.

The main findings obtained in the present study are as follows.

The streamwise velocity is varied significantly in the spanwise direction within the canopy, due to the local deceleration behind the vegetation. This trend is more remarkable in the denser vegetation. In contrast, over the canopy, the lateral variations become smaller, because the local effects of vegetations become negligibly small.

The vertical profiles of the space-averaged streamwise velocity reveals that the typical drag effects of vegetation decelerate the streamwise velocity more largely in the canopy layer as the vegetation density becomes larger. Consequently, a significant inflectional point appears near the canopy edge, the feature of which is consistent with that of plant canopy flows. The measured shear length scale decreases with an increase of the vegetation density. Furthermore, a second peak is observed near the bottom-bed, which may be caused by three-dimensional dynamics of wakes.

The friction velocity was evaluated as the peak value of the Reynolds stress, which is consistent with the method of plant canopy flows as reviewed by Finnigan (2000). The results suggest that the bed friction becomes larger with an increase of the vegetation density.

The vegetation has much significant effects on the space-averaged velocity and Reynolds stress within the canopy rather than over the canopy. Therefore, a universal formula, i.e. the log-law, may be applied to the velocity profiles over the canopy.

It is inferred from the inflectional profiles of velocity as well as the Reynolds stress profiles that coherent eddies are generated by the velocity shear near the vegetation edge, and, consequently, they cause large momentum exchanges between the low-speed flow within the canopy and the high-speed flow over the canopy. In order to evaluate these properties quantitatively, the quadrant conditional analysis was conducted for the instantaneous Reynolds

stress. It revealed that the sweep event was greater than the ejection event, near the canopy edge.

The sweep and ejection events are related with skewness. It was found from the skewness distributions that there were noticeable coherent structures within the canopy, and the significant momentum exchange occurs between the within-canopy and the over-canopy.

In over-canopy layers, the spectral distributions obey the Kolmogoroff's power law in the inertial subrange. Within the canopy, the spectral distribution fits to the Kolmogoroff's power law in a narrower range, and the spectrum increases in the high frequency range. This suggests that there may be a turbulence energy supply caused by the wake eddies generated behind the vegetation elements. This property is more remarkable nearer the bottom bed, whereas the spectral profile nearer the free surface is closer to that of boundary layer since the effects of coherent motions are smaller farther from the vegetation layer.

The turbulent kinetic energy (TKE) budget was examined in order to reveal the dispersive contributions of turbulence due to vegetations. Of particular significance is that the turbulent fluctuations are generated strongly near the vegetation edge and the wake generation is comparable or larger than the shear generation. This suggests that the wake generation plays an important role on the turbulence generation within the canopy.

Furthermore, it is demonstrated significantly that the coherent motion, such as sweeps, transports high-speed momentum toward the inner vegetation layer, causing significant energy loss.

10.1.3 Aim and organisation of the Chapter

In the following paragraphs 10.2 and 10.3 of this Chapter the effects on a turbulent boundary layer flow of two different models of rigid fully submerged vegetation will be described. The first model was made by brass cylinders of different height, arranged in rectangular or square shapes; the second one was made by a synthetic grass carpet.

Paragraph 10.1.1 has presented elder and more recent researches on boundary layer. In particular, it was shown that the most intriguing type of boundary layer is the one which rises when the free-stream is a turbulent one. Always in paragraph 10.1.1, it was stated that the presence of turbulence in streams of various types is a very frequent condition, and often the boundary layers that might rise within them are of this type.

In parallel to boundary layer researches, paragraph 10.1.2 has presented also recent literature researches on vegetated surfaces. Such literature has been limited only to the case of rigid submerged vegetation, because of the type of researches the authors were inclined to carry out and which will be hereafter presented.

It is now obvious that a type of current where turbulence is strongly present is just the case of a vegetated one. It is possible that in such a type of current some boundary layer would rise. For instance, when an abrupt change in the nature of the vegetated wall happens. In this case, it could be important to know which the rapidity of changes of the current behaviour is: i.e. to discover how wall vegetation can affect the boundary layer dynamic development, the values of its thickness at different distances from the leading edge, and the mean velocity distributions inside.

In the already examined growing literature on streams flowing over vegetated surfaces, the effects of vegetation on the characteristics of possibly present boundary layers has not yet been considered, at least in relation to the authors' knowledge. In fact, literature is limited to the cases of uniform or at the most of permanent flow, but a boundary layer flowing over a vegetated bed has never been taken into consideration.

Consequently, the authors recently decided to open a new research line, just in relation to boundary layers with turbulent free-stream rising over vegetated beds. In any case, in order to limit the topic, only rigid submerged vegetation has been taken into consideration so far.

The specific aim of this research line was to give first contributions to the topic through suitable comparison between the behaviour of a boundary layer with turbulent free-stream flowing on a smooth flat plate and a boundary layer with turbulent free-stream too, but developing itself on differently vegetated surfaces.

After all, since 2004 the authors' papers appeared in international literature (and will be specifically remembered afterwards) on this topic. The history of this research can be, till now, subdivided into three different steps.

In the first step, a sparse vegetation was considered, modelled through brass cylinders positioned at the vertices of rectangular or even square meshes. Some new results could be therefore obtained with regard to boundary layers behaviour in these circumstances, and, in particular, on their possible equilibrium characteristics as a function of the different used vegetation models.

In the second step, a dense vegetation was considered, modelled through an artificial continuous grass carpet. In this case, the results obtained, showing a total loss of the equilibrium boundary layer, could be compared in any case to the previous ones, relative to sparse vegetation, and allowed the authors to attain some new general results on the overall behaviour of a boundary layer, flowing over a vegetated bottom, either sparse or even dense, but always rigid and submerged.

Finally, the third step has now scarcely begun and has not yet reached final results.

This step will regard the possibility to present all the previous experimental measurements through a new methodology, in order to unify, in a unique "universal" law, all the obtained velocity distributions, either in sparse or in dense vegetation cases.

In the following paragraphs, the Chapter will present the aforementioned results related to the first and second step. Paragraph 10.2 will present the first step; paragraph 10.3 will present the second step; in the Conclusion paragraph 10.4, some idea of the trend which will be followed in the third step will be outlined too.

10.2 BOUNDARY LAYER ON A VEGETATED SURFACE WITH A SUBMERGED, RIGID, SPARSE VEGETATION

10.2.1 Generalities about experimental plant, data acquisition systems and experiments planning

A whole series of experimental surveys, whose results are reported in four previous works (Gualtieri *et al.*, 2004b; Gualtieri *et al.*, 2004c; De Felice *et al.*, 2004; De Felice and Gualtieri, 2005), have been undertaken some years ago by the authors so as to determine the effects of a particular vegetated bottom on the main hydrodynamic characteristics—such as local mean velocity distributions and thickness values—of an equilibrium boundary layer stream flowing over it. The vegetation bottom considered was of a submerged, rigid and sparse type.

The vegetation was modelled by means of brass 4 mm diameter cylinders (Fig. 10.5) with three different heights (5 mm, 10 mm, 15 mm) placed according to two different regular geometries (rectangular and square meshes) pointed out synthetically as single and double density. For the rectangular meshes the sides measurements were 5 cm longitudinally and 2.5 cm transversely; for the square meshes the sides measurements were 2.5 cm. Consequently, the projected area of vegetation per unit volume of water in the flow direction (Tsujimoto *et al.*, 1992) were, respectively, $0.032\,\mathrm{cm}^{-1}$ and $0.064\,\mathrm{cm}^{-1}$ (Figs. 10.6 and 10.7).

These cylinders were glued within suitable holes arranged in a plexiglas plate. The plate was then inserted onto the bottom of the channel close to its inlet. In order to avoid the plate disturbing the entry of the stream into the channel, a connecting ramp between the channel

Figure 10.5. View of vegetation obtained through rigid cylinders.

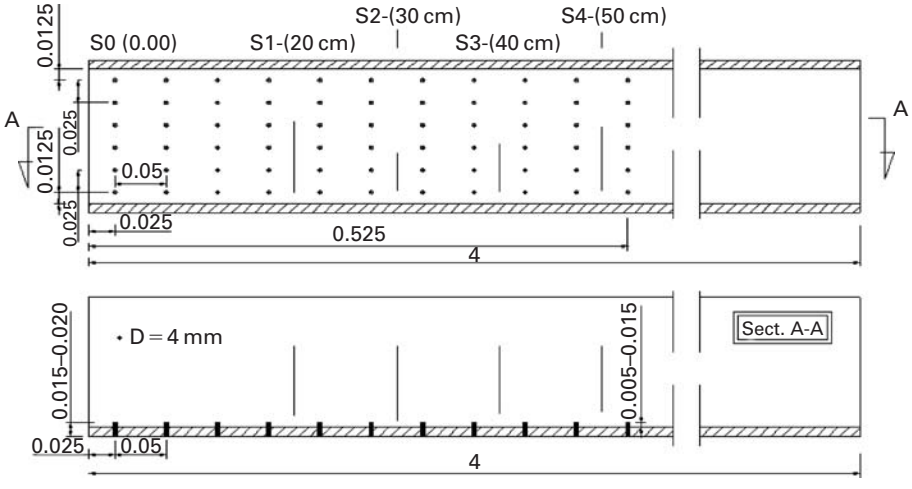

Figure 10.6. Scheme of the plate with single density.

inlet and the plate itself had been installed. Combinations of three different heights and two different densities produced six different vegetation types.

In order to compare the experimental data with previous data obtained from studies of the equilibrium boundary layer over a smooth surface, and obtain some general conclusions, it was necessary to preserve some fundamental hydraulic parameters unchanged with regard to the previous studies. As a consequence, the Run 1 data of the Gualtieri paper (Gualtieri *et al*., 2004a) was taken in consideration as reference experiment.

Consequently the same experimental setting of that run was considered. In particular the height of the sluice gate was set at 7.49 cm so that the height in the vena contracta was at 4.62 cm; the load on the vena contracta at 10.34 cm, and finally the resultant velocity of the free-stream at 1.424 m/s.

Moreover it was necessary to ensure the possible equilibrium of the boundary layer, in each one of the six considered vegetation types. This condition, as already recalled, corresponded to the physical condition of holding the free surface of the current horizontal, at least in the first 50 cm where the boundary layer developed and was measured. In order to achieve

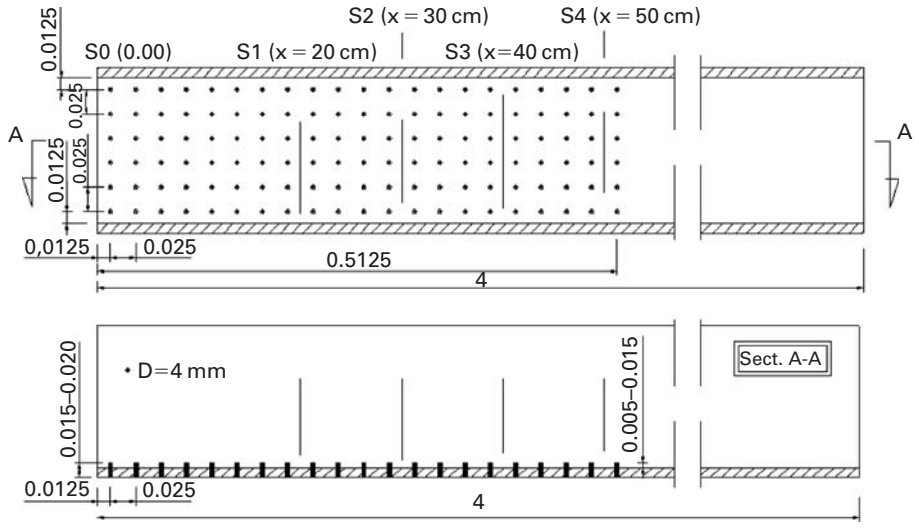

Figure 10.7. Scheme of the plate with double density.

Table 10.3. Slopes used in different cases.

Veget. height or density	Smooth bottom	Veget. 5 mm	Veget. 10 mm	Veget. 15 mm
Single Density	0.25%	0.92%	1.60%	2.27%
Double Density	0.25%	1.15%	2.05%	2.95%

this requirement, it was necessary to suitably raise the slope of the channel, taking into account the vegetation type, whose possible increase in height and density would generate a corresponding increase of head losses, which would need to be balanced by a suitable increase of channel slope. Hereafter, in Table 10.3, the slope values relative to smooth bottom and to the six vegetation types are reported.

As in the previous smooth surface experiments, the test sections were set at 20, 30, 40 and 50 centimetres from the channel inlet. In each test section two particular measuring verticals were considered. The first one was exactly at the centre of the test section, and also at the centre of either a rectangular or a square mesh (respectively in single or double density) generated by cylinders. This position corresponded exactly to the measurements previously carried out with a smooth bottom. The second position was laterally displaced by 1.25 cm, and consequently was located along a cylinder row and at the centre of the lateral side of the same rectangular or square mesh (always respectively in single or double density). It is clear that in the case of a smooth bottom there was no need of such a measurement position. In the authors' literature, the (De Felice *et al.*, 2004) paper relates to results for measurement points of the first type and the (De Felice and Gualtieri, 2005) paper relates to results for measurement points of the second type.

In each test section, for every one of the six different flow conditions, and for measurements at both vertical positions, the experimental study was carried out in a standardized way.

Figure 10.8. LDA in course of data collection.

Specifically, a number of about 20–30 experimental points were chosen along the measurement verticals, so as to fully describe the behaviour of the current from bottom to free surface. Measurements of instant velocities were carried out at each one of these points through the LDA technique. An LDA compact system (Fig. 10.8) was used, working in back-scattering, equipped with a Bragg cell and frequency shifter, whose signal was processed through a frequency tracker (Fig. 10.9). The focal length of the lens was 310 mm, the output power of the ray was 65 mW and its wave-length 825 nanometres (infrared light). In the course of data collection it turned out that the use of an infrared camcorder was very useful in order to be able to monitor the position of the measurement point at every moment, minimizing the possibility of pointing errors.

The frequency tracker was also able to process the experimental data so as to obtain the mean value (with an average time that could be chosen freely) of the instantaneous velocity data collected at each point of measurement. Each value of the local mean velocity was obtained through an acquisition time of 200 s, which was considered to be enough to reduce the major part of turbulent velocity fluctuations.

10.2.2 Velocity measurements and relative processing

Some examples of the obtained velocity distributions are shown in Figs. 10.10, 10.11, 10.12, 10.13. In each diagram the velocity distributions relative to only one vegetation type and only one measurement vertical position is considered, but representing in any case all the three possible vegetation heights always compared with the smooth bottom results.

Only four diagrams among the 16 available are reported here, having chosen those which present the extreme hydrodynamic characteristics.

Starting from these local mean velocity distributions, the values of the δ_{99} thickness of the boundary layer were obtained. These values are reported in Tables 10.4 and 10.5 where in

Figure 10.9. LDA system.

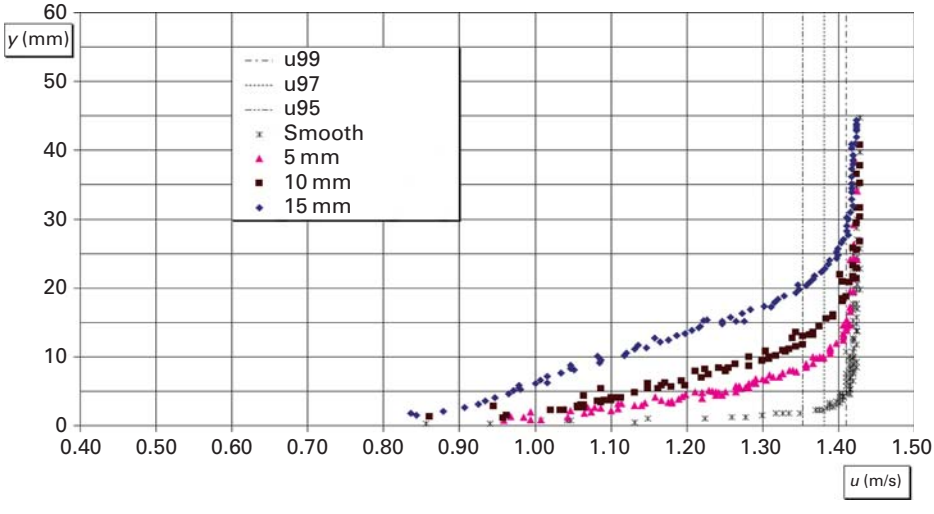

Figure 10.10. Local mean velocity distributions in test section n. 1, central vertical (single density).

the thin lines represent the central vertical measurements and in bold lines the lateral vertical measurements. In all diagrams some verticals are traced relative to the 95%, 97% and 99% values of u_0. The 99% values are obviously necessary in order to calculate the δ_{99} thickness, but it is important to point out that the direct reading of the δ_{99} is not straightforward or even possible in all the local mean velocity distributions. Therefore it has been necessary to

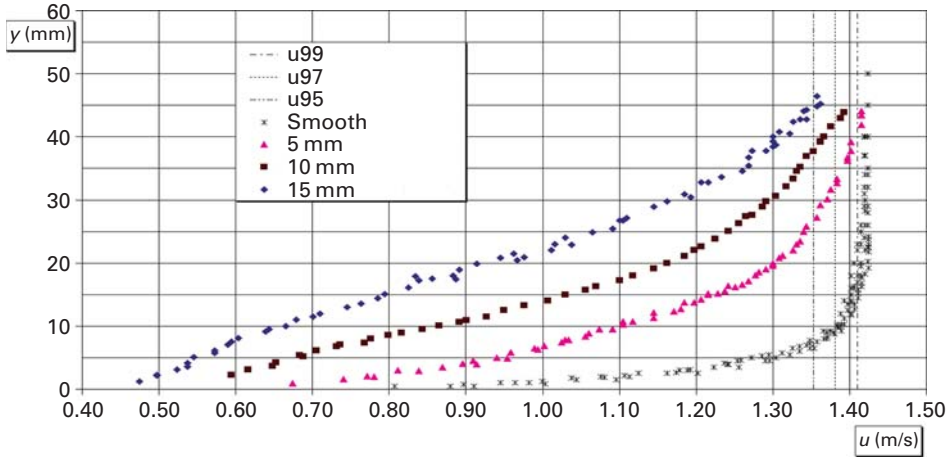

Figure 10.11. Local mean velocity distributions in test section n. 4, central vertical (double density).

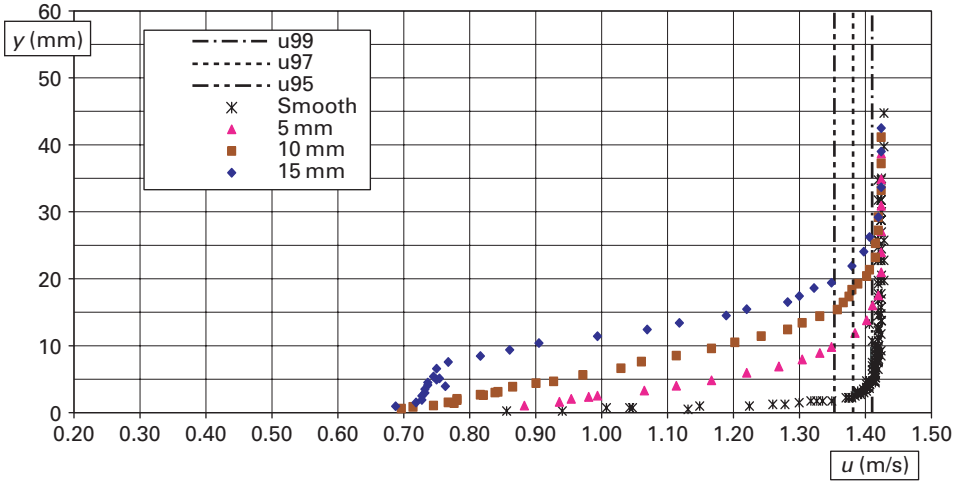

Figure 10.12. Local mean velocity distributions in test section n.1, lateral vertical (single density).

adopt a method of computing the δ_{99} based on the readings of the δ_{95} and the δ_{97} (Gualtieri *et al.*, 2004b). Obviously δ_{99}, δ_{97}, and δ_{95} are, respectively, the boundary layer thicknesses based on 99%, 97%, and 95% of the free-stream velocity.

It is useful to underline the fact that sometimes the thickness shown in Tables 10.4 and 10.5 exceeds the thickness of the flow, and therefore, it must be considered as "virtual thickness", stressing through this definition the characteristics that have been described in the final part of paragraph 10.1.1.3. The concept of "virtual thickness" can be found also in previous works of authors on the boundary layer (Greco and Pulci Doria, 1983) and it has the following definition: the "virtual thickness" represents the equivalent δ_{99} (for instance) "scale" to make non dimensional the heights of the points corresponding to the local mean velocities values when the boundary layer "breaks" the free surface of the current.

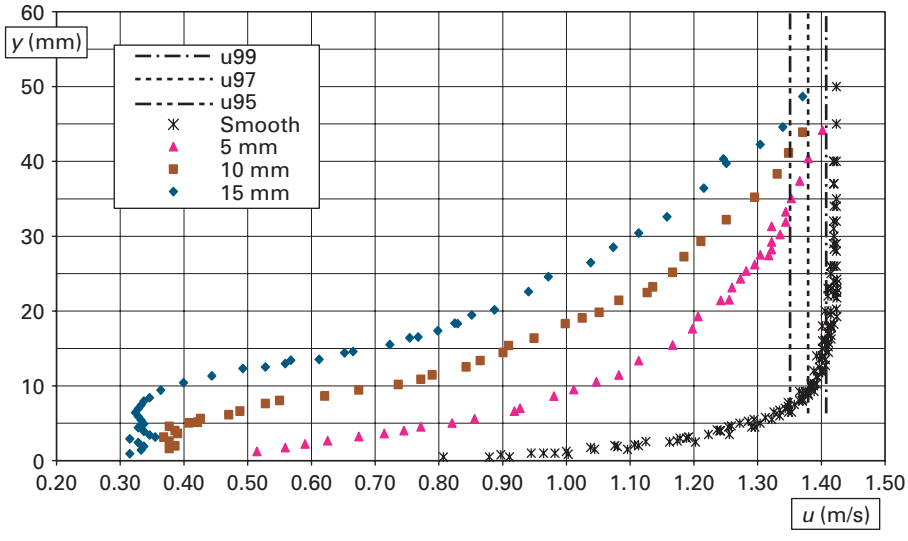

Figure 10.13. Local mean velocity distributions in test section n.4, lateral vertical (double density).

Table 10.4. Thickness of the boundary layers (single density).

Boundary layer thickn.	Smooth bottom	Veget. 5 mm	Veget. 10 mm	Veget. 15 mm
δ_{S1}(mm)	3.8	14.6–16.5	20.0–22.8	29.5–27.2
δ_{S2}(mm)	7.1	25.6–22.7	31.4–30.4	43.5–39.5
δ_{S3}(mm)	10.9	32.0–33.0	42.1–45.0	56.8–51.7
δ_{S4}(mm)	13.5	42.2–41.3	51.3–53.2	64.1–59.2

Table 10.5. Thickness of the boundary layers (double density).

Boundary layer thickn.	Smooth bottom	Veget. 5 mm	Veget. 10 mm	Veget. 15 mm
δ_{S1}(mm)	3.8	16.0–16.3	22.0–25.4	31.5–34.2
δ_{S2}(mm)	7.1	26.3–28.0	33.9–35.4	45.5–46.0
δ_{S3}(mm)	10.9	35.1–41.0	47.7–49.4	56.7–55.9
δ_{S4}(mm)	13.5	44.0–52.7	52.4–54.7	62.2–57.1

Starting from the two tables it is possible to state some general characteristics of boundary layers over a vegetated surface:

1) Vegetation increases boundary layer thickness.
2) Previous increase is greater as vegetation is higher or denser.
3) Boundary layer thickness, either measured in the current centreline or measured in correspondence to a row of cylinders, is practically the same.

At this point, the local mean velocity distributions obtained for each test section and each flow condition was changed into non dimensional values, through use of the velocity in the free-stream and the boundary layer thickness.

This operation was performed to stress possible equilibrium characteristics of the considered boundary layers.

As regards to this operation, it is suitable to remember that, according to the rule given in paragraph 10.1.1, a boundary layer on a flat plate is called an equilibrium one when, in its free-stream pressures (or piezometric heads for liquids), it has a streamwise zero gradient, and consequently velocity distributions, once they have been made non dimensional in the shape of velocity defect law, appear to superimpose on one another.

In the case we are dealing with, it is very hard even to try representing velocity distributions in the shape of velocity defect law, because, in order to obtain such a representation, it would be necessary to refer to friction velocities. Now, in the flows considered over a vegetated surface, the friction velocities are variable from a point to another even in the same section (as happens to velocity distributions too) because of the presence of sparse cylinders. Therefore, in previous papers, the possibility to refer to friction velocity was discarded at all.

Furthermore, the distances of the test sections from the leading edge of the boundary layer considered (from 20 cm to 50 cm), were of the same order one another, and, in this conditions, the friction velocities in the standard boundary layer differ very little one another. Consequently, the superposition of velocity distributions, in the shape of velocity defect law, implies, with good approximation, also superposition of diagrams made non dimensional in the simpler way previously specified, and vice-versa. This conclusion is fully confirmed, for instance, by the diagrams of Figs. 10.10, . . . ,10.13, where also velocity distributions of the equilibrium boundary layers case over smooth bottom are presented. These last specific diagrams are made non dimensional through the aforementioned technique. Now, they certainly should be superimposed in the shape of velocity defect law, and, in fact, appear to be superimposed even in this new shape.

As a result of this reasoning, the condition of equilibrium flow can be assessed also taking into consideration the superposition of diagrams made non dimensional in the simpler way previously specified.

10.2.3 Non dimensional velocity distributions and relative processing

The local mean velocity distributions relative to all the vegetation types considered and to both measurement verticals taken in consideration are represented in Figs. 10.14, . . . ,10.25.

In each of the diagrams the non dimensional velocity distributions of all the four test sections relative to one single vegetation type are reported. Some different behaviours can be observed between the least high and least dense vegetation (for instance 5 mm single density) on one side, and the highest and most dense vegetation (for instance 15 mm and double density) on the other. In the first cases the non dimensional distributions superimpose one another perfectly; in the second case this superimposition is limited to the higher side of the diagrams (practically higher than the vegetation height).

It is evident that in the second case, vegetation disturbance is so great that the velocity distribution within the vegetated layer comes close to a constant value, and that it is this behaviour that prevents the velocity distributions superimposing one another.

Recalling that superposition of non dimensional velocity distributions is the main characteristic of equilibrium boundary layers, it is possible to state that, in conditions where the vegetation perturbation to the stream is lower, the equilibrium characteristics completely hold; whereas, in conditions where the vegetation perturbation to the stream is higher, the equilibrium characteristics hold only in that part of the stream which is not directly

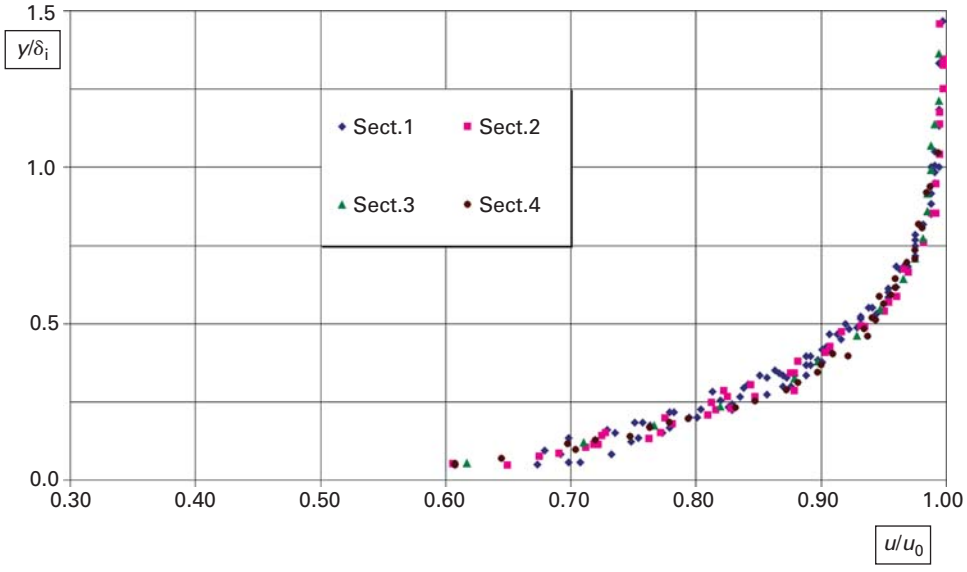

Figure 10.14. Non dimensional local mean velocity distributions, central verticals (5 mm cylinders single density).

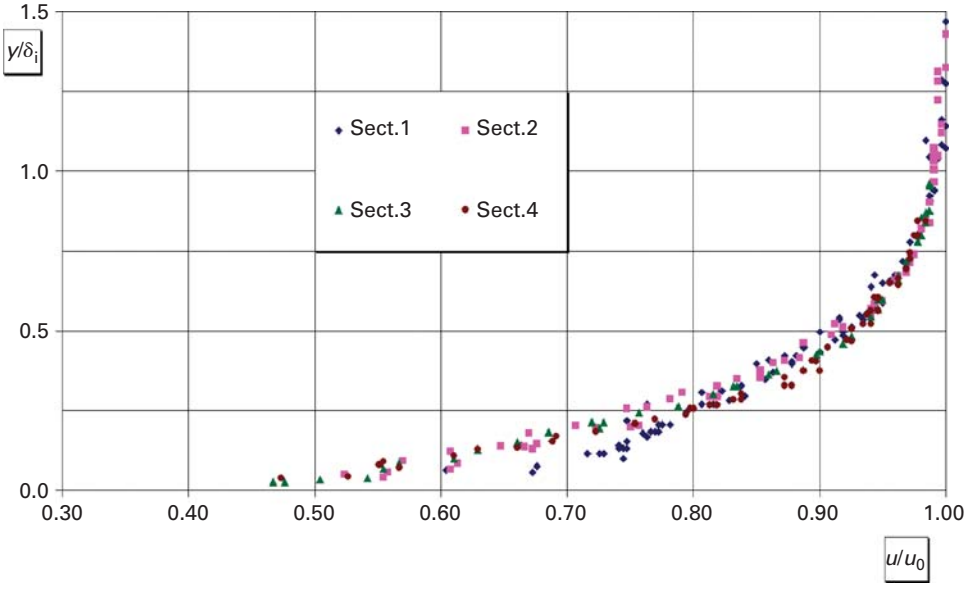

Figure 10.15. Non dimensional local mean velocity distributions, central verticals (10 mm cylinders single density).

influenced by the cylinders. in previous papers the authors coined the definitions of "full equilibrium" and "partial equilibrium" for these two cases.

This behaviour is present either in the velocity distributions obtained in correspondence to the central verticals, or in the velocity distributions obtained in correspondence to the

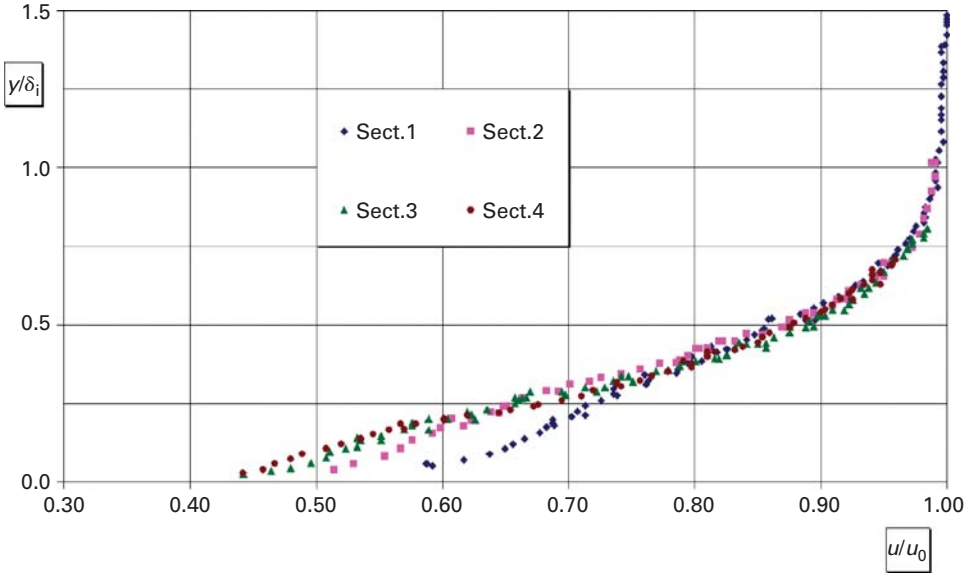

Figure 10.16. Non dimensional local mean velocity distributions, central verticals (15 mm cylinders single density).

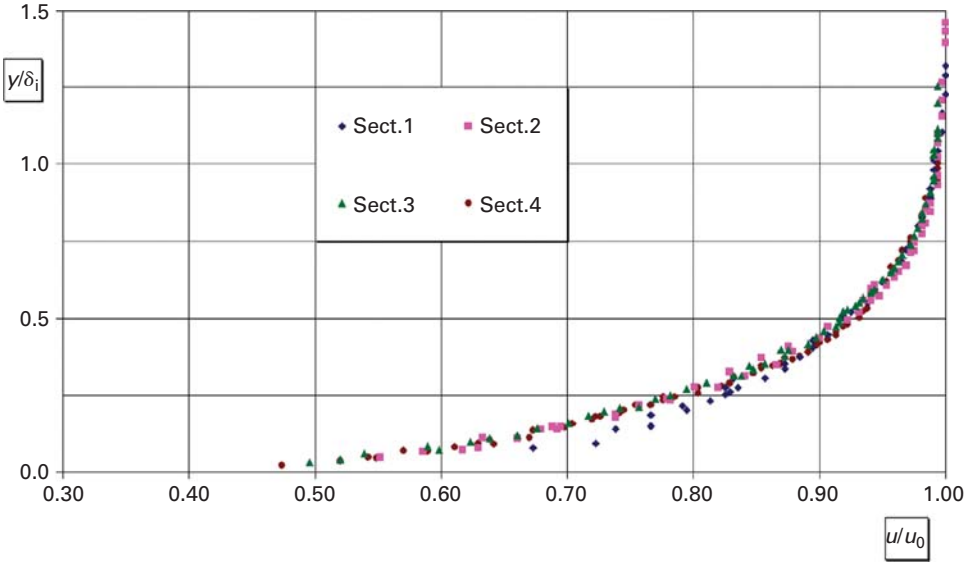

Figure 10.17. Non dimensional local mean velocity distributions, central verticals (5 mm cylinders double density).

lateral verticals. A deep insight into this phenomenon also permits a mathematical rule to be derived to determine its presence or its absence. In particular, it was stressed that the main parameter that defines the presence or the absence of the phenomenon can be considered to be the ratio between the cylinder height and the boundary layer thickness. Whether in central verticals or in lateral verticals, the phenomenon does not appear as long as this ratio

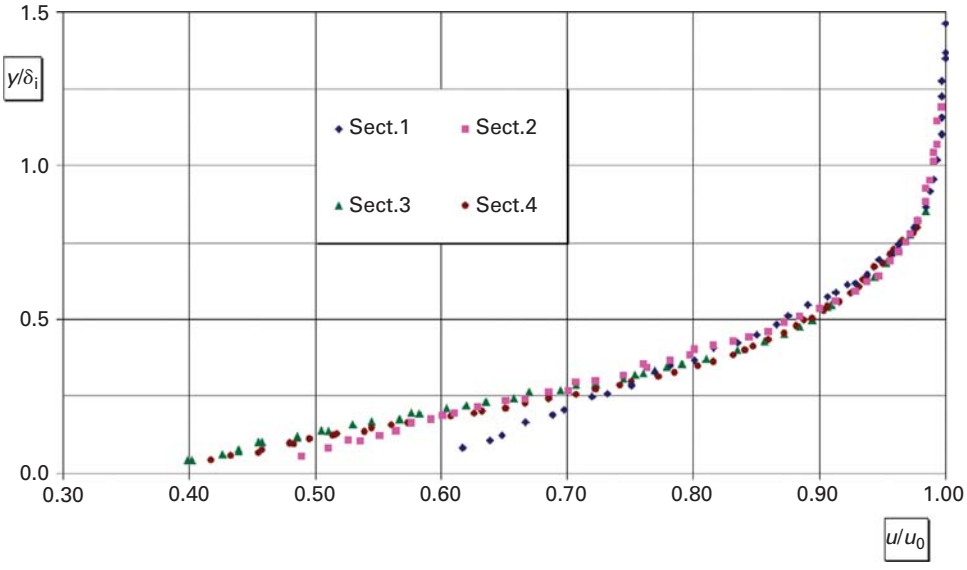

Figure 10.18. Non dimensional local mean velocity distributions, central verticals (10 mm cylinders double density).

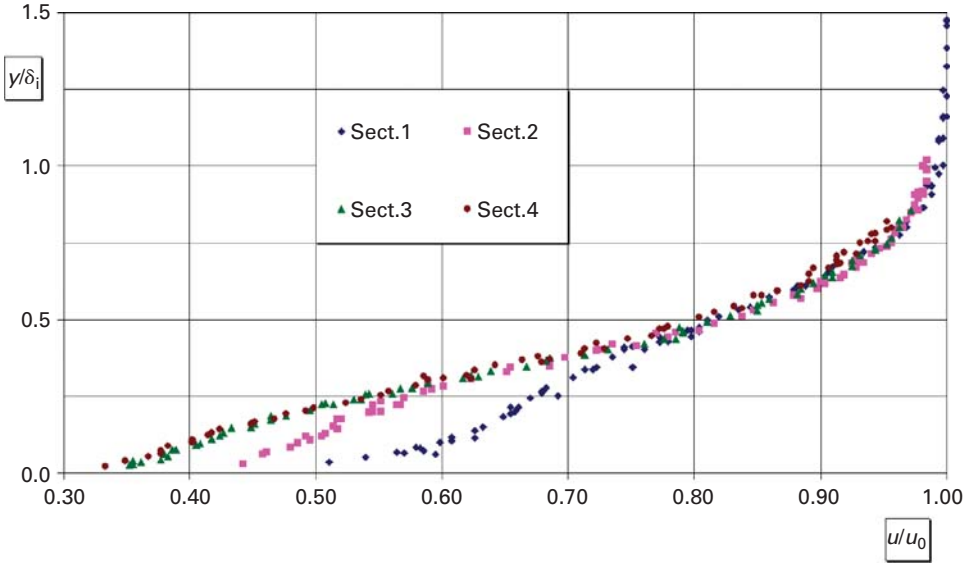

Figure 10.19. Non dimensional local mean velocity distributions, central verticals (15 mm cylinders double density).

does not approach the values of 0.35 in the case of single density and 0.28 in the case of double density.

Interestingly these observations can be matched with some experimental data referred by Tsujimoto (1999), even if relative to uniform flows. This author presents some velocity

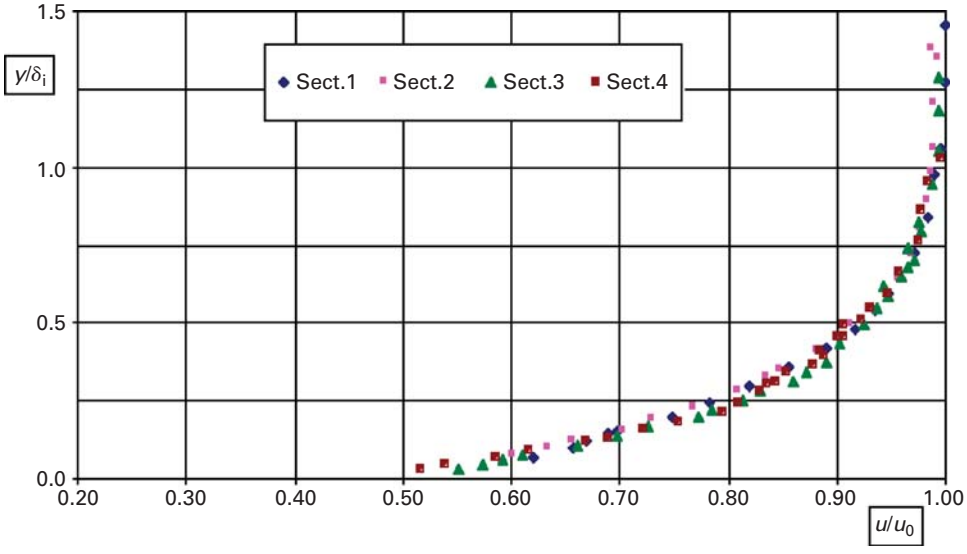

Figure 10.20. Non dimensional local mean velocity distributions, lateral verticals (5 mm single density).

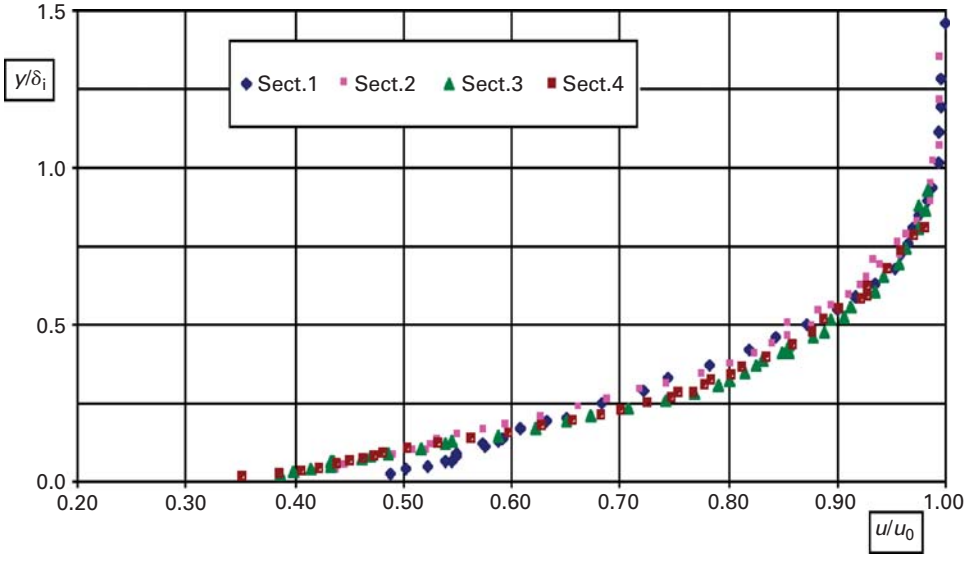

Figure 10.21. Non dimensional local mean velocity distributions, lateral verticals (10 mm single density).

distributions in currents with submerged cylinders as vegetated bottom, whose density can be compared to our case of single density. In these data the distribution part within the vegetated layer has shapes very similar to those found in the present paper in the case where equilibrium no longer exists. Not surprisingly, the ratio between the cylinder height and the full current height (for uniform flow the full current height can obviously be compared with the boundary layer thickness) is 0.50; i.e. more than 0.35, which is further confirmation of our previous conclusions.

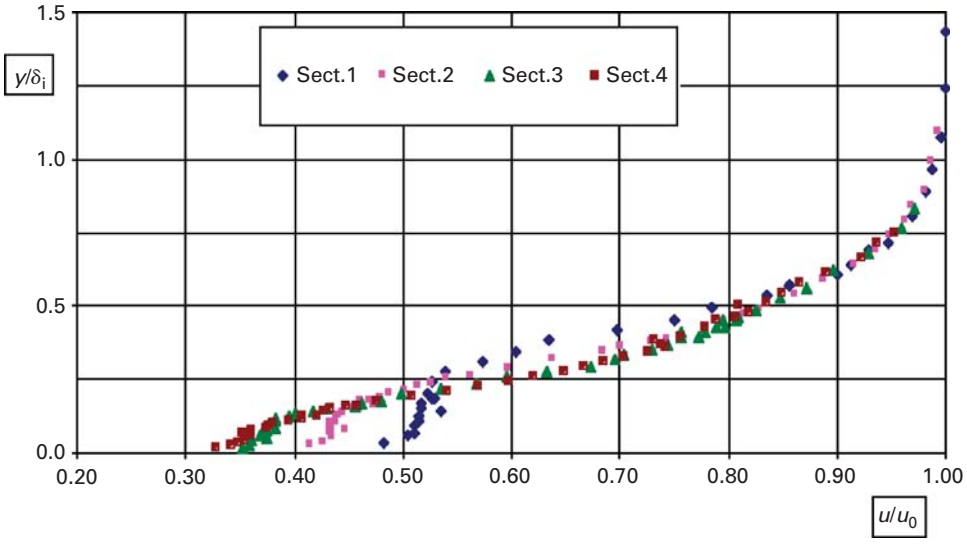

Figure 10.22. Non dimensional local mean velocity distributions, lateral verticals (15 mm single density).

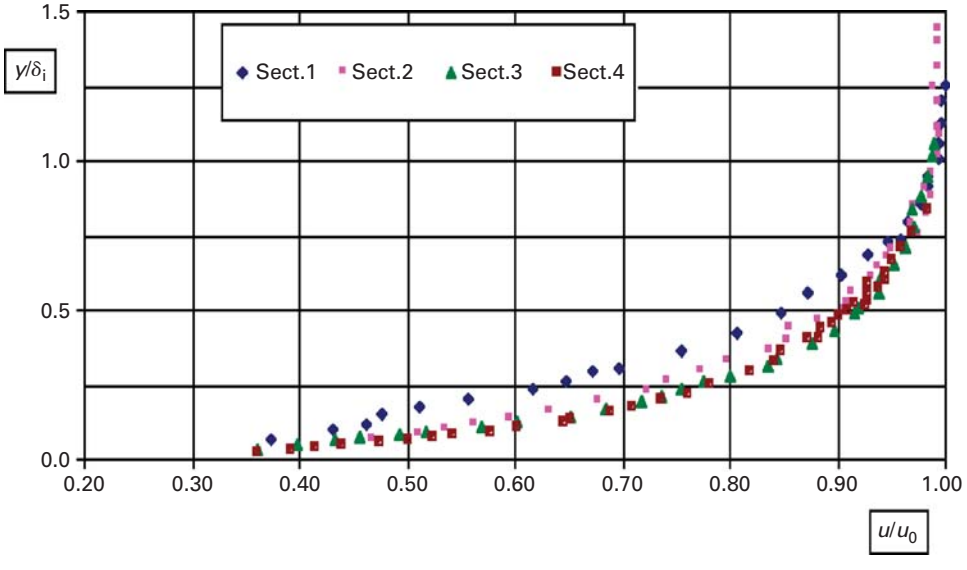

Figure 10.23. Non dimensional local mean velocity distributions, lateral verticals (5 mm double density).

Previous observations can also show that, if we do not take into consideration the test sections where vegetation is too high with respect to the boundary layer thickness, or also if in these last test sections we take into consideration only the part of the distribution diagrams higher than cylinder thickness, then a complete equilibrium holds.

Figs. 10.26–10.29 show the non dimensional velocity distributions related only to their equilibrium portions. They have been collected together in four groups, each one relative to

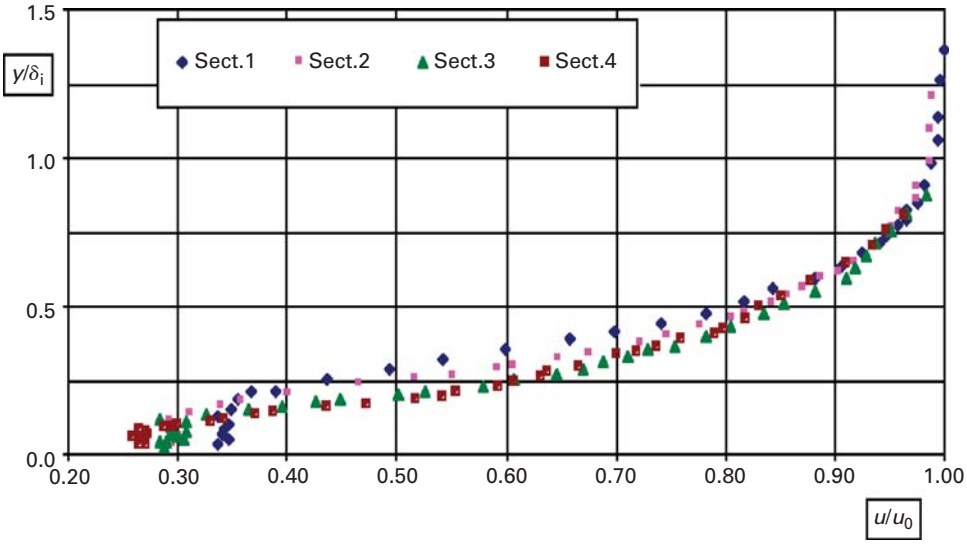

Figure 10.24. Non dimensional local mean velocity distributions, lateral verticals (10 mm double density).

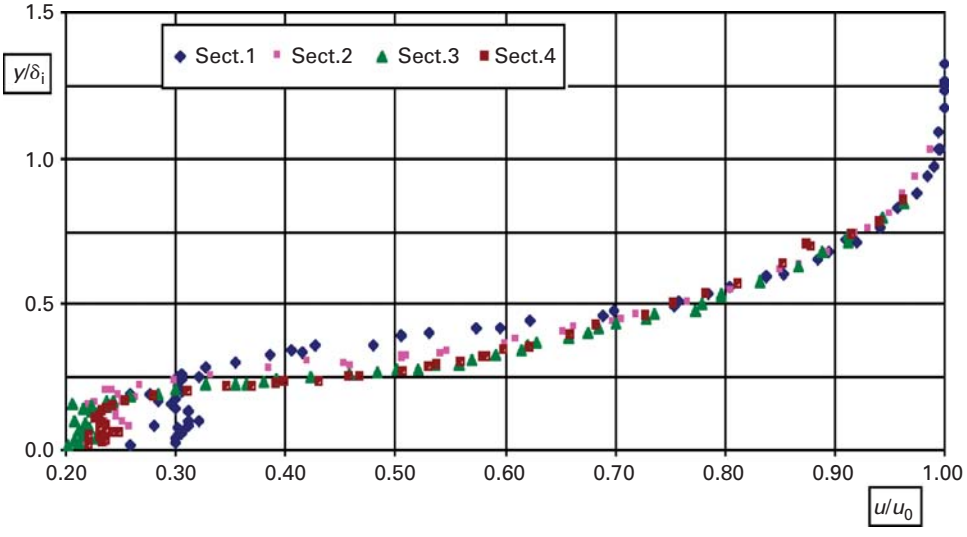

Figure 10.25. Non dimensional local mean velocity distributions, lateral verticals (15 mm double density).

one type of density and one well defined measurement vertical position. In each figure all the three cylinder heights are considered and also the smooth bottom case as a comparison.

The main point that emerges from this new representation is that, even if we consider the equilibrium portion of the diagrams, this equilibrium shape is not the same for each vegetation type or even for the smooth bottom, but on the contrary is strongly dependent on the vegetation characteristics. Perhaps this behaviour is due just to the circumstance that the non dimensionalization has been performed not in the shape of velocity defect with respect

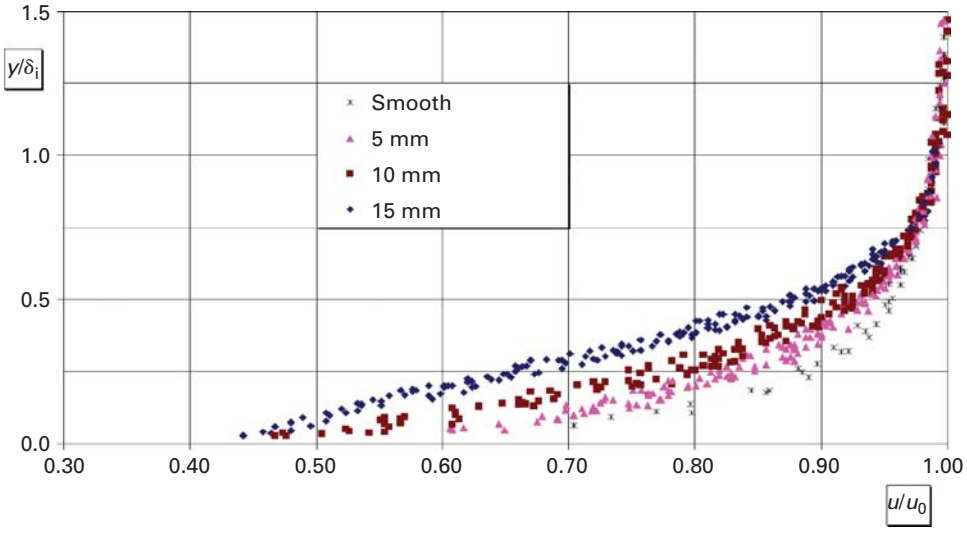

Figure 10.26. Non dimensional local mean velocity distributions (0, 5, 10, 15 mm single density).

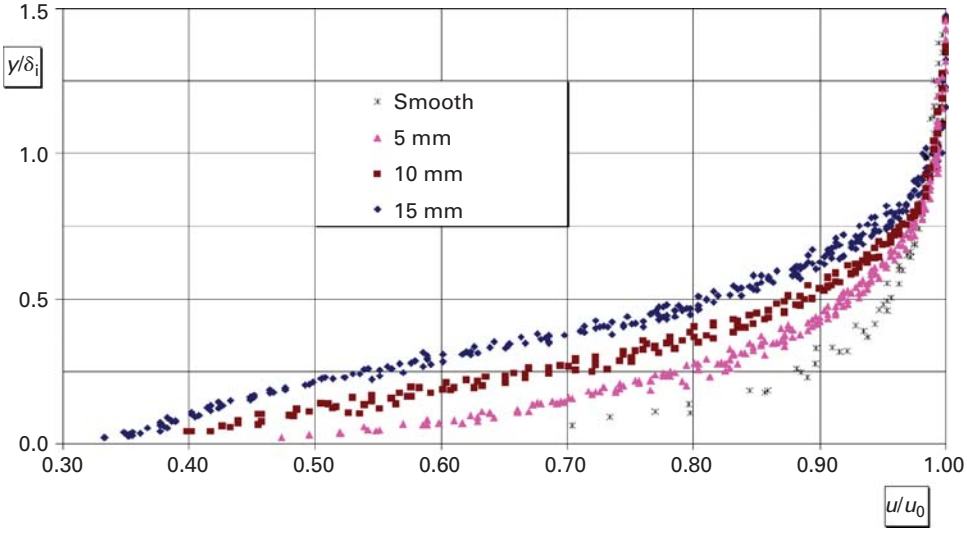

Figure 10.27. Non dimensional local mean velocity distributions (0, 5, 10, 15 mm double density).

of the friction velocity as scaling velocity, but necessarily in the simpler way recalled. In fact, with this processing modality, any reference to the different values of friction velocity, no more among different test sections of a single type of vegetated current, but among different types of vegetated currents, has been discarded. In Conclusion paragraph 10.4, a possible new data processing which could overcome this difficulty will be outlined.

In order to characterize this behaviour using only a single value, a new definition was coined by the authors: the "shape factor" of the distribution. In particular the characteristic

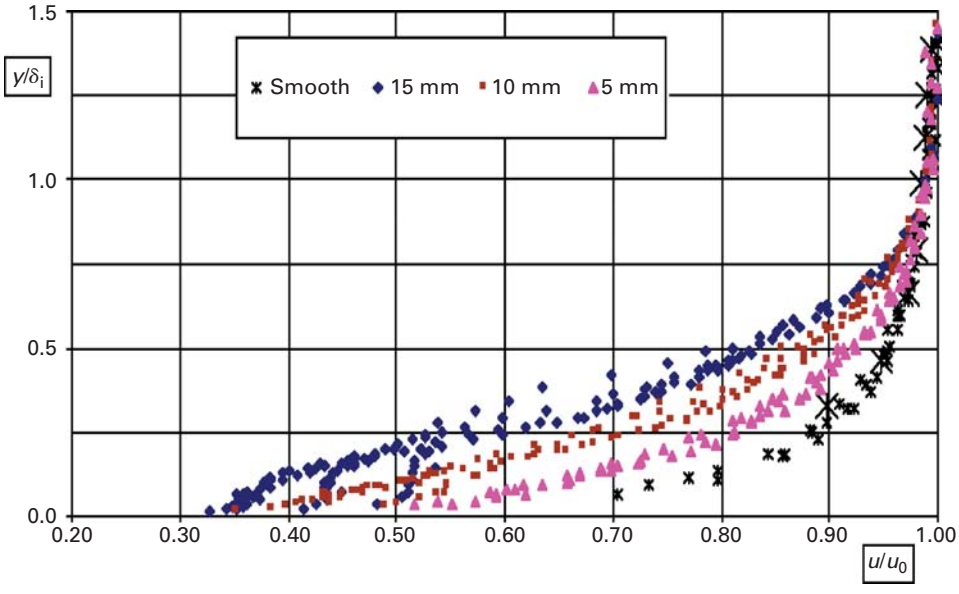

Figure 10.28. Non dimensional local mean velocity distributions (single density).

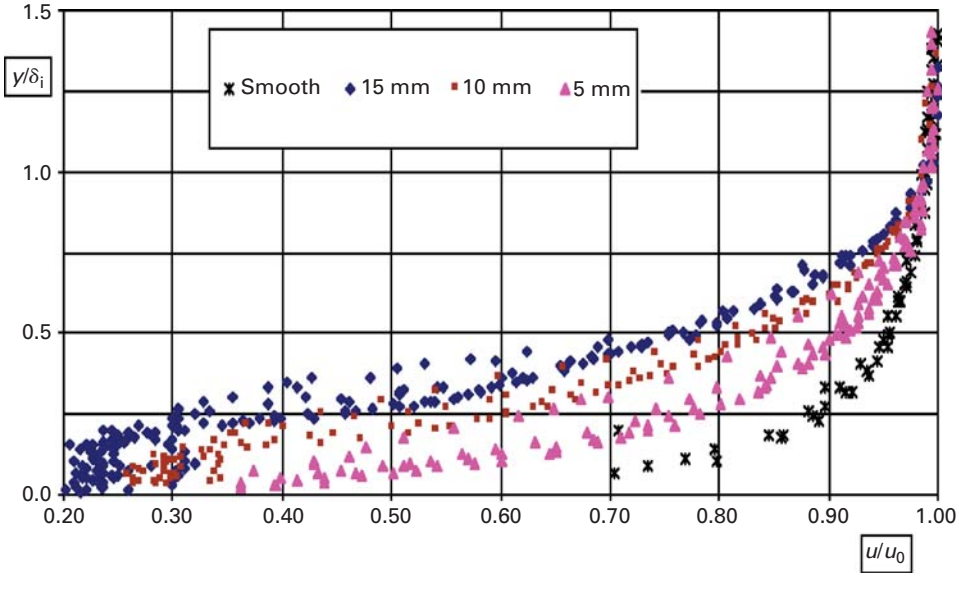

Figure 10.29. Non dimensional local mean velocity distributions (double density).

ratio δ_{99}/δ_{97} was defined as the "shape factor" of the distribution and was calculated for all the cases considered. The values obtained are reported in Table 10.6, where, again, thin lines represent the central vertical measurements and bold lines the lateral vertical measurements.

Table 10.6. Different Shape Factors for the various flow conditions.

Boundary layer thickness	Zero density	Single density	Double density
Height 0 mm	1.65–1.65	1.65–1.65	1.65–1.65
Height 5 mm	1.65–1.65	1.50–1.38	1.38–1.30
Height 10 mm	1.65–1.65	1.40–1.27	1.25–1.19
Height 15 mm	1.65–1.65	1.32–1.22	1.20–1.12

It is clear that the "shape factor" establishes a particular function, which is decreasing in a monotonic way with increasing cylinder height, cylinder density, and proximity of measurement vertical to a cylinder.

10.2.4 First partial conclusions

In conclusion, in previously cited papers the effects of a rigid fully submerged vegetated bed on the hydrodynamics of a turbulent boundary layer developing over it have been experimentally investigated. In these papers the boundary layer was a zero piezometric head gradient, the vegetation was submerged, rigid and sparse and was modelled through use of rigid cylinders; the dimensions and density of the cylinders generated six different vegetation types; and finally experimental measurements of the instantaneous velocities were carried out in verticals placed either along the axis of the flow or 1.25 cm apart (along a cylinder row). The main results of these investigations were the following:

1) The shifting of the measurement verticals along the transverse test section does not give rise to meaningful changes of the boundary layer thickness values;
2) The local mean velocity distributions made non dimensional with the boundary layer thickness and the external stream velocity, show a "total" or "partial" equilibrium characteristic (velocity distributions relative to the four test sections superimposing one another) with every kind of vegetation (that is cylinder height and density) and in relation to both vertical positions considered. The loss of "total" equilibrium in a section depends on the ratio between the height of the cylinders and the thickness of the boundary layer in the section: the limit values of this ratio depend on the density type of the vegetation (0.35 for the single density and 0.28 for the double one), and are the same apart from the measurements at vertical positions. In other words, therefore, when vegetation is sufficiently sparse and/or low, this same vegetation acts simply as a bottom roughness even in relation to distances from the bottom less than the vegetation height; whereas when vegetation is more dense and/or higher, it significantly influences at least the zone of the current lower than the cylinders height.
3) Taking into account only the "total equilibrium" distributions, the shape of these non dimensional distributions depends on the chosen vegetation type and measurement vertical. This circumstance perhaps must be attributed to the impossibility of non dimensionalizing referring to both the velocity defect diagrams and friction velocity scaling.
4) It is possible to define a particular "Shape Factor", which sums up with just a single value the characteristics of the shapes of the velocity distributions;
5) Finally the "Shape Factor" values are a decreasing function of vegetation height, vegetation density and proximity of measurement vertical to a single cylinder.

10.3 BOUNDARY LAYER ON A VEGETATED SURFACE WITH A SUBMERGED, RIGID, DENSE VEGETATION

10.3.1 Generalities about experimental plant, data acquisition system and experiments planning

The previous paragraph detailed an extensive survey carried out by the authors regarding a non equilibrium boundary layer stream flowing over submerged, rigid, sparse vegetation.

Vegetation was represented by cylinders of differing heights (5, 10, 15 mm) and densities (rectangular meshes $2.5 * 5.0\ cm^2$ or square meshes $2.5 * 2.5\ cm^2$).

Various interesting conclusions have been obtained about the behaviour of such a current.

In a more recent paper (Gualtieri *et al*., 2006) the authors investigated a boundary layer current of the same type, but flowing over submerged, rigid, dense vegetation, very similar to natural vegetation, such as that of Fig 10.30. This vegetation was modelled using a commercial carpet of plastic grass 18 mm in height, glued onto a similar Plexiglas bottom as previously used for the cylinders. The artificial grass was sufficiently resistant so that it could be considered as rigid vegetation.

Figure 10.30. View of the submerged, almost rigid, thick vegetation.

The aim of this new approach was to investigate any differences in the behaviour of the stream with respect to the former vegetation type. For this reason most of the hydrodynamic characteristics of the previous current were kept unaltered.

In particular the boundary layer was still a zero piezometric head gradient, obtained by assuming a channel slope of 2.25%. Moreover the head on the vena contracta was set again equal to 10.34 cm, so that the velocity in the recovery layer would be maintained at 1,424 m/s.

However, as regards the sluice gate height, two values of 8 cm and 10 cm were adopted, in contrast to the 7.49 cm previously used. The reason for this choice lay in the fact that the differing nature of the vegetation increased the boundary layer thickness at corresponding

test sections, so that the free-stream became so thin as to make it doubtful that the velocity distributions would remain independent of the flow height (even from the first test section onwards). Consequently a first experimental run using a slightly greater sluice height (8 cm) followed by a second run with greater sluice height again (10 cm) were carried out.

In relation to the acquisition surveys, for both the different flows similar surveys as with cylinders were carried out. Furthermore, the acquisition instrumentation (LDA) was exactly the same as in previous works. It is worth noting that in the case of the grass carpet, measurements within the vegetation were not possible due to the technical limits of the LDA instrumentation.

10.3.2 Velocity measurements and relative processing

The local mean velocity distributions were obtained experimentally and are reported in Figs. 10.31, 10.32, 10.33, 10.34. In each diagram the distributions relative to "Sluice gate opening 8 cm" and "Sluice gate opening 10 cm" are reported together with the distributions relative to smooth bottom and to that with cylinders of 15 mm height displaced in double density (i.e. the maximum height and the maximum density obtained with the cylinders). From the bottom to the top of the diagrams the following are reported in the order: smooth bottom; cylinders; grass with sluice gate opening 10 cm; grass with sluice gate opening 8 cm. As previously, the verticals relative to the 95%, 97% and 99% of u_0 values are traced.

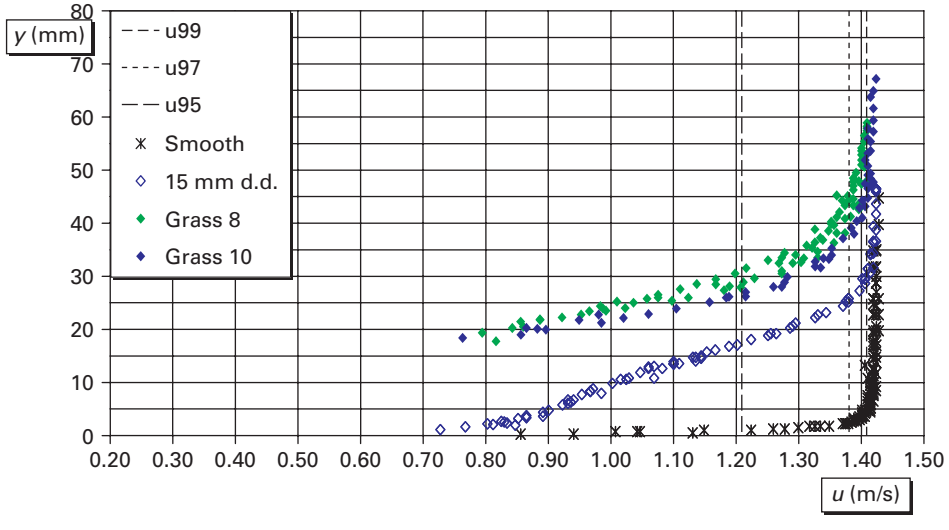

Figure 10.31. Velocity distributions in test section 20 cm.

A preliminary observation of velocity distributions suggested some first considerations.

First of all it was possible to observe that, in presence of the vegetal carpet, the local mean velocities were lower and consequently the boundary layer thickness was larger with respect to the case when cylinders were used. This outcome is due either to the larger height of the grass carpet with respect to the cylinders or to the much greater density of the carpet vegetation.

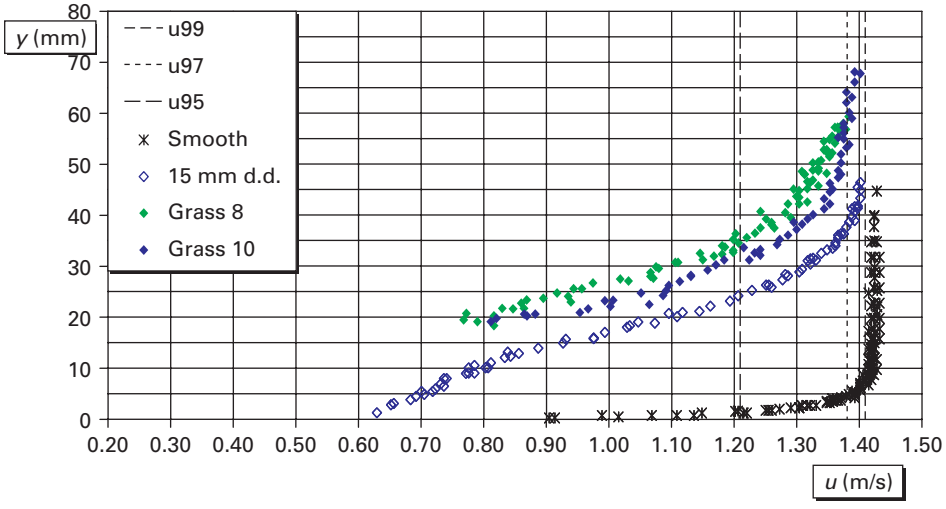

Figure 10.32. Velocity distributions in test section 30 cm.

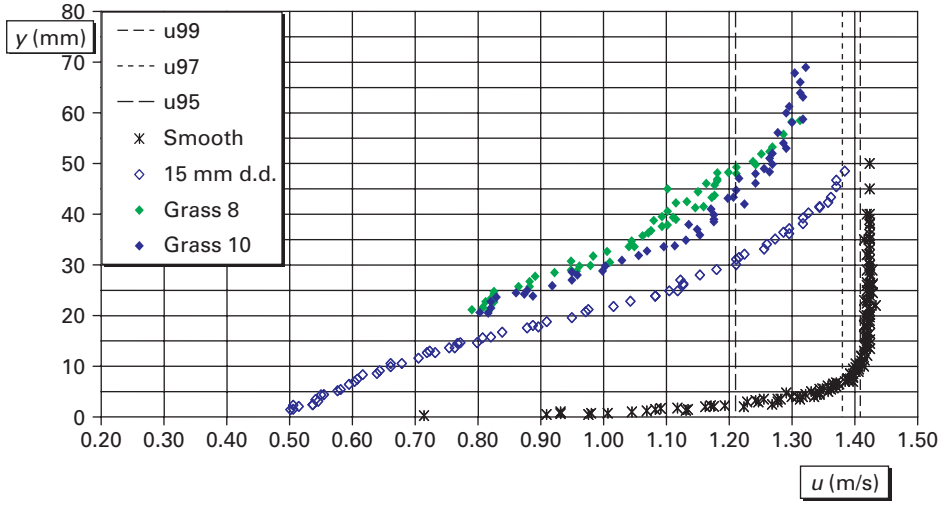

Figure 10.33. Velocity distributions in test section 40 cm.

It was moreover evident that, in the same test section, velocity distributions relative to "Sluice gate opening 8 cm" and "Sluice gate opening 10 cm" did not superimpose on one another, so that, as had been foreseen, the independence of the velocity profiles from the flow height could no longer be verified. This characteristic is certainly due to smallness or, in the last test sections, even a lack of a free-stream. It is worth noting that it is possible to demonstrate through continuity considerations that lack of free-stream prevents any possible superposition.

More detailed results could be obtained through non dimensional distributions observations.

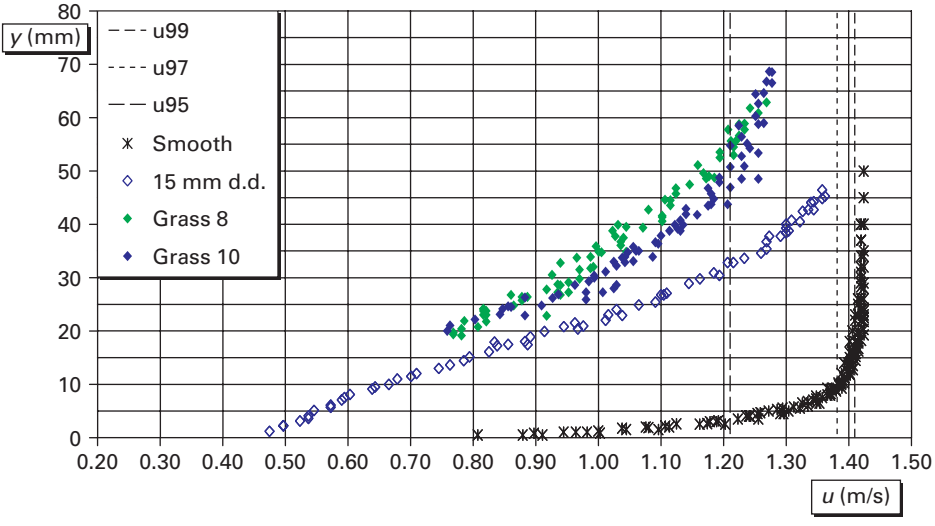

Figure 10.34. Velocity distributions in test section 50 cm.

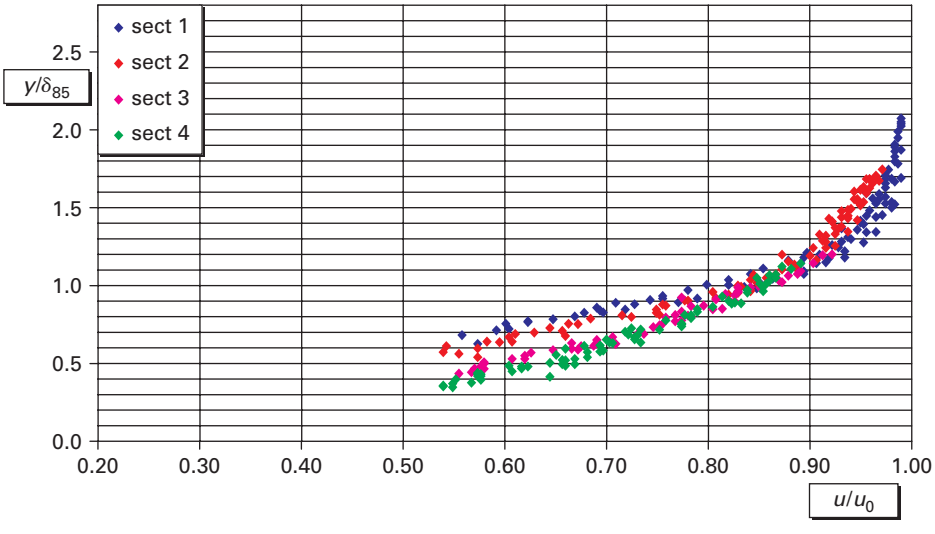

Figure 10.35. Non dimensional velocity distributions, sluice gate opening 8 cm.

In Figs. 10.35 and 10.36 non dimensional velocity distributions are reported, with regard to "Sluice gate opening 8 cm" and "Sluice gate opening 10 cm" respectively.

In these distributions velocities are scaled always with $u_0 = 1{,}424$ m/s, whereas the heights are scaled with the boundary layer thickness obtained through the 85% value of u_0 velocity (obviously called δ_{85}). This last choice was a result of the fact that it was impossible to obtain the δ_{99} values in all test sections and with both sluice gate openings.

Comparing the corresponding distributions of the two different diagrams, it could be clearly observed that they did not superimpose, as had been foreseen: a fact due to the

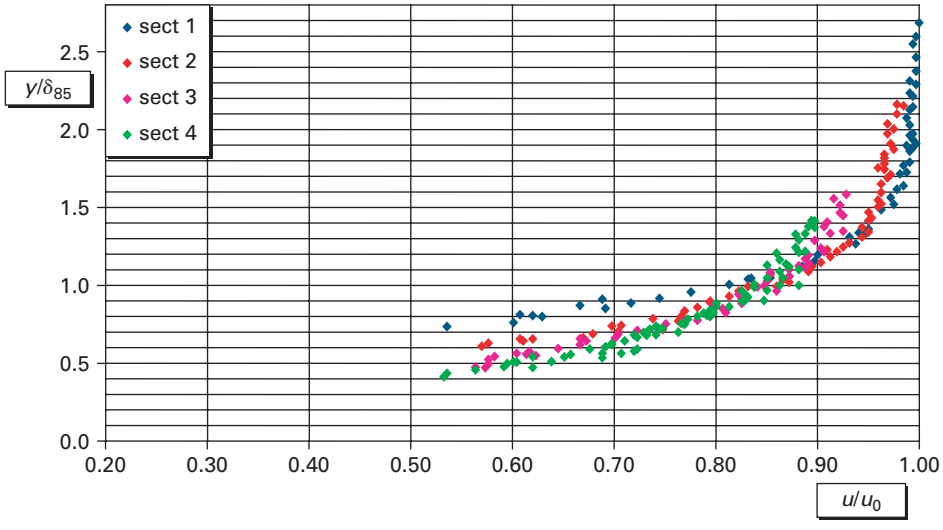

Figure 10.36. Non dimensional velocity distributions, sluice gate opening 10 cm.

different shapes of the dimensional distributions. The main observation, however, was that even the four diagrams relative to the four test sections for the same flow did not superimpose on one another, so that it appeared clear that with this type of vegetation the obtained boundary layer was no more an equilibrium boundarylayer.

10.3.3 Second partial conclusions

In conclusion, in the papers cited in paragraph 10.2, the effects of a rigid fully submerged vegetated bed on the hydrodynamics of a turbulent boundary layer developing over it have been experimentally investigated. In the paper cited in this paragraph, the boundary layer was characterised by a zero piezometric head gradient, the vegetation was submerged, rigid and dense and was modelled using a carpet of commercial plastic grass; moreover, there were two flows investigated, both equal except for the aperture value of the initial sluice gate (8 cm and 10 cm respectively). The main result of this investigation was the following.

When the vegetation is no longer sufficiently sparse and low and instead is very dense and possibly quite high, and the height of the flow is no longer sufficient with respect to this new vegetation typology, the boundary layer loses its main characteristics.

In particular, even considering a case of zero pressure (or piezometric head) gradient in the free-stream, the boundary layer no longer displays the other equilibrium characteristics. That is, it does not display superposition of the non dimensional velocity distributions in subsequent test sections. Moreover, under such circumstances, the boundary layer does not even display the simpler characteristics of standard boundary layers (i.e. superposition of dimensional and non dimensional velocity distributions with changing of current height).

10.4 CONCLUSIONS

This Chapter reports the results of a long-term experimental research.

The experimental research refers to a topic that appears to be new at all in international literature, at least as far as the authors know. This topic is relative to the behaviour of water boundary layers flowing over a vegetated surface.

In order to limit the possible extension of the argument, either the possible boundary layers or vegetation types have been strictly selected. As for boundary layers, the type with zero piezometric head gradient has been chosen. As for vegetation, the rigid submerged vegetation has been taken into consideration. Many types of rigid submerged vegetation have been considered, starting from a very sparse and very low type, and reaching a very dense and higher type.

The most intriguing result of the first step of the research has been that, in case of very sparse and very low vegetation, the boundary layer totally holds its equilibrium characteristics, typical of boundary layers with zero piezometric head gradient flowing over a smooth bottom. Surely, this was not a result expected.

In cases of vegetation more dense and/or high, this characteristic behaviour holds only in the layers of the flow not directly obstructed by vegetation (partial equilibrium).

In any case, in presence of a total or partial equilibrium, the characteristic shape of the considered suitable non dimensional velocity distribution depends on the vegetation typology present on the currents' bed. This property perhaps depends on the particular choice of the non-dimensionalizing procedure, which is due to the difficulty of defining and computing a friction velocity in this type of current.

The second step of the research allows to supplement results relative to boundary layer behaviour with sparse rigid submerged vegetation with the alternative boundary layer behaviour in case of dense rigid submerged vegetation. In fact, when the vegetation is no longer sufficiently sparse and low and instead is very dense and possibly quite high, and the height of the flow is no longer sufficient with respect to this new vegetation typology, the boundary layer loses its main characteristics.

The comments above now allow a simplified and unified description of the characteristics of a boundary layer flowing over a bed covered with submerged, rigid, sparse or dense vegetation In fact, referring now to both types of vegetation investigated (submerged, rigid sparse; and submerged, rigid, dense), and drawing on a concept introduced in paragraph 10.2.4 relative to total and partial equilibrium characteristics, it is possible to roughly divide the effects of vegetation on velocity distributions into three principal cases.

First case: Vegetation very sparse and/or low—the boundary layer with zero piezometric head gradient holds its total equilibrium characteristics, even in the lower layers of the stream, but with velocity distribution shapes that depend on vegetation characteristics.

Second case: Vegetation more dense and/or higher—the boundary layer with zero piezometric head gradient holds its equilibrium characteristics only partially, in particular in the layers more distant from the bottom than the vegetation height, still with velocity distribution shapes that depend on vegetation characteristics.

Third case: Vegetation very dense and high so that the free-stream becomes very thin or at worst no longer exists. The boundary layer with zero piezometric head gradient no longer behaves either as an equilibrium boundary layer or as a standard boundary layer.

Finally, the third step of the research has scarcely begun. Its main aim is to overcome the difficulties relative to the different shapes of the equilibrium velocity distributions as a function of the vegetation typology, or even to the total lack of equilibrium in cases of more dense and higher vegetation.

The method that authors are pursuing is to limit the velocity distributions in so far as they relate to distances from the bottom that are greater than the vegetation height.

Moreover, the velocity distributions will become "differential velocity distributions", if we consider as starting points the distributions relative to the vegetation height in the ordinate, and the water velocity at the vegetation height in the abscissa.

APPENDIX—LIST OF SYMBOLS

List of Symbols

Symbol	Definition	Dimensions or Units
F	first experimentally based PDT distribution function	
F′	second experimentally based PDT distribution function	
Q	volumetric flow rate of the current	$[L^3T^{-1}]$
TKE	turbulent kinetic energy	$[ML^2T^{-2}]$
W	Coles' wake function	
h	height of canopies in Poggi' paper	[L]
k	turbulent kinetic energy per unit mass	$[L^2T^{-2}]$
n	Manning's roughness coefficient	
u	longitudinal velocity at a distance y from the bottom	$[LT^{-1}]$
u_k	longitudinal velocity at the interface vegetation layer and surface layer	$[LT^{-1}]$
u_0	longitudinal velocity in the free-stream layer	$[LT^{-1}]$
u_0'	fluctuating velocity in the streamwise direction at $y = \delta$	$[LT^{-1}]$
$u^* = (\tau/\rho)^{1/2}$	friction velocity	$[LT^{-1}]$
y	distance from the bottom of a point of the flow	[L]
z	distance from the bottom of a point of the flow in Poggi' paper	[L]
z	vegetation height in Klopstra model	[L]
Π	Coles' wake parameter	
α	exponent in Tsujimoto Reynolds stress law coefficient in Poggi' paper	
α	characteristic length in Klopstra model	[L]
β	exponent in Tsujimoto velocity law	
δ	boundary layer thickness	[L]
δ_{85}	boundary layer thickness at 85% of u_0	[L]
δ_{97}	boundary layer thickness at 97% of u_0	[L]
δ_{99}	boundary layer thickness at 99% of u_0	[L]
ε	dissipation rate of k	$[L^2T^{-3}]$
κ	von Kàrmàn constant	
ν	water kinematic viscosity	$[L^2T^{-1}]$
π	pi greek value	
ρ	water Density	$[ML^{-3}]$
τ	shear stress	$[ML^{-1}T^{-2}]$
τ_k	shear intensity at the interface vegetation layer and surface layer	$[ML^{-1}T^{-2}]$
ω	dissipation rate of TKE per unit kinetic energy	$[T^{-1}]$

REFERENCES

Ackermann, J.D. and Okubo, A. 1993, Reducted mixing in a marine macrophyte canopy, *Funct. Ecol.*, **7**, pp. 305–309.

Balachandar, R. and Ramachandran, S., 1999, Yurbulent Boundary Layers in Low Reynolds Number Shallow Open Channel Flows, *Journal of Fluids Engineering, Transactions of ASME*, **123** (2), pp. 394–400 (jan.).

Balachandar, R., Blakely, D., Tachie, M. and Putz, G., 2001, A Study on Turbulent Boundary Layers on a smooth Flat Plate in an Open Channel, *Journal of Fluids Engineering, Transactions of ASME*, **121**, pp. 684–689 (sept.).

Bandypadhyay, P.R., 1992, Reynolds Number Dependence of the Freestream Turbulence Effects on Turbulent Boundary layers, *AIAA Journal*, **30** (7), pp. 1910–1912.

Baptist, M.J., V. Babovic, J. Rodriguez Uthurburu, M. Keijzer, R.E. Uittenbogaard, A. Mynett, and A. Vevey, 2006, On inducing equations for vegetation resistance, Journal of Hydraulic Research, accepted.

Ben Meftah M., De Serio F., Malcangio D., Petrillo A. and Mossa M., 2006, Experimental study of flexible and rigid vegetation in an open channel, *Proceedings of River Flow 2006*, Lisbona, Portugal.

Blair, M.F., 1983a, Influence of Free-Stream Turbulence on Turbulent Boundary Layer Heat Transfer and Mean Profile Development. Part I Experimental Data, *Transactions of the ASME Journal of Heat and Mass* Transfer, **105** (feb), pp. 33–40.

Blair, M.F., 1983b, Influence of Free-Stream Turbulence on Turbulent Boundary Layer Heat Transfer and Mean Profile Development. Part II Analysis of results, *Transactions of the ASME Journal of Heat and Mass* Transfer, **105** (sep), pp. 41–47.

Burke, R.W. and Stolzenbach, K.D., 1983, Free surface flow through salt marsh grass, *MIT-Sea Grant. Rep. MITSG 83-16*, Cambridge, Massachusetts, USA, 252.

Carollo, F.G., Termini, D. and Ferro, V., 2005, Flow resistance law in channels with flexible submerged vegetation, Journal of Hydraulic Engineering, **131** (7), pp. 554–564.

Carollo, F.G., Termini, D. and Ferro, V., 2005, Flow velocity measurements in vegetated channels, Journal of Hydraulic Engineering, **128** (7), pp. 664–673.

Castro, I.P., 1984, Effects of Free Stream Turbulence on Low Reynolds Number Boundary Layers, *Transactions of ASME Journal of Fluid Engineering*, **106** (sep), pp. 298–306.

Charnay, G., Mathieu, J. and Comte-Bellot, G. 1976, Response of a turbulent boundary layer to random fluctuations in an external stream, *The Physics of Fluids*, **19** (9) pp. 1261–1272.

Charney, G., Comte-Bellot, G. and Mathieu J., 1971, Development of a turbulent boundary layer on a flat plate in an external turbulent flow, *AGRD CCP*, 93–71, pp. 27.1–27.10.

Choi S. and Kang H., 2003, Reynolds stress modelling of vegetated open-channels flows, *Journal of Hydraulic Research*, **42** (1), pp. 3–11.

Chow Ven Te, 1959, Open-Channel Hydraulics, McGraw-Hill Classic Textbook Reissue Series.

Clauser, F.H., 1956, The turbulent boundary layer, *Advances in Applied Mech*, **4**, pp. 1–51.

Coles, D., 1956, The law of the wake in the turbulent boundary layer, *Journal of Fluids Mechanics*, **1**, pp. 191–226.

Cui J. and Neary V.S., 2002, Large eddy simulation (LES) of fully developed flow through vegetation, *Proceedings of the 5th International Conference on Hydroinformatics*, Cardiff, UK.

Cui J., 2000, Large-eddy simulation of turbulent flow over rough surfaces, PhD dissertation Mechanical Engineering, University of Iowa, Iowa City, Iowa, USA.

De Felice, S. and Gualtieri, P., 2005, Interactions between turbulent Boundary Layer and rigid vegetated beds: Comparison among hydrodynamic characteristics in different points around the cylinders, *I.A.H.R. Congress, Seoul (Corea)*, 11–16 september, pp. 2434–2445.

De Felice, S., Gualtieri, P. and Pulci Doria, G., 2004, Study of the interactions between turbulent boundary layer and vegetated beds through an LDA system, *A.I.VE.LA. National Conference*, Naples, Italy, www.aivela.org.

Dean, R.B., 1976, A single formula for the complete velocity profile in a turbulent boundary layer, *ASME Journal. of Fluid Engineering*, **98**, pp. 723–727.

Defina, A. and Bixio, A.C., 2005, Mean Flow and turbulence in vegetated open channel flow, *Water Resources Research*, **41** (7), pp. 1–12.

Evans, R.L. and Horlock, J.K. 1974 Calculation of the Development of Turbulent Boundary Layers With a Turbulent Free-Stream, *Transactions of the ASME Journal of Fluid Engineering*, 1974 (dec), pp. 348–352.

Evans, R.L., 1985, Free-Stream Turbulence Effects on Turbulent Boundary Layers in an Adverse Pressure Gradient, *AIAA Journal*, **23** (11), pp. 1814–1816.

Fenzl, R.N., 1962, Hydraulic resistance of broad shallow vegetated channels, PhD Thesis, University of California at Davis, Davis, California, USA.

Finnigan, J., 2000, Turbulence in plant canopies, *Annual Review of Fluids Mechanics*, **32** (1), pp. 519–571.

Fischer-Antze, T., T. Stoasser, P. Bates, and N.R.B. Olson, 2001, 3D numerical modeling of open-channel flow with submerged vegetation, *Journal of Hydraulic Research* **39** (3) pp. 303–310.

Freeman, G.E., R.E. Copeland, W. Rahmeyer, & D.L. Derrick, 1998, Field determination of Manning's n value for shubs and woody vegetation, *Engineering Approaches to Ecosystem Restoration, Proc. Wetlands Engrg. And River restoration, Conf. ASCE*, New York, USA.

Gad-el-Hak, M. and Bandyopadhyay, P.R., 1994, Reynolds number effects in wall-bounded flows, *Applied Mechanics Review* **47** (8) pp. 307–365.

George, W.K. and Casillo, L., 1997, Zero pressure-gradient turbulent boundary layer, *Applied Mechanics Review* **50** (11), pp. 689–729.

Ghisalberti M. and Nepf H., 2006, The structure of shear layer flow over rigid and flexible canopy, *Environmental Fluid Mechanics*, **6**, pp. 277–301.

Gioia G. and F.A. Bombardelli, 2002, Scaling and similarity in rough channel flows, *Physical Review Letters*, **88** (1), pp. 14501–14504.

Granville, P.S., 1976, A modified law of the wake for turbulent shear layers, *ASME Journal of Fluid Engineering*, **98**, pp. 578–580.

Greco, M. and Pulci Doria, G., 1983, Strato limite in una corrente originariamente turbolenta (Boundary Layer in a current with turbulent free-Stream), *Simposio su l'Anemometria Laser-Doppler nella sperimentazione idraulica*, Roma, pp. 156–175.

Green J.C., 2005, Modelling flow resistance in vegetated streams: review and development of a new theory, *Hydrological Processes*, **19**, pp. 1245–1259.

Gualtieri, P. and Pulci Doria, G. 1998, A proposal of a physically based thickness definition and of a new mean velocities distribution law in a turbulent boundary-layer on the ground of LDA measurements, *13th Australasian Fluid Mechanics Conference*, Melbourne, pp. 845–848.

Gualtieri, P. and Pulci Doria, G. 1999, Boundary Layer Intermittency Model, *Int. IUTAM Symp. on Geometry and Statistics of Turbulence Hayama Japan*, pp. 379–384.

Gualtieri, P. and Pulci Doria, G., 1997, Non dimensional distribution of longitudinal integral length scales in a turbulent boundary layer *FLUCOME '97 Congress Hayama Japan*, pp. 161–166.

Gualtieri, P. and Pulci Doria, G., 1998a, Skewness, Kurtosis and Length Scales experimental distributions laws based on a three bands model in a turbulent boundary layer, *Excerpta of Italian contributions to the field of hydraulic engineering*, **12**, pp. 155–194.

Gualtieri, P. and Pulci Doria, G., 1998b, A proposal of a physically based thickness definition and of a new mean velocities distribution law in a turbulent boundary-layer on the ground of LDA measurements, *13th Australasian Fluid Mechanics Conference, Melbourne*, pp. 845–848.

Gualtieri, P. and Pulci Doria, G., 2001, A Correct Model of Variance, Skewness, Kurtosis in Boundary Layer with Turbulent External Layer, *14th Australasian Fluid Mechanics Conference Melbourne*, pp. 259–262.

Gualtieri, P. and Pulci Doria, G., 2003, A correct model of longitudinal integral length scales in boundary layer with turbulent external layer, *2nd International Conference on*

Heat Transfer, Fluid Mechanics, and Thermodynamics H.E.F.A.T., Victoria Falls Zambia, produced on CD-ROM.

Gualtieri, P., Pulci Doria, G. and Taglialatela, L., 2004a, Experimental validation of turbulent boundary layers in channels *3rd International Conference on Heat Transfer, Fluid Mechanics, and Thermodynamics H.E.F.A.T.*, Cape Town South Africa, June, produced on CD-ROM.

Gualtieri, P., Pulci Doria, G. and Tagliatatela, L., 2004b, Effect of vegetation on boundary layer with turbulent external stream, *2nd International Conference on Fluvial Hydraulics RiverFlow*, Naples, Italy, pp. 381–388.

Gualtieri, P., Pulci Doria, G. and Tagliatatela, L., 2004c, Density vegetation influence on boundary layer, *15th Australasian Fluid Mechanics Conference on Fluvial Hydraulics AFMC*, Sydney, Australia, pp. 195–198.

Gualtieri, P., Pulci Doria, G., De Felice, S. and Catapano, 2006, Studio tramite LDA degli effetti di un fondo fittamente vegetato su di uno strato limite turbolento (Study through LDA of the effects on a turbulent Boundary Layer of a densely vegetated bottom) *XXX Convegno di Idraulica e Costruzioni Idrauliche IDRA 2006*, 11–15 sept., Roma, Published on CD-ROM pp. 1–14.

Hancock, P.E. and Bradshaw, P., 1983, Influence of Free-Stream Turbulence on Turbulent Boundary Layers, *Transactions of the ASME Journal of Fluids Engineering*, **105** (sep), pp. 284–289.

Hancock, P.E. and Bradshaw, P., 1989, Turbulent structure of a boundary layer beneath a turbulent free stream, *Journal of Fluid Mechanics*, **205** pp. 45–76.

Hoffmann, J.A. and Mohammady, K., 1991, Velocity Profiles for Turbulent Boundary Layers Under Free-Stream Turbulence, *Transactions of the ASME Journal of Fluid Engineering*, **113** (sep), pp. 399–404.

Huffman, G.D., Zimmerman, D.R. and Bennett, W. A., 1972, The effect of Free-Stream turbulence leel on turbulent boundary layer behaviour, *AGARDograph 164 Paper I-5*, pp. 91–115.

Huthoff, F., Augustijn, D.C.M. and Hulscher, S.J.M.H., 2006, Depth-averaged flow in presence of submerged cylindrical elements, *Proceedings of River Flow 2006*, Lisbona, Portugal.

Keijzer, M., Baptist, M., Babovic, V. and Uthurburu, J.R., 2005, Determining equation for vegetation induced resistance using genetic programming, *Proceedings of GECCO'05*, Washington, DC, USA.

Kline, S. J., Lisin, A.V. and Waitman, B.A., 1960 Preliminary experimental investigation of effect of free-Stream turulence on turbulent boundary-layer growth, *N.A.C.A. TN D-368*, pp. 1–60.

Klopstra, D., Barneveld, H.J., Van Noortwijk, J.M. and Van Velzen, E.H., 1997, Analytical model for hydraulic roughness of submerged vegetation, *Proceedings of the 27th IAHR Congress*, San Francisco, USA, pp. 775–780.

Kutija, V. and Hong, H.T.M., 1996, A numerical model for assessing the additional resistance to flow introduced by flexible vegetation, *Journal of Hydraulic Research*, **34** (5), pp. 99–114.

Lopez, F. and Garcia, M., 1997, Open-Channel Flow Through Simulated Vegetation: Turbulence Modeling and Sediment Transport, *US Army of Engineers Waterway Experiment Station Wetlands Research Program Technical Report WRP-CP-10*.

Lopez F. and Garcia M., 1998, Open channel flow through simulated vegetation: Suspended sediment transport modeling, *Water Resources Research*, **34** (9), pp. 2341–2352.

Lopez F. and Garcia M., 2001a, Mean Flow and Turbulence Structure of Open-Channel Flow Through Non-Emergent Vegetation, *Journal of Hydraulic Engineering*, **127** (5), pp. 392–402.

Mc Donald, H. and Kreskowsky, J.P., 1974, Effects of free stream turbulence on the turbulent boundary layer, *International Journal of Heat and Mass* Transfer, **17**, pp. 705–716.

Meier, H.U. and Kreplin, H.P., 1980, Influence of Freestream Turbulence on Boundary-Layer Development, *AIAA Journal*, **18** (1), pp. 11–15.

Mejier, D.G. and Van Velzen, E.H., 1998, Prototype-scale flume experiments on hydraulic roughness of submerged vegetation, *Proceedings of the 28th IAHR Congress*, Graz, Austria.

Mellor, G.L. and Herring, H.J., 1973, A survey of mean turbulent filed closure, *AIAA J.*, **11**, pp. 590–599.

Neary, V.S., 1995, Numerical modelling of diversion flows, PhD dissertation, Civil and Environmental Engineering, University of Iowa, Iowa City, Iowa, USA.

Neary, V.S., 2000, Numerical model for open-channel flow with vegetative resistance, *IAHR's 4th International Conference on Hydroinformatics*, July 23–27, Cedar Rapids, Iowa, USA.

Neary, V.S., 2003, Numerical solution of fully developed flow with vegetative resistance, *Journal of Engineering Mechanics*, **129** (5), pp. 558–563.

Nepf, H.M. and E.R. Vivoni, 1999, Drag, turbulence and diffusion in flow through emergent vegetation, *Journal of Geophysical Research*, **105** (2), pp. 479–489.

Nezu, I. and Nakagawa, H., 1993, Turbulence in open-channel flows, Monograph, Balkema, Rotterdam, The Netherlands.

Nezu, I., Sanijou, M. and Okamoto, T., 2006, Turbulent structure and dispersive properties in vegetated canopy, *Proceedings of River Flow 2006*, Lisbona, Portugal.

Patel, V.C. and Yoon, J.Y., 1995, Application of turbulence models to separated flows over rough surfaces, *Journal of Fluids Engineering* **117** (2), pp. 234–241.

Poggi, D., Porporato, A. and Ridolfi, L., Albertson, J.D., Katul G.G. 2004, The effect of vegetation on canopy sub-layer turbulence, *Boundary-Layer Meteorology*, **111**, pp. 565–587.

Prandtl, L., 1904, Über Flüssigkeitsbewegungen bei sehr kleiner Reibung (On Fluid Motions with Very Small Friction), *Verhandlungen des III Internaztionalen Mathematiker Kongresses (Heidelberg 1904)*, Leipzig 1905.

Pulci Doria, G. and Tagliatatela, L., 1990, Ipotesi di distribuzioni adimensionali di velocità media e di agitazione in correnti turbolente (An hypothesis about non dimensional distributions of local mean velocity and turbulent velocity fluctuations in turbulent streams) *Giornate di Studio per la celebrazione della nascita di Girolamo Ippolito*, Lacco Ameno, Italy, pp. 223–245.

Pulci Doria, G., 1991, Statistical quantities distributions and the use of the entropy concept *International Conference on Entropy and Energy Dissipation on Water Resources*, Maratea, Italy, pp. 541–586.

Raupach, M.R. and Shaw, R.H., 1982, Averaging procedures for flow within vegetation canopies, *Boundary Layer Meteorology*, **22**, pp. 79–90.

Raupach, M.R. and Thom, A.S., 1981, Turbulence in and above plant canopies, *Annual Review of Fluids Mechanics*, **13**, pp. 97–129.

Righetti, M. and Armanini, A., 2002, Flow resistance in open channel with sparsely distributed bushes, *Journal of Hydrology*, **269**, pp. 375–395.

Robertson, J.M. and Holt, C., 1972, Stream turbulence effects on turbulent boundary layer, *Journal of Hydraulic Division Proceedings of the American Society of Civil Engineers*, **98** (HY6), pp. 1095–1099.

Rodi W., 1980, Turbulence models and their application: state of art paper, Monograph, IAHR, Delft, The Netherlands.

Russo Spena, A., 1954, Contributo allo studio delle correnti di strato limite (A contribution to boundary layer streams research), *Printed by Stabilimento Tipografico Bavarese for the Istituto di Idraulica e Costruzioni Idrauliche*, Napoli, June, pp. 3–35.

Russo Spena, A., 1957, Correnti di strato limite lungo lastre scabre (Boundary Layer streams over a rough bottom), *L'Energia Elettrica*, **XXXIV** (1) pp. 1–23.

Schlichting, H. and Gersten, K., 2003, *Boundary Layer Theory (transl. by Mayes K.)*, 8th revised and Enlarged Edition 2000, Corrected Printing 2003, Springer-Verlag, Berlin-Heidelberg.

Schlichting, H., 1955, *Boundary Layer Theory (transl. by Kestin J.)*, Pergamon Press LTD, London.

Shi Z., J. Pethick, and K. Pye, 1995, Flow structure in and above the various heights of a salt-marsh canopy: a laboratory flume study, *Journal of Coastal Research*, **11**, pp. 1204–1209.

Shimizu Y. and Tsujimoto T., 1994, Numerical analysis of turbulent open-channel flow over a vegetation layer using a k-ε model, *Journal of Hydroscience and Hydraulic Engineering*, **11** (2), pp. 57–67.

Smart, G.M., M.J. Duncan, and J.M. Walsh, 2002, Relatively rough flow resistance equations, *Journal of Hydraulic Engineering*, **128** (6), pp. 568–578.

Speziale C.G., Sarkar S., and Gatski T., 1991, Modeling the pressure strain correlation of turbulence: an invariant dynamical systems approach, *Journal of Fluids Mechanics*, **227**, pp. 245–272.

Sreenivasan, K.R., 1989, Turbulent boundary layer, in "*Frontiers in Experimental Fluid Mechanics*", M. Gad-el-Hak (ed), pp. 159–209.

Stone B.M. and Tao Shen H., 2002, Hydraulic Resistance of Flow in Channels with Cylindrical Roughness, *Journal of Hydraulic Engineering*, **128** (5), pp. 500–506.

Tachie, M.F., Balachandar, R. and Bergstrom, D.J., 2003, Low Reynolds number effects in open-channel turbulent boundary layers, *Experiments in Fluids*, **35**, pp. 338–346, (jan).

Tachie, M.F., Balachandar, R., Bergstrom, D.J. and Ramachandran S., 2001, Skin Friction Correlation in Open Channel Boundar Layers, *Journal of Fluids Engineering, Transactions of ASME*, **123**, pp. 953–956, (dec).

Tachie, M.F., Bergstrom, D.J. and Balachandar, R., 2000, Rough Wall Turbulent Boundary Layers in Shallow Open Channel Flow, *Journal of Fluids Engineering, Transactions of ASME*, **122**, pp. 533–541. (sept.)

Timoschenko S., 1955, Strength of materials; Part I: Elementary theory and Problems, D. Van. Nostrand Company, Inc. pp. 137–165.

Tsuijimoto, T., Shimizu, Y., Kitamura, T. and Okada, T., 1992, Turbulent open-channel flow over bed covered by rigid vegetation, *Journal of Hydroscience and Hydraulic Engineering*, **10** (2), pp. 13–25.

Tsujimoto, T. and Kitamura, T., 1990, Velocity profile of flow in vegetated-bed channels, *KHL Progressive Report, Hydraulic Laboratory, Kanazawa University*.

Tsujimoto, T. and T. Kitamura, 1998, A model for flow over flexible vegetation-covered bed, *Proc. Int. Water Resourches Engrg. Conf ASCE*, New York, USA, pp. 1380–1385.

Tsujimoto T., Shimizu Y., Kitamura T. and Okada T., 1992, Turbulent open-channel flow over bed covered by rigid vegetation, *Journal of Hydroscience and Hydraulic Engineering*, **10** (2), pp. 13–25.

Uittenbogaard, R., 2003, Modelling turbulence in vegetation aquatic flows, *Proceedings of Riparian Forest Vegetate Channels Workshop*, Trento, Italy.

Wilson, N.R. and Shaw, R.H., 1977, A higher closure model for canopy, *Journal of Applied Meteorology*, **16**, pp. 1197–1205.

Yen, B.C., 2002, Open channel flow resistance, *Journal of Hydraulic Engineering*, **128** (1), pp. 20–39.

CHAPTER ELEVEN

Mass transport in aquatic environments

Gregory N. Nishihara[1] & Josef Daniel Ackerman[2]
[1,2]*Department of Integrative Biology and* [2]*Faculty of Environmental Sciences, University of Guelph, Guelph, Ontario, Canada*

ABSTRACT

All forms of aquatic life rely on the surrounding fluid for the transport of resources and the products of metabolic activity. The processes that affect the transport of material to and from the surface of an organism include molecular and turbulent diffusion. However, since the viscosity of water is about 55 times that of air, the scales at which these processes occur are different and may represent considerable constraints to aquatic organisms. Transport processes in aquatic environments are considered for both pelagic (i.e., those in the water column) and benthic organisms (i.e., those at the bottom). The relevant issues related to mass transfer to and from benthic plants and animals are considered in detail.

11.1 INTRODUCTION

The concept of mass transfer is essential in aquatic environments where the fluid medium—water—serves to facilitate myriad biological processes. These include the delivery of gases used in the most basic and fundamental biochemical reactions related to the fixing of dissolved inorganic carbon (DIC; largely CO_2) via photosynthesis or chemosynthesis and the oxidation of oxygen (O_2) in respiration. They also include more complex ecological processes related to suspension feeding—the selective removal of nutritious particles from a virtual soup of material—and sexual reproduction—where sperm and eggs broadcast into a seemingly infinite spatial domain must contact one another to continue the cycle of life. All of these examples involve the physical transport of dissolved and/or particulate matter to and from aquatic organisms. The transport of these scalar quantities, whether it is generated by the organism or through environmental flows, is dictated by the principles of fluid dynamics. There is nothing magical involved, but scientific insights continue to provide intriguing examples of how aquatic organisms have evolved to use fluids.

In the parlance of fluid dynamics, it is the flux of scalar quantities (i.e., $J = UC$, where U is the velocity, and C is the concentration of the scalar) that links physics and biology in aquatic environments. It is relevant to note that it is the product of the vector and the scalar that is important rather than either the velocity or concentration alone. Too often the emphasis in many biological studies, including those of the authors, has focused on comparisons across a range of velocities; the classical experimental approach of holding one variable constant. However, a simple thought experiment will reveal that it is possible to generate the same value for J using different combinations of values for U and C. This observation should not lead the reader to think that it is physics alone that is important, rather it is evident that biology is complex and cannot be understood solely through the examination of physical principles (c.f., Pennycuick, 1992).

The focus of this chapter is mass transport in aquatic environments. From the onset this may appear to be a relatively simple task until the spatial and temporal scale and diversity of processes involved are considered. For example, aquatic organisms span eight orders of magnitude in terms of length ($10^{-7}-10^{1}$ m) and 21 orders of magnitude ($10^{-16}-10^{5}$ kg) in terms of mass (McMahon and Bonner, 1983; Niklas, 1994). It would be inconceivable to think, for example, that the same physical processes apply to a bacterium moving at μm s^{-1} and a whale swimming at many m s^{-1}, however the truth or falsehood of this statement is scale dependent. Moreover, there are at least two scales that need to be considered, namely spatial and temporal (via velocity) scales. The familiar non-dimensional Reynolds number ($Re = lU/\nu$; where l is the length, and ν the molecular diffusivity of momentum), which relates inertial to viscous forces, provides the context by which to make this comparison (e.g., Vogel, 1994; White, 1999). A comparison of processes that occur at Re based on the scale of the whale ($Re >> 10^{3}$) are turbulent in nature whereas those that occur at Re based on the scale of the bacterium ($Re << 1$) are creeping. Similarly, transport in the former is advective, whereas it is diffusive for the latter. There are exchange processes at the whale's surface however, that occur at the "bacterium scale", but the bacterium will never experience processes at the "whale scale" given that its environment is circumscribed within the smallest oceanic eddies (i.e., the Kolmogorov microscale; $\eta \sim$ several mm in the upper mixed layer; see Mann and Lazier, 2006). In other words, at large spatial and velocity scales conditions are turbulent and transport is advective, and simultaneously they are laminar and diffusive when examined at very small spatial and velocity scales within the external flow environment. Dealing with this continuum of scales will appear throughout this chapter, but the majority of the examples chosen are biased toward the 10s of cm and cm s^{-1} scales and smaller. In addition, this chapter is not meant to be an exhaustive review, rather it was written to provide some historical context along with the state of the art developments, which are leading to some new understanding of aquatic environments (see for example, Niklas, 1992; Okubo and Levin, 2002; Mann and Lazier, 2006).

11.2 AQUATIC ENVIRONMENTS

When dealing with any problem or idea, it is first necessary to define the appropriate boundary conditions. This chapter will be restricted to mass transport processes in organisms inhabiting surface waters (e.g., Fischer *et al.*, 1979), and will not deal with groundwater and other interstitial environments (e.g., transport in porous material; de Beer *et al.*, 1994; de Beer and Kühl, 2001). There are a large number of ways in which to classify the structure of surface waters due largely to the availability of light and tidal forcing, which lead to different categorizations between marine and freshwater ecosystems (Fig. 11.1). For example the regions closest to shore are referred to as intertidal zones in marine ecosystems and littoral zones in both marine and freshwater systems. This is quite reasonable in the former given that the tidal influence can be so pronounced in terms of the periodic variation of conditions imparted on the resident organisms (Ingmanson and Wallace, 1995). An analogous approach is used to discriminate among freshwater ecosystems as to whether they are lotic (flowing waters, such as streams and rivers) or lentic (standing waters, such as ponds and lakes) (Kalff, 2001; Wetzel, 2001). From the perspective of this chapter, the real issue is whether the organism is pelagic (living freely within the water column) or benthic (attached to the bottom or a surface). Several important distinctions emerge from this perspective. Pelagic organisms exist in a Lagrangian reference frame as they are transported along with the water and where they may experience relative motions. This concept, which was introduced above, holds that organisms smaller than η (i.e., several mm in the upper mixed layer; e.g., many species of phyto- and zooplankton) live within the shelter of eddies. Conversely,

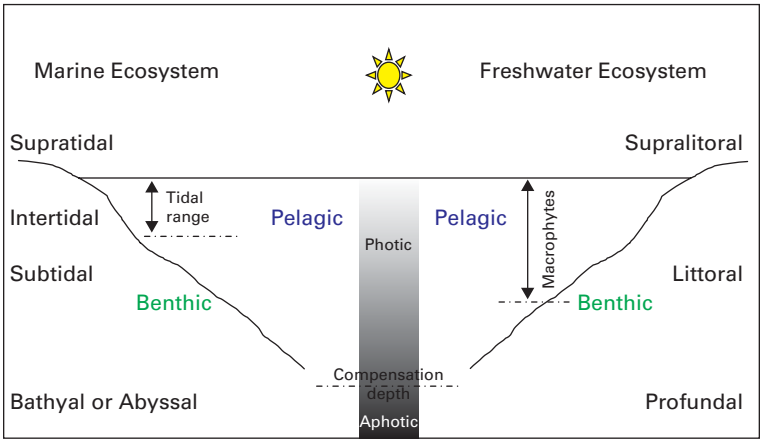

Figure 11.1. The principle classification of aquatic environments and some of the classification used in marine and freshwater ecosystems. Both ecosystems include an open water or pelagic zone (limnetic zone in freshwater) and a bottom oriented or benthic zone. The penetration of light is relevant in both cases, where the compensation depth marks the limit of the photic zone where phytoplankton can survive. In freshwater, the depth limit of rooted macrophytes delimits the bottom of the littoral zone, whereas tidal exchanges provide the various demarcations in marine systems. Note that the depth scales is much compressed in marine ecosystem.

benthic organisms, which are fixed to the bottom, inhabit an Eulerian reference frame and may experience both relative and absolute motions depending on their length. For most benthic organisms this has led to diminutive size in highly energetic environments where the whiplash-like forces of breaking waves can cause tissue damage or detachment (Denny, 1988). There are exceptions however, where long lengths can provide an escape from the breaking waves through the response known as "going with the flow" (see review in Okubo *et al.*, 2002). Recognizing these patterns and distinctions, it is possible to apply the principles of mass transport equally well to organisms living in the benthos of an estuary, a river, a coast, or a lake.

11.2.1 Aquatic ecosystems

It would be relevant to develop further the ecosystem concept, which can be defined as the sum total of the biotic (living) and abiotic (non-living) elements and processes that occur within a particular designation (e.g., Ricklefs and Miller, 2000). In this way we can define a marine ecosystem, an estuarine ecosystem, an eelgrass ecosystem, an epiphytic ecosystem, and so forth to as many scales as one could envision (note that this example was chosen to demonstrate the hierarchy of scales; e.g., Nybakken and Bertness, 2005). The term has merit as a concept in that it is all encompassing within a system-based perspective, which provides for an understanding of the mechanistic basis of the system and allows for the comparison among ecosystems. It is also limiting because of its lack of precision of how to designate the unit, and thus avoid confusion. This is somewhat analogous to the other hierarchical scaling phenomena discussed above.

The systems analogy allows for the definition of the constituent biological components as: (1) producers (autotrophs), which are the organisms that fix chemical energy from sunlight or other sources of electron transfer (e.g., chemosynthesis), such as planktonic algae [photosynthetic protists], macroalgae, seagrasses, aquatic, marsh plants, etc.; (2) consumers

(heterotrophs), which are the organisms that eat the producers such as herbivorous zooplankton, bivalves, snails, fish, turtles, sea urchins, etc.; (3) predators, which are the organisms that eat the consumers, such as large zooplankton, fish, snails, birds, etc.; and (4) detritivores, which are the organisms that utilize waste products such as fungi, bacteria, protists, and annelids. There are of course many exceptions whereby organisms may be omnivorous and feed on more than one trophic level (Ricklefs and Miller, 2000). It is also possible to define the nature of the aquatic ecosystem through its trophic status, which provides a short hand indication of the nutrient status and productivity—either as gross primary productivity (GPP) or net primary productivity (NPP) after the subtraction of the production used for respiration (Ricklefs and Miller, 2000). Productivity in this case refers to the fixation of carbon (usually gC m^{-2} yr^{-1}, i.e., flux) via the photosynthesis of cyanobacteria (blue-green algae), photosynthetic protists (algae) both planktonic (phytoplankton) and macrophytic (macroalgae or seaweeds), and nonvascular (i.e., mosses) and vascular plants (ferns, seagrasses, aquatic angiosperms or aquatic weeds).

Given that productivity is driven by nutrient levels it is not surprising that nutrient status is used to describe the trophic state of the aquatic environment (Kalff, 2001; Wetzel, 2001; Nybakken and Bertness, 2005). These states can represent the natural progression of temporal changes that occur as a newly formed water basin ages through time (note that this can also apply to a coastal embayment). In this scenario, the water body begins with relatively clear water with few nutrients, low productivity and biodiversity (i.e., oligotrophic) and through time as nutrients and sediments accumulate in the basin it progresses through mesotrophic, eutrophic and finally dystrophic where the accumulated organic matter can render the water acidic in freshwater systems (Table 11.1). Not surprisingly, excess nutrient input (principally phosphorus in freshwater and nitrogen in marine) through human activity has resulted in cultural eutrophication. Much of the past 40 years of research and engineering have been devoted to the elimination of these nutrient inputs and many researchers are describing the oligotrophication of previously culturally eutrophic environments.

Table 11.1. Trophic status of aquatic environments, which follow a continuum of sorts from low nutrient levels, productivity and biodiversity to higher levels, which can be disrupted in the extreme case of dystrophic conditions.

	Trophic status			
Condition	Oligotrophic	Mesotrophic	Eutrophic	Dystrophic
Nutrients	Low	Moderate	High	Excess
Productivity	Low	Moderate	High	Low
Biodiversity	Low	Moderate	High	Low

11.3 THEORY DEVELOPMENT

As indicated above, water flowing around organisms (e.g., macrophytes, sediments, corals, and mussel beds) provides a mechanism that supplies and removes scalar quantities (e.g., dissolved gases, nutrients, seston, and gametes). Therefore, the mass transport of these scalars is an essential process for aquatic organisms (Jørgensen and Des Marais, 1990; Falter *et al.*, 2004; Larned *et al.*, 2004; Nishihara and Ackerman, 2006, 2007a). Mass transport is also a complex process involving diffusion (i.e., molecular and turbulent diffusion),

advection, and boundary layer reactions, which are influenced by the properties and flow characteristics of the water, the biological and physical characteristics of the organism, the concentration and diffusional characteristics of the scalar quantity, and the kinetics and mechanism of the boundary layer reactions (Chambré and Acrivos, 1956; Acrivos and Chambré, 1957; Chambré and Young, 1958; Libby and Liu, 1966; Dang, 1983; Nishihara and Ackerman, 2006, 2007a).

11.3.1 Momentum and concentration boundary layers

Water flowing over a surface forms a momentum boundary layer (MBL) that can have laminar, transitional, or turbulent characteristics, depending on spatial and velocity scales that can be determined through the local Reynolds number ($Re = xU/\nu$, where x is the downstream distance). The MBL forms as a result of the tendency of water to adhere to surfaces (i.e., the no-slip condition; $U = 0$), which produce tangential forces (i.e., shear stresses; τ) that are greatest at the water-surface interface (i.e., wall shear stress; Ackerman and Hoover, 2001). The laminar MBL in two-dimensions can be described by solving the continuity equation and the equation of motion and their exact and approximate solutions are well known (Schlichting and Gersten, 2000). More importantly, the solutions provide a measure of the MBL thickness (δ_{MBL}), and in the case where the organisms can be approximated as a flat plate (Fig. 11.2), the δ_{MBL} at a given distance downstream (x) from the leading edge is

$$\delta_{\mathrm{MBL}} \approx \frac{5\,x}{Re_x^{1/2}} \tag{11.1}$$

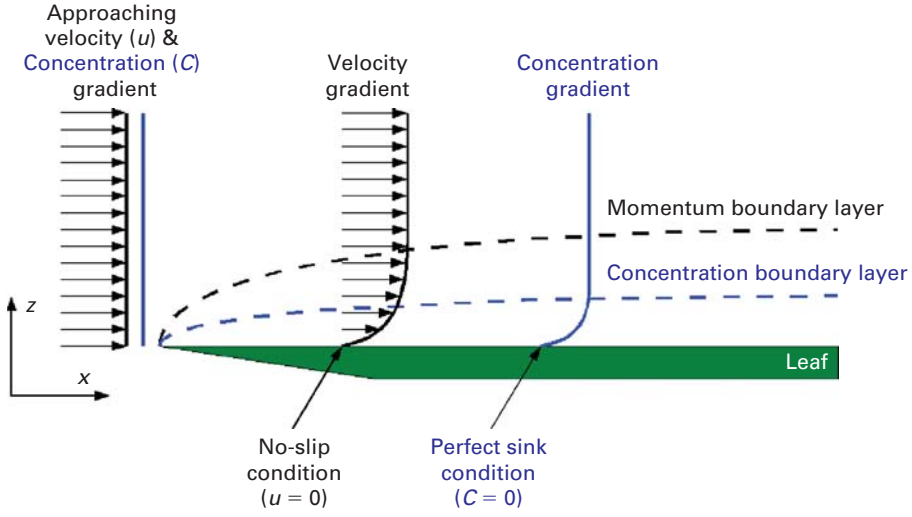

Figure 11.2. The momentum boundary layer and concentration boundary layer over a model leaf. The velocity gradient is a result of the no-slip condition at the water-surface interface and the concentration gradient occurs, given that the leaf surface acts as a sink and consumes all of the scalar arriving to the surface ($C = 0$).

The turbulent MBL has vertical structure with three regions extending from the surface: (i) the viscous sublayer (VSL) where forces are largely viscous in nature; (ii) the logarithmic

layer where inertial forces begin to dominate; and (iii) the outer layer where conditions approach those of the free stream (Nishihara and Ackerman, 2006, 2007b; see Table 11.2). Within the VSL, there is a very thin diffusional sublayer (DSL) where processes are largely diffusive in nature (see below).

Table 11.2. A comparison of momentum and concentration boundary layer definitions and theoretical values of their thickness (δ) over flat plates.

Distribution of momentum	Distribution of scalar
Momentum Boundary Layer (MBL) region from the surface to $0.99U$ Laminar[1] $\delta_{\mathrm{MBL}} = \frac{5x}{Re_x^{1/2}}$ Turbulent $\delta_{\mathrm{MBL}} = \frac{0.16x}{Re_x^{1/7}}$	Concentration Boundary Layer (CBL) region from the surface to $0.99C_{\mathrm{bulk}}$ Laminar $\delta_{\mathrm{CBL}} = \frac{5x}{Re_x^{1/2}Sc^{1/3}}$ Turbulent $\delta_{\mathrm{CBL}} = \frac{0.16x}{Re_x^{1/7}Sc^{1/3}}$
Outer Region (Eckman Layer[2]) region where $\partial u/\partial z \rightarrow 0$ –	Outer Region region where $\partial C/\partial z \rightarrow 0$ $(K_D \approx K_\nu) > D$ –
Inertial Sublayer region where $\partial u/\partial z$ is exponential; ν negligible $\delta_{\mathrm{ISL}} \sim 0.15\delta_{\mathrm{MBL}}$	Exponential Region region where $\partial C/\partial z$ is exponential; D negligible –
Viscous Sublayer (VSL) region where $K_\nu = \nu$ $\delta_{\mathrm{VSL}} = 10\frac{\nu}{u_*}$	– – –
Diffusional Sublayer (DSL) region where D dominates $\delta_{\mathrm{DSL}} = \delta_{\mathrm{VSL}}Sc^{-1/3}$	Diffusional Boundary Layer (DBL) region where $(K_D \approx K_\nu) < D$ depends on the nature of scalar sink/source; $\delta_{\mathrm{DBL}} \leq \delta_{DSL}$

[1] $Re_x = 3 - 5 \times 10^5$ marks the transition to turbulence; [2] where Coriolis effects are relevant.

By analogy, when scalars are consumed or produced at the surface of organisms, concentration boundary layers (CBL) will form. The CBL can be described in two-dimensions as

$$u\frac{\partial C}{\partial x} + w\frac{\partial C}{\partial z} = \frac{\partial}{\partial z}\left[(D + K_D)\frac{\partial C}{\partial z}\right] + R \tag{11.2}$$

where u and w are the velocities in the x and z (vertical) directions, D is the molecular diffusivity of the scalar, K_D is the turbulent analogue to D, and R is a homogeneous reaction that occurs within the CBL (Fig. 11.3; Nishihara and Ackerman, 2006, 2007a). Consider the simplest cases where the boundary conditions at the water-surface interface is constant (i.e., where the surface concentration or flux is invariant), there are no homogeneous reactions, and the turbulent diffusivity of the scalar (K_D) is much smaller than D and can be neglected (Hanratty, 1956; Shaw and Hanratty, 1977; Na and Hanratty, 2000). In this case, Eqn. (11.2)

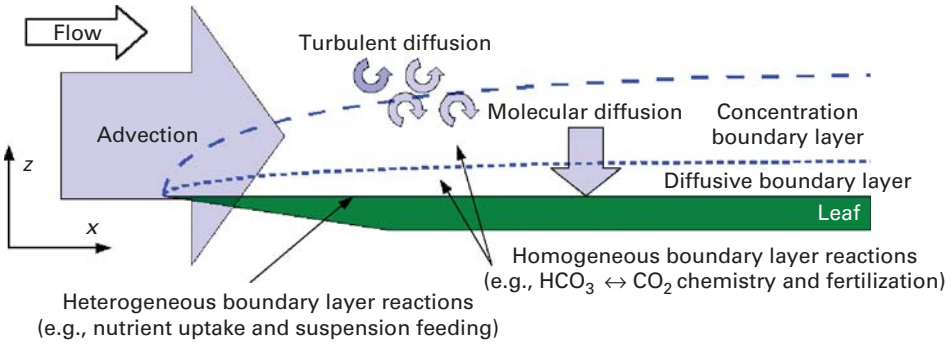

Figure 11.3. A schematic of the process occurring in the concentration boundary layer (CBL) important to mass transport in aquatic systems. Mass transfer is a function of advection, turbulent and molecular diffusion, as well as heterogeneous and homogeneous boundary layer reactions that occur at the surface and in the CBL.

can be solved using the similarity principle (Schlichting and Gersten, 2000) and the thickness of the CBL (δ_{CBL}) is given by

$$\delta_{CBL} \approx \frac{5\,x}{Re_x^{1/2} Sc^{1/3}} \tag{11.3}$$

where Sc is the Schmidt number defined as the ratio of the ν to D. Note that δ_{CBL} is thinner than the δ_{MBL} by a factor of $Sc^{1/3}$ (i.e., compare Eqn. (11.1) and (11.3); see Table 11.2).

The CBLs in aquatic systems may have a structure similar to that of a MBL (Fig. 11.3; Levich, 1962; Nishihara and Ackerman, 2006; see Table 11.2). Adjacent to the surface there is a thin region of fluid, the diffusive boundary layer (DBL), where the $K_D < D$ and molecular diffusion is the dominant form of mass transport. The thickness of this region, which is incorrectly equated to the DSL of the MBL, extends to a height where $K_D = D$. It is relevant to note that advective transport parallel to the surface is also present in this region; therefore, diffusion is the primary mode of mass transport only in the fluid nearest to the surface where the no-slip condition is valid. Above the DSL, K_D begins to dominate D (Levich, 1962; Shaw and Hanratty, 1977; Bird *et al.*, 2002) and further from the surface, in the outer region, $K_D >> D$, and the concentration gradient is small (Bird *et al.*, 2002; Nishihara and Ackerman, 2006).

11.3.2 Surface and CBL Reactions

Unfortunately, the boundary conditions at the water-surface interface of biological systems can be complex (Nishihara and Ackerman, 2006, 2007a, b), which invalidates the assumptions of constant concentration or flux used to derive Eqn. (11.3). This is due to the variety of boundary layer reactions (i.e., heterogeneous and homogeneous boundary layer reactions) that can occur as a result of physiological activity, such as photosynthesis, nutrient uptake, and bicarbonate-carbonate chemistry (Table 11.3; Tortell *et al.*, 1997; Wolf-Gladrow and Riebesell, 1997; Martin and Tortell, 2006; Nishihara and Ackerman, 2007a). Heterogeneous reactions, occurring at the water-surface interface, serve to control the flux of material in and out of the CBL (Fig. 11.3). The kinetics can be linear or nonlinear and can vary with the concentration of the reactant and the location of the reaction (Jørgensen and Revsbech, 1985; Ploug *et al.*, 1999; Nielsen *et al.*, 2006; Nishihara and Ackerman, 2007a). Homogeneous

Table 11.3. Examples of heterogeneous and homogeneous boundary layer reactions that may influence the boundary conditions of the mass transport equations.

Biological processes	Type of reaction	Reference
Nutrient uptake in oligotrophic water	Constant concentration, heterogeneous	Thomas *et al.,* 1985, 1987, 2000; Sanford and Crawford, 2000; Phillips and Hurd, 2003; Larned *et al.*, 2004
Nutrient uptake in eutrophic water	Constant flux, heterogeneous	Sanford and Crawford, 2000
Ammonium uptake in *Laurencia brongniartii*	Linear flux, heterogeneous	Nishihara *et al.,* 2005
Photosynthesis in *Vallisneria americana*	Nonlinear flux, heterogeneous	Nishihara and Ackerman, 2006, 2007b
Suspension feeding activity of mussels	Nonlinear, heterogeneous	Ackerman, 1999; Ackerman *et al.*, 2001; Ackerman and Nishizaki, 2004; Tweddle *et al.*, 2005
Pollen and spore dispersal	Nonlinear, heterogeneous	Ackerman, 2000, 2006; Okubo and Levin, 2002
Fertilization by broadcast spawning	Linear/Nonlinear, homogeneous	Okubo *et al.*, 2002; Okubo and Levin, 2002
Bicarbonate–carbon dioxide chemistry above photosynthesizing organisms	Linear, homogeneous	Wolf-Gladrow and Riebesell, 1997; Tortell *et al.*, 1997; Nishihara and Ackerman, 2006, 2007a, b

reactions, which occur in the CBL, will also influence the concentration gradient in the CBL and violate the assumptions made to derive Eqn. (11.2) (Fig. 11.3). When reactions occur in the CBL, they serve to decrease and increase δ_{CBL} as the reaction consumes and produces the scalar, respectively (Bird *et al.*, 2002). Therefore, Eqn. (11.2) developed through the assumptions of constant concentration or flux does not apply when the heterogeneous reactions vary or when there are homogeneous reactions occurring in the CBL.

The deviations from Eqn. (11.3) have been examined in detail from a chemical engineering perspective (Chambré and Acrivos, 1956; Acrivos and Chambré, 1957; Chambré and Young, 1958; Freeman and Simpkins, 1965; Chung, 1969). Along a flat-plate undergoing a heterogeneous linear reaction where a scalar quantity is consumed, the δ_{CBL} is influenced by the magnitude of the reaction and its proximity to the leading edge. Near the leading edge, if mass transfer rates are greater than the reaction rate, mass transport is kinetically limited (Chambré and Acrivos, 1956; Acrivos and Chambré, 1957). Therefore, the concentration at the surface ($C_{surface}$) is approximately that of the bulk concentration (C_{bulk}). Much further downstream from the leading edge where the CBL is thick, mass transfer can be slower than the reaction rate (i.e., mass transfer limitation), and the concentration at the surface is significantly lower than the bulk concentration (Chambré and Acrivos, 1956; Acrivos and Chambré, 1957). Therefore, the ratio of the CBL to the MBL may vary (Eqn. (11.3)) with regards to space, the reaction rate, and the reaction mechanism. For example,

consider the case where mass transfer does not limit nutrient uptake (J) and J is not a function of the surface concentration. In this case, the surface concentration will decrease on the order of $x^{0.5}$ within a laminar CBL (Fig. 11.4). However, it has been suggested (Chambré and Acrivos, 1956; Acrivos and Chambré, 1957) that if a heterogeneous boundary layer reaction is a first-order (i.e., linear) process, a similar monotonic decrease in surface concentration will be observed, although the initial decrease of the scalar quantity will be of a smaller magnitude than for a constant reaction rate (Fig. 11.4). Moreover, it appears that for more complex reaction mechanisms (i.e., Michaelis-Menten-like reactions; Nishihara and Ackerman in review), there will be little change in surface concentrations near the leading edge, however a large decrease will be observed further downstream (Fig. 11.4) after which, the surface concentrations are predicted to asymptote to some finite value.

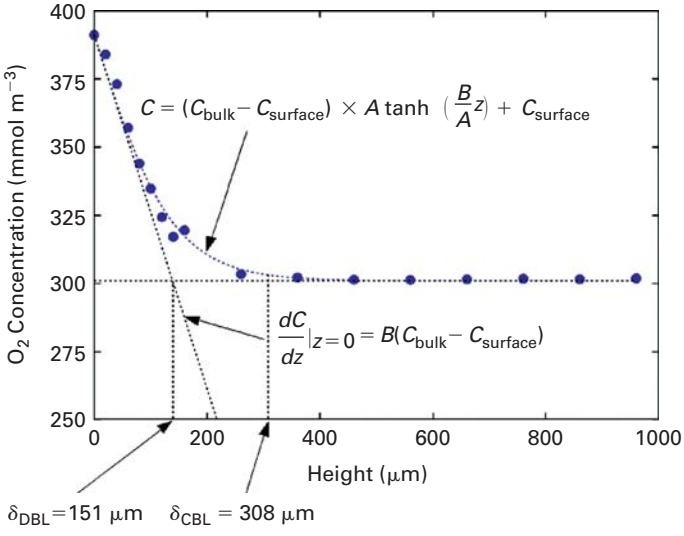

Figure 11.4. The measured and modeled oxygen gradient over a photosynthesizing leaf of the freshwater macrophyte, *Vallisneria americana* (modified after Nishihara and Ackerman, 2007b). The concentration boundary layer thickness (δ_{CBL}) and the diffusive boundary layer thickness (δ_{DBL}) are also given.

For homogeneous reactions that consume scalars, the CBL is thinner than predicted by Eqn. (11.3) (Bird *et al.*, 2002), and it will decreases monotonically in thickness with increasing distance from the leading edge (Chambré and Young, 1958). However, if the homogeneous reaction serves to produce a scalar quantity, the shape of the CBL and the concentration gradient is not as simple. Specifically, the shapes of the gradient and CBL will be similar to that of a non-homogeneous reactions near the leading edge, however further downstream, the scalar begins to accumulate in the CBL drastically altering the shape of the gradient and the characteristics of the CBL (Chambré and Young, 1958).

The combined effects of heterogeneous and homogeneous boundary layer reactions on mass transfer are not well known, however along the axial length of a pipe homogeneous reactions were suggested to have a greater influence on the consumption of scalar quantities (Dang, 1983). Biological systems involve reactions as complex as their chemical engineering analogues. Given that heterogeneous boundary layer reactions common to biology cannot always be described by simple linear or power-law functions (e.g., Michaelis-Menten kinetics), analytical solutions to determine characteristics of the CBL (e.g., Dang, 1983)

are difficult to derive. Consequently, the δ_{CBL} and concentration gradients must be determined experimentally, to ensure that the fluxes and mass transfer rates derived from the concentration gradient are not based on violations of the assumptions made in Eqn. (11.3).

11.3.3 Concentration boundary layer measurements

It is relatively simple to determine the concentration gradient over the surface provided the scalar quantity can be measured easily. Unfortunately there are few scalars for which this can be achieved. The widespread use of oxygen microsensors (Glud *et al.*, 1999; Ploug *et al.*, 1999; Hondzo *et al.*, 2005; Nishihara and Ackerman, 2006, 2007a, b) has facilitated the measurement of O_2 CBLs over respiring and photosynthesizing surfaces. By appropriately positioning the microsensor, the concentration gradient over the surface can be recorded and analyzed to provide the δ_{CBL}, the thickness of the diffusive boundary layer (δ_{DBL}, where the DBL is a layer of fluid adjacent to the surface, where diffusion is the primary form of mass transfer), and the oxygen flux at the water-surface interface. It is important to make the distinction between the concept of the DSL and the DBL (Table 11.2). Whereas the DSL is a sublayer of the VSL and the ratio of the DSL to VSL is $\sim Sc^{-1/3}$ (Levich, 1962; Bird *et al.*, 2002), the DBL is a region within the CBL and will not necessarily scale with the VSL thickness uniformly over the surface of a flat plate (i.e., an organism) (Nishihara and Ackerman, 2007b, in review).

Typically, only the flux and the δ_{DBL} could be determined from the oxygen gradient due to the limited spatial resolution. Flux was evaluated by determining the slope of a line fit to the data points closest to the surface, in the region before the points became nonlinearly distributed, and multiplying the slope by the molecular diffusivity (D) for oxygen (Jørgensen and Des Marais, 1990; Ploug *et al.*, 1999; Køhler-Rink and Kühl, 2000). The δ_{DBL} was then estimated by extrapolating the line out so that it would intercept a line drawn through the data point in the bulk water (Fig. 11.4). The location of the intercept of these two lines was used to provide an estimate of the δ_{DBL}. This approach is limited because it ignores the nonlinearity observed in many of the datasets involving oxygen concentration gradients, and it is subject to errors in estimate due to the small number of data points used to determine the slope (Nishihara and Ackerman, 2007b). The solution to this problem is to select an appropriate function that can be used to model the concentration gradient determined with a microsensor.

Whereas there are a number of exponential and transcendental functions available, the hyperbolic tangent function provides an excellent solution to the problem of determining CBL properties from scalar gradients (Nishihara and Ackerman, 2006, 2007b). This function has the property that (i) far from the surface, the curve is asymptotic (i.e., models the bulk concentration) and (ii) adjacent to the surface, the first derivative of the curve is nonzero (i.e., can approximate the slope at the water-surface interface). Moreover, by making the concentration gradient dimensionless (θ) the hyperbolic tangent can be easily fit to the data regardless of whether the surface is a sink or source, by normalizing the concentration gradient [$C(z)$] to values from 0 to 1 (Fig. 11.4)

$$\theta(z) = \frac{C - C_{surface}}{C_{bulk} - C_{surface}} \tag{11.4}$$

A two-parameter hyperbolic tangent function can also be fit using nonlinear regression to the dimensionless concentration gradient (θ)

$$\theta(z) = A\tanh\left(\frac{B}{A}z\right) \tag{11.5}$$

where parameter A and B are constants. At the water-surface interface, the no-slip condition is valid and there is no advective component to mass transfer. Therefore, Fick's law

$$J_{(z=0)} = -D\frac{\partial C}{\partial z} \tag{11.6}$$

can be used to determine the flux through the interface by combining Eqn. (11.4) and (11.5)

$$\frac{C - C_{\text{surface}}}{C_{\text{bulk}} - C_{\text{surface}}} = A\tanh\left(\frac{B}{A}z\right) \tag{11.7}$$

solving for C

$$C = A\tanh\left(\frac{B}{A}z\right)(C_{\text{bulk}} - C_{\text{surface}}) + C_{\text{surface}} \tag{11.8}$$

and evaluating the derivative of C with respect to z

$$\frac{\partial C}{\partial z} = A\tanh\left(\frac{B}{A}z\right)(C_{\text{bulk}} - C_{\text{surface}}) + C_{\text{surface}} \tag{11.9}$$

Evaluating Eqn. (11.9) at $z = 0$ leads to

$$\frac{\partial C}{\partial z} = B(C_{\text{bulk}} - C_{\text{surface}}) \tag{11.10}$$

By substituting Eqn. (11.10) into Eqn. (11.6), the flux at the water-surface interface is

$$J_{(z=0)} = -DB\,(C_{\text{bulk}} - C_{\text{surface}}) \tag{11.11}$$

The δ_{DBL} can also be determined, by evaluating where the line with the slope determined in Eqn. (11.10) intercepts a point with a concentration of C_{bulk}. Therefore the δ_{DBL} is

$$\delta_{\text{DBL}} = \frac{C_{\text{bulk}}}{B(C_{\text{bulk}} - C_{\text{surface}})} \tag{11.12}$$

The δ_{CBL} can also be determined, following the definition for the laminar MBL, by solving for z in Eqn. (11.7), when the concentration is 99 % of the bulk (i.e., when $\theta = 0.99$). Therefore, the δ_{CBL} is

$$\delta_{\text{CBL}} = \frac{A}{B}\tanh^{-1}\left(\frac{0.99}{A}\right) \tag{11.13}$$

The mass transfer coefficient (k_c) can also be determined from Eqn. (11.11)

$$J = k_c(C_{\text{bulk}} - C_{\text{surface}}) \tag{11.14}$$

where k_c is the product of the D and parameter B.

Through k_c, a characteristic local Sherwood number, which is the ratio of the advective to diffusive flux ($Sh_x = k_c x D^{-1}$), can then be determined. In laminar flat plate boundary layer theory, Sh_x can be described by

$$Sh_x = aRe_x^b Sc^{0.33} \tag{11.15}$$

and for ideal boundary conditions, parameter a has a value of 0.339 and 0.464 for constant surface concentration and constant flux, respectively and parameter b is equal to 0.50 (Schlichting and Gersten, 2000; Bird *et al.*, 2002). For turbulent boundary layers, a has a value of 0.030 and 0.028 for constant concentration and flux, respectively and parameter b is equal to 0.80 (Schlichting and Gersten, 2000; Bird *et al.*, 2002).

Note that for laminar CBLs with the aforementioned values of a and b, Eqn. (11.15) is the dimensionless solution to the concentration boundary layer equation (Eqn. (11.2)), when $R = 0$. The parameters a and b will deviate according to the boundary conditions involved and the hydrodynamics of the system.

11.4 SETTING THE BOUNDARY CONDITIONS

As indicated above, the boundary conditions for aquatic organisms are complicated by the diverse variety of scalar quantities of interest and, most importantly, the physiological and chemical processes that create the source or sink necessary for CBL formation (Table 11.3). This is in contrast to the boundary conditions used to model purely abiotic phenomena such as water velocity or energy through the dissolution of gypsum etc. (e.g., Porter *et al.*, 2000).

Regardless, whereas it is possible to classify boundary layer reactions into two groups (heterogeneous and homogeneous boundary layer reactions) it is also possible to classify the transported material as particulate (or suspended; e.g., gametes, plankton, bacteria) and as dissolved (or in solution; e.g., gases such as oxygen and carbon dioxide and nutrients such as phosphate, nitrate and ammonium).

Heterogeneous reactions are those processes such as nutrient uptake, photosynthesis, and respiration that directly influence the flux of material through the water-surface interface (Nishihara and Ackerman, 2007a). The flux at the water-surface interface is defined by the physiological processes, which creates the sink or source. In the simplest case, the heterogeneous reaction proceeds so that the surface concentration or flux is constant and does not vary with increases in the supply or removal of the scalar (Levich, 1962). For example, marine algae in nutrient-poor water (i.e., oligotrophic conditions) suffering from nutrient limitation, will consume all the nutrients that arrive at its surface. Consequently, the concentration of nutrients at the water-surface interface would be zero (i.e., the perfect-sink condition; Vogel, 1994) and the uptake rate would be directly proportional to the flux of nutrients towards the surface. In contrast, under nutrient-rich conditions (i.e., eutrophic conditions) and where the nutrients are in excess of the alga's requirements, the uptake rate would saturate at some maximum and is invariant. The flux of nutrients at the surface would not depend on the external mass transport processes and the surface concentrations may increase if the flux through the water-surface interface is lower than the flux due to mass transport, in the case of where the surface acts as a source.

As a result of heterogeneous reactions, the flux at the water-surface interface will deviate from the constant concentration and flux boundary conditions and variations are likely to occur due to the physiological characteristics of the organism. For example, the kinetics of nutrient uptake by aquatic macrophytes can vary with the nutrient (Thomas *et al.*, 1985; Thomas *et al.*, 1987; Nishihara *et al.*, 2005) as well as the spatial location on the leaf (Nishihara and Ackerman, 2007a). Moreover, uptake kinetics and the flux can be linear or

nonlinear. If the nutrient can diffuse freely into the organism, the flux at the water-surface interface will be directly proportional to that of the surface (i.e., mass transfer limited). Typically however, the concentrations of nutritionally important ions (e.g., DIC, DIN) are higher in the organism than in the water (Lobban and Harrison, 1996), and thus an active uptake mechanism is required. Such active mechanisms can saturate under high nutrient concentrations (e.g., Michaelis-Menten kinetics) and hence the flux is a nonlinear function of the concentration.

Homogeneous reactions occurring in the concentration boundary layer may also alter the local concentration of material within the CBL. In the ideal case, $R = 0$ and there are no reactions present. In the natural environment however, homogeneous boundary layer reactions are likely to be relatively more common than the ideal condition. For example, the conversion of bicarbonate to CO_2 may increase the availability of CO_2 to photosynthetic organisms such as coral symbionts, algae and plants (Tortell *et al.*, 1997; Wolf-Gladrow and Riebesell, 1997; Riebesell *et al.*, 2000; Nishihara and Ackerman, 2007a). Similarly, spawning over the bed of mussels will consume eggs and sperm and produce fertilized eggs in the CBL. Ultimately these homogeneous processes affect the concentration of the material in question and clearly deviate from the ideal processes modeled by Eqn. (11.3) and Eqn. (11.14).

11.4.1 Boundary conditions for nutrient uptake

The diversity of boundary conditions discussed above is present in benthic systems, whether they are sediments, biofilms, mussel beds, or the surfaces of photosynthetic organisms. Research suggests that there is significant spatial heterogeneity in the O_2 concentrations at the water-surface interface in sediment (Jørgensen and Revsbech, 1985; Glud *et al.*, 1994; Lorke *et al.*, 2003) and biofilm systems (Nielsen *et al.*, 1990; Kuehl *et al.*, 1996). For example, the O_2 consumption in sediments were found to saturate with increasing water velocities (Jørgensen and Revsbech, 1985), indicating that the uptake mechanism is a nonlinear process. Although, there is little evidence on whether O_2 flux and nutrient flux is a linear or nonlinear process, it is more than likely that the flux is a nonlinear function. Given that the biomass in any given organism is limited, there will be some finite capacity to consume oxygen or nutrients. Therefore, for large mass transfer rates, the kinetics of the system will saturate and supply will outweigh demand. The situation is also similar in autotrophic systems, where phytoplankton, algal mats and macrophytes (e.g., macroalgae and aquatic angiosperm) consume nutrients and produce oxygen. As with sediments and biofilms, there is marked heterogeneity of flux with respect to spatial location (Nielsen *et al.*, 2006; Nishihara and Ackerman, 2007a). For example in colonies of *Phaeocystis*, oxygen flux varied along its axis (Ploug *et al.*, 1999) as was the case for algal mats, where oxygen flux was spatially heterogeneous (Glud *et al.*, 1999). Variation in oxygen flux was also evident in the leaves of the aquatic angiosperms, *Vallisneria americana*, where the flux was higher near the leading edge of the leaf than the trailing edge (Nishihara and Ackerman, 2007a). It is relevant to note that the uptake kinetics of macrophyte systems is better understood than those in multispecies arrangements (i.e., ecosystems) in sediments, biofilms, and marine aggregates (marine snow).

It is evident that uptake kinetics range from linear to nonlinear and the nonlinear behavior can be modeled as a rectangular hyperbola (i.e., Michaelis-Menten kinetics) or a more complex function as in the case of the biphasic uptake of nitrate in the diatom *Skeletonema costatum* (Serra *et al.*, 1978). The nonlinearity of the uptake kinetics can lead to spatial heterogeneity in the flux and influence the observed kinetics of the physiological process. This was the case in *Vallisneria spiralis* where the flux of oxygen saturated at both leading and trailing edges when mass transfer rates were high (i.e., high nutrient concentrations),

but oxygen flux did not saturate at the trailing edge when mass transfer rates were low (i.e., low nutrient concentrations) (Nishihara and Ackerman, 2007a). Spatial heterogeneity in nutrient uptake was also observed in *Elodea canadensis*, where nutrients accumulation was highest at the edges of the leaves where mass transfer rates would be greatest (Nielsen *et al.*, 2006). It is likely that the flux through the water-surface interface is inherently nonlinear in nature with respect to concentration and space.

11.4.2 Boundary conditions for external fertilization

Reproduction involves complex boundary layer conditions with respect to the transport of gametes in and out of the momentum boundary layer, given the diversity of broadcast spawning observed in animal and macrophyte systems (see review in Okubo *et al*., 2002). For example, the wide variety of reproductive processes seen in macroalgae limits the possibility of developing a more general theory on how mass transport processes influence reproduction. In particular, sexual reproduction in most brown algae (e.g., kelps) involves the release of male and female gametes into the water column where fertilization occurs (Lobban and Harrison, 1996). This is case of a homogeneous reaction where gametes are consumed and fertilized zygotes are produced, which would also apply to broadcast spawning invertebrates. Moreover, attractants (e.g., pheromones) are released to encourage fertilization, which would in practice enhance the production of zygotes (Lobban and Harrison, 1996). In contrast, sexual reproduction involves a heterogeneous boundary condition in the brown algal order Fucales and in red algae where the male gamete (i.e., spermatia in reds) must be transported to the female gametes that remain on the surface of the macrophyte. This is also the case in the submarine pollination of aquatic angiosperms including seagrasses (Ackerman, 2000, 2006). Similar comparisons and contrasts are also possible for the large diversity of marine and freshwater benthic animals.

11.5 SEDIMENT SYSTEMS AND BIOFILMS

Sediments and biofilms can play an important role in the exchange of dissolved organic and inorganic compounds and gases (Jørgensen and Revsbech, 1985; Glud *et al.*, 1994; Lorke *et al.*, 2003). Fortunately, microsensors have been used for some time to measure the concentration gradient and hence determine the CBL and fluxes in these systems (Jørgensen and Revsbech, 1985; Gundersen and Jørgensen, 1990; Glud *et al.*, 1994; Lorke *et al.*, 2003). There appears to be considerable the spatial heterogeneity in O_2 (Jørgensen and Revsbech, 1985; Røy *et al.*, 2002), and a recent analysis of these data revealed the nonlinear nature of the CBL of O_2 (Nishihara and Ackerman, 2007b). These studies have relied on a linear estimate of the diffusive boundary thickness (δ_{DBL}) and the assumption that advection does not occur within the DBL. In addition, the CBL thickness (δ_{CBL}) was generally not determined given that there were no objective methods to do so prior to Hondzo *et al*. (2005). As indicated above, the DBL was typically determined graphically by assuming that the oxygen gradient adjacent to the surface was linear (Jørgensen and Revsbech, 1985) and the flux through the water-surface interface was determined from the slope of the oxygen gradient. This method make two assumptions: (i) that mass transfer occurs only through diffusion in the diffusional boundary layer (DBL); and (ii) that the flux can be modeled as a one-dimensional problem (Jørgensen and Revsbech, 1985; see review in Nishihara and Ackerman, 2007b). However, it is well known that horizontal advection (e.g., mass transfer parallel to the surface and turbulent diffusion) also influences the concentration gradient near the surface (Shaw and Hanratty, 1977; Dade, 1993; Hondzo *et al.*, 2005). A power-law scaling of the concentration gradient and information on the momentum boundary layer

(MBL) over the sediment revealed estimates of the δ_{DBL} that were 30% thinner than that of the linear model (Hondzo *et al.*, 2005). Moreover, a model of the CBL could be expressed in terms of the *Sc,* the turbulent *Sc*, and the MBL through the use of similarity arguments for the concentration gradient (Hondzo *et al.*, 2005). This model incorporates the fact that advective mass transport processes can be important in the CBL and discounts the notion that the DBL is a stagnant layer of water.

11.6 AUTOTROPHIC SYSTEMS

11.6.1 Pelagic producers

There has been considerable interest in the large-scale mass transport of nutrients to phytoplankton as these organisms drive pelagic ecosystems, especially in the seasonal blooms when mixing of the water column bring nutrient-rich waters to the upper water column, and in upwelling events/regions when other physical processes do the same (Ingmanson and Wallace, 1995; Kalff, 2001; Mann and Lazier, 2006). Similar interest has existed on the scale of individual cells and aggregates in an attempt to understand the mechanistic basis of blooms and hence determine parameters that can be used for modeling (e.g., Kiørboe, 2001; Kiørboe *et al*., 2001).

Presently, the influence of mass transport on the photosynthetic rates of phytoplankton are not well understood. However, from studies of the fluid dynamics of mass transport of sinking marine snow (Kiørboe *et al.*, 2001; Ploug *et al.*, 2002; see below), it is possible to infer that the local photosynthesis rate will vary spatially over the surface of the phytoplankton and produce oxygen-rich microenvironments. Regions of low CO_2 concentrations can also develop, which would influence mass transfer rates and hence, photosynthesis. For example, diatoms, which experience a Langrangian reference frame, have $Re < 10$ and are likely to produce relative thick and heterogeneous CBLs (Ploug *et al.*, 2002). Moreover, the depletion of CO_2 within the CBL will decrease the availability of substrate for photosynthesis (Tortell *et al.,* 1997; Wolf-Gladrow and Riebesell, 1997; Nishihara and Ackerman, 2006, 2007a). The mass transport processes dominating these microscopic organisms are believed to be primarily from diffusion (Wolf-Gladrow and Riebesell, 1997; Ploug *et al.*, 2002). However, diatoms are able to enhance CO_2 supply by changing the CO_2 concentration through the acidification of their surrounding water thereby altering the balance of bicarbonate and CO_2 (Tortell *et al.,* 1997; Wolf-Gladrow and Riebesell, 1997). Moreover, the biosilica (Milligan and Morel, 2002) in the cell wall of diatoms also have the ability to buffer seawater, allowing them to convert bicarbonate enzymatically to CO_2 enhancing the availability of CO_2. The magnitude of the enhancement in the supply of CO_2 through these boundary layer reactions relative to advection and diffusion are not clear. However, a numerical model of the diffusion-reaction equation (i.e., neglecting advection) suggests that 5% of the CO_2 supply is from reactions occurring in the CBL (Wolf-Gladrow and Riebesell, 1997). Given the morphological and physiological diversity of diatoms, further studies are needed to explore the relationships between their biology and physical environment, through investigations of their mass transport and fluid dynamic characteristics.

11.6.2 Benthic macrophytes

The effect of mass transport processes on aquatic macrophytes has long been recognized (e.g., Conover, 1968) and remains a topic of increased activity (see reviews in Hurd, 2000; Okubo *et al.,* 2002). For example, mass transfer has been shown to affect the rates of photosynthesis (e.g., Sand-Jensen *et al.*, 1985; Nishihara and Ackerman, 2006, 2007a, b),

nutrient uptake (e.g., Borchardt *et al.*, 1994; Cornelisen and Thomas, 2004), and the timing of spore release (Serrão *et al.*, 1996; see review in Gaylord *et al.*, 2004). Macrophytes have three-dimensional structure at a larger spatial scale than sediments and biofilms (c.f., Larned *et al.*, 2004), and the momentum boundary layers that form around these organisms can be complex (Hurd *et al.*, 1997; Hurd and Stevens, 1997; Stevens and Hurd, 1997). It is not surprising that most studies have simplified this complexity by configuring the macrophytes as flat plates (Wheeler, 1980; Koch, 1993; Hurd *et al.*, 1996; Nishihara and Ackerman, 2006, 2007a, b), although there has been some efforts devoted to parameterizations and the Stanton number (*St*) analogy, where the *St* is the ratio of the flux to a surface divided by the advection past the surface (e.g., Thomas *et al.,* 2000). Moreover, a conceptual model has been advanced to explain the relative importance of mass transport under the influence of different scales of the DBL (i.e., individual DBLs and substratum DBLs) (Larned *et al*., 2004). Regardless, significant details of the CBL and the mass transport properties of these organisms have been elucidated.

Most studies related to mass transport in macrophyte systems have focused their discussion using the Schmidt number scaling of the viscous sublayer thickness (δ_{VSL}) to determine the thickness of the diffusive sublayer (δ_{DSL})

$$\delta_{DSL} \approx \delta_{VSL} Sc^{-1/3} \tag{11.16}$$

which is referred to, incorrectly, as the thickness of the diffusive boundary layer (δ_{DBL}) (Larned *et al.,* 2004). Recall that the DBL is a component of the CBL and consequently

$$\delta_{DBL} \neq \delta_{DSL} \tag{11.17}$$

Moreover, when the DBL and mass flux at the water-surface interface was determined, it was by assuming a linear one-dimensional model of the concentration gradient near the surface (see above). Based on the one-dimensional model and a further simplifying assumption that the surface concentration of the nutrient was zero at the water-surface interface (i.e., a perfect-sink condition; Vogel, 1994), the δ_{DBL} of nutrients such as dissolved inorganic nitrogen (DIN) (Hurd *et al.*, 1996) and dissolved inorganic carbon (DIC) have been estimated (Wheeler, 1980). However, the concept that higher water velocities, and thus thinner δ_{DSL} and by analogy thinner δ_{DBL}, are alone responsible for increased rates of uptake or photosynthesis is false and has wasted much effort in the field. As mentioned above, it is the flux (i.e., product of the velocity and concentration) of nutrients that affects the rates of physiological processes. This was demonstrated in the case of oxygen flux in *V. americana*, which has flat ribbon-like leaves, where the effect of higher velocities (and thinner δ_{DBL}) on photosynthetic rates was observed at low nutrient concentrations and declined linearly with nutrient concentration (Nishihara and Ackerman, 2006; see below). This realization is likely one of the reasons that mass-transfer limitation has yet to be demonstrated under field conditions.

As indicated above, there has been limited success in matching predictions from linear models of the concentration gradient made using flat-plate analogies with simple boundary conditions (i.e., constant concentration and flux) and experimental results (see discussions in Hondzo *et al.*, 2005; Nishihara and Ackerman, 2006, 2007b). Several non nonlinear approximations have been used to better describe the concentration gradient measured by O_2 microsensors, and of these, the hyperbolic tangent function provides the ability to estimate both the δ_{CBL} and the δ_{DBL} of the scalar. In addition, the first derivative of the model provided estimates of the O_2 flux, which were more accurate than the typically used linear model (Nishihara and Ackerman, 2007b). The development of these techniques should provided objective methods that can be used for macrophytes as well as other organisms.

Both hydrodynamics and the concentration of DIC influenced the rates of photosynthesis in *Vallisneria americana* (Nishihara and Ackerman, 2006, 2007a, b). Increasing the DIC concentration effectively increased the mass transport of DIC to the leaf surface and decreased the saturation velocity (i.e., the velocity required to saturate photosynthesis rates). Moreover photosynthetic rates were observed to be in a state of mass transfer limitation at very low velocities even though the mass transfer of DIC through the DBL (assuming that the surface was a perfect sink) was much greater than the observed carbon uptake rates in the DBL (Nishihara and Ackerman in review). This indicates that other processes (e.g., homogeneous reactions) are likely limiting the supply of carbon.

There were also physiological differences observed between closely related species in terms of the effects of mass transfer on photosynthesis. For example, photosynthesis rates in *V. spiralis* and *V. americana* saturated at leading and trailing regions of the leaf at high DIC concentrations, however the kinetics of photosynthesis was significantly different at lower DIC concentrations (Nishihara and Ackerman, 2007a)—O_2 fluxes were much lower at the trailing edge and did not saturate with increased water velocities. There are a number of possible explanations for the differences observed at different leaf locations: (i) the physiology may differ along the leaf surface; (ii) nutrient concentrations may decline along the leaf surface; or (iii) there may be differences in the homogeneous reactions (e.g., the bicarbonate-carbon dioxide chemistry) over the leaf surface. Both of these species are known to acidify water adjacent to the surfaces, which encourages the production of CO_2 from the bicarbonate in the water (Prins *et al.*, 1980). Physiological differences may influence the rates of these homogeneous reactions and therefore affect the concentration of CO_2 that is available. It is also likely that upstream processes remove the CO_2 from the CBL and thus reduce the CO_2 availability downstream (Nishihara and Ackerman, 2007a, in review). In addition, both the δ_{CBL} and δ_{DBL} are much thinner than predictions based on Eqn. (11.3) (Nishihara and Ackerman, 2007a) and given that homogeneous reactions have non-linear responses that tend to change the thicknesses of the boundary layer, the situation is even more complicated. Evidently, more effort will be required to identify the mechanism(s) responsible for the decrease in photosynthetic rates observed downstream on the leaf surface.

The morphology of macrophytes can be quite complicated involving much branching, highly dissected leaf and frond morphologies, and surface roughness and rugosity (e.g., Sculthorpe, 1967; Lobban and Harrison, 1996). In other words, macrophytes are not simple two-dimensional organisms that can modeled as flat plates, with some obvious exception (e.g., *V. americana*). A functional explanation for this diversity is lacking, however the potential effects of some of these morphologies on the local hydrodynamic environment has long been the subject of inquiry, especially in species that have low and high energy phenotypes (i.e., smooth versus rugose and corrugated surfaces) (Wheeler, 1980; see reviews in Hurd, 2000 and Okubo *et al.*, 2002). For example, it has been long suggested that the features such as spines and corrugations along *Macrocystis* sp. (giant kelp) fronds serve to trip the boundary layer and thus periodically infuse the CBL with fresh nutrient rich water from the overlying bulk water (Hurd *et al.*, 1996). Currently, there is little evidence to support this hypothesis, and experimental results have been equivocal. For example, the twist in *V. spiralis* leaves did not appear to enhance photosynthesis rates compared to the flat leaves of *V. americana* (Nishihara and Ackerman, 2007a), but the local flow environment made it difficult to resolve O_2 measurements within the thin DBL under higher velocities. Clearly, one of the failings of this type of approach is the lack of characterization of the hydrodynamics of the flow (i.e., the MBL) and the lack of measurement of the scalar (i.e., the CBL).

It has also been suggested that the complex branching and large surface area to volume ratio enhance the ability of macrophytes to uptake nutrients (Hurd, 2000). For example, the surface area to volume ratio is large in the whorled macrophyte, *Elodea canadensis*. However at low water velocities, the boundary layers around the whorls and leaves are thick and can overlap. Most of the accumulation of carbon occurs near the edges of the leaves and whorls,

where the boundary layer is thinnest and the entire leaf does not perceive the hydrodynamics in the same way (Nielsen *et al.,* 2006). Moreover, flow-induced configurational changes to the shape of macrophytes may reduce their ability to undergo photosynthesis through self-shading or the reduction of area available for nutrient uptake (Stewart and Carpenter, 2003). There are a large number of unresolved questions that remain to be answered at both small and large spatial scales around aquatic macrophytes.

11.7 HETEROTROPHIC SYSTEMS

11.7.1 Pelagic zooplankton

Mass transport issues are relevant in pelagic environments for a number of reasons including those related to trophic and reproductive relations. In the former, there are a large number of suspension feeders and ambush predators that rely on the delivery of nutrients, chemical signals, and prey (Mann and Lazier, 2006). Chemical signals are also relevant to reproductive interactions such as mate recognition and tracking (Strickler, 1998). Both of these examples can be conceived of as encounter rate problems, which have been applied to aggregates and their formation through the application of coagulation theory (Jackson and Burd, 1998).

A key issue for pelagic mass transport at the smallest scales involves the identification of resources by small heterotrophic bacteria and protists in a well-mixed environment. In other words, this is a problem of locating a resource that has a patchy distribution in space and time. Microscale patchiness has been demonstrated to exist on the mm scale and persist on the scale of 10 min in the laboratory (Blackburn *et al.*, 1998). These patches are created by lysing cells and from sinking algal cells (which can be quite leaky) and from aggregates. Aggregates (marine snow and flocs) are composed of the lysed cells, algae, and bacteria, as well as detritus and transparent exopolymer (TEP) matter (see review in Okubo *et al.*, 2002). The chemical plumes from sinking aggregates have been examined for $Re \leq 20$ by solving the Navier-Stokes and the advection-diffusion equations numerically (Kiørboe *et al.*, 2001). Results indicate that long slender plumes, which extend from reasonably small aggregates, can have significant concentration and length depending on the flow field. An analogous phenomenon has been inferred from observations of reproductive female copepods pursed by males; the males tracking a pheromone signal released by the females (Yen *et al.*, 1998).

The case of zooplankton mass transport it is not merely an issue of flux of seston because turbulence can also affect the outcomes. As indicated above, organisms smaller than the Kolmogorov microscale are predicted to experience the relative motions within small eddies. However, this does not appear to be the case as many organisms have a dome-shaped response in which moderate levels of turbulence enhance encounter and ingestion rates for predators, whereas large levels can be inhibitory to growth in other groups, due perhaps to increased energy expenditures (Peters and Marrasé, 2000). It is evident that small-scale unsteady motion and length scales other than organism size are likely to be more relevant to these ecological processes (Peters and Marrasé, 2000).

11.7.2 Benthic animals

The diversity and ecological and economic importance of benthic suspension-feeding organisms has generated considerable interest into the biology and mechanisms of particle capture (Shimeta and Jumars, 1991; Riisgård and Larsen, 2001) and more recently the effect of suspension feeders on ecosystems (Wildish and Kristmanson, 1997; Okubo *et al.*, 2002). Concentration boundary layers have been observed over bivalves in lakes and estuaries (Dame, 1996; Ackerman *et al.,* 2001; Tweddle *et al.*, 2005) and over coral reefs (Yahel *et al.*,

1998), which indicates the important impact that suspension feeding can have on aquatic environments. Mass transport is of particular importance to suspension-feeding organisms as it is a process driven by the delivery of seston (water borne material) in the water to organisms. Suspension-feeding organisms can be classified as: (i) passive suspension feeders, such as corals, gorgonians, polychaete worms, brittle stars, sand dollars, and caddisfly and black fly larvae, which extend their feeding appendages into the water column; and (ii) active suspension feeders, such as sponges, bivalves, lophophorates, crustaceans, and ascidians, which use various pumping mechanisms to move fluid. In the former, it is the delivery of seston through horizontal advection and turbulent mixing in the vertical direction that is important—analogous to what has been described above for autotrophic organisms (see Eqn. (11.2))—although in this case additional terms describing the settling velocity (w_s) of the seston (particulate matter) must be added

$$U\frac{\partial C}{\partial x} + w_s\frac{\partial C}{\partial z} = \frac{\partial}{\partial z}\left((K_D + D)\frac{\partial C}{\partial z}\right) + R \tag{11.18}$$

In addition, the heterogeneous reaction of suspension feeding (ϕ) must be considered. There are many factors that can affect ϕ ranging from physical factors such as seston concentration (C), ambient velocity and the height above the bottom to biological ones including the spacing and orientation of the collecting elements (f_d; tentacles, fibers, cilia, etc.), the number (n) and numerical density (A_n) of organisms, the time (t_I) for moving the material to the site of ingestion, and the efficiency of the capture process (η_ϕ)

$$\phi = f\,(C, U, z, f_d, n, A_n, t_I, \eta_\phi) \tag{11.19}$$

The circumstances are similar for active suspension feeders, but the situation requires that a term pertaining to the hydrodynamics of the pumping mechanisms used to move water through the organisms (Riisgård and Larsen, 1995) be added to ϕ in Eqn (11.19). This is of course a simplification of reality as many of the factors in Eqn. (11.19) are known to covary. For example, both the quantity and quality of the seston can affect η_ϕ, as can the product $f_d A_n$ through the potential refiltration of water (O'Riordan *et al.*, 1995). Moreover, bivalves have behavioral responses to fluid dynamics that can affect ϕ (Ackerman, 1999).

One of the most interesting responses of suspension feeders is their unimodal response to velocity (Wildish and Kristmanson, 1997; Ackerman, 1999; Ackerman and Nishizaki, 2004). In this case, increases in velocity lead to increases in capture, clearance and/or growth rates to some peak mode after which further increases in U are inhibitory to the aforementioned rates. The phenomena has been observed in a wide variety of passive and active suspension feeders including corals, gorgonians, and bivalves (for review of bivalves see Ackerman and Nishizaki, 2004), although the mechanism responsible is not well understood. It may be, however, somewhat analogous to the model for autotrophic organisms where increased flux can saturate the physiology of the organism and other processes at high velocities can interfere with their physiology (see Fig. 11.1 in Nishihara and Ackerman, 2006). In the case of bivalves it has been suggested that it is behavioral instability due to lift and drag forcing, acting at the scale of siphons and/or shells, rather than hydrodynamic instability of the pumping mechanism or some grazing optimization that is responsible for the physiological interference (Ackerman, 1999). Regardless it indicates the importance of understanding the role of fluid dynamics at the scale of the organism for mass transport.

Environmental flows are relevant to both passive and active suspension feeding in that the formation of a CBL will be a function of the relative strength of the turbulent mixing in the water column and the sink of seston at the benthos (Fig. 11.5). CBL formation is based on the principle that the rate of seston uptake (ϕ) by suspension feeders is greater than the rate

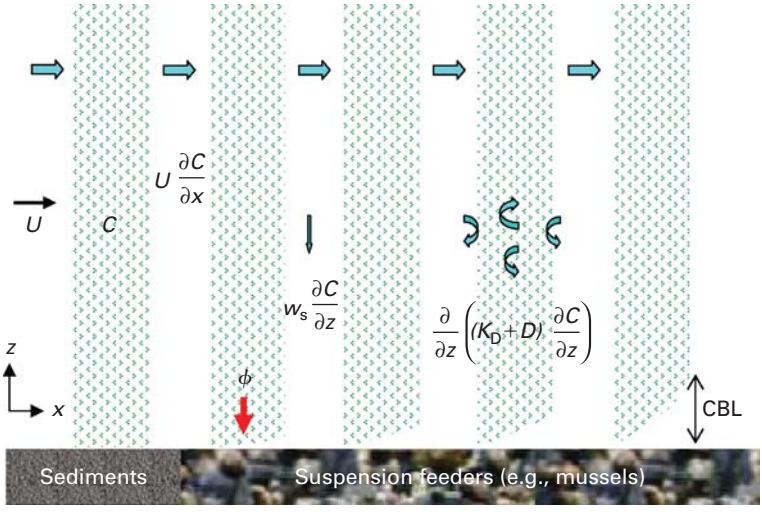

Figure 11.5. The formation of a concentration boundary layer (CBL) as seston (C) travels over a region of sediment to a region of suspension-feeding benthos. The stippled seston-containing region represents a slice of the water column at a particular instant in time at different downstream locations. The flux of seston to the bed is a function of advection, settling, and turbulent mixing. The CBL will be a function of the strength of the sink of seston (ϕ) and mixing of the scalar in the water column (K_D) that serves to eliminate the signal. In most cases, the time scale for turbulent mixing of the water column is faster than the time scale for benthic grazing.

of seston delivery through mass transport. Processes such as turbulent mixing (e.g., K_D) act to obliterate the CBL through the transport of the scalar to regions where it has been depleted (Hanratty, 1956; Shaw and Hanratty, 1977). In other words, if the rate of scalar mixing (i.e., K_D) is small, it is possible that a CBL will form but if K_D is large, the CBL may not form (or may be too thin to observe) as water column mixing will eliminate it and/or cause the size of the CBL to fluctuate in thickness (Hanratty, 1956; Shaw and Hanratty, 1977). It is not surprising, therefore, that it can be difficult to detect CBLs in the field except under particular circumstances where the biomass of suspension feeders is quite large (Tweddle *et al.*, 2005) and/or mixing processes are minimized (e.g., during stratification, Ackerman *et al.*, 2001). Similar arguments can be advanced for the autotrophic systems described above.

Corals reefs represent an important component of the benthos in shallow water regions (generally <50 m) where the average annual water temperatures are $>20°$C. This is due in large part to their symbiotic zooxanthellae (dinoflagellate algae), which, as autotrophs, require sunlight and nutrients (e.g., DIC, DIN) for photosynthesis. The corals, being heterotrophic, also feed via the capture of particles and zooplankton on their tentacles, mucous sheets, and the extended mesenterial filaments of the gut wall. There has been considerable effort devoted to mass transport of particulate matter in terms of particle capture (Wildish and Kristmanson, 1997; Sebens *et al.*, 1998), and nutrient uptake (e.g. Atkinson and Bilger, 1992) in corals. The latter has included numerical and physical modeling as well as laboratory and field experiments (see review in Monismith, 2007). Indirect measurements of mass transfer using the dissolution of plaster has been popular recently, with experiments conducted within the skeletons of the complexly branched corals of a number of species under unidirectional and oscillatory flow in laboratory flow chambers (Reidenbach *et al.*, 2006). As might be expected, mass transfer was reduced by $\sim$50% within the branches and mass transfer was enhanced many fold under oscillatory flow. This confirmed field results that indicated that mass transfer of gypsum blocks of various surface configurations

was 30–40% higher under oscillatory flow in the field (Falter *et al.*, 2005). Importantly, the magnitude of the difference between oscillatory and linear flow declined with velocity. How these indirect measurements translate biologically for corals under natural conditions remains to be determined (c.f., Atkinson and Bilger, 1992). It has been possible, however, to ignore the intricacies of the flow-coral morphological interaction, by considering the roughness of the coral reef and parameterizing the process through the use of the Stanton number, which relates the mass transfer coefficient (k_c) to the velocity (e.g., Atkinson and Bilger, 1992). This technique has been applied recently at the scale of a reef flat community where the dissipation of waves allowed for estimates of the bottom friction (Falter *et al.*, 2004). The ability to use a measurement of the canopy friction has also made this an attractive approach for macrophyte canopies (see above).

The manner by which large-scale fluid dynamic processes in surface waters affect benthic organisms and *visa versa* is becoming better understood (Jonsson *et al.*, 2005; Loewen *et al.*, 2007). Simple measurements such as velocity are likely to provide some indication that locally depleted resources may be replenished with fresh seston. However, a description of the physical mixing processes rather than a mere reliance on simple metrics is necessary. Unfortunately, neither the physical mixing of surface waters nor the response of suspension feeders to this mixing can be predicted or easily modeled. Additional studies at a variety of spatial scales are, therefore, warranted to better understand the role of mass transport to benthic organisms.

11.8 EMERGING PRINCIPLES

Although aquatic environments involve a great diversity of organisms, biological and ecological processes and habitats, there are some common principles that emerge when they are considered from the perspective of mass transport:

(i) There are similarities among systems in terms of the relevance of the flux of dissolved and/or particulate scalars to the processes under consideration. Specifically flux applies equally well to the transport of nutrients to autotrophs as it is does to the flux of seston to suspension feeders. It is important to note that flux is the product of velocity and a concentration gradient, therefore, experiments should examine both the vector and the scalar.

(ii) Concentration boundary layers (CBL) are formed when a concentration gradient forms next to a biological surface that acts as a source or sink of a scalar. CBLs are analogous to momentum boundary layers (MBL) but their structure differs. Importantly, the diffusional sublayer thickness (δ_{DSL}) defined using the MBL is not a good predictor of the much thinner diffusional boundary layer thickness (δ_{DBL}) of the CBL.

(iii) The development and use of microsensors continues to advance our ability to examine and understand mass transport issues through the direct measurement of the concentration gradients. A hyperbolic-tangent model provides the ability to estimate the δ_{CBL}, δ_{DBL}, and the flux at the surface in a rigorous and unambiguous manner.

(iv) CBLs can be difficult to measure under moderate and turbulent flows in the laboratory due to the small spatial scales involved and in the field due to turbulent mixing (i.e., temporal scales) that eliminate the gradients.

(v) Both homogeneous and heterogeneous boundary layer reactions can and do occur in the CBL associated with biological and ecological processes. This realization should help to facilitate the further modeling of mass transport phenomena in aquatic systems.

(vi) Further research into the role of physiology on the dynamics of heterogeneous reactions, especially those involving nutritiously important molecules, is required to advance our understanding of biologically relevant mass transport beyond simple physical models.

(vii) Our current understanding of mass transport is based largely on morphological systems whereby the organism is fixed naturally to a surface or held static in experiments. Realistically, however, many biological systems are flexible and undergo complex undulations and may reconfigure morphologically under environmental flows. Unfortunately there are few techniques that can provide measurements of MBLs under these conditions, let alone characterize CBLs that vary temporally and spatially. Advances in technology and approach are needed in this area.

(viii) Although significant advances have been made with respect to mass transport there are many unresolved problems, including processes that occur under turbulent and unsteady environmental flows. This last realization provides a degree of optimism in the sense that research into mass transport will continue to be at the leading edge of aquatic research for the foreseeable future.

APPENDIX—LIST OF SYMBOLS

List of Symbols

Symbol	Definition	Units
A, B	parameters for Eqn. (11.5)	–
A_n	numerical density of organisms	indv m^{-2}
C	concentration	mol m^{-3}
C_{bulk}	bulk concentration	mol m^{-3}
$C_{surface}$	surface concentration	mol m^{-3}
CBL	concentration boundary layer	–
D	molecular diffusivity of the scalar	m^2 s^{-1}
DBL	diffusive boundary layer	m
DIC	dissolved inorganic carbon	mol m^{-3}
DIN	dissolved inorganic nitrogen	mol m^{-3}
DSL	diffusive sublayer	m
J	mass flux, scalar (e.g., nutrient) uptake rate	mol m^{-2} s^{-1}
K_D	turbulent diffusivity of the scalar	m^2 s^{-1}
K_v	turbulent diffusivity of momentum	m^2 s^{-1}
MBL	momentum boundary layer	–
R	homogeneous boundary layer reaction	mol m^{-2} s^{-1}
Re	Reynolds number	–
Re_x	local Reynolds number	–
Sc	Schmidt number	–
Sh_x	local Sherwood number	–
St	Stanton number	–
U	freestream or bulk velocity	m s^{-1}
f_d	collecting fiber diameter	m
k_c	mass transfer coefficient	m s^{-1}
l	length	m

(*Continued*)

List of Symbols

Symbol	Definition	Units
n	number of individuals	–
t_I	ingestion time	s
u	velocity in the x direction	m s^{-1}
w	velocity in the z direction	m s^{-1}
w_s	settling velocity	m s^{-1}
x	distance in the x (downstream) direction	m
z	distance in the z (vertical) direction	m
δ	boundary layer (BL) thickness	m
δ_{CBL}	thickness of the concentration BL	m
δ_{DBL}	thickness of the diffusive BL	m
δ_{DSL}	thickness of the diffusive sublayer	m
δ_{ISL}	thickness of the inertial sublayer	m
δ_{MBL}	thickness of the momentum BL	m
δ_{VSL}	thickness of the viscous sublayer	m
η	Kolmogorov microscale	m
η_ϕ	efficiency of suspension feeding	–
θ	dimensionless concentration gradient	–
ν	molecular diffusivity of momentum	m^2 s^{-1}
τ	shear stress	Pa
ϕ	flux due to suspension feeding	kg m^{-2} s^{-1}

REFERENCES

Ackerman J.D. 1999. Effect of velocity on the filter feeding of dreissenid mussels (*Dreissena polymorpha* and *Dreissena bugensis*): implications for trophic dynamics. *Canadian Journal of Fisheries and Aquatic Sciences* **56**:1551–61.

Ackerman, J.D. 2000. Abiotic pollen and pollination: Ecological, functional, and evolutionary perspectives. *Plant Systematics and Evolution* **222**:167–185.

Ackerman, J.D. 2006. Sexual reproduction of seagrasses: Pollination in the marine context. pp. 89–109. In: A.W.D. Larkum, J.J. Orth, and C.M. Duarte (eds.) *Seagrasses: Biology, Ecology and Their Conservation*. Springer, New York. pp. 691.

Ackerman, J.D. and Hoover, T. 2001. Measurement of local bed shear stress in streams using a Preston-static tube. *Limnology and Oceanography* **46**:2080–2087.

Ackerman, J.D., Loewen, M.R. and Hamblin, P.F. 2001. Benthic-pelagic coupling over a zebra mussel bed in the western basin of Lake Erie. *Limnology and Oceanography* **46**:892– 904.

Ackerman, J.D. and Nishizaki, M.T. 2004. The effect of velocity on the suspension feeding and growth of the marine mussels *Mytilus trossulus* and *M. californianus*: Implications for competition and niche separation. *Journal of Marine Systems* **49**:195–207.

Atkinson, M. and Bilger, R.W. 1992. Effects of water velocity on phosphate uptake in coral reef-flat communities. *Limnology and Oceanography* **37**:273–279.

Acrivos, A. and Chambré, P.L. 1957. Laminar boundary layer flows with surface reactions. *Industrial and Engineering Chemistry* **59**:1025–1029.

Bird, R.B., Stewart, W. E. and Lightfoot, E.N. 2002. *Transport Phenomena*. John Wiley & Sons, New York. pp. 895.

Blackburn, N. Fenchel, T. and Mitchell, J. 1998. Microscale nutrient patches in planktonic habitats shown by chemotactic bacteria. *Science* **282:**2254–2256.

Borchardt, M.A., Hoffman, J. and Cook, P. 1994. Phosphorus uptake kinetics of *Spirogyra fluviatilis* (Charophyceae) in flowing water. *Journal of Phycology* **30**:403–417.

Chambré, P.L. and Acrivos, A. 1956. On chemical surface reactions in laminar boundary layer flows. *Journal of Applied Physics* **27**:1322–1328.

Chambré, P. L. and Young, J.D. 1958. On the diffusion of a chemically reactive species in a laminar boundary layer flow. *The Physics of Fluids* **1**:48–54.

Chung, P.M. 1969. Periodic fluctuation of chemical species over a reactive surface. *The Physics of Fluids* **12**:53–63.

Conover J.T. 1968. The importance of natural diffusion gradients and transport of substances related to benthic marine plant metabolism. *Botanica Marina* **11**:1–9.

Cornelisen, C.D. and Thomas, F.I.M. 2004. Ammonium and nitrate uptake by leaves of the seagrass *Thalassia testudinum*: impact of hydrodynamic regime and epiphyte cover on uptake rates. *Journal of Marine Systems* **49**:177–194.

Dade, W. 1993. Near-bed turbulence and hydrodynamic control of diffusional mass-transfer at the sea-floor. *Limnology and Oceanography* **38**:52–69.

Dame, R. 1996. *Ecology of Marine Bivalves: An Ecosystem Approach*. CRC Marine Science Series, Boca Raton. pp. 272.

Dang, V.D. 1983. Steady-state mass transfer with homogeneous and heterogeneous reactions. *AIChE Journal* **29**:19–25.

de Beer, D. and Kühl, M. 2001. Interfacial microbial mats and biofilms. 374–394. In: *The Benthic Boundary Layer*, Boudreau, B.P. and Jørgensen, B.B. (eds.). Oxford University Press, New York. pp. 404.

de Beer, D., Stoodley, P., and Lewandowski, Z. 1994. Liquid flow in heterogeneous biofilms. *Biotechnology and Bioengineering* **44**:636–641.

Denny, M.W. 1988. *Biology and Mechanics of the Wave-Swept Environment.* Princeton University Press, Princeton. pp. 344.

Falter, J.L., Atkinson, M.J. and Merrifield, M.A. 2004. Mass transfer limitation of nutrient uptake by a wave-dominated reef flat community. *Limnology and Oceanography* **49**:1820–1831.

Falter, J.L., Atkinson, M.J. and Coimbra, C.F.M. 2005. Effects of surface roughness and oscillatory flow on the dissolution of plaster forms: Evidence for nutrient mass transfer to coral reef communities. *Limnology and Oceanography* **50**:246–254

Fischer, H., List, J., Koh, C., Imberger, J., and Brook, N. 1979. *Mixing in Inland and Coastal Waters*. Academic Press, San Diego. pp. 302.

Freeman, N.C. and Simpkins, P.G. 1965. On the diffusion of species in similar boundary layers with finite recombination rate at the wall. *Quarterly Journal of Mechanics and Applied Mathematics* **18**:213–229.

Gaylord, B., Reed, D.C., Washbun, L. and Raimondi, P.T. 2004. Physical-biological coupling in spore dispersal of kelp forest macroalgae. *Journal of Marine Systems* **49**:19–39.

Glud, R.N., Gundersen, J.K., Jørgensen, B.B., Revsbech, N.P. and Schulz, H.D. 1994. Diffusive and total oxygen uptake of deep-sea sediments in the eastern South Atlantic Ocean: In Situ and laboratory measurements. *Deep-Sea Research Part I Oceanographic Research Papers* **41**:1767–1788.

Glud, R.N., Kühl, M., Kohls, O. and Ramsing, N.B. 1999. Heterogeneity of oxygen production and consumption in a photosynthetic microbial mat as studied by planar optodes. *Journal of Phycology* **35**:270–279.

Gundersen, J.K. and Jørgensen, B.B. 1990. Microstructure of diffusive boundary-layers and the oxygen-uptake of the sea-floor. *Nature* **345**:604–607.

Hanratty, T.J. 1956. Turbulent exchange of mass and momentum with a boundary. *AIChE Journal* 2:359–362.

Hondzo, M., Feyaerts, T., Donovan, R. and O'Connor, B.L. 2005. Universal scaling of dissolved oxygen distribution at the sediment-water interface: A power law. *Limnology and Oceanography* **50**:1667–1676.

Hurd, C.L. and Stevens, C.L. 1997. Flow visualization around single- and multiple-bladed seaweeds with various morphologies. *Journal of Phycology* **33**:360–367.

Hurd, C.L. 2000. Water motion, marine macroalgal physiology, and production. *Journal of Phycology* **36**:453–472.

Hurd, C.L., Harrison, P.J. and Druehl, L.D. 1996. Effect of seawater velocity on inorganic nitrogen uptake by morphologically distinct forms of *Macrocystis integrifolia* from wave-sheltered and exposed sites. *Marine Biology* **126**:205–214.

Hurd, C.L., Stevens, C.L., Laval, B., Lawrence, G. and Harrison, P.J. 1997. Visualization of seawater flow around morphologically distinct forms of the giant kelp *Macrocystis integrifolia* from wave-sheltered and exposed sites. *Limnology and Oceanography* **42**: 156–163.

Ingmanson, D.E. and Wallace, W.J. 1995. *Oceanography 5th Ed*. Wadsworth, Belmont, CA. pp. 528.

Jackson, G.A. and Burd, A.B. 1998. Aggregation in the marine environment. *Environmental Science and Technology* **32**:2805–2814.

Jonsson, P.R., Petersen, J.K., Karlsson, Ö., Loo, L.O. and Nilsson, S. 2005. Particle depletion above experimental bivalve beds: In situ measurements and numerical modeling of bivalve filtration in the boundary-layer. *Limnology and Oceanography* **50**:1989–1998.

Jørgensen, B.B. and Des Marais, D.J. 1990. The diffusive boundary layer of sediments: Oxygen microgradients over a microbial mat. *Limnology and Oceanography* **35**: 1343–1355.

Jørgensen, B.B. and Revsbech, N.P. 1985. Diffusive boundary layers and the oxygen uptake of sediments and detritus. *Limnology and Oceanography* **30**:111–122.

Kalff, J. 2001. Limnology. Prentice Hall, Upper Saddle River, NJ. pp. 592.

Kiørboe, T. 2001. Formation and fate of marine snow: small-scale processes with large-scale implications. *Scientia Marina* **65**:57–71.

Kiørboe, T., Helle Ploug, H. and Thygesen, U.H. 2001. Fluid motion and solute distribution around sinking aggregates. I. Small-scale fluxes and heterogeneity of nutrients in the pelagic environment. *Marine Ecology Progress Series* **211**:1–13.

Koch, E.W. 1993. The effect of water flow on photosynthetic processes of the alga *Ulva lactuca* L. *Hydrobiologia* **260–261**:457–462.

Køhler-Rink, S. and Kühl, M. 2000. Microsensor studies of photosynthesis and respiration in larger symbiotic foraminifera. I The physico-chemical microenvironment of *Marginopora vertebralis*, *Amphistegina lobifera* and *Amphisorus hemprichii*. *Marine Biology* **137**:473–486.

Kuehl, M., Glud, R.N., Ploug, H. and Ramsing, N.B. 1996. Microenvironmental control of photosynthesis and photosynthesis-coupled respiration in an epilithic cyanobacterial biofilm. *Journal of Phycology* **32**:799–812.

Larned, S.T., Nikora, V.I. and Biggs, B.J.F. 2004. Mass-transfer-limited nitrogen and phosphous uptake by stream periphyton: a conceptual model and experimental evidence. *Limnology and Oceanography* **49**:1992–2000.

Levich, V.G. 1962. *Physicochemical Hydrodynamics*. Prentice Hall. pp. 700.

Libby, P.A. and Liu, T. 1966. Laminar boundary layer with surface catalyzed reactions. *The Physics of Fluids* **9**:436–445.

Lobban, C.S. and Harrison, P.J. 1996. *Seaweed Ecology and Physiology*. Cambridge University Press, Cambridge. pp. 376.

Loewen, M.R., Ackerman, J.D. and Hamblin, P.F. 2007. Environmental implications of stratification and turbulent mixing in a shallow lake basin. *Canadian Journal of Fisheries and Aquatic Sciences* **64**:43–57.

Lorke, A., Müller, B., Maerki, M. and Wüest, A. 2003. Breathing sediments: The control of diffusive transport across the sediment-water interface by periodic boundary-layer turbulence. *Limnology and Oceanography* **48**:2077–2085.

Mann, K.H. and J.R.N. Lazier. 2006. *Dynamics of Marine Ecosystems, 3rd Ed.* Blackwell Science, Oxford. pp. 512.

Martin, C.L. and Tortell, P.D. 2006. Bicarbonate transport and extracellular carbonic anhydrase activity in Bering Sea phytoplankton assemblages: Results from isotope disequilibrium experiments. *Limnology and Oceanography* **51**:2111–2121.

McMahon, T.A. and Bonner, J.T. 1983. *On Size and Life*. W.H. Freeman, New York. pp. 255.

Milligan, A.J. and Morel, F.M.M. 2002. A proton buffering role for silica in diatoms. *Science* **297**:1848–1850.

Monismith, S.G. 2007. Hydrodynamics of coral reefs. *Annual Review of Fluid Mechanics* **39**:37–55.

Na, Y. and Hanratty, T.J. 2000. Limiting behavior of turbulent scalar transport close to a wall. *International Journal of Heat and Mass Transfer* **43**:1749–1758.

Nielsen, H.D., Nielsen, S.L. and Madsen, T.V. 2006. CO_2 uptake patterns depend on water velocity and shoot morphology in submerged stream macrophytes. *Freshwater Biology* **51**:1331–1340.

Nielsen, L.P., Christensen, P.B., Revsbech, N.P. and Sørensen, J. 1990. Denitrification and oxygen respiration in biofilms studied with a microsensor for nitrous oxide and oxygen. *Microbial Ecology* **19**:63–72.

Niklas, K.J. 1992. *Plant Biomechanics*. University of Chicago Press, Chicago. pp. 622.

Niklas, K.J. 1994. *Plant Allometry.* University of Chicago, Chicago. pp. 395.

Nishihara, G.N. and Ackerman, J.D. 2006. The effect of hydrodynamics on the mass transfer of dissolved inorganic carbon to the freshwater macrophyte *Vallisneria americana*. *Limnology and Oceanography* **51**:2734–2745.

Nishihara, G.N. and Ackerman, J.D. 2007a. The interaction of CO_2 concentration and spatial location on O2 flux and mass transport in the freshwater macrophytes *Vallisneria spiralis* and *V. americana*. *Journal of Experimental Biology* **210**:522–532.

Nishihara, G.N. and Ackerman, J.D. 2007b. On the determination of mass transfer in a concentration boundary layer. *Limnology and Oceanography Methods* **5**:88–96+ Appendix.

Nishihara, G.N., Terada, R. and Noro, T. 2005. Effect of temperature and irradiance on the uptake of ammonium and nitrate by *Laurencia brongniartii* (Rhodophyta, Ceramiales). *Journal of Applied Phycology* **17**:371–377.

Nybakken, J.W. and Bertness, M.D. 2005. *Marine Biology: An Ecological Approach (6th Edition).* Benjamin Cummings, San Francisco. pp. 592.

Okubo, A. and Levin, S.A. 2002. *Diffusion and Ecological Problems, 2nd Ed.* Springer, New York. pp. 488.

Okubo, A., Ackerman, J.D. and Swaney, D.P. 2002. Passive Diffusion in Ecosystems. pp. 31–106 in A. Okubo and S. Levin (eds.) *Diffusion and Ecological Problems: New Perspectives, 2nd Ed*. Springer Verlag, New York. pp. 467.

O'Riordan, C.A., Monismith S.G. and Koseff , J.R. 1995. The effect of bivalve excurrent jet dynamics on mass transfer in a benthic boundary layer. *Limnology and Oceanography* **40**:330–44.

Pennycuick, C.J. 1992. *Newton Rules Biology.* Oxford University Press, Oxford. 128 pp.

Peters, F. and Marrasé, C. 2000. Effects of turbulence on plankton: an overview of experimental evidence and some theoretical considerations. *Marine Ecology Progress Series* **205**:291–306.

Phillips, J.C. and Hurd, C.L. 2003. Nitrogen ecophysiology of intertidal seaweeds from New Zealand: N uptake, storage and utilisation in relation to shore position and season. *Marine Ecology Progress Series* **264**:31–48.

Ploug, H., Stolte, W., Epping, E.H.G. and Jørgensen, B.B. 1999. Diffusive boundary layers, photosynthesis, and respiration of the colony-forming plankton algae, *Phaeocystis* sp. *Limnology and Oceanography* **44**:1949–1958.

Ploug, H., Hietanen, S. and Kuparinen, J. 2002. Diffusion and advection within and around sinking, porous diatom aggregates. *Limnology and Oceanography* **47**:1129–1136.

Porter, E.T., Sanford, L.P. and Suttles, S.E. 2000. Gypsum dissolution is not a universal integrator of 'water motion'. *Limnology and Oceanography* **45**:145–158.

Prins, H.B.A., Snel, J.F.H., Helder, R.J. and Zanstra, P.E. 1980. Photosynthetic HCO_3^- utilization and OH^- excretion in aquatic angiosperms. Plant Physiology **66**:818–822.

Ricklefs, R.E. and Miller, G. 2000. *Ecology 4th ed*. W.H. Freeman, New York. pp. 896.

Riebesell, U., Zondervan, I., Rost, B., Tortell, P.D., Zeebe, R.E. and Morel, F.M.M. 2000. Reduced calcification of marine plankton in response to increased atmospheric CO_2. *Nature* **407**:364–367.

Reidenbach M.A., Koseff, J.R., Monismith, S.G., Steinbuck, J.V. and Genin, A. 2006. Effects of waves, unidirectional currents, and morphology on mass transfer in branched reef corals. *Limnology and Oceanography* **51**:1134–1141.

Riisgård, H.U. and Larsen, P.S. 2001. Minireview: Ciliary filter feeding and bio-fluid mechanics – present understanding and unsolved problems. *Limnology and Oceanography* **46**:882–891.

Riisgård, H.U. and Larsen, P.S. 1995. Filter-feeding in marine macro-invertebrates: pump characteristics, modelling and energy cost. *Biological Reviews* **70**:67–106.

Røy, H., Hüettel, M. and Jørgensen, B.B. 2002. The role of small-scale sediment topography for oxygen flux across the diffusive boundary layer. *Limnology and Oceanography* **47**:837–847.

Sand-Jensen, K., Revsbech, N.P. and Jørgensen, B.B. 1985. Microprofiles of oxygen in epiphyte communities on submerged macrophytes. *Marine Biology* **89**:55–62.

Sanford, L.P. and Crawford, S.M. 2000. Mass transfer versus kinetic control of uptake across solid-water boundaries. *Limnology and Oceanography* **45**:1180–1186.

Schlichting, H. and Gersten, K. 2000. *Boundary-Layer Theory*. Springer, New York. pp. 801.

Sculthorpe, C.D. 1967. *The Biology of Aquatic Vascular Plants.* Edward Arnold, London. pp. 610.

Sebens, K.P., Grace, S. P., Helmuth, B., Maney, E.J. Jr. and Miles, J.S. 1998. Water flow and prey capture by three scleractinian corals, *Madracis mirabilis*, *Montastrea cavernosa* and *Porites porites*, in a field enclosure. *Marine Biology* **131**:347–360.

Serra, J.L., Llama, M.J. and Codenas, E. 1978. Nitrate utilization by the diatom *Skeletonema costatum*. 2. Regulation of nitrate uptake. *Plant Physiology* **62**:991–994.

Serrão, E.A., Pearson, G., Kautsky, L. and Brawley, S.H. 1996. Successful external fertilization in turbulent environments. *Proceedings of the National Academy of Science (USA)* **93**:5286–5290.

Shaw, D.A. and Hanratty, T.J. 1977. Turbulent mass transfer to a wall for large Schmidt numbers. *AIChE Journal* **23**: 28–37.

Shimeta, J. and Jumars, P.A. 1991. Physical mechanisms and rates of particle capture by suspension-feeders. *Oceanography and Marine Biology Annual Review* 29:191–257.

Stevens, C.L. and Hurd, C.L. 1997. Boundary-layers around bladed aquatic macrophytes. *Hydrobiologia* **346**:119–128.

Stewart, H.L. and Carpenter, R.C. 2003. The effects of morphology and water flow on photosynthesis of marine macroalgae. *Ecology* **84**:2999–3012.

Strickler, J.R. 1998. Observing free-swimming copepods mating. *Philosophical Transactions of the Royal Society (London) Series B* **353**:671–680.
Thomas F.I.M., Cornelsen, C.D. and Zande, J.M. 2000. Effects of water velocity and canopy morphology on ammonium uptake by seagrass communities. *Ecology* **81**:2704–2713.
Thomas, T.E., Harrison, P.J. and Taylor, B.E. 1985. Nitrogen uptake and growth of the germlings and mature thalli of *Fucus distichus*. *Marine Biology* **84**:267–274.
Thomas, T.E., Harrison, P.J. and Turpin, D.H. 1987. Adaptations of *Gracilaria pacifica* (Rhodophyta) to nitrogen procurement at different intertidal locations. *Marine Biology* **93**:569–580.
Tortell, P.D., Reinfelder, J.R. and Morel, F.M.M. 1997. Active uptake of bicarbonate by diatoms. *Nature* **390**:243–244.
Tweddle, J.F., Simpson, J.H. and Janzen, C.D. 2005. Physical controls of food supply to benthic filter feeders in the Menai Strait, UK. *Marine Ecology Progress Series* **289**:79–88.
Vogel, S. 1994. *Life in Moving Fluids, 2nd Ed.*. Princeton University Press. pp. 476.
Wetzel, R.G. 2001 *Limnology 3rd ed.* Academic Press, San Diego pp. 1006.
Wheeler, W.N. 1980. Effect of boundary layer transport on the fixation of carbon by the giant kelp *Macrocystis pyrifera*. *Marine Biology* **56**:103–110.
White, F.M. 1999. Fluid Mechanics, 4th Ed. WCB McGraw Hill, New York.
Wildish, D. and Kristmanson, D. 1997. *Benthic Suspension Feeders and Flow.* Cambridge University Press, Cambridge. pp. 409.
Wolf-Gladrow, D. and Riebesell, U. 1997. Diffusion and reactions in the vicinity of plankton: A refined model for inorganic carbon transport. *Marine Chemistry* **59**:17–34.
Yahel, G., Post, A.F., Fabricius, K.E., Marie, D., Vaulot, D. and Genin, A. 1998. Phytoplankton distribution and grazing near coral reefs. *Limnology and Oceanography* **43**:551–563.
Yen, J., Weissburg, M.J. and Doall, M.H. 1998.The fluid physics of signal perception by mate-tracking copepods. *Philosophical Transactions of the Royal Society (London) Series B* **353**:787–804.

Author Index

Arsenić, I. 17
Ackerman, J. 299

Chanson, H. 163
Cushman-Roisin, B. 1

Djurdjević, V. 49

Grsić, Z. 17
Gualtieri, C. 1, 131
Gualtieri, P. 241

Kallos, G. 97
Kapor, D. 71
Katsafados, P. 97

Lalić, B. 221

Mihailović, D.T. 1, 71, 199, 221

Nishihara, G. 299

Pulci Doria, G. 131, 241

Rajković, B. 17, 49

Subject Index

Acoustic Doppler Velocimeter (ADV) 267
advection 23, 27, 300, 303, 306, 314–315, 318–320
aeration processes 163–196
aerodynamic resistances 203, 205, 207, 214
aggregation 72–76, 80, 87–89
air bubble entrainment 163–196
air-sea interaction 50–51, 64–66
albedo 72, 75, 80–81, 83–87
Algebraic Stress Model (ASM) 260–261
angle of attack 242

benthic 299, 301, 312, 314, 319–321
bicarbonate 306–307, 312, 315, 317
blending height 72, 74–76
bottom-shear generated turbulence 142–144; *see also* unsheared interface
broadcast spawning/external fertilization 307, 312–314
boundary layer 241–249; equilibrium 241, 243–245, 247–249, 271, 278–284, 286, 292; experimental thickness of 273–277, 290; laminar 242; rotational 242; standard 241–244, 247; structures 249, 251; thickness of 242, 244–245, 247, 267; turbulent 242, 269, 286; with turbulent free-stream 243–245, 249, 269–270; zero pressure (or piezometric head) gradient 242–244
boundary layer velocity distribution or profile 241–245, 248, 251–254, 256, 263, 265, 268; defect 243–244; measured velocity distributions 273–276, 288–290; measured non dimensional velocity distributions 277–286, 290–291; fluctuations of 244; gradient of 242, 251, 260; power and logarithmic (or log-law) 243, 268; shape factor of 285–286, 286
Bragg cell 273
bubble clustering 181–186
bubbly flow structure 181–189
bubble breakup 168–169
bubble rise velocity 169–170
bulk boundary resistance 202
buoyancy effects on submerged air bubbles 169–170

Chézy coefficient 253–254, 262
Computational Fluid Dynamics (CFD) 258
concentration boundary layer (CBL) 134–142, 147–148, 152, 155, 304–309, 311–312, 314–317, 319–322
constant flux layer 51, 54
CO_2 299, 306–307, 312, 315, 317
correlation analysis 186–189
creeping 99

Darcy-Weisbach friction coefficient 151
deposition 42, 45
deposition of dust 98–99, 101, 107, 110–111, 118–121
desert dust cycle 99
diffusion 299–300, 303–306, 309, 314–315, 318
diffusion equation 107, 138
diffusive boundary layer 305–306, 308–309, 311, 314, 316–317, 322
diffusive sublayer 304–306, 309, 316
dimensional analysis 145–146
displacement height 76–80
dissipation rate 264
distance-neighbour function 18, 31–32
Direct Numerical Simulation (DNS) 144, 155–156
drag 251–252, 255, 257–258, 264–266; drag coefficient 52
dry deposition 42, 45
dust 97–98, 101–105; cycle of 111–118; dispersion of 108–110; mobilization of dust 99, 101, 106, 116; settling of 110–111; sinks of 118–121;

source regions of 102–105; transport of 97–103, 105, 114–117

ecology 249
ecosystem 301–302, 313, 319
eddy viscosity 54, 139, 147, 150, 232; model 252–253, 259–260, 264 *see also* turbulence
Environmental Fluid Mechanics (EFMC) 2–3; scope of 2–3; scale, processes and systems of 7–8
environmental interfaces 10–11

Fick's law 19
flat plate 242
flow resistance or resistance of the bed 249–250, 252–253, 256–257, 262, 265–266
flux aggregation 72, 75, 87–89
forest canopy 221–223, 225, 323, 234–235
free-stream 242–243, 248; thickness 247; turbulence 244–245
frequency shifter 273; tracker 273
friction 224, 227–228, 230
friction velocity 6, 51, 54, 56, 59, 106–107, 141, 145, 147, 150, 243
frictionless flow 241
Froude number 145–146

gas-transfer 131–157; coefficient of 136; Atkinson model of 147–148; Gualtieri and Gualtieri model of 148; Higbie-Danckwerts model of 148–149; large-eddy and small-eddy models of 150–151; Lewis-Whitman model of 146–147; surface-renewal model of 148; surface divergence model of 152–153
Gaussian plume 41; model 34–40
genetic programming 262–263
grid cell 72, 76–84, 86–90

head loss 249
heat flux 50, 56–57, 59–60, 62, 67
Henry's law 133
Henry's constant 133–137
heterogeneous surface 72, 74, 76, 80–81, 87
homogeneous and heterogeneous reactions 304, 306–309, 311–312, 322
humidity flux 54
hydraulic jumps 174–176

inception of air entrainment 166–178
interfacial aeration 176–181
irrotational flow 242; motion 241

"K"-theory 199
Kelvin-Helmholtz instability 267
kinematic viscosity 243
Kolmogorov scale or microscale 147, 150, 255, 264, 266; power-law 268

laminar flow 242
land surface scheme 214
large eddies 255
Large Eddy Simulation (LES) 144, 154–155, 258
Land Air Parameterization Scheme (LAPS) 199–220
Laser Doppler Anemometer (LDA) 241, 261, 273–274
leading edge of a plate 242
leaf area density 221–223, 233

macrophytes 301, 303, 308, 312–318, 321
Manning/Strickler equation 266; coefficient 256–257
mixing length 76–77, 225–227, 233–234, 250, 253, 267–268
molecular diffusivity 132, 138–141, 147, 149
molecular dispersion 19
momentum 221, 223, 225, 230–236; flux of 51, 54
momentum boundary layer 303–304, 306, 308, 311, 314–315, 317, 322; *see also* velocity boundary layer
Monin-Obukhov theory 54–58, 60; length 106

Navier-Stokes equations 245, 268; Reynolds Averaged Navier-Stokes (RANS) equations 258
nutrient uptake 302–303, 306–308, 312–313, 315, 318, 321

parameter aggregation 75, 87–89
parameterization 222–223, 225, 232–235

parameterization of energy fluxes 201–204
parameterization of hydrology 212–214
parameterization of radiation 204–205
parameterization of resistances 205–215
Particle Image Velocimeter (PIV) 143, 258
particulate matter 97, 101
penetration depth 264
photosynthesis 299, 302, 306, 309, 312–313, 316–318, 321
plankton 302, 311, 314–315, 318, 321
plunging jets 172–174
point source 18, 21–22, 25, 34–35, 39–41
puff model 40–42

quadrant analysis 268

reaeration 131
Reynolds analogy 139
Reynolds number 6, 145–146, 241, 243, 260; friction 148, 150–151
Reynolds stress 250–252, 255, 258, 260–262, 264, 266, 268; model (RSM) 260–261; tensor 255
"resistance" representation 201
resuspension 10
Richardson's theory 31–34
roughness 223–226, 228–230, 234–235; coefficient 249; length 74–76, 78–80

salinity flux 64
saltation 99–101, 105, 112
Schmidt number 141–142, 145–148, 150–151, 153, 155–156; turbulent 140
secondary currents 251
sedimentation 10
sediments 302–303, 312–315, 320
settling 10, 101–102, 107–108, 110, 119
sheared interface 143; *see also* wind-shear generated turbulence
shear stress 243, 250, 252–254, 257, 259, 263–264, 266, 268
singular aeration 172–176
smooth plate 270
spectral analysis 261
spillway chutes 170–172
stability class 37
stepped spillways 179–181
stomatal resistance 202, 210
stratification 4–6
streamlined body 241–242
surface divergence parameter 152
surface resistance 203, 210–211, 214
suspension 98–100, 103, 106, 109–110
suspension feeding 299, 307, 319–320

Taylor's theorem 18, 28–31, 34–35
transport process 249
turbulence 6–7, 27, 53, 75–76, 98–101, 108–109, 132, 134, 138–144, 149–156, 167–169, 171, 181, 186–190, 223, 225–226, 232–235, 242, 244, 248, 264, 316; and gas-transfer 132, 138–143; and wind above the forest 223–232; and wind within the forest 232–236; in bubbly flows 163–196; intensity 186; distribution 265; eddy viscosity model 252–253, 259–260, 264; k-ε model 251, 255, 258–261, 263–264; k-ω model 255, 258–260, 264; statistical quantities or characteristics or properties of or statistics of 244–245, 247, 250–251, 254, 256, 262, 266, 268; structures of 143, 255; wind and 105–106
turbulent diffusion 17–19, 27–28, 31, 34, 40, 118, 140–141, 173, 305; coefficient of 139–141, 169
turbulent length scale in bubble flows 186–189
turbulent transfer 221–222, 225, 227, 232–234
turbulent time scale in bubbly flows 186–189
Turbulent Kinetic Energy (TKE) 27, 39, 51, 53, 117, 153, 255, 263–264, 268; dissipation rate of 140, 150
turbulent vortices 266
two-layer approach 263–264

uniform flow 242
unsheared interface 142–144; *see also* bottom-shear generated turbulence
uptake 104

vegetated surface, or bed or bottom or layer 241, 249–270, 286

vegetation 249–250; artificial 250; dense 241, 268, 270; density of 250, 268; flexible 249–250, 252–253, 256–257, 265, 267–268; hydraulic roughness of 253–254; open-channel 251; model of 249; natural 250; rigid or inflexible 249–250, 252, 256–257, 265, 267–268, 286; rigid submerged 241, 255, 292; sparse 241, 270, 286; submerged 250; rigid, submerged and dense 287–292; rigid, submerged and sparse 273–286, 292
velocity boundary layer (VBL) 140–142, 148; *see also* momentum boundary layer
viscosity 6, 139–141, 145, 147, 241–242
viscous friction 241; sub-layer 51, 58–59, 61, 111, 115–116, 118, 242–243
visualization experiments 143–144, 261
void fraction 169, 171–172, 176–177, 180–181, 183–184, 186, 188, 190
volatilization 131
Von Kármán constant 7, 56, 106, 140, 205, 208, 224–229, 243; vortex street 262
vortex coherent structures 143–144, 267
vortex street 267

wake function 243
wake law 243–244
water jets 176–180
Weber number 145–146
wet deposition 42, 45
wind profile 77–79, 223, 225, 228–230, 232, 234–235
wind speed 106, 143
wind speed above a canopy 205
wind speed within a canopy 208
wind-shear generated turbulence 143; *see also* sheared interface